
UNIVERSITY OF LIVERPOOL

# Optimising Polymeric Nanocarrier Environments to Encapsulate and Deliver Highly Potent Anti-Cancer Drug SN-38

Thesis submitted in accordance with the requirements of the University of Liverpool for the degree of Doctor in Philosophy by

**Claire Iris May Armstrong**

January 2021

Dedicated to my dearest Dad, Malcolm.

*Always loved, never forgotten, forever missed.*

# Acknowledgements

Firstly, I would like to extend my warmest gratitude to Professor Steve Rannard for believing in me and giving me the opportunity to carry out this Ph.D. research within his research group at the University. Over the past 4 years, Steve has been a constant pillar of support, for both scientific and personal guidance, for which I am ever so grateful for. His positive and enthusiastic approach to research is highly contagious and I have absolutely loved being part of his team, particularly enjoying sinking a few raki shots together at the EPF conference, Crete 2018. I will really miss working with Steve and I believe that any Ph.D. student is lucky to work under his supervision.

This leads me to giving special thanks to Dr Pierre Chambon and Dr Andrew Dwyer who have been involved with this project from day one. Providing their ideas, feedback and support, whilst encouraging and allowing me to expand my own scientific capabilities and understanding. I would also like to say thanks to Dr Sean Flynn, who listened to many of my scientific and personal rambles with no judgement. The Rannard group is very much a friendly team, with many different personalities that contribute to the enjoyable working environment. I have made many friends working within the group, far too many too mention, but thanks for all the gins and the laughs! With regards to the pharmacology work presented in this thesis, I would like to thank Usman Ashard who conducted the pharmacological studies in the Department of Molecular and Clinical Pharmacology under the supervision of Professors Andrew Owen and Chris Goldring, Dr Jo Sharpe and Dr Helen Box. I would also like to acknowledge CRUK for making this PhD possible with their funding and say thanks for the many different opportunities.

Last but foremost, I would like to thank my family, friends and Mr Jones for their continuous support and for loving me unconditionally during what has proven to be one of the most difficult and challenging periods of my young adult life. Ultimately, utmost thanks to my Mum and Dad, both my role models growing up. They have always encouraged me to reach my goals and potential, whilst supporting me both financially and emotionally. I hope I've made you both proud.

As by the Armstrong clan moto *"Invictus Maneo" – I remain unbeaten*.

# Abstract

**Optimising polymeric nanocarrier environments to encapsulate and deliver highly potent anti-cancer drug SN-38**

Chemotherapy is undeniably a highly effective cancer treatment, which has saved or prolonged many patients' lives. However, its indiscriminate nature, acute toxicities and low aqueous solubility has limited the ability to achieve maximum therapeutic effectiveness and usage clinically. Irinotecan, a water-soluble prodrug of highly potent SN-38, is used clinically to treat multiple cancers. The active metabolite, SN-38, exhibits 100- to 1000- fold more cytotoxicity compared to irinotecan, but the metabolism of irinotecan to SN-38 is highly inefficient with significant interpatient variability. Direct administration of SN-38 is highly desirable; however, the extreme hydrophobicity exhibited by SN-38 has prevented its clinical use. Herein, branched vinyl copolymer nanoparticles have been utilised to encapsulate SN-38, offering sustained release profiles and superior *in vitro* cytotoxic behaviour compared to irinotecan. Co-nanoprecipitation has proven to be a fast, reproducible and efficient nanoformulation technique for the preparation of sterically stabilised SN-38 loaded branched vinyl copolymer aqueous nanoparticle dispersions. The preparation of which involved the simultaneous nanoprecipitation of highly branched hydrophobic vinyl copolymers with amphiphilic PEG-based AB block copolymers and SN-38. Methanolic atom transfer radical polymerisation, a versatile polymerisation technique, was used for the production of novel hydrophobic branched vinyl polymers and AB block copolymers; this provided an easy synthetic strategy to impart different polymer characteristics through varying different monomer chemistries. Fundamental studies were carried out to gain an understanding of how these differing polymer chemistries affected the formation of the nanoparticles and their stability, and in-turn influenced the drug loading capabilities and subsequent *in vitro* and *in vivo* pharmacological behaviour. The SN-38 loaded nanoparticles were characterised with small sizes (< 180 nm), slight negative charges (< -20 mV) and respectable drug loadings (< 10 wt.%) with high drug encapsulation efficiencies (> 88%) and extremely low $IC_{50}$ values following *in vitro* analyses in both human and murine cancer cell lines. Radiometric labelling of SN-38 allowed for the release profiles to be accurately determined and highlighted that the particles offer sustained, slow release at physiological relevant conditions (< 17% release). Overall, it has been demonstrated that SN-38 can be successfully encapsulated within aqueous branched vinyl copolymer nanoparticle dispersions, which display promising *in vitro* behaviour; thereby providing an opportunity to further explore the potential of these systems *in vivo* as an anti-cancer drug treatment.

**Table of Contents**

# List of General Abbreviations

| | |
|---|---|
| ATRA | Atom Transfer Radical Addition |
| ATRP | Atom Transfer Radical Polymerisation |
| CRC | Colorectal Cancer |
| CRP | Conventional Radical Polymerisation |
| Cu-ATRP | Copper-Catalysed Atom Transfer Radical Polymerisation |
| Đ | Dispersity |
| $D_n$ | Number Average Hydrodynamic Diameter |
| $D_z$ | Z-average Hydrodynamic Diameter |
| DDS | Drug Delivery System |
| DLS | Dynamic Light Scattering |
| DLVO | Derjaguin Landau Verway and Overbeek Theory |
| $DP_n$ | Number Average Degree of Polymerisation |
| DSC | Differential Scanning Calorimetry |
| EE | Encapsulation Efficiency |
| EPR | Enhanced Permeation and Retention |
| FDA | Food and Drug Administration |
| FRP | Free Radical Polymerisation |
| HIV | Human Immunodeficiency Virus |
| IV | Intravenous |
| LALS | Low-Angle Light Scattering |
| LSC | Liquid Scintillation Counting |
| $M_n$ | Number Average Molecular Weight |
| $M_w$ | Weight Average Molecular Weight |
| MPS | Mononuclear Phagocytic System |
| MWCO | Molecular Weight Cut Off |
| MW | Molecular Weight |
| NHS | National Health Service |
| NMR | Nuclear Magnetic Resonance |
| PBS | Phosphate Buffer Solution |
| PDI | Polydispersity Index (DLS) |
| RALS | Right-Angle Light Scattering |
| RDRP | Reversible Deactivation Radical Polymerisation |
| RI | Refractive Index |
| SDN | Solid Drug Nanoparticles |
| SEM | Scanning Electron Microscopy |
| SLN | Solid Lipid Nanoparticle |
| TD-SEC | Triple Detection Size Exclusion Chromatography |
| TLC | Thin Layer Chromatography |
| VDW | Van Der Waal Forces |
| WHO | World Health Organisation |
| ζ | Zeta Potential (mV) |

# List of Chemical Abbreviations

| | |
|---|---|
| $^{3}H$ | Tritium |
| ACN | Acetonitrile |
| Bpy | 2,2'-Bipyridine |
| BPDMA | Bisphenol A Dimethacrylate |
| BPGDMA | Bisphenol A Glycerolate Dimethacrylate |
| BuMA | Butyl Methacrylate |
| $CDCl_3$ | Deuterated Chloroform |
| $CHCl_3$ | Chloroform |
| CT-26 | Murine Colon Carcinoma Cell Line |
| Cu | Copper |
| DCC | *N,N'*-Dicyclohexylcarbodiimide |
| DCM | Dichloromethane |
| DLD-1 | Human Colorectal Adenocarcinoma Cell line |
| DMAP | Dimethylaminopyridine |
| DMF | Dimethylformamide |
| DMSO | Dimethyl sulfoxide |
| DSDMA | Bis(2-methacryloyl)oxyethyl Disulfide Dimethacrylate |
| EBiB | Ethyl α-bromoisobutyrate |
| EGDMA | Ethylene Glycol Dimethacrylate |
| EHMA | 2-Ethyl Hexyl Methacrylate |
| GDMA | Glycerol Dimethacrylate |
| HCT116 | Human Colon Carcinoma cell line |
| HPMA | 2-hyroxypropyl methacrylate |
| IPA | Isopropyl alcohol |
| IR | Irinotecan |
| LoVo | Dukes' Type C Colorectal Adenocarcinoma |
| MeO-$PEG_{114}$-Br | Poly(ethylene glycol) Macroinitiator (5000 g $mol^{-1}$) |
| MeOD | Deuterated Methanol |
| MeOH | Methanol |
| PCL | Poly(caprolactone) |
| PEG | Poly(ethylene glycol) |
| PLA | Poly(lactic acid) |
| PLGA | Poly(lactic-*co*-glycolic acid) |
| PMMA | Poly(methyl methacrylate) |
| SN-38 | 7-ethyl-10-hydroxyl camptothecin |
| TEA | Triethylamine |
| THF | Tetrahydrofuran |
| UDMA | Urethane Dimethacrylate |

# Chapter 1

Introduction

## 1.1 Cancer

The term cancer is given to a group of diseases in which there is an accumulation of abnormal cells as a consequence of a mutation to one or more genes.[1] This usually results in the uncontrollable proliferation of the cancerous cells and the rapid growth of the malignant tumour - a clear violation to the maintenance of a healthy cell system. These tumours are also capable of metastasis, where cells from the primary tumour can relocate to secondary sites within the body, thereby causing the spread of the disease. The World Health Organisation (WHO) reported that in 2018, cancer was the second leading cause of death globally and accounted for 9.6 million deaths.[2] There are over 200 different variants of the disease and it can be noted that there is an increasing prevalence and diagnosis within economically developed countries. In the UK, there was 367,000 incidences of cancer (2017) and the four most common diagnosed were breast, prostate, lung and bowel; cumulatively, they accounted for over half (53%) of all new cancer cases, as highlighted in Figure 1.1.[3]

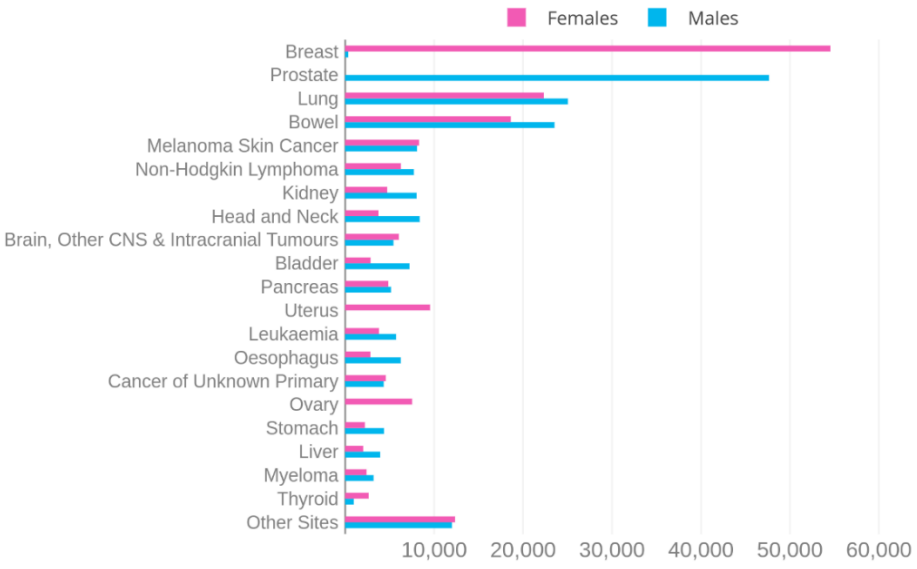


**Figure 1.1** The 20 most common cancers in the UK (2017) and their respective numbers of cases for both males (blue bar) and females (pink bar). Graphic Credit: Cancer Research UK.

It is predicted that the number of new cancer cases diagnosed in the UK will rise to over half a million per year by 2035, an increase of over 40% compared to 2015.[4,5] Whilst the risk of developing cancer depends on many different factors including genetics, sex, age and risk exposure, the rise in incidence can be attributed to our

lifestyle choices, increasing populations and rising life expectancies. Although the quality of services available to cancer patients has dramatically improved UK survival rates in recent decades, with a 10-year survival rate progressing from 1-in-4 during the 1970s to 1-in-2 in 2010, the UK still finds itself with a lower five-year survival rate in comparison to other developed countries such as Australia, Sweden, New Zealand and Canada.[6] It is believed that this difference is likely due to the variances in the treatments given to patients, together with the fact that diagnoses in the UK are typically made later in the disease development.[6] Clearly, cancer has a huge and devastating impact on human life, but it also places huge financial stress on to the National Health Service (NHS), with the National Audit Office estimating an annual expenditure of approximately £6.7 billion in 2009; given that the incidence of cases has increased, it is certain that this figure of expenditure will have increased too.[7]

In 2011, the Department for Health and Social Care aimed to address these issues by launching the National Cancer Strategy in partnership with cancer charities, research institutes and healthcare professionals.[8] The aims of the strategy were to: (1) raise further awareness of the disease and increase screening processes to enable earlier diagnosis, (2) provide funding opportunities for researchers to improve the range and efficacy of available treatments, and finally, (3) challenge societal unhealthy lifestyles and advocate the reduction in risk factors, such as occupational exposure to harmful materials. By investing into the research and development of new and existing treatments and diagnostic tests, and generating resources to educate society about lifestyle choices, it could help to reduce the financial outlay on the NHS. Successful research in those areas could lower the cost by: reducing the overall incidence of cancer; increasing the number of cancer cases detected early in the disease development, thereby providing opportunity for more cost-effective treatment options; reducing the therapeutic dose by improving the efficiency of existing treatments.

Whilst providing financial relief to the NHS is clearly advantageous, the ultimate driving force behind research investments comes from our societal conscience to improve the outcomes for patients diagnosed with cancer, not just in the UK but worldwide.

### 1.1.2 Bowel Cancer

The continual regeneration of the epithelial cells lining the bowel is essential to maintaining good health; however, gene mutation can result in the formation of polyps, common amongst the older population.[9] Most polyps are not typically cancerous and can be removed easily. However, bowel cancer, alternatively referred to as colorectal cancer (CRC), arises from a polyp that has shown abnormal behaviour and has developed into an advanced adenoma.[10]

In 2018, approximately 1.8 million new cases of CRC were diagnosed worldwide, making it the third most commonly diagnosed malignancy.[11] CRC incidence has been growing steadily worldwide and is forecast to rise to 2.2 million cases annually by 2030,[12] indicating that there is a growing demand for effective treatments of CRC.[13] The main contributing factors to the increase in incidence cases are: sedentary lifestyles, rising prevalence of obesity, and excessive alcohol, tobacco and red meat consumption. Case numbers are rapidly rising in developing countries who are undergoing speedy economic and societal changes and transitioning to a more western lifestyle.[14]

As previously mentioned, CRC is the fourth most commonly diagnosed cancer within the UK, accounting for approximately 11% of all new cancer cases (2017), but it is the second most common cause of cancer death within the UK, accounting for 10% of all UK cancer deaths (2017).[15] As with all cancers, when a tumour has developed in CRC, the course of treatment recommended will depend on what stage the cancer is and the individual patient.

### 1.1.3 Conventional Cancer Treatments

Cancer treatment's first aim is to cure the disease where possible by shrinking, or stopping the progression of cancer cells. Should that not be possible due to advanced disease then the treatment should look to palliate.[16, 17] There are many different types of cancer treatments available and the type of cancer and how advanced it is will dictate which treatment option is most applicable. The most commonly known options are: radiation therapy, chemotherapy and surgery, which is appropriate in cases where physical tumour mass can be accessed, with minimal risk, and removed. The latter being the preferred option for complete cure by removal of the tumour

tissue, if localised.[18, 19] Other alternative, lesser known treatments include, hormone therapy, immunotherapy and stem cell therapies. [18, 19]

The inherent ability of metastasis from cancer cells usually means that the most applicable form of treatment is chemotherapy, since the cancer is no longer localised. This involves the intravenous (IV) administration of cytotoxic drugs, henceforth referred to as chemotherapeutics, which are designed to kill cells. The mechanism of which is complex and drug dependent, but in brief they typically disrupt the cells ability to divide. This is achieved by causing damage to the RNA or DNA which is responsible for informing a cell's replication during the division process.[20] Simply, if the cancer cells cannot divide they will die. IV infusion allows for the rapid entry of molecules into the systemic circulation. It also provides predictable pharmacokinetics and offers the quickest drug absorption time compared to other methods, such as oral administration.[21]

Chemotherapy is often administered in cycles to patients and a combination of chemotherapeutics can be used. Which chemotherapeutic is used is decided based on a number of different factors such as: the type of the cancer cells, the rate of cell division and also whether there are any secondary cancer sites present.[22] There are two different types of chemotherapeutics: cell-cycle specific therapies, which target the cancer cell when they are dividing and, on the contrary, cell-cycle nonspecific therapies, which kill the cells when they are at rest. Chemotherapeutics can be typically categorised as platinum based or non-metallic,[23, 24] the latter leading to the discovery and development of a number of organic chemotherapeutics, such as: doxorubicin, fluorouracil, taxanes and campothecin derived agents.

#### 1.1.3.1 Bowel Cancer Treatments

There have been significant advances made in the treatment of CRC over the past 30 years, which have resulted in patients having a higher chance of cure and, when cure is not achievable, longer survival times with their disease.[25] The choice of treatment for bowel cancer is based on several factors, including stage at presentation, location, and the conditions of the patient. The preferential and most common treatment option for patients with bowel cancer is surgery, with 66% of patients diagnosed with

CRC receiving surgery as part of their primary cancer treatment.[15] Surgery is dependent on a substantial proportion of the tumour being able to be removed. Often, this is done in combination with a cycle of chemotherapy to cause tumour shrinkage (and therefore make the surgery easier) or to reduce the risk of the cancer returning after tumour removal. However, when surgery is not a viable option, chemotherapy is the secondary preferred route of treatment. Approximately 31% of bowel cancer patients will receive some form of chemotherapy as part of their primary cancer treatment. Reasons why surgery is not viable include late stage diagnosis meaning that the cancer has spread to other parts of the body, such as the liver or lungs, or that the patient is not a suitable candidate for surgery due to other health complications or poor recovery predictions.

There are many different chemotherapeutic agents that can be administered for the treatment of CRC but the most common are 5-fluorouracil (5-FU), oxaliplatin and irinotecan (IR).[26] Often, these are administered in combination and can be given as a tablet or intravenously infused. IR, a prodrug which is converted *in vivo* to biologically active metabolite 7-ethyl-10-hydroxy-campothecien (SN-38; Scheme 1.1), has also been established as an effective treatment as a single agent.[27]

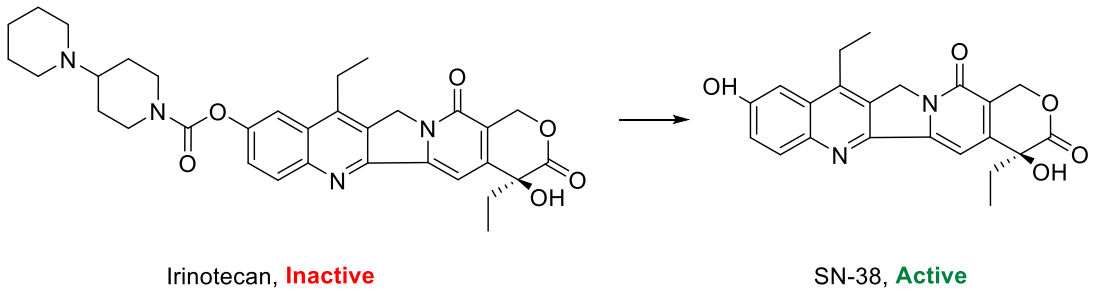


**Scheme 1.1** Schematic representation of the conversion of inactive prodrug irinotecan to the active metabolite SN- 38.

It has been shown that the potent anti-cancer activity of IR is due to this rapid formation of SN- 38. The potency of SN-38 relative to IR varies between patients but it is reported to have 100- to 1000-fold higher cytotoxic activity compared to the original parent drug dependant on conversion rates.[28] [29] Although, conversion between the prodrug and SN-38 suffers from interindividual variability and the mechanism of which, and its effects on the variability, are still being investigated and

are discussed in more detail in Chapter 4.[30] Direct administration of SN-38, although desirable, is not possible due to the extremely low water solubility and other associated pharmacological problems it presents.

#### 1.1.3.2 Limitations to Chemotherapy Treatments

Whilst the use of chemotherapeutics has played a major role in the reduction to morbidity and enhancement of the quality of patients' lives, there are often concerns associated with their use and other factors which decrease the clinical effectiveness of these agents.

The nonspecific distribution of chemotherapeutics within the body can result in severe off-target toxicities and, as effective as chemotherapeutics are at causing cell death, the chemotherapeutics unfortunately cannot distinguish between healthy and non-healthy (or cancerous) cells; thereby accumulation of these highly toxic drugs also occurs within healthy cells. This results in some adverse side effects such as: diarrhoea, nausea, mouth sores, low blood counts and hair loss. These are the most commonly experienced side effects since the cells found in hair follicles, bone marrow, gut epithelium and skin often display high mitotic activity and thereby are most likely to respond to chemotherapeutics that affect cell division.[31] These side effects are caused by most chemotherapeutics, but there are some side effects which are drug-specific, such as cardiotoxicity experienced by administration of anthracyclines (a class of chemotherapeutics).[32]

In addition to the poor specificity chemotherapeutics display, they are also presented with a variety of different obstacles upon their administration into the body which also limits their effectiveness. Chemotherapeutics often will extensively bind to body tissues and serum proteins upon administration in an unpredictable manner in comparison to other drug classes. This offers unique problems and unfavourable pharmacokinetic profiles such as short half-life in blood circulation, high clearance rates and susceptibility to induce drug resistance within cancer cells.[33]

Other factors which constrain the clinical effectiveness of chemotherapeutics also include the suboptimal penetration into tumour tissue and their poor aqueous solubility.

Approximately 40% of developed pharmaceuticals are practically insoluble in water, rendering them unsuitable for purpose and many of the commonly used chemotherapeutics are no exception, often displaying high lipophilicity and low water-solubility characteristics.[34] As specified by the Biopharmaceuticals Classification System a drug is considered to be poorly water soluble "*if the maximum dose strength is insoluble in 250 mL or less aqueous media over a pH range from 1 – 7.5*." [35] This poor water solubility typically arises due to two reasons: (1) the hydrophobic nature of the drug molecule meaning that they have limited ability to form hydrogen bonds with surrounding water molecules and (2) the typical bulky cyclic nature of most chemotherapeutics and the subsequent high lattice energy required to break down the solid molecule. This poor water solubility is one of the main reasons why most new drug molecules fail to fulfil their potential as therapeutic candidates and do not make it to clinic. Given that chemotherapeutics are generally administered in aqueous solutions, this poses a problem.

Currently, to overcome the poor solubility issues displayed, the chemotherapeutics are often mixed with various different solubilisers or co-solvents in order to maximise their water solubility and improve their therapeutic efficacy. However, the efficiency of solubilisation is directly related to the polarity of the compound which can limit the use of this technique.[36-38] Also, when using co-solvents and stabilising agents, it is important to consider the effects that these may have to the overall toxicity experienced directly or indirectly by the patient.[39]

Whilst the use of solubilizers or co-solvents may improve the observed saturation solubility, it does not address the other aforementioned issues associated with the use of chemotherapeutics. The combination of inherent problems results in only a small fraction of the administered dose reaching the tumour site and thereby reducing the therapeutic efficacy and increasing systemic drug toxicity. These challenges are diverse and complex and must be overcome by the chemotherapeutics in order to successfully perform their anti-cancer functions in a safe and efficient manner *in vivo*.

To overcome the aforementioned problems associated with the administration of chemotherapeutics, an attractive strategy that has received considerable interest and research development over the last few decades involves the formulation of chemotherapeutics within nanoscale drug carrying platforms, which will be discussed in detail in Section 1.2. Such systems have been used for disease treatment and prevention and some of the key advantages of using these drug carrying platforms include improved pharmacokinetics, longer circulation half-lives and targeted drug delivery thereby decreasing off-target toxicity.[40]

## 1.2 Nanomedicine

Given the huge scientific and technological developments that have been made in the last 60 years, it would be fair to assume that this would have aided new drug discovery. However, it has somewhat had the opposite effect with more drugs failing during their clinical development now than in the 1970s.[41] A combination of stricter regulations, reproducibility issues and rising research and development costs can all be assumed to be contributing factors. As disease incidence continues to rise, pressures of finding new drugs to "cure" disease, particularly cancer, remains at the forefront of discussion. Yet due to the complexity of the stages involved in drug discovery, research has slowed with limited outputs. There are also significant financial and time costs associated with new drug discovery.

Nanomedicine provides an attractive strategy to overcome these limitations. The main objective is not to discover new drugs but to improve therapeutic outcomes of existing medicines or those that have failed late stage clinical tests, and to develop new therapeutic strategies of administration.

### 1.2.1 What is Nanomedicine?

Nanomedicine is an evolving sub-discipline of nanotechnology, but its official definition continues to be an area of controversy and one would find many different definitions. For the clarity of the work being presented within this thesis, nanomedicine is the use and application of a material, whose size exists within a region between 1-1000 nm, within a medicinal environment.[35, 42] The concept of working at the nanoscale is not novel, but the developments in the ability to be able to characterise and understand the physical phenomena occurring when materials

are organised at the nanoscale has propelled the area into becoming one of the key areas of research in the 21st century,[43] receiving significant attention from funding agencies, regulatory bodies, academic research groups and global government agencies.[44, 45]

Developing a nanomedicine is a time-consuming process which is usually divided into three main stages: development of a proof-of-concept demonstration, clinical development and investigations, followed by the generation of a commercialised product.[46] The first stage generally occupies the most time, typically up to 20 years, since it can be subdivided into three sections: preliminary research, development of the intended application followed by preclinical animal studies. There are many biomedical applications which exploit the use of nanomedicines such as diagnosis and treatment of disease, regenerative medicine and molecular imaging. [47, 48]

One area in which nanomedicine has proven to be particularly advantageous is its application within the field of oncology.[49] The utilisation of such has seen improvements made to imaging and treatments of cancer.[50] The inherent problems conventional cancer treatments possess - low specificity, rapid drug clearance, biodegradation and limited targeting - can be potentially addressed by the use of nanocarriers.[51, 52] Nanocarriers can be referred to as drug delivery systems (DDS), which are engineered materials in the nanoscale size region used for the targeted delivery and/or release of therapeutic agents.[53] The DDS utilised may offer several advantageous attributes and opportunities such as, size, high surface area to volume ratio, targeting modifications and stimuli responsive behaviour, all of which can favourably work in unison or complement each other to deliver drugs in a stable, controlled manner.[51, 54] There are many different type of nanocarriers, with the most relevant examples being discussed below.

### 1.2.2 The Different Types of DDS

DDS can be applied to a wide range of different disease treatments including: Human Immunodeficiency Virus (HIV),[55] respiratory disease,[56] Alzheimer's disease,[57] diabetes[58] and cancer.[59]

The desire to deliver potent therapeutic agents intact to their intended site of action whilst minimising adverse side effects can be achieved by utilising a DDS.[60] Other advantages include improving the drug bioavailability, enhancing therapeutic effect, improved permeation of drugs across biological barriers (e.g. gut and blood brain barrier), and the alteration of the pharmacological properties of the drugs (e.g. stability) in the hope to see improvements without altering the active drug molecule itself.[61, 62] There are a wide variety of material platforms being investigated as DDS candidates: inorganic,[63] lipid-based,[64] polymer-based[65] and drug conjugates (Figure 1.2). [66-68]

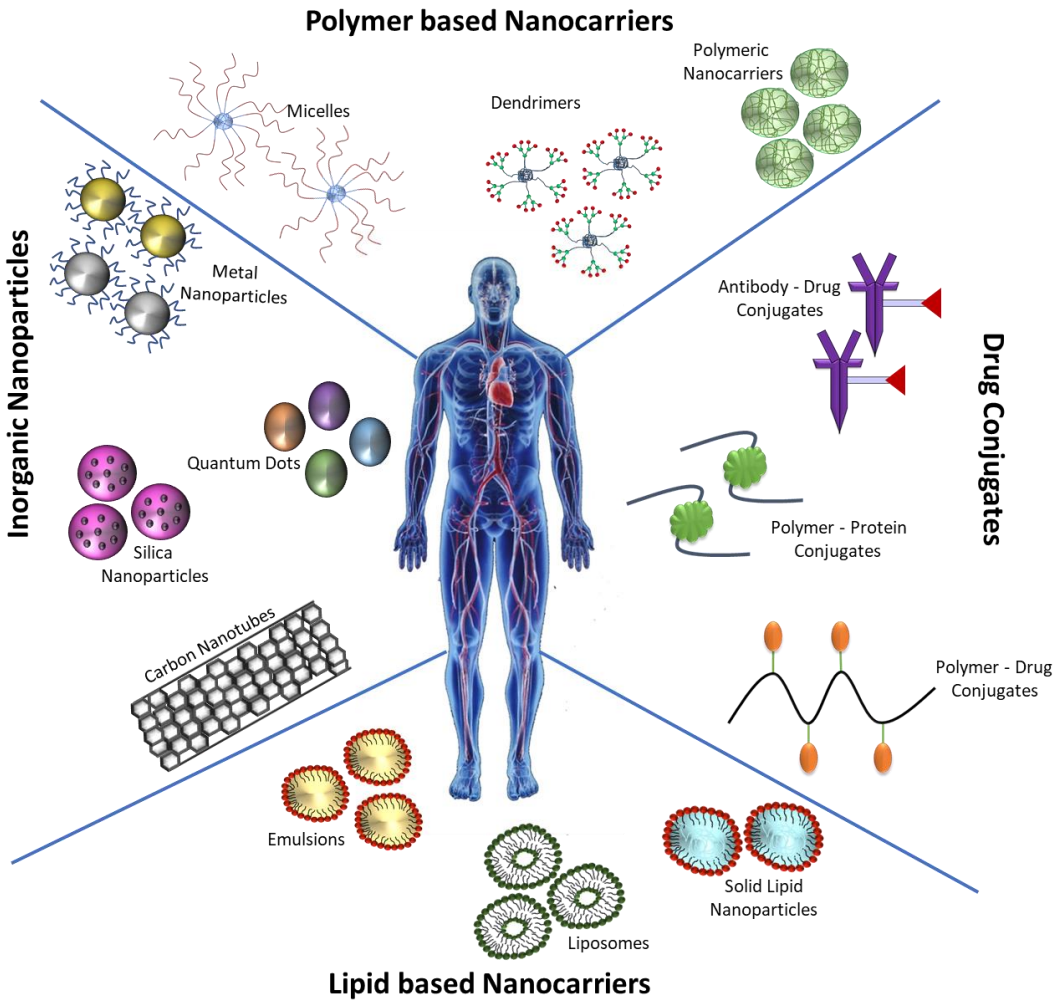


**Figure 1.2** Overview of the material platforms currently being investigated as drug delivery systems. Figure adapted from reference [69].

An example of a lipid-based DDS is a liposome, which is formed when phospholipids self-assemble upon exposure to an aqueous environment.[70] First reported by

Bangham and co-workers in the 1960s, who observed the spontaneous formation of a three-dimensional intricate structure that was formed when egg lecithin was exposed to water.[71] A liposome consists of a phospholipid bilayer which is amphiphilic in nature, thereby providing liposomes with the capability to encapsulate both hydrophilic and hydrophobic payloads. They also exhibit high levels of biocompatibility.[72] In addition to this, liposomes, like other DDS, can protect drug molecules from degradation and reduce the premature removal from the body by opsonisation.[35] This is the process, whereby opsonin proteins can bind to the surface of the nanoparticles, allowing immune recognition and subsequently trigger clearance from the body by various different mechanisms.[73]

Some of the drawbacks associated with the use of liposomes include: their complex manufacture, leakage of encapsulated drugs/molecules, low solubility and the potential for oxidation and hydrolysis of the phospholipids.[74]

In 1995, a liposome-based DDS, known as Doxil, was approved by the Food and Drug Administration (FDA) for use in anti-cancer treatments. The formulation encapsulated the chemotherapeutic, Doxorubicin.[75] The success of Doxil is owed to its prolonged systemic circulation that enables the DDS to exploit the Enhanced Permeation and Retention effect (EPR) - a pharmacokinetic principle that will be discussed in further detail in Section 1.2.3. In 2017, there were fifteen clinically available liposomal formulations being used to treat a variety of diseases, seven of which were specific to anti-cancer treatments.[76] In addition to these, there are numerous other formulations that have made it through to various stages of clinical trial. One of interest is a liposomal encapsulation of SN-38 (LE-SN38) developed by Neopharm for the treatment of late stage CRC. The work was inspired by the clinical success of Camptosar (irinotecan) that had been developed by Pfizer, and aimed to directly encapsulate SN-38. It was hoped that this formulation would improve efficacy of the treatment whilst ensuring that the overall toxicity of the drug was not increased. LE-SN38 was evaluated successfully in phase I, but failed phase II trials.[77,78] Despite the formulation preventing any further disease growth, the tumours did not display any sign of shrinkage and it was concluded that the formulation did not meet the prespecified activity, so no further evaluation was conducted.[79]

Another example of a lipid-based DDS is a solid lipid nanoparticle (SLN), which consists of a solid lipid core, which can carry lipophilic payloads, that is typically stabilised by a range of polymer-based surfactants to prevent particle agglomeration. The main advantages of SLNs include: the water-based synthesis thus avoiding organic solvent use; the ease of scale-up compared to liposomal formulations; the cost of manufacturing is typically less than other polymer-based DDS; and finally, their excellent biodegradability and biocompatibility.[80] However, one disadvantage of SLNs is that they typically display low drug loadings due to the limited solubility of the drug in the lipid melt: if the structure of the lipid matrix comprises molecules that are too similar in nature, a highly crystalline matrix is formed that hinders drug encapsulation. Therefore, more complex lipids are required in order to facilitate high drug loadings. There are many different types of lipids that can be used to yield SLNs. These include triglycerides, steroids, waxes and fatty acids, all of which offer different opportunities to the formulation. A lot of research has been conducted into SLNs and they have many applications ranging from gene vector carriers to cosmeceuticals to applications in agriculture. The use of SLNS within cancer research has been extensively researched, examples including docetaxel, doxorubicin and SN-38.[33, 81]

Micelles based DDS are formed from the self-assembly of amphiphilic molecules, including block copolymers, upon their addition to water. Amphiphilic block copolymers are comprised of 2 segments: one hydrophobic and one hydrophilic. The self-assembly is driven by the unfavourable interaction between water and the hydrophobic segment of the block copolymer. [82] The shape of these DDS is dictated by: (1) the head group size and the degree of steric hinderance, (2) the length of the hydrophobic tail, and (3) whether the surfactant is ionic or non-ionic in nature. Typical shapes include spheres, cylinders and rods. It is possible for micelles to encapsulate hydrophobic drug molecules within their cores.[83] This has resulted in this form of DDS receiving significant attention as drug nanocarriers in the treatment of many cancers. Examples include the encapsulation of paclitaxel for the treatment of ovarian, breast and small cell lung cancer.[84, 85] These formulations showed high drug loading capacities and good treatment efficiency in patients.[86] Similarly this was also observed for the micellar formulations of encapsulated doxorubicin.[87] Disadvantages

associated with the use of micelles as DDS include: (1) the potential for drug-leakage from the polymer assembly, thereby reducing drug circulation half-life, and (2) the poor stability of the micelles within the blood stream.[88, 89]

A leading class of DDS system for clinical translation are solid drug nanoparticles (SDNs). They do not employ a guest-host mechanism, as the active pharmaceutical ingredient is not encapsulated but instead forms the solid core of the nanoparticle, which is stabilised by polymers and surfactants.[90] This, in principle, means that higher drug loadings, relative to stabilisers, can be achieved in comparison to systems made up of other chemical entities which simply host the payload, such as micelles and liposomes. One method of preparation for SDNs is the emulsion templated freeze-drying method, which is a relatively simple process.[91-94] Firstly, the formation of an oil-in-water emulsion is achieved by sonication. Following this, it is then rapidly frozen in liquid nitrogen, thereby entrapping droplets within a solid emulsion template. Then, the sample is subjected to freeze drying to remove the aqueous and non-aqueous phase leaving behind a monolith of water-soluble polymers and surfactants, with particles of drug dispersed within the solid. This monolith is then re-dispersed in water to form aqueous nanodispersions, thereby generating an aqueous nano-dispersion. Materials of similar nature can also be formed using a spray drying technique.[95-97] Due to the relative ease and scalability of these formulations, SDNs have become attractive candidates as DDS in the treatment of various diseases and infections such as HIV and cancer.[98-101]

Drug nanocrystals are also a class of SDN that are commonly researched. They are an attractive class of DDS as they also consist solely of drug particles stabilised by polymers and surfactants. Nanocrystals can be obtained by adopting a top-down or bottom-up approach. Top down technologies typically use high energy methodology, such as milling, to break down larger drug crystals into smaller drug crystals. Whereas bottom up processes see the formation of drug nanocrystals from dissolved drug molecules. In the production of commercial drug nanocrystals, it is not common to utilise bottom up technologies as difficulties in controlling the process can be experienced. Additionally, the process requires removal of large volumes of solvent

and most drugs exhibit poor solubility in both aqueous and organic media, often rendering this processing technique unsuitable.

### 1.2.3 Passive Targeting of DDS in Tumours via Enhanced Permeation Retention (EPR) Effect

A pharmacokinetic principle which is often exploited in the design of DDS for cancer therapies is the EPR effect, see Figure 1.3. It was initially discovered in the 1950s following *in vivo* studies involving the administration of small molecule dyes into tumour bearing animals; the results showed extravasation from systemic circulation and accumulation within tumour tissue.[102-104]

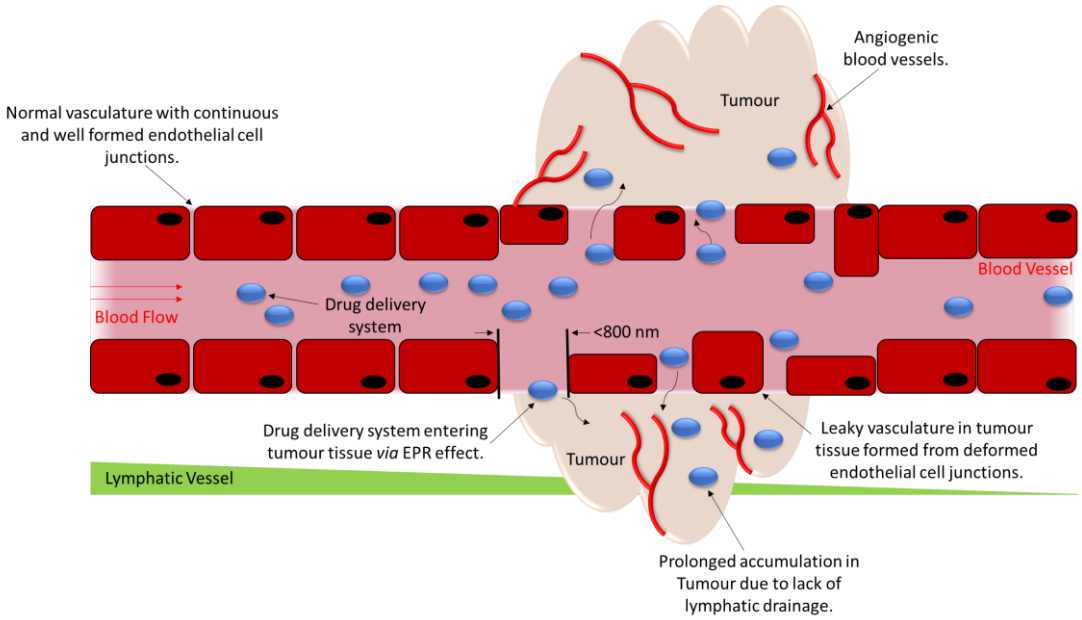


**Figure 1.3** Passive targeting of DDS *via* the EPR effect.

This was subsequently developed further in 1986 by Matsumura and Maeda whose initial publication has since been cited within > 6500 publications.[105] The study investigated the mechanism of accumulation of radioactive proteins within tumour-bearing mice. It found that there was noticeable accumulation of proteins within the tumour tissue and it was speculated, and later confirmed, that the accumulation was due to the high degree of vasculature within the tumour microenvironment and its increased permeability compared to that within healthy cells. The results also highlighted little lymphatic recovery of the macromolecules from the tumour tissue. The article concludes that the findings presented were of "potential value" to macromolecular tumour therapeutics. The seminal study has made a huge

contribution to the development of drug delivery, specifically by recognising the opportunity for enhanced passive targeting capabilities of drug nanocarriers.

In principle, when a tumour grows, the centre of the tumour gets further away from the supply of blood supply, oxygen and nutrients, all of which are required to promote growth. As a result of this, the cancerous cells send out an angiogenic signal which encourages new blood vessels to form within that area, thereby providing the tumour with the vasculature necessary for further growth as depicted in Figure 1.3. However, the fast, dysregulated nature of the growth of this tumour vasculature leads to structural and physiological defects. These defects often lead to hyperpermeability within the tumour tissue and give rise to the increased permeation of macromolecules. The tumour vasculature can be described as 'leaky'; typically, macromolecules with prolonged circulation will exploit this characteristic the most. Another unique property of the tumour microenvironment is the lack of a properly functioning lymphatic recovery system, which is responsible for the clearance of macromolecules; this results in poor lymphatic drainage and the retention of macromolecules within the tumour tissue.[106] These unique characteristics presented within the tumour environment can be utilised to help increase the delivery of nanoparticles *via* passive targeting, provided the nanoparticle can remain stable and avoid clearance, the strategies of which will be discussed later.

#### 1.2.3.1 Limitations Associated with the EPR Effect

The EPR effect has been described as the "pillar of cancer nanomedicine research" and has been validated for particles up to 400 nm in size.[107, 108] However, the development of such nanomedicines is somewhat stalling and the relevance of the EPR effect has been under considerable debate.[108-112] The main drawback of the EPR dogma is that it has been somewhat over-generalised. There is no question that the EPR effect does exist,[51, 113-117] but it should be recognised that the effect cannot be simply generalised as a feature of all cancers, and that there is a degree of variance exhibited due to the heterogenous nature of the disease. Variances of the effect can also occur between patients and different types of cancers.[118,119] For example, a study investigating the effect of nanoformulated doxorubicin in the treatment of

both breast cancer and Kaposi's sarcoma found that the nanoparticle accumulation was different between the two cancers due to the differences in the degree of "leakiness" in the vasculature. The extent of deformation of the endothelial membrane in the case of Kaposi's sarcoma was larger than in the case of the breast cancer tumour, resulting in a more effective accumulation of nanoformulated doxorubicin for the Kaposi's sarcoma. [120]

The preclinical investigations of DDS have often been conducted using animal models, typically murine, to assess the EPR effect in tumours. These tumours are systematically grown within the model in a controlled environment. However, since the tumours have been forced to grow rapidly, it is thought that the blood vessels that have developed are somewhat leakier than those developed within a tumour under normal conditions, which can often take many years. This can lead to an overestimation of the actual passive targeting capabilities of the formulated nanomedicines, as seen when radio-labelled soluble (2-hydroxypropyl)methacrylamide copolymers were administered to different tumour models. The results showed an increased accumulation (0.5% per gram administered) observed for the tumour model which had grown by one centimetre in two weeks compared to the accumulation observed (0.2% per gram administered) in a tumour model which had taken over a year to grow by one centimetre.[121, 122]

Despite these limitations, pre-clinical data on DDS for anti-cancer treatments has undergone meta-analysis for the past 10 years and the results seem to suggest that delivery efficiency of chemotherapeutics from DDS is higher than the delivery efficiency of most chemotherapeutics which dominate the clinic. Calculations suggest that a median of about 0.7% of the injected dose of DDS reaches the target tumours.[123] Whilst this number may seem small, this delivery efficiency is higher than that of conventionally used chemotherapeutics. A study conducted by Vlerken *et al*. on nanoformulated paclitaxel compared to free paclitaxel, showed that the delivery efficiency increased from 0.2% to 0.6% of injected dose when the chemotherapeutic was formulated into DDS.[124] The study concludes that this is encouraging and clearly indicates advantages of using DDS for drug delivery in anti-cancer treatments.

The delivery efficiency of DDS can be improved to maximize their therapeutic benefit. An alternative method of increasing the accumulation of polymeric nanoparticles within tumour sites is the utilisation of a strategy known as *active targeting*. Whereby, a ligand which is complimentary in nature to an over expressed receptor on the tumour surface can be incorporated onto the nanoparticle corona so that an increase in binding and affinity of polymeric nanoparticles to a tumour is observed.[125]

**1.3 Polymeric Nanoparticles**

Advancements made within the polymer chemistry field has provided opportunities for chemists to generate macromolecular structures with a high degree of control. These structures can then be utilised to generate nanoparticles. Their attractiveness as DDS stems from a variety of different reasons but mainly from the ability to design and control the polymer functionality to compliment individual drug properties and delivery requirements. This makes polymers a desirable material platform to utilise in the development of new/improved disease treatments with pre-existing drug candidates. Incorporation of drug molecules within polymeric nanoparticles can be achieved by adsorption, covalent linkage, entrapment and encapsulation. Polymer nanoparticle preparation, in short, utilises polymeric material that is hydrophobic in nature, which spontaneously collapses upon addition to water. The hydrophobic core of these nanoparticles would therefore provide a suitable environment for a hydrophobic guest molecule to reside, in this case a hydrophobic drug. This type of encapsulation is classified as non-covalent since there are no chemical bonds created to entrap the drug, only supramolecular interactions based on hydrophobic interactions, and if applicable, π-π interactions.[126]

The formation of nanoparticles can be categorised into two strategies: *in situ* synthesis of nanoparticles starting from solubilised small molecules; or the creation of polymeric nanostructures *via* various different preparative techniques such as spray drying, milling processes and nanoprecipitation. The latter is a facile, low energy and mild technique which can be used to generate nanoparticular material of organic, inorganic or hybrid nature.[127-129] This simple and highly convenient technique offers applicability to wide field applications, since the incorporation of many differing functionalities and characteristics comes with ease due to the facile

nature of this method. In non-specific terms, it is the precipitation of dissolved material, of low or high molecular weight, as nanoparticles, upon the rapid exposure to a non-solvent environment. Given the context of this thesis, the discussion will be focussed on the nanoprecipitation of polymeric material. The applications of which can be generalised into two main category types: a formulation technique to create value-added desired end-products, such as pay loaded nanoparticles, or as an intermediate step during polymer processing.

### 1.3.1 Nanoprecipitation

The process of nanoprecipitation originated long before the emergence of nanotechnology as a concept, and its applicability was verified by the broad scope of patents that were filed during the latter half of the 19$^{th}$ century.[129-133] For some time after, however, interest in the technique waned until it was utilised as a cost-effective purification technique for polyolefins.[129] The use of nanoprecipitation was also patented by Fessi *et al* in 1992, following the presentation of a simple, novel procedure to synthesise indomethacin loaded polylactic acid nanoparticles (200 nm) *via* the deposition of poly(lactic acid) (PLA) polymer at an oil-water interface following acetone displacement from the oily nanodroplets.[134, 135] The inventors of the patent highlight that the main advantage of the technique was the instantaneous, reproducible way of producing monodisperse nanoparticles with long-term stability.[134] The versatility of this procedure was demonstrated by the extension of the study to include the nanoprecipitation of different polymeric species (polyvinylacetate, polyvinylchloride and polycaprolactone) and the incorporation of various hydrophobic moieties (essential oils, anticancer drugs and magnetic resonance imaging contrast agents), thereby reflecting the extended potential of such a technique.[136, 137]

Polymers which possess charge can also be used to form nanoparticles *via* nanoprecipitation and examples of such have been used for efficient gene delivery.[138] The theory and mechanism of nanoparticle formation is discussed in detail below.

### 1.3.2 Nanoprecipitation Theory

Nanoprecipitation as a preparative method is a simple and easy way to generate nanoparticles from polymers or small molecules in solution.[139] Theoretically, nanoprecipitation is based on the reduction of the quality of the solvent in which the polymer is dissolved, which subsequently causes the precipitation of this material into nanoparticles. This can be achieved by various strategies such as: altering the pH, varying the salt concentration or introducing a non-solvent phase, such as water. Formation of nanoparticles *via* the latter strategy can be broken down into four different steps which will be discussed in more detail below: 1) the generation of a supersaturated solution, 2) nucleation, 3) growth, and finally, 4) stabilisation as outlined in Figure 1.4.

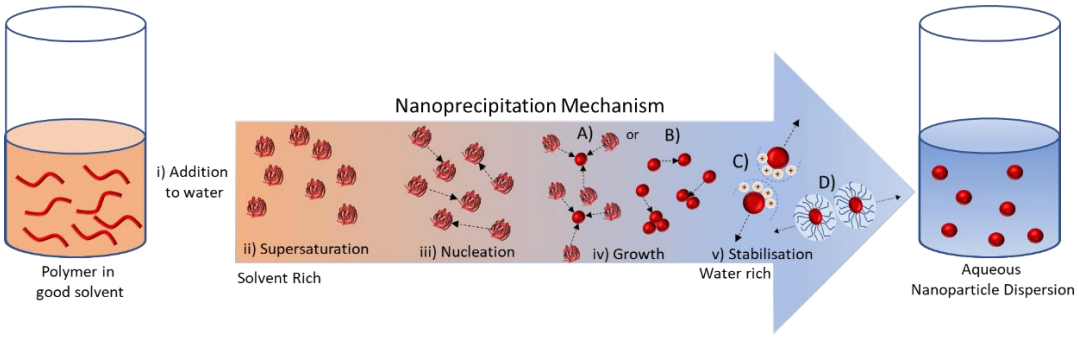


**Figure 1.4** Schematic representation of the formation of nanoparticles *via* nanoprecipitation. Following i) the addition of polymer to water, ii) generation of state of supersaturation, iii) nucleation of polymer chains, iv) growth *via* 2 mechanisms: A) nucleation and diffusion or B) coagulation. Followed by v) stabilisation *via* C) charge repulsion of cationic nuclei or D) steric repulsion.

Each of these steps play a role in the control of the particle size and morphology.[140-142] It is worth noting that the mechanistic understanding of these four stages are complex, and often in literature, scientists will suggest that the primary principle of nanoprecipitation is based on the classical nucleation theory (CNT). However, this has been criticised with suggestions that CNT over-simplifies the process and Gebauer and Colfen provide a detailed review on non-classical nucleation.[143] These alternative mechanisms suggest that the CNT is based on the assumptions that supersaturation is uniformly distributed in the solution. However, in a state of precipitation, supersaturation is often not uniformly distributed throughout the total solution volume and it is local fluctuations in concentration, caused by supersaturation, which leads to the formation of the primary nuclei. Regardless, given the ambiguity in literature presented and the lack of concise understanding

into the mechanistic detailing, for the purpose of this thesis, the reader will be redirected back to the typical representation of the mechanism of nanoprecipitation.

### 1.3.2.1 Supersaturation and Nucleation

The initial step of the mechanism involves the formation of a supersaturated solution following the rapid addition of polymeric materials which are dissolved in a 'good' solvent to an anti-solvent, typically water (Figure 1.5).[140]

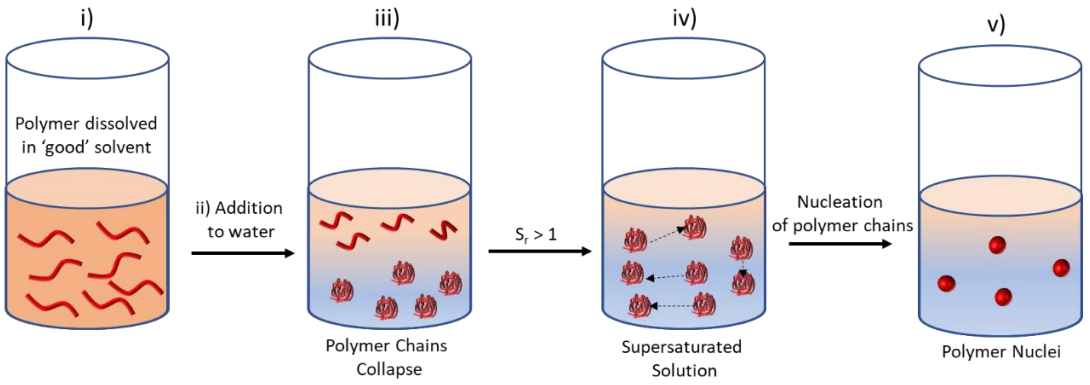


**Figure 1.5** Schematic representation of the initial stages of the nanoprecipitation mechanism, i) polymer dissolved in 'good' solvent, ii) polymer in 'good' solvent added to anti-solvent (water), iii) exchange of anti-solvent and 'good' solvent causing polymer chains to collapse, iv) generation of a supersaturated solution, where Sr > 1, followed by the nucleation of polymer chains to form v) polymer nuclei.

This occurs because the addition of the organic solution to the non-solvent phase decreases the solvent potency for the dissolved polymer solute and creates a solution with a dissolved solute concentration that is greater than the thermodynamic solubility limit, thereby creating a system defined as a state of supersaturation. The extent of which can be represented by the simple equation $S_r = C/C_{eq}$, where $S_r$ represents the supersaturation limit, C is the concentration of the polymer in the nanoprecipitation medium, and $C_{eq}$ is the thermodynamic equilibrium solubility limit. The extent of supersaturation can influence the final nanoparticle properties, such as the particle size.[144] Only when a state of supersaturation is achieved (i.e. the value of Sr > 1) will the spontaneous formation of nuclei occur in order to gain thermodynamic stability within the system. The formation of nuclei occurs through the random collapsing of the polymer chains in order to minimise the interfacial energy between the polymer and the surrounding solvent environment (Figure 1.5iii and iV). The nuclei that are initially formed increase in size by association of solute molecules until a critical size has been achieved, at which point they are then stable

against dissolution (Figure 1.5v). Once this is achieved these nuclei will then continue to grow until a state of colloidal stability is established.

### 1.3.2.2 Growth

The mechanism of growth can be described by either: 1) nucleation and diffusion limited growth, or 2) coagulation or the diffusion limited cluster-cluster aggregation (Figure 1.6).[145, 146]

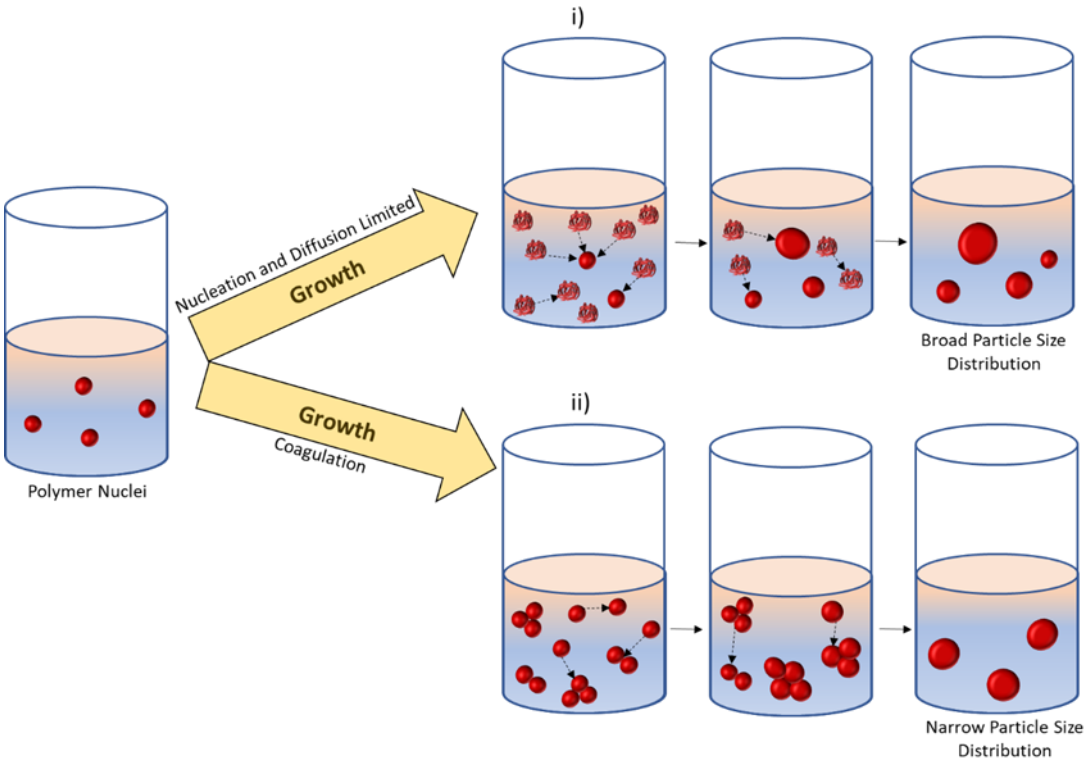


**Figure 1.6** Schematic representation of the growth mechanisms which follow after the initial formation of polymer nuclei. Growth *via* i) nucleation and diffusion limited mechanism and ii) coagulation mechanism.

Growth by nucleation and diffusion limited growth mechanism involves the addition of solute molecules to the particle surface and proceeds *via* two steps.[147] Initially, solute molecules diffuse from the bulk fluid through the solution to the surface of the nuclei, then a deposition step occurs where the adsorbed solute molecules are integrated onto the nuclei matrix (Figure 1.6i). This growth will continue until the non-adsorbed solute concentration is reduced to that of the equilibrium saturation concentration. This mechanism is limited by the rate of nucleation and the diffusion of the solute to the particle surface.

Alternatively, growth may occur by coagulation, which in short is the adhesion of particles to one another following a random collision (Figure 1.6ii).[148] Typically, this adhesion will occur when the attractive interactions are stronger than that of the repulsive interactions of the particles. This is controlled and limited by the collision frequency, which is dependent on the rate of diffusion and can be affected by the particle concentration and the particle size. The collision efficiency is primarily dependent on the attractive and repulsive forces between the particles.

The mechanism of growth that is favoured is typically dependent on two factors: 1) the initial nuclei concentration, and 2) the extent of supersaturation.[149] If the degree of supersaturation is high, the mechanism of growth is predominantly coagulation driven.[146] This is because the rate of nucleation is enhanced. Since there is a high concentration of nuclei and that the probability of collisions is proportional to the square of the number of nuclei present, the chances of random collisions between nuclei increases.[150] If the degree of supersaturation is low, the mechanism of growth will proceed by nucleation and diffusion. Since the nucleation rate is lower, there is less chance of random collisions occurring between particles; instead, the particle growth will be limited by the diffusional rate of solute molecules. Preferentially, to obtain small particle sizes with narrow particle size distributions, it would be desirable if the growth mechanism followed coagulation.[150, 151]

#### 1.3.2.3 Stabilisation

In order to minimise the thermodynamically unfavourable high total surface energy that nanoparticles possess, the particles will tend to agglomerate leading to macroscopic precipitates, rendering them useless for nanoscale applications. To prevent this from occurring, it is typical that a stabiliser will be introduced into the formulation or the polymeric material will have been designed to possess characteristics that provide stability. Stability can be provided to the colloidal suspension by two main methods: steric stabilisation and electrostatic stabilisation (Figure 1.7). Both works to ensure that the attractive Van der Waals (VDW) forces are exceeded by the repulsive forces, preventing the particles coming together and subsequently forming larger aggregates.[147]

Stabilisation by electrostatic charge is based on the mutual repulsion of like charges and can be described by the well-known Derjaguin-Landau-Verwey-Overbeek (DLVO) theory.[152-155] This theory is well understood for aqueous suspensions and assumes that there are two main forces acting on the particle within the medium: attractive VDW forces and repulsive electrostatic forces (Figure 1.7A). As previously mentioned, the interplay between these two is the driving force behind the stabilisation. The origin of the repulsive forces is caused by the overlapping of the electrical double layer, which surround the particles in the medium. This double layer consists of two different layers: (1) the stern layer, which is generated by counter ions attracted to the particle surface to maintain electrical neutrality, and (2) the diffuse layer, which is a result of the diffusion of ions.[156-158] One parameter that can be used to predict suspension stability is the zeta potential, which is defined as the electrical potential at the boundary between the diffuse layer and the bulk liquid. Solutions which have a high zeta potential (negative or positive) will generally exhibit more stability than the solutions which have a lower value.[159]

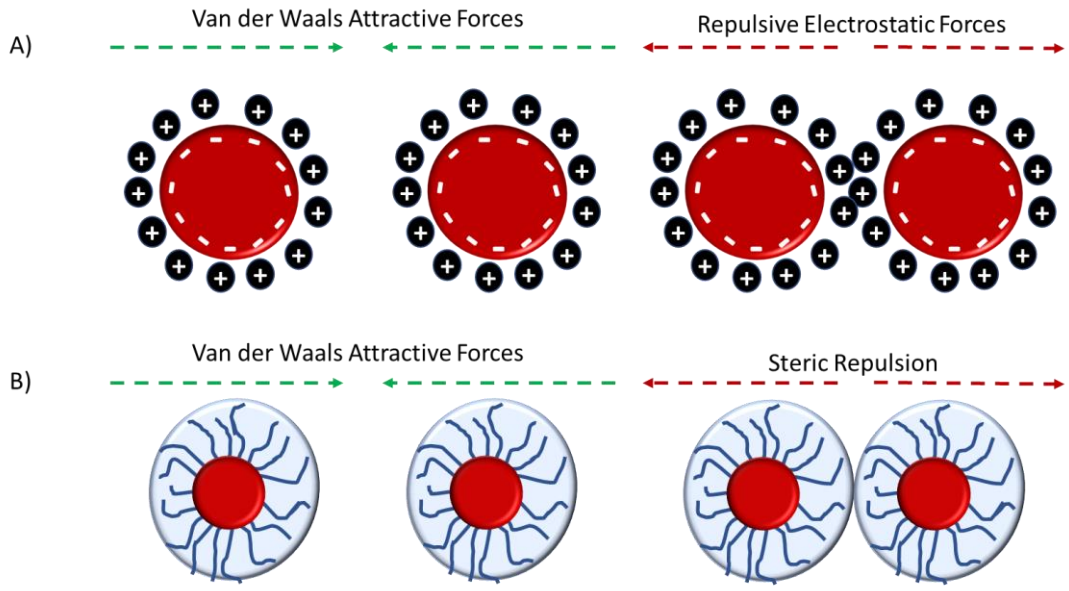


**Figure 1.7** Schematic representation of nanoparticle stabilisation mechanism *via* A) electrostatic repulsion between two cationic nanoparticles and B) steric repulsion caused through extended solvated polymer chains.

On the contrary, steric stabilisation is achieved by a solvation effect and the presence of a well solvated polymer chain on the particle surface (Figure 1.7B).[160] This can be attained by the incorporation of an amphiphilic copolymer into the formulation process or synthetic incorporation of an amphiphilic moiety within the polymer

species.[161, 162] Coagulation of particles is prevented through the unfavoured interactions of the solvated surface polymer chains as two particles approach each other.[163] These stabilising segments may interpenetrate, which can cause a compression to the surface polymer chains and a subsequent increase in osmotic pressure that ejects solvent molecules located within the inter-particulate space into the bulk medium.[164] This is thermodynamically unfavoured, since this would result in an increase in the Gibbs free energy of the system. This process is minimised when the bulk solvent is a good environment for that of the stabilising block. These extended solvated polymeric chains do not get within a close enough distance of each other to allow for the attractive VDW forces to act. Stabilisation *via* this mechanism offers some benefits which are of interest if the particles are intended for biomedical applications. A common stabilising segment used in such applications is polyethylene glycol (PEG); this polymer functionality has increased systemic circulation of nanoparticles within the blood stream by providing them with stealth properties, which will be discussed in more detail in Section 1.4. Rannard and co-workers have demonstrated the applicability and ease of the incorporation of PEG functionalities into nanoprecipitating polymers that were subsequently included within nanoprecipitations to produce sterically stabilised polymeric nanoparticles.[165-167] Consideration of the length, and subsequent surface density, of the stabilising block is something to be taken into consideration to ensure that particle-particle interactions are minimised through the steric barrier.[168]

### 1.4 Nanoparticles in the Body

When designing nanoparticles for use in drug delivery, it is important to acknowledge that the nanoparticles are faced with a variety of different physiological barriers as soon as they are administered. The success of a DDS will depend on how well it can overcome these barriers. The DDS must circulate within the body for an extended period of time to allow it to ultimately reach the site of therapeutic need. The journey of any IV administered DDS injected directly into the blood stream is the same as any foreign matter; however, it is their interactions with the cells within the body that differs and it is these interactions which can be the DDS's biggest limitation when considering drug delivery.[169]

The journey begins with the injection of the DDS directly into the blood, where the nanoparticles are immediately covered in biomolecules which can modify their size and physiochemical properties.[170] These molecules are adsorbed onto the external surface of the nanoparticles to form a corona; the composition of this corona will include proteins and other extracellular components, which will be discussed in further detail below. The DDS is then transported *via* venous networks to the heart, specifically into the right ventricle. From here, it will be pumped into the lungs where it will then enter pulmonary circulation. The capillaries that line the lungs are the smallest blood vessels within the body, approximately 2-13 μm in diameter, and act as the first initial sieving process for removing any foreign material from the blood stream; it is therefore the first hurdle a DDS must overcome. If the DDS is too large or rigid in nature, this will result in the DDS being sequestered in the lungs. If the DDS passes through it is then transported back to the heart, specifically the left ventricle, where it is then pumped into systemic circulation. Here, the DDS continues to face interactions with the different components of the blood.

Blood consists of leukocytes (white blood cells), erythrocytes (red blood cells), thrombocytes (platelets), and a solution of proteins and low molecular weight solutes commonly known as plasma. Typically, interactions between blood cells and DDS are minimal, as red blood cells and platelets exhibit a non-phagocytic nature and the defence mechanism of white blood cells will only be activated at the site of an injury. However, it is the proteins found in plasma that will interact with the DDS and it is the physicochemical properties of the DDS, specifically the particle size and surface functionality, that will determine to what extent these interactions occur.[14,171] These interactions, if significant, can subsequently influence the behaviour of the DDS within the body.

The plasma proteins form a dynamic corona on the particle surface and can increase or decrease the clearance of the DDS by the mononuclear phagocyte system (MPS) - the system responsible for the elimination of foreign material.[172, 173] This interaction of proteins with the surface of the DDS can either be minimised or exploited during the design of the nanocarrier.[173, 174] An example of using surface protein as an advantage is the use of the human albumin protein. Albumin is the most abundant

protein found in plasma and acts as a carrier for many different molecules whilst also regulating osmotic pressure.[175] Compared to other proteins, it exhibits a long half-life (~22 days) as it is protected from elimination by recognition from neonatal receptors, which ensure the reabsorption of the protein during liver filtration. The non-specific interactions of albumin and the surface of the DDS can be exploited to increase the circulatory time of a nanoparticle therapy.[176] However, since these interactions are transient, albumin can be displaced easily by proteins that have a higher affinity for the nanoparticle surface.[177] There have been studies that have physically adsorbed albumin to the surface of the DDS, but these show only a marginal increase in circulation time.[178]

DDS that have avoided clearance this far, and have therefore remained in systemic circulation, are now exposed to different filtration mechanisms within the kidney, liver and spleen, all of which are usually size dependent.[179]

The kidney is responsible for blood filtration and, in short, is made up of about a million filtering units called nephrons, which are comprised of a glomerular capillary network. Simplistically, this network has fenestrations present in their endothelium layer that are typically around 60-80 nm in size. The molecules that are able to pass through these gaps are passed into the tubule where they will either be reabsorbed into the blood or they will be excreted as waste in urine.[180] Molecules with larger sizes will not pass through these gaps and will subsequently remain in the blood unless there has been prior biodegradation.[181]

It is approximated that around 60-90% of nanomaterials are sequestered by the liver.[182] The liver receives the blood from the gut and brain *via* the portal and hepatic veins respectively, and it engages in numerous endocrine, metabolic and immunological functions. To enter these veins and subsequently the liver, blood circulates through a permeable discontinuous network known as the sinusoids, which have fenestrations present (100-150 nm).[183, 184] These sizes will typically allow for unrestricted passage of most plasma components, including most DDS, into the presinusoidal space. Within this space, there are hepatocytes that have multiple functions: protein synthesis, bile synthesis and many more.[185] One of the main

hepatocytic cell type present within the space is the Kupffer cell, which is responsible for phagocytotic behaviour within the liver.[186] Phagocytosis occurs between cells and DDS when there is recognition of opsonins on the particle surface. The macrophage will spread its cell membrane around the particle and engulf it. Once engulfed, the particle will be degraded by digestive proteins and the acidic internal environment that these cells possess. Following this process, the degradation products are released for excretion as waste. For DDS, this type of capture by the Kupffer cells needs to be minimised in order to sustain a long circulatory time and subsequent enhanced tumour accumulation. The most common synthetic strategy to minimise this is to coat the particle surface with an antifouling agent such as PEG or through manipulation of particle size and shape.[187, 188] An alternative study which sought to improve the delivery efficiency of DDS has investigated whether removal of the macrophage cells within the liver would increase the delivery efficiency of DDS to tumour sites. The results showed that the depletion of the macrophage cells in the liver increased the delivery efficiency from the median value of 0.7% to maximum value of 2%.[182]

In selected cases of anti-cancer treatments where the liver is the target organ, this large accumulation of DDS in the liver can be advantageous, enabling the pharmacological effects to be exerted provided the DDS is not engulfed by the phagocytes.[189]

It is commonly thought that the spleen does not play a role in the clearance of classical drug molecules, but instead its physiological roles are: removal of old blood cells, immunological surveillance and the regulation of blood volume.[189, 190] However, this perspective has changed since the development of nanomaterials for drug delivery, with the current understanding that the spleen is actually accountable for taking up approximately 2 – 20% of DDS from the blood stream. [189] This is likely due to the increased size of nanoparticles and their complex chemical structures (compared to classical drug molecules) triggering the physiological response of the spleen.

This therefore highlights the additional physicochemical responses that need to be accounted for when designing DDS, and the parameters that need to be considered to achieve accumulation within different tumour sites.

### 1.4.1 Design Considerations for Nanoparticles in the Body

When designing nanoparticles for drug delivery purposes, it is important to take into consideration how a nanoparticle behaves when administered into systemic circulation and how the nanoparticle will behave in a physiological environment. The physicochemical properties of a nanoparticle determine the immediate pharmacological response and the pharmacokinetics observed. These physiological barriers are typically the main limiting factor for the efficacy of nanoparticles.[191, 192] A number of parameters must be considered when generating polymer materials intended for drug delivery, all of which will collectively contribute to the action and fate of the nanoparticle within the body (Figure 1.8).

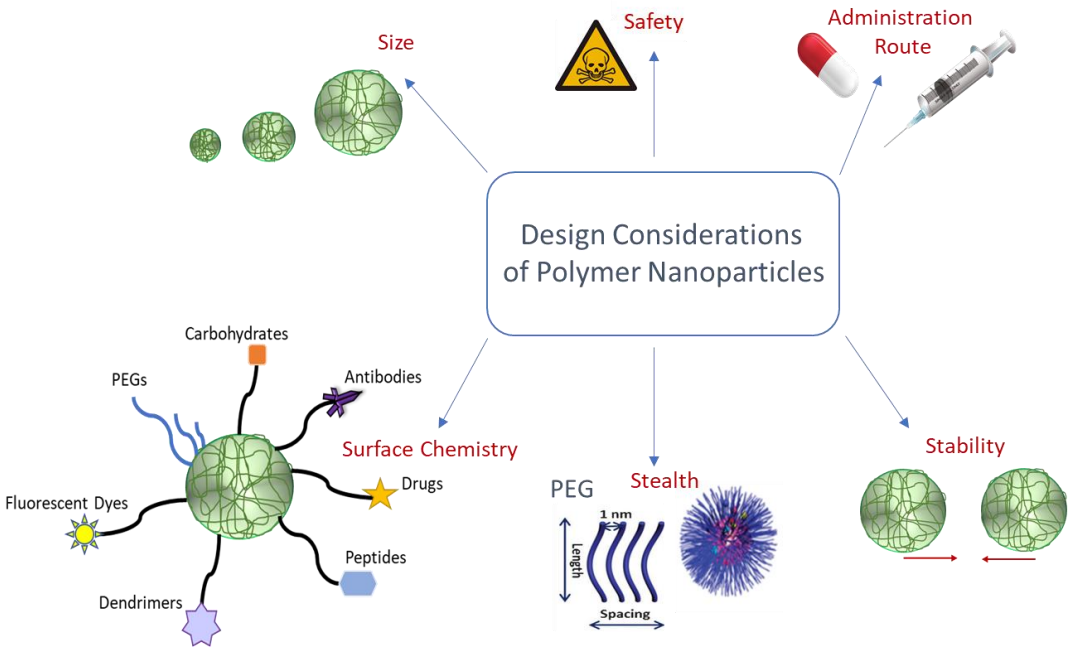


**Figure 1.8** A schematic summary of the design considerations of the properties of polymeric nanoparticles. *Information from ref*[193].

Firstly, the most important parameter to consider is whether the polymer is deemed "safe" for such an application. To determine this, toxicology studies would need to be performed to assess the suitability of the bulk material with respect to the possible detrimental effects it could have on the body. Additionally, it is also important to consider the materials suitability in a physiological environment and to

understand the potential detrimental or beneficial effects it may have, which is often thought of as a materials biocompatibility. These two observations lead to the understanding of the materials safety.[194]

Secondly, consideration must also be given to the route of administration and the different physiological barriers that each present. As previously mentioned, the primary administrative route of chemotherapeutics is *via* IV injection. This is advantageous when designing drug nanocarriers as it avoids the complex issues often associated with oral dosing. These often refer to how the nanocarrier will enter the systemic circulation and whether its structural integrity will remain intact upon administration after being subjected to the harsh acidic environment of the GI tract. IV administration is the most efficient and reproducible route of administration but it does present different obstacles and negative side effects compared to oral dosing. These include pulmonary complications, thrombophlebitis and infection risks.[195]

One of the primary obstacles to overcome in the delivery of nanoparticles is to prevent their premature removal from systemic circulation, whilst maintaining stability within blood and ensuring optimum biodistribution and bioavailability. The size, shape, charge and surface functionality of nanoparticles can all contribute to the fate of the nanoparticle. Polymeric nanoparticles can be modified to circumvent some of these challenges.

#### 1.4.1.1 Nanoparticle Size

When designing polymeric nanoparticles for applications in drug delivery, there really isn't a 'one size fits all' approach that can be adopted; instead, the intended use and the delivery target should be carefully considered. It has been reported previously that nanoparticles designed for use in cancer treatments should have particle sizes between 70 – 200 nm.[115, 193] If the particles are too small (< 30 nm) they will be cleared rapidly by the renal system,[196] too large and the particles will be taken up by the MPS.[197] The liver and spleen will often accumulate nanoparticles that are between 150-300 nm, whilst particles below 150 nm will generally locate in the heart, kidney, stomach and bone marrow.[198] Hobbs *et al* determined that most tumours have a characteristic pore cut-off size between 380 and 780 nm.[199]

### 1.4.1.2 Charge of Nanoparticle

The charge exhibited by the surface of nanoparticles can influence: (1) the degree of opsonisation, (2) the degree of particle stability in biological media, and (3) the degree of cytotoxicity.[200] Particles of high charge, negative or positive, will promote protein adsorption and therefore increase the particle's recognition and subsequent clearance by the MPS.[115, 201] The magnitude of charge can also determine how stable the nanoparticles are when exposed to various ions and proteins present in biological media. [165]

Particles of positive charge typically exhibit high levels of toxicity and have demonstrated deleterious effects when administered *in vivo*, since their ability to rupture cells is enhanced due to the electrostatic attractions between the particles and the negatively charged cell membranes.[202] Particles which display negative surface charge are generally less toxic and have shown decreased recognition and subsequent clearance by the MPS when compared to positively charged particles. This is due to their repulsion from the negatively charged cell membranes.[203, 204] Although, other studies have suggested that this is model-dependent: when negatively charged formulations were administered to rats rather than mice, little increase in circulatory time was observed compared to formulations of neutral charge.[205, 206] The administration of particles with neutral charge have shown minimal interactions within the body. [207]

### 1.4.2 Incorporating Stealth Properties

Drug containing nanoparticles must circulate within the blood stream for as long as possible if they are to deliver adequate concentrations of therapeutic payloads to tumour tissue. Once in the blood stream, however, opsonin proteins can bind to the surface of the nanoparticles, allowing immune recognition and subsequently trigger clearance from the body by various different mechanisms.[73] The macrophages involved with this process of removal have the capabilities to remove nanoparticles from the bloodstream within minutes of administration, thus rendering them ineffective with regard to drug delivery.[208] One method to overcome this rapid clearance is to incorporate an inert polymer on to the surface of the nanoparticle, which will aid in resisting or preventing interactions with components of the blood

and therefore help to avoid immune recognition. There are several different polymers that have been used for this purpose: poly(acrylic acid)[209], poly(vinyl alcohol) and polysaccharides.[210] However, the most widely used polymer to impart stealth properties onto nanoparticles is PEG and is termed PEGylation.[208, 211-213] This hydrophilic polymer contains subunits which are capable of forming tight associations with water molecules, creating a hydrating layer that prevents protein adsorption on the surface of the nanoparticle, therefore reducing the recognition by the MPS.[214] This was demonstrated for the first time when PEG was covalently attached to bovine serum albumin, resulting in an increase in circulation time due to a lack of an immunological response.[213] Additionally, incorporation of PEG chains within the nanomaterial whilst increasing circulation time, can also help to provide steric stabilisation to the particles and prevent aggregation, as described in Section 1.3.2.4. The PEG chains at the surface help to form a sterically hindering layer to stabilise the surface charge exhibited by charged nanoparticles and providing stability.[73]

There are different factors that can influence the circulation time of PEGylated nanoparticles, one of which is the chain length of the PEG chains. In a study of PEGylated micelles, it was found that an increase in circulation time *in vivo* was observed as the MW of the PEG was increased (from 2 to 20 kg $mol^{-1}$).[215] Likewise, when liposomes were PEGylated with PEG of MW 5 kg $mol^{-1}$, a prolonged blood circulation and reduced clearance was observed when compared to the non-PEGylated and liposomes bearing PEG with an MW = 750 g $mol^{-1}$; the latter behaved almost identically to the liposomes without PEG.[216] Whilst modification of a liposome surface with PEG is known to increase circulation time by reducing the opsonisation clearance and increase accumulation within tumours *via* the EPR effect, it has been demonstrated that it can inhibit cellular uptake capabilities and reduce endosomal escape - this is known as the PEG dilemma.[217-219] In addition to this, the dense PEGylated shell may also prevent targeting ligands on the nanoparticle surface from binding to the desired receptor. This dilemma means that a balance is required between having a long enough PEG chain present to reduce opsonisation and increase circulatory time for the nanoparticle to accumulate, whilst also ensuring the

chain is not too long that the cellular uptake is impacted. Synthetically, there are strategies for overcoming this dilemma, but generally the most utilised is designing a cleavable PEG linker.[217]

Despite the early literature reports suggesting that all these strategies discussed to improve the fate of nanoparticles in the body were shown to be very promising strategies at overcoming some of the described problems.[220] Progress has somewhat stalled in the development of clinically relevant materials and paradoxically, the upsurge in published papers does not compliment with therapeutic advances.[121, 221, 222] This is likely due to the fact that the pathophysiological and physiological interactions between nanoparticles and biological systems are somewhat complex and often unique between patients, thereby hindering the clinical translation. Simple chemical modifications that can be made to the nanoparticles seem to offer easy ways to strategically overcome the bodies response systems, and when investigated in animal models, most will show potential.[223] However, it is typical that when these systems are extended to human models, they will fail because our understanding of how the body actually responds to nanoparticles is somewhat still in its infancy. An interesting article eloquently summarised that the clinical success of nanoparticles is limited by: 1) the biobarriers, 2) fate at the disease site, and 3) safety issues.[222]

**1.5 Research Hypothesis**

For the successful treatment of cancer, chemotherapeutic agents need to be delivered in a safe and effective manner but as previously discussed there are still some challenges associated with the delivery of these potent, hydrophobic molecules. It has been shown that the use of nanocarriers offers the opportunity to encapsulate and deliver these drugs in aqueous media. The use of DDS also provides opportunities to nano-formulate drugs which previously have had to be administered in a prodrug formulation to overcome insolubility issues. Of interest in this thesis is SN-38, which is the active metabolite of irinotecan administered for the treatment of CRC. Research has shown that high molecular weight branched hydrophobic polymers can be utilised to generate nanoprecipitate nanocarriers. This branched material has numerous chemical modification options. It is hypothesised that nanocarriers can be produced and optimised for encapsulation and delivery of SN-38

through the manipulation of the chemical structure of this branched material and subsequent polymer-drug interactions of the nanoparticles.

### 1.5.1 Project Aim

The aim of the research presented within this thesis is to investigate and optimise the encapsulation of the anti-cancer drug SN-38, within a novel polymeric based drug delivery platform and assess its applicability as a biologically relevant pharmaceutical candidate (Figure 1.9).

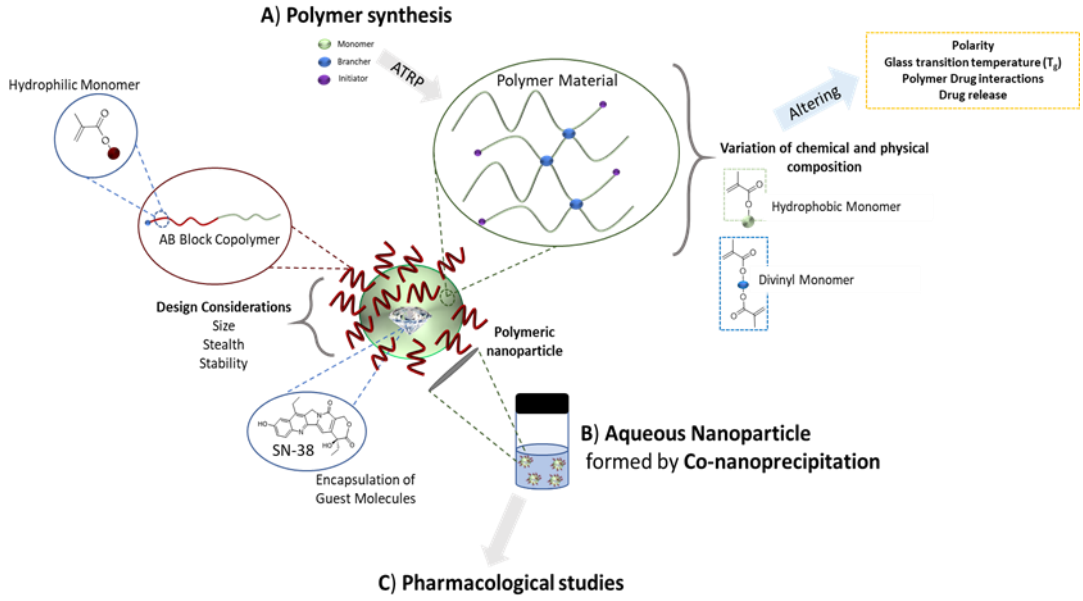


**Figure 1.9** Schematic representation of the aims of this research project. Highlighting the formation of SN-38 loaded polymeric nanoparticles formed *via* co-nanoprecipitation of AB block and branched copolymers indicating the various different modifications that can be made.

Building from previous reports, it is proposed that by combining highly branched, high molecular weight methacrylate-based copolymers and amphiphilic AB block copolymers, sterically stabilised polymeric nanoparticles can be generated *via* co-nanoprecipitation. Thereby, presenting opportunity for the potential encapsulation and delivery of guest molecules, such as therapeutic agents. [165-167, 224, 225] Methanolic ATRP, a proven robust synthetic strategy, will be utilised to generate a large library of polymeric materials including, linear homo and statistical copolymers, statistical branched and AB block copolymers. The chemical compositions of these materials will be varied through the incorporation of different monomer, divinyl monomer and initiator chemistries (Figure 1.9A). The effects of these chemical alterations on the polymers physical properties such as, polarity and glass transition temperature will

also be studied. Nanoprecipitation and co-nanoprecipitation studies will then follow the successful synthesis of this broad range of polymer materials (Figure 1.9B). Co-nanoprecipitation presents an opportunity to generate sterically stabilised nanoparticles under controlled conditions through the addition of an AB block copolymer. Previously, this steric stabilisation has been achieved through the incorporation of an AB block copolymer which possessed complimentary chemistry on the B block to the branched methacrylate polymer. However, the aim here is to investigate the effects on nanoparticle formation when the chemistry of the B Block on the AB block copolymer is varied. Additionally, variance in the nanoparticles' composition of branched polymer: AB block copolymer ratio, will also be explored to determine the optimum ratio to achieve steric stabilisation. Given the intended application for these nanoparticles their stability *in vitro* is essential for pharmacological assessment; therefore, to mimic physiological conditions nanoparticles stability to PBS addition will also be tested.

The ultimate aim of the nanoparticles is to encapsulate the hydrophobic anti-cancer drug SN-38. Given, the role of an additional hydrophobic guest within the co-nanoprecipitation has not been explored, SN-38 will be included in all polymer co-nanoprecipitate regimes to determine whether it has any influence on the outcome. The evaluation of drug loading capacity and efficiency will be assessed for the successful drug loaded nanoparticles. It is anticipated that the different physical properties of the polymers, imparted through chemical variance during synthesis, will in turn effect polymer-drug interactions. These differing interactions and the relationship between the physical properties of the polymers and its effects on drug loading and release rates will be explored *via* radiometric release experiments.

Promising candidates of stable SN-38 loaded polymer nanoparticles will have their pharmacological behaviour explored *in vitro* and *in vivo* to determine their potential and suitability as a CRC treatment (Figure 1.9C). The PhD is funded by Cancer Research UK and sees the collaboration between the Departments of Chemistry and Molecular & Clinical Pharmacology at the University of Liverpool.

## 1.6 References


1. National Cancer Institute, https://www.cancer.gov/publications/dictionaries/cancer-terms/def/cancer, (accessed Sept 2020).
2. World Health Organisation, Health topics - Cancer https://www.who.int/health-topics/cancer#tab=tab_1, (accessed 12/03/2020).
3. Cancer Research UK, *Cancer incidence for common cancers*, https://www.cancerresearchuk.org/health-professional/cancer-statistics/incidence/common-cancers-compared#heading-Zero, (accessed 13/03/2020).
4. *Cancer in the UK 2019*, Cancer Research UK, 2019.
5. Cancer Research UK, *Cancer Research UK's proposals for the NHS 10-year plan*, 2018.
6. M. P. Coleman, D. Forman, H. Bryant, J. Butler, B. Rachet, C. Maringe, U. Nur, E. Tracey, M. Coory, J. Hatcher, C. E. McGahan, D. Turner, L. Marrett, M. L. Gjerstorff, T. B. Johannesen, J. Adolfsson, M. Lambe, G. Lawrence, D. Meechan, E. J. Morris, R. Middleton, J. Steward, M. A. Richards and I. M. W. Group, *Lancet*, 2011, **377**, 127-138.
7. National Audit Office, NHS England and Public Health England, Department of Health, *Progress in improving cancer services and outcomes in England*, 2015.
8. Department of Health, *Improving Outcomes: A Strategy for Cancer* 2011.
9. Macmillan Cancer Support, *Statistics fact sheet*, 2019.
10. Bowel Cancer UK, https://www.bowelcanceruk.org.uk/about-bowel-cancer/bowel-cancer/, (accessed 13/03/2020).
11. World Cancer Research Fund, Colorectal cancer statistics, https://www.wcrf.org/dietandcancer/cancer-trends/colorectal-cancer-statistics, (accessed 13/03/2020).
12. M. Arnold, M. S. Sierra, M. Laversanne, I. Soerjomataram, A. Jemal and F. Bray, *Gut*, 2017, **66**, 683-691.
13. Cancer Research UK, Bowel Cancer Statistics https://www.cancerresearchuk.org/health-professional/cancer-statistics/statistics-by-cancer-type/bowel-cancer#heading-Zero, (accessed 13/03/2020).
14. T. Cedervall, I. Lynch, M. Foy, T. Berggård, S. C. Donnelly, G. Cagney, S. Linse and K. A. Dawson, *Angewandte Chemie International Edition*, 2007, **46**, 5754-5756.
15. Cancer Research UK, https://www.cancerresearchuk.org/health-professional/cancer-statistics/statistics-by-cancer-type/bowel-cancer#heading-Four, (accessed Sept 2020).
16. F. A. Khan, S. S. Akhtar and M. K. Sheikh, *The Malaysian journal of medical sciences,* 2005, **12**, 3.
17. F. M. Balis, *The oncologist*, 1998, **3**, 373-389.
18. M. Arruebo, N. Vilaboa, B. Sáez-Gutierrez, J. Lambea, A. Tres, M. Valladares and A. González-Fernández, *Cancers (Basel)*, 2011, **3**, 3279-3330.
19. National Cancer Institue, Cancer Treatment, https://www.cancer.gov/about-cancer/treatment, (accessed 12/03/2020).
20. ChemoCare, Cancer Cells and Chemotherapy, http://chemocare.com/chemotherapy/what-is-chemotherapy/cancer-cells-chemotherapy.aspx, (accessed 13/03/2020).
21. ChemoCare, How is chemotherapy given?, http://chemocare.com/chemotherapy/what-is-chemotherapy/how-chemotherapy-is-given.aspx, (accessed 13/03/2020).
22 Cancer Chemotherapy, https://alteredstatesinstructions.com/ZAPPERS/Super%20Sweep%20Function%20Zapper/Cancer%20Chemotherapy.pdf, (accessed April 2020).
23. X. Kang, H.-H. Xiao, H.-Q. Song, X.-B. Jing, L.-S. Yan and R.-G. Qi, *Cancer Biology & Medicine*, 2015, **12**, 362-374.
24. J. I. Hare, T. Lammers, M. B. Ashford, S. Puri, G. Storm and S. T. Barry, *Advanced Drug Delivery Reviews*, 2017, **108**, 25-38.
25. M. S. Braun and M. T. Seymour, *Theraputic Advances Medical Oncology*, 2011, **3**, 43-52.
26. Bowel Cancer UK, Chemotherapy, https://www.bowelcanceruk.org.uk/about-bowel-cancer/treatment/chemotherapy/, (accessed 13/03/2020).
27. D. Cunningham, S. Pyrhönen, R. D. James, C. J. Punt, T. F. Hickish, R. Heikkila, T. B. Johannesen, H. Starkhammar, C. A. Topham, L. Awad, C. Jacques and P. Herait, *The Lancet*, 1998, **352**, 1413-1418.

28. F. Kanzawa, Y. Sugimoto, K. Minato, K. Kasahara, M. Bungo, K. Nakagawa, Y. Fujiwara, L. F. Liu and N. Saijo, *Cancer Research*, 1990, **50**, 5919-5924.
29. Y. Kawato, M. Aonuma, Y. Hirota, H. Kuga and K. Sato, *Cancer Research*, 1991, **51**, 4187-4191.
30. M. Shingyoji, Y. Takiguchi, R. Watanabe-Uruma, Y. Asaka-Amano, H. Matsubara, K. Kurosu, Y. Kasahara, N. Tanabe, K. Tatsumi and T. Kuriyama, *Cancer Science*, 2004, **95**, 537-540.
31. R. Oun, Y. E. Moussa and N. J. Wheate, *Dalton Transactions*, 2018, **47**, 6645-6653.
32. P. Lu, *Seminars in Nuclear Medicine*, 2005, **35**, 197-201.
33. H. L. Wong, R. Bendayan, A. M. Rauth, Y. Li and X. Y. Wu, *Advanced Drug Delivery Reviews*, 2007, **59**, 491-504.
34. K. T. Savjani, A. K. Gajjar and J. K. Savjani, *ISRN Pharmacology*, 2012, **2012**, 195727-195727.
35. M. Narvekar, H. Y. Xue, J. Y. Eoh and H. L. Wong, *AAPS PharmSciTech*, 2014, **15**, 822-833.
36. Y. He, S. E. Tabibi and S. H. Yalkowsky, *Journal of Pharmaceutical Sciences*, 2006, **95**, 97-107.
37. W. J. Loos, J. Szebeni, A. J. ten Tije, J. Verweij, D. M. van Zomeren, K. Chung, K. Nooter, G. Stoter and A. Sparreboom, *Anti-Cancer Drugs*, 2002, **13**, 767-775.
38. R. Chadha, V. Kapoor, D. Thakur, R. Kaur, P. Arora and D. Jain,*Journal of Scientific & Industrial Research,* 2008,**67**,185-197.
39. J. E. Kipp, *International Journal of Pharmaceutics*, 2004, **284**, 109-122.
40. S. Parveen, R. Misra and S. K. Sahoo, *Nanomedicine*, 2012, **8**, 147-166.
41. J. W. Scannell and J. Bosley, *PLOS ONE*, 2016, **11**, e0147215.
42. British Society of Nanomedicine, *What is Nanomedicine,* https://www.britishsocietynanomedicine.org/what-is-nanomedicine/, (accessed 12/03/2020).
43. H. F. Tibbals, in *Medical Nanotechnology and Nanomedicine*,Taylor and Francis Group, 2017.
44. M. Krukemeyer, V. Krenn, F. Huebner, W. Wagner and R. Resch, *Journal of Nanomedicine & Nanotechnology*, 2015, **6**, 336.
45. M. Kumar Teli, S. Mutalik and G. Rajanikant, *Current Pharmaceutical Design*, 2010, **16**, 1882-1892.
46. M. L. Etheridge, S. A. Campbell, A. G. Erdman, C. L. Haynes, S. M. Wolf and J. McCullough, *Nanomedicine: Nanotechnology, Biology and Medicine*, 2013, **9**, 1-14.
47. K. K. Jain, *Clinica chimica acta*, 2005, **358**, 37-54.
48. S. A. Wickline and G. M. Lanza, in *Applications of Nanotechnology to Atherosclerosis Thrombosis and Vascular Biology*, 2003,1092-5.
49. L. Salvioni, M. A. Rizzuto, J. A. Bertolini, L. Pandolfi, M. Colombo and D. Prosperi, *Cancers (Basel)*, 2019, **11**, 1855.
50. F. Mottaghitalab, M. Farokhi, Y. Fatahi, F. Atyabi and R. Dinarvand, *Journal of Controlled Release*, 2019, **295**, 250-267.
51. S. Tran, P.-J. DeGiovanni, B. Piel and P. Rai, *Clinical and Translational Medicine*, 2017, **6**, 44-44.
52. S. Rannard and A. Owen, *Nano Today*, 2009, **4**, 382-384.
53. National Institue of Biomedical Imaging and Bioengineering, Drug Delivery Systems, https://www.nibib.nih.gov/science-education/science-topics/drug-delivery-systems-getting-drugs-their-targets-controlled-manner (accessed Sept 2020).
54. A. Wicki, D. Witzigmann, V. Balasubramanian and J. Huwyler, *Journal of controlled release*, 2015, **200**, 138-157.
55. P. Curley, N. J. Liptrott and A. Owen, *Future Science*, 2017, **4**, FSO230.
56. M. Bahadori and F. Mohammadi, *Tanaffos*, 2012, **11**, 18-22.
57. M. Gregori, M. Masserini and S. Mancini, *Nanomedicine*, 2015, **10**, 1203-1218.
58. O. Veiseh, B. C. Tang, K. A. Whitehead, D. G. Anderson and R. Langer, *Nature reviews. Drug discovery*, 2015, **14**, 45-57.
59. S. Senapati, A. K. Mahanta, S. Kumar and P. Maiti, *Signal Transduction and Targeted Therapy*, 2018, **3**, 7.
60. A. Z. Wilczewska, K. Niemirowicz, K. H. Markiewicz and H. Car, *Pharmacological Reports*, 2012, **64**, 1020-1037.
61. K. Werengowska-Ciećwierz, M. Wiśniewski, A. P. Terzyk and S. Furmaniak, *Advances in Condensed Matter Physics*, 2015, **2015**.
62. N. Kamaly, Z. Xiao, P. M. Valencia, A. F. Radovic-Moreno and O. C. Farokhzad, *Chemical Society Reviews*, 2012, **41**, 2971-3010.

63. M. Vallet-Regí, M. Colilla, I. Izquierdo-Barba and M. Manzano, *Molecules (Basel, Switzerland)*, 2017, **23**, 47.
64. B. García-Pinel, C. Porras-Alcalá, A. Ortega-Rodríguez, F. Sarabia, J. Prados, C. Melguizo and J. M. López-Romero, *Nanomaterials (Basel)*, 2019, **9**, 638.
65. W. B. Liechty, D. R. Kryscio, B. V. Slaughter and N. A. Peppas, *Annual Review of Chemical and Biomolecular Engineering*, 2010, **1**, 149-173.
66. E. L. Sievers and P. D. Senter, *Annual Review of Medicine*, 2013, **64**, 15-29.
67. F. Greco and M. J. Vicent, *Advanced Drug Delivery Reviews*, 2009, **61**, 1203-1213.
68. M. Thanou and R. Duncan, *Current opinion in investigational drugs (London, England: 2000)*, 2003, **4**, 701-709.
69. S. Tran, P.-J. DeGiovanni, B. P. Piel and P. Rai, *Clinical and Translational Medicine*, 2017, **6**, 44.
70. W. Gao, C.-M. J. Hu, R. H. Fang and L. Zhang, *Journal of Materials Chemistry B*, 2013, **1**, 6569-6585.
71. A. D. Bangham, *Annual Review of Biochemistry*, 1972, **41**, 753-776.
72. T. L. Doane and C. Burda, *Chemical Society Reviews*, 2012, **41**, 2885-2911.
73. J. S. Suk, Q. Xu, N. Kim, J. Hanes and L. M. Ensign, *Advanced drug delivery reviews*, 2016, **99**, 28-51.
74. A. Akbarzadeh, R. Rezaei-Sadabady, S. Davaran, S. W. Joo, N. Zarghami, Y. Hanifehpour, M. Samiei, M. Kouhi and K. Nejati-Koshki, *Nanoscale Research Letters*, 2013, **8**, 102-102.
75. B. Uziely, S. Jeffers, R. Isacson, K. Kutsch, D. Wei-Tsao, Z. Yehoshua, E. Libson, F. M. Muggia and A. Gabizon, *Journal of Clinical Oncology*, 1995, **13**, 1777-1785.
76. U. Bulbake, S. Doppalapudi, N. Kommineni and W. Khan, *Pharmaceutics*, 2017, **9**, 12.
77. T. C. Chang, H. S. Shiah, C. H. Yang, K. H. Yeh, A. L. Cheng, B. N. Shen, Y. W. Wang, C. G. Yeh, N. J. Chiang, J. Y. Chang and L. T. Chen, *Cancer Chemother Pharmacolgy*, 2015, **75**, 579-586.
78. A. J. Ocean, D. Niedzwiecki, J. N. Atkins, B. Parker, B. H. O'Neil, J. W. Lee, S. Wadler and R. M. Goldberg, *Journal of Clinical Oncology*, 2008, **26**, 4109-4109.
79. Outsourcing pharma, https://www.outsourcing-pharma.com/Article/2007/04/04/Neopharm-faces-uncertain-future-after-lacklustre-trial-results (Accessed Jan 2021)
80. P. Ghasemiyeh and S. Mohammadi-Samani, *Research in Pharmaceutical Science*, 2018, **13**, 288-303.
81. N. Mosallaei, A. Mahmoudi, H. Ghandehari, V. K. Yellepeddi, M. R. Jaafari and B. Malaekeh-Nikouei, *European Journal of Pharmaceutics and Biopharmaceutics*, 2016, **104**, 42-50.
82. Y. Mai and A. Eisenberg, *Chemical Society Reviews*, 2012, **41**, 5969-5985.
83. Y. Lu and K. Park, *International journal of pharmaceutics*, 2013, **453**, 198-214.
84. H. Cabral, K. Miyata, K. Osada and K. Kataoka, *Chemical Reviews*, 2018, **118**, 6844-6892.
85. D. W. Kim, S. Y. Kim, H. K. Kim, S. W. Kim, S. W. Shin, J. S. Kim, K. Park, M. Y. Lee and D. S. Heo, *Annals of Oncology*, 2007, **18**, 2009-2014.
86. N. A. N. Hanafy, M. El-Kemary and S. Leporatti, *Cancers (Basel)*, 2018, **10**, 238.
87. S. Danson, D. Ferry, V. Alakhov, J. Margison, D. Kerr, D. Jowle, M. Brampton, G. Halbert and M. Ranson, *British Journal of Cancer*, 2004, **90**, 2085-2091.
88. S. C. Owen, D. P. Y. Chan and M. S. Shoichet, *Nano Today*, 2012, **7**, 53-65.
89. H. Cabral and K. Kataoka, *Journal of Controlled Release*, 2014, **190**, 465-476.
90. H. Zhang, D. Wang, R. Butler, N. L. Campbell, J. Long, B. Tan, D. J. Duncalf, A. J. Foster, A. Hopkinson, D. Taylor, D. Angus, A. I. Cooper and S. P. Rannard, *Nature Nanotechnology*, 2008, **3**, 506-511.
91. U. Wais, A. W. Jackson, T. He and H. Zhang, *Nanoscale*, 2016, **8**, 1746-1769.
92. L. M. Tatham, S. P. Rannard and A. Owen, *Therapeutic Delivery*, 2015, **6**, 469-490.
93. H. Zhang, D. Wang, R. Butler, N. L. Campbell, J. Long, B. Tan, D. J. Duncalf, A. J. Foster, A. Hopkinson and D. Taylor, *Nature Nanotechnology*, 2008, **3**, 506.
94. U. Wais, A. W. Jackson, Y. Zuo, Y. Xiang, T. He and H. Zhang, *Journal of Controlled Release*, 2016, **222**, 141-150.
95. R. RoSièRe, M. Gelbcke, V. Mathieu, P. Van Antwerpen, K. Amighi and N. Wauthoz, *International journal of oncology*, 2015, **47**, 1131-1142.
96. K. Tomoda, T. Ohkoshi, K. Hirota, G. S. Sonavane, T. Nakajima, H. Terada, M. Komuro, K. Kitazato and K. Makino, *Colloids and Surfaces B: Biointerfaces*, 2009, **71**, 177-182.

97. D. K. Jensen, L. B. Jensen, S. Koocheki, L. Bengtson, D. Cun, H. M. Nielsen and C. Foged, *Journal of Controlled Release*, 2012, **157**, 141-148.
98. L. M. Tatham, A. C. Savage, A. Dwyer, M. Siccardi, T. Scott, M. Vourvahis, A. Clark, S. P. Rannard and A. Owen, *European Journal of Pharmaceutics and Biopharmaceutics*, 2019, **138**, 92-98.
99. R. P. Bakshi, L. M. Tatham, A. C. Savage, A. K. Tripathi, G. Mlambo, M. M. Ippolito, E. Nenortas, S. P. Rannard, A. Owen and T. A. Shapiro, *Nature Communications*, 2018, **9**, 315.
100. T. O. McDonald, M. Giardiello, P. Martin, M. Siccardi, N. J. Liptrott, D. Smith, P. Roberts, P. Curley, A. Schipani, S. H. Khoo, J. Long, A. J. Foster, S. P. Rannard and A. Owen, *Advanced Healthcare Materials*, 2014, **3**, 400-411.
101. J. J. Hobson, A. Al-khouja, P. Curley, D. Meyers, C. Flexner, M. Siccardi, A. Owen, C. F. Meyers and S. P. Rannard, *Nature Communications*, 2019, **10**, 1413.
102. R. Goldacre and B. Sylven, *Nature*, 1959, **184**, 63-64.
103. L. Owen, *Nature*, 1960, **187**, 795-796.
104. R. J. Goldacre and B. Sylven, *British journal of cancer*, 1962, **16**, 306-322.
105. Y. Matsumura and H. Maeda, *Cancer Research*, 1986, **46**, 6387-6392.
106. H. Kobayashi, R. Watanabe and P. L. Choyke, *Theranostics*, 2013, **4**, 81-89.
107. F. Yuan, M. Dellian, D. Fukumura, M. Leunig, D. A. Berk, V. P. Torchilin and R. K. Jain, *Cancer Research*, 1995, **55**, 3752.
108. Y. Nakamura, A. Mochida, P. L. Choyke and H. Kobayashi, *Bioconjugate Chemistry*, 2016, **27**, 2225-2238.
109. D. Luo, K. A. Carter and J. F. Lovell, *Wiley Interdisciplinary Reviews: Nanomedicine and Nanobiotechnology*, 2015, **7**, 169-188.
110. U. Prabhakar, H. Maeda, R. K. Jain, E. M. Sevick-Muraca, W. Zamboni, O. C. Farokhzad, S. T. Barry, A. Gabizon, P. Grodzinski and D. C. Blakey, *Cancer Research*, 2013, **8**, 2412-2417
111. H. Nakamura, F. Jun and H. Maeda, *Expert opinion on drug delivery*, 2015, **12**, 53-64.
112. J. W. Nichols and Y. H. Bae, *Journal of Controlled Release*, 2014, **190**, 451-464.
113. T. M. Allen and P. R. Cullis, *Science*, 2004, **303**, 1818-1822.
114. D. Peer, J. M. Karp, S. Hong, O. C. Farokhzad, R. Margalit and R. Langer, *Nature Nanotechnology*, 2007, **2**, 751-760.
115. M. E. Davis, Z. Chen and D. M. Shin, *Nature Reviews Drug Discovery*, 2008, **7**, 771-782.
116. T. Lammers, W. E. Hennink and G. Storm, *British Journal of Cancer*, 2008, **99**, 392-397.
117. R. K. Jain and T. Stylianopoulos, *Nature Reviews Clinical Oncology*, 2010, **7**, 653-664.
118. R. van der Meel, T. Lammers and W. E. Hennink, *Expert opinon on Drug Delivery*, 2017,**14**, 1-5.
119. S. K. Golombek, J.-N. May, B. Theek, L. Appold, N. Drude, F. Kiessling and T. Lammers, *Advanced drug delivery reviews*, 2018, **130**, 17-38.
120. M. E. O'Brien, N. Wigler, M. Inbar, R. Rosso, E. Grischke, A. Santoro, R. Catane, D. G. Kieback, P. Tomczak, S. P. Ackland, F. Orlandi, L. Mellars, L. Alland and C. Tendler, *Annals of Oncology*, 2004, **15**, 440-449.
121. T. Lammers, F. Kiessling, W. E. Hennink and G. Storm, *Journal of Controlled Release*, 2012, **161**, 175-187.
122. T. Lammers, P. Peschke, R. Kühnlein, V. Subr, K. Ulbrich, J. Debus, P. Huber, W. Hennink and G. Storm, *Journal of Controlled Release*, 2007, **117**, 333-341.
123. S. Wilhelm, A. J. Tavares, Q. Dai, S. Ohta, J. Audet, H. F. Dvorak and W. C. Chan, *Nature reviews materials*, 2016, **1**, 1-12.
124. L. E. van Vlerken, Z. Duan, S. R. Little, M. V. Seiden and M. M. Amiji, *Molecular Pharmaceutics*, 2008, **5**, 516-526.
125. Y. Zhong, F. Meng, C. Deng and Z. Zhong, *Biomacromolecules*, 2014, **15**, 1955-1969.
126. X. Jin, L. Zhu, B. Xue, X. Zhu and D. Yan, *National Science Review*, 2019, **6**, 1128-1137.
127. C. J. Martínez Rivas, M. Tarhini, W. Badri, K. Miladi, H. Greige-Gerges, Q. A. Nazari, S. A. Galindo Rodríguez, R. Román, H. Fessi and A. Elaissari, *Inter national Journal of Pharmaceutics*, 2017, **532**, 66-81.
128. A. Minost, J. Delaveau, M. A. Bolzinger, H. Fessi and A. Elaissari, *Recent Patents on Drug Delivery & Formulation*, 2012, **6**, 250-258.
129. S. Schubert, J. J. T. Delaney and U. S. Schubert, *Soft Matter*, 2011, **7**, 1581-1588.
130. G. A. Engelhard (1860), 00027540.

131. J. W. Hyatt and I. S. Hyatt, 1874, 00156354.
132. D. M. Lamb, 1877, 00196677.
133. E. A. Wallendahl, 1888, 00389875.
134. H. Fessi, F. Puisieux, J. P. Devissaguet, N. Ammoury and S. Benita, *International Journal of Pharmaceutics*, 1989, **55**, R1-R4.
135. H. Fessi, J.P Devissaguet, F. Puisiuex, C. Thies, 1992, US Patent: 593 522, 1992.
136. D. Lemoine, C. Francois, F. Kedzierewicz, V. Preat, M. Hoffman and P. Maincent, *Biomaterials*, 1996, **17**, 2191-2197.
137. D. Sharma, T. P. Chelvi, J. Kaur, K. Chakravorty, T. K. De, A. Maitra and R. Ralhan, *Oncology Research Featuring Preclinical and Clinical Cancer Therapeutics*, 1996, **8**, 281-286.
138. S. K. Lai, K. Hida, S. T. Man, C. Chen, C. Machamer, T. A. Schroer and J. Hanes, *Biomaterials*, 2007, **28**, 2876-2884.
139. T. Govender, S. Stolnik, M. C. Garnett, L. Illum and S. S. Davis, *Journal of Controlled Release*, 1999, **57**, 171-185.
140. W. S. Saad and R. K. Prud'homme, *Nano Today*, 2016, **11**, 212-227.
141. C. Zhang, V. J. Pansare, R. K. Prud'Homme and R. D. Priestley, *Soft Matter*, 2012, **8**, 86-93.
142. J. Aubry, F. Ganachaud, J.-P. Cohen Addad and B. Cabane, *Langmuir*, 2009, **25**, 1970-1979.
143. D. Gebauer and H. Cölfen, *Nano Today*, 2011, **6**, 564-584.
144. C. S. Kim, K. Okuyama and J. F. de la Mora, *Aerosol Science & Technology*, 2003, **37**, 791-803.
145. E. Lepeltier, C. Bourgaux and P. Couvreur, *Advanced Drug Delivery Reviews*, 2014, **71**, 86-97.
146. N. T. K. Thanh, N. Maclean and S. Mahiddine, *Chemical Reviews*, 2014, **114**, 7610-7630.
147. J. Polte, *CrystEngComm*, 2015, **17**, 6809-6830.
148. J. Aubry, F. Ganachaud, J.-P. Cohen Addad and B. Cabane, *Langmuir*, 2009, **25**, 1970-1979.
149. J. Aubry, F. Ganachaud, J. P. Cohen Addad and B. Cabane, *Langmuir*, 2009, **25**, 1970-1979.
150. A. J. Mahajan and D. J. Kirwan, *Journal of crystal growth*, 1994, **144**, 281-290.
151. S. V. Dalvi and R. N. Dave, *Industrial & Engineering Chemistry Research*, 2009, **48**, 7581-7593.
152. E. J. W. Verwey, *The Journal of Physical Chemistry*, 1947, **51**, 631-636.
153. V. M. Muller, B. V. Derjaguin and Y. P. Toporov, *Colloids and Surfaces*, 1983, **7**, 251-259.
154. B. Derjaguin, *Transactions of the Faraday Society*, 1940, **35**, 203-215.
155. E. J. W. Verwey and J. T. G. Overbeek, *Journal of Colloid Science*, 1955, **10**, 224-225.
156. M. Gouy, 1910.
157. D. L. Chapman, *The London, Edinburgh, and Dublin philosophical magazine and journal of science*, 1913, **25**, 475-481.
158. P. Hiemenz, *Principle of Colloid and Surface Chemistry , New York, USA*, 1986.
159. C. Chirayil, J. Abraham, R. Mishra, S. George and S. Thomas, *Journal of Saudi Chemical Society,* 2017,**22,** 1-36.
160. R. Gref, M. Lück, P. Quellec, M. Marchand, E. Dellacherie, S. Harnisch, T. Blunk and R. Müller, *Colloids and Surfaces B: Biointerfaces*, 2000, **18**, 301-313.
161. B. K. Johnson and R. K. Prud'homme, *Australian Journal of Chemistry*, 2003, **56**, 1021-1024.
162. C. Lourenco, M. Teixeira, S. Simões and R. Gaspar, *International Journal of Pharmaceutics*, 1996, **138**, 1-12.
163. T. Tadros, *General Principles of Colloid Stability and the Role of Surface Forces*, Wiley, 2006. 1-22.
164. Th. F. Tadros, B. Vincent,in Encyclopedia of EmulsionTechnology,Marcel Dekker, 1983, 22.
165. J. Ford, P. Chambon, J. North, F. L. Hatton, M. Giardiello, A. Owen and S. P. Rannard, *Macromolecules*, 2015, **48**, 1883-1893.
166. F. L. Hatton, L. M. Tatham, L. R. Tidbury, P. Chambon, T. He, A. Owen and S. P. Rannard, *Chemical Science*, 2015, **6**, 326-334.
167. F. L. Hatton, P. Chambon, T. O. McDonald, A. Owen and S. P. Rannard, *Chemical Science*, 2014, **5**, 1844-1853.
168. T. Cosgrove, T. L. Crowley, K. Ryan and J. R. P. Webster, *Colloids and Surfaces*, 1990, **51**, 255-269.
169. D. Walczyk, F. B. Bombelli, M. P. Monopoli, I. Lynch and K. A. Dawson, *Journal of the American Chemical Society*, 2010, **132**, 5761-5768.
170. M. Hadjidemetriou and K. Kostarelos, *Nature nanotechnology*, 2017, **12**, 288.
171. M. Lundqvist, J. Stigler, G. Elia, I. Lynch, T. Cedervall and K. A. Dawson, *Proceedings of the National Academy of Sciences*, 2008, **105**, 14265-14270.

172. P. M. Lavoie and O. Levy, in *Fetal and Neonatal Physiology (Fifth Edition)*, Elsevier, 2017, pp. 1208-1216.
173. J. H. Senior, *Critical Reviews in Theraputic Drug Carrier Systems*, 1987, **3**, 123-193.
174. R. Cagliani, F. Gatto and G. Bardi, *Materials (Basel)*, 2019, **12**, 1991.
175. M. W. Semler, E. D. Siew and A. Shaw, in *Critical Care Nephrology (Third Edition)*, Philadelphia, 2019, 350-353.
176. M. Karimi, S. Bahrami, S. B. Ravari, P. S. Zangabad, H. Mirshekari, M. Bozorgomid, S. Shahreza, M. Sori and M. R. Hamblin, *Expert opinion on drug delivery*, 2016, **13**, 1609-1623.
177. C. Röcker, M. Pötzl, F. Zhang, W. J. Parak and G. U. Nienhaus, *Nature Nanotechnology*, 2009, **4**, 577-580.
178. K.-i. Ogawara, K. Furumoto, S. Nagayama, K. Minato, K. Higaki, T. Kai and T. Kimura, *Journal of Controlled Release*, 2004, **100**, 451-455.
179. M. Longmire, P. L. Choyke and H. Kobayashi, *Nanomedicine (Lond)*, 2008, **3**, 703-717.
180. B. Haraldsson, J. Nyström and W. M. Deen, *Physiological reviews*, 2008, **88**, 451-487.
181. N. Bertrand and J.-C. Leroux, *Journal of Controlled Release*, 2012, **161**, 152-163.
182. A. J. Tavares, W. Poon, Y.-N. Zhang, Q. Dai, R. Besla, D. Ding, B. Ouyang, A. Li, J. Chen, G. Zheng, C. Robbins and W. C. W. Chan,*Proceedings of the National Academy of Sciences* USA, 2017, **114** 10871-10880.
183. E. Wisse, F. Jacobs, B. Topal, P. Frederik and B. De Geest, *Gene Therapy*, 2008, **15**, 1193-1199.
184. F. Jacobs, E. Wisse and B. De Geest, *The American Journal of Pathology*, 2010, **176**, 14-21.
185. J. Fusion, What Are the Functions of a Liver Cell?, https://sciencing.com/functions-liver-cell-5106552.html, (accessed 13/03/2020).
186. B. J. Potter, in *Reference Module in Biomedical Sciences*, Elsevier, 2019.
187. C. D. Walkey, J. B. Olsen, H. Guo, A. Emili and W. C. W. Chan, *Journal of the American Chemical Society*, 2012, **134**, 2139-2147.
188. Q. Dai, C. Walkey and W. C. W. Chan, *Angewandte Chemie International Edition*, 2014, **53**, 5093-5096.
189. M. Cataldi, C. Vigliotti, T. Mosca, M. Cammarota and D. Capone, *International journal of molecular sciences*, 2017, **18**, 1249.
190. R. E. Mebius and G. Kraal, *Nature Reviews Immunology*, 2005, **5**, 606-616.
191. I. Khan, K. Saeed and I. Khan, *Arabian Journal of Chemistry*, 2019, **12**, 908-931.
192. O. S. Thomas and W. Weber, *Frontiers in Bioengineering and Biotechnology*, 2019, **7**, 415-415.
193. M. Elsabahy and K. L. Wooley, *Chemical Society Reviews*, 2012, **41**, 2545-2561.
194. R. Gaspar and R. Duncan, *Advanced Drug Delivery Reviews*, 2009, **61**, 1220-1231.
195. A. Vijayakumar, E. V. Sharon, J. Teena, S. Nobil and I. Nazeer, *Journal of Basic Clinical and Pharmacy*, 2014, **5**, 49-53.
196. S. M. Moghimi, A. C. Hunter and J. C. Murray, *Pharmacological reviews*, 2001, **53**, 283-318.
197. N. Hoshyar, S. Gray, H. Han and G. Bao, *Nanomedicine*, 2016, **11**, 673-692.
198. M. Gaumet, A. Vargas, R. Gurny and F. Delie, *European Journal of Pharmaceutics and Biopharmaceutics*, 2008, **69**, 1-9.
199. S. K. Hobbs, W. L. Monsky, F. Yuan, W. G. Roberts, L. Griffith, V. P. Torchilin and R. K. Jain, *Proceedings of the National Academy of Sciences of the United States of America*, 1998, **95**, 4607-4612.
200. A. Sukhanova, S. Bozrova, P. Sokolov, M. Berestovoy, A. Karaulov and I. Nabiev, *Nanoscale Research Letters*, 2018, **13**, 44-44.
201. N. Welsch, Y. Lu, J. Dzubiella and M. Ballauff, *Polymer*, 2013, **54**, 2835-2849.
202. N. M. Schaeublin, L. K. Braydich-Stolle, A. M. Schrand, J. M. Miller, J. Hutchison, J. J. Schlager and S. M. Hussain, *Nanoscale*, 2011, **3**, 410-420.
203. A. Gabizon and D. Papahadjopoulos, *Proceedings of the National Academy of Sciences*, 1988, **85**, 6949.
204. A. Mori, A. L. Klibanov, V. P. Torchilin and L. Huang, *FEBS Letters*, 1991, **284**, 263-266.
205. D. Liu, F. Liu and Y. K. Song, *Pharmaceutical research*, 1995, **12**, 508-512.
206. D. Liu, Q. Hu and Y. K. Song, *Biochimica et Biophysica Acta (BBA) - Biomembranes*, 1995, **1240**, 277-284.
207. E. Fröhlich, *International journal of nanomedicine*, 2012, **7**, 5577-5591.
208. D. E. Owens and N. A. Peppas, *International Journal of Pharmaceutics*, 2006, **307**, 93-102.

209. Y. Hu, X. Jiang, Y. Ding, H. Ge, Y. Yuan and C. Yang, *Biomaterials*, 2002, **23**, 3193-3201.
210. M. Božič, T. Elschner, D. Tkaučič, M. Bračič, S. Hribernik, K. Stana Kleinschek and R. Kargl, *Cellulose*, 2018, **25**, 6901-6922.
211. L. E. van Vlerken, T. K. Vyas and M. M. Amiji, *Pharmaceutical Research*, 2007, **24**, 1405-1414.
212. Z. Amoozgar and Y. Yeo, *Wiley Interdisciplinary Reviews: Nanomedicine and Nanobiotechnology*, 2012, **4**, 219-233.
213. A. Abuchowski, J. R. McCoy, N. C. Palczuk, T. van Es and F. F. Davis, *Journal of Biological Chemistry*, 1977, **252**, 3582-3586.
214. J. S. Suk, Q. Xu, N. Kim, J. Hanes and L. M. Ensign, *Advanced drug delivery reviews*, 2016, **99**, 28-51.
215. M. Miteva, K. C. Kirkbride, K. V. Kilchrist, T. A. Werfel, H. Li, C. E. Nelson, M. K. Gupta, T. D. Giorgio and C. L. Duvall, *Biomaterials*, 2015, **38**, 97-107.
216. A. Mori, A. L. Klibanov, V. P. Torchilin and L. Huang, *FEBS letters*, 1991, **284**, 263-266.
217. H. Hatakeyama, H. Akita and H. Harashima, *Biological and Pharmaceutical Bulletin*, 2013, **36**, 892-899.
218. H. Hatakeyama, H. Akita and H. Harashima, *Advanced drug delivery reviews*, 2011, **63**, 152-160.
219. P. Mishra, B. Nayak and R. Dey, *asian journal of pharmaceutical sciences*, 2016, **11**, 337-348.
220. A. A. Gabizon, Y. Patil and N. M. La-Beck, *Drug Resistance Updates*, 2016, **29**, 90-106.
221. Y. H. Bae and K. Park, *Journal of Controlled Release*, 2011, **153**, 198-205.
222. T. J. Anchordoquy, Y. Barenholz, D. Boraschi, M. Chorny, P. Decuzzi, M. A. Dobrovolskaia, Z. S. Farhangrazi, D. Farrell, A. Gabizon, H. Ghandehari, B. Godin, N. M. La-Beck, J. Ljubimova, S. M. Moghimi, L. Pagliaro, J.-H. Park, D. Peer, E. Ruoslahti, N. J. Serkova and D. Simberg, *ACS Nano*, 2017, **11**, 12-18.
223. S. Mitragotri, T. Lammers, Y. H. Bae, S. Schwendeman, S. De Smedt, J.-C. Leroux, D. Peer, I. C. Kwon, H. Harashima, A. Kikuchi, Y.-K. Oh, V. Torchilin, W. Hennink, J. Hanes and K. Park, *Journal of Controlled Release*, 2017, **246**, 183-184.
224. J. Ford, *PhD Thesis*, Univerisity of Liverpool, 2015. (https://livrepository.liverpool.ac.uk/2052220/1/FordJan_Sept2015_2052220.pdf.pdf)
225. S. Flynn, *PhD Thesis*, Univeristy of Liverpool, 2019. (https://livrepository.liverpool.ac.uk/3079211/1/200670082_Sep2019.pdf).

# Chapter 2

Synthesis of Methacrylate Based Polymers *via* Copper Catalysed Methanolic Atom Transfer Radical Polymerisation

## 2.1 Introduction

### 2.1.1 Controlled Polymer Synthesis

The desire to produce well-defined functional materials under simple reaction conditions led to the development of controlled radical polymerisation (CRP) techniques.[1] These were formed from a combination of the principles of 'living' polymerisation and conventional free radical polymerisations (FRP).[2] Unlike FRP, however, CRP offers the potential to synthesise macromolecular structures with control over the molecular weight, molecular weight distribution, chain-end functionality, polymer architecture and composition.[3-5] These advantages complement the existing advantages associated with FRP, such as mild reaction conditions and the applicability to a wide range of monomers. [1, 6-9]

The success of CRP can be attributed to two general characteristics: firstly, all the polymer chains are formed at the same time *via* initiation which is faster than propagation and secondly, the number of active species has to be constant throughout the reaction (i.e. termination reactions have to be minimal). This can be achieved by minimising the concentration of active radical species to suppress any undesirable side reactions.

The combination of these two factors allows the equal growth rate of polymer chains, producing polymers with narrow molecular weight distributions. These attributes have steered CRP into becoming a widely researched synthetic route since its discovery in the 1990s, contributing to the development of numerous materials with potential applications ranging from coatings, adhesives, personal care products, biomaterials and many more.[10, 11]

Since 2010, the international union of pure and applied chemicals (IUPAC) recommends that CRP is referred to as reversible-deactivation radical polymerisation (RDRP),[12] which is how it will be referred to throughout the remainder of this thesis.

### 2.1.2 Atom Transfer Radical Polymerisation

Atom transfer radical polymerisation (ATRP) is a specific type of RDRP that is commonly utilised to generate functional polymers since the technique is robust,

applicable to a wide range of monomers and presents opportunity to introduce site specific tailored functionalities.[6] The first reports of ATRP were published in 1995 describing the work conducted by Wang and Matyjaszewski,[13] and Sawamoto and co-workers.[14] These seminal studies were built on the concept of atom transfer radical addition (ATRA), which is an efficient and well recognised method in organic chemistry for the formation of carbon–carbon bonds between olefins and alkyl halides. These studies showed that transition metal catalysts commonly employed in ATRA could also be employed in ATRP to polymerise vinyl monomers with a high degree of control.[13, 15]

The control exerted by ATRP arises from the equilibrium between dormant species (R-X) and propagating radicals (R˙), outlined in Scheme 2.1.[10, 16] ATRP is a reversible redox process which is catalysed by a transition metal complex $TM^n/L$ ($TM^n$ represents the transition metal species in oxidation state n and L represents the ligand). The most commonly used complexes are Cu-based, but other studies have been conducted using different metals such as Fe, Ru and Mo.[17]

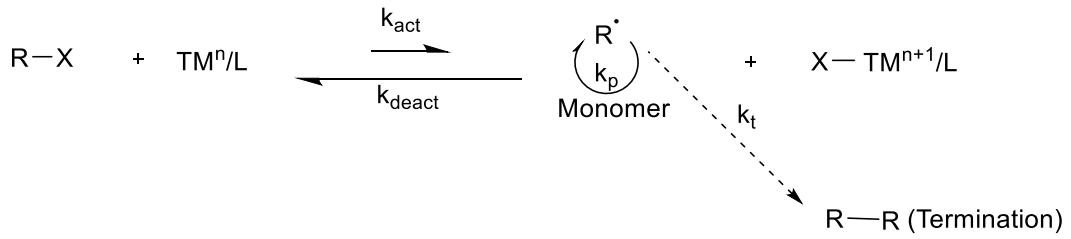


**Scheme 2.1** General mechanism for transition metal catalysed ATRP.

The reaction proceeds *via* the activation of the dormant species R-X, which involves the abstraction of the halide atom and the simultaneous one-electron oxidation of the transition metal complex to form the species $X – TM^{n+1}/ L$ and the active radical R˙; this activation step proceeds *via* the rate constant $k_{act}$. The active radical species R˙ can then propagate with vinyl monomer (rate constant $k_p$) to grow the polymer chain. A reverse reaction (rate constant $k_{deact}$) sees the deactivation of the active radical by capping it with the halide to form the dormant species once more. Termination reactions of the activated radical species can also occur (rate constant $k_t$), although these are negligible under ideal conditions because the concentration

of active radical species is minimised since the rate of deactivation is much greater than the rate of activation ($k_{deact}$ >> $k_{act}$). Additionally, the occurrence of any termination reactions minimises further termination reactions by what is known as the *persistent radical effect*.[18, 19] Here, the irreversible formation of a radical-radical species generates two equivalents of the halide complex, X – $M_t^{n+1}$ / L, and thus further drives the equilibrium towards the dormant species in accordance with Le Chatelier's principle.

The values of the rate constants can all be strongly influenced by experimental parameters such as: reaction solvent, temperature, pressure, and the chemical structure of the monomer, the initiating species and the ligand. The main control over the polymerisation arises from two factors: (i) the rate of deactivation ($k_{deact}$) is much larger than the rate of propagation ($k_p$) and therefore only a small number of monomer units are added to the chain at each time i.e. the propagating radical is only active for a short period of time before capping. And (ii) the rate of deactivation ($k_{deact}$) is far greater than the rate of activation ($k_{act}$), which means that the dormant dominates and the local concentration of active radicals is kept low. Due to the nature of the mechanism it is extremely important that the reaction is completed without the presence of oxygen as this would lead to: (i) the poisoning of the transition metal catalyst, and (ii) the scavenging of the active radicals. The control of ATRP can be studied through kinetic experiments and detailed proton nuclear magnetic resonance ($^1$H NMR) spectroscopy and triple detection size exclusion chromatography (TD- SEC) analysis. A semi-logarithmic plot of ln($[M]_0$/[M]) *vs.* time, where $[M]_0$ represent monomer concentration at t=0 and [M] represent monomer concentration and a plot of number average molecular weight ($M_n$) *vs.* conversion should both yield linear correlations, which would highlight that a constant radical concentration was maintained throughout the polymerisation and that termination and chain-transfer reactions were negligible.

ATRP has attracted both research and commercial interest for the following reasons: the relatively straight forward experimental setup, compatibility with a wide range

of different monomers, use of readily available and inexpensive catalytic components and commercially available or easily prepared (macro)initiators.[20]

### 2.1.3 The Synthesis of Various Polymer Compositions and Architectures by ATRP

The use of ATRP has facilitated the straightforward synthesis of a wide range of polymeric architectures including: stars, brushes, linear polymers and branched (co)polymers.[20] The design of polymeric compositions and architectures can involve the variation of: the monomer functionality, the number of monomer types, their distribution within a polymer chain and how the polymer chains are arranged, i.e. the polymer topology (Figure 2.1).[21, 22] There are many different types of copolymers such as: alternating copolymers, statistical copolymers and block copolymers.[23, 24]

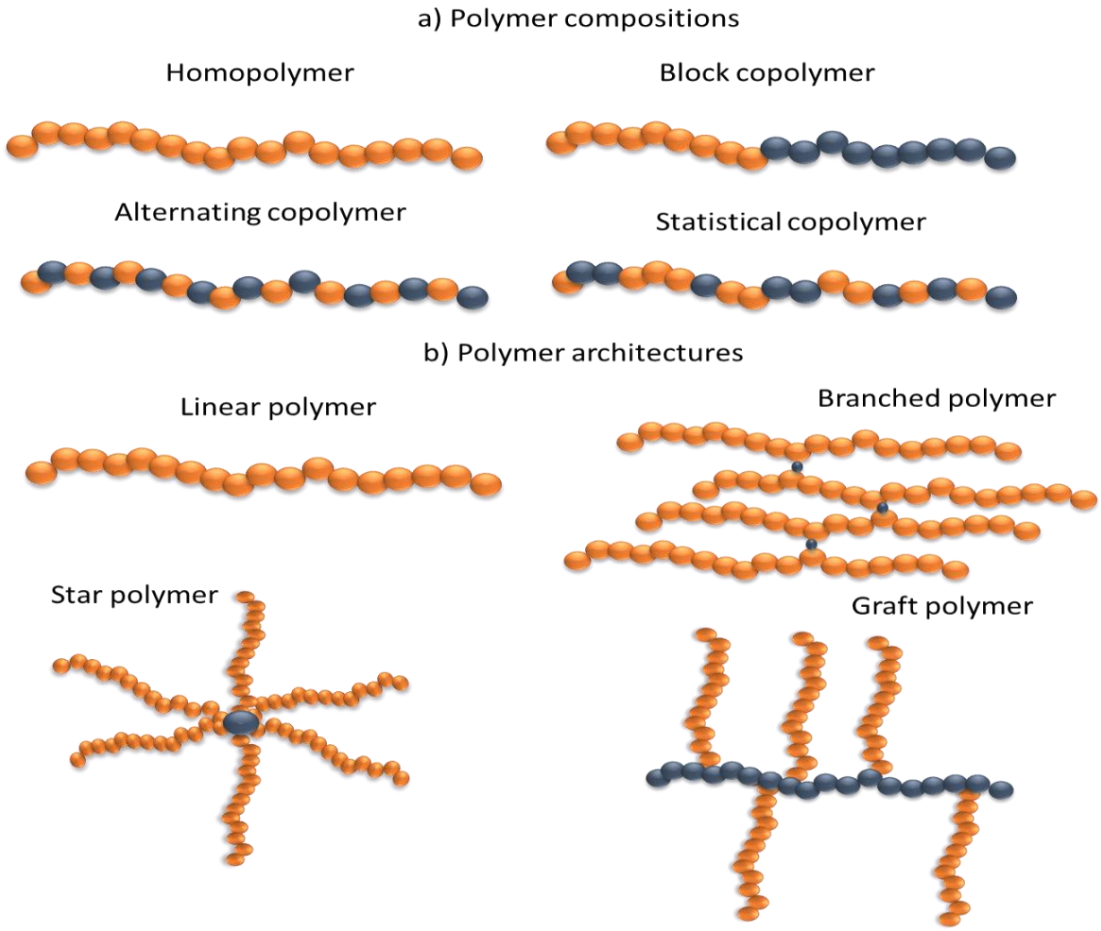


**Figure 2.1** Schematic representation of the different examples of polymer structures: a) examples of the different compositions, and b) examples of the different polymer architectures achievable *via* ATRP.

#### 2.1.3.1 Controlled Polymerisation for the Synthesis of Amphiphilic Block Copolymers

Block copolymers, as previously discussed (Chapter 1.2.1), are copolymers consisting of two or more distinct block sequences of monomer residue functionalities within a

given chain. There is huge scope for their use as advanced materials in different applications that include their use as porous materials, electronics, and drug delivery.[25] Significant research interest arises from the inherent ability of amphiphilic block copolymers to self-assemble, which is a process that requires well-defined polymers with distinct block functionalities and narrow molecular weight distributions. In addition to the relative functionalities of the block segments, the length and ratio of each are also important contributory factors to the formation of such self-assembled structures. Therefore, the required method of synthesis must control these characteristics and ATRP has already proven to be a particularly attractive route for their synthesis. [26, 27] There are two main methodologies for the synthesis of block copolymers *via* ATRP, both of which involve growth from a pre-existing polymer chain.

The first approach involves the sequential addition of two monomer, A and B. with the propagation of B from the end of the first chain comprising of monomer A residues. This type of approach is typically referred to as chain extension to produce an A-B di-block copolymer structure, as depicted in Figure 2.2.

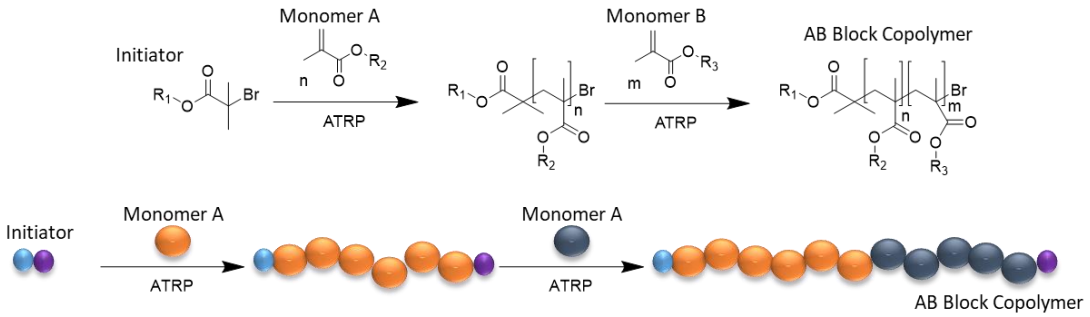


**Figure 2.2** Schematic representation of the generation of an AB di-block copolymer *via* chain extension. Whereby, the (re)initiation of polymer A that has retained its alkyl halide chain-end functionality occurs *via* sequential polymerisation with monomer B to generate AB block copolymers.

The order of monomer addition plays an important role since the reactivity of the carbon-halogen bond of the dormant species will depend on the chemical structure of the first monomer used. The reactivity decreases as follows: acrylonitrile > alkyl methacrylate > styrene ~ alkyl acrylate > acrylamide.[28] Further sequential additions can be made under suitable conditions following the chain extension method, which provides an opportunity to generate a wide variety of different block copolymer structures such as A-B-A tri-block copolymers (Figure 2.3i) and A-B-C tri-block

terpolymers (Figure 2.3ii). The success of chain extension is dependent on the preservation of the alkyl halide chain-end functionality, and the successful and efficient re-initiation of the polymer chains.

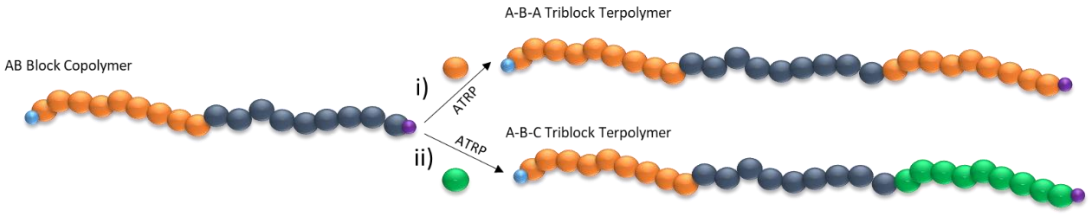


**Figure 2.3** Schematic representation of the generation of ABA block copolymers and ABC triblock terpolymers via tertiary polymerisation of an AB block copolymer.

The second approach to A-B block copolymer formation involves the chain-end modification of polymer A in order to generate a macro-initiator capable of initiating an alternative polymerisation (Figure 2.4i). This macro-initiator can then be used to produce an AB di-block copolymer by initiating a polymerisation of monomer B (Figure 2.4ii).[27, 28]

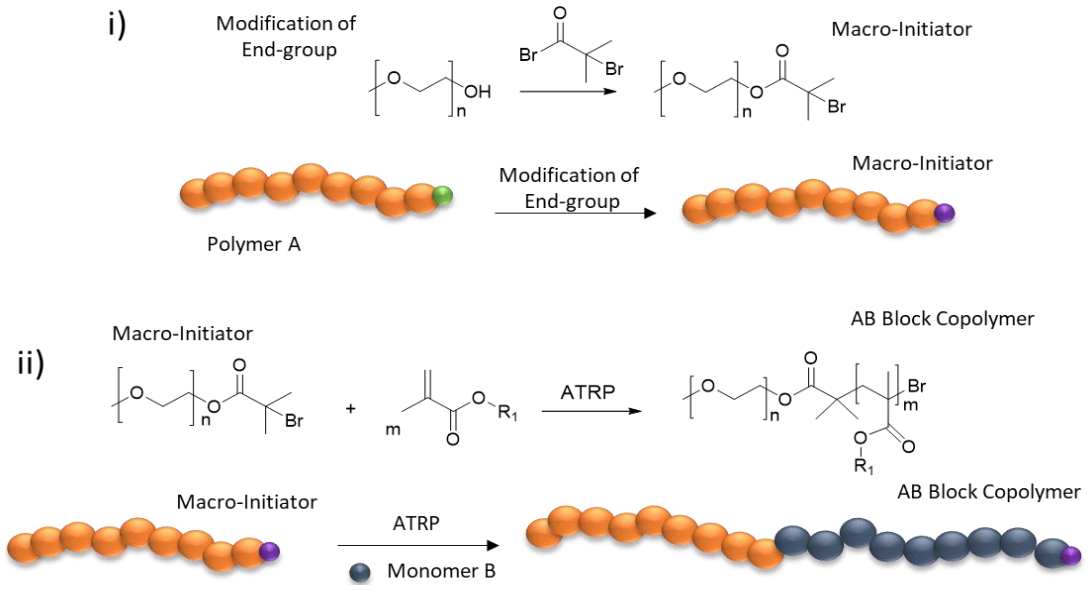


**Figure 2.4** Schematic representation of the generation of an AB block copolymer following the synthesis of a PEG macro-initiator. The figure shows i) the post polymerisation modification of poly(ethylene glycol) monomethyl ether (polymer A) with α-bromoisobutyryl bromide (or another initiating species) and ii) its subsequent utilisation within ATRP of methacrylate-based monomer B.

Polymers that have been synthesised from alternative methods such as ring-opening polymerisation,[29] anionic polymerisation,[30] and cationic polymerisation,[31, 32] can be

used to generate macro-initiators, which therefore increases the scope and chemical variability of the available block co-polymers.

There are several potential limitations of this model of macro-initiator synthesis. Firstly, poor efficiency of the end group modification on the primary polymer chain; if the modification of the end group is not efficiently achieved, and if purification is difficult, this could result in the presence of polymer chains which are incapable of initiating the subsequent polymerisation. Secondly, if the initiator efficiency is low, this would result in the generation of a mixture of unreacted original polymer and AB block copolymer. Additionally, the rate of initiation can also be a limitation. If it is slow then the polydispersity of the resulting AB block copolymer will be broad and will result in undesirable variability of the ratio of the segments.

It is common for amphiphilic block copolymers intended for drug delivery applications to incorporate a hydrophilic PEG component. The successful incorporation of PEG within AB block copolymers can be achieved by the use of a PEG isobutryl bromide macroinitiator, which can be utilised to initiate ATRP polymerisations of different monomers, examples of which include hydrophilic,[33-35] hydrophobic and ionic chemistries.[36, 37]

### 2.1.3.2 Synthesis of Branched Statistical Copolymers by ATRP

A branched polymer can be defined as a macromolecule with chains or branches of significant length bonded to the main chain at branching points (Figure 2.5). Such species can be characterised by the size and number of branches. Branched polymeric materials, although architecturally complex, are relatively economical and facile to synthesise compared to other complex branched architectures such as dendrimers.[38, 39]

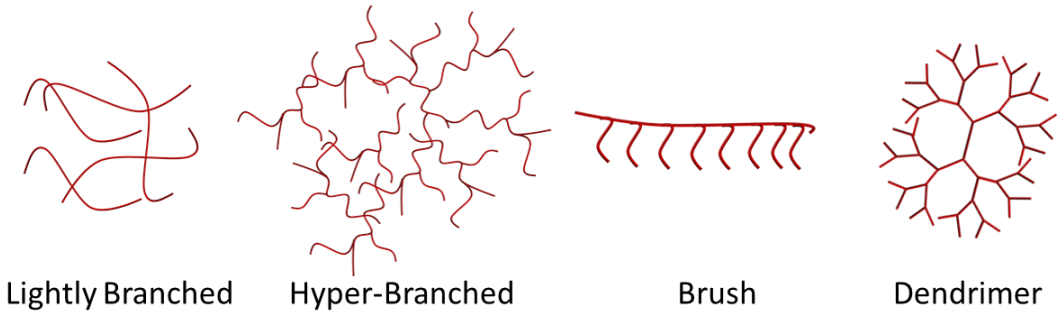


**Figure 2.5** Schematic representation of different branched polymer architectures.

Branched copolymer materials can be synthesised through the copolymerisation of a monofunctional monomer and a bifunctional monomer (Figure 2.6). A bifunctional monomer, as the name suggests, is a monomer that contains two functional groups which are capable of partaking in propagation reactions between separate growing polymer chains. This inclusion between two propagating chains generates a single branching point, with the generation of further intermolecular branching points resulting in a large number of primary polymer chains being covalently linked together.

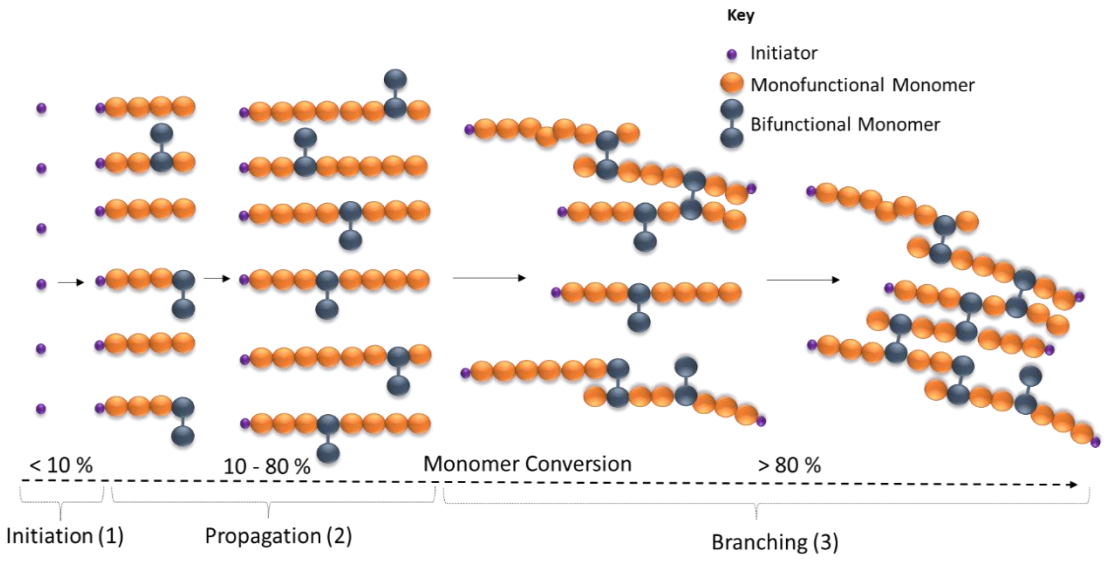


**Figure 2.6** Schematic formation of a branched copolymer. Figure adapted from reference[40]

In the initial stages of the copolymerisation of a monofunctional and bifunctional monomer, the incorporation between the two monomers is statistical and results in the formation of linear primary polymer chains presenting unreacted pendant double bonds. At low monomer conversion, the concentration of unreacted monovinyl

monomer is much greater than that of pendant vinyl bonds, and only at high conversion of the monovinyl monomer does the spontaneous intermolecular coupling of the chains begin – subsequently producing branched polymers.[40] This generates materials with significantly higher molecular weights and broader molecular weight distributions compared to that of the corresponding primary chains synthesised in the absence of divinyl monomer. Gelation of a polymer can occur when primary polymer chains forms large interconnected networks *via* cross-linking through the incorporation of more than one on average divinyl monomers per polymer primary chain (Figure 2.7).

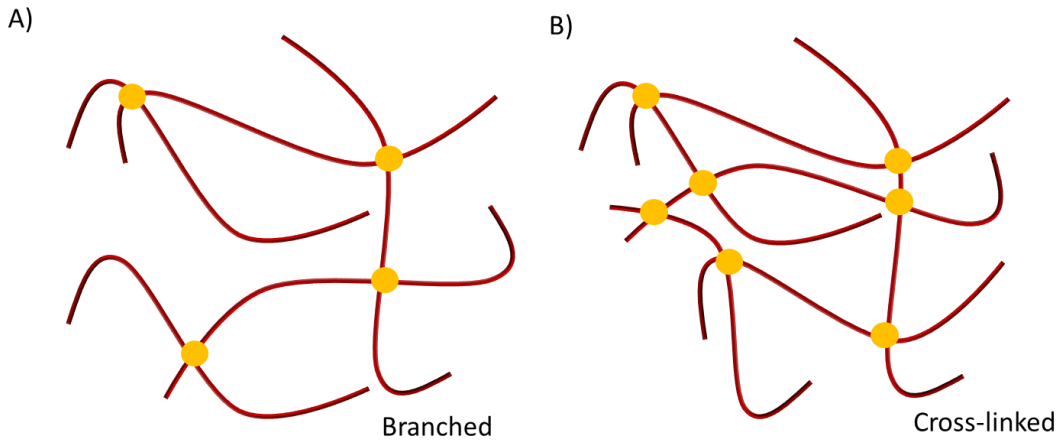


**Figure 2.7** Schematic representation illustrating a: A) branched polymer and B) cross linked polymer.

The initial quantitative description of gelation was developed in the 1940s by Flory and Stockmayer, which is termed the Flory-Stockmayer theory.[41-45] Which allows for the identification of a gel point of a polymerisation between monomer A and B and is based on three assumptions: 1) all vinyl groups are equally reactive, 2) that all reactions occur between monomer A and B and 3) there are no intramolecular reactions.

There are several synthetic strategies that can be utilised in the synthesis of branched materials, which include chain transfer mediated FRP, reversible addition-fragmentation chain-transfer (RAFT) polymerisation and ATRP.[11, 46-53]

Characteristically, FRP proceeds in an uncontrolled manner, and high molecular weight chains with very broad distributions are produced. FRP has a fast rate of

propagation compared to a slow rate of initiation; and due to the highly reactive nature of the free radicals, termination and chain transfer are inevitable. When even a small percentage of divinyl monomer is incorporated, these high molecular weight chains are very easily cross-linked i.e. an average two or more branch points per chain has been introduced into each chain resulting in gelation as described by Flory.[54] Due to the polydisperse nature of the polymers produced *via* FRP, gelation can occur even at low monomer conversions since some chains will be significantly longer than average, making cross-linking even easier.[55] This has somewhat limited the production of branched polymers *via* FRP. To try and avoid gelation, high dilution could be employed.

Alternatively, Sherrington and co-workers reported the synthesis of branched vinyl polymers *via* FRP but with the inclusion of a chain transfer agent (CTA) (typically a thiol) to a copolymerisation of a vinyl and divinyl monomer. Scheme 2.2 illustrates an example of how chain transfer occurs when a radical from a propagating styrene chain is transferred to a chain transfer agent, butyl mercaptan, in exchange for a proton, terminating the chain.

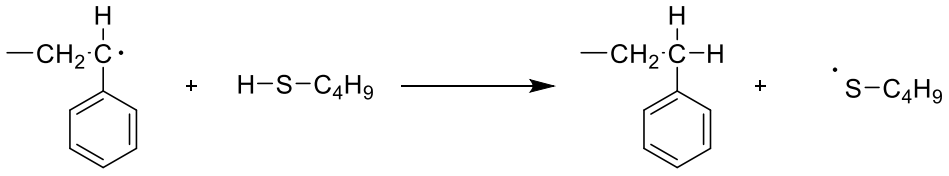

**Scheme 2.2** Schematic representation of how butyl mercaptan, a CTA, can be used to transfer a radical from a propagating styrene chain.

The incorporation of a chain transfer agent within a copolymerisation of a vinyl and divinyl monomer suppresses gelation by limiting the molecular weight of the primary polymer chains by transferring the radical of a growing polymer chain to another molecule and therefore reducing the average number of branch points per chain (Scheme 2.3).

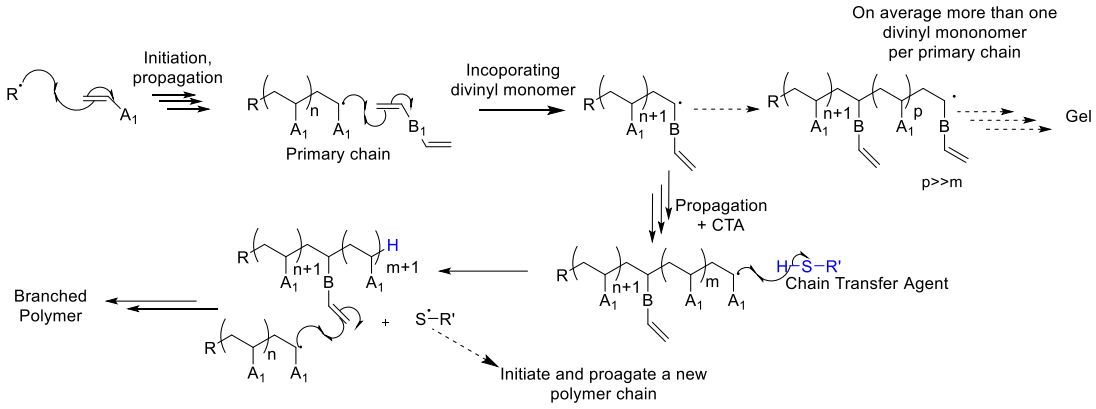


**Scheme 2.3** Schematic representation of copolymerisation of a vinyl and divinyl monomer with and without the presence of a CTA.

This is known as the "Strathclyde" technique, which was built upon pre-existing knowledge that chain transfer agents could be used to supress gelation by ensuring that primary chain length is too short.[56] However, Sherrington and co-workers were the first to show that this method could be used to generate soluble branched copolymers of high molecular weight with high monomer conversion.[57-61] The branched polymers produced, contain a large number of conjoined primary chains and due to the statistical nature of branching possess a broad molecular weight distribution. The Strathclyde methodology has received significant attention in the literature with the majority of the work focussing on the polymerisation of hydrophobic monomers.[62-65]

ATRP can be utilised for the synthesis of high molecular weight soluble branched copolymers as part of a modified Strathclyde technique.[66-68] These branched copolymers can be prepared *via* the statistical copolymerisation between a vinyl and divinyl monomer without the need of a CTA. Gelation is minimised in the case of ATRP since the degree of polymerisation (i.e. primary chain length) can be controlled without CTA presence, through adjustment of monomer and initiation molar ratio. Since the amount of initiator is known, gelation can also be controlled through the accurate incorporation of a divinyl monomer. Additionally, the relatively low polydispersity values minimise the probability of primary polymer chains incorporating more than two branching units. Whilst ATRP does provide a degree of synthetic control to minimise gelation, in order to fully avoid gelation of the branched

polymer, the molar ratio of divinyl monomer: initiator should be less than 1. This is in keeping with the Flory Stockmayer theory.[41-45] Employing ATRP to obtain soluble branched copolymers provides several advantages. Firstly, the degree of branching, and therefore the number of primary chains which are joined together, can be varied by targeting various [B]/[I] molar ratios, where [B] represents brancher concentration and [I] represent initiator concentration. Secondly, the degree of polymerisation of the primary polymer chain can be varied by simply targeting different [M]/[I] ratios, where [M] represents monomer concentration. Finally, since polymers prepared by ATRP contain two chain ends: the α-end derived from the initiator and the ω-end, which is normally a labile end-group, such as a bromine atom, an array of different chain-end functionalities is possible, through careful design and synthesis of the initiator (Figure 2.8).

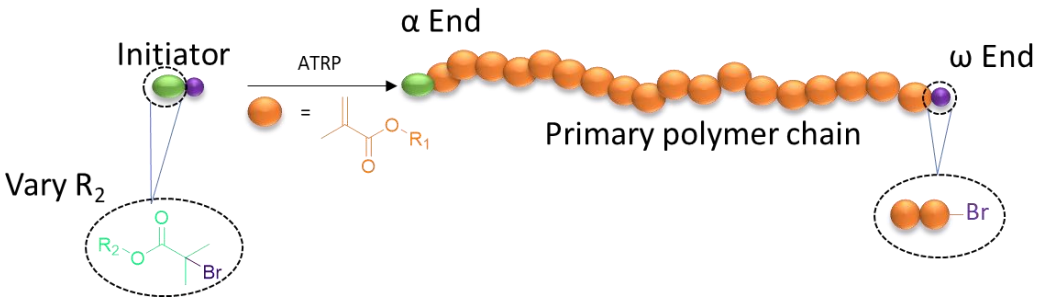


**Figure 2.8** Schematic representation of a primary polymer chain highlighting the two different chain ends and how different functionalities can be introduced.

First reports of soluble branched polymers produced *via* ATRP and utilising a modified Strathclyde methodology was published in 2004 when Isaure *et al*. reported the copolymerisation of methyl methacrylate and divinyl monomer ethylene glycol dimethacrylate (EGDMA) in a one pot synthesis to produce *p*(MMA$_x$-*co*-EGDMA$_y$).[69] Other reports of soluble branched material being synthesised by ATRP include *p*(HPMA$_x$-*co*-EGDMA$_y$) [40] and *p*(styrene-*co*-divinylbenzene).[70]

## 2.2 Research Aims of Chapter 2

Literature reports have shown that ATRP is a versatile technique which exhibits compatibility with a wide range of functional monomers. The synthetic process, methanolic ATRP, has already proven to be robust and efficient at generating well-defined polymer materials.[50, 53, 71] The aim of this research chapter is to expand on

the polymer materials which have been previously reported, by synthesising a wide range of methacrylate-based hydrophobic polymers *via* methanolic ATRP. Three different methacrylate hydrophobic monomers with varying hydrophobicity will be used: butyl methacrylate (BuMA), 2-ethyl hexyl methacrylate (EHMA) and 2-hydroxylpropyl methacrylate (HPMA) (Figure 2.9i). Employing the monomer chemistries outlined above, polymers of varying architectures will be targeted. These include: linear homopolymers, branched copolymers through copolymerisation of a vinyl and divinyl monomer using the modified Strathclyde approach following the Flory-Stockmayer theory; amphiphilic A-B block copolymers by incorporating a macroinitiator and statistical copolymers, both linear and branched through mixing of monomers (Figure 2.9ii). These materials in-turn, would later be utilised generate hydrophobic amphiphilic polymer nanoparticles.

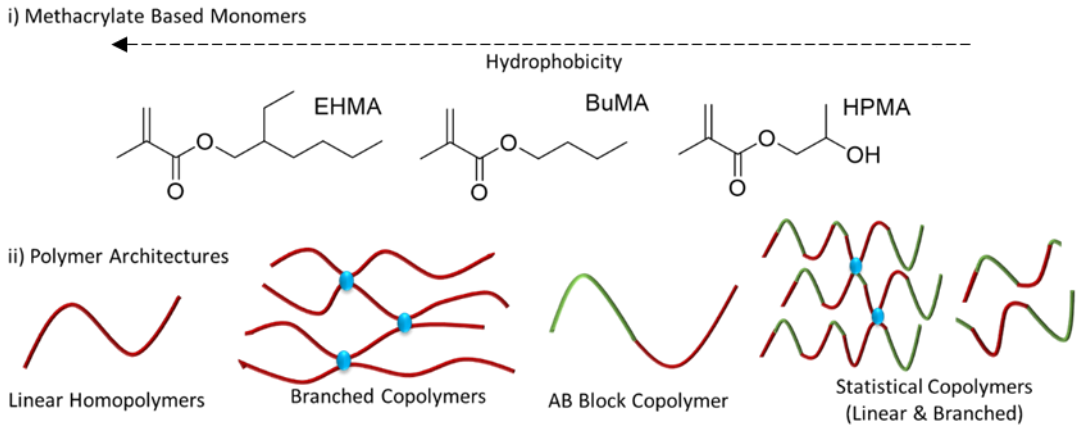


**Figure 2.9** Schematic representation of i) the different methacrylate monomers selected and ii) the varying polymer architectures.

This chapter also aims to explore how different functionalities can be imparted into the polymer species during the synthesis of high molecular weight branched copolymers using six different divinyl monomers: bisphenol A dimethacrylate (BPDMA), bisphenol glycerol dimethacrylate (BPGDMA), Bis(2-methacryloyl)oxyethyl disulphide dimethacrylate (DSDMA), ethylene glycol dimethacrylate (EGDMA), glycerol dimethacrylate (GDMA) and urethane dimethacrylate (UDMA). Polymers of different primary chain lengths will also be synthesised. The polymer materials generated will be characterised by $^{1}$H NMR and TD-GPC and their thermal characteristics analysed *via* DSC.

## 2.3 Results and Discussion

### 2.3.1 Synthesis of Linear p(BuMA)$_n$ Homopolymers *via* Methanolic ATRP

A series of polymerisations were performed using a method previously reported by Dwyer *et.al*, whereby linear poly(*n*-butyl methacrylate) p(BuMA)$_n$ was synthesised *via* methanolic ATRP to yield p(BuMA)$_n$ of controlled molecular weight and low dispersity values.[51,53] Therefore, the monomer BuMA was chosen as a control to verify the controlled nature of ATRP.

The homopolymerisation of commercially available monomer BuMA was performed in anhydrous methanol (MeOH) at 50 °C using a copper (I) chloride ($Cu^{(I)}Cl$): 2,2-bipyrine (bpy) catalytic system and a commercially available initiator, ethyl α-bromoisobutyrate (EBiB). A molar ratio of BuMA:EBiB:$Cu^{(I)}Cl$:bpy of X:1:1:2 was used for all reactions, were X also represents the targeted $DP_n$ of the resulting linear polymer. The amount of MeOH added was set to 50 wt. % wrt to total solids content. The $DP_n$ was varied and targeted 20, 60, 80 and 100 monomer units (Scheme 2.4), which was achieved by increasing the monomer concentration relative to initiator and catalyst within the reactions and maintaining the 50 wt.% total solids content. All of the polymerisations remained as homogenous dark brown solutions throughout the reactions and achieved high vinyl conversions (≥ 98%), as calculated by $^1$H NMR (Table 2.1).

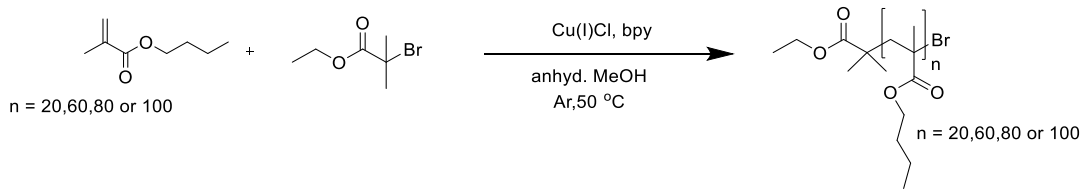


**Scheme 2.4** Linear polymerisation of hydrophobic BuMA monomer *via* Cu-catalysed methanolic ATRP.

As the targeted $DP_n$ value increased, the reaction time required to reach these high monomer conversions also increased from 18 hours to 75 hours to allow for the longer polymer chain length to be generated. The reactions were then poisoned *via* the addition of THF and exposure to oxygen to prevent further reaction. A change in colour was observed for all the polymerisations from dark opaque brown to a transparent bright green solution during this process as the Cu catalyst was oxidised

from oxidation state +1 to +2. The polymers were then purified *via* a two-stage process. Firstly, the catalytic system was removed by passing the diluted reaction mixture through a neutral alumina column using THF as the mobile phase. The removal of catalyst is evident by the presence of a green band at the top of the column, and the catalyst-free polymer solutions were subsequently concentrated *in vacuo* and precipitated into cold MeOH to remove any unreacted monomer, residual initiator and free ligand. The polymers were obtained as white solids and were then dried *in vacuo* at 35 °C for 24 hours to ensure complete solvent removal. Analysis of the polymers was conducted *via* $^1$H NMR ($CDCl_3$) to confirm the complete removal of residual initiator, unreacted monomer and free ligand. $^1$H NMR analysis of the vinyl monomers are presented in the Appendix Figure A1-3. Subsequent analysis *via* TD-SEC using a THF/TEA (98/2 v/v %) eluent, was used to determine the molecular weights and dispersities of the synthesised linear homopolymers (Table 2.1).

**Table 2.1** Methanolic Cu-ATRP of BuMA at 50 °C for linear polymer synthesis targeting various $DP_n$.

| | | | | TD-SEC (THF)[d] | | | |
|---|---|---|---|---|---|---|---|
| [a] Target $DP_n$ | Time (hr) | [b] Conversion (%) | [c] $M_n$ Theory (g mol$^{-1}$) | $M_n$ (g mol$^{-1}$) | $M_w$ (g mol$^{-1}$) | Đ | Mark - Houwink α value |
| 20 | 18 | > 99 | 3 010 | 5 100 | 6 400 | 1.24 | 0.591 |
| 60 | 24 | 98 | 8 550 | 10 930 | 12 110 | 1.11 | 0.735 |
| 80 | 48 | > 99 | 11 460 | 18 850 | 20 910 | 1.11 | 0.807 |
| 100 | 75 | > 99 | 14 280 | 20 200 | 23 050 | 1.14 | 0.676 |

[a] Target $DP_n$ calculated *[BuMA] / [EBiB]*, [b] Calculated by $^1$H-NMR *spectroscopy* of polymerisation mixture at t=final. [c] Theoretical $M_n$ calculated as ((target $DP_n$ x MW monomer) x (conversion/100)) + initiator residue. [d] Calculated by TD-SEC using THF/TEA mobile phase (98/2 v/v%) at 35 °C, flow rate of 1mL min$^{-1}$.

Analysis by TD-SEC revealed monomodal chromatograms that indicated that the polymerisations had proceeded in a controlled manner to yield well-defined polymers with narrow molecular weight distributions ($1.11 \leq Đ \leq 1.24$). The obtained $M_n$ values (5,100 – 20,200 g mol$^{-1}$) increased as the targeted $DP_n$ increased, and all showed an appreciable targeting of the molecular weights; however, these values did vary slightly from that of the theoretical values, which could be attributed to a lower initiator efficiency of EBiB than expected. Overlay of the refractive index chromatograms showed a decrease in retention volumes for the increasing primary

polymer chain length relative to the shortest $DP_n$ targeted of 20 monomer units (Figure 2.10).

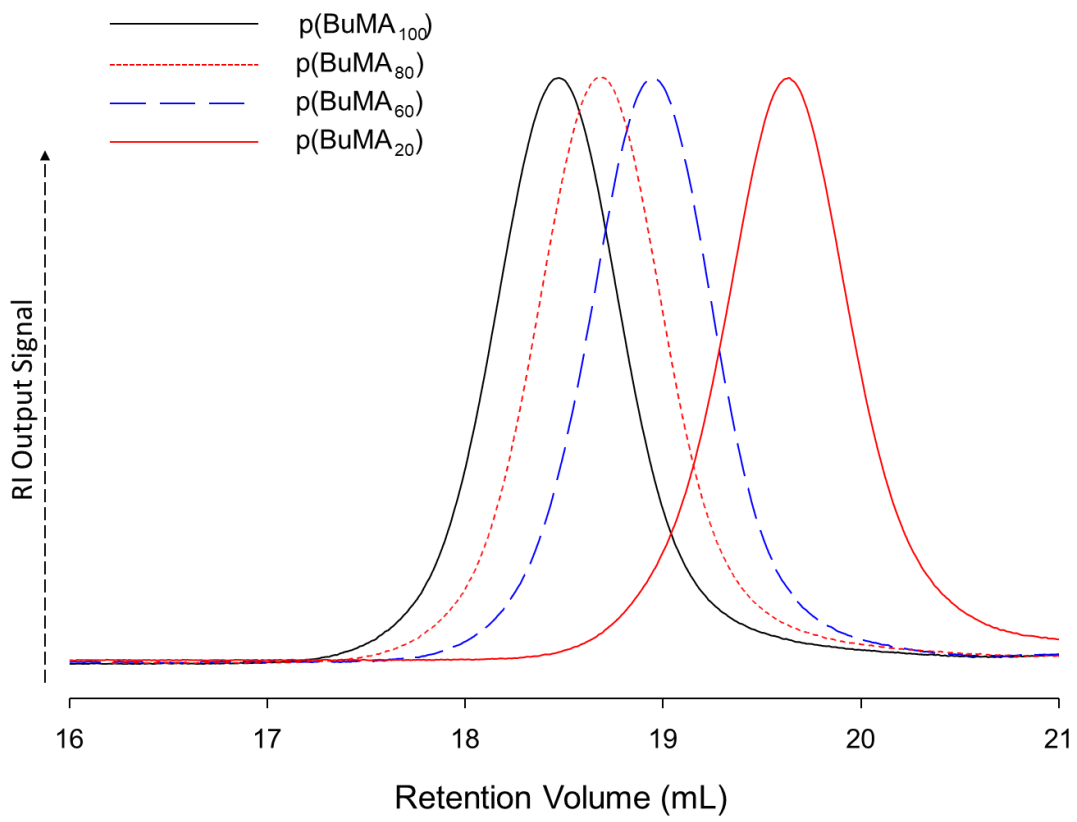


**Figure 2.10** Overlaid TD-SEC refractive index chromatograms of p(BuMA) at varying different degrees of polymerisation: a) 100 (black solid line), b) 80 (red dashed line), c) 60 (blue long dashed line) and c) 20 (red solid line) monomer units showing molecular weight distributions.

Confirmation of linear architectures was provided by analysis of the Mark-Houwink α values; these values are obtained from the Mark-Houwink-Sakurada equation (Equation 2.1). The analysis describes the relationship between the molecular weight (M), the intrinsic viscosity (η) of a polymer in a given solvent and α, which represents parameters which depend on the nature of the interaction with the polymer and solvent.

$$[\eta] = \mathrm{KM}^{\alpha} \qquad \textbf{(2.1)}$$

Typically, when in solution, a linear polymer will adopt a random coil conformation and the polymer will experience a high level of solvent interaction. Therefore, values for α are reported between 0.5 and 1.0 for linear polymers. Those obtained for the

$p(BuMA)_n$ homopolymers (0.591 - 0.807) are consistent with values expected of linear polymers.

In summary, methanolic ATRP has been utilised successfully as a technique to synthesise $p(BuMA)_n$, where n represents a varying degree of polymerisation. The polymers produced were generated with a high level of control and the experiment has shown that ATRP is a suitable polymerisation technique for targeting polymers with different $DP_n$ values.

### 2.3.2 Kinetic Studies on the Formation of Linear $p(BuMA)_{60}$ in Anhydrous Methanol *via* ATRP

Kinetic experiments are performed on controlled polymerisations to confirm that reactions proceed *via* first order kinetics with respect to monomer concentration. It provides evidence that control was maintained throughout the polymerisation and that termination reactions were negligible. Monitoring the evolution of molecular weight with respect to monomer conversion can also provide evidence that chain transfer reactions were negligible and that predictable number average molecular weights may be achieved. Methanolic ATRP reactions were conducted as previously described at 50°C for 24 hours, but aliquots were removed at nine different time points and analysed by $^1$H NMR and TD- SEC. It is important that throughout the kinetic experiment the reaction mixture is not poisoned *via* exposure to oxygen and that a dark brown homogenous solution remains in order to maintain the validity of the experiment. The kinetic study targeting $p(BuMA)_{60}$ was homogeneous throughout the polymerisation and the reaction was terminated at 98 % conversion after 24 hours. The data provided linear correlations of both $\ln([M]_0/[M])$ *vs.* time, and $M_n$ *vs.* conversion (Figure 2.11), indicating that the polymerisation of BuMA followed first order kinetics and that the concentration of active species remained constant throughout the polymerisation and irreversible termination reactions were negligible. The linear plot of $M_n$ *vs.* conversion (Figure 2.11b) provides an indication that all the chains were formed at the same time i.e. the initiation was faster than the propagation and that the chains grow homogenously throughout the polymerisations.

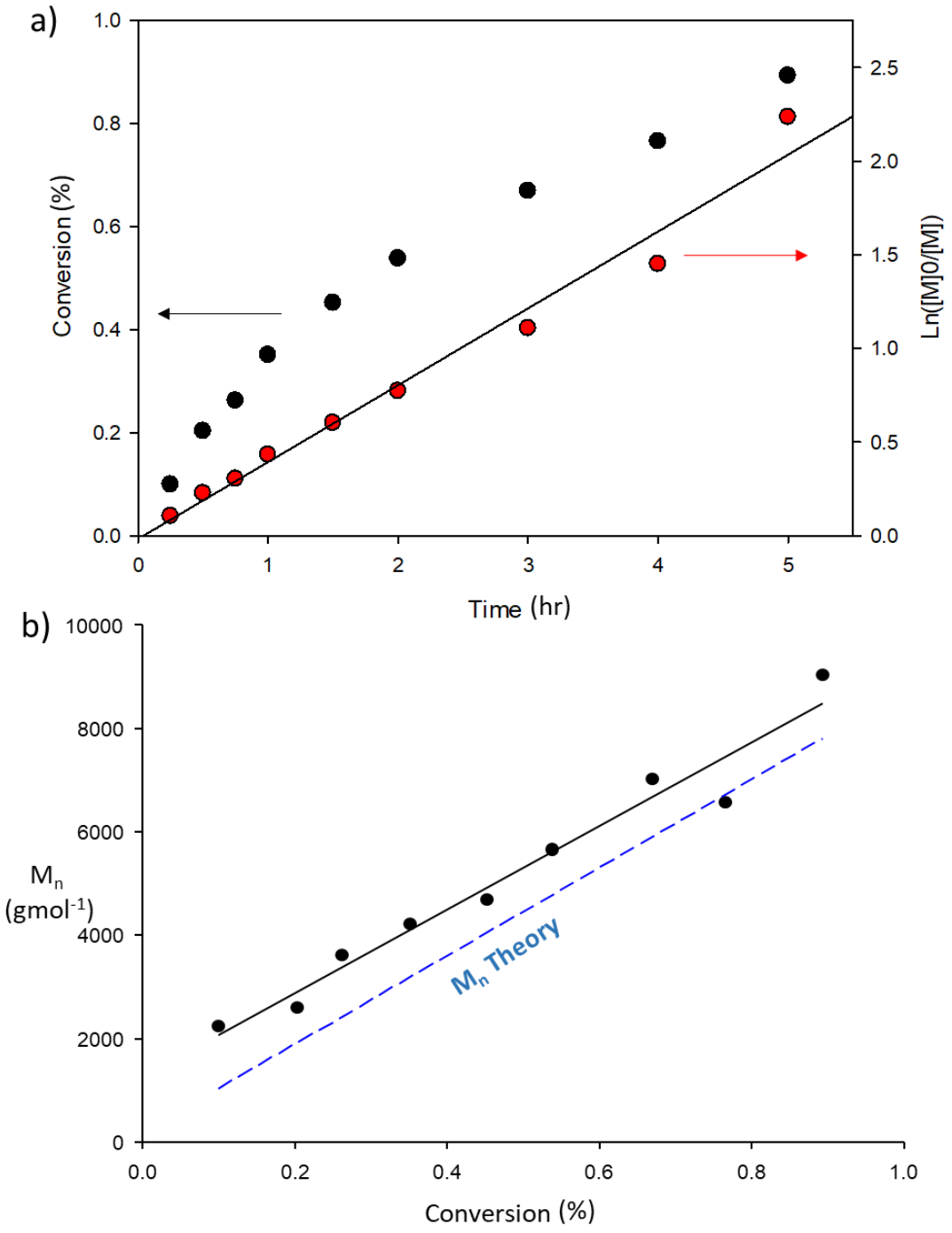


**Figure 2.11** Kinetic studies of targeted p(BuMA)$_{60}$ by ATRP in anhydrous MeOH at 50 °C: (a) conversion and semi-logarithmic plots *vs.* time (hr), and (b) evolution of $M_n$ (gmol$^{-1}$) with conversion.

### 2.3.3 Synthesis of AB Block Copolymers

Given the success of the methanolic ATRP of BuMA to yield p(BuMA) homopolymers, this method was considered as an attractive synthetic strategy to synthesise AB diblock copolymers with well-defined structural characteristics. The only difference between the preparations was the replacement of the commercially available EBiB initiator with a synthesised polymer-based macro-initiator. Therefore, the generation of the amphiphilic AB diblock copolymer consisted of two stages: firstly, the synthesis of a poly(ethylene glycol) monomethyl ether bromo isobutyrate macro-initiator (MeO-$PEG_{114}$-Br) *via* an end group modification that involved a reaction between α-bromoisobutyryl bromide and the hydroxyl chain-end functionality of poly(ethylene glycol) monomethyl ether ($PEG_{114}$-OH). The chain length of the macroinitiator (MeO-$PEG_{114}$-Br) was chosen as it is widely used within nanomedicine and detailed in literature that the higher molecular weight chain can reduce the likelihood of opsonisation from the body as discussed in Section 1.5.[72, 73] From previous data obtained, it has also been shown that AB block copolymers which are comprising of $PEG_{114}$ compared to $PEG_{45}$ produce nanoparticles which are smaller in size.[36] Following successful synthesis, the second stage is the methanolic ATRP of BuMA, initiated by the synthesised PEG macro-initiator, thereby yielding an amphiphilic AB diblock copolymer consisting of a hydrophilic PEG block covalently bonded to a hydrophobic p(BuMA) block. The targeted $DP_n$ of the BuMA B block segment was fixed at $DP_n$ 100 monomer units for consistency. Since the intended use of the AB block copolymer is to be used to provide steric stabilisation to nanoparticles, the $DP_n$ of the hydrophobic segment needs to be long enough to ensure that the chances of its incorporation within the nanoparticle core is maximised and therefore can provide maximum stabilisation. The synthesis and characterisation of the macroinitiators and copolymers will be discussed below.

### 2.3.4 Synthesis of $PEG_{114}$ Macroinitiator

The $PEG_{114}$-Br macroinitiator, (MeO-$PEG_{114}$-Br), was synthesised as previously reported *via* an esterification reaction between poly(ethylene glycol) monomethyl ether (MeO-$PEG_{114}$-OH; average molecular weight ~5000 g $mol^{-1}$) and α-bromoisobutyryl bromide (Scheme 2.5).[74-76]

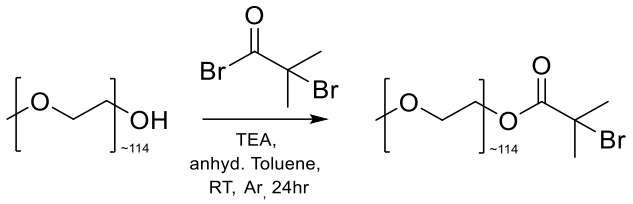


**Scheme 2.5** Synthesis of MeO-PEG$_{114}$-Br macroinitiator *via* an esterification of poly(ethylene glycol) monomethyl ether.

The monomethoxy PEG, MeO-PEG$_{114}$-OH ($M_n$ ~5000 g mol$^{-1}$) was dissolved in anhydrous toluene with the addition of triethylamine and the reaction mixture was heated to 45 °C to aid solubilisation. The solution was degassed with argon for 30 minutes and then allowed to cool to room temperature before α-bromoisobutyryl bromide was added drop-wise over a period of 30 minutes. The formation of a white precipitate indicated the progress of the reaction and the formation of a triethylammonium bromide salt. The reaction medium was left to stir for 24 hours at room temperature under Ar. After reaction completion, a hot filtration (50 °C) was performed and the crude product was washed with small amounts of hot toluene (~ 10 mL, 50 °C). The solvent was then concentrated *in vacuo*. The resulting product was diluted in THF and passed through a short basic alumina column before further purification by precipitation into room temperature hexane. The precipitation process was repeated and the product (white powder) was dried under vacuum at 35 °C for 24 hours. The MeO-PEG$_{114}$-Br macro-initiator was characterised using a number of analytical techniques: $^{1}$H-NMR, $^{13}$C-NMR and TD-SEC (Figures 2.12-2.13). $^{1}$H-NMR analysis of the macro-initiator and assignment of environments was obtained by normalising the integration of the methoxy group (Figure 2.8, proton a, δ = 3.38 ppm) to 3H. Assignment of the MeO-PEG$_{114}$-Br is assigned to two methylene groups i.e. 4 protons, (Figure 2.12, protons b-f, δ = 3.65 ppm) gave an integration value of 452, which is expected for a ~5000 g mol$^{-1}$ MeO-PEG$_{114}$-Br macroinitiator. The two methyl groups (6 protons) of the initiator end group (Figure 2.8, protons h, δ = 1.94 ppm) and its relative intensity compared to the methoxy, provide confirmation that the end group modification had been successful and confirmed the structure of the desired compounds. The integral ratio theoretically should be 6:3 for the two methyl groups and the methoxy respectively, however the integration value was slightly lower (5.37) than the theoretical value (6) which suggested a purity of 90

% which may be indicative that there may have been an impurity present within the sample, likely to be the starting material, MeO-PEG$_{114}$-OH. The success of the reaction however was further supported by $^{13}$C NMR and the assignment of the resonances attributed to the two methyl groups (Figure 2.13, carbons j, δ = 30 ppm).

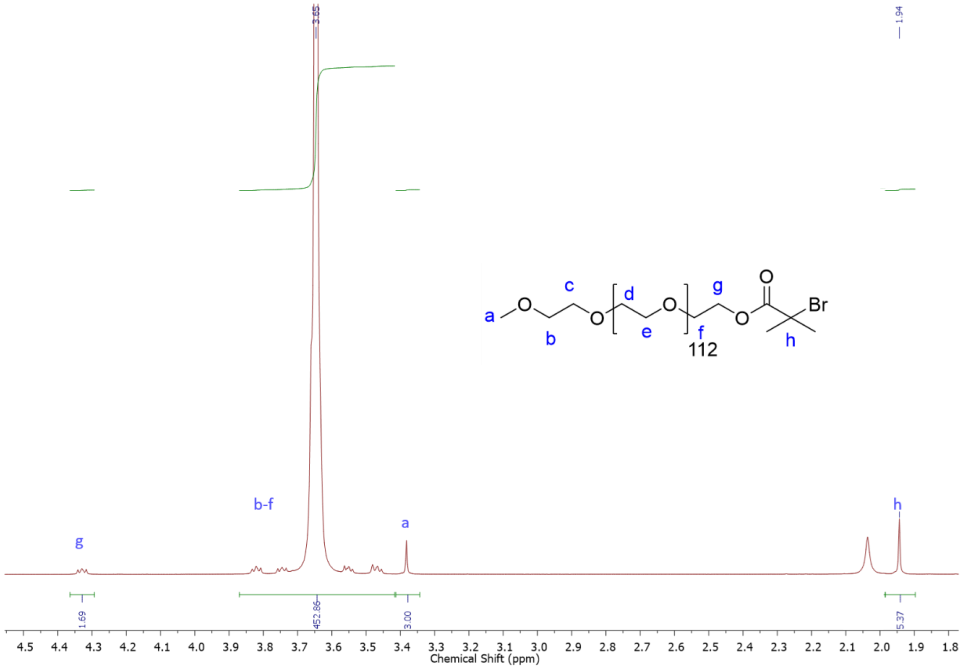


**Figure 2.12** $^{1}$H NMR ($CDCl_3$) spectrum of MeO-PEG$_{114}$-Br macro-initiator.

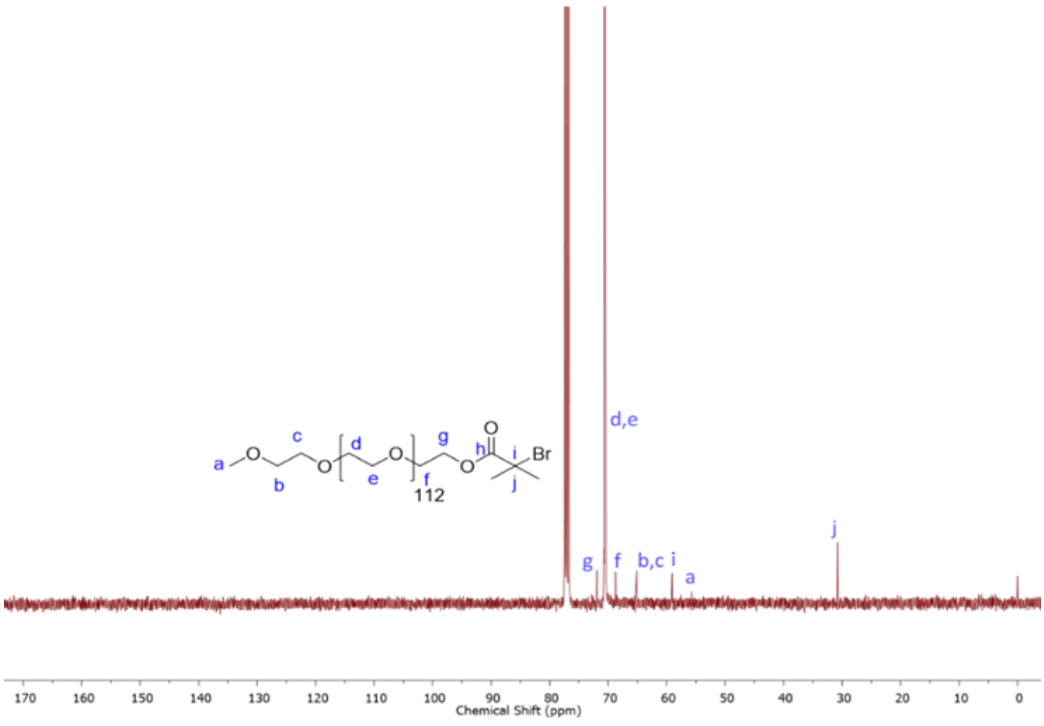


**Figure 2.13** $^{13}$C NMR ($CDCl_3$) spectrum of MeO-PEG$_{114}$-Br macro-initiator.

It is noted that the carbon associated with the carbonyl group (h) is absent from the $^{13}C$ NMR spectra, which is likely due to the polarity of the $CDCl_3$. However, all other expected resonances are present. TD-SEC analysis of MeO-$PEG_{114}$-Br (Table 2.2) showed that monomodal traces were observed and that the macro-initiator had a narrow molecular weight distribution (Đ = 1.03), and a $M_n$ value (4 950 g $mol^{-1}$) was obtained which was in good agreement compared to the $M_n$ theory (5 150 g $mol^{-1}$).

### 2.3.5 Synthesis of AB Diblock Copolymers *via* Methanolic ATRP of BuMA

The ATRP polymerisations of BuMA initiated by the PEG macroinitiator (MeO-$PEG_{114}$-Br) targeted a $DP_n$ of 100 monomer units and was carried out at 50 °C in anhydrous MeOH utilising the same catalytic system of Cu(I)Cl:bpy (1:2) discussed in Section 2.3 (Scheme 2.6).

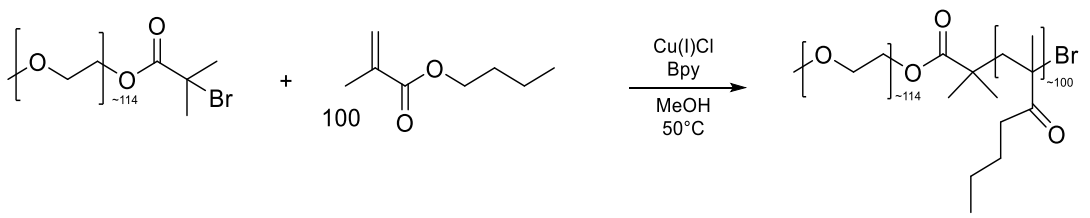


**Scheme 2.6** A reaction scheme for the methanolic ATRP synthesis of AB block copolymer using MeO-$PEG_{114}$-Br as macroinitiator and BuMA as the monomer with a target $DP_n$ of 100 monomer units.

The reaction was conducted at 50 wt. % solids in MeOH, as done previously. The polymerisation proceeded homogenously with the typical dark brown colour associated with Cu catalysed ATRP. The reaction proceeded for 96 hours and was terminated *via* exposure to oxygen before an aliquot was taken and diluted with $CDCl_3$ for $^1H$ NMR analysis to determine the monomer conversion. As before, the catalytic system was removed *via* a neutral alumina column and the polymer solution was concentrated *in vacuo* before being precipitated into ice cold hexane to yield a white solid. The polymer was then dried *in vacuo* at 35 °C for 24 hours to ensure complete solvent removal. Analysis of the AB block copolymer was conducted *via* $^1H$ NMR ($CDCl_3$) and confirmed the complete removal of the unreacted monomer by the disappearance of the resonances associated with the vinyl protons (c.a. 6.09 and 5.54 ppm ($CDCl_3$)). Characterisation of the purified AB diblock copolymer was conducted *via* TD-SEC (Table 2.2).

**Table 2.2** TD-SEC data of $PEG_{5k}$ macroinitiator and AB block copolymer synthesised *via* methanolic ATRP of BuMA at 50 °C targeting a $DP_n$ of 100 monomer units.

| | | | TD-SEC (THF)[c] | | |
|---|---|---|---|---|---|
| Polymer composition | [a] Conversion (%) | [b] $M_n$ Theory (g $mol^{-1}$) | $M_n$ (g $mol^{1}$) | $M_w$ (g $mol^{-1}$) | Đ |
| MeO-$PEG_{114}$-Br | - | 5 150 | 4 950 | 5 100 | 1.03 |
| p($PEG_{114}$-*b*-$BuMA_{100}$) | 98 | 19 200 | 27 700 | 37 300 | 1.21 |

[a] Calculated by $^1$H-NMR *spectroscopy* of polymerisation mixture at t=final. [b] Theoretical $M_n$ calculated as ((target $DP_n$ x MW monomer) x (conversion/100)) + initiator residue. [c] Calculated by TD-SEC using THF/TEA mobile phase (98/2 v/v%) at 35 °C, flow rate of 1mL $min^{-1}$.

The polymerisation achieved a high monomer conversion (98%) to yield a well-defined AB diblock copolymer with a narrow molecular weight distribution (Đ = 1.21), suggesting the polymerisation had proceeded with control. The calculated $M_n$ (NMR) value (21 150 g $mol^{-1}$) correlated well with the $M_n$ theory (19 200 g $mol^{-1}$) based on monomer conversion. However, the calculated $M_n$ (TD-SEC) value (27 700 g $mol^{-1}$) was higher (by a factor of 1.4) than the $M_n$ theory (19 200 g $mol^{-1}$), which may indicate a poor initiation efficiency. An approximate estimation of initiator efficiency can be determined using a simple calculation of ((Theoretical $M_n$)/ (Observed $M_n$ (TD-SEC)) x 100 %), which in this case gave a value of 70% for MeO-$PEG_{114}$-Br; this is consistent with a previously reported value of 73%.[53] One possible reason for this is that not all chain-ends of the macro-initiator were bromide functionalised and therefore exist as dead chains (i.e. not capable of initiating polymerisations). Ideally, these dead chains should have been removed during the purification step of the macro-initiator synthesis, but the almost identical nature of the starting material and the final product rendered this very difficult. The initiator efficiency has also been calculated using $^1$H NMR (91%), which is higher than that calculated by TD-SEC (70 %). This is likely due to residual amount of unreacted macroinitiator in the sample, highlighted by the slight shoulder in the overlaid RI chromatograms (Figure 2.14). However, the relative success of the polymerisation is highlighted in the overlaid RI chromatograms through the elution of AB block copolymer at a decreased retention volume relative to MeO-$PEG_{114}$-Br macro-initiator.

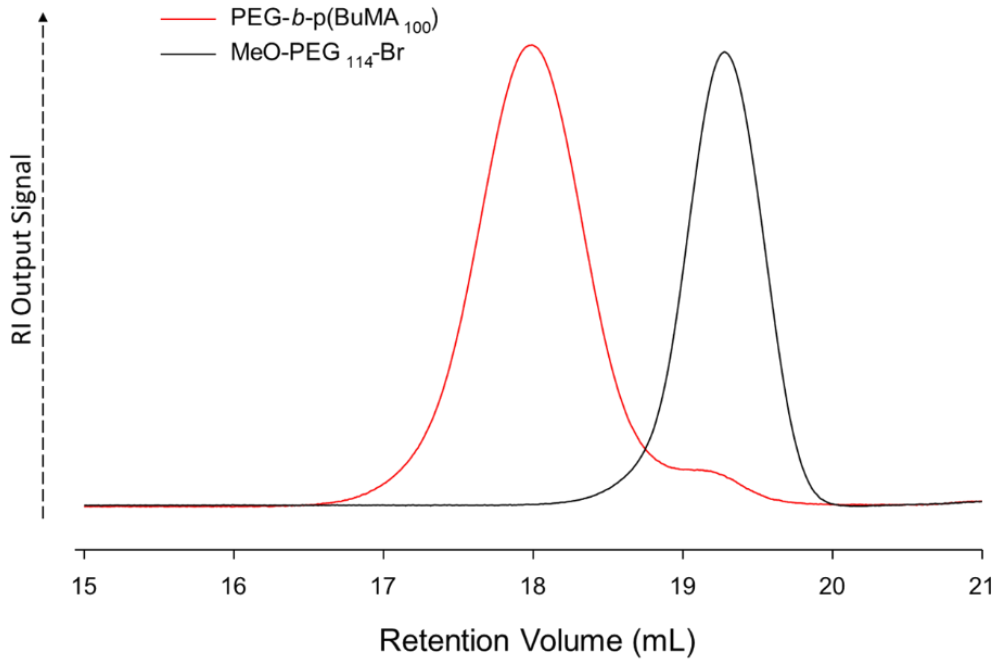


**Figure 2.14** TD-SEC analysis of p($PEG_{114}$-*b*-$BuMA_{100}$) generated *via* polymerisation from MeO-$PEG_{114}$-Br initiator with BuMA using Cu-ATRP. Overlaid TD-SEC chromatograms showing molecular weight distributions of a) p($PEG_{114}$-*b*-$BuMA_{100}$) (red) and b) MeO-$PEG_{114}$-Br (black).

### 2.3.6 Synthesis of Linear Polymers *via* Methanolic ATRP of Various Methacrylate Monomers

The physicochemical properties of polymers are largely determined by the chemistry of their monomer repeat units.[77] Therefore, the methanolic ATRP of other hydrophobic monomers was investigated in order to expand the library of linear polymers already synthesised by this method. The two monomers that were chosen were EHMA and HPMA (Figure 2.15), both of which are commercially available. Their chemistries differ by the pendant group and therefore their hydrophobicity. These variations in the monomer chemistry, such as the presence of a hydroxy group in the HPMA monomer and the longer alkyl chain in the EHMA monomer, is hoped to introduce different polarities, hydrophobicity and hydrogen bonding to the polymer and the subsequent nanoparticles that are to be generated (Chapter 3.3.1). Optimum polymerisation conditions of HPMA *via* ATRP had previously been determined from research within the Rannard group to produce p(HPMA).[74, 78-80]

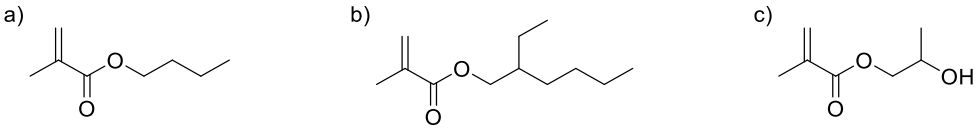


**Figure 2.15** Chemical structures of: a) BuMA, b) EHMA and c) HPMA.

Polymerisations generating p(EHMA)$_n$ *via* methanolic ATRP had not been investigated in significant detail at the time of this study. Although, recent reports from the Rannard group have described the synthesis of both linear and branched (co)polymers of p(EHMA) in MeOH.[50]

### 2.3.6.1 Synthesis of Linear Homopolymers *via* Methanolic ATRP

The polymerisations of EHMA and HPMA with a targeted DP$_n$ of 100 and 20 monomer units per chain were conducted as previously described. The polymerisations were carried out at 50 °C in anhydrous MeOH with Cu(I)Cl:(bpy) as the catalytic system (Scheme 2.7). An initial molar ratio of monomer:EBiB:Cu(I)Cl:bpy was set at 100:1:1:2 for the reactions targeting a DP$_n$ of 100 monomer units, and 20:1:1:2 for those reactions targeting a DP$_n$ of 20 monomer units. The amount of MeOH added was set to 50% wrt to total solid mass, as before.

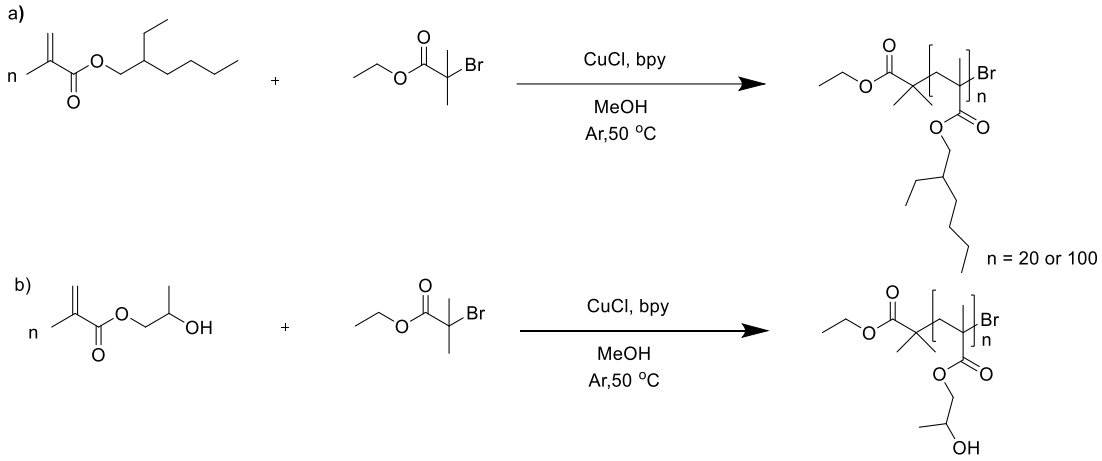


**Scheme 2.7** Linear homopolymerisation of EHMA and HPMA methacrylate monomers *via* copper catalysed methanolic ATRP targeting DP$_n$ of 20 and 100 monomer units.

The polymerisations of HPMA and EHMA with DP$_n$ = 20 monomer units proceeded for 24 hours, whereas when the DP$_n$ was increased to 100 monomer units the reactions proceeded for a longer period of time of 48 and 72 hours for the HPMA and EHMA polymerisations, respectively.

The HPMA polymerisation reactions all proceeded with the classic Cu-ATRP characteristic of a dark brown homogenous solution being observed throughout the polymerisation. Interestingly, however, the EHMA polymerisations targeting the DP$_n$ of 100 and 20 monomer units both showed phase-separation after the first few hours

of the reactions. More specifically, the polymerisation medium had turned biphasic with an opaque dark brown liquid above a cream solid-like layer. In light of previous studies in the group investigating the UCST behaviour of pBuMA in various monomer-MeOH mixtures, the differences observed between the homogeneity between the polymerisations could be due to the poor solubility of p(EHMA) in the monomer-MeOH mixtures. It is likely that in the early stages of the polymerisation, low molecular weight oligomers/polymers are retained in solution due to the co-solvency effect of the EHMA monomer. However, as the polymerisation progresses, and the monomer is depleted, the co-solvency effect may not be enough to retain the polymer in solution. Phase separation observed early on in the polymerisations highlights that the co-solvency effect was minimal in its thermodynamic contribution to the Gibbs free energy of mixing. [81]

After the HPMA polymerisations had reached high monomer conversions (≥ 98%), determined by $^{1}$H-NMR analyses, the polymerisations were terminated by exposure to air and addition of THF solvent. Due to the biphasic nature of the EHMA polymerisations, they were terminated *via* the addition of $CDCl_3$ instead of THF, which enabled a crude NMR sample to be taken directly from the reaction mixture once solubilised. Integration of the resonances attributed to the vinyl protons within the $^{1}$H NMR spectra showed that despite the biphasic nature, the polymerisation was still able to achieve high monomer conversions (≥ 99%). A change in colour was observed for both the HPMA polymerisations from dark opaque brown to a transparent green solution. This colour change was also observed for the EHMA polymer mixture but with the additional observation that the biphasic mixture only became solvated and homogenous with stirring for 1 hour. The polymers were then purified *via* a two-stage process. Firstly, the catalytic system was removed by passing the diluted reaction mixture over a neutral alumina column using either $CHCl_3$ or THF as the mobile phase for the purifications of p(EHMA) and p(HPMA), respectively. The polymer solutions were then precipitated, as before, to remove any unreacted monomer, residual initiator and free ligand. The linear p(EHMA) homopolymers were precipitated into cold MeOH and the linear p(HPMA) homopolymers into room temperature hexane. The polymers were then dried *in vacuo* at 35 °C for 24 hours to

ensure complete solvent removal. Analysis of the polymers was then conducted *via* $^{1}$H-NMR spectroscopy to confirm the complete removal of any residual initiator, unreacted monomer and free ligand. Subsequent analysis *via* TD-SEC in THF/TEA (98/2 v/v %), was used to determine the molecular weights and dispersities of the synthesised linear homopolymers (Table 2.3).

**Table 2.3** Methanolic Cu-ATRP of hydrophobic monomers, EHMA and HPMA, for linear polymer synthesis at 50 °C with target $DP_n$ of 100 and 20 monomer units.

| | | | | TD-SEC (THF)[d] | | | |
|---|---|---|---|---|---|---|---|
| [a] Target Polymer composition | Time (hr) | [b] Conversion (%) | [c] $M_n$ Theory (g mol$^{-1}$) | $M_n$ (g mol$^{-1}$) | $M_w$ (g mol$^{-1}$) | Đ | Mark Houwink α Value |
| $p(EHMA)_{20}$ | 24 | > 99 % | 4 050 | 7 530 | 10 450 | 1.38 | 0.486 |
| $p(EHMA)_{100}$ | 72 | 99 % | 19 850 | 23 900 | 35 300 | 1.48 | 0.621 |
| $p(HPMA)_{20}$ | 24 | 98 % | 3 000 | 4 300 | 7 200 | 1.67 | 0.480 |
| $p(HPMA)_{100}$ | 48 | 99 % | 14 500 | 24 500 | 30 400 | 1.24 | 0.526 |

[a] Target $DP_n$ calculated by [Monomer]/[EBiB]. [b] Calculated by $^{1}$H NMR spectroscopy of polymerisation mixture at t=final. [c] Theoretical $M_n$ calculated as ((target $DP_n$ x mw monomer) x (conversion/100)) + initiator residue). [d] Calculated by TD-SEC using THF/TEA mobile phase (98/2 v/v%) at 35 °C, flow rate of 1mL min$^{-1}$.

The TD-SEC analysis of the polymers revealed that the $M_n$ values did vary slightly from that of the theoretical values, which again may be attributed to the initiator efficiency of EBiB. The initiator efficiencies were calculated as previously described and values were obtained as follows: $p(EHMA)_{20}$ (54%), $p(EHMA)_{100}$ (84%), $p(HPMA)_{20}$ (70%) and $p(HPMA)_{100}$ (60%). The dispersity values obtained for these homo-polymerisations were higher compared to that of the BuMA homo-polymerisations. It is not surprising that $p(EHMA)_n$ possessed higher dispersity values of $Đ$ = 1.38 and 1.48 for the $DP_n$ 20 and 100 monomer units, respectively. This is because it is likely to be a result of the phase separation that occurred during the polymerisation, which would have isolated polymer chains from the monomer/MeOH solution and subsequently impeded further growth. Whereas, the higher dispersities of $p(HPMA)_n$ compared to that of $p(BuMA)_n$ could be due the equilibrium of ATRP being impacted by the relative reactivity of the two monomers. Although higher than that of p(BuMA), the dispersity value of $p(HPMA)_{100}$ ($Đ$ = 1.24) suggested that the polymerisation still proceeded with control. However, the dispersity value obtained for $p(HPMA)_{20}$ ($Đ$=1.69) is significantly higher than what would be anticipated for that of a controlled polymerisation, however, it is common that low molecular weight material will have

a higher dispersity values due to the nature of the calculation. The Mark-Houwink α values obtained for the homopolymers (0.480 - 0.621) are consistent with that expected of linear polymers.

### 2.3.7 Synthesis of Statistical Linear Copolymers *via* Methanolic ATRP

Statistical copolymers can be generated by using a mixed monomer feed of different monomers before initiation and is typically done to manipulate the chemical and physical properties of the copolymers that are produced. In this study, linear statistical copolymers were generated by blending 2 of the 3 monomers with the target DPn set to 100 and the comonomers selected were used at an equal molar ratio to generate 50 monomer units each with respect to the initiator concentration.

The polymerisations were conducted as before *via* methanolic ATRP at 50 ˚C using the same catalytic system as that used in earlier polymerisations. The reactions all proceeded for 72 hours and were terminated by exposure to oxygen and *via* addition of THF, with the exception of p($BuMA_{50}$-co-$EHMA_{50}$); this was poisoned with $CDCl_3$ due to the biphasic nature of the polymerisation. Purification was conducted as before, passing the crude polymers through a neutral alumina column before conducting a precipitation into an appropriate antisolvent. TD-SEC and $^1$H NMR analyses were conducted on the purified polymers (Table 2.4).

**Table 2.4** Methanolic Cu-ATRP of hydrophobic monomers at 50 °C to generate statistical linear copolymers with overall target $DP_n$ of 100 monomer units.

| | | | TD-SEC (THF)[d] | | | |
|---|---|---|---|---|---|---|
| [a] Target Polymer composition | [b] Conversion (%) | [c] $M_n$ Theory (g mol$^{-1}$) | $M_n$ (g mol$^1$) | $M_w$ (g mol$^{-1}$) | Đ | Mark - Houwink α value |
| p($BuMA_{50}$-co-$EHMA_{50}$) | > 99 % | 16 900 | 19 800 | 22 500 | 1.13 | 0.686 |
| p($BuMA_{50}$-co-$HPMA_{50}$) | 98 % | 14 000 | 18 100 | 22 200 | 1.22 | 0.620 |
| p($EHMA_{50}$-co-$HPMA_{50}$) | 99 % | 17 100 | 22 100 | 26 100 | 1.18 | 0.628 |

[a] Target $DP_n$ calculated *[Monomer] / [EBiB]*, [b] Calculated by $^1$H-NMR *spectroscopy* of polymerisation mixture at t=final. [c] Theoretical $M_n$ calculated as ((target $DP_n$ x mw monomer) x (conversion/100)) + initiator residue. [d] Calculated by TD-SEC using THF/TEA mobile phase (98/2 v/v%) at 35 °C, flow rate of 1mL min$^{-1}$.

The reactions all reached high monomer conversions (> 98%) and the polymers produced were generated with control, as indicated by the low dispersity values ($1.13 \leq Đ \leq 1.22$). As previously observed, the $M_n$ values (19 800 – 22 100 g mol$^{-1}$) did deviate slightly from the $M_n$ theory values, again likely due to initiator efficiency, but

still highlighted a reasonable control of the molecular weight of the primary polymer chains. The obtained Mark-Houwink α values ($0.620 \leq \alpha \leq 0.686$) indicated that the polymers were linear in architecture.

Interestingly, p($HPMA_{50}$-co-$EHMA_{50}$) did not precipitate from the reaction medium, and instead remained homogenous and yet for the polymerisation of p($BuMA_{50}$-co-$EHMA_{50}$), biphasic behaviour was observed at the late stages of the polymerisation. Homopolymerisation of EHMA have been shown to proceed with a biphasic nature.[50] However, from the inclusion of HPMA monomer this behaviour was altered. The difference in behaviour observed could be rationalised by the simple fact that MeOH is a much better solvent for HPMA than EHMA and therefore the HPMA monomer residues in the polymer chain enable the chain to remain solvated. Despite the polymerisation of p($BuMA_{50}$-co-$EHMA_{50}$) yielding a biphasic reaction mixture, a low dispersity value (1.13) was still obtained. The biphasic nature was only observed after the reaction had proceeded for at least 60 hours, so it is likely the polymerisation had already reached high conversion. The obtained Đ value for p($HPMA_{50}$-co-$EHMA_{50}$) (1.18) was also lower than the values obtained for the corresponding homopolymerisation of HPMA and EHMA, which could be as a result of the polymer remaining in solution for longer and therefore was more likely to polymerise better.

### 2.3.8 Synthesis of $PEG_{114}$ AB Diblock Copolymers *via* Methanolic ATRP using EHMA and HPMA as the Monomers

In order to expand the library of the amphiphilic AB block copolymers available, the synthesis of p($PEG_{114}$-*b*-$EHMA_{100}$) and p($PEG_{114}$-*b*-$HPMA_{100}$) was conducted. The ATRP polymerisations were initiated by the PEG macroinitiator (MeO-$PEG_{114}$-Br), targeting a $DP_n$ of 100 monomer units and was carried out at 50 °C in anhydrous MeOH. The same catalytic system of Cu(I)Cl:bpy (1:2) was used as discussed in Section 2.3. The MeOH concentration was set to 50% with respect to total solid mass, as done previously (Scheme 2.8).

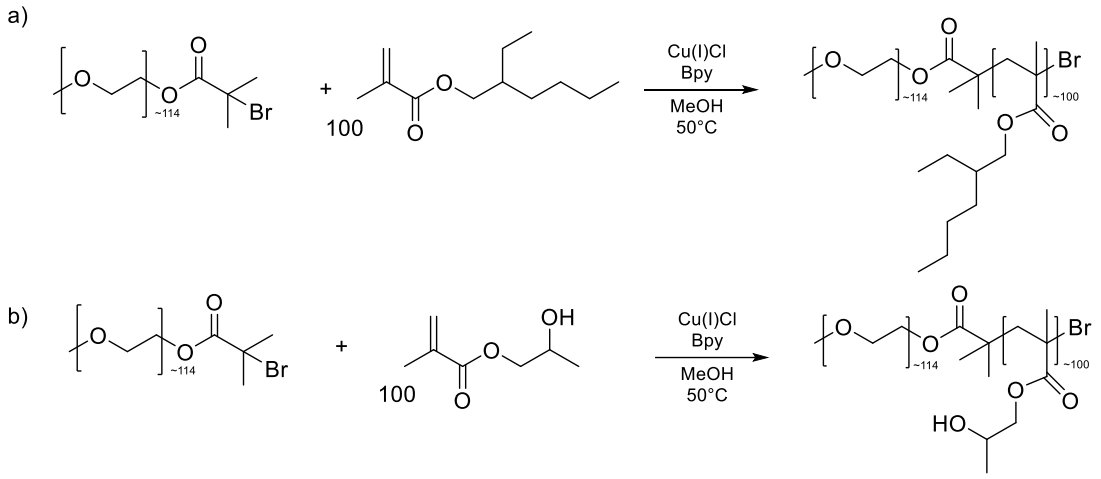


**Scheme 2.8** Schematic representation of the synthesis of a) p($PEG_{114}$-*b*-$EHMA_{100}$) and b) p($PEG_{114}$-*b*-$HPMA_{100}$).

The polymerisation proceeded homogenously with the typical dark brown colour associated with Cu catalysed ATRP and was terminated *via* exposure to oxygen before an aliquot was taken and diluted with $CDCl_3$ for $^1$H NMR analysis to determine the monomer conversion. As before, the catalytic system was removed *via* a neutral alumina column and the polymer solution was concentrated *in vacuo* before being precipitated into ice cold hexane to yield a white solid. The polymer was then dried *in vacuo* at 35 °C for 24 hours to ensure complete solvent removal. Analysis of the AB block copolymer was conducted *via* $^1$H-NMR ($CDCl_3$) (Appendix, Figure A4 and A5) and confirmed the complete removal of any residual initiator, unreacted monomer and free ligand. Characterisation of the purified AB diblock copolymer was conducted *via* $^1$H NMR spectroscopy and TD-SEC (Table 2.5).

**Table 2.5** TD-SEC data of AB block copolymers synthesised *via* methanolic ATRP at 50 °C with target $DP_n$ of 100 monomer units.

| | | | TD-SEC (THF)[d] | | |
|---|---|---|---|---|---|
| [a] Target Polymer composition | [b] Conversion (%) | [c] $M_n$ Theory ($gmol^{-1}$) | $M_n$ ($gmol^1$) | $M_w$ ($gmol^{-1}$) | Đ |
| p($PEG_{114}$-*b*-$EHMA_{100}$) | > 99 % | 24 400 | 32 400 | 39 000 | 1.19 |
| p($PEG_{114}$-*b*-$HPMA_{100}$) | 98 % | 14 000 | 18 100 | 22 200 | 1.71 |

[a] Target $DP_n$ calculated *[Monomer] / [EBiB]*, [b] Calculated by $^1$H-NMR *spectroscopy* of polymerisation mixture at t=final. [c] Theoretical $M_n$ calculated as ((target $DP_n$ x mw monomer) x (conversion/100)) + initiator residue. [d] Calculated by TD-SEC using THF/TEA mobile phase (98/2 v/v%) at 35 °C, flow rate of 1mL $min^{-1}$.

The polymerisations proceeded for 72 hours until high monomer conversions were reached, determined by $^1$H NMR. Both polymerisations proceeded under

homogeneous reaction conditions with a dark brown colour observed throughout; in the case of the EHMA polymerisation, this observation was in contrast to that observed during the synthesis of the p(EHMA) homopolymers, which proceeded with a biphasic nature. It is believed that the hydrophilic PEG functionality had a significant effect on retaining the block copolymer within the methanolic solution. The refractive index trace obtained for p($PEG_{114}$-*b*-$HPMA_{100}$) showed a small shoulder on the right-hand side of the peak at a higher retention time that had a significant contribution to this high dispersity value (Figure 2.16).

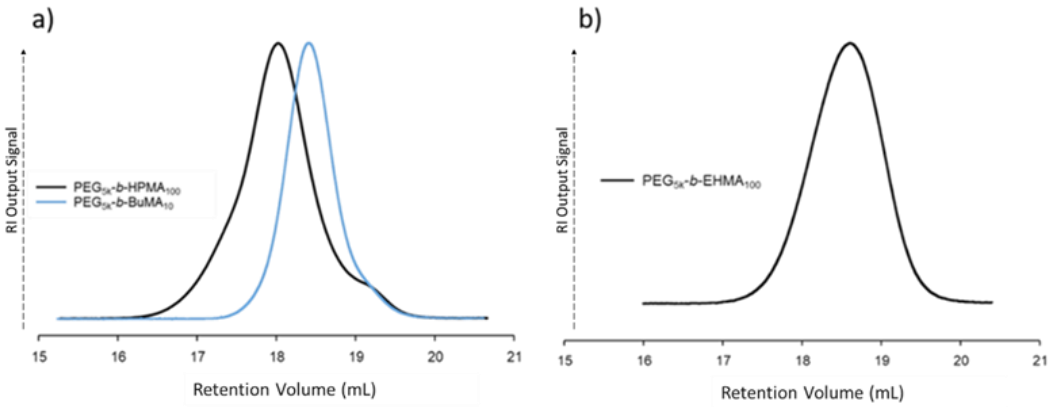


**Figure 2.16** TD-SEC overlay of a) $PEG_{113}$-*b*-p($BuMA_{100}$) vs $PEG_{113}$-*b*-p($HPMA_{100}$) obtained with DMF containing 0.01M LiBr at 60˚C, 1 mL $min^{-1}$ flow rate and b) $PEG_{114}$-*b*-p($EHMA_{100}$) obtained with THF containing 2% TEA (v/v) at 35˚ C, 1 mL $min^{-1}$ flow rate.

This shoulder was believed to be unreacted MeO-$PEG_{114}$-Br macro-initiator that has not been successfully removed during the purification *via* precipitation. This was further confirmed by overlaying the RI traces of p($PEG_{114}$-*b*-$HPMA_{100}$) and MeO-$PEG_{114}$-Br (Figure 2.17), which showed that the shoulder eluted at a very similar retention time to that of the macro-initiator. The purification of the AB block copolymers involved the precipitation into an antisolvent of hexane. This is also an anti-solvent for the macro-initiator, meaning purification was challenging. It could also be presence of MeO-$PEG_{114}$-OH which was not removed successfully during the purification of the macro-initiator and has subsequently been carried forward in the AB block copolymer synthesis when using the macro-initiator.

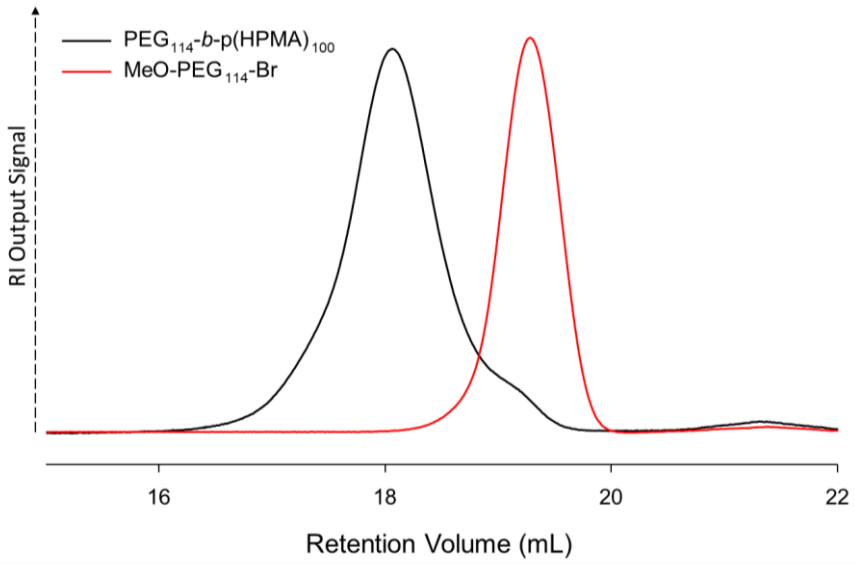


**Figure 2.17** Overlaid TD-SEC chromatograms of p($PEG_{114}$-*b*$HPMA_{100}$) (black line) and MeO-$PEG_{114}$-Br (red line). Obtained with THF containing 2% TEA (v/v) at 35˚C, 1 mL $min^{-1}$ flow rate.

### 2.3.9 Synthesis of Statistical Branched Copolymers with EGDMA via Methanolic ATRP

Having established the viability of methanolic ATRP as technique suitable for the controlled synthesis of linear polymers varying in functionality and composition, this technique was extended towards the synthesis of high molecular weight branched statistical copolymer architectures. These materials were synthesised following a modified Strathclyde approach *via* Cu-catalysed ATRP of BuMA. The polymerisation was conducted as described previously for the generation of linear p(BuMA) homopolymers (Section 2.4.1) but with the addition of small amounts of a divinyl monomer - ethylene glycol dimethacrylate (EGDMA) - within the synthesis, which led to the inter-chain branching of primary polymer chains (Scheme 2.9). It is important to note that the equivalence of the divinyl monomer had to be on average less than one equivalent per primary chain to avoid gelation of the polymeric material, as described by the Flory-Stockmayer theory.[41-44]

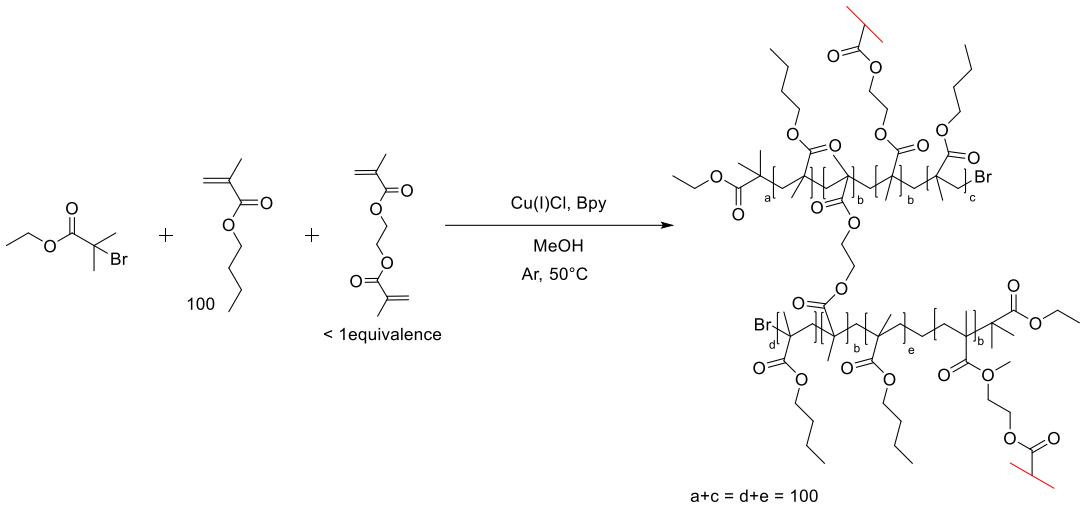


**Scheme 2.9** The methanolic ATRP of BuMA with the inclusion of divinyl monomer EGDMA at equivalence X (0.85-1) using the EBiB initiator, targeting a $DP_n$ =100 monomer units, to yield branched copolymer p($BuMA_{100}$-co-$EGDMA_x$).

The incorporation of EGDMA with [EGDMA]/[EBiB] molar equivalences varying between 0.85 and 0.95 yielded materials with varying molecular weights. The weight average number of chains within the branched species was calculated *via* a crude calculation, by dividing the $M_w$ value of the branched copolymers by the $M_n$ of the linear counterpart (Table 2.6). The polymerisations targeting a $DP_n$ of 100 monomer units proceeded *via* Cu-catalysed methanolic ATRP at 50 ˚C. An initial molar ratio of BuMA:EGDMA:EBiB:CuCl:bpy was set at 100:X:1:1:2, where X represents the varying equivalences of the divinyl monomer. All the reactions proceeded for 72 hours with the characteristic brown homogenous solution as previously observed for $p(BuMA)_{100}$. The monomer conversions were high for all polymerisations (≥ 98%), as determined by $^1$H-NMR analysis. This is essential for the formation of high $M_w$ branched copolymers following a modified Strathclyde method, as the propagation through the pendent vinyl group only occurs during the latter stages of the reaction (Section 2.2.3).[40] Reactions were terminated following exposure to oxygen and subsequent dilution with THF, the catalytic system was removed by passing the polymer solution through a neutral alumina column and all polymers were purified by precipitation into MeOH. The branched copolymers were then characterised by $^1$H-NMR (Appendix, Figure A6) and TD-SEC (Table 2.6).

**Table 2.6** Methanolic Cu-ATRP of BuMA at 50 °C using varying equivalences of divinyl monomer EGDMA to generate branched statistical copolymers with a targeted $DP_n$ of 100 monomer units.

| | | TD-SEC (THF)[c] | | | | |
|---|---|---|---|---|---|---|
| [a] Target polymer composition | [b] Conversion (%) | $M_n$ (g mol[1]) | $M_w$ (g mol$^{-1}$) | Đ | Mark - Houwink α value | [d] Weight average number of chains |
| p(BuMA$_{100}$-co-EGDMA$_{0.85}$) | > 99 % | 35 950 | 99 100 | 2.76 | 0.430 | 4 |
| p(BuMA$_{100}$-co-EGDMA$_{0.90}$) | 98 % | 39 700 | 271 250 | 6.83 | 0.405 | 11 |
| p(BuMA$_{100}$-co-EGDMA$_{0.95}$) | > 99 % | 125 700 | 2 140 000 | 17.02 | 0.428 | 105 |
| p(BuMA$_{100}$-co-EGDMA$_{1.00}$) | Insoluble Gel | | | | | |

[a] Target $DP_n$ calculated by *[nBuMA] / [EBiB]*, [b] Calculated by $^1$H NMR *spectroscopy* of polymerisation mixture at t=final. [c] Calculated by TD-SEC using THF/TEA mobile phase (98/2 v/v%) at 35 °C, flow rate of 1mL min$^{-1}$. [d] Calculated by $M_w$ of branched copolymer (TD-SEC)/$M_n$ of corresponding linear polymer (TD-SEC).

Analysis of the branched p(BuMA-co-EGDMA) copolymers by TD-SEC (THF) showed that the $M_w$ and $M_n$ values were significantly higher than the linear homopolymer analogues (Section 2.3.1, Table 2.1), which clearly indicates that the incorporation of the divinyl monomer EGDMA had an influence on the polymer architecture and that branched structures have been generated. Furthermore, an increase in $M_w$ and $M_n$ values was observed as the [EGDMA]/[EBiB] molar ratio was increased. The branched copolymer, *p*(BuMA$_{100}$-*co*-EGDMA$_{0.95}$) exhibited the highest molecular weight ($M_n$ = 125 kg mol$^{-1}$; $M_w$ = 2140 kg mol$^{-1}$) within the series. As expected, when the molar equivalence of EGDMA relative to EBiB was increased to 1, the formation of an insoluble gel occurred. The molecular weight distributions (2.76 ≤ Đ ≤ 17.02) were significantly broader than that of the linear homopolymer (Đ = 1.14), which again indicates the statistical inter-chain branching of the primary polymer chains in the presence of EGDMA. The Mark-Houwink α values (0.405-0.430) were significantly lower compared to the linear analogue (0.676). It has been reported that for branched polymers, depending on the degree/extent of branching within the branched architecture, that the α value will typically vary between 0.2 and 0.5, which further validates that branched copolymer architectures have been obtained. From a crude calculation, the weight average number of chains within the branched species was calculated by dividing the $M_w$ value of the branched copolymers by the $M_n$ of the linear counterpart. The number of chains branched together increased considerably with the increasing ratios of EGDMA, further validating that the EGDMA is incorporated within the growing polymer species. The values calculated suggested

that the branched polymers structures consisted of at least 4 conjoined primary polymer chains and this increased to 105 as the equivalence of EGDMA increased.

Overlays of the TD-SEC refractive index (RI) (Figure 2.18A) and right-angle light scattering (RALS) (Figure 2.18B) chromatograms obtained for p(BUMA)$_{100}$ and p(BuMA$_{100}$-co-EGDMA$_{0.95}$), highlights the difference between the linear and branched architectures obtained. Analysis of RI traces illustrates narrow monomodal molecular weight distribution for linear p(BuMA)$_{100}$ and broad multi-modal distributions for branched p(BuMA$_{100}$-co-EGDMA$_{0.95}$) copolymer. This is typical for the analysis of branched polymers synthesised in this way due to the statistical nature of incorporating EGDMA into the polymer species. A range of species is generated; linear, lightly branched and highly branched architectures which has been reported for polymers synthesised in this way.[80] This is further confirmed by the close correlation between the overlays of the RI traces of the linear homopolymer and the lower $M_w$ species of the branched material. The differences between the obtained RALS chromatograms provides evidence for the presence of large size (high $M_w$) species since material which has larger size will scatter significantly more light than smaller polymer molecules.

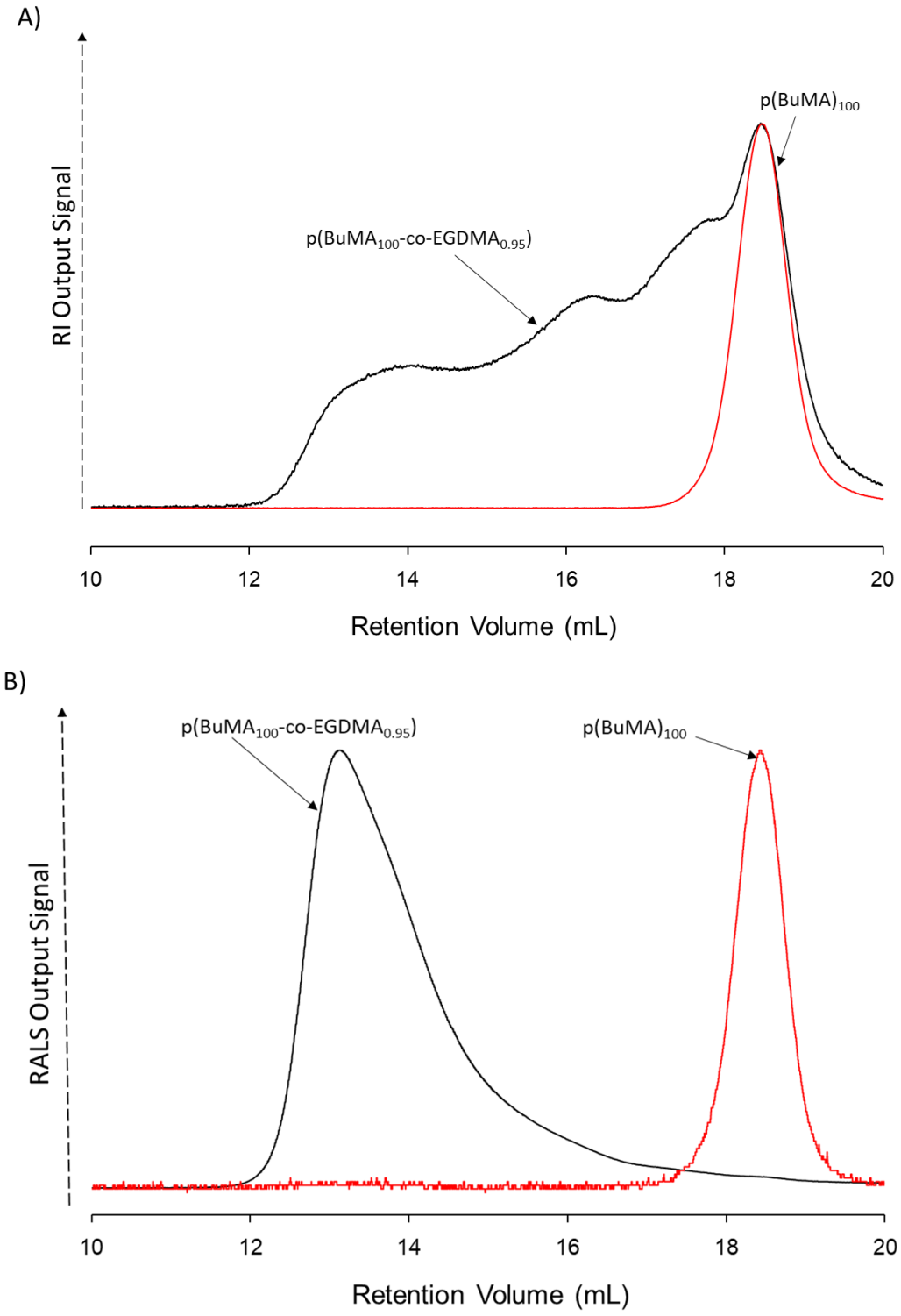


**Figure 2.18** Overlaid TD-SEC analysis of a) RI chromatograms and b) RALS chromatograms for p(BuMA$_{100}$-co-EGDMA$_{0.95}$) (black) and p(BuMA)$_{100}$ (red).

The copolymerisation of BuMA with varying equivalences of EGDMA was also conducted targeting a $DP_n$ of 20 monomer units for the primary chains and the

polymerisations proceeded for 24 hours. Compared to the $DP_n$ of 100 monomer units, this copolymerisation required a lower equivalence (0.85 eqv.) of divinyl monomer EGDMA relative to EBiB in order to avoid gelation and yield a soluble branched polymer. Equivalences above this value generated insoluble polymeric gels. Since the monomer mass is fixed during the polymerisations, the lower gelation point could be explained by the increased density of pendant vinyl bonds, which has increased from 1 in 100 to 1 in 20 and hence the potential for intermolecular reaction has increased and loop formation (cyclisation) is less likely. Analysis by TD-SEC showed that p($BuMA_{20}$-co-$EGDMA_{0.85}$) was highly branched with an $M_w$ value of 4856 kg $mol^{-1}$(Table 2.7).

**Table 2.7** Methanolic Cu-ATRP of hydrophobic monomer BuMA and varying equivalences of divinyl monomer EGDMA for branched statistical copolymers synthesis at 50 °C with target $DP_n$ 20 monomer units.

| | | TD-SEC (THF)[c] | | | | |
|---|---|---|---|---|---|---|
| [a] Target Polymer composition | [b] Conversion (%) | $M_n$ (g $mol^1$) | $M_w$ (g $mol^{-1}$) | Đ | Mark - Houwink α value | [d]Weight average number of chains |
| p($BuMA_{20}$-co-$EGDMA_{0.85}$) | > 99 % | 57 050 | 4 856 000 | 85. 14 | 0.402 | 952 |
| p($BuMA_{100}$-co-$EGDMA_{0.90}$) | | | Insoluble Gel | | | |
| p($BuMA_{20}$-co-$EGDMA_{0.95}$) | | | Insoluble Gel | | | |

[a] Target DP calculated *[nBuMA] / [EBiB],* [b] Calculated by $^1$H NMR *spectroscopy* of polymerisation mixture at t=final hr. [c] Calculated by TD-SEC using THF/TEA mobile phase (98/2 v/v%) at 35 °C, flow rate of 1mL $min^{-1}$. [d] Calculated by $M_w$ of branched copolymer (TD-SEC)/$M_n$ of corresponding linear polymer (TD-SEC).

Calculation of the weight average number of chains revealed that there were 952 primary polymer chains branched together, which is significantly more than that calculated for p($BuMA_{100}$-co-$EGDMA_{0.95}$) that had 105 primary polymer chains branched together. The Mark-Houwink α value (0.402) is indicative of a branched polymer. The broad dispersity value (Đ = 85) was consistent with that expected for a branched polymer produced by this technique (i.e. modified Strathclyde.) The broad value suggests that there is a wide variety of species present within the sample.

### 2.3.9.2 Variation of the Hydrophobic Monomer to Produce Branched Statistical Copolymers

Statistical branched copolymers were also generated using EHMA and HPMA as the monomers. Both $DP_n$ = 100 and 20 monomer units were targeted for the primary chain length and, as before, varying equivalences of EGDMA were incorporated into the polymerisations. For the polymerisations targeting a $DP_n$ of 100 monomer units,

a molar ratio of monomer:EGDMA:EBiB:Cu(I)Cl:bpy was set at 100:X:1:1:2. The polymerisations proceeded for 48 and 72 hours for HPMA and EHMA, respectively, during which the observed phase behaviours were identical to that of the corresponding linear polymerisations as previously described; the polymerisation of HPMA remained homogeneous in nature throughout the reaction, whereas the polymerisation of EHMA induced a phase-separation during the reaction. Analysis of the polymerisation mixtures by $^1$H NMR showed that the polymers had achieved high monomer conversions (97 - 99%) (Table 2.8). Polymers were purified by removal of the Cu(I)Cl:Bpy catalytic system by passing through a neutral alumina column and subsequent precipitation into an anti-solvent. The purified branched copolymers were characterised by TD-SEC (Table 2.8) and $^1$H NMR (Appendix, Figure A7 and A8).

**Table 2.8** Methanolic Cu-ATRP of hydrophobic monomers, EHMA and HMPA, with varying equivalences of divinyl monomer EGDMA for branched statistical copolymers with target $DP_n$ = 100 monomer units at 50 °C.

| | | TD-SEC (THF)[c] | | | | |
|---|---|---|---|---|---|---|
| [a] Target Polymer composition | [b] Conversion | $M_n$ (g mol$^1$) | $M_w$ (g mol$^{-1}$) | Đ | Mark - Houwink α value | [d]Weight average number of chains |
| p(EHMA$_{100}$-co-EGDMA$_{0.80}$) | 97 % | 44 100 | 687 950 | 15.60 | 0.419 | 20 |
| p(EHMA$_{100}$-co-EGDMA$_{0.85}$) | | Insoluble Gel | | | | |
| p(HPMA$_{100}$-co-EGDMA$_{0.85}$) | > 99 % | 60 350 | 359 500 | 5.96 | 0.314 | 12 |
| p(HPMA$_{100}$-co-EGDMA$_{0.90}$) | > 99 % | 71 500 | 1 427 000 | 19.97 | 0.359 | 47 |
| p(HPMA$_{100}$-co-EGDMA$_{0.95}$) | | Insoluble Gel | | | | |

[a] Target DP calculated *[Monomer] / [EBiB]*, [b] Calculated by $^1$H NMR *spectroscopy* of polymerisation mixture at t=final. [c] Calculated by TD-SEC using THF/TEA mobile phase (98/2 v/v%) at 35 °C, flow rate of 1mL min$^{-1}$. [d] Calculated by $M_w$ of branched copolymer (TD-SEC)/$M_n$ of corresponding linear polymer (TD-SEC).

In both cases, soluble high molecular weight copolymers were obtained, p(EHMA$_{100}$-co-EGDMA$_{0.80}$) ($M_w$ = 687 950 g mol$^{-1}$) and p(HPMA$_{100}$-co-EGDMA$_{0.90}$) ($M_w$ = 1427 kg mol$^{-1}$). It was observed that the branched copolymerisation of EHMA required a much lower equivalence of EGDMA (0.80 eqv.) compared to the polymerisations of BuMA and HPMA in order to avoid gelation and generate soluble branched material. As oligomers and polymers concentrate during phase separation, it is likely that they are swollen by the monomer mixture and a relative high concentration of EGDMA is present that may lead to higher incorporation in some chains and the potential for network formation and gelation.

Despite the lower molecular weight, analysis of the Mark-Houwink α value (0.419) and the broad dispersity (Đ = 15.60) still indicate that the polymer is branched with approximately 20 primary chains attached together. Analysis of p($HPMA_{100}$-co-$EGDMA_{0.90}$) showed that branched copolymer architecture had been obtained with a broad dispersity value (19.97) with approximately 47 primary chains attached together.

The polymerisations targeting a reduced $DP_n$ of 20 monomer units were also conducted as described above using a molar ratio of monomer:EGDMA:EBiB:Cu(I)Cl: bpy was set at 20:X:1:1:2. The reactions all proceeded for 24 hours and the same phase behaviour was observed. The polymerisations were poisoned *via* the exposure to oxygen and *via* the addition of THF for p($HPMA_{20}$-co-$EGDMA_x$) and $CDCl_3$ for p(EHMA-co-$EGDMA_x$). Analysis of the polymerisations *via* $^1$H-NMR spectroscopy showed that high monomer conversions (> 99%) were achieved. The catalytic system was removed by passing the polymeric solution over a neutral alumina column and subsequent precipitation into an appropriate anti-solvent. The polymers were characterised by TD-SEC and $^1$H NMR spectroscopy (Table 2.9).

**Table 2.9** Methanolic Cu-ATRP of hydrophobic monomers, EHMA and HMPA, with varying equivalences of divinyl monomer EGDMA for branched statistical copolymers with target $DP_n$ = 20 monomer units at 50 °C.

| | | TD-SEC (THF)[c] | | | | |
|---|---|---|---|---|---|---|
| [a] Target Polymer composition | [b] Conversion (%) | $M_n$ (g mol$^1$) | $M_w$ (g mol$^{-1}$) | Đ | Mark - Houwink α value | [d] Weight average number of chains |
| p($EHMA_{20}$-co-$EGDMA_{0.80}$) | > 99 | 18 900 | 1 200 000 | 63.16 | 0.372 | 159 |
| p($EHMA_{20}$-co-$EGDMA_{0.85}$) | | | Insoluble Gel | | | |
| p($HPMA_{20}$-co-$EGDMA_{0.80}$) | > 99 | 21 300 | 119 900 | 5.63 | 0.365 | 28 |
| p($HPMA_{20}$-co-$EGDMA_{0.90}$) | > 99 | 138 950 | 1.02 x $10^7$ | 73.74 | 0.179 | 2 372 |
| p($HPMA_{20}$-co-$EGDMA_{0.95}$) | | | Insoluble Gel | | | |

[a] Target DP calculated *[monomer] / [EBiB],* [b] Calculated by $^1$H NMR *spectroscopy* of polymerisation mixture at t=final. [c] Calculated by TD-SEC using THF/TEA mobile phase (98/2 v/v%) at 35 °C, flow rate of 1 mL min$^{-1}$. [d] Calculated by $M_w$ of branched copolymer (TD-SEC)/$M_n$ of corresponding linear polymer (TD-SEC).

The obtained $M_w$ and dispersity values indicated that branched polymeric structures had been synthesised: p($EHMA_{20}$-co-$EGDMA_{0.80}$) ($M_w$ = 1200 kg mol$^{-1}$, $Đ$ = 63.16) and p($HPMA_{20}$-co-$EGDMA_{0.90}$) ($M_w$ =10 200 kg mol$^{-1}$, $Đ$ = 73.74). The weight average number of chains calculated were 159 and 28 for p($EHMA_{20}$-co-$EGDMA_{0.80}$) and

p(HPMA$_{20}$-co-EGDMA$_{0.90}$), respectively. Additionally, the corresponding Mark-Houwink α values obtained for the EHMA and HPMA branched copolymers (0.372 and 0.179, respectively) also provide indication that the materials are branched in nature. As observed for the copolymerisation of EHMA and HPMA with EGDMA targeting the higher $DP_n$ of 100 monomer units, the required molar equivalences of EGDMA to avoid gelation and produce soluble branched material varied between the polymerisations of the two monomers. Polymerisation of EHMA incorporated a maximum of 0.80 equivalences ([B]/[I] ratio) of EGDMA, whereas the polymerisation of HPMA incorporated a maximum of 0.90 equivalences of EGDMA.

### 2.3.10 Synthesis of Statistical Branched Copolymers

Since the viability of methanolic ATRP has been proven for the synthesis of high molecular weight branched polymers following a modified Strathclyde approach, the synthesis was extended to the generation of statistical branched copolymers using two monofunctional monomers in the presence of the divinyl monomer, EGDMA, and targeting an overall $DP_n$ of 100 monomer units for the primary chains. This resulted in each monovinyl monomer being set to 50 equivalences with respect to the initiator concentration. The polymerisations were conducted as before *via* methanolic ATRP at 50 ˚C using the same catalytic system as previously described. The reactions all proceeded for 72 hours and were terminated by exposure to oxygen and *via* addition of THF. Interestingly, there was no phase separation observed for any of these polymers. Purification was conducted by passing the polymer mixture through a neutral alumina column before performing a precipitation into an appropriate antisolvent. Once again, the formation of branched statistical copolymers was confirmed by TD-SEC and $^1$H-NMR spectroscopy (Table 2.10). In all cases high monomer conversions (≥ 98%) were achieved and the calculated $M_w$ (≥ 501.6 kg mol$^{-1}$) and $M_n$ (≥ 51.3 kg mol$^{-1}$) values were significantly higher than the values obtained for the linear statistical copolymers (Section 2.4.3.3). Broad molecular weight distributions were also observed (Đ = 7.51 – 20.75) and the calculated Mark-Houwink α values were highly indicative of branched copolymer structures (α = 0.389 - 0.423).

**Table 2.10** Methanolic Cu-ATRP of hydrophobic monomers at 50 °C to generate statistical branched copolymers with overall target $DP_n$ = 100 monomer units.

| | | TD-SEC (THF)[c] | | | |
|---|---|---|---|---|---|
| [a]Target Polymer composition | [b] Conversion (%) | $M_n$ (g mol[1]) | $M_w$ (g $mol^{-1}$) | Đ | Mark - Houwink α value |
| p($BuMA_{50}$-co-$EHMA_{50}$-co-$EGDMA_{0.95}$) | 98 % | 51 250 | 1 060 000 | 20.75 | 0.389 |
| p($BuMA_{50}$-co- $HPMA_{50}$-co-$EGDMA_{0.95}$) | 99 % | 66 750 | 939 000 | 14.07 | 0.399 |
| p($HPMA_{50}$-co-$EHMA_{50}$-co-$EGDMA_{0.95}$) | 99 % | 66 800 | 501 600 | 7.51 | 0.423 |

[a] Target DP calculated [monomer] / [EBiB], [b] Calculated by 1H NMR spectroscopy of polymerisation mixture at t=final hr. [c] Calculated by TD-SEC using THF/TEA mobile phase (98/2 v/v%) at 35 °C, flow rate of 1 mL $min^{-1}$.

## 2.4 Determining the Glass Transition Temperature of the Polymers

The physical properties of polymers such as rigidity and viscosity in the bulk state can be influenced by temperature. Polymeric materials that are semi-crystalline in nature, such as p(caprolactone), p(lactic acid) and PEG, will exhibit two characteristic thermal transitions in the solid state.[82] One of the thermal transitions is associated with a first order phase change of the polymer and occurs at the temperature at which the crystalline polymer (or domain) melts thereby increasing the molecular motion of the polymer chains. This is known and reported as the crystalline melting temperature ($T_m$). This transition is only present in (semi-)crystalline species and is absent from materials that are amorphous in nature. The other thermal transition is known as the glass-transition and is represented by the glass transition temperature ($T_g$). The $T_g$ represents a second order transition and can be thought of as the temperature at which local segmental motion starts to occur within an amorphous polymer. It is important to note that $T_g$ proceeds over a certain temperature range and not as a discrete temperature value. The $T_g$ value is affected by the mobility and flexibility of the polymer chains, which in turn is governed by the free volume and the backbone and pendent group chemistry. The free volume describes how much space a polymer chain has to move and achieve different physical conformations with respect to other polymer chains. If the free volume around the polymer chain is large, the polymer chain can move and undergo conformational changes more freely with a lower energy input and will exhibit a low $T_g$ value. On the contrary, if the polymer chain has limited free volume (i.e. the mobility of the chain is restricted), more energy is required for the polymer chains to exhibit conformational changes and they will therefore exhibit a higher $T_g$ value.

There are many different factors that can affect the $T_g$ of a polymer including: molecular weight, molecular structure, intermolecular forces, chain stiffness and cross-linking. In general, factors that increase the energy required for the onset of molecular motion will increase $T_g$; factors that decrease the energy required will lower $T_g$. Polymers of different architectures and monomer composition will also typically exhibit different $T_g$ values. It has been reported that even minimal changes such as increasing the carbon number by one on the pendant group of the repeat unit can have a dramatic impact on the $T_g$ value. As seen when comparing analyses of poly(methyl methacrylate) and poly(ethyl methacrylate); in the latter case, there is a significant decrease in the recorded $T_g$ by approximately 40 °C.[83] This observed change illustrates how easily the thermal characteristics of any polymer can be altered by relatively small manipulations of polymer structure and chemistry.

Changes to the primary polymer chain length and therefore the molecular weight will also alter the $T_g$ value. The relationship between polymer molecular weight and $T_g$ can be explained by the Flory-Fox approximation, which describes the relationship between $T_g$ and $M_n$ (Equation 2.2).[84, 85]

$$T_g(M_n) \approx T_{g,\infty} - K/M_n \qquad \textbf{(2.2)}$$

Where $T_{g,\infty}$ represents maximum $T_g$ temperature at a theoretical infinite molecular weight and K is the empirical parameter relating to polymer free volume. This $T_g$ dependence on $M_n$ can be explained with the free volume theory; chain ends typically exhibit greater mobility than chain segments, and consequently free volume increases with the number of chain-ends in a given volume. Higher $DP_n$ values yield polymers with higher $M_n$ values and lower numbers of chain-ends for any given mass, thereby reducing the free volume and mobility that can be exhibited and increasing the $T_g$ value. $T_g$ will continue increasing with molecular weight until it reaches a limiting value ($T_{g,\infty}$) at moderate to high molecular weights. However, the Flory-Fox equation does not give accurate estimations for the entire range of molecular weights; at short chain lengths (low molecular weight oligomers), the accuracy of the prediction is much lower. This is because there is a strong dependency on the constant physical properties and molecular weight. The transition from oligomer to

polymer is not precisely defined, but it is generally accepted that this point will be located at around 50 to 100 monomer units.[86]

### 2.4.1 Determining the Thermal Behaviour of Linear Homopolymers *via* Differential Scanning Calorimetry

The thermal characteristics of the linear homopolymers were assessed using a DSC Q 2000 TA Instrument (Table 2.11). The instrument was calibrated for heat flow and temperature using an indium reference. All samples were purged with pure nitrogen at a flow rate of 50 mL $min^{-1}$ and the thermal history was erased by an initial heat/cool cycle and then the $T_g$ values were determined from the second heat cycle by taking the inflection point of the heat flow curve.

**Table 2.11** $T_g$ temperatures (°C) obtained for linear homopolymers of $DP_n$ 20 and 100 monomer units.

| Polymer Composition | [a]Obtained $T_g$ Value (°C) |
|---|---|
| $p(EHMA)_{20}$ | - 34 |
| $p(BuMA)_{20}$ | 8 |
| $p(HPMA)_{20}$ | 39 |
| $p(EHMA)_{100}$ | - 17 |
| $p(BuMA)_{100}$ | 24 |
| $p(HPMA)_{100}$ | 53 |

[a] Tg values were determined from the second heat cycle by taking the inflection point of the heat flow curve. Thermogram was obtained on a DSC Q 2000. The instrument was calibrated for heat flow and temperature using an indium reference and all samples were purged with pure nitrogen at a flow rate of 50 mL $min^{-1}$. Measurements were obtained *via* two heat/cool/heat cycles between 25 and 250 °C at a heating rate of 5 °C $min^{-1}$.

For all of the polymers within the series, a single $T_g$ endotherm was obtained without the presence of any additional transitional temperatures (such as melting), suggesting that the polymers are amorphous in nature. Examples thermograms are provided for $p(EHMA)_{20}$, $p(HPMA)_{20}$, $p(BuMA)_{100}$ and $p(HPMA)_{100}$ (Appendix, Figure A9-A12). The $T_g$ values obtained for the linear homopolymers all varied for the $DP_n$ = 20 monomer units, ($-34 \leq T_g \leq 39$ °C) and $DP_n$ = 100 monomer units ($-17 \leq T_g \leq 53$ °C). Literature values have been reported as -10 °C for EHMA, 24 °C for BuMA and 76 °C for HPMA based polymers,[87] but it is important to note that literature values are usually reported as $T_{g,\infty}$ and at much higher $M_n$ values than these materials. The $T_g$ values obtained for all of the linear homopolymers are consistently lower than the

literature values reported, with the exception of $p(BuMA)_{100}$ and it is likely that the values that have been experimentally obtained for the polymer series described above have not yet reached $T_{g,\infty}$.

When comparing the functionality of the homopolymers, it is not surprising that those consisting of HPMA monomer residues exhibited the highest $T_g$ values for both the targeted $DP_n$ 20 and 100 chain lengths, which were 39 °C and 53 °C, respectively. This can be explained by the presence of the hydroxyl groups on the pendant chain of the repeat units, which increases the intermolecular interactions between the polymer chains and therefore decreases their mobility and flexibility. This decrease in free volume increases the energy required to impart conformational changes on the polymer chains and subsequently increases the observed $T_g$ value. As expected, the polymers consisting of EHMA monomer residues exhibited the lowest $T_g$ values for both the targeted $DP_n$ 20 and 100 chain lengths, which were -34 °C and -17 °C, respectively. Since the EHMA repeat units contain a long aliphatic side group, this creates more free volume between the polymeric chains and thus in turn decreases the energy required for chain mobility and therefore decreases the $T_g$ value.

### 2.4.2 Determining the Thermal Characteristic Behaviour of the Branched Copolymers *via* Differential Scanning Calorimetry

The DSC thermograms of the branched copolymer series consisting of EGDMA divinyl monomer residues were also acquired under identical DSC conditions, and provided insight into $T_g$ changes associated with changing the polymer architecture from linear to branched (Table 2.12). Examples of DSC thermograms obtained for branched copolymers are presented in Appendix, Figure A13 – A17.

**Table 2.12** $T_g$ temperatures (°C) obtained for EGDMA branched statistical copolymers of $DP_n$ 20 and 100 monomer units compared to the $T_g$ temperatures obtained for linear homopolymers $DP_n$ 20 and 100 monomer units.

| Polymer Composition | Obtained $T_g$ Value (°C) | $M_n$ (SEC) (g mol$^{-1}$) | Đ |
|---|---|---|---|
| $p(EHMA)_{20}$ | - 34 | 7 530 | 1.38 |
| $p(BuMA)_{20}$ | 8 | 5 100 | 1.24 |
| $p(HPMA)_{20}$ | 39 | 4 300 | 1.67 |
| $p(EHMA_{20}\text{-co-}EGDMA_{0.80})$ | - 16 | 18 900 | 63 |
| $p(BuMA_{20}\text{-co-}EGDMA_{0.95})$ | 24 | 57 050 | 85 |
| $p(HPMA_{20}\text{-co-}EGDMA_{0.85})$ | 58 | 138 950 | 74 |
| $p(EHMA)_{100}$ | - 17 | 19 850 | 1.48 |
| $p(BuMA)_{100}$ | 24 | 20 200 | 1.14 |
| $p(HPMA)_{100}$ | 53 | 14 500 | 1.24 |
| $p(EHMA_{100}\text{-co-}EGDMA_{0.80})$ | - 6 | 44 100 | 16 |
| $p(BuMA_{100}\text{-co-}EGDMA_{0.95})$ | 26 | 125 700 | 17 |
| $p(HPMA_{100}\text{-co-}EGDMA_{0.90})$ | 78 | 71 500 | 20 |

[a]$T_g$ values were determined from the second heat cycle by taking the inflection point of the heat flow curve. Thermogram was obtained on a DSC Q 2000. The instrument was calibrated for heat flow and temperature using an indium reference and all samples were purged with pure nitrogen at a flow rate of 50 mL min$^{-1}$. Measurements were obtained *via* two heat/cool/heat cycles between 25 and 250 °C at a heating rate of 5 °C min$^{-1}$.

In general, the observed $T_g$ values were higher for all branched polymers compared to the corresponding linear homopolymers with same targeted $DP_n$ value. The rationalisation of this increase could follow the very classic approach of using the Flory-Fox equation, since the actual $M_n$ of the copolymers had increased with the introduction of the divinyl monomer. However, it is important to note that $T_g$ studies reported in the literature that also follow this trend are typically of linear samples that are relatively monodisperse with unimodal molecular weight distributions. In this study, the branched polymeric materials have broad molecular weight distributions and therefore the effects of this distribution on the $M_n$ value and therefore $T_g$ must be accounted for. Rannard and co-workers have shown that a more general equation can be applied to consider samples that have a wide variation in $M_n$ and $M_w$ (Equation 2.3).[88]

$$T_g = T_{g,\infty} - \frac{K}{\sqrt{M_n M_w}} \quad \textbf{(2.3)}$$

Clearly, when incorporating a branching agent within a polymerisation, the $M_n$ and $M_w$ values will increase. Therefore, an increase in $T_g$ value could be expected until values of $T_{g,\infty}$ are obtained due to the molecular weight dependency. When $T_{g\infty}$ is obtained, increases in molecular weight can no longer be the only contributory factor to changes in the $T_g$. However, what is of interest is the influence of changing the polymer architecture from linear to branched from an architectural perspective once $T_g$ is no longer dependant on molecular weight. Rannard and co-workers reported that variations to $T_g$ of polystyrene based materials were observed when branched polymers were produced.[88] Initially, these variations were clearly due to molecular weight influence. However, once the observed $T_g$ values were at $T_{g\infty}$, an interesting observation was made; when the $DP_n$ was increased to 100 monomer units, the $T_g$ value observed for the branched polystyrene materials were systematically lower than the respective linear counterpart despite the significant increase in MW of the branched species. This suggested that architecture may be now playing a contributory role in the influence over $T_g$. The paper concludes that there was no direct correlation with branched polymer molecular weight but instead highlighted a strong relationship between the primary polymer chain length of the individual chains and its influence on $T_g$.[88]

Studying the DSC analyses of the polymers presented here, higher $T_g$ values were observed for the branched copolymers targeting a $DP_n$ of 20 monomer units compared to their linear homopolymer analogues, which can be explained by their higher molecular weights. These increases in $T_g$ values when changing from linear to branched architectures are consistent with that reported by Rannard and co-workers for a linear polystyrene homopolymer of $DP_n$ = 10 monomer units ($T_g$ = 37 °C) compared to the corresponding branched polystyrene with primary chains of $DP_n$ = 10 monomer units ($T_g$ = 62 °C).

The $T_g$ values obtained for all branched materials containing primary chains of $DP_n$ = 20 monomer units are lower than the reported $T_g$ literature values, which is believed to be because the obtained $T_g$ values are lower than that of $T_{g,\infty}$. This is also

consistent with the work by Rannard and co-workers for the linear and branched polystyrene materials containing primary chains of $DP_n$ = 10 monomer units. This significant difference with $T_{g,\infty}$ for high molecular weight species can be explained by the significant population of unbranched linear polymers within the branched polymer samples are believed to act as plasticisers at short primary chain lengths, which therefore decreases the $T_g$ values.[88]

With reference to the Alhilfi *et al.* paper once more, when the $DP_n$ was increased to 100 monomer units, the reported $T_g$ value for the branched material was lower than that of the corresponding linear homopolymer.[88] In the study presented here, however, the $T_g$ of the branched materials of $DP_n$ = 100 monomer units are still higher than the corresponding linear homopolymers. In the present work, the values obtained for the different linear homopolymers of $DP_n$ = 100 monomer units are systematically lower than the reported $T_{g,\infty}$ and therefore it is believed that the overall molecular weight is still the primary parameter influencing $T_g$ as would be expected in a classic Flory-Fox model. It is also worth noting that the polymers produced within this study are synthesised *via* a much less controlled polymerisation technique (ATRP) compared to the method of synthesis used by Alhilfi *et al*. (living anionic polymerisation) and therefore samples containing primary chains with much broader molecular weight distributions were obtained. As expected, branched polymers with $DP_n$ = 100 monomer units exhibited higher $T_g$ higher than branched $DP_n$ = 20 monomer units. HPMA still had the highest $T_g$ value and branched copolymers of EHMA still had the lowest $T_g$ values following the incorporation of EGDMA divinyl monomer residues. However, no clear conclusion regarding this can be drawn given the complexity of the systems and the varying molecular weights, composition and architecture. We have shown that $T_g$ can be varied by using different monomers, varying the primary chain length and changing the polymer architecture by incorporation of a divinyl monomer. It is now of interest to see how the $T_g$ can be influenced following the mixing of two monomers to produce statistical linear copolymers and mixing of two monomers with EGDMA incorporation to produce statistical branched copolymers by varying the composition of the primary

polymer chains within linear and branched statistical copolymers through the copolymerisation of two monofunctional monomers.

### 2.4.3 Determining the Thermal Characteristic Behaviour of Linear and Branched Statistical Copolymers via Differential Scanning Calorimetry

The thermal characteristics of the linear statistical copolymers were assessed by DSC using the same conditions as previously described (Table 2.13).

**Table 2.13** $T_g$ temperatures (°C) obtained for statistical linear copolymers of $DP_n$ = 100 monomer units.

| Polymer Composition | [a]Obtained $T_g$ Value (°C) |
|---|---|
| p($BuMA_{50}$-co-$EHMA_{50}$) | 5 |
| p($HPMA_{50}$-co-$EHMA_{50}$) | 40 |
| p($BuMA_{50}$-co-$HPMA_{50}$) | 53 |

[a] $T_g$ values were determined from the second heat cycle by taking the inflection point of the heat flow curve. Thermogram was obtained on a DSC Q 2000. The instrument was calibrated for heat flow and temperature using an indium reference and all samples were purged with pure nitrogen at a flow rate of 50 mL $min^{-1}$. Measurements were obtained *via* two heat/cool/heat cycles between 25 and 250 °C at a heating rate of 5 °C $min^{-1}$.

The thermograms showed a single transition with no melting point observed, therefore we can conclude that these materials are amorphous (Appendix, Figure A18-A20). Only one $T_g$ value was recorded for each of the statistical copolymers. This is indicative of a copolymer that has a statistical distribution of the two monomer functionalities along the chain and has not developed polymer blocks of each individual monomer functionality.

Finding comparative values of $T_g$ for these type of materials within the literature is difficult since the combination of monomers and polymer composition vary significantly. One relationship that can be used to calculate the theoretical $T_g$ of statistical copolymers is the DiMarzio-Gibbs equation. This relationship links the molar composition of statistical copolymers and the $T_g$ of each component to the $T_g$ of the final material (Equation 2.4). Where m represents the mole fraction of each monomer (A and B). This equation was used to calculate the theoretical $T_g$ values of the linear statistical copolymers (Table 2.14).

$$T_g(theoretical) = \left(m(MonomerA)xT_{gMonomerA}\right) + \left(m(MonomerB)xT_{gMonomerB}\right) \quad \textbf{(2.4)}$$

**Table 2.14** Table of theoretical $T_g$ values calculated using the Dimarzio-Gibbs relationship compared to the experimentally obtained $T_g$ values for linear statistical copolymers using literature $T_g$ values.

| Polymer Composition | [a]$T_g$ HomoA Literature Value (°C) | [a]$T_g$ HomoB Literature Value (°C) | [b]Theo $T_g$ Value (°C) | [c]Obtained $T_g$ Value (°C) |
|---|---|---|---|---|
| p(BuMA$_{50}$-*stat*-EHMA$_{50}$) | 20 | -10 | 5 | 5 |
| p(HPMA$_{50}$-*stat*-EHMA$_{50}$) | 76 | -10 | 33 | 40 |
| p(BuMA$_{50}$-*stat*-HPMA$_{50}$) | 20 | 76 | 48 | 53 |

[a,] $T_g$ values were obtained from literature. [b] $T_g$ calculated *via* the Dimarzio-Gibbs relationship.[c] $T_g$ values were determined from the second heat cycle by taking the inflection point of the heat flow curve. Thermogram was obtained on a DSC Q 2000. The instrument was calibrated for heat flow and temperature using an indium reference and all samples were purged with pure nitrogen at a flow rate of 50 mL/min. Measurements were obtained *via* two heat/cool/heat cycles between 25 and 250°C at a heating rate of 5°C/min.

There seemed to be a good correlation between experimental and theoretical $T_g$ values. Interestingly, the experimental $T_g$ values for the two statistical copolymers containing HPMA monomer residues were both observed to be above the theoretical $T_g$ values. The rationale for this is beyond the scope of this manuscript, but it could be speculated that perhaps the hydrogen-bonding capabilities of the HPMA monomer residues were having a strong influence on $T_g$ compared to the other monomer residue functionalities. Especially when considering that the $T_{g,\infty}$ of the statistical copolymers may not have been reached.

Despite it being a complicated relationship, it is clear that simple manipulation of the polymer composition has resulted in considerable differences between experimental $T_g$ values of the linear statistical copolymers and the respective linear homopolymers. For example, when comparing the difference between p(BuMA$_{50}$-*stat*-EHMA$_{50}$) and p(BuMA$_{50}$-*stat*-HPMA$_{50}$) a difference of 48 °C was observed.

The thermal characteristics of branched statistical copolymers were assessed using DSC under the same conditions (Table 2.15). Incorporation of EGDMA within the statistical copolymers produced amorphous materials as only one $T_g$ value was recorded for each of the statistical copolymers (Appendix, Figure A21-A23). Once again, it was observed that a considerable difference between $T_g$ values can be produced by this simple material modification ($\Delta T_g$ = 41 °C). $T_g$ values increased when

the architecture was changed from linear to branched, which may be related to the changes in free volume associated with the architectural change.

**Table 2.15** $T_g$ temperatures (°C) obtained for statistical branched copolymers of $DP_n$ = 100 monomer units.

| Polymer Composition | [a]Obtained $T_g$ Value (°C) |
|---|---|
| p(BuMA$_{50}$-*stat* -EHMA$_{50}$-co-EGDMA$_{0.95}$) | 17 |
| p(HPMA$_{50}$-*stat*-EHMA$_{50}$-co-EGDMA$_{0.95}$) | 47 |
| p(BuMA$_{50}$-stat-HPMA$_{50}$-co-EGDMA$_{0.90}$) | 58 |

[a] $T_g$ values were determined from the second heat cycle by taking the inflection point of the heat flow curve. Thermogram was obtained on a DSC Q 2000. The instrument was calibrated for heat flow and temperature using an indium reference and all samples were purged with pure nitrogen at a flow rate of 50 mL min$^{-1}$. Measurements were obtained *via* two heat/cool/heat cycles between 25 and 250 °C at a heating rate of 5 °C min$^{-1}$.

### 2.4.4 Determining the Thermal Characteristic Behaviour of AB Block Copolymers *via* Differential Scanning Calorimetry

When considering AB block copolymers which incorporate a PEG segment, the copolymer may be described as semi-crystalline. Therefore, it would be expected that both a $T_m$ and a $T_g$ value would be observed. The thermal characteristics of AB block copolymers were determined using DSC as previously described (Table 2.16).

**Table 2.16** $T_m$ temperatures (°C) obtained for AB block copolymers and MeO-PEG$_{114}$-Br.

| Polymer Composition | [a]Obtained $T_m$ Value (°C) |
|---|---|
| MeO-PEG$_{114}$ -Br | 57 |
| p(PEG$_{114}$ -b-BuMA$_{100}$) | 52 |
| p(PEG$_{114}$ -*b*-HPMA$_{100}$) | 52 |
| p(PEG$_{114}$ -*b*-EHMA$_{100}$) | 43 |

[a] $T_g$ values were determined from the second heat cycle by taking the inflection point of the heat flow curve. Thermogram was obtained on a DSC Q 2000. The instrument was calibrated for heat flow and temperature using an indium reference and all samples were purged with pure nitrogen at a flow rate of 50 mL min$^{-1}$. Measurements were obtained *via* two heat/cool/heat cycles between 25 and 250 °C at a heating rate of 5 °C min$^{-1}$.

Analysis of the obtained thermograms showed the presence of only one thermal transition, which can be assigned as the $T_m$ of the PEG block (Appendix, Figure A24-A26). In comparison to the MeO-PEG$_{114}$-Br macroinitiator, the effect of polymerisation with a B block seemed to lower the melting point of the PEG block. The lack of $T_g$ recorded from the B block could be due to the endotherm dwarfing the $T_g$ transition or the PEG domain restricting the mobility of the hydrophobic domain.

## 2.5 Varying the Divinyl Methacrylate Monomer in the Synthesis of Branched Copolymers

As has been shown above, changes to the polymer architecture and monomer composition resulted in changes to the polymer bulk characteristics. It was therefore of interest to investigate whether changes to the functionality of the divinyl monomer residues would also result in such changes to the polymer bulk characteristics. The monomer composition of the primary polymer chain was fixed to EHMA and five different divinyl monomers were incorporated into the branched copolymerisations: bisphenol A dimethacrylate (BPDMA), bisphenol A glycerolate dimethacrylate (BPGDMA), bis(2-methacrylol)oxyethyl disulphide dimethacrylate (DSDMA), glycerol dimethacrylate (GDMA) and urethane dimethacrylate (UDMA) (Figure 2.19).

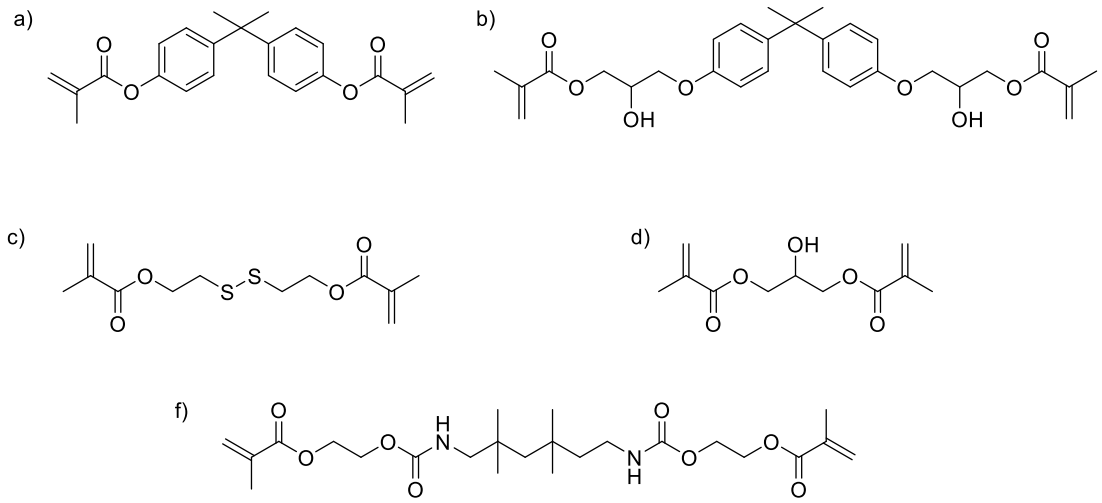


**Figure 2.19** Chemical structures of divinyl monomers; a) BPDMA, b) BPGDMA, c) DSDMA, d) GDMA and f) UDMA.

Once again, these polymerisations targeted a $DP_n$ of 20 and 100 monomer units. The reason why EHMA was selected as the monofunctional monomer instead of BuMA or HPMA was because it would yield polymers with the lowest $T_g$ value, and therefore any changes to this value as a result of the divinyl monomer residue would be easily observable. Also, since the intended use of the polymer nanoparticles is to act as drug carriers and release chemotherapeutics *in vivo*, working with a polymer that is above its $T_g$ at body temperature would potentially offer the best drug release profile.[89]

The divinyl monomers were chosen as they all had differing chemical structures, which would in turn influence the bulk polymer properties in different ways. The different branching agents allowed for the introduction of: bulkiness, rigidity, aromaticity, hydrophilicity, hydrogen bonding and possible degradation sites (S-S bonds).

As previously indicated, it is well established that the level of branching that occurs during the copolymerisation of monofunctional and bifunctional monomers is significantly impacted by the molar ratio of divinyl monomer to initiator. As previously outlined for the copolymerisation of the monofunctional monomers with EGDMA, the molar ratio of these divinyl monomers relative to the initiator must be less than 1 to avoid gelation in the absence of significant cyclisation. Given the differences in chemical structure for these divinyl monomers, it is likely that their subsequent incorporation into the primary polymer chains, and therefore their gelation point, will vary. This was studied for all of the divinyl monomers and EHMA combinations at the two different $DP_n$ values by conducting copolymerisations at decreasing divinyl monomer: initiator ratios starting from 0.95 equivalences. The polymerisations were carried out following the same experimental methods as before, that is at 50 °C in MeOH using Cu(I)Cl: bpy as the catalytic system. An initial molar ratio of monomer: EBiB: CuCl: bpy : divinyl monomer was set at 100:1:1:2:X for the reactions targeting a $DP_n$ of 100 monomer units and 20:1:1:2:X for those reactions targeting a $DP_n$ of 20 monomer units. The reaction was completed with 50 wt. % solids in MeOH as before. All of the copolymerisations proceeded with a dark brown colour and under biphasic reaction conditions. Termination occurred after 72 hours ($DP_n$ = 100) and 48 hours ($DP_n$ = 20) *via* exposure to oxygen and dilution with $CDCl_3$, which enabled the monomer conversion to be determined by $^1$H-NMR. Polymer mixtures were passed through a neutral alumina column, concentrated *in vacuo* and precipitated into ice-cold MeOH. Analysis *via* $^1$H-NMR and TD-SEC was conducted. Subsequent comparison of copolymer compositions and molecular weight distributions were made and show that varying equivalences of the different divinyl monomers were copolymerised with EHMA monomer to produce soluble branched material (Table 2.17).

**Table 2.17** Table of EHMA branched copolymers synthesised *via* methanolic Cu-ATRP at 50 °C with varying divinyl monomer incorporated.

| | | TD-SEC (THF)[c] | | | | |
|---|---|---|---|---|---|---|
| [a] Target Polymer composition | [b] *Monomer Conversion (%)* | $M_n$ (g mol[1]) | $M_w$ (g mol$^{-1}$) | Đ | Mark - Houwink α value | [d] Weight average number of chains |
| p(EHMA$_{100}$-co-BPDMA$_{0.85}$) | > 99 | 57 100 | 832 300 | 14.58 | 0.362 | 42 |
| p(EHMA$_{100}$-co-BPGDMA$_{0.85}$) | >99 | 36 750 | 197 400 | 5.37 | 0.443 | 8 |
| p(EHMA$_{100}$-co-DSDMA$_{0.75}$) | >99 | 85 100 | 1 386 000 | 16.28 | 0.487 | 58 |
| p(EHMA$_{100}$-co-GDMA$_{0.85}$) | 98 | 44 600 | 306 600 | 6.89 | 0.390 | 13 |
| p(EHMA$_{100}$-co-UDMA$_{0.85}$) | 98 | 50 800 | 377 000 | 7.42 | 0.426 | 16 |
| p(EHMA$_{20}$-co-BPDMA$_{0.85}$) | >99 | 16 250 | 148 000 | 9.11 | 0.341 | 19 |
| p(EHMA$_{20}$-co-BPGDMA$_{0.80}$) | 99 | 208 200 | 1 791 000 | 8.60 | 0.572 | 243 |
| p(EHMA$_{20}$-co-DSDMA$_{0.75}$) | >99 | 41 650 | 1 986 000 | 47.27 | 0.403 | 267 |
| p(EHMA$_{20}$-co-GDMA$_{0.85}$) | >99 | 12 100 | 117 300 | 9.68 | 0.366 | 16 |
| p(EHMA$_{20}$-co-UDMA$_{0.90}$) | >99 | 19 100 | 502 100 | 26.28 | 0.80 | 67 |

[a] Target DP calculated [EHMA] / [EBiB], [b] Calculated by $^1$H NMR spectroscopy of polymerisation mixture at t = final. [c] Calculated by TD-SEC using THF/TEA mobile phase (98/2 v/v%) at 35 °C, flow rate of 1 mL min$^{-1}$. [d] Calculated by *M*w of branched copolymer (SEC)/*M*n of corresponding linear polymer (SEC).

The results presented within the table are those of the soluble branched polymers that were obtained using the highest possible concentration of divinyl monomer; higher concentrations yielded insoluble gel network structures. The results show that the polymerisations involving each divinyl monomer had different gelation points, and that the [B]/[I] ratios for each varied between 0.75 and 0.9. As expected, the incorporation of the different divinyl monomers into the copolymerisations yielded soluble branched copolymers with significantly higher molecular weights and broader molecular weight distributions compared to the corresponding linear homopolymer of EHMA. This was observed by TD-SEC with the $M_w$, Đ, Mark-Houwink α value, and the weight averaged number of primary chains incorporated into the branched architecture *via* intermolecular branching reactions confirming that the material produced was indeed branched in nature, therefore suggesting that the divinyl monomers had been successfully incorporated within the polymer species.

### 2.5.1 Determining the Thermal Characteristic Behaviour of Branched Copolymers with Varying Divinyl Monomer

The thermal characteristics of the EHMA branched copolymers with $DP_n$ = 20 monomer units were assessed *via* DSC using a DSC Q 2000 TA Instrument (Table 2.18).

**Table 2.18** Glass transition ($T_g$) temperatures (°C) obtained for EHMA branched copolymers with varying divinyl monomers with a targeted of $DP_n$ = 20 monomer units.

| Divinyl Monomer Used | Obtained $T_g$ Value (°C) |
|---|---|
| **EGDMA** | **-16** |
| UDMA | 6 |
| DSDMA | -2 |
| BPDMA | -8 |
| GDMA | -17 |
| BPGDMA | -10 |

[a] $T_g$ values were determined from the second heat cycle by taking the inflection point of the heat flow curve. Thermogram was obtained on a DSC Q 2000. The instrument was calibrated for heat flow and temperature using an indium reference and all samples were purged with pure nitrogen at a flow rate of 50 mL $min^{-1}$. Measurements were obtained *via* two heat/cool/heat cycles between 25 and 250 °C at a heating rate of 5 °C $min^{-1}$.

The instrument was calibrated for heat flow and temperature using an indium reference. All samples were purged with pure nitrogen at a flow rate of 50 mL $min^{-1}$ and the $T_g$ values were determined from the second heat cycle by taking the inflection point of the heat flow curve**.**

For all of the polymers, a single $T_g$ endotherm was obtained without the presence of any additional transitional temperatures (such as melting), suggesting that the polymers are amorphous in nature (Appendix, Figure A27-A30). The $T_g$ values obtained for the branched copolymers all varied, ($-16 \leq T_g \leq 6$ °C). Using EGDMA as a reference point, the comparison of the different divinyl monomers showed that different thermal properties of the resulting polymer could be obtained when this was varied. The effect was quite dramatic when comparing EGDMA to UDMA. The magnitude of difference was large ($\Delta T_g$ = 22 °C). However, when considering the mass contribution (%) of the divinyl monomer to the polymer mass, UDMA has the highest mass contribution (11%) compared to the mass contribution of EGDMA (5%) (Table 2.19). The incorporation of UDMA is likely to have increased the hydrogen bonding within the polymer. This increase in intramolecular bonding between the polymer

chains may result in it behaving more like an entangled network, therefore having less chain mobility and less free volume. This would mean that more energy is required to exhibit conformational changes to the polymer segments and therefore an increase in $T_g$.

**Table 2.19** Mass contributions of the divinyl monomers to the overall mass of polymer at $DP_n$ = 20 monomer units.

| Divinyl Monomer | Mw of Divinyl Monomer (g $mol^{-1}$) | [a] Mass Contribution of Divinyl Monomer (%) |
|---|---|---|
| EGDMA | 198.22 | 4.76 |
| GDMA | 228.24 | 5.44 |
| DSDMA | 290.44 | 6.82 |
| BPDMA | 364.4 | 8.41 |
| UDMA | 470.53 | 10.61 |
| BPGDMA | 484.54 | 10.89 |

[a]Calculated by $M_{w\ (divinyl\ monomer)}$/ ($M_{w\ (divinyl\ monomer)}$ + $DP_n$* $Mw_{(monomer)}$)

The magnitude of difference between EGDMA and the differing divinyl monomers did decrease. It has already been shown how complex it is to rationalise material thermal characteristics when architecture and molecular weight have an influence. This study is even more complex due to the incorporation of an additional monomer which can influence intermolecular bonding, hydrogen bonding strength and the rigidity of the polymer chains. The effect of which was more noticeable for the DP 20, since the ratio of divinyl monomer to monomer is greatest at this lower DP value.

The thermal characteristics of the EHMA branched copolymers with $DP_n$ = 100 monomer units were also assessed *via* DSC using a DSC Q 2000 TA Instrument (Table 2.20).

**Table 2.20** Glass transition ($T_g$) temperatures (°C) obtained for EHMA branched copolymers with varying divinyl monomers with a targeted of $DP_n$ = 100 monomer units.

| Divinyl Monomer Used | Obtained $T_g$ Value (°C) |
|---|---|
| **EGDMA** | **-6** |
| GDMA | 6 |
| DSDMA | 4 |
| UDMA | -5 |
| BPDMA | -7 |
| BPGDMA | -8 |

[a] $T_g$ values were determined from the second heat cycle by taking the inflection point of the heat flow curve. Thermogram was obtained on a DSC Q 2000. The instrument was calibrated for heat flow and temperature using an indium reference and all samples were purged with pure nitrogen at a flow rate of 50 mL $min^{-1}$. Measurements were obtained *via* two heat/cool/heat cycles between 25 and 250 °C at a heating rate of 5 °C $min^{-1}$.

Again, when using EGDMA as a reference (-6 °C), varying the divinyl monomer changed the $T_g$ behaviour. However, the difference between the divinyl monomers was not as significant in magnitude compared to the DP 20 analogues. ($\Delta T_{g\ DPn\ =\ 100}$ = 12 °C) This observation is in line with what would be expected for the increase in polymer primary chain length since the percentage contribution of brancher to monomer is now significantly less (Table 2.21).

**Table 2.21** Mass contribution of divinyl monomer to the overall polymer mass

| Divinyl Monomer | Mw of Divinyl Monomer (g $mol^{-1}$) | [a] Mass Contribution of Divinyl Monomer (%) |
|---|---|---|
| EGDMA | 198.22 | 0.99 |
| GDMA | 228.24 | 1.14 |
| DSDMA | 290.44 | 1.44 |
| BPDMA | 364.4 | 1.80 |
| UDMA | 470.53 | 2.32 |
| BPGDMA | 484.54 | 2.39 |

[a]Calculated by $M_{w\ (divinyl\ monomer)}$/ ($M_{w\ (divinyl\ monomer)}$ + $DP_n$* $M_{w\ (monomer)}$)

Generally, as before, the $T_g$ for polymers with $DP_n$ = 20 monomer units was lower than when the polymers were $DP_n$ = 100 monomer units, except for UDMA which goes against this trend. When the primary polymer chain length was decreased from 100 to 20 monomer units, the $T_g$ did not decrease like we have observed for every other polymer but instead it increased (6 to -5 °C), so the $T_g$ value actually decreased with a decrease in free volume which is counter intuitive to what would be expected.

The main observation from this is that through the synthetic manipulation of incorporating different divinyl monomer chemistries within the polymer imparts different physical properties. This in turn may or may not influence the behaviour of this material with respect to the encapsulation and release of the drug.

## 2.6 Conclusion

Methanolic ATRP has proven to be a robust way of generating hydrophobic methacrylate-based polymers and expanding on the library which has been previously reported. A range of linear homopolymers were synthesised using monofunctional monomers BuMA, EHMA and HPMA with control over primary polymer chain length ($DP_n$ = 100 and 20 monomer units), low Đ values and targeted molecular weight. Statistical linear copolymers were also obtained by the mixing of these monomers. Soluble high molecular weight branched statistical copolymer architectures (2.1 x $10^6$ g $mol^{-1}$) were generated with relative ease through the incorporation of divinyl monomer EGDMA at low concentrations. Variations to the divinyl monomer chemistries using BPGDMA, BPDMA, DSDMA, UDMA and GDMA yielded, to the best of authors knowledge, the first report on the preparation of these branched statistical copolymers containing EHMA monomer residues using methanolic Cu-ATRP. Through the incorporation of a PEG based macro-initiator within a linear polymerisation at the expense of EBiB, amphiphilic AB block copolymers were obtained with varying hydrophobic block chemistry. The thermal characteristics of these materials was assessed *via* DSC and it was seen that the bulk polymer materials had different properties.

## 2.7 References


1. K. Matyjaszewski and J. Spanswick, *Materials Today*, 2005, **8**, 26-33.
2. G. Moad, E. Rizzardo and S. H. Thang, *Accounts of chemical research*, 2008, **41**, 1133-1142.
3. S. Yamago, *Chemical reviews*, 2009, **109**, 5051-5068.
4. P. B. Zetterlund, Y. Kagawa and M. Okubo, *Chemical Reviews*, 2008, **108**, 3747-3794.
5. K. Matyjaszewski and N. V. Tsarevsky, *Nature chemistry*, 2009, **1**, 276.
6. K. Matyjaszewski, in *Overview: Fundamentals of controlled/living radical polymerization,*ACS Publications, 1998.
7. K. Matyjaszewski and T. P. Davis, *Handbook of radical polymerization*, John Wiley & Sons, 2003.
8. N. V. Tsarevsky and K. Matyjaszewski, in *Fundamentals of Controlled/Living Radical Polymerization*, The Royal Society of Chemistry, 2013, 287-357.
9. K. Matyjaszewski, in *Overview: Fundamentals of controlled/living radical polymerization,*ACS Publications, 1998.
10. K. Matyjaszewski and J. Xia, *Chemical reviews*, 2001, **101**, 2921-2990.

11. H. Gao and K. Matyjaszewski, *Progress in Polymer Science*, 2009, **34**, 317-350.
12. A. D. Jenkins, R. G. Jones and G. Moad, *Pure and Applied Chemistry*, 2009, **82**, 483-491.
13. J.-S. Wang and K. Matyjaszewski, *Journal of the American Chemical Society*, 1995, **117**, 5614-5615.
14. M. Kato, M. Kamigaito, M. Sawamoto and T. Higashimura, *Macromolecules*, 1995, **28**, 1721-1723.
15. F. Minisci, *Accounts of Chemical Research*, 1975, **8**, 165-171.
16. K. Matyjaszewski, *Macromolecules*, 2012, **45**, 4015-4039.
17. Y. Wang, Y. Zhang, B. Parker and K. Matyjaszewski, *Macromolecules*, 2011, **44**, 4022-4025.
18. H. Fischer, *Macromolecules*, 1997, **30**, 5666-5672.
19. W. Tang, N. V. Tsarevsky and K. Matyjaszewski, *Journal of the American Chemical Society*, 2006, **128**, 1598-1604.
20. K. Matyjaszewski and N. V. Tsarevsky, *Nature Chemistry*, 2009, **1**, 276-288.
21. T. E. Patten and K. Matyjaszewski, *Advanced Materials*, 1998, **10**, 901-915.
22. B. I. Voit and A. Lederer, *Chemical Reviews*, 2009, **109**, 5924-5973.
23. Y. Matsushita, in *Encyclopedia of Polymeric Nanomaterials*, Springer,Berlin Heidelberg,2014, 1-5.
24. A. Noshay and J. E. McGrath, *Block copolymers: overview and critical survey*, Elsevier, 2013.
25. M. L. Adams, A. Lavasanifar and G. S. Kwon, *Journal of pharmaceutical sciences*, 2003, **92**, 1343-1355.
26. M. Hua, T. Kaneko, X.-Y. Liu, M.-q. Chen and M. Akashi, *Polymer journal*, 2005, **37**, 59-64.
27. H. Feng, X. Lu, W. Wang, N.-G. Kang and J. W. Mays, *Polymers*, 2017, **9**, 494.
28. K. Sugiyama, in *Encyclopedia of Polymeric Nanomaterials*, Springer, Berlin Heidelberg,2014, 1-10.
29. S. Coca, H.-j. Paik and K. Matyjaszewski, *Macromolecules*, 1997, **30**, 6513-6516.
30. M. H. Acar and K. Matyjaszewski, *Macromolecular Chemistry and Physics*, 1999, **200**, 1094-1100.
31. K. Matyjaszewski, J. Saget, J. Pyun, M. Schlögl and B. Rieger, *Journal of Macromolecular Science, Part A*, 2002, **39**, 901-913.
32. W. Jakubowski, N. V. Tsarevsky, T. Higashihara, R. Faust and K. Matyjaszewski, *Macromolecules*, 2008, **41**, 2318-2323.
33. F. Wolf, A. Hofmann and H. Frey, *Macromolecules*, 2010, **43**.
34. C. Yuan, H.-C. Lu, Q.-Z. Li, S. Yang, Q.-L. Zhao, J. Huang and L.-H. Wei, *Journal of Polymer Science A Polymer Chemistry*, 2012, **50**, 2398-2405.
35. L. Yuan, W. Chen, J. Li, J. Hu, J. Yan and D. Yang, *Journal of Polymer Science Part A: Polymer Chemistry*, 2012, **50**, 4579-4588.
36. J. Ford, *PhD Thesis*, Univerisity of Liverpool, 2015. (https://livrepository.liverpool.ac.uk/2052220/1/FordJan_Sept2015_2052220.pdf.pdf)
37. N. M. Nizardo, D. Schanzenbach, E. Schönemann and A. Laschewsky, *Polymers (Basel)*, 2018, **10**.
38. J. M. J. Fréchet, C. J. Hawker, I. Gitsov and J. W. Leon, *Journal of Macromolecular Science, Part A*, 1996, **33**, 1399-1425.
39. M. Jikei and M.-a. Kakimoto, *Progress in Polymer Science*, 2001, **26**, 1233-1285.
40. I. Bannister, N. C. Billingham, S. P. Armes, S. P. Rannard and P. Findlay, *Macromolecules*, 2006, **39**, 7483-7492.
41. P. J. Flory, *Journal of the American Chemical Society*, 1941, **63**, 3083-3090.
42. P. J. Flory, *Journal of the American Chemical Society*, 1941, **63**, 3091-3096.
43. P. J. Flory, *Journal of the American Chemical Society*, 1941, **63**, 3096-3100.
44. W. H. Stockmayer, *The Journal of chemical physics*, 1943, **11**, 45-55.
45. W. H. Stockmayer, *The Journal of Chemical Physics*, 1944, **12**, 125-131.
46. Z. Wang, J. He, Y. Tao, L. Yang, H. Jiang and Y. Yang, *Macromolecules*, 2003, **36**, 7446-7452.
47. Y. Li and S. P. Armes, *Macromolecules*, 2005, **38**, 8155-8162.
48. J. Rosselgong, S. P. Armes, W. R. S. Barton and D. Price, *Macromolecules*, 2010, **43**, 2145-2156.
49. D. Konkolewicz, A. Gray-Weale and S. Perrier, *Polymer Chemistry*, 2010, **1**, 1067-1077.
50. S. Flynn, A. B. Dwyer, P. Chambon and S. Rannard, *Polymer Chemistry*, 2019, **10**, 5103-5115.

51. A. B. Dwyer, P. Chambon, A. Town, T. He, A. Owen and S. P. Rannard, *Polymer Chemistry*, 2014, **5**, 3608-3616.
52. F. Y. Hern, A. Hill, A. Owen and S. P. Rannard, *Polymer Chemistry*, 2018, **9**, 1767-1771.
53. A. B. Dwyer, P. Chambon, A. Town, F. L. Hatton, J. Ford and S. P. Rannard, *Polymer Chemistry*, 2015, **6**, 7286-7296.
54. P. J. Flory, *Principles of polymer chemistry*, Cornell University Press, 1953.
55. O. Wichterle and D. LÍM, *Nature*, 1960, **185**, 117-118.
56. S. G. Cohen and D. B. Sparrow, *Journal of Polymer Science*, 1948, **3**, 693-703.
57. N. O'brien, A. McKee, D. Sherrington, A. Slark and A. Titterton, *Polymer*, 2000, **41**, 6027-6031.
58. P. A. Costello, I. K. Martin, A. T. Slark, D. C. Sherrington and A. Titterton, *Polymer*, 2002, **43**, 245-254.
59. P. Besenius, S. Slavin, F. Vilela and D. C. Sherrington, *Reactive and Functional Polymers*, 2008, **68**, 1524-1533.
60. F. Isaure, P. A. Cormack and D. C. Sherrington, *Macromolecules*, 2004, **37**, 2096-2105.
61. A. T. Slark, D. C. Sherrington, A. Titterton and I. K. Martin, *Journal of Materials Chemistry*, 2003, **13**, 2711-2720.
62. P. Chambon, L. Chen, S. Furzeland, D. Atkins, J. V. M. Weaver and D. J. Adams, *Polymer Chemistry*, 2011, **2**, 941-949.
63. S. Graham, S. P. Rannard, P. A. G. Cormack and D. C. Sherrington, *Journal of Materials Chemistry*, 2007, **17**, 545-552.
64. U. Wais, A. W. Jackson, Y. Zuo, Y. Xiang, T. He and H. Zhang, *J Control Release*, 2016, **222**, 141-150.
65. J. V. M. Weaver, R. T. Williams, B. J. L. Royles, P. H. Findlay, A. I. Cooper and S. P. Rannard, *Soft Matter*, 2008, **4**, 985-992.
66. K. Robinson, M. Khan, M. de Paz Banez, X. Wang and S. Armes, *Macromolecules*, 2001, **34**, 3155-3158.
67. K. H. Kim, J. Kim and W. H. Jo, *Polymer*, 2005, **46**, 2836-2840.
68. M. Ranger, M. C. Jones, M. A. Yessine and J. C. Leroux, *Journal of Polymer Science Part A: Polymer Chemistry*, 2001, **39**, 3861-3874.
69. F. Isaure, P. A. Cormack, S. Graham, D. C. Sherrington, S. P. Armes and V. Butun, *Chemical Communications (Camb)*, 2004, **9**, 1138-1139.
70. W. Huang, H. Yang, X. Xue, B. Jiang, J. Chen, Y. Yang, H. Pu, Y. Liu, D. Zhang, L. Kong and G. Zhai, *Polymer Chemistry*, 2013, **4**, 3204-3211.
71. A. Dwyer, P. Chambon, A. Town, T. He, A. Owen and S. Rannard, *Polymer Chemistry*, 2014, **5**, 3608-3616.
72. A. Mori, A. L. Klibanov, V. P. Torchilin and L. Huang, *FEBS Letters*, 1991, **284**, 263-266.
73. M. Miteva, K. C. Kirkbride, K. V. Kilchrist, T. A. Werfel, H. Li, C. E. Nelson, M. K. Gupta, T. D. Giorgio and C. L. Duvall, *Biomaterials*, 2015, **38**, 97-107.
74. F. L. Hatton, L. M. Tatham, L. R. Tidbury, P. Chambon, T. He, A. Owen and S. P. Rannard, *Chemical Science*, 2015, **6**, 326-334.
75. F. Y. Hern, S. Auty, O. Andren, M. Malkoch and S. Rannard, *Polymer Chemistry*, 2017.
76. M. Giardiello, F. L. Hatton, R. A. Slater, P. Chambon, J. North, A. K. Peacock, T. He, T. O. McDonald, A. Owen and S. P. Rannard, *Nanoscale*, 2016, **8**, 7224-7231.
77. A. B. Cook and S. Perrier, *Advanced Functional Materials*, 2020, **30**, 1901001.
78. J. Ford, P. Chambon, J. North, F. L. Hatton, M. Giardiello, A. Owen and S. P. Rannard, *Macromolecules*, 2015, **48**, 1883-1893.
79. F. L. Hatton, P. Chambon, T. O. McDonald, A. Owen and S. P. Rannard, *Chemical Science*, 2014, **5**, 1844-1853.
80. R. A. Slater, T. O. McDonald, D. J. Adams, E. R. Draper, J. V. M. Weaver and S. P. Rannard, *Soft Matter*, 2012, **8**, 9816-9827.
81. Q. Zhang and R. Hoogenboom, *Progress in Polymer Science*, 2015, **48**, 122-142.
82. G. M. Kelly, J. F. Elman, Z. Jiang, J. Strzalka and J. N. L. Albert, *Polymer*, 2018, **143**, 336-342.
83. S. Rogers and L. Mandelkern, *The Journal of Physical Chemistry*, 1957, **61**, 985-991.
84. T. G. Fox, Jr. and P. J. Flory, *Journal of Applied Physics*, 1950, **21**, 581.
85. T. G. Fox and P. J. Flory, *Journal of Polymer Science*, 1954, **14**, 315-319.
86. M. E. Cates, *Macromolecules*, 1987, **20**, 2289-2296.

87. Polymer Properties Database, http://polymerdatabase.com/polymer%20physics/Polymer%20Tg%20C.html, (accessed October 2020).
88. T Alhilfi, P Chambon, S. P. Rannard, *Journal. Polymer. Science., Part A: Poly. Chem., 2020, **58**, 1426-1438*
89. S Lappe, D Mulac, K. Langer, International Journal of Pharmaceutics, 2017, **517**, 338-347

# Chapter 3

Nanoprecipitation Studies:

Preparation of Branched Vinyl Copolymer Nanoparticles

*via* Co-nanoprecipitation with Varying Amphiphilic AB

Block Copolymers

## 3.1 Introduction

Nanoprecipitation is a technique that can be used to generate polymer nanoparticles from a wide range of polymer materials. These nanomaterials are of particular interest as they possess different chemical and physical properties to that of the bulk materials, which in turn renders them useful for many applications. The mechanism of nanoparticle formation and stabilisation *via* nanoprecipitation was discussed in detail Chapter 1, Section 1.3.1. Nanoprecipitation has been a successful technique for the large-scale generation of polymeric nanoparticles under clinically relevant conditions.[1-3] The majority of nanoprecipitations reported in the literature use biodegradable polyesters and polystyrenes.[4-6] Over recent years, however, there has been an increase in research studies that utilise more hydrophobic polymers to generate aqueous polymer nanoparticle dispersions *via* nanoprecipitation.[7-9]

As previously discussed, it is essential that polymer nanoparticles possess some form of stabilisation mechanism, either steric or charge, in order to avoid the polymeric nanoparticles being unstable and prone to aggregation and sedimentation. Rannard and co-workers showed that the utilisation of a polymer that generates electrostatic charge at the nanoparticle surface can prevent particle-particle aggregation *via* electrostatic repulsion and yield stable nanoparticles without the requirement of additional stabilisers.[7-9] However, these nanoparticle dispersions were prone to aggregation upon exposure to salts, likely due to the masking of the electrostatic charges on the surface of the nanoparticle. Consequently, this rendered them unsuitable for drug delivery applications as it is vital that such nanoparticle formulations remain stable in biological media. To overcome this issue, Rannard and co-workers reported the first example of the simultaneous nanoprecipitation of linear AB block copolymers, specifically PEG-based amphiphilic block copolymers, and hydrophobic branched copolymers to yield sterically stabilised branched vinyl copolymer nanoparticles. This approach was termed 'co-nanoprecipitation'.[10]

### 3.1.1 Co-nanoprecipitation

Co-nanoprecipitation describes the precipitation of a polymer with a secondary polymer that can act as a stabilising species. This differs from conventional nanoprecipitation in that there are now two different polymers present in the

system. There are two methods in which the mixing of these two polymers can occur. The first method involves the mixing of the polymer and the stabilising polymer within the good solvent phase prior to precipitation into water. Whereas, the second method involves dissolving the polymer in the good solvent and the stabilising polymer (or surfactant) in water prior to the mixing of the two phases. The first method has greater relevance to the research presented in this thesis and will therefore be discussed in greater detail below. The second method is beyond the scope of this research and the reader is directed to publications by McDonald and co-workers for further details.[11]

The formation of branched vinyl copolymer nanoparticles *via* co-nanoprecipitation is presented in Figure 3.1. The experimental process of which is nearly identical to that of nanoprecipitation, as discussed in Chapter 1.3.1. The only difference is the inclusion of an amphiphilic AB block copolymer, which is solvated with the branched copolymer in a water-miscible good solvent.

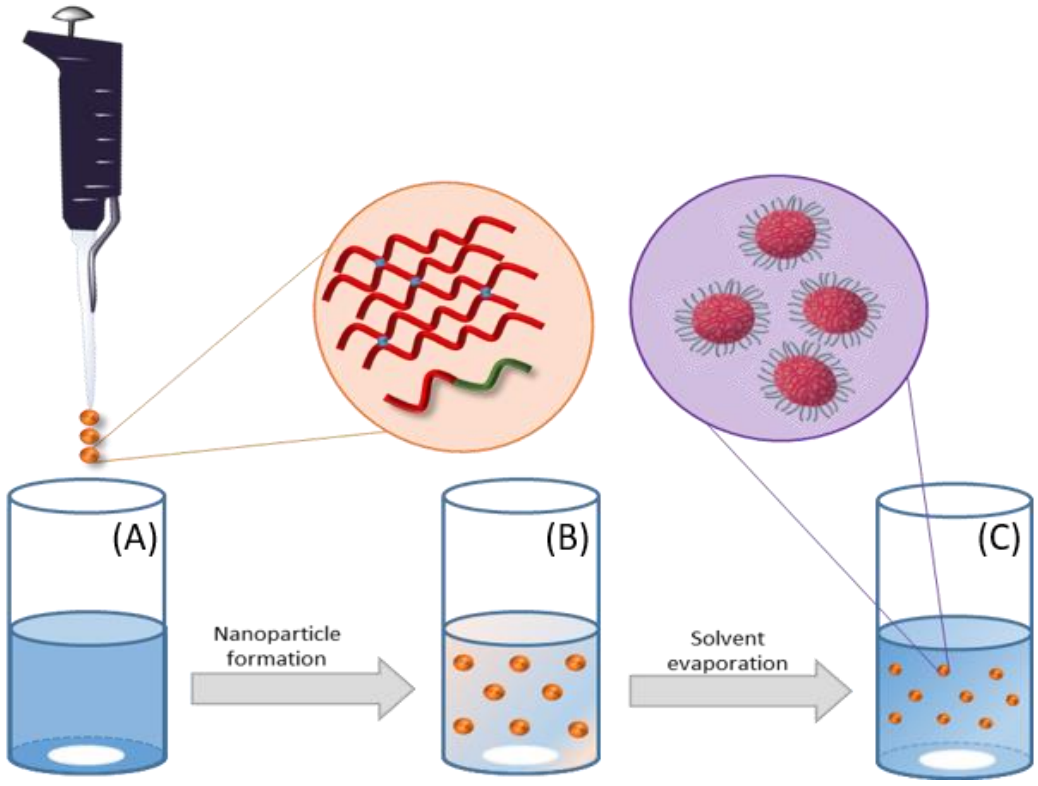


**Figure 3.1** Schematic representation of the formation of branched vinyl copolymer nanoparticles *via* co-nanoprecipitation. (A) The rapid addition of AB block copolymers and hydrophobic branched copolymers - both dissolved in a good solvent - to water. (B) Nanoparticle formation immediately following the addition to the bad solvent (water), yielding swollen nanoparticles. (C) Subsequent solvent evaporation over time, giving aqueous sterically stabilised branched vinyl copolymer nanoparticles.

Rannard and co-workers reported that the addition of the AB block copolymer within the nanoprecipitation did not interfere with the nanoprecipitation process of poly(hydroxypropyl methacrylate) (p(HPMA)) but instead yielded highly monodisperse nanoparticles with intensity-derived hydrodynamic diameters ranging between 70 – 300 nm.[10] These nanoparticles were sterically stabilised and could tolerate the addition of sodium chloride at high concentrations, thereby showing that this method can be utilised to generate polymer nanoparticles with potential applications as drug delivery vehicles. In brief, the co-nanoprecipitation technique enables the one pot production of sterically stabilised branched vinyl copolymer nanoparticles by mixing the branched vinyl copolymer with the amphiphilic AB block copolymer within a good solvent. This is rapidly added to water (a bad solvent environment), which causes a state of supersaturation and subsequent nucleation of both polymers. Nanoparticle formation then occurs *via* a growth mechanism, details of which are described in Chapter 1.3.2.3. As demonstrated by the authors, nanoparticle formation occurs immediately after addition of the solution of polymers to the anti-solvent (water) and solvent evaporation leads to an aqueous dispersion of sterically stabilised branched vinyl copolymer nanoparticles.

More recent work conducted *by* Rannard and co-workers expanded the scope of co-nanoprecipitation as a technique and investigated the branched vinyl copolymer nanoparticle formation from differing hydrophobic vinyl polymers such as poly(hexyl methacrylate), poly(lauryl methacrylate), poly(butyl methacrylate) (p(BuMA)) and poly(ethylhexyl methacrylate) (p(EHMA)).[12] Stabilisation was provided by the incorporation of AB block copolymers that had a matching hydrophobic domain derived from the same hydrophobic monomer that produced the branched vinyl copolymers. This preliminary study further illustrated the attractiveness of co-nanoprecipitation as a nano-formulation technique since, with the exception of p(HPMA) previously reported, none of the hydrophobic branched polymers studied alone (i.e. without amphiphilic blocks copolymers) were capable of forming stable aqueous nanoparticle dispersions, but were successful with the inclusion of the respective AB block copolymer.[12] In addition to this advantageous attribute of co-nanoprecipitation, there are a few other advantages that are worth noting. Firstly,

the composition of the nanoparticle and degree of steric stabilisation can be pre-determined prior to synthesis. This is due to the ability to vary the branched vinyl copolymer and AB block copolymer weight ratios within the initial good solvent mixture. Secondly, in order to drive nucleation, co-nanoprecipitation utilises high molecular weight branched copolymers. This opens up an opportunity to utilise complex macromolecular architectures that have been prepared by RDRP techniques, such as those discussed in Chapter 2. The design space of these materials can be explored to produce polymeric nanoparticles that have been specifically designed to facilitate and maximise incorporation of guest molecules, such as drugs. And thirdly, since steric stabilisation is achieved by the utilisation of the hydrophilic domains of the amphiphilic AB block copolymers, this also presents an opportunity for improving the behaviour of the polymer nanoparticle within the body and therefore the suitability of the polymeric nanoparticle as a drug delivery platform.

### 3.2 Chapter Aims

The primary aim of the work presented within this chapter is to build on the successful co-nanoprecipitations of hydrophobic vinyl-based copolymers and AB block copolymers that have been previously reported. The initial report focused on the co-nanoprecipitation of hydrophobic branched copolymers, comprised predominantly of p(HPMA) containing a low molar concentration of EGDMA, in the presence of an amphiphilic linear AB block copolymer to yield sterically stabilised aqueous vinyl polymer nanoparticles. As discussed, the co-nanoprecipitation process relies upon the simultaneous nucleation between amphiphilic block copolymers and hydrophobic vinyl branched copolymers. This has been previously achieved by ensuring that both hydrophobic domains of the copolymers are derived from the same monomer residue functionality. However, in this study we aim to vary the hydrophobic B block of the amphiphilic block copolymer to investigate any changes that this may impart to the co-nanoprecipitation process and the resulting polymeric nanoparticles. The library of polymer materials synthesised in Chapter 2 are to be utilised herein and their ability to form stable nanoparticle dispersions in aqueous media *via* co-nanoprecipitation will be assessed. The impact of the two different $DP_n$ values and the differing monofunctional and difunctional monomer chemistries on

nanoparticle formation will be explored. Given the contrasting role that each polymers plays, investigative studies into the optimal composition will be conducted and their stability to dilution with PBS will be evaluated. Another important aim of this study is to try and encapsulate a guest molecule, pyrene, as a model system to explore: (i) whether the presence of a hydrophobic guest molecule, which may crystalise, within the co-nanoprecipitation process has any significant influence on the mechanism of co-nanoprecipitation, and (ii) whether these polymer nanoparticles have encapsulation capabilities and therefore can be eventually utilised as a potential drug delivery system. In-turn, pyrene encapsulation will also provide opportunity to obtain information about the nanoparticle core polarity.

## 3.3 Results and Discussion

### 3.3.1 Nanoprecipitation Studies

Co-nanoprecipitation is more complex than a traditional nanoprecipitation process, since there is no longer just one polymer contributing to the formation of nanoparticles.[10] Therefore, it was important to gain an understanding of the behaviour (e.g. solubility, particle formation or aggregation) of each individual polymer component under nanoprecipitation conditions before assessing how they each contributed to the formation of polymer nanoparticles during the co-nanoprecipitation process. Each polymer was therefore nanoprecipitated as a single component to act as a control experiment.

#### 3.3.1.1 Single-component Nanoprecipitation Studies

As previously discussed, nanoprecipitation is a reproducible and efficient synthetic technique to generate polymeric nanoparticles.[13, 14] There are many different parameters that can control and influence the population, particle size, particle size distribution and ultimately whether it is successful in producing polymer nanoparticles. These parameters include the solvent:water ratio, the polymer:solvent ratio, the polymer molar mass and the selection of the organic solvent.

Regarding the selection of solvent, it must be water-miscible and ideally volatile. These characteristics of the solvent will allow for the rapid mixing of the good and

bad solvents and for the easy removal of the good solvent under ambient conditions to yield aqueous polymeric nanoparticles and avoid the need for lengthy dialysis. There are many organic solvents that meet these criteria including: acetone, acetonitrile, MeOH, isopropyl alcohol and tetrahydrofuran (THF). It has been reported that the mean size of nanoparticles is dependent on the nature of the organic solvent used to solubilise the polymer before nanoprecipitation. The impact of solvent miscibility with water and its effect on nanoparticle size has been investigated by Cheng *et al.* who reported that a decrease in mean nanoparticle size was observed with increasing water/solvent miscibility.[1] It has also been reported that when comparing the use of THF and acetone under identical nanoprecipitation conditions, nanoparticles obtained from acetone solutions had smaller particle sizes regardless of the polymer used.[15, 16] Acetone has a lower viscosity and higher diffusion coefficient in water compared to THF, and it has been suggested that this could promote faster mixing of acetone and water. This faster mixing would result in a more uniform supersaturation. Acetone would therefore make an obvious solvent choice. However, since the co-nanoprecipitation process would hopefully advance to include a chemotherapeutic drug (SN-38) solubilised within the polymer mixture, discussed in Chapter 4, the solubility of the chemotherapeutic drug in the organic solvent also needed to be considered. SN-38 exhibits extremely limited solubility in most organic solvents, however, it is soluble in THF. Therefore, the solvent selected as the good solvent for all aqueous nanoprecipitations and co-nanoprecipitations conducted throughout this research was THF.

Solubility of all the polymers was tested in THF and was conducted by preparing polymer solutions at an initial polymer concentration ($[P]_0$) = 5 mg $mL^{-1}$ in THF. It has been reported previously that the hydrodynamic diameter of the polymer nanoparticles can be influenced by the polymer concentration within the organic solvent.[17] We have reported in our group that nanoparticles produced *via* co-nanoprecipitation had intensity-average hydrodynamic diameters ($D_z$) in the range of 50 – 200 nm, which was dependent on the chemical nature of the polymer. These nanoparticles were produced at $[P]_0$ = 5 mg $mL^{-1}$. [7-10, 18] The effect of varying $[P]_0$ in the good solvent has also been investigated by varying the concentration from

0.5 mg $mL^{-1}$ to 5 mg $mL^{-1}$ and a small decrease in hydrodynamic diameter was observed as the $[P]_0$ decreased; although this change was modest and was again dependent on the chemical nature of the polymer.

In addition, the nanoprecipitation process also involves careful consideration of other design parameters, such as the good solvent/bad solvent volume ratio and the final polymer concentration in water ($[P]_f$), both of which contribute to the success of the technique. It has been established and demonstrated for a number of polymers with similar functionalities and structures that $[P]_f$ = 1 mg $mL^{-1}$ is sufficient to facilitate the nucleation and subsequent nanoparticle formation. With this is mind, and given that the nanoparticles produced from $[P]_0$ = 5 mg $mL^{-1}$ were within the size range that is optimal for anti-cancer DDS, this was the initial polymer concentration used within this study. Solutions were sealed and placed on a roller mixer overnight to ensure complete solubilisation of polymer. In all cases, the polymers showed full solubility in THF as clear solutions were obtained.

Nanoprecipitation of all materials synthesised in Chapter 2 was conducted following the general protocol outlined below and depicted in Figure 3.2. The polymer was dissolved in THF (the good solvent) until complete solubilisation was achieved. Into 5 mL of stirred deionised (DI) water, 1 mL of the polymer stock solution ($[P]_0$ = 5 mg $mL^{-1}$) was rapidly added using a manual air displacement pipette. The solution was allowed to stir at ambient temperature for 24 hours to facilitate the evaporation of the THF solvent. Confirmation of complete THF removal was conducted by performing the nanoprecipitation in $D_2O$ and then analysing *via* $^1$H-NMR spectroscopy, which showed that no THF was remaining. To ensure the final concentrations were targeted accurately, the mass of water was recorded before and after evaporation and topped up as required. Aqueous nanoparticle dispersions were obtained at $[P]_f$ = 1 mg $mL^{-1}$ .

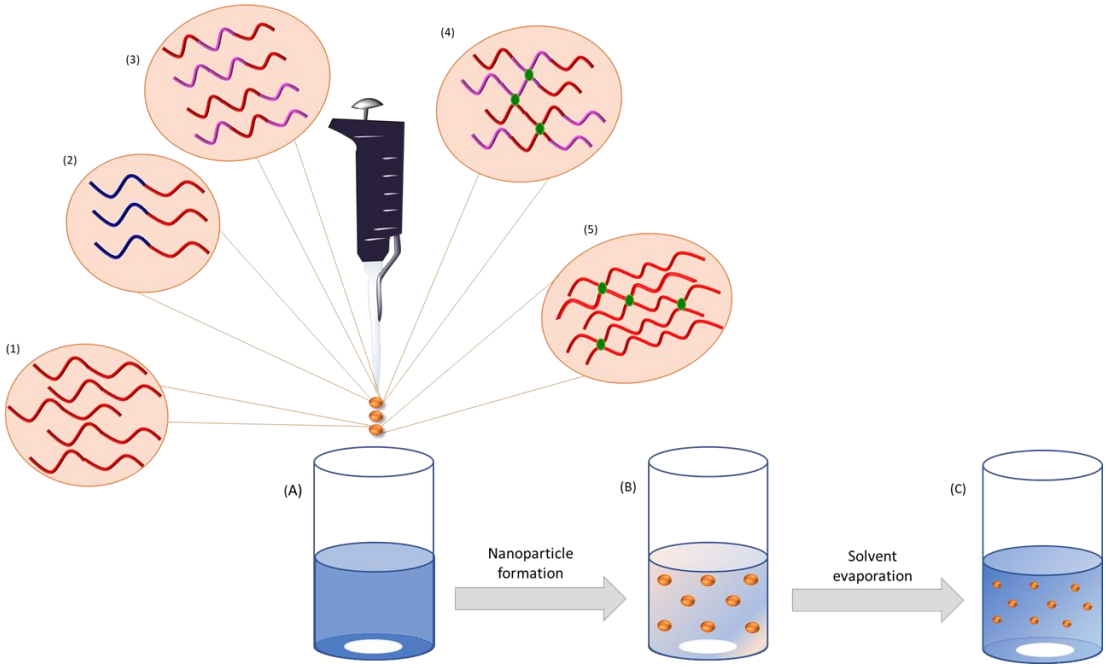


**Figure 3.2** Schematic representation of how nanoprecipitations of 1) linear homopolymers, 2) AB block copolymers, 3) statistical linear copolymers, 4) statistical branched copolymers and 5) branched copolymers were conducted *via* co-nanoprecipitation. A) Good solvent containing polymer at $[P]_0$=5 mg $mL^{-1}$ rapidly added to 5 mL $H_2O$ with stirring, (B) nanoparticle formation and (C) evaporation of THF over 24 hours yielding aqueous nanoparticle dispersion at $[P]_f$ =1 mg $mL^{-1}$.

Sole nanoprecipitation of all 31 polymers, with the exception of p(HPMA)$_{100}$, p(HPMA)$_{20}$, p(HPMA$_{100}$-co-EGDMA$_{0.90}$), p(HPMA-co-EGDMA$_{0.95}$) and p(PEG$_{114}$-*b*-HPMA$_{100}$), were unsuccessful in forming stable polymer nanoparticles; a mere success rate of 13%. The other 87% of nanoprecipitated samples failed, which was evident after the THF had evaporated leading to macroscopic polymer precipitation and subsequent sedimentation within the glass vial. The successful nanoprecipitations of p(HPMA) based polymers agreed with the literature and its success is owed to its ability to provide electrostatic stabilisation, discussed in more detail below. Turbid aqueous nanoparticle dispersions were obtained for p(HPMA)$_{100}$ and p(HPMA)$_{20}$, whilst transparent aqueous nanoparticle dispersions were obtained for p(HPMA$_{100}$-co-EGDMA$_{0.90}$), p(HPMA$_{20}$-co-EGDMA$_{0.85}$) and p(PEG$_{114}$-*b*-HPMA$_{100}$), whereby no macroscopic aggregation was observed (Figure 3.3).

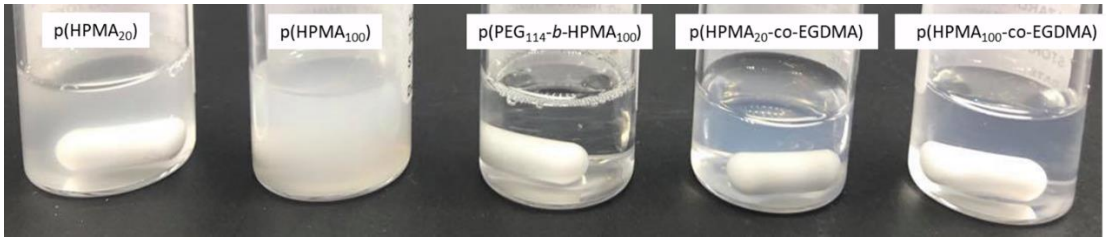


**Figure 3.3** Photograph of the successful sole nanoprecipitations of the HPMA based polymeric systems.

Particle size distributions of the p(HPMA) based polymer nanoparticles were obtained by dynamic light scattering (DLS) (Table 3.1, Figure 3.4). Differences between polymer architectures yielded different hydrodynamic diameters. Linear homopolymers had larger hydrodynamic diameters and significantly increased polydispersity values compared to the branched copolymers; for example, $p(HPMA)_{20}$ ($D_z$ = 570 nm, PDI = 0.217) compared to $p(HPMA_{20}\text{-co-}EGDMA_{0.85})$ ($D_z$ = 80 nm, PDI = 0.047). This result is not surprising, since it has been reported previously that high molecular weight p(HPMA-co-EGDMA) copolymers play an important role in promoting homogenous and rapid nucleation, which leads to smaller hydrodynamic diameters and narrower particle size distributions.[8, 9] It was also observed that the sole nanoprecipitation of $p(HPMA)_{20}$ when compared to $p(HPMA)_{100}$ produced particles with a significantly larger hydrodynamic diameter (570 vs 190 nm). This is likely due to $p(HPMA)_{20}$ having a higher thermodynamic equilibrium solubility limit and therefore a lower degree of supersaturation. This may have, in turn led to a slower nucleation rate and a small number of nuclei.

**Table 3.1** DLS analysis of the stable aqueous nanoparticle dispersions produced *via* sole nanoprecipitation of the HPMA based polymers.

| Polymer | $D_z$ (nm)[a] | PDI[a] | Derived count rate (kcps)[a] | ζ (mV)[b] | Attenuator Value |
|---|---|---|---|---|---|
| *$p(HPMA)_{100}$** | *190* | *0.154* | *286 323* | *-31.2* | *4* |
| *$p(HPMA)_{20}$** | *570* | *0.217* | *21 800* | *-37.1* | *7* |
| $p(HPMA_{100}\text{-co-}EGDMA_{0.90})$ | 60 | 0.047 | 99 734 | -32.6 | 6 |
| $p(HPMA_{20}\text{-co-}EGDMA_{0.85})$ | 80 | 0.080 | 238 220 | -40.4 | 5 |
| $p(PEG_{114}\text{-}b\text{-}p(HPMA)_{100})$ | 40 | 0.042 | 10 000 | -12.9 | 8 |

[a] Measured using DLS analysis at a concentration of 1 mg $mL^{-1}$, $D_z$ values have been rounded to the nearest 5 nm. [b] Obtained *via* measurement of the electrophoretic mobility of aqueous nanoparticle dispersions within zeta cell. *Samples were not stable 7 days after generation and sedimentation had occurred.

The success of the nanoprecipitations of p(HPMA) based polymers is often attributed to the high charge that the generated nanoparticles exhibit. The zeta potential value

(ζ) obtained for the HPMA-based polymer nanoparticles (avg. -35 mV) is considered of a sufficient magnitude to be able to provide charge stabilisation to a moderate level and would explain why these were successful at forming nanoparticles without the addition of stabilisers (e.g. AB block copolymers or additional surfactants).

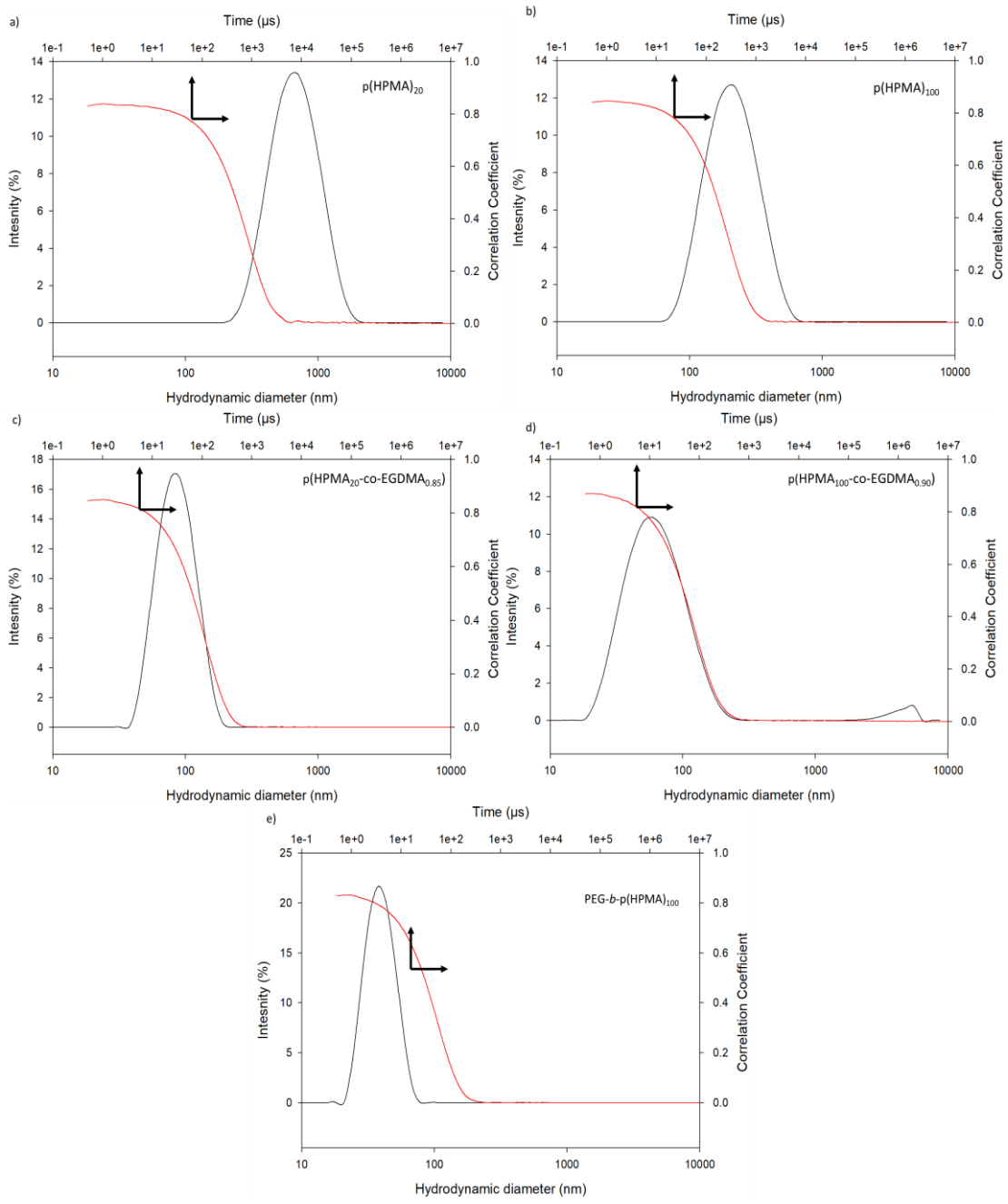


**Figure 3.4** Nanoparticle size distributions obtained by DLS analysis of the successful sole nanoprecipitations: a) $p(HPMA)_{20}$, b) $p(HPMA_{100})$, c) $p(HPMA\text{-}co\text{-}EGDMA_{0.85})$, d) $p(HPMA_{100}\text{-}co\text{-}EGDMA_{0.90})$ and e) $p)PEG_{114}\text{-}b\text{-}HPMA_{100})$ obtained at 1 mg $mL^{-1}$ with no filtration.

It is worth emphasising that the nanoparticle dispersions obtained from linear polymers $p(HPMA)_{20}$ and $p(HPMA)_{100}$ were unstable and visible aggregation was

noticed after several days without stirring. This difference in behaviour observed between linear homopolymers and branched copolymers is consistent with that previously reported, whereby, our group have shown that the architecture of the nanoprecipitated polymer can have a large influence on the production of stable nanoparticles and that stability is greatly facilitated by high molecular weight branched material.[7]

When the sole nanoprecipitations of the AB block copolymers were conducted, it was assumed that the addition of the hydrophilic PEG group would provide the nanoparticles with steric stabilisation and thereby produce stable polymer nanoparticles from polymers with differing methacrylate-based B block domains varying in hydrophobicity. However, the only successful nanoprecipitation of AB block copolymers was that of p($PEG_{114}$-*b*- $HPMA_{100}$), producing a transparent dispersion with no visible aggregates present (Figure 3.5a). The other AB block copolymers were unsuccessful in forming stable nanoparticles and generated fine white macroscopic aggregates in solution (Figure 3.5b&c).

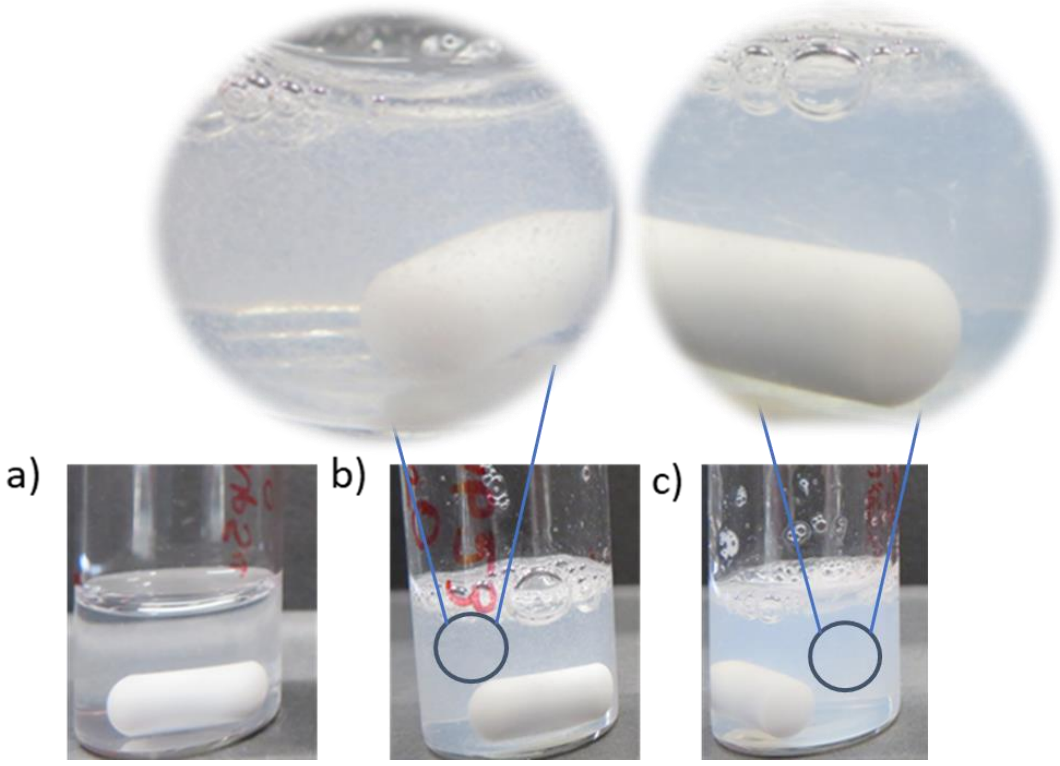


**Figure 3.5** Photographs showing the successful sole nanoprecipitation of a) p($PEG_{114}$-*b*-$HPMA_{100}$) producing a transparent aqueous nanoparticle dispersion compared to the unsuccessful nanoprecipitation of b) p($PEG_{114}$-*b*-$BuMA_{100}$) and c) p($PEG_{114}$-*b*-$EHMA_{100}$), which generated turbid solutions and resulted in macroscopic sedimentation.

From this experiment, it was evident that the sole nanoprecipitation of each individual polymer component was not a feasible method for producing stable aqueous nanoparticle dispersions, with the exception of HPMA-based branched copolymer systems. To potentially produce stable aqueous nanoparticle dispersions of the hydrophobic branched copolymers consisting of BuMA and EHMA monomer residues, there is a need for the addition of a stabilising species, such as an AB block copolymer. Co-nanoprecipitation is a technique whereby two polymers can be mixed to potentially generate sterically stabilised nanoparticles and therefore further studies focussed on utilising this approach.

### 3.4 Determining Co-Nanoprecipitation Parameters

Despite the failure to nanoprecipitate the majority of the polymer library individually, it was of interest to conduct co-nanoprecipitations on the full material library generated in Chapter 2 but with the inclusion of an AB block co-polymer in each case. This would provide insight into whether or not the material behaved differently during co-nanoprecipitation when combined with an AB block co-polymer, whilst also providing a greater understanding of the co-nanoprecipitation process and the different types of polymer material that can be used to generate nanoparticles. In particular, it was of interest to gain an understanding of how the nanoparticle composition, specifically branched copolymer:AB block copolymer weight ratio, could affect the size and stability of the polymer nanoparticles. Given that the hydrophobic linear polymers exhibited limited stability during the sole nanoprecipitations (Section 3.3.1), this study focussed on the co-nanoprecipitation of hydrophobic branched copolymers and amphiphilic linear AB block copolymers only, and aimed to determine an optimum weight ratio of branched copolymer:AB block copolymer that could then be utilised in the rest of the studies.

#### 3.4.1 Varying the Weight Compositional Ratio of Each Polymeric Component Within Co-nanoprecipitation

When two polymers are co-nanoprecipitated, they must associate simultaneously in order to avoid the formation of two different species, which may also result in two distinct size populations or visible macroscopic aggregation from unstabilised nanoparticles. Given the contrasting roles of each polymer component within the nanoprecipitation, whereby the branched copolymer contributes to the core

composition and the AB block provides stabilisation, it could be expected that by varying the weight percentages (wt. %) of these components with respect to the total polymer mass that it would alter or impact the properties of the final polymer nanoparticle. Specifically, the particle stability, size, dispersity and core characteristics. Therefore, there is a need to select consistent values to provide direct comparisons and aid identification of the role of varying polymer chemistry and structure. In order to successfully form stabilised nanoparticles, the concentration of AB block copolymer must be sufficient enough to provide steric stabilisation, but low enough to avoid also forming nanoprecipitates that comprise predominantly AB block copolymer.

Co-nanoprecipitations were conducted following the same protocol as previously described. Initial polymer concentration was maintained at $[P]_0$ = 5 mg $mL^{-1}$ and the ratio of branched copolymer and AB block copolymer incorporated within the good solvent varied systematically between 100:0 to 0:100 wt.% with respect to total solid mass (Figure 3.6). It is worth noting that the weight percentages discussed below correspond to branched copolymer:AB block copolymer, respectively.

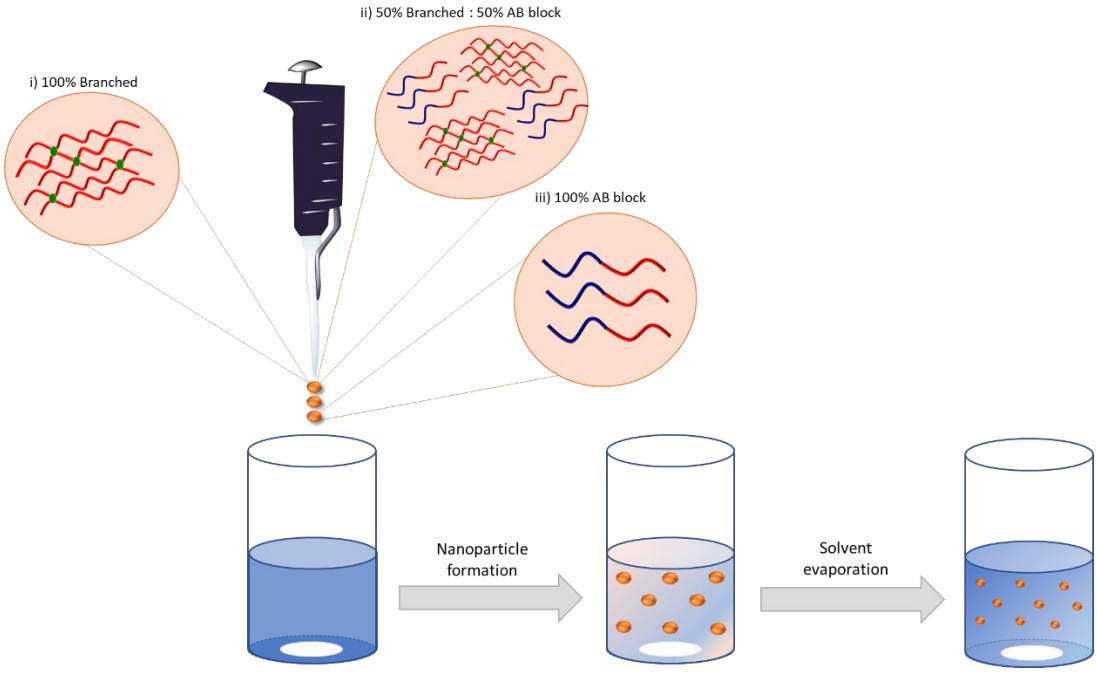


**Figure 3.6** Schematic representation of the experimental design used to vary the weight ratio of branched copolymer: AB block copolymer within the initial THF solution. Co-nanoprecipitation conducted as before to yield varying nanoparticle compositions containing i) 100 wt.% branched copolymer, (ii) 50 wt.% branched copolymer and 50 wt.% A block copolymer and (iii) 100 wt.% AB block copolymer.

Given that p($PEG_{114}$-b-$HPMA_{100}$) is stable when nanoprecipitated on its own, it was the ideal choice of AB block copolymer to conduct this study as it would allow for the full range of weight ratios to be explored. It would also help develop an understanding of the influence of monomer chemistry from the branched (co)polymers on the co-nanoprecipitation process, as only one polymer component would be changing. Three branched vinyl copolymers were selected: p($HPMA_{100}$-co-$EGDMA_{0.90}$), p($BuMA_{100}$-co-$EGDMA_{0.95}$) and p($EHMA_{100}$-co-$EGDMA_{0.80}$). Rapid addition of polymer stock solution (1 mL) was added to DI water (5 mL) and left to evaporate for 24 hours for complete THF removal. Particle size distributions of the aqueous nanoparticle dispersions were obtained using DLS at a concentration of 1 mg $mL^{-1}$ (Table 3.2, Figure 3.7). Samples where visible macroscopic aggregation had occurred, for example like the sole nanoprecipaiton of p($EHMA_{100}$-co-$EGDMA_{0.80}$) and p($BuMA_{100}$-co-$EGDMA_{0.95}$), were passed through a 1 µm fibreglass filter prior to DLS analysis, as indicated by an Asterix and red italic font (Figure 3.8). These samples would normally be classified as a failed nanoprecipitation but have been utilised within this study for information purposes.

**Table 3.2** DLS analyses of branched vinyl copolymer nanoparticles produced by co-nanoprecipitation with p($PEG_{114}$-*b*-$HPMA_{100}$) at varied branched and AB block copolymer compositions from 100-0 wt.%, respectively.

| Monomer Residue | Wt. % of Branched Polymer | Wt. % of AB Block Co-Polymer | $D_z$ (nm)[a] | | PDI[a] | | Derived Count Rate [a](kcps) |
|---|---|---|---|---|---|---|---|
| | | | Day 1 | Day 10 | Day 1 | Day 10 | |
| HPMA | 100 | 0 | 60 | 60 | 0.210 | 0.207 | 119 330 |
| | 90 | 10 | 60 | 60 | 0.159 | 0.154 | 99 990 |
| | 80 | 20 | 60 | 60 | 0.121 | 0.110 | 97 500 |
| | 70 | 30 | 60 | 60 | 0.149 | 0.135 | 122 100 |
| | 60 | 40 | 60 | 60 | 0.112 | 0.100 | 89 700 |
| | 50 | 50 | 55 | 55 | 0.093 | 0.083 | 110 700 |
| | 40 | 60 | 55 | 55 | 0.068 | 0.055 | 103 400 |
| | 30 | 70 | 55 | 55 | 0.055 | 0.046 | 100 800 |
| | 20 | 80 | 55 | 55 | 0.066 | 0.061 | 89 500 |
| | 10 | 90 | 50 | 50 | 0.082 | 0.090 | 57 850 |
| | 0 | 100 | 40 | 40 | 0.060 | 0.048 | 19 150 |
| BuMA | *100** | *0* | *190* | - | *0.111* | - | *263 100* |
| | *90** | *10* | *170* | - | *0.122* | - | *321 700* |
| | *80** | *20* | *160* | - | *0.098* | - | *426 900* |
| | *70** | *30* | *150* | - | *0.081* | - | *578 100* |
| | 60 | 40 | 140 | 140 | 0.068 | 0.091 | 567 500 |
| | 50 | 50 | 130 | 130 | 0.090 | 0.083 | 463 700 |
| | 40 | 60 | 130 | 130 | 0.108 | 0.090 | 458 600 |
| | 30 | 70 | 120 | 120 | 0.106 | 0.118 | 316 400 |
| | 20 | 80 | 110 | 110 | 0.126 | 0.130 | 230 000 |
| | 10 | 90 | 80 | 80 | 0.148 | 0.0157 | 108 250 |
| | 0 | 100 | 40 | 40 | 0.060 | 0.048 | 19 150 |
| EHMA | *100** | *0* | *220* | - | *0.179* | - | *186 900* |
| | *90** | *10* | *165* | - | *0.107* | - | *445 000* |
| | *80** | *20* | *160* | - | *0.091* | - | *465 600* |
| | *70** | *30* | *145* | - | *0.078* | - | *586 200* |
| | *60** | *40* | *170* | - | *0.133* | - | *318 300* |
| | *50** | *50* | *140* | - | *0.099* | - | *481 150* |
| | *40** | *60* | *125* | - | *0.089* | - | *371 100* |
| | 30 | 70 | 125 | 125 | 0.137 | 0.095 | 358 600 |
| | 20 | 80 | 110 | 110 | 0.140 | 0.135 | 233 150 |
| | 10 | 90 | 95 | 100 | 0.187 | 0.172 | 130 850 |
| | 0 | 100 | 40 | 40 | 0.060 | 0.048 | 19 150 |

[a] Measured using DLS analysis at a concentration of 1 mg $mL^{-1}$, $D_z$ values have been rounded to the nearest 5 nm. *Sample contained visible aggregate and required filtration 1 µm glass filter to obtain DLS results.

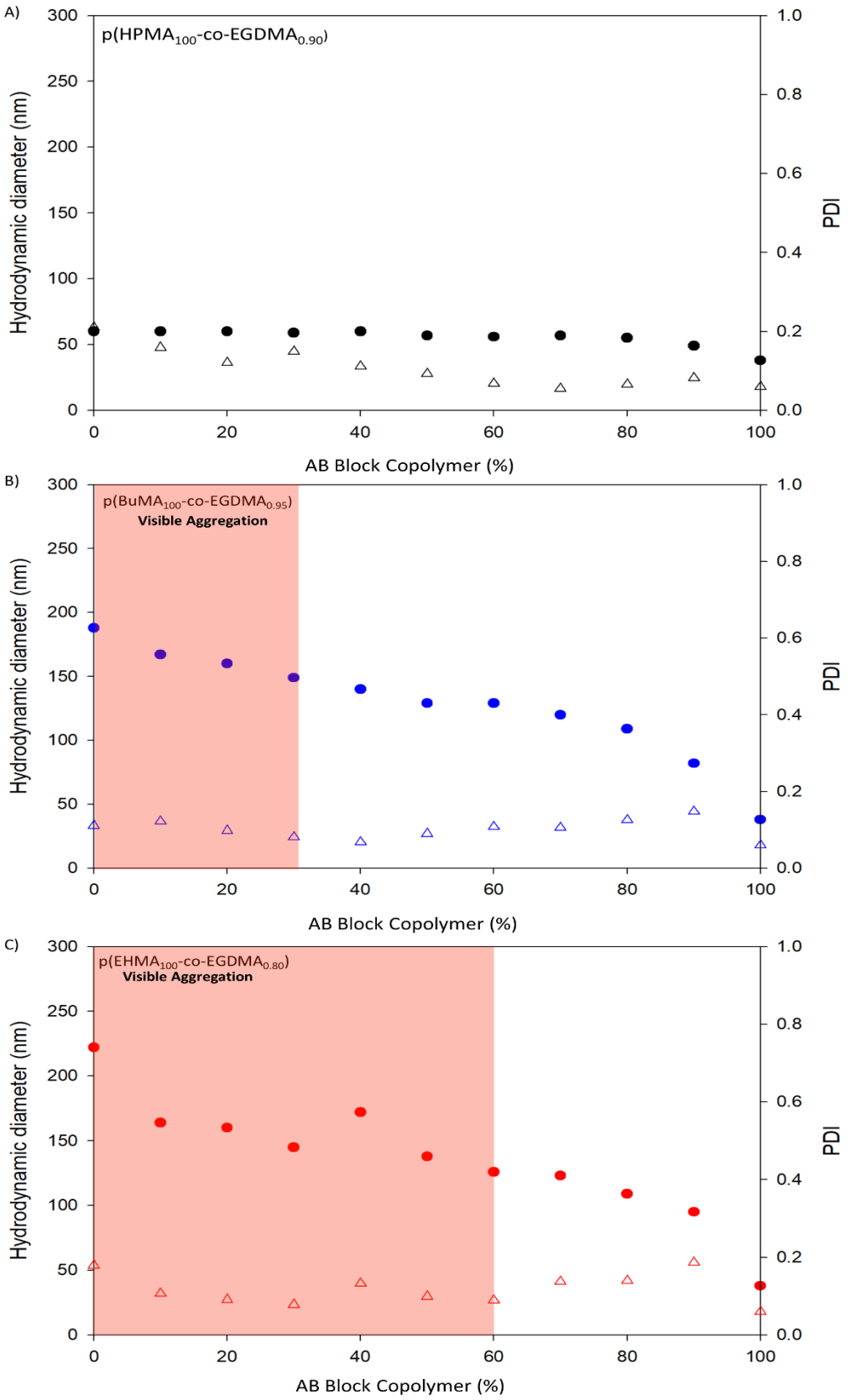


**Figure 3.7** Graphical representation of the impact of varying the branched copolymer wt.% in the initial THF solution on the $D_z$ (nm) (closed circles) and the PDI (open triangles) of the branched vinyl copolymer nanoparticles generated *via* co-nanoprecipitation: A) p(HPMA$_{100}$-co-EGDMA$_{0.90}$), B) p(BuMA$_{100}$-co-EGDMA$_{0.95}$) and C) p(EHMA$_{100}$-co-EGDMA$_{0.80}$). The wt. % ratios of branched copolymer at which visible aggregation was observed is indicated in red.

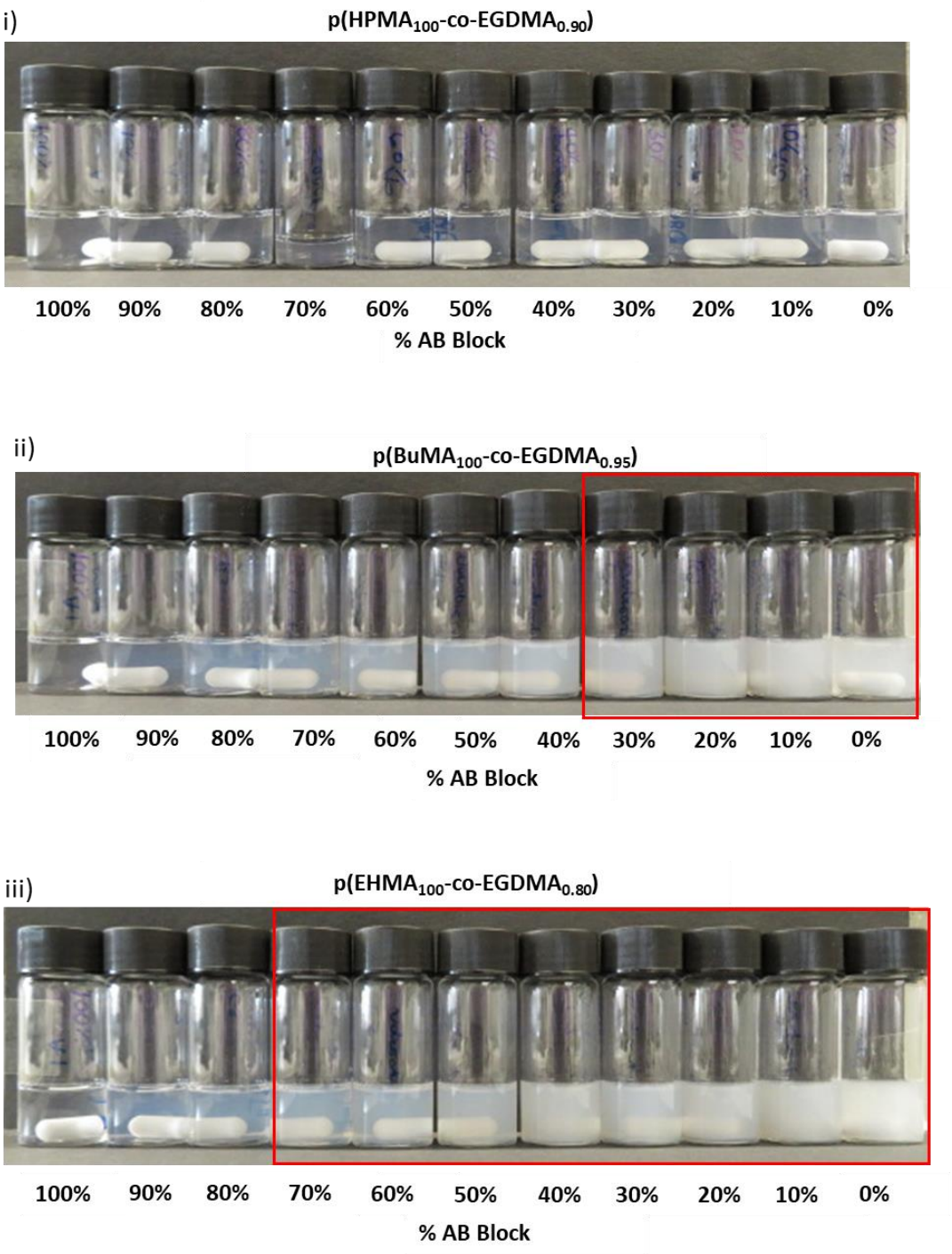


**Figure 3.8** A photograph of the co-nanoprecipitations of p($PEG_{114}$-*b*-$HPMA_{100}$) and i) p($HPMA_{100}$-co-$EGDMA_{0.90}$), ii) p($BuMA_{100}$-co-$EGDMA_{0.95}$) and iii) p($EHMA_{100}$-co-$EGDMA_{0.80}$) at varying wt.% ratios of AB block decreasing from left to right. The wt.% at which macroscopic aggregation occurred is illustrated with the red box.

In all cases, DLS analysis of the aqueous nanoparticle dispersions showed monomodal particle size distributions consisting of highly monodisperse nanoparticles with $D_z$ values ranging from 40 to 220 nm. A general trend was observed where the nanoparticle hydrodynamic diameters decreased linearly as the weight composition of the AB block copolymer increased (Figure 3.7). The extent of

this decrease was dependent on the chemical nature of the branched copolymer utilised within the co-nanoprecipitation. Interestingly, the extent of this decrease in hydrodynamic diameter was small whilst the AB block copolymer composition was between 0 and 50 wt.%, but became more significant as the composition increased beyond 50 wt.%. For example, when analysing the results of the co-nanoprecipitation of p($HPMA_{100}$-co-$EGDMA_{0.90}$) with p($PEG_{114}$-*b*-$HMPA_{100}$), an increase in the AB block copolymer composition from 0 to 50 wt.% resulted in a decrease in hydrodynamic diameter from 60 to 55 nm - a relatively insignificant change. However, as the composition of AB block copolymer increased from 50 to 100 wt.%, the change in hydrodynamic diameter was more significant, decreasing from 55 to 40 nm. This was also observed for the other two polymer systems. The rationale for this is that the increasing composition, and therefore mass, of AB block copolymer within the system results in a decrease in composition, and therefore mass, of hydrophobic branched copolymer. As the role of the AB block copolymer is to provide steric stabilisation, nanoparticle growth would likely be arrested at an earlier stage resulting in smaller hydrodynamic diameters.

In all cases, the co-nanoprecipitation of p($HPMA_{100}$-co-$EGDMA_{0.90}$) and p($PEG_{114}$-b-$HMPA_{100}$) was successful in forming sterically stabilised polymer nanoparticles regardless of the weight ratio of AB block copolymer utilised. DLS analysis of the aqueous nanoparticle dispersions showed monomodal size distributions with hydrodynamic diameters ranging from 40 – 60 nm. The hydrodynamic diameter of the nanoparticles remained consistent (60 nm) as the composition of hydrophobic branched copolymer decreased from 100 to 60 wt.%. This control in size could be derived from the electrostatic stabilisation that p($HPMA_{100}$-co-$EGDMA_{0.90}$) provides during the nanoparticle growth capping mechanism, even at low wt.% ratios of AB block copolymer. The PDI values (0.210 – 0.055) decreased as the wt.% of AB block copolymer increased from 0 – 70 wt.% and branched copolymer decreased from 100 – 30 wt.%, but then began to increase at 80 wt.% AB block copolymer and above.

When the branched copolymer was changed to p($BuMA_{100}$-co-$EGDMA_{0.95}$), samples that contained ≤ 30 wt.% AB block copolymer were not sterically stabilised and

macroscopic aggregation was observed (Figure 3.8). This suggests that the nanoparticles generated at these compositions had an insufficient density of PEG stabilising chains to achieve steric stabilisation and colloidal stability. This is also in line with what was observed during the sole nanoprecipitation of p($BuMA_{100}$-co-$EGDMA_{0.95}$) without the presence of AB block copolymer, which also resulted in macroscopic aggregation. However, these samples were still analysed *via* DLS following filtration to provide some indication about size trends. There was a large decrease in hydrodynamic diameter (190 to 40 nm) as the composition of AB block copolymer increased from 0-100 wt.%. Again, this is likely due to the increasing levels of steric stabilisation afforded to the polymer nanoparticles. Interestingly, however, the magnitude of change in hydrodynamic diameter was significantly larger ($\Delta D_z$ = 150 nm) than what was observed for p($HPMA_{100}$-co-$EGDMA_{0.90}$). This is likely due to the lack of electrostatic stability provided to the growing nuclei by p($BuMA_{100}$-co-$EGDMA_{0.95}$). When 50 - 90 wt.% of AB block copolymer was present and sterically stabilised nanoparticles were formed, the PDI values increased up to a value of 0.148. This broader PDI and decrease in size suggests a loss of control during the co-nanoprecipitation may be occurring. This is likely due to differences in supersaturation within the co-nanoprecipitations. As the amount of AB block copolymer increases and the amount of branched vinyl copolymer decreases, there is a decrease in the levels of supersaturation of the core-forming material. This decrease in supersaturation causes a slower nucleation relative to the growth phase and hence produces samples that have a broader PDI. As before, the stability of the branched vinyl polymer nanoparticles was checked by repeating the DLS measurements on the original samples following 10 days of storage under ambient conditions. These measurements showed a lack of significant variation from the original nanoparticle diameters, suggesting that the samples all remained stable.

Finally, when changing the polymer to p($EHMA_{100}$-co-$EGDMA_{0.80}$), co-nanoprecipitations with ≤ 60 wt.% of AB block copolymer present resulted in macroscopic aggregation and failed co-nanoprecipitations. The boundary between the success and failure of these co-nanoprecipitations was observed at higher compositions of AB block copolymer compared to the p($BuMA_{100}$-co-$EGDMA_{0.95}$)

series. As previously explained, EHMA is more hydrophobic than BuMA, therefore the EHMA branched copolymer may possibly require more stabiliser to achieve steric stabilisation. Those samples with visible polymer aggregates were still studied using DLS, following filtration. Particle hydrodynamic diameters decreased (220 to 40 nm) as the composition of AB block copolymer increased.

The results of the study highlighted that each polymer species has different roles within the co-nanoprecipitation process, with the hydrophobic branched copolymers driving the particle nucleation and the amphiphilic AB block copolymer arresting particle growth through steric stabilisation. In the cases of the p($BuMA_{100}$-co-$EGDMA_{0.95}$) and p($EHMA_{100}$-co-$EGDMA_{0.80}$) series, a combination of these components was essential in order to generate colloidally stable nanoparticles. In the case of the p($HPMA_{100}$-co-$EGDMA_{0.90}$) series, such a combination was not essential and colloidally stable nanoparticles consisting of 100 wt.% hydrophobic branched copolymer could be obtained through charge stabilisation; however, the presence of the AB block copolymer is still deemed necessary if such nanoparticles are to fulfil their potential as drug delivery vehicles, for the reasons discussed previously. Furthermore, the results highlighted that the AB block copolymer composition had a direct impact on the particle size and the success of the co-nanoprecipitations, with the p($EHMA_{100}$-co-$EGDMA_{0.80}$) nanoprecipitates requiring a greater content of p($PEG_{114}$-b-$HPMA_{100}$) (≥ 70 wt.%) compared to the p($BuMA_{100}$-co-$EGDMA_{0.95}$) nanoprecipitates (≥ 40 wt.%) in order to achieve colloidal stability. With regard to the latter point, it was assumed that the nanoprecipitates of the EHMA-based polymers may be unsuitable candidates as DDS unless their behaviour is altered when a guest molecule is introduced to the co-nanoprecipitation process.

### 3.4.2 Stability of Co-nanoprecipitated Nanoparticles Upon the Addition of PBS

To be considered as a potential drug delivery vehicle, it is important that the nanoparticles can maintain their structural integrity upon exposure to physiological relevant conditions. These conditions include high dilution and the presence of salts. Failure of the nanoparticles to withstand these conditions is likely to result in the faster clearance from systemic circulation and the uncontrolled release of the encapsulated drug shortly after IV administration into systemic circulation. Previous

studies within our group have reported the stability of branched p(HPMA) based nanoparticles upon addition of salt (NaCl).[10] It was shown that nanoparticles without AB block copolymer present were immediately prone to aggregation and sedimentation following this addition due to the screening of the electrostatic charges that otherwise provided stability.[19] However, it was found that incorporation of AB block copolymer (≥ 20 wt.%) led to greater stability of the polymer nanoparticles upon addition of the salt. It is likely that this was due to the steric stabilisation of the hydrophilic PEG domain of the AB block copolymer. This stabilisation effect was seen to diminish when ≥ 70 wt.% AB block copolymer was incorporated, as particle size began to increase dramatically. This indicated that branched vinyl copolymer nanoparticles should compromise ≤ 60 wt.% AB block copolymer if they are to be utilised as DDS.

Given that these polymer nanoparticles were to be assessed in both *in vitro* and *in vivo* pharmacological evaluations, it is important to understand their behaviour when diluted in buffered media and it was therefore necessary to conduct a study to determine the effects of the addition of phosphate buffer solution. Experimentally, p(HPMA$_{100}$-co-EGDMA$_{0.90}$) was co-nanoprecipitated into DI water with p(PEG$_{114}$-*b*-HPMA$_{100}$); as before, the compositions varied from 100:0 – 50:50 wt.%, respectively. The volatile organic solvent was allowed to evaporate and $D_z$, PDI and derived count rate were determined *via* DLS at $[P]_f$ = 1 mg mL$^{-1}$. The stability of these branched vinyl copolymer nanoparticles in response to dilution and exposure to salts was assessed *via* a serial dilution with PBS over a 100-fold dilution factor to produce final polymer concentrations at 0.5, 0.25, 0.1 and 0.01 mg mL$^{-1}$. The aqueous nanoparticle dispersions were left to gently mix overnight following dilution and then assessed using DLS (Table 3.3). The samples that were diluted to 0.1 and 0.01 mg mL$^{-1}$ have been omitted from this discussion as the DLS data obtained was not credible due to insufficient light scattering (Appendix, Table A1)

**Table 3.3** DLS analyses of p($HPMA_{100}$-co-$EGMDA_{0.90}$) co-nanoprecipitates varying in wt. % of p($PEG_{114}$-*b*- $HPMA_{100}$) from 0 – 50 wt.%, respectively, following the serial dilution with PBS addition. $D_z$ values have been rounded to the nearest 5 nm

| Polymer Concentration | Wt.% of Branched Polymer | Wt.% of AB block co-polymer | $D_z$ (nm) | PDI | Derived count rate (kcps) | Attenuator Setting |
|---|---|---|---|---|---|---|
| 1 mg $mL^{-1}$ (no PBS) | 100 | 0 | 65 | 0.261 | 47 900 | 6 |
| | 90 | 10 | 60 | 0.197 | 46 500 | 6 |
| | 80 | 20 | 75 | 0.239 | 54 550 | 6 |
| | 70 | 30 | 70 | 0.170 | 69 950 | 6 |
| | 60 | 40 | 60 | 0.152 | 40 720 | 6 |
| | 50 | 50 | 60 | 0.115 | 31 800 | 7 |
| 0.5 mg $mL^{-1}$ (PBS) | *100* | *0* | *Polymer aggregation* | | | |
| | *90* | *10* | *Polymer aggregation* | | | |
| | 80 | 20 | 180 | 0.277 | 249 700 | 5 |
| | 70 | 30 | 90 | 0.093 | 81 050 | 6 |
| | 60 | 40 | 60 | 0.097 | 19 500 | 7 |
| | 50 | 50 | 60 | 0.113 | 18 300 | 7 |
| 0.25 mg $mL^{-1}$ (PBS) | *100* | *0* | *Polymer aggregation* | | | |
| | *90* | *10* | *Polymer aggregation* | | | |
| | 80 | 20 | 180 | 0.272 | 84 600 | 5 |
| | 70 | 30 | 95 | 0.195 | 38 300 | 6 |
| | 60 | 40 | 105 | 0.269 | 11 000 | 7 |
| | 50 | 50 | 90 | 0.291 | 10 600 | 7 |

[1]Italic numbers represent sample which resulted in polymer aggregation.

As expected, the sample without AB block co-polymer present precipitated immediately upon dilution with PBS to a polymer concentration of 0.5 mg $mL^{-1}$. It was also observed that the nanoprecipitates consisting of 10 wt.% of AB block copolymer also precipitated (Figure 3.9). These two samples were consequently not diluted further. However, stability was observed when ≥ 20 wt.% of AB block copolymer was incorporated. Although precipitation was not observed, it is thought that 20 wt.% may be on the cusp of providing a sufficient density of surface PEG chains from the AB block copolymer for steric stabilisation since an approximate doubling in $D_z$ was observed (75 to 180 nm). It is worth noting, however, that little variation was seen from this point with further dilutions (Figure 3.10).

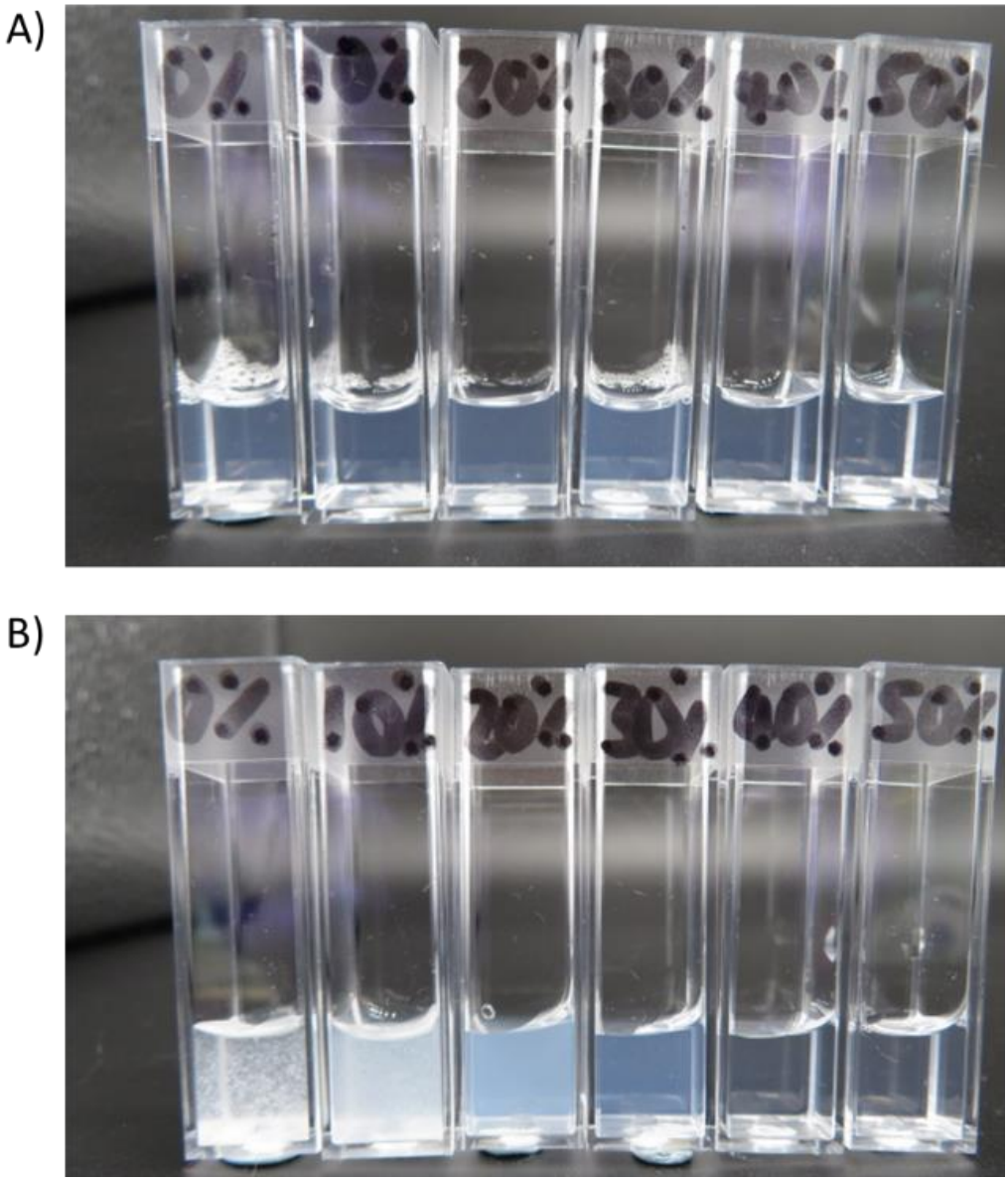


**Figure 3.9** Photographs showing the effects of the addition of PBS to the samples of p($HPMA_{100}$-co-$EGDMA_{0.90}$) with varying amounts of AB block copolymer from 0-50 wt.% from left to right. Measured at A) polymer concentration = 1 mg $mL^{-1}$ in $H_2O$ and B) polymer concentration = 0.5 mg $mL^{-1}$ following dilution with PBS.

Further increases in AB block copolymer composition (≥ 30 wt.%) led to greater stability of nanoparticles upon exposure to PBS, as demonstrated by the smaller changes in $D_z$ values observed before and after PBS addition. Although, the sample with 30 wt.% AB block copolymer did increase in size from 70 to 90 nm upon dilution to 0.5 mg $mL^{-1}$. The size and PDI values of samples with 60:40 and 50:50 wt.% branched copolymer:AB block copolymer were the least affected by addition of PBS. This study has indicated that ≥ 40 wt.% of AB block copolymer is required to provide sufficient steric stabilisation upon dilution and exposure to salt.

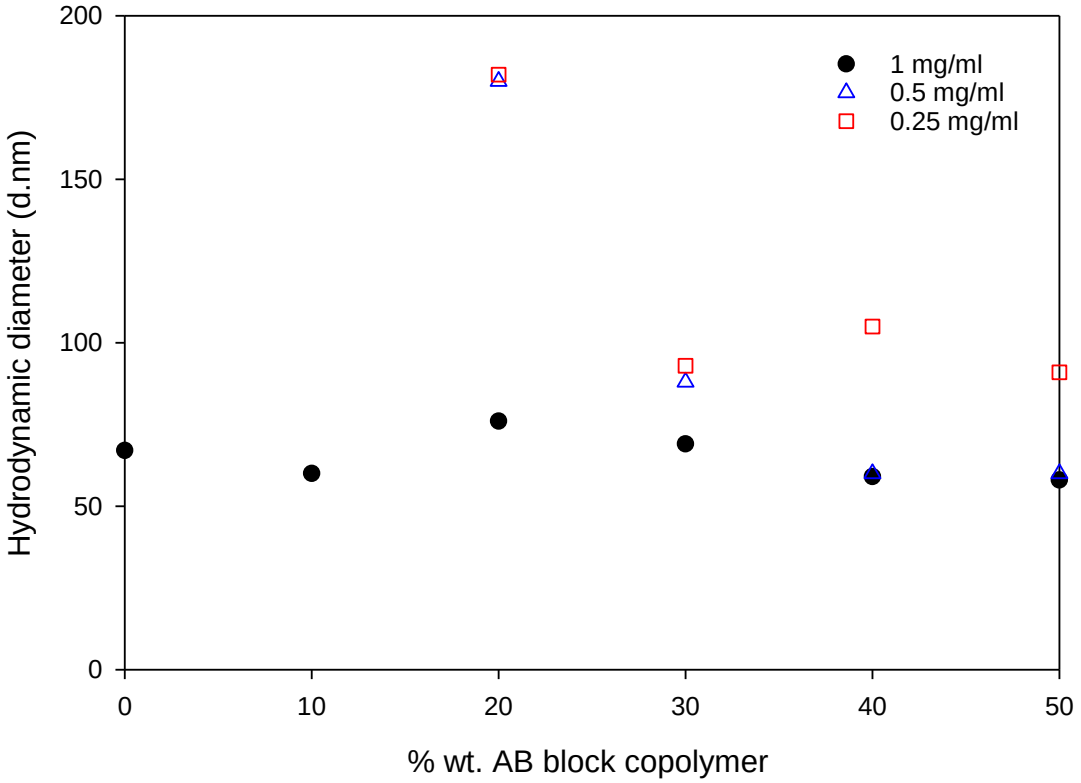


**Figure 3.10** Graphical representation of changes to the hydrodynamic diameter (nm) following the dilution of p(HPMA-co-EGDMA) nanoparticles with varying % wt. of p($PEG_{114}$-*b*-$HPMA_{100}$) with PBS from 1 mg $mL^{-1}$ to 0.25 mg $mL^{-1}$.

### 3.5 Co-nanoprecipitation of Varying Polymer Architectures with Varying Amphiphilic AB Block Copolymers.

The co-nanoprecipitations were attempted using combinations of the (co)polymers and varying AB block copolymers that had been previously described in Chapter 2. In total, there were 48 different co-nanoprecipitation combinations.

Co-nanoprecipitations were attempted using: 1) linear homopolymers, 2) linear statistical copolymers, 3) branched copolymers and 4) branched statistical copolymers (Figure 3.11). Each of which were co-nanoprecipitated with an AB block copolymer. Previous reports of co-nanoprecipitation saw the use of compatible AB block copolymers, where the hydrophobic domain of the AB block copolymer matched the hydrophobic domain of the branched vinyl copolymer. This study incorporated AB block copolymers with varying hydrophobic domains that sometimes differed from that of the hydrophobic vinyl copolymer. This approach was taken to determine if this would have any effect on the formation of colloidally stable co-nanoprecipitates.

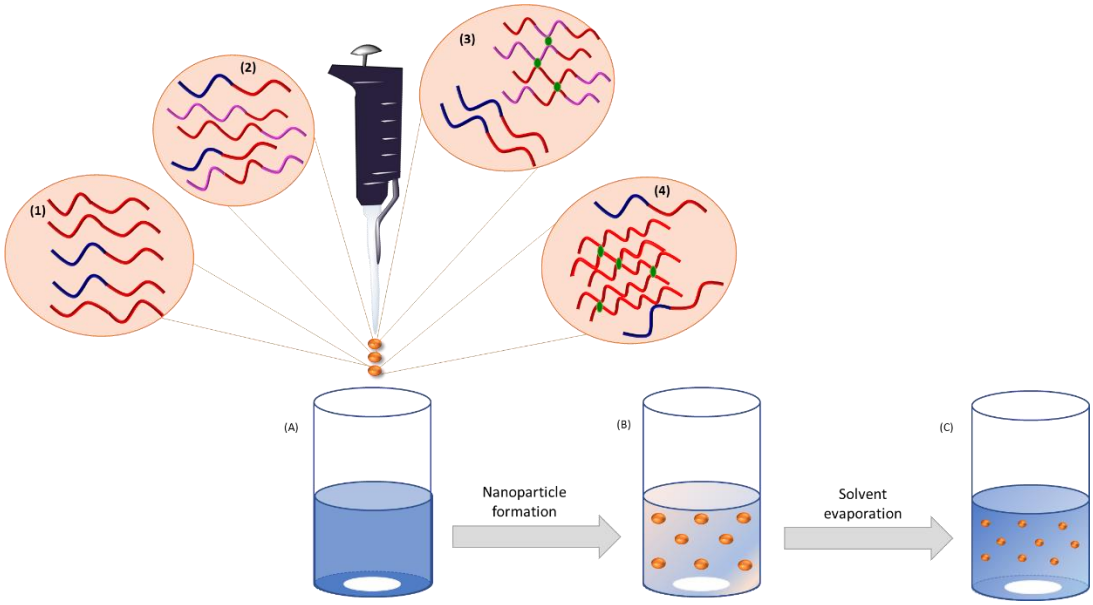


**Figure 3.11** Schematic representation of the co-nanoprecipitation process. Combinations of polymers include 1) linear homopolymer and AB block copolymer, 2) Linear statistical copolymer and AB block copolymer, 3) branched statistical copolymer and AB block copolymer and 4) branched polymer and AB block copolymer. Co-nanoprecipitation proceeded as A) addition of 1 mL of polymer-THF solution into 5 mL DI water, B) rapid nanoparticle formation, followed by C) solvent evaporation after 24 hours, yielding aqueous polymer nanoparticles.

### 3.5.1 Co-nanoprecipitation of Linear Homopolymers with Varying Amphiphilic AB Block Copolymers.

Co-nanoprecipitations were conducted in an identical manner to those reported in Section 3.4. Linear homopolymers were combined with AB block copolymers in THF to form a solution with polymer concentration of 1 mg $mL^{-1}$, and the THF solution (1 mL) was added into stirred DI water (5 mL) (Figure 3.12). Solutions were left for 24 hours for THF removal *via* evaporation. In all cases, the combination of hydrophobic linear homopolymer:AB block copolymer consisted of a 60:40 wt.% ratio, respectively. This ratio was chosen as it had been previously suggested by Ford et al that incorporation of AB block copolymer above 60 wt.% may lead to a loss of control within the nanoprecipitation process and potentially form a secondary population of smaller nanoscale objects from the self-assembly of the AB block copolymer.[10]

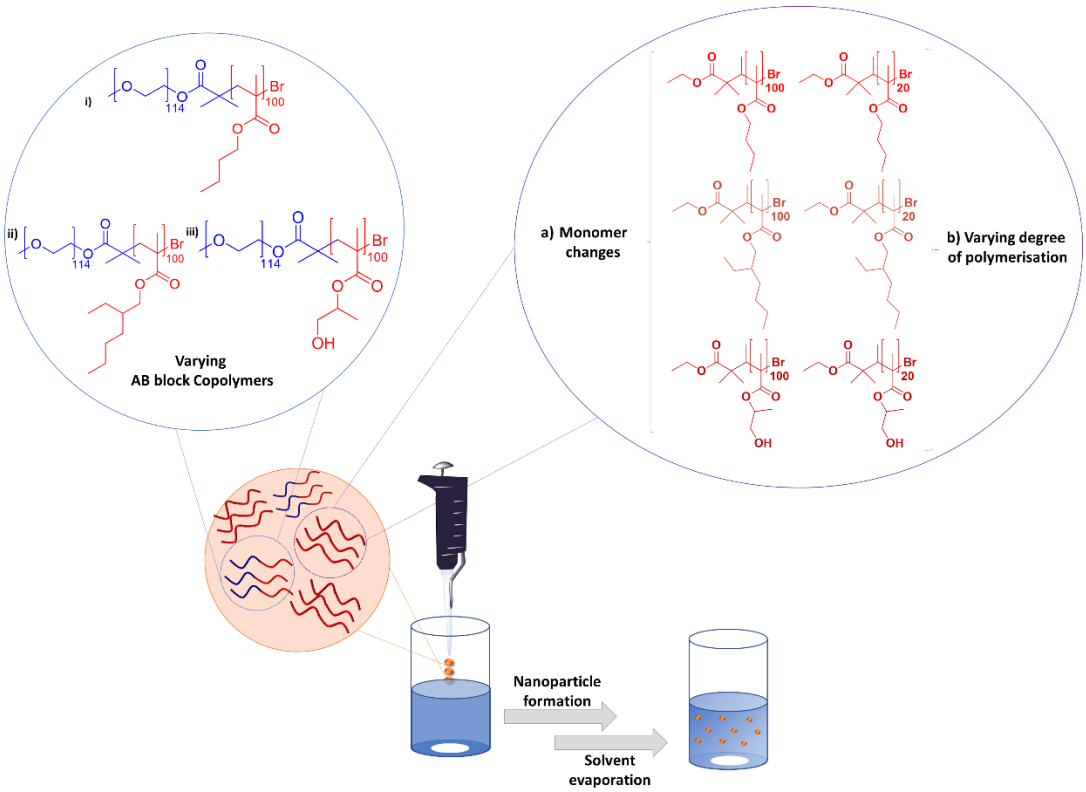


**Figure 3.12** Schematic representation of the co-nanoprecipitation of varying linear homopolymers with a) different monomer chemistry and b) different degrees of polymerisation, and with differing AB block copolymers: i) p($PEG_{114}$-*b*-$BuMA_{100}$), ii) p($PEG_{114}$-*b*-$EHMA_{100}$) and iii) p($PEG_{114}$-*b*-$HPMA_{100}$).

Aqueous nanoparticle dispersions were assessed *via* DLS and zeta potential analysis (Table 3.4). With the exception of the linear p(HPMA) homopolymers, all co-nanoprecipitations of p(BuMA) and p(EHMA) linear homopolymers with the three varying AB block copolymers were unsuccessful and resulted in macroscopic aggregation. Unsurprisingly, the co-nanoprecipitation of $p(HPMA)_{20}$ and $p(HPMA)_{100}$ with p($PEG_{114}$-*b*-$HPMA_{100}$) yielded sterically stabilised nanoparticles with hydrodynamic diameters of 90 and 120 nm, and PDI values of 0.310 and 0.093, respectively. These hydrodynamic diameters were lower than those from sole nanoprecipitations of $p(HPMA)_{20}$ and $p(HPMA)_{100}$ (= 570 and 190 nm, respectively), suggesting that the AB block copolymer has capped the growth of the nanoparticles during the co-nanoprecipitation process and provided steric stabilisation. Negative zeta potential values (= -33 and -17 mV) were obtained.

**Table 3.4** DLS characterisation of linear homopolymers with varying AB block copolymers.

| | AB Block Copolymer (40 wt.%) | | | | | | | | | | | |
|---|---|---|---|---|---|---|---|---|---|---|---|---|
| | p(PEG$_{114}$-*b*-BuMA$_{100}$) | | | | p(PEG$_{114}$-*b*-EHMA$_{100}$) | | | | p(PEG$_{114}$-*b*-HPMA$_{100}$) | | | |
| **Polymer** | **$D_z$ (nm)[a]** | **PDI[a]** | **Derived count rate (kcps)[a]** | **ζ (mV)[b]** | **$D_z$ (nm)[a]** | **PDI[a]** | **Derived count rate (kcps)[a]** | **ζ (mV)[b]** | **$D_z$ (nm)[a]** | **PDI[a]** | **Derived count rate (kcps)[a]** | **ζ (mV)[b]** |
| p(BuMA)$_{20}$ | *Polymer Aggregation* | | | | *Polymer Aggregation* | | | | *Polymer Aggregation* | | | |
| p(EHMA)$_{20}$ | *Polymer Aggregation* | | | | *Polymer Aggregation* | | | | *Polymer Aggregation* | | | |
| p(HPMA)$_{20}$ | *Polymer Aggregation* | | | | *Polymer Aggregation* | | | | 90 | 0.310 | 79 200 | -33 |
| p(BuMA)$_{100}$ | *Polymer Aggregation* | | | | *Polymer Aggregation* | | | | *Polymer Aggregation* | | | |
| p(EHMA)$_{100}$ | *Polymer Aggregation* | | | | *Polymer Aggregation* | | | | *Polymer Aggregation* | | | |
| p(HPMA)$_{100}$ | 215 | 0.294 | 329 350 | -27 | 175 | 0.235 | 351 200 | -24 | 120 | 0.093 | 358 100 | -17 |

[a]Measured using DLS analysis at a concentration of 1 mg mL$^{-1}$, $D_z$ values have been rounded to the nearest 5 nm. [b] Obtained *via* measurement of the electrophoretic mobility of aqueous nanoparticle dispersions within zeta cell.

Interestingly, p(HPMA)$_{100}$ successfully co-nanoprecipitated with the contrasting AB block copolymers p(PEG$_{114}$-*b*-BuMA$_{100}$) and p(PEG$_{114}$-*b*-EHMA$_{100}$) to form turbid and translucent aqueous nanoparticle dispersions with hydrodynamic size diameters of 215 and 175 nm and PDI values of 0.294 and 0.235, respectively. The sole nanoprecipitations of these two AB block copolymers were unsuccessful, so this observation once again highlights the importance of the hydrophobic polymers within the co-nanoprecipitation process. However, p(HPMA)$_{20}$ did not co-nanoprecipitate successfully with p(PEG$_{114}$-*b*-BuMA$_{100}$) or p(PEG$_{114}$-*b*-EHMA$_{100}$), but instead yielded polymer aggregates.

The failure of the co-nanoprecipitations involving the linear p(BuMA) and p(EHMA) homopolymers, both $DP_n$ 100 and 20 monomer units, is not that surprising. The role of high molecular weight copolymers in promoting rapid homogeneous nucleation in co-nanoprecipitation has been reported previously.

### 3.5.2 Co-nanoprecipitation of Linear Statistical Copolymers with Varying Amphiphilic AB Block Copolymers.

Co-nanoprecipitations were conducted with statistical linear copolymers and varying AB block copolymers as before. Both were solvated in THF and added to stirred water with $[P]_f$ = 1 mg mL$^{-1}$. Following the evaporation of THF overnight, aqueous polymer nanoparticle dispersions were obtained and $D_z$, PDI and ζ were determined using DLS

and zeta potential analysis (Table 3.5). These co-nanoprecipitations proved more successful than the co-nanoprecipitations of the linear homopolymers (Section 3.5.1). Interestingly, the presence of HPMA monomer residues within the statistical linear copolymers appeared to provide additional stabilisation and enabled the formation of colloidally stable nanoparticles.

**Table 3.5** DLS and zeta potential analyses following the co-nanoprecipitations of linear statistical copolymers with varying AB block copolymers.

| | **AB Block Copolymer (40 wt.%)** | | | | | | | | | | | |
|---|---|---|---|---|---|---|---|---|---|---|---|---|
| | **p(PEG$_{114}$-*b*-BuMA$_{100}$)** | | | | **p(PEG$_{114}$-*b*-EHMA$_{100}$)** | | | | **p(PEG$_{114}$-*b*-HPMA$_{100}$)** | | | |
| **Polymer** | **$D_z$ (nm)[a]** | **PDI[a]** | **Derived count rate (kcps)[a]** | **ζ (mV)[b]** | **$D_z$ (nm)[a]** | **PDI[a]** | **Derived count rate (kcps)[a]** | **ζ (mV)[b]** | **$D_z$ (nm)[a]** | **PDI[a]** | **Derived count rate (kcps)[a]** | **ζ (mV)[b]** |
| p(BuMA$_{50}$-*s*-EHMA$_{50}$) | *Polymer Aggregation* | | | | *Polymer Aggregation* | | | | 165 | 0.102 | 773 250 | -13.3 |
| p(BuMA$_{50}$-*s*-HPMA$_{50}$) | 100 | 0.056 | 359 300 | -7.95 | 125 | 0.015 | 804 550 | -8.04 | 105 | 0.082 | 329 300 | -11.7 |
| p(HPMA$_{50}$-*s*-EHMA$_{50}$) | *Polymer Aggregation* | | | | 140 | 0.033 | 523 000 | -10.6 | 90 | 0.310 | 79 200 | -33 |

[a]Measured using DLS analysis at a concentration of 1 mg mL$^{-1}$, $D_z$ values have been rounded to the nearest 5 nm. [b] Obtained *via* measurement of the electrophoretic mobility of aqueous nanoparticle dispersions within zeta cell.

The resulting $D_z$ values were in the range of 100 – 165 nm, where p(BuMA$_{50}$-*s*-HPMA$_{50}$) and p(HPMA$_{50}$-*s*-EHMA$_{50}$) produced smaller particles than p(BuMA$_{50}$-*s*-EHMA$_{50}$), likely due to the stabilisation from HPMA monomer residues providing some charge stabilisation through the adsorption of hydroxide ions and therefore preventing further growth of the particle. Uniform and narrow particle size distributions were obtained (< 0.102), which is indicative of a homogenous nucleation and rapid growth period. In all cases, ζ values were low (-7.95 to -13.3 mV), which suggests that the stabilisation of the nanoparticles is not entirely maintained by electrostatic forces, as previously observed, but is instead likely provided by steric stabilisation from the hydrated PEG coronas.

Interestingly, it was observed that the co-nanoprecipitation of p(BuMA)$_n$ with p(PEG$_{114}$-*b*-HPMA$_{100}$), and the co-nanoprecipitation of p(EHMA)$_n$ with p(PEG$_{114}$-*b*-HPMA$_{100}$) both failed, but the co-nanoprecipitation of p(BuMA$_{50}$-*s*-EHMA$_{50}$) with p(PEG$_{114}$-*b*-HPMA$_{100}$) was a success. This may be as a result of the compatibility being

improved between the statistical copolymer and the AB block copolymer compared to the homopolymers.

### 3.5.3 Co-nanoprecipitation of EGDMA-Based Branched Copolymers with Varying Amphiphilic AB Block Copolymers.

Co-nanoprecipitations were conducted with EGDMA-based branched copolymers that were described in Chapter 2. Branched vinyl copolymers were each combined with an AB block copolymer in THF. Co-nanoprecipitations were completed following the same protocol as previously used, whereby polymer-THF solution (1 mL) at $[P]_0$ = 5 mg $mL^{-1}$ was added to stirred DI water (5 mL). Again, the solutions consisted of 60:40 wt.% ratio of branched copolymer: AB block copolymer. Co-nanoprecipitations were left to stir for 24 hours to allow for THF removal (Figure 3.13).

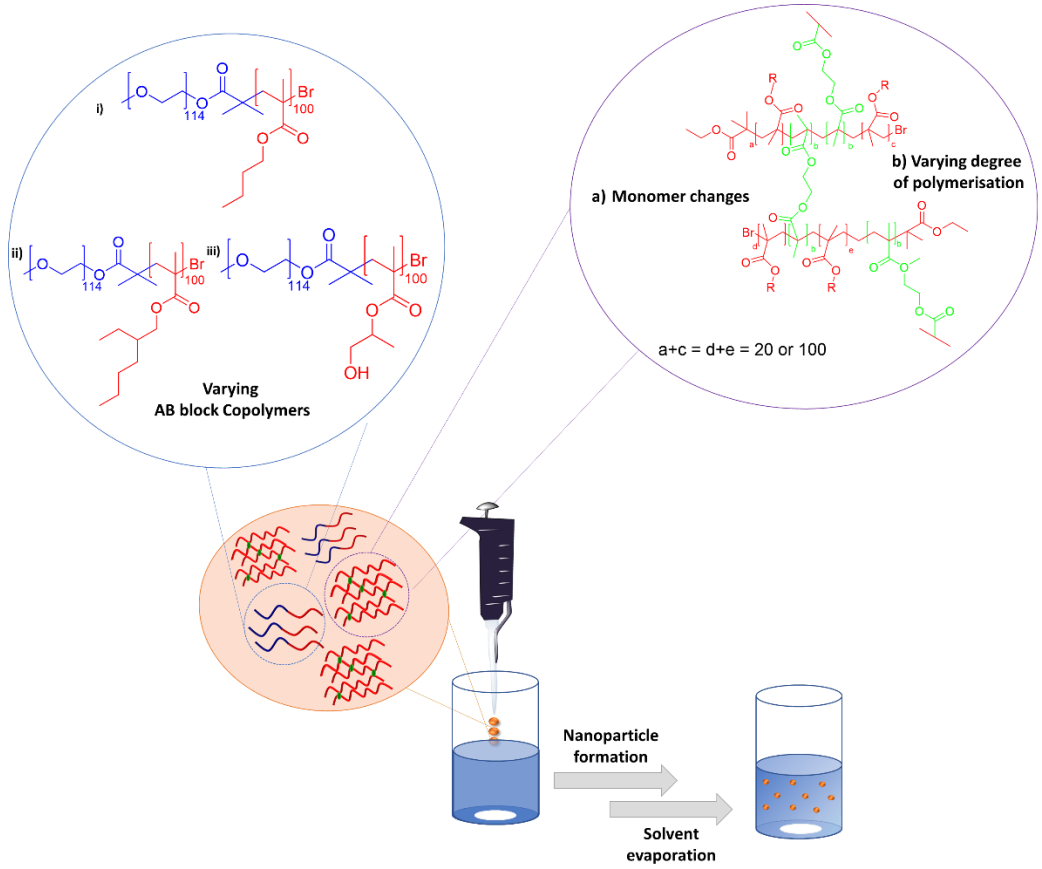


**Figure 3.13** Schematic representation of the co-nanoprecipitations of varying branched copolymers with a) different monomer chemistry and b) different degrees of polymerisation, with differing AB block copolymers: i) p($PEG_{114}$-*b*-$BuMA_{100}$), ii) p($PEG_{114}$-*b*-$EHMA_{100}$) and iii) p($PEG_{114}$-*b*-$HPMA_{100}$).

Co-nanoprecipitations of branched copolymers and AB block copolymers were generally successful. In the majority of cases, the nanoprecipitations remained stable

following THF evaporation, with the exception of: p($BuMA_{20}$-co-$EGDMA_{0.85}$) and p($EHMA_{20}$-co-$EGDMA_{0.80}$) when co-nanoprecipitated with p($PEG_{114}$-*b*-$BuMA_{100}$), and p($EHMA_{100}$-co-$EGDMA_{0.80}$) when co-nanoprecipitated with p($PEG_{114}$-*b*-$EHMA_{100}$) and p($PEG_{114}$-*b*-$HPMA_{100}$), which did not remain stable following THF evaporation; macroscopic polymer aggregation was observed with subsequent sedimentation. The other combinations formed turbid aqueous nanoparticle dispersions, which were assessed *via* DLS and zeta potential analysis (Table 3.6).

**Table 3.6** DLS and zeta potential analyses of aqueous branched copolymer nanoparticle dispersions produced *via* co-nanoprecipitation with varying AB block copolymers.

| | AB Block Copolymer (40 wt.%) | | | | | | | | | | | |
|---|---|---|---|---|---|---|---|---|---|---|---|---|
| | p($PEG_{114}$-*b*-$BuMA_{100}$) | | | | p($PEG_{114}$-*b*-$EHMA_{100}$) | | | | p($PEG_{114}$-*b*-$HPMA_{100}$) | | | |
| **Polymer** | **$D_z$ (nm)[a]** | **PDI[a]** | **Derived count rate (kcps)[a]** | **ζ (mV)[b]** | **$D_z$ (nm)[a]** | **PDI[a]** | **Derived count rate (kcps)[a]** | **ζ (mV)[b]** | **$D_z$ (nm)[a]** | **PDI[a]** | **Derived count rate (kcps)[a]** | **ζ (mV)[b]** |
| p($BuMA_{20}$-co-$EGDMA_{0.85}$) | *Polymer Aggregation* | | | | *95* | *0.024* | *387 500* | *-14.7* | 155 | 0.098 | 788 000 | -10.8 |
| p($EHMA_{20}$-co-$EGDMA_{0.80}$) | *Polymer Aggregation* | | | | 95 | 0.065 | 341 000 | -17.7 | 150 | 0.133 | 592 300 | -12.2 |
| p($HPMA_{20}$-co-$EGDMA_{0.85}$) | 100 | 0.088 | 325 600 | -10.1 | 115 | 0.067 | 400 000 | -4.34 | 110 | 0.111 | 397 500 | -8.0 |
| p($BuMA_{100}$-co-$EGDMA_{0.95}$) | 80 | 0.135 | 116 100 | -14.1 | 95 | 0.039 | 346 100 | -12.7 | 145 | 0.088 | 481 250 | -10.8 |
| p($EHMA_{100}$-co-$EGDMA_{0.80}$) | 85 | 0.120 | 239 150 | -11.6 | *Polymer Aggregation* | | | | *Polymer Aggregation* | | | |
| p($HPMA_{100}$-co-$EGDMA_{0.90}$) | 70 | 0.088 | 75 050 | -16.5 | 75 | 0.056 | 102 200 | -17.9 | 60 | 0.112 | 89 700 | -11.9 |

[a]Measured using DLS analysis at a concentration of 1 mg $mL^{-1}$, $D_z$ values have been rounded to the nearest 5 nm.
[b]Obtained *via* measurement of the electrophoretic mobility of aqueous nanoparticle dispersions within zeta cell.

The polymer nanoparticles that were generated were uniform and had monomodal particle size distributions without the need for sample filtration. The nanoparticles that were obtained had varying hydrodynamic diameters ($70 < D_z < 155$ nm) and polydispersity values ($0.024 < PDI < 0.135$). Compared to the sole nanoprecipitation of these branched materials, whereby all but HPMA-based polymers failed, incorporation of an AB block copolymer within the polymer-THF solution yielded much more successful results. Only four out of the eighteen co-nanoprecipitations failed. This observation highlights how important the AB block copolymer is and how it can provide sufficient levels of steric stabilisation to prevent nanoparticle-nanoparticle aggregation. This steric stabilisation was once again confirmed by the

moderately negative ζ values obtained for the aqueous polymer nanoparticle dispersions (-8.0 to -17.9 mV). SEM analyses of the nanoparticles produced *via co*-nanoprecipitation of p(BuMA$_{100}$-*co*-EGDMA$_{0.95}$):p(PEG$_{114}$-*b*-HPMA$_{100}$) and p(EHMA$_{20}$-*co*-EGDMA$_{0.80}$):*p*(PEG$_{114}$-*b*-HPMA$_{100}$) at 60:40 wt.% ratio respectively, indicated spherical particle morphology (Figure 3.14).

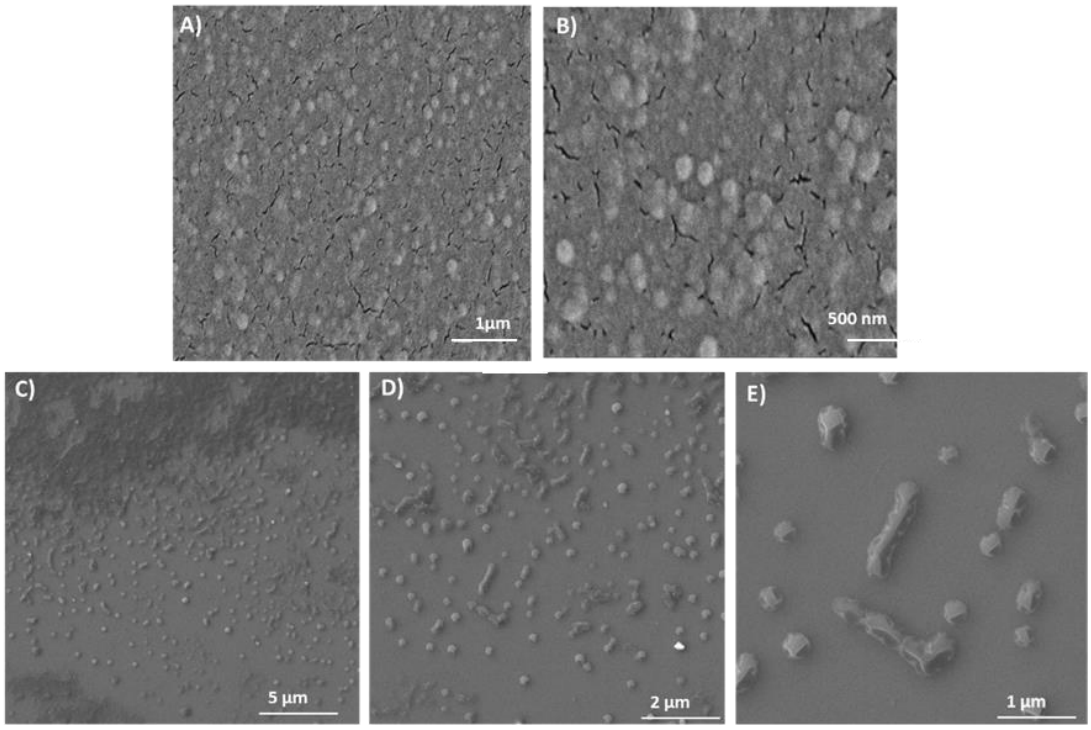


**Figure 3.114** SEM images of co-nanoprecipitates produced using (A and B) p(BuMA$_{100}$-*co*-EGDMA$_{0.95}$):p(PEG$_{114}$-*b*-HPMA$_{100}$) and (C-E) p(EHMA$_{20}$-*co*-EGDMA$_{0.80}$):*p*(PEG$_{114}$-*b*-HPMA$_{100}$) at 60:40 wt.% ratio, respectively.

Co-nanoprecipitations of branched statistical copolymers with varying AB block copolymers were also conducted following the same standard protocol. Stable aqueous nanoparticle dispersions were analysed *via* DLS (Table 3.7). With the exception of p(BuMA$_{50}$-s-EHMA$_{50}$-co-EGDMA$_{0.95}$):p(PEG$_{114}$-*b*-BuMA$_{100}$), all cases gave monomodal particle size distributions with intensity-averaged hydrodynamic diameters ranging from 90-175 nm. In the case of p(BuMA$_{50}$-s-EHMA$_{50}$-co-EGDMA$_{0.95}$):p(PEG$_{114}$-*b*-BuMA$_{100}$), visible aggregation occurred. In the majority of cases, narrow PDI values were obtained (< 0.1), indicating that the nanoparticles are monodisperse. Nanoparticle stability obtained through steric stabilisation conferred by the AB block copolymer was indicated by the low negative ζ values (-8.6 to -16.9 mV).

**Table 3.7** DLS and zeta potential analyses of aqueous branched statistical copolymer nanoparticle dispersions produced *via* co-nanoprecipitation with varying AB block copolymers.

| | AB Block Copolymer (40 wt.%) | | | | | | | | | | | |
|---|---|---|---|---|---|---|---|---|---|---|---|---|
| | p(PEG$_{114}$-*b*-BuMA$_{100}$) | | | | p(PEG$_{114}$-*b*-EHMA$_{100}$) | | | | p(PEG$_{114}$-*b*-HPMA$_{100}$) | | | |
| Polymer | $D_z$ (nm)[a] | PDI[a] | Derived count rate (kcps)[a] | ζ (mV)[b] | $D_z$ (nm)[a] | PDI[a] | Derived count rate (kcps)[a] | ζ (mV)[b] | $D_z$ (nm)[a] | PDI[a] | Derived count rate (kcps)[a] | ζ (mV)[b] |
| p(BuMA$_{50}$-*s*-EHMA$_{50}$-*co*-EGDMA$_{0.95}$) | *Polymer Aggregation* | | | | 90 | 0.047 | 379 600 | -16.9 | 175 | 0.094 | 470 050 | -12.0 |
| p(HPMA$_{50}$-*s*-EHMA$_{50}$-*co*-EGDMA$_{0.95}$) | *100* | *0.162* | *130 160* | *-10.5* | 140 | 0.051 | 562 700 | -12.8 | 140 | 0.091 | 489 650 | -11.6 |
| p(HPMA$_{50}$-*s*-BuMA$_{50}$-*co*-EGDMA$_{0.90}$) | 115 | 0.071 | 320 250 | -8.6 | 135 | 0.037 | 690 000 | -9.8 | 125 | 0.099 | 444 900 | -10.1 |

[a]Measured using DLS analysis at a concentration of 1 mg mL$^{-1}$, $D_z$ values have been rounded to the nearest 5 nm.
[b]Obtained *via* measurement of the electrophoretic mobility of aqueous nanoparticle dispersions within zeta cell.

Clearly, when developing polymer nanoparticles for DDS, the ability to generate stable aqueous dispersions is essential. As shown throughout all of the studies, co-nanoprecipitation offers the opportunity to generate sterically stabilised aqueous nanoparticle dispersions. In order to assess the potential of the co-nanoprecipitates as DDS of therapeutic compounds, the next stage of the research and development is to investigate whether the identified co-nanoprecipitation options can be used successfully to encapsulate small hydrophobic guest molecules.

### 3.6 Encapsulating a Hydrophobic Guest Molecule *via* Co-nanoprecipitation

For polymer nanoparticles to be utilised as DDS they must be able to encapsulate hydrophobic drug molecules within their core. The following experiments aimed to investigate whether it was possible to encapsulate a hydrophobic guest molecule within the core of branched vinyl copolymer nanoparticles prepared *via* co-nanoprecipitation before utilising this strategy for encapsulation of hydrophobic drug molecules to generate DDS. Encapsulation of such can be achieved by dissolving the hydrophobic guest molecule within the copolymer-THF solution before addition to water. Pyrene was used as the selected guest molecule in the following studies (Figure 3.15).

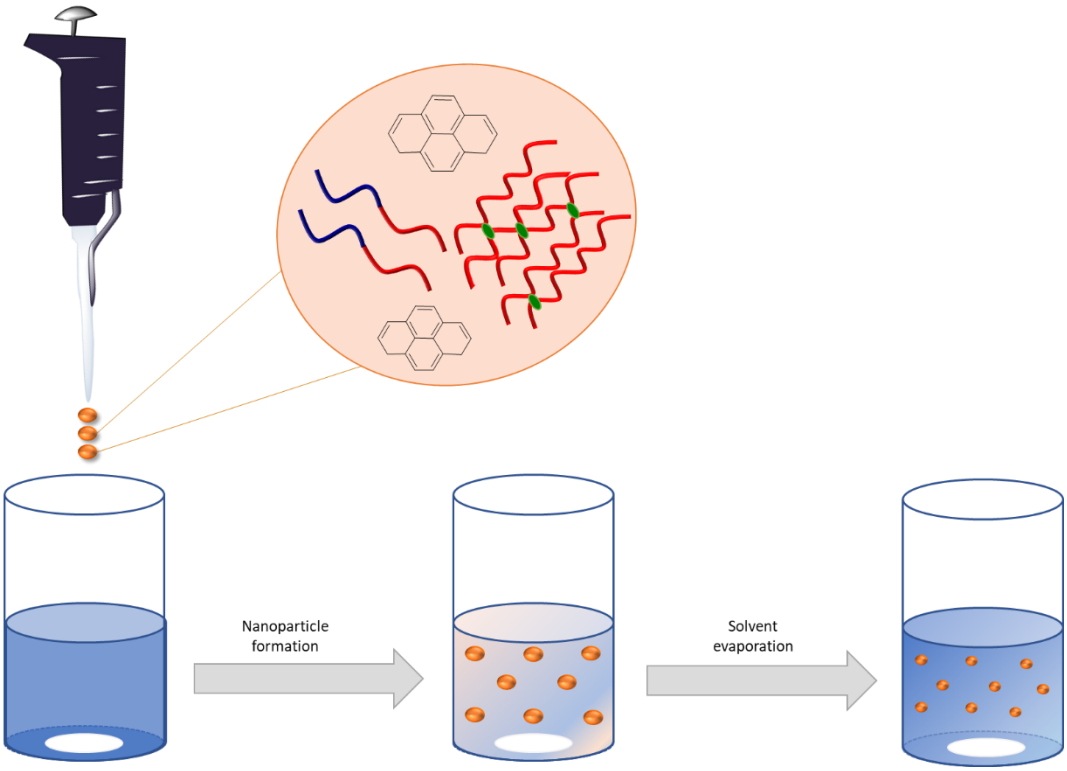


**Figure 3.15** Schematic representation of the encapsulation of the hydrophobic guest molecule, pyrene, *via* co-nanoprecipitation.

Pyrene is a hydrophobic aromatic molecule consisting of four fused benzene rings, and has been used as a fluorescent probe to evaluate solvent polarity (Figure 3.16).[20].

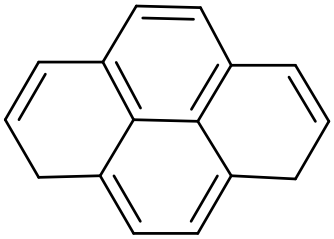

**Figure 3.16** The chemical structure of pyrene.

The fluorescence of pyrene ($\pi \rightarrow \pi^*$) generates an emission spectrum consisting of five vibrational bands that are sensitive to solvent polarity. The first vibrational band (373 nm, $I_1$) of pyrene is enhanced in polar solvents (or environments) relative to the third vibrational band (385 nm, $I_3$). Therefore, the ratio of intensities between these two bands ($I_1/I_3$) can be used to provide information on the local environment of the pyrene molecules (i.e. the internal environment of nanoparticles). $I_1/I_3$ values obtained for pyrene in polar solvents such as water have been reported at 1.87. Which decreases significantly to 0.58 when the solvent is changed to the non-polar solvent, hexane.[21] The impact of nanoparticle composition on the internal core

polarity can also be assessed using fluorescence emission spectroscopy of pyrene. Pyrene can be encapsulated at low loadings (1 wt.% with respect to total polymer mass) during the co-nanoprecipitation process, and its fluorescence emission spectra can help to provide insight into where the hydrophobic guest molecule locates itself (i.e. within the core or on the surface) and subsequent information about the characteristics of that environment.

The co-nanoprecipitation studies that were conducted using pyrene aimed to provide information on the following: 1) did the incorporation of pyrene alter the co-nanoprecipitation process, 2) can a hydrophobic molecule be encapsulated within the core, and 3) how was the polarity of the nanoparticle core altered when varying the monomer residue functionality, the AB block copolymer and the divinyl monomer residue functionality. In addition to this, results obtained from the fluorimetry measurements could also provide indication of how the AB block copolymer is interacting with the nanoparticle during the co-nanoprecipitation process.

### 3.6.1 Evaluation of the Impact of Pyrene Encapsulation During Co-nanoprecipitation

Encapsulation experiments were conducted in an identical manner to those in previous co-nanoprecipitation studies but with the addition of pyrene into copolymer-THF solutions. Given the hydrophobic nature of pyrene, it was anticipated that it would become entrapped and therefore encapsulated within the core of the polymeric nanoparticles during its co-nanoprecipitation with the AB block copolymer and branched vinyl copolymer. Pyrene was incorporated within the copolymer-THF solutions with a 1 wt.% loading with respect to total polymer mass. As before, the copolymer-THF solutions consisted of $[P]_o$ = 5 mg $mL^{-1}$ and contained 60:40 wt.% branched vinyl copolymer:AB block copolymer. Co-nanoprecipitations were conducted by addition of copolymers and pyrene/THF solutions (1 mL) into stirred DI water (5 mL). Samples were left stirring overnight to allow for THF evaporation to yield aqueous nanoparticle dispersions with $[P]_f$ = 1 mg $mL^{-1}$ and a pyrene concentration of 1 µg $mL^{-1}$. Nanoparticle size distributions were obtained *via* DLS analysis (Table 3.8)

**Table 3.8** DLS of aqueous branched copolymer nanoparticle dispersions produced *via* co-nanoprecipitation with varying AB block copolymers and pyrene.

| | AB Block Copolymer (40 wt.%) | | | | | | | | |
|---|---|---|---|---|---|---|---|---|---|
| | p($PEG_{114}$-*b*-$BuMA_{100}$) | | | p($PEG_{114}$-*b*-$EHMA_{100}$) | | | p($PEG_{114}$-*b*-$HPMA_{100}$) | | |
| **Polymer** | **$D_z$ (nm)[a]** | **PDI[a]** | **Derived count rate (kcps)[a]** | **$D_z$ (nm)[a]** | **PDI[a]** | **Derived count rate (kcps)[a]** | **$D_z$ (nm)[a]** | **PDI[a]** | **Derived count rate (kcps)[a]** |
| p($BuMA_{20}$-co-$EGDMA_{0.85}$) | 65 | 0.071 | 77 200 | 80 | 0.032 | 266 300 | 135 | 0.088 | 304 600 |
| p($EHMA_{20}$-co-$EGDMA_{0.80}$) | 75 | 0.071 | 117 350 | 90 | 0.035 | 325 550 | 70 | 0.156 | 59 200 |
| p($HPMA_{20}$-co-$EGDMA_{0.85}$) | 110 | 0.287 | 77 450 | 90 | 0.287 | 80 700 | 165 | 0.087 | 749 250 |
| p($BuMA_{100}$-co-$EGDMA_{0.95}$) | 80 | 0.143 | 230 100 | 90 | 0.094 | 300 250 | 145 | 0.088 | 578 300 |
| p($EHMA_{100}$-co-$EGDMA_{0.80}$) | 75 | 0.090 | 128 400 | 90 | 0.070 | 409 300 | 145 | 0.100 | 542 100 |
| p($HPMA_{100}$-co-$EGDMA_{0.90}$) | 50 | 0.166 | 105 900 | 50 | 0.143 | 118 500 | 60 | 0.101 | 117 500 |

[a]Measured using DLS analysis at a concentration of 1 mg $mL^{-1}$, $D_z$ values have been rounded to the nearest 5 nm.

In all of the cases, turbid aqueous nanoparticle dispersions were obtained which closely resembled those obtained without pyrene present. Monomodal particle size distributions were obtained, and pyrene loaded nanoparticles were produced with hydrodynamic diameters between 50 - 165 nm and PDI values between 0.032 - 0.287. Different observations were made regarding the impact of loading pyrene within the nanoparticles.

Firstly, and most commonly, was that there was no difference in the hydrodynamic diameters of pyrene loaded polymer nanoparticles compared to unloaded versions of the same polymer composition. For example, pyrene loaded p($HPMA_{100}$-co-$EGDMA_{0.90}$):p($PEG_{114}$-*b*-$HPMA_{100}$) nanoparticles had a hydrodynamic diameter of 60 nm and a PDI of 0.101, whereas in the absence of pyrene the polymer nanoparticles had a hydrodynamic diameter of 60 nm and a PDI of 0.112. Another example is pyrene loaded p($BuMA_{100}$-co-$EGDMA_{0.95}$):p($PEG_{114}$-*b*-$HPMA_{100}$) nanoparticles having a hydrodynamic diameter of 145 nm and a PDI of 0.088, whereas in the absence of pyrene the nanoparticles had a hydrodynamic diameter of 145 nm and a PDI of 0.088 (Figure 3.17).

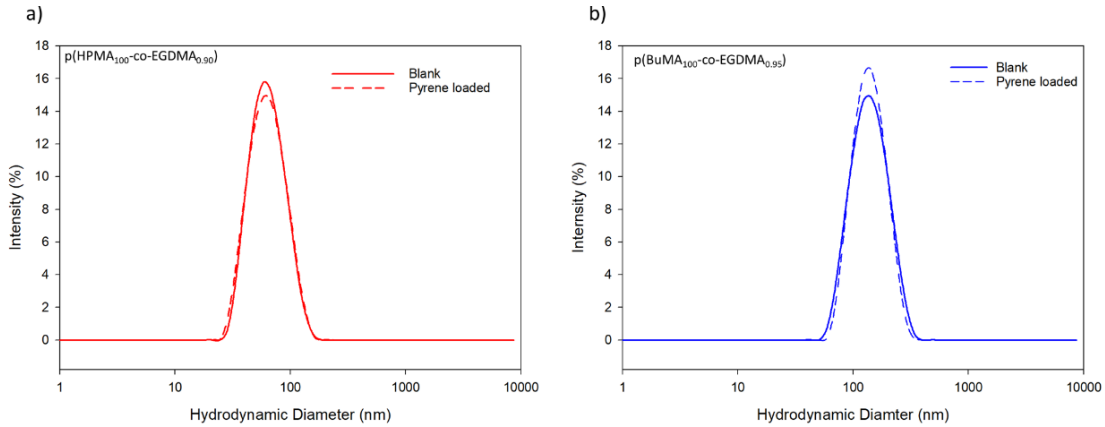


**Figure 3.17** Overlaid nanoparticle size distributions obtained by DLS analysis of unloaded (solid lines) and 0.1 wt.% pyrene loaded (dashed lines) aqueous nanoparticle dispersions prepared by co-nanoprecipitation of a) p(HPMA$_{100}$-co-EGDMA$_{0.95}$), and b) p(BuMA$_{100}$-co-EGDMA$_{0.95}$), with p(PEG$_{114}$-*b*-HPMA$_{100}$) at a composition of 60:40 wt.%, respectively.

There were four cases where the incorporation of pyrene within the co-nanoprecipitation caused a significant decrease in the hydrodynamic diameters observed. Pyrene loaded p(HPMA$_{100}$-co-EGDMA$_{0.90}$):p(PEG$_{114}$-*b*-BuMA$_{100}$) nanoparticles had a hydrodynamic diameter of 50 nm and a PDI of 0.166, but in the absence of pyrene, the polymer nanoparticles had a hydrodynamic diameter of 70 nm and a PDI of 0.088. A decrease in hydrodynamic diameter of approximately 20 nm. Another example of this is pyrene loaded p(HPMA$_{100}$-co-EGDMA$_{0.95}$):p(PEG$_{114}$-*b*-EHMA$_{100}$) nanoparticles having a hydrodynamic diameter of 50 nm and a PDI of 0.143, but in the absence of pyrene the nanoparticles had a hydrodynamic diameter of 75 nm and a PDI of 0.056. This was also observed for nanoparticles comprising of p(BuMA$_{20}$-co-EGDMA$_{0.85}$): p(PEG$_{114}$-*b*-HPMA$_{100}$), which also saw a decrease in hydrodynamic diameter from 155 nm to 135 nm when pyrene was loaded. Finally, this was also observed for p(EHMA$_{20}$-co-EGDMA$_{0.80}$): p(PEG$_{114}$-*b*-HPMA$_{100}$), which saw a decrease in hydrodynamic diameter from 150 nm to 70 nm when pyrene was loaded. These observations suggest that pyrene may be playing a positive role in driving the nucleation process. Its incorporation within the co-nanoprecipitation process may lead to an increase in the number of nuclei formed in the initial stages which may lead to a greater nucleation rate and a consequent decrease in nanoparticle size.

Perhaps the most interesting observation was that not only did the incorporation of pyrene reduce particle size, it also led to the success of co-nanoprecipitations that

previously failed in its absence. For example, the co-nanoprecipitation of p($BuMA_{20}$-co-$EGDMA_{0.85}$) with p($PEG_{114}$-*b*-$BuMA_{100}$) in the absence of pyrene resulted in macroscopic aggregation (Section 3.5.3). When pyrene was incorporated, however, a monomodal particle size distribution was obtained consisting of monodisperse nanoparticles with a hydrodynamic diameter of 65 nm and PDI of 0.071. Another example is the co-nanoprecipitation of p($EHMA_{100}$-co-EGDMA) with p($PEG_{114}$-*b*-$HPMA_{100}$) without pyrene, which once again resulted in macroscopic aggregation (Section 3.5.3); however, when pyrene was included, a monomodal particle size distribution was obtained consisting of monodisperse nanoparticles with a hydrodynamic diameter of 145 nm and PDI of 0.100. Since these co-nanoprecipitations were conducted at the standard 60:40 branched copolymer:AB block copolymer wt.% ratio, the full range of ratios from 0-100 wt.% were studied to see if this influence of pyrene was observed throughout the whole series of compositions (Section 3.6.2)

In contrast, there was one example, p($HPMA_{20}$-co-$EGDMA_{0.85}$):p($PEG_{114}$-*b*-$HPMA_{100}$) nanoparticles, where incorporation of pyrene caused an increase in hydrodynamic diameter compared to the blank nanoparticles, from 110 to 165 nm. Both chemistries of the branched copolymer and the AB block copolymer consist of HPMA hydrophobic monomer residues. Hydrophobic interfaces have been shown to promote the adsorption of hydroxide ions and leading to a negative ζ values.[22-24] This adsorption may confer some charge stabilisation to the resulting nanoparticles. Therefore, the increase in particle size could have arisen from some incompatibilities between the pyrene and the charge exhibited from these species.

### 3.6.2 Varying the Composition of the Nanoparticle Core and the Effect on the Encapsulation of Pyrene

In the co-nanoprecipitations described above, the ratio of branched copolymer and AB block copolymer was set at a constant 60:40 wt.%, respectively, unless otherwise stated. It has been shown that each constituent copolymer plays a different role during the co-nanoprecipitation process and that the manipulation of this ratio between the two polymers in the initial THF solution has an effect on particle stability and size (Section 3.4.1). It has also been shown that through the incorporation of a

guest molecule, the outcome of some co-nanoprecipitations differed from that of the respective co-nanoprecipitation without a guest molecule present (Section 3.6.1). It was of interest to see whether this effect was observed at the full range of compositional ratios and whether such compositional manipulation also impacted the nanoparticle internal polarity. Therefore, a range of co-nanoprecipitations were conducted as previously described, with pyrene incorporated within copolymer-THF solution with a loading of 1 wt.% with respect to total polymer mass. As before, copolymer/THF solutions consisted of $[P]_o$ = 5 mg $mL^{-1}$ and branched vinyl copolymer: AB block copolymer was systematically varied from 0-100 wt.%, respectively. The AB block copolymer utilised in this study was p($PEG_{114}$-*b*-$HPMA_{100}$), given its stability when solely nanoprecipitated. Co-nanoprecipitations were conducted by addition of copolymers and pyrene/THF solution (1 mL) into stirred DI water (5 mL). Samples were left stirring overnight to allow for THF evaporation to yield aqueous nanoparticle dispersions with $[P]_f$ = 1 mg $mL^{-1}$ and a pyrene concentration of 1 µg $mL^{-1}$. The effects of the encapsulation of pyrene within branched vinyl copolymer nanoparticles during co-nanoprecipitation was confirmed using DLS (Figure 3.18) and fluorescence emission spectroscopy (Figure 3.19). Analysis *via* DLS for all the stable pyrene loaded polymer nanoparticles showed that the co-nanoprecipitations produced monodisperse nanoparticles with monomodal particle size distributions, and that the particle sizes did not vary with any significance compared to their unloaded counterpart.

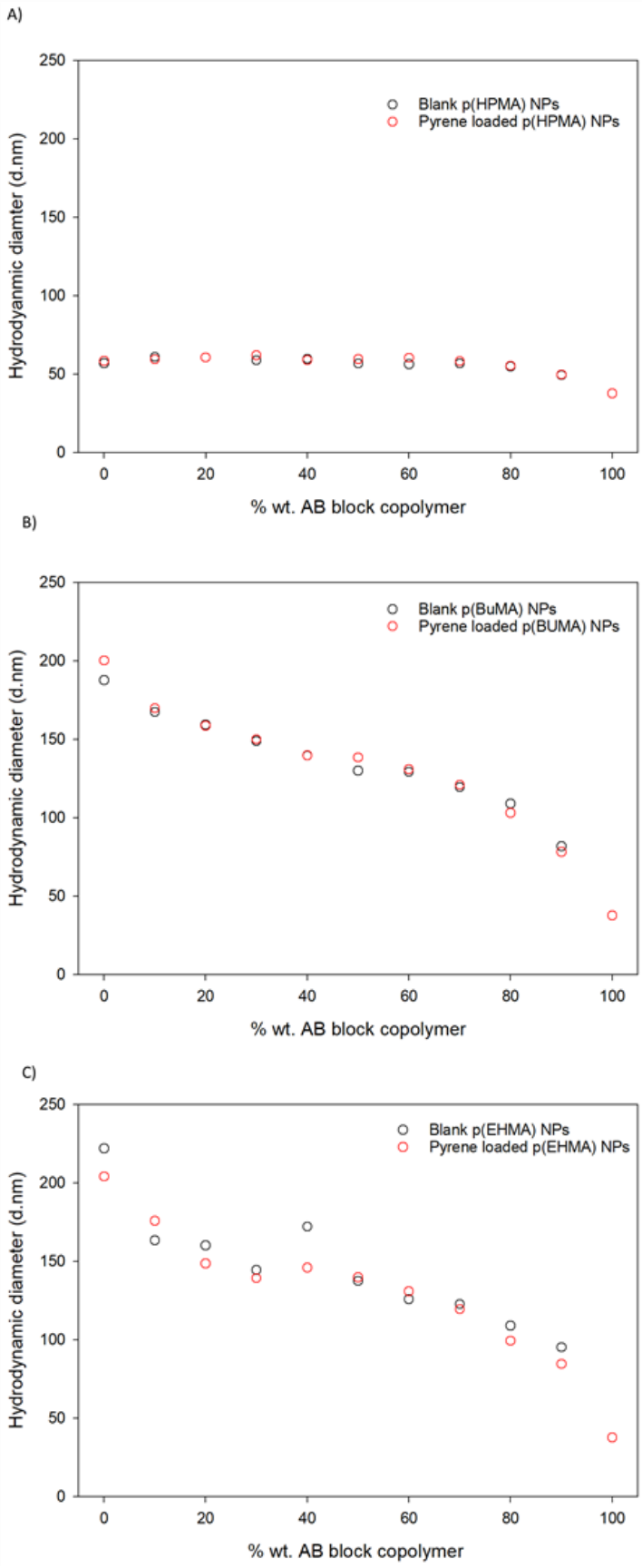


**Figure 3.18** Nanoparticle sizes from DLS analysis of blank nanoparticles (black circles) and with 1 wt.% pyrene encapsulated (red circles) for A) p($HPMA_{100}$-co-$EGDMA_{0.90}$), B) p($BuMA_{100}$-co-$EGDMA_{0.95}$) and C) p($EHMA_{100}$-co-$EGDMA_{0.80}$), with varying wt.% p($PEG_{114}$-*b*-$HPMA_{100}$) from 0-100 wt.%.

Encapsulation of pyrene within all p(HPMA$_{100}$-co-EGDMA$_{0.90}$) nanoparticles was successful and had little, if any, effect to the nanoprecipitation regime regardless of the wt.% of AB block copolymer present. Interestingly, when the polymer was changed to p(EHMA$_{100}$-co-EGDMA$_{0.80}$), the wt.% of AB block copolymer required to produce sterically stabilised nanoparticles changed when comparing the co-nanoprecipitations with and without pyrene. When pyrene was incorporated, all wt.% of AB block copolymer produced stable co-nanoprecipitates of p(EHMA-co-EGDMA). This is a stark contrast to what was observed when no pyrene was included, which required at least 70 wt.% AB block copolymers to yield sterically stabilised nanoparticles. This observation suggests that the incorporation of a guest molecule such as pyrene has had an influence on the co-nanoprecipitation process to produce stabilised nanoparticles. The guest molecules may be coming together to form zoned areas which may be presented on the surface (or partially presented) which could be providing additional stabilisation through charge.

Analysis of the pyrene fluorescence spectra showed two different trends between nanoparticle internal polarity and the wt.% ratio of AB block copolymer present within the co-nanoprecipitation (Figure 3.19). In the case of p(HPMA$_{100}$-co-EGDMA$_{0.90}$), increasing the weight composition of the AB block copolymer had little impact on the internal polarity of the nanoparticle core. The $I_1/I_3$ ratio increased slightly from 1.69 when the polymer nanoparticle consisted entirely of p(HPMA$_{100}$-co-EGDMA$_{0.90}$), to 1.71 as the environment was changed to consist solely of p(PEG$_{114}$-*b*-HPMA$_{100}$). This result is consistent with what would be expected since there is little change to the chemical composition of the nanoparticle core; both of the hydrophobic domains within each polymer component contain hydroxyl functional groups and therefore bring an associated level of polarity to the nanoparticle core.

Changing the polymer to those with more hydrophobic monomer residues, BuMA and EHMA, presented a different trend. Increasing the content of AB block copolymer from 0 to 100 wt.% caused a general increase to the $I_1/I_3$ value, suggesting that the core of polymeric nanoparticle was increasing in polarity with the increasing AB block copolymer. Specifically, p(BuMA$_{100}$-co-EGDMA$_{0.95}$) showed an increase in $I_1/I_3$ value

from 1.22 to 1.71 and p(EHMA$_{100}$-co-EGDMA$_{0.80}$) increased from 1.07 to 1.71. Interestingly, this influence on the internal core polarity seemed to begin when the AB block composition was > 50 wt.%. This observation suggests that when the AB diblock copolymer composition is < 50 wt.%, the chemical composition of the nanoparticle core is dominated by the branched copolymer and not the AB block copolymer.

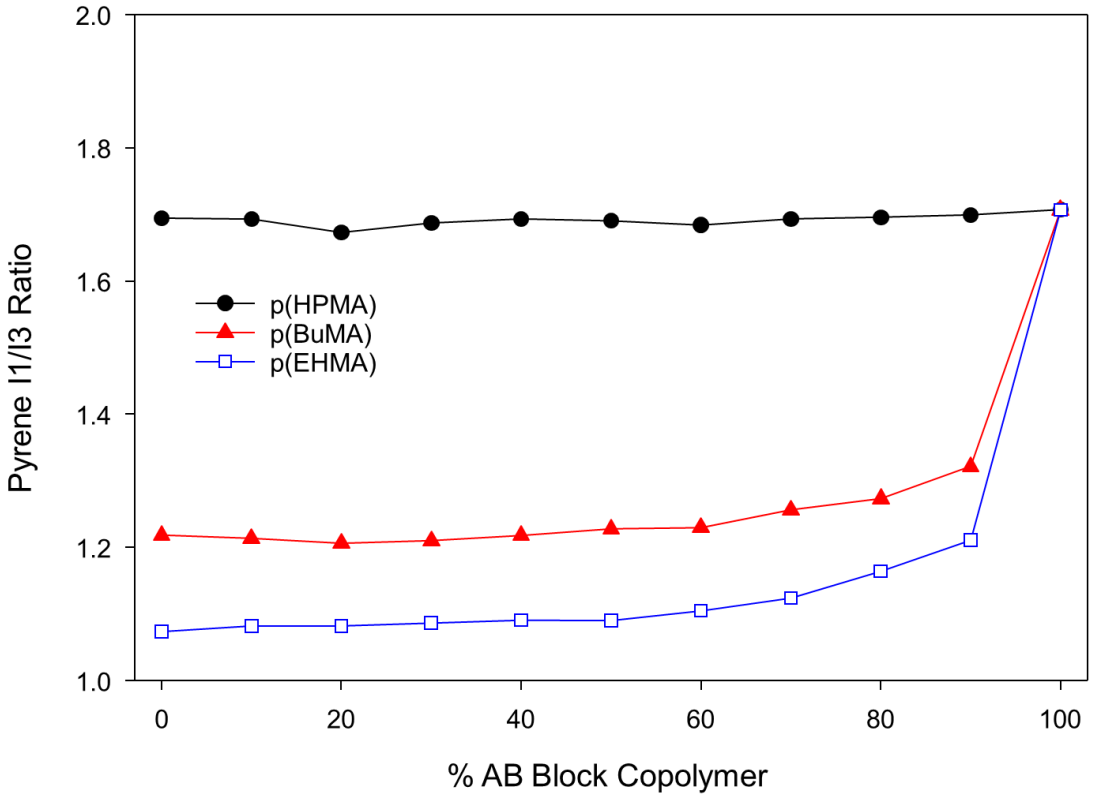


**Figure 3.19** Graphical representation of how the $I_1/I_3$ ratio changed as the wt.% of p(PEG$_{114}$-*b*-HPMA$_{100}$) increased within co-nanoprecipitates of p(HPMA$_{100}$-co-EGDMA$_{0.90}$) (black line, circles), p(BuMA$_{100}$-co-EGDMA$_{0.95}$) (red line, triangles) and p(EHMA$_{100}$-co-EGDMA$_{0.80}$) (blue line, open squares).

Clearly, increasing the amount of AB block copolymer altered the nanoparticle core polarity, suggesting that the hydrophobic domain of the AB block copolymer was in fact anchored within the core of the particle in some way and the hydrophilic counterpart was located on the surface. Incorporation of AB block copolymer within co-nanoprecipitation clearly changes the nanoparticle core otherwise it could be expected that the $I_1/I_3$ values would remain the same. Also, it is worth reiterating that since the $I_1/I_3$ values do change, it further confirms that some of the encapsulated pyrene is located within the core of the particle and not present on the particle surface.

### 3.6.3 The Evaluation of Nanoparticle Core Polarity of EGDMA Branched Vinyl Copolymers with Varying Monomer compositions and Varying AB block Copolymers *via* the Encapsulation of Pyrene

The encapsulation of pyrene within branched vinyl co-polymer nanoparticles enabled investigations into the physical properties of the internal environment. This was achieved through analysis of the fine structure of the fluorescence emission of pyrene, specifically the $I_1$ and $I_3$ vibrational bands. It was hypothesised that comparison of the fluorescence spectra of pyrene within co-nanoprecipitates of varying composition, including different branched vinyl copolymers and different AB block copolymers, would potentially provide information of the core environment (specifically polarity) and a more-clear indication on the role of AB block copolymer within the co-nanoprecipitation process.

To compare the $I_1/I_3$ values of the co-nanoprecipitates derived from the three different monomers, pyrene was encapsulated within p(HPMA$_{100}$-co-EGDMA$_{0.90}$), p(BuMA$_{100}$-co-EGDMA$_{0.95}$) and p(EHMA$_{100}$-co-EGDMA$_{0.80}$) co-nanoprecipitated with p(PEG$_{114}$-b-HPMA$_{100}$), p(PEG$_{114}$-b-BuMA$_{100}$) and p(PEG$_{114}$-b-EHMA$_{100}$), (60:40 wt.%). The nanoparticles were prepared as previously described in Section 3.6. A similar study has been previously conducted for hyp-polydendron nanoparticles.[9] In all cases, the fluorescence emissions of the aqueous nanoparticle dispersions, obtained following excitation at λ = 335 nm, showed that the encapsulation of pyrene during co-nanoprecipitation had been successful. This was confirmed by the lower $I_1/I_3$ values obtained for pyrene encapsulated polymer nanoparticles ($I_1/I_3$ = 1.10-1.62) compared to that of pyrene dissolved in water ($I_1/I_3$ = 1.81) (Table 3.9).

**Table 3.9** Polarity data obtained from pyrene emission spectroscopy for aqueous nanoparticle dispersions obtained *via* co-nanoprecipitation of varying branched polymers, AB block copolymers and pyrene.

| | **AB block copolymer** | | |
|---|---|---|---|
| | **p(PEG$_{114}$-*b*-HPMA$_{100}$)** | **p(PEG$_{114}$-*b*-BuMA$_{100}$)** | **p(PEG$_{114}$-*b*-EHMA$_{100}$)** |
| **Branched Copolymer** | | **[a] $I_1/I_3$** | |
| p(EHMA$_{100}$-co-EGDMA$_{0.80}$) | 1.10 | 1.12 | 1.10 |
| p(BuMA$_{100}$-co-EGDMA$_{0.95}$) | 1.22 | 1.17 | 1.12 |
| p(HPMA$_{100}$-co-EGDMA$_{0.90}$) | 1.62 | 1.26 | 1.14 |

[a] Obtained using fluorescence emission spectroscopy of aqueous nanoparticle dispersions following attempted encapsulation of pyrene during co-nanoprecipitation.

The lower $I_1/I_3$ values obtained suggests that pyrene is located in an environment which is of lower polarity than water, indicating that pyrene may be located within the core of the polymer nanoparticles (i.e. it has been successfully encapsulated during co-nanoprecipitation). Polymer nanoparticles produced with p($PEG_{114}$-b-$HPMA_{100}$) as constant but with varying branched vinyl polymer showed varying $I_1/I_3$ values (Figure 3.20).

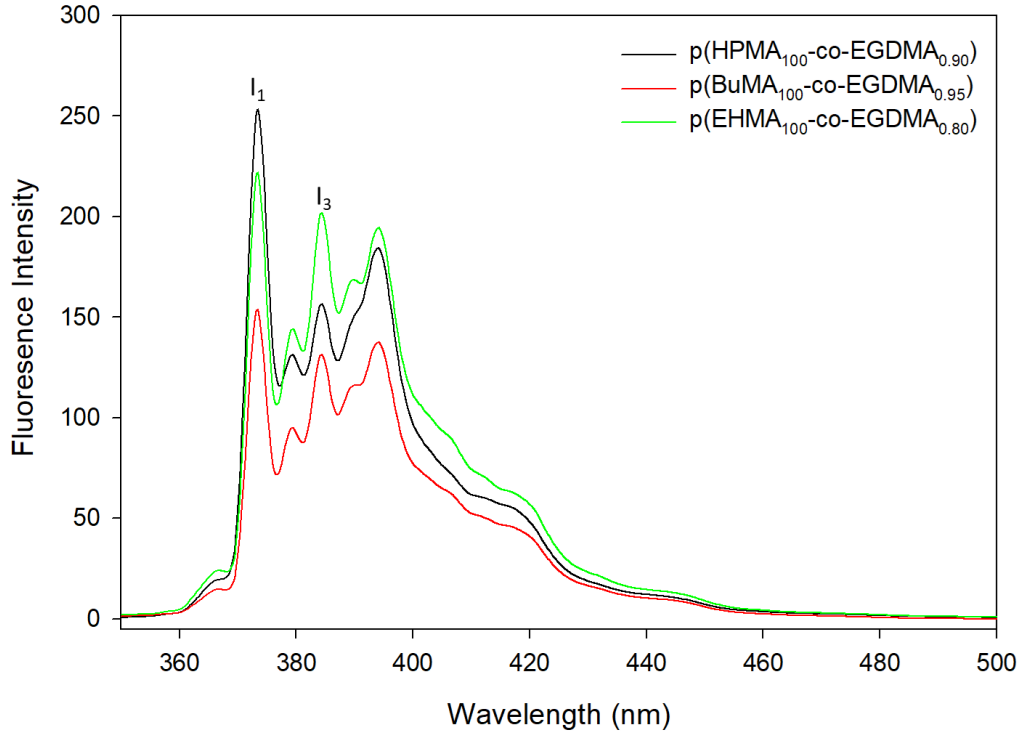


**Figure 3.20** Fluorescence emissions spectra for pyrene loaded p($HPMA_{100}$-co-$EGDMA_{0.90}$) (Black line), p($BuMA_{100}$-co-$EGDMA_{0.95}$) (red line) and p($EHMA_{100}$-co-$EGDMA_{0.80}$) (green line) branched copolymers with AB block copolymer, p($PEG_{114}$-*b*-$HPMA_{100}$) (60:40 wt. % composition respectively). Showing the difference in $I_1$ and $I_3$ values between the branched copolymers.

Since the AB block copolymer composition was kept constant during the co-nanoprecipitation process, the changes to the $I_1/I_3$ ratio value has provided indication that the monomer residue chemistry is having an impact on the nanoparticle core chemistry and therefore the internal polarity. This was also observed when the AB block was changed to p($PEG_{114}$-b-$BuMA_{100}$) and p($PEG_{114}$-b-$EHMA_{100}$). Analysis of the values obtained for p($PEG_{114}$-b-$HPMA_{100}$) co-nanoprecipitates showed that polymer nanoparticles consisting of branched copolymers with HPMA monomer residue functionalities exhibit the most polar nanoparticle cores, as demonstrated by the

highest $I_1/I_3$ value (1.62). This value decreased when the monomer residue of the branched copolymer was changed to BuMA (1.22) and then to EHMA (1.10). This suggests that when varying monomer residue chemistry, a decrease in polarity of the nanoparticle core is observed with increasing monomer residue hydrophobicity. As previously discussed, BuMA and EHMA functionalities are more hydrophobic than that of HPMA and therefore it would be expected that a less polar core would be generated. The difference in values between BuMA and EHMA functionalities further suggests that the increasing hydrophobicity between the two has an impact on the core polarity. This increase in hydrophobicity can be readily rationalised as being due to the longer and branched aliphatic chains that are present in p(EHMA) and the subsequent changes this would have on the calculated octanol-water partition coefficients (cLogP).

To provide some indication of the mode of AB block copolymer incorporation during co-nanoprecipitation, the AB block copolymer was changed to p($PEG_{114}$-*b*-$BuMA_{100}$) and p($PEG_{114}$-*b*-$EHMA_{100}$). If the hydrophobic segment of the AB block locates within the core of the polymer nanoparticle, then changing the hydrophobic segment on the AB block copolymer should alter the nanoparticle core polarity and, in turn, the $I_1/I_3$ ratios. Polymer nanoparticles were prepared with pyrene, as described previously. The fluorescence emissions of the aqueous nanoparticle dispersions, obtained following excitation at $\lambda$ = 335 nm, showed that the encapsulation of pyrene during these co-nanoprecipitations had been successful.

Different $I_1/I_3$ values were obtained for the nanoparticles prepared with different AB block copolymers (Table 3.9). The polymer nanoparticles that were prepared with p($PEG_{114}$-*b*-$EHMA_{100}$) produced the lowest $I_1/I_3$ ratios, which is consistent with this being the most hydrophobic AB block copolymer. These differing values presented here demonstrate that the nanoparticle internal core is comprised not just of branched copolymer, but also the hydrophobic segment from the AB block copolymer. Additionally, it also indicates that the hydrophilic PEG-based domain is not located within the core of the nanoparticle as these values suggest that pyrene is located in a low polarity environment.

### 3.6.4 Evaluation of Stability of Pyrene Loaded p(EHMA-co-EGDMA) Nanoparticles Following the Addition of PBS.

As previously mentioned, the co-nanoprecipitation of p($EHMA_{100}$-co-$EGDMA_{0.85}$) seemed to be improved by the incorporation of the guest molecule, pyrene. It was of interest to see how the co-nanoprecipitates incorporating pyrene behaved following the addition of PBS. Experimentally, p($EHMA_{100}$-co-$EGDMA_{0.85}$) was co-nanoprecipitated with pyrene into DI water with p($PEG_{114}$-*b*-$HPMA_{100}$) at varying compositional ratios of 100:0 – 50:50 wt. %, respectively. Solvent was allowed to evaporate and $D_z$, PDI and derived count rate were determined *via* DLS at a $[P]_f$ =1 mg $mL^{-1}$. The stability to dilution and exposure to salts of these branched vinyl copolymer nanoparticles was assessed *via* a serial dilution with PBS over a 100-fold dilution factor to produce final polymer concentrations at 0.5, 0.25, 0.1 and 0.01 mg $mL^{-1}$. Aqueous nanoparticle dispersions were diluted and left to gently mix overnight before being analysed *via* DLS (Table 3.10).

The sample without AB block co-polymer present was translucent but contained visible aggregation on the stirrer bar before addition of PBS, again indicating that the AB block copolymer is required to provide a degree of steric stabilisation during the co-nanoprecipitation process (Figure 3.21). The importance of such steric stabilisation was also evident as the sample was diluted with PBS to 0.5 mg $mL^{-1}$, which resulted in a dramatic increase in particle hydrodynamic diameter from 140 to 306 nm, coupled with a decrease in count rate from 72 700 to 15 400 kcps, which suggests that the sample was precipitating out of solution and sedimenting, resulting in a reduced scattering of light. The samples that contained ≥ 20 wt.% AB block copolymer remained stable upon addition of PBS up to a dilution of 0.01 mg $mL^{-1}$, with minimal variation in hydrodynamic diameter observed (Figure 3.22). The sample with 10 wt.% AB block copolymer showed signs of instability and polymer aggregation at 0.25 mg $mL^{-1}$ as a multimodal DLS trace was obtained; no further dilution was conducted with this sample (Appendix, Figure A31). Interestingly, the sample that showed the least difference between measurements was that consisting of 40 wt.% AB block copolymer.

**Table 3.10** DLS analyses of pyrene loaded p($EHMA_{100}$-co-$EGMDA_{0.90}$) polymer nanoparticles conanoprecipitated at varying wt. % of p($PEG_{114}$-*b*-$HPMA_{100}$) from 0-50 wt.%, respectively, following the serial dilution with PBS. $D_z$ values have been rounded to the nearest 5 nm.

| Polymer Concentration | Wt.% of Branched Polymer | Wt.% of AB block copolymer | $D_z$ (nm) | PDI | Derived count rate (kcps) | Attenuator Setting |
|---|---|---|---|---|---|---|
| 1 mg $mL^{-1}$ (no PBS) | *100** | *0* | *140* | *0.073* | *72 700* | 6 |
| | 90 | 10 | 175 | 0.093 | 781 300 | 4 |
| | 80 | 20 | 175 | 0.239 | 773 500 | 4 |
| | 70 | 30 | 175 | 0.170 | 816 700 | 4 |
| | 60 | 40 | 160 | 0.152 | 781 300 | 4 |
| | 50 | 50 | 140 | 0.115 | 579 800 | 4 |
| 0.5 mg $mL^{-1}$ (PBS) | *100** | *0* | *305* | *0.115* | *15 400* | *7* |
| | *90* | *10* | 185 | 0.130 | 518 900 | *4* |
| | 80 | 20 | 180 | 0.118 | 305 100 | 5 |
| | 70 | 30 | 170 | 0.126 | 340 300 | 5 |
| | 60 | 40 | 160 | 0.106 | 389 850 | 4 |
| | 50 | 50 | 150 | 0.089 | 276 150 | 5 |
| 0.25 mg $mL^{-1}$ (PBS) | *100* | *0* | *Polymer aggregation* | | | |
| | *90*** | *10* | *215* | *0.233* | *260 100* | *5* |
| | 80 | 20 | 175 | 0.088 | 227 100 | 5 |
| | 70 | 30 | 175 | 0.078 | 248 150 | 5 |
| | 60 | 40 | 160 | 0.099 | 222 750 | 5 |
| | 50 | 50 | 140 | 0.095 | 93 510 | 6 |
| 0.1 mg $mL^{-1}$ (PBS) | *100* | *0* | *Polymer aggregation* | | | |
| | *90* | *10* | *Polymer aggregation* | | | |
| | 80 | 20 | 175 | 0.106 | 61 750 | 6 |
| | 70 | 30 | 180 | 0.105 | 59 200 | 6 |
| | 60 | 40 | 160 | 0.099 | 58 100 | 6 |
| | 50 | 50 | 140 | 0.104 | 43 100 | 6 |

*sample contained visible aggregation on stirrer bar. **Size distribution by intensity graph was multimodal

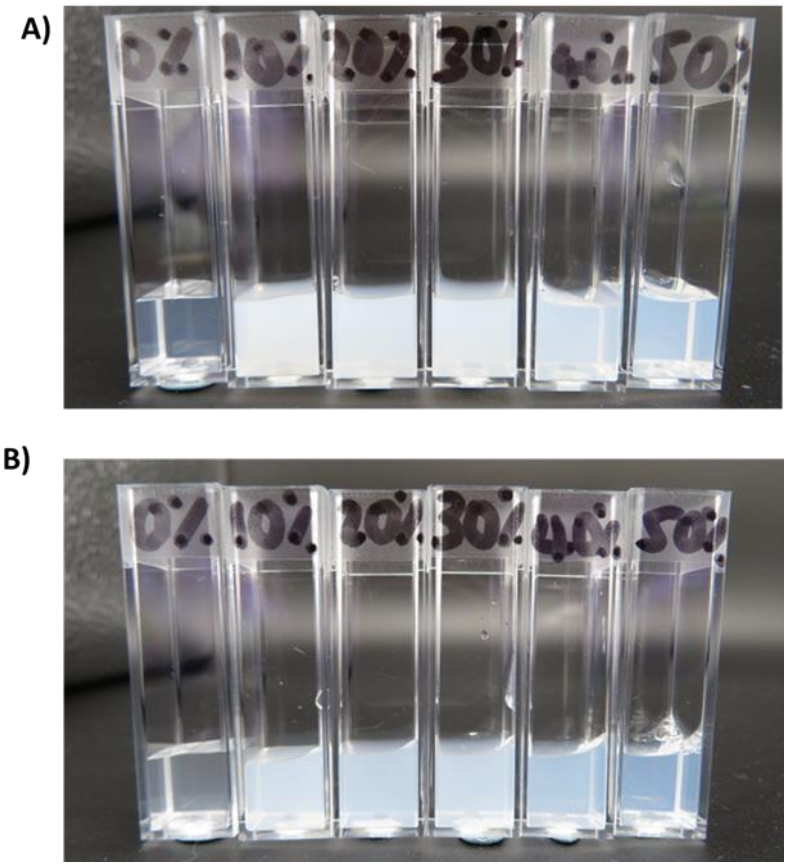


**Figure 3.21** Photographs showing the effects of the addition of PBS to the samples of p($EHMA_{100}$-co-$EGDMA_{0.85}$) with varying amounts of p($PEG_{114}$-*b*-$HPMA_{100}$) from 0-50 wt.% from left to right. Measured at A) polymer concentration = 1 mg $mL^{-1}$ in $H_2O$ and B) polymer concentration = 0.5 mg $mL^{-1}$, following dilution with PBS.

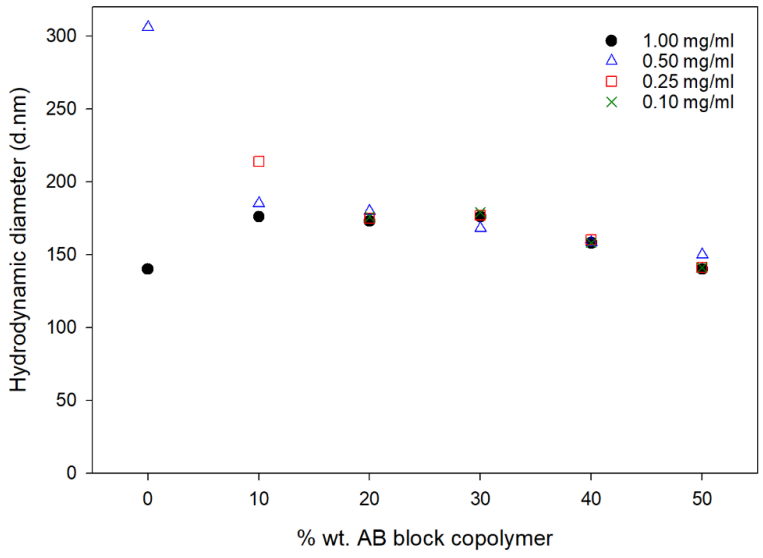


**Figure 3.22** A graph showing the hydrodynamic diameters (nm) obtained for the pyrene loaded p($EHMA_{100}$-co-$EGDMA_{0.85}$) nanoparticles with varying amounts compositions of p($PEG_{114}$-*b*-$HPMA_{100}$) from 0-50 wt.%. Data collected at different final polymer concentrations: 1 mg $mL^{-1}$ (black closed circles), and 0.5 mg $mL^{-1}$ (blue open triangles), 0.25 mg $mL^{-1}$ (red open squares) and 0.1 mg $mL^{-1}$ (green crosses) following dilutions with PBS.

### 3.7 Co-nanoprecipitation of p($PEG_{114}$-*b*-$HPMA_{100}$) and Branched Copolymers with Varying Divinyl Monomer Residue Chemistries

Co-nanoprecipitations were conducted by fixing the AB block copolymer as p($PEG_{114}$-b-$HPMA_{100}$) and by using branched copolymers consisting of EHMA monomer residues but varying in divinyl monomer residue chemistries. A ratio of branched copolymer:AB block polymer of 60:40 wt.% was used, as before. Co-nanoprecipitations were conducted as previously described (Section 3.5.3). Co-nanoprecipitation of all the branched p(EHMA) with varying divinyl monomer residue chemistry was successful except for p($EHMA_{100}$-co-$EGDMA_{0.80}$), which resulted in macroscopic aggregation, as previously described. Analysis *via* DLS showed monomodal distributions for all the aqueous nanoparticle dispersions obtained (Table 3.11).

**Table 3.11** DLS and zeta potential analyses of aqueous nanoparticle dispersions produced *via* co-nanoprecipitation of the AB block copolymer, p($PEG_{114}$-b-$HPMA_{100}$), with branched p(EHMA) varying in divinyl monomer residue chemistry.

| | | AB Block copolymer: p($PEG_{114}$-*b*-$HPMA_{100}$) | | | |
|---|---|---|---|---|---|
| **$DP_n$ of branched copolymer (monomer units)** | **Branching Agent** | **$D_z$ (nm)[a]** | **PDI[a]** | **Derived count rate (kcps)[a]** | **ζ (mV)[b]** |
| 20 | EGDMA | 150 | 0.133 | 592 300 | -17.7 |
| | BPDMA | 150 | 0.066 | 698 750 | -10.7 |
| | GDMA | 150 | 0.090 | 738 500 | -11.7 |
| | BPGDMA | 110 | 0.018 | 456 000 | -13.5 |
| | UDMA | 155 | 0.090 | 785 700 | -9.86 |
| | DSDMA | 145 | 0.042 | 790 350 | -13.2 |
| 100 | EGDMA | Polymer Aggregation | | | |
| | BPDMA | 165 | 0.087 | 637 150 | -11.1 |
| | GDMA | 160 | 0.084 | 833 450 | -11.2 |
| | BPGDMA | 150 | 0.063 | 731 550 | -8.64 |
| | UDMA | 155 | 0.080 | 785 400 | -8.58 |
| | DSDMA | 165 | 0.086 | 815 600 | -11.9 |

[a] Measured using DLS analysis at a concentration of 1 mg $mL^{-1}$. [b] Obtained via measurement of the electrophoretic mobility of aqueous nanoparticle dispersions within zeta cell.

Nanoparticles were produced with varying hydrodynamic diameters ($110 \leq D_z \leq 165$ nm) and polydispersity values ($0.018 \leq PDI \leq 0.133$). Repeat analyses were performed on p($EHMA_{100}$-co-$GDMA_{0.85}$), p($EHMA_{20}$-co-$GDMA_{0.85}$), p($EHMA_{100}$-co-$UDMA_{0.85}$) and p($EHMA_{20}$-co-$GDMA_{0.90}$) after 80 days of storage following co-nanoprecipitation, which showed little deviation from the original data collected and that all samples

were stable (Appendix, Table A.2). Therefore, suggesting that changes in the branching agent chemistry imparted minimal differences on the nanoparticle formation.

### 3.7.1 Investigating the Effect of Divinyl Monomer Residue Chemistries on Nanoparticle Core Polarity

Pyrene was encapsulated within EHMA-based branched copolymers consisting of varying branching agent chemistries to study its effect on the core properties of the polymer nanoparticles. Co-nanoprecipitations with pyrene were conducted as previously described with p(EHMA$_{20}$-co-EGDMA), p(EHMA$_{20}$-co-BPGDMA), p(EHMA$_{20}$-co-GDMA), p(EHMA$_{20}$-co-UDMA), p(EHMA$_{20}$-co-DSDMA) and p(EHMA$_{20}$-co-BPDMA) combined with p(PEG$_{114}$-*b*-HPMA$_{100}$). Co-nanoprecipitations with pyrene were also conducted with EHMA-based branched copolymer analogues with $DP_n$ of 100 monomer units. All co-nanoprecipitations were conducted at 60:40 wt.% ratio of branched copolymer:AB block copolymer, respectively, and produced stable aqueous nanoparticle dispersions following THF evaporation. Analysis of these dispersions by DLS showed minimal differences in the hydrodynamic diameters compared to their unloaded counterparts. Fluorescence emission spectroscopy confirmed the encapsulation of pyrene in the core of the polymer nanoparticles (Table 3.12).

**Table 3.12** Polarity data obtained from pyrene emission spectroscopy for aqueous nanoparticle dispersions obtained *via* co-nanoprecipitation of varying branched EHMA polymers at $DP_n$ = 20 and 100 monomer units with p(PEG$_{114}$-*b*-HPMA$_{100}$) and pyrene (1 wt.%).

| | | p(PEG$_{114}$-*b*-HPMA$_{100}$) |
|---|---|---|
| **$DP_n$ of branched copolymer (monomer units)** | **Branching Agent** | **[a] $I_1/I_3$** |
| 20 | EGDMA | 1.09 |
| | BPDMA | 1.11 |
| | GDMA | 1.10 |
| | DSDMA | 1.11 |
| | UDMA | 1.11 |
| | BPDMA | 1.10 |
| 100 | EGDMA | 1.10 |
| | BPGDMA | 1.07 |
| | GDMA | 1.06 |
| | UDMA | 1.07 |
| | DSDMA | 1.07 |
| | BPDMA | 1.07 |

[a] Obtained using fluorescence emission spectroscopy of aqueous nanoparticle dispersions following attempted encapsulation of pyrene during co-nanoprecipitation.

$I_1/I_3$ values were determined for $DP_n$ = 20 monomer units (1.09 - 1.11) and for $DP_n$ = 100 monomer units (1.06 - 1.10). The slightly higher $I_1/I_3$ values obtained for the polymers of $DP_n$ = 20 monomer units is likely to be as a result of the higher concentration of branching comonomers for any given mass of branched copolymer. However, these results showed that the variations in the branched copolymer core chemistries had negligible effect on the nanoparticle core polarity.

### 3.8 Conclusion

The work completed within this chapter aimed to expand on the scope of materials that have been previously reported to produce polymer nanoparticles *via* co-nanoprecipitation. The initial findings from model co-nanoprecipitation studies of linear and branched copolymers with AB block copolymers reiterated previous findings in that there is a clear advantage to using high molecular weight branched vinyl polymer material to promote faster rates of nucleation for the formation of sterically stabilised nanoparticles with narrow and monomodal size distributions.

This provided an opportunity to utilise complex macromolecular architectures that have been prepared by RDRP techniques, such as those discussed in Chapter 2. The design space of these materials was explored and the impact on producing polymeric nanoparticles and the effect this may have on the nanoparticle properties, such as size, appeared to be dependent on chemical nature of the polymer materials used. The results also reinforced that co-nanoprecipitation was a viable technique to produce polymer nanoparticles consisting of BuMA and EHMA functional copolymers, whose sole nanoprecipitation regimes failed to produce stable nanoparticles in the absence of AB diblock copolymers. Previously, the chemistry of the AB block copolymer hydrophobic domain has always been complimentary to that of the branched vinyl copolymer. However, systematically varying the AB block copolymer chemistries within the co-nanoprecipitation process allowed for the previously unreported co-nanoprecipitation of linear and branched vinyl (co)polymers whose functionality differed from that of the hydrophobic domains of the AB block copolymer. This in turn developed a further understanding of how the hydrophobic domain incorporates itself within the polymer nanoparticles.

It was also of interest to gain an understanding of whether these polymer nanoparticles would be suitable candidates for the encapsulation of hydrophobic guest molecules. The use of pyrene as a hydrophobic guest molecule demonstrated that these polymer nanoparticles have the capability to encapsulate small hydrophobic molecules within their core during the co-nanoprecipitation process and that this approach may therefore be suitable for the use of encapsulating chemotherapeutics. It was also indicated through this incorporation that the co-nanoprecipitation process is a complex mechanism, which can be influenced by the presence of small molecules. The presence of pyrene may be introducing a degree of charge stabilisation through the possible adsorption of hydroxide ions, as has been previously reported for hydrophobic polymers with HPMA monomer residue functionalities.

The chemical nature of pyrene also allowed for the probing of the internal environment of the polymer nanoparticles *via* fluorescence spectroscopy, which showed that the nanoparticle core polarities were influenced by the monomer residue chemistries and the hydrophobic domain chemistries of the AB block copolymer. These sterically stabilised pyrene loaded branched vinyl copolymer nanoparticles withstood dilution with biological media, which was relevant for future pharmacological investigations. This also suggests that the encapsulated guest molecules will remain within the nanoparticles and release at a rate dependent on diffusion and not by the degradation of the polymer nanoparticles.

### 3.9 References


1. J. Cheng, B. A. Teply, I. Sherifi, J. Sung, G. Luther, F. X. Gu, E. Levy-Nissenbaum, A. F. Radovic-Moreno, R. Langer and O. C. Farokhzad, *Biomaterials*, 2007, **28**, 869-876.
2. O. C. Farokhzad, S. Jon, A. Khademhosseini, T.-N. T. Tran, D. A. LaVan and R. Langer, *Cancer research*, 2004, **64**, 7668-7672.
3. N. Kamaly, G. Fredman, M. Subramanian, S. Gadde, A. Pesic, L. Cheung, Z. A. Fayad, R. Langer, I. Tabas and O. C. Farokhzad, *Proceedings of the National Academy of Sciences*, 2013, **110**, 6506-6511.
4. C. Zhang, V. J. Pansare, R. K. Prud'Homme and R. D. Priestley, *Soft Matter*, 2012, **8**, 86-93.
5. S. Khoee and M. Yaghoobian, *European journal of medicinal chemistry*, 2009, **44**, 2392-2399.
6. B. Le Droumaguet, J. Nicolas, D. Brambilla, S. Mura, A. Maksimenko, L. De Kimpe, E. Salvati, C. Zona, C. Airoldi and M. Canovi, *ACS nano*, 2012, **6**, 5866-5879.
7. R. A. Slater, T. O. McDonald, D. J. Adams, E. R. Draper, J. V. Weaver and S. P. Rannard, *Soft Matter*, 2012, **8**, 9816-9827.

8. F. L. Hatton, P. Chambon, T. O. McDonald, A. Owen and S. P. Rannard, *Chemical Science*, 2014, **5**, 1844-1853.
9. F. L. Hatton, L. M. Tatham, L. R. Tidbury, P. Chambon, T. He, A. Owen and S. P. Rannard, *Chemical science*, 2015, **6**, 326-334.
10. J. Ford, P. Chambon, J. North, F. L. Hatton, M. Giardiello, A. Owen and S. P. Rannard, *Macromolecules*, 2015, **48**, 1883-1893.
11. E. Niezabitowska, J. Smith, M. R. Prestly, R. Akhtar, Felix W. von Aulock, Y. Lavallée, H. Ali-Boucetta and T. O. McDonald, *RSC Advances*, 2018, **8**, 16444-16454.
12. S. Flynn, *PhD Thesis*, Univeristy of Liverpool, 2019. (https://livrepository.liverpool.ac.uk/3079211/1/200670082_Sep2019.pdf).
13. S. Schubert, J. T. Delaney Jr and U. S. Schubert, *Soft Matter*, 2011, **7**, 1581-1588.
14. H. Fessi, F. Puisieux, J. P. Devissaguet, N. Ammoury and S. Benita, *International journal of pharmaceutics*, 1989, **55**, R1-R4.
15. P. Legrand, S. Lesieur, A. Bochot, R. Gref, W. Raatjes, G. Barratt and C. Vauthier, *International Journal of Pharmaceutics*, 2007, **344**, 33-43.
16. M. Beck-Broichsitter, E. Rytting, T. Lebhardt, X. Wang and T. Kissel, *European Journal of Pharmaceutical Sciences*, 2010, **41**, 244-253.
17. W. S. Saad and R. K. Prud'homme, *Nano Today*, 2016, **11**, 212-227.
18. H. E. Rogers, P. Chambon, S. E. R. Auty, F. Y. Hern, A. Owen and S. P. Rannard, *Soft Matter*, 2015, **11**, 7005-7015.
19. J. Goodwin, *Colloids and Interfaces with Surfactants and Polymers*, John Wiley & Sons, 2nd Edition, UK, 2009.
20. M. Li, M. Jiang, Y.-x. Zhang and Q. Fang, *Macromolecules*, 1997, **30**, 470-478.
21. D. C. Dong and M. A. Winnik, *Canadian Journal of Chemistry*, 1984, **62**, 2560-2565.
22. K. N. Kudin and R. Car, *Journal of the American Chemical Society*, 2008, **130**, 3915-3919.
23. S. Inphonlek, N. Pimpha and P. Sunintaboon, *Colloids Surf B Biointerfaces*, 2010, **77**, 219-226.
24. R. Van Wagenen, D. Coleman, R. King, P. Triolo, L. Brostrom, L. Smith, D. Gregonis and J. Andrade, *Journal of Colloid and Interface Science*, 1981, **84**, 155-162.

# Chapter 4

Encapsulation of the Anti-Cancer Drug SN-38 *via* Co-Nanoprecipitation and the Release from Branched Vinyl Copolymer Nanoparticles

## 4.1 Introduction

One of the most common treatments for a wide range of cancers is systemic chemotherapy, however, high doses are required to achieve a high drug concentration in target tissues, and thus a therapeutic effect, which frequently results in a broad toxicity experienced by the patients. Additionally, many chemotherapeutics exhibit poor aqueous solubility and stability issues. Over the last few decades there has been an increase in the preparation of drug loaded nanocarriers that have shown promising potential in overcoming the inherent problems associated with conventional dosing of chemotherapy drugs. Examples of such nanocarriers include liposomes, dendrimers, micelles and polymeric nanoparticles, which were discussed in detail in Chapter 1 section 1.2.1. When compared to conventional administration, encapsulation of chemotherapeutics offers several specific advantages, such as protection from degradation in systemic circulation, enhanced drug stability and solubility, decreasing toxic side effects and improved pharmacokinetic and pharmacodynamic profiles.

### 4.1.1 Irinotecan - An Anticancer Chemotherapy Drug

Camptothecin-11, more commonly known as irinotecan (IR), is a non-metallic chemotherapeutic that is commonly administered as a single agent or in combination therapy for the treatment of colorectal and small cell lung cancer.[1] It is derived from the natural compound, camptothecin (CPT), a plant alkaloid that is found in the Chinese ornamental tree, *Camptotheca acuminate.* CPT was first discovered in the 1960s and demonstrated positive anti-tumour effects in mice with experimental tumours.[2] However, its clinical development was halted as it exhibited unpredictable and severe toxicity in both animal experiments[3] and clinical trials.[4-6] These unpredictable toxic effects were determined to be as a result of the water insolubility CPT exhibited.[7] Therefore, CPT is not utilised as a clinical chemotherapeutic. However, an analogue with increased water solubility and more predictable toxicity was created, which led to the development of IR (Figure 4.1).[8, 9] IR demonstrated potent anti-tumour activity in multiple murine models[10-12] and became commercially available in Japan (1994) for the treatment of lung, cervical and ovarian cancers, and

soon after gained approval for treatment of metastatic colorectal cancer in the USA (1996).[8]

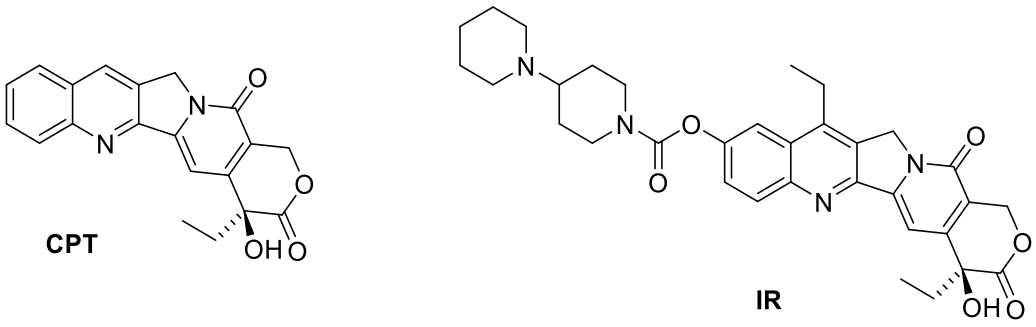


**Figure 4.1** Chemical structures of camptothecin (CPT) and irinotecan (IR).

The use of IR prevents cells from dividing by inhibiting topoisomerase I, a nuclear enzyme.[13] More specifically, it prevents the DNA from re-ligating by binding to topoisomerase I through hydrogen bonding, therefore causing DNA damage and resulting in apoptosis. However, IR itself actually possesses limited anti-tumour activity and its pharmacological profile is dependent on an extensive and complex metabolic conversion *in vivo* by varying enzyme systems (Figure 4.2).

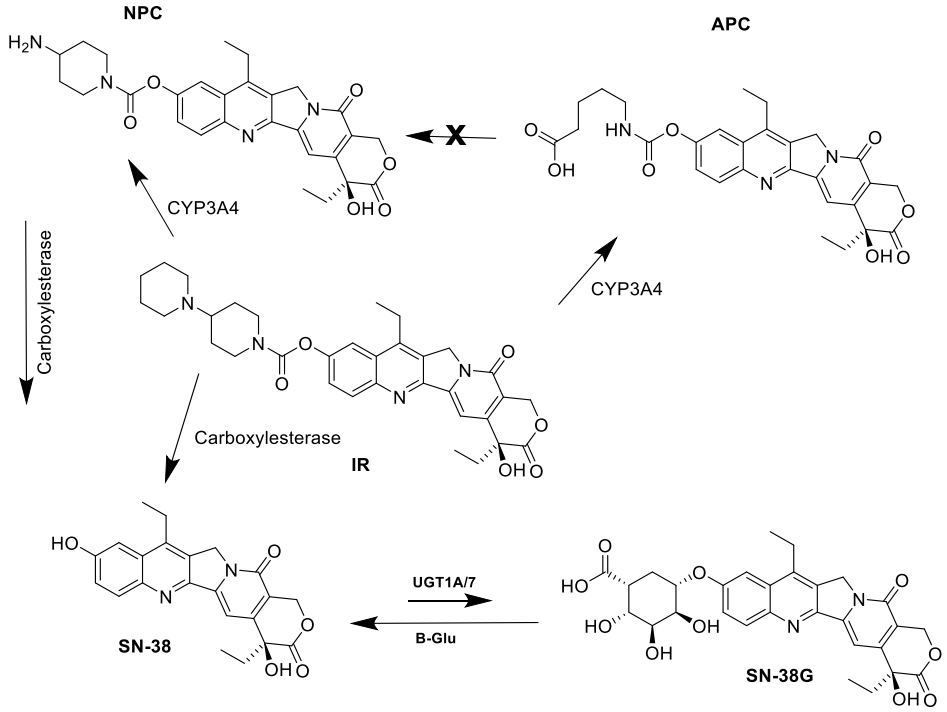


**Figure 4.2** Metabolic pathway of IR showing the esterase mediated formation of the active metabolite SN-38 and its subsequent conversion to a glucuronide derivative (SN-38G) by enzymes UGT1A and 1A7. SN-38G can undergo deglucuronidation by β-glucuronidase. IR can also undergo enzyme mediated oxidation to form APC and NPC, the latter can be hydrolysed by carboxylesterase to form SN-38. Figure adapted from reference.[7]

The enzymatic hydrolysis of IR in the liver by carboxylesterase leads to the formation of the active metabolite, SN-38, which is 100-1000 times more potent than IR.[14] Unfortunately, only 1-9% of an injected dose of IR is converted to SN-38 in humans due to the low rates of carboxylesterase mediated cleavage which occurs in the liver.[15, 16]

IR is also metabolised by cytochrome enzymes into less active metabolites, 7-ethyl-10-[4-N-(5-aminopentanoic acid)-1-piperidino] carbonyloxycamptothecin (APC) and 7-ethyl-10-[4-amino-1-piperidino] carbonyloxycamptothecin (NPC). The latter can be further converted to SN-38 by carboxylesterase. SN-38 is inactivated by 5'-diphospho-glucuronosyltransferase enzymes (UGT) into SN-38G, which increases the polarity of the drug and promotes its elimination from the body.[17]

The high potency of SN-38 makes it a highly desirable chemotherapeutic for the treatment of lung, ovarian, breast and colorectal cancer, but the clinical applications have been significantly limited due to the poor solubility in aqueous solutions (< 5 μg $mL^{-1}$)[18, 19] and most pharmaceutically accepted solvents.[20] However, the preparation of SN-38 within DDS offers an opportunity to formulate and evaluate it as a directly administrated therapy.

### 4.1.2 SN-38 Nanoformulations

Currently, SN-38 is not directly administered due to its hydrophobic nature. In addition, SN-38 also possesses pH sensitivity, whereby SN-38 is converted from closed-lactone ring form to the open carboxylate form at physiological pH, the latter of which is inactive (Figure 4.3).[21] The rate of this hydrolysis is dependent on pH[22], ionic strength[23] and protein concentration.[24, 25] This consequently limits its clinical application.

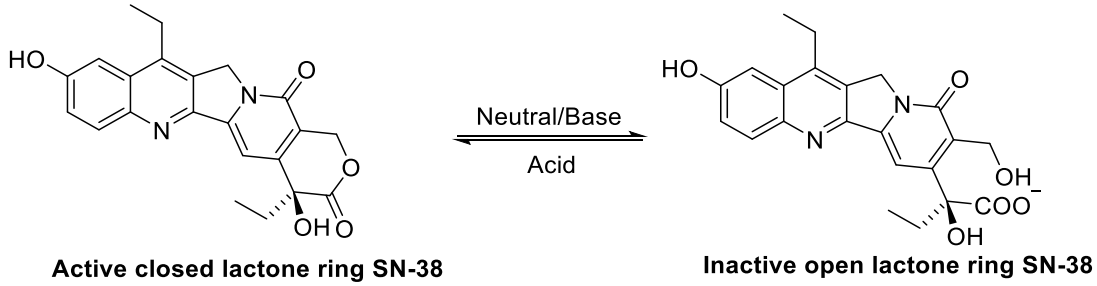


**Figure 4.3** Conversion of the lactone and carboxyl forms of SN-38.

The preparation of SN-38 DDS is fairly limited as a consequence of these factors; however, a variety of different DDS have been developed and reported, which include polymer-drug conjugates,[26, 27] liposomes,[28-30] micelles[31], and polymer nanoparticles.[32-35]

Perhaps the most significant DDS of SN-38 to date is NK012, which has been evaluated in Phase II clinical trials.[36] NK012 is a micellar formulation of SN-38, which was prepared by the self-assembly of a PEG-poly(glutamic acid) based block copolymer. Binding of SN-38 to the poly(glutamate) block *via* an ester bond saw SN-38 incorporated at ca. 20% (w/w), and generated mean particle sizes of 20 nm with narrow size distributions. Release rates of SN-38 were determined in PBS at 37 °C, and were 57% and 74% at 24 and 48 hours, respectively. In comparison to treatment with IR, NK012 demonstrated significantly greater anti-tumour activity in a wide variety of pre-clinical experimental tumours such as: lung,[36-38] pancreatic,[39] renal,[40] gastric,[38] and colorectal cancer.[41] Another polymer-drug conjugate that progressed to Phase I clinical trials is EZN-2208, synthesised *via* PEGylation of SN-38 with drug loadings between 2.5-3.7 wt.%, which showed potent *in-vitro* cytotoxicity against human cell lines.[42, 43]

Alternatively, there have been reports of SN-38 loaded polymer nanocarriers, which have been prepared *via* different methods including thin film hydration[44] or nanoprecipitation.[25, 26] Whereas, Roger *et al* formulated SN-38 within a liposomal formulation using a variety of different excipients, which had a mean particle size of 40 nm and a drug loading of approximately 0.43 mg $g^{-1}$; release of SN-38 was determined to be 10% after 6 hours at pH 1.2.[45] Gu *et al* described loading SN-38 into micelles (ca. 125 nm) consisting of Pluronic F-108 and p($PEG_{114}$-*b*-PCL), at an

estimated drug loading of 20 wt.%. Release of SN-38 was determined to be < 68% in PBS after 24 hours.[31] Polymer nanoparticles prepared from PLGA and a PVA stabiliser with a drug loading of approximately 6 wt.% SN-38 and an average diameter of 170 nm have also been reported.[16] Although, the preparation of these required the presence of DMSO as a co-solvent to increase SN-38 solubility.

Each of these different strategies have their own merits and demerits. For example, polymer-drug conjugates improve the drug bioavailability, but the preparation involves multiple complex reaction steps, which in-turn can result in low product yields. Co-nanoprecipitation of hydrophobic branched vinyl copolymers and AB block copolymers, as previously demonstrated, offers a potentially facile way to incorporate hydrophobic guest molecules, which may in turn provide a route to encapsulate SN-38 at clinically-relevant drug loadings and offer sustained release profiles.

### 4.1.3 Chapter Aim

In Chapter 3, the preparation of sterically stabilised polymer nanoparticles with varying chemical composition was explored. It was highlighted that co-nanoprecipitation was a versatile way of generating aqueous nanoparticle dispersions. It was also shown that the chemistry of both branched vinyl polymer and AB block copolymer had an influence on the nanoparticle properties, such as size, core polarity and stability. The ability to tune the chemistry means that the nanoparticle can be tailored for the encapsulation of a desired hydrophobic drug molecule. This research chapter ultimately aims to assess and optimise the encapsulation capabilities of the co-nanoprecipitated materials explored in Chapter 3 using the potent chemotherapeutic SN-38 and to assess the rate of drug release from the nanoparticles. These studies will determine the maximum drug loading of SN-38 attainable without causing significant disruption to the co-nanoprecipitation process or generating large quantities of un-encapsulated drug. The influence of different parameters that may modulate the drug loading, encapsulation efficiency (EE), such as polymer functionality and composition, and nanoprecipitation environment (pH), will also be studied. Following this, investigations will be conducted to determine whether encapsulating SN-38 within polymer nanoparticles

enables sustained release profiles by quantifying the release rate of SN-38 using radiometric analysis.

## 4.2 Preparation of SN-38 Loaded Aqueous Nanoparticles

Co-nanoprecipitation as a technique has been shown to produce sterically stabilised branched vinyl copolymer nanoparticles capable of encapsulating hydrophobic guest molecules (Chapter 3.6). Since SN-38 is a small hydrophobic guest, it is theorised that it could be encapsulated during the co-nanoprecipitation process. However, as previously discussed, SN-38 exhibits extremely limited solubility in most organic solvents and the solubility is limited to acetonitrile, dimethyl sulfoxide (DMSO) and THF. The $^{1}$H-NMR and $^{13}$C-NMR analysis of SN-38 in deuterated DMSO is presented in the Appendix, Figure A32 & A33. SEM analyses of the sole nanoprecipitation of SN-38 [1 mg mL$^{-1}$] from THF (1 mL) into water (5 mL) shows the crystalline nature of the drug (Figure 4.4).

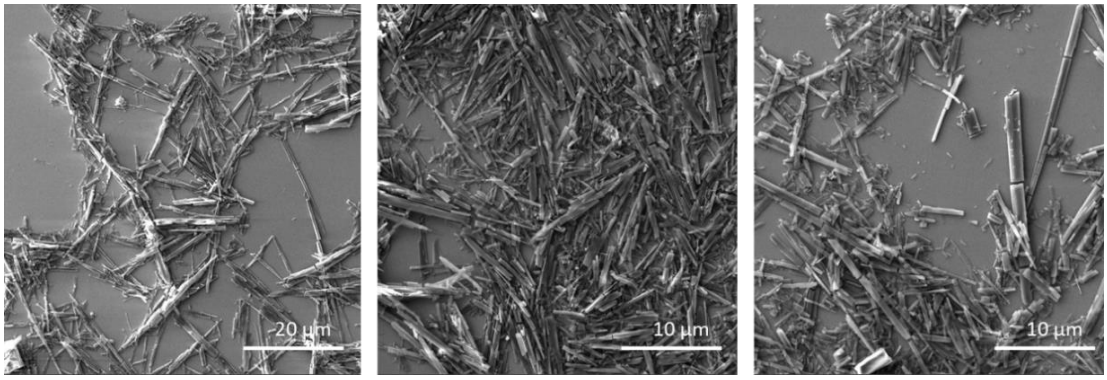


**Figure 4.4** SEM images of nanoprecipitated SN-38 from THF into water.

### 4.2.1 Preparation of SN-38 Loaded Aqueous Nanoparticles *via* Co-nanoprecipitation

SN-38 encapsulation experiments were conducted by the co-nanoprecipitation of branched vinyl polymers and AB block copolymers in the presence of SN-38. Since there was a large number of co-nanoprecipitation options, a standard set of conditions were determined for all co-nanoprecipitations involving SN-38. Following on from the successful conditions developed in Chapter 3.4, all of these co-nanoprecipitations were conducted from THF (1 mL, $[P]_o$= 5 mg mL$^{-1}$) into stirred water (5 mL, $[P]_f$= 1 mg mL$^{-1}$). SN-38 was incorporated within the initial THF solution to target drug loadings of 2.5 and 5 wt.% wrt. the total solid mass. All co-nanoprecipitations were conducted using a 60:40 wt.% composition of branched

vinyl polymer:AB block copolymer, respectively. A general overview of the SN-38 encapsulation experiments is presented in Figure 4.5.

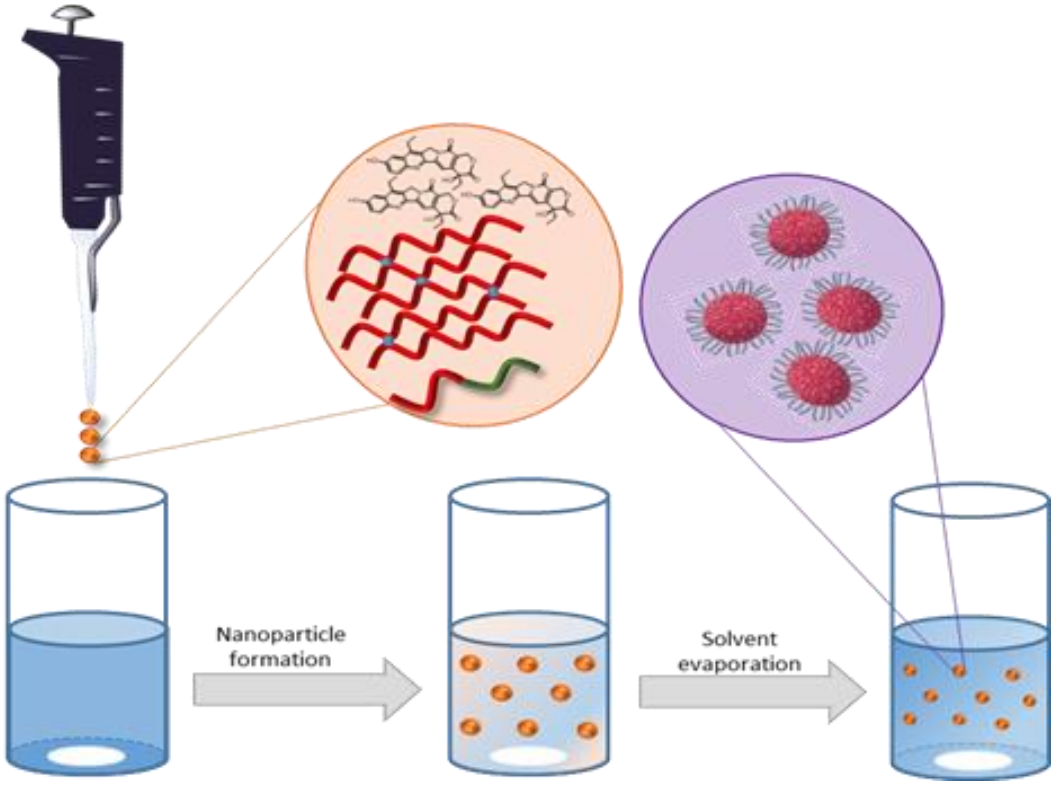


**Figure 4.5** Schematic representation of the co-nanoprecipitation of branched vinyl copolymers and AB block copolymers with SN-38 to produce SN-38 loaded branched vinyl copolymer nanoparticles.

In all cases, the addition of the polymer/SN-38 THF solution to water resulted in the instantaneous formation of a turbid mixture. The mixtures were left to stir for 24 hours at ambient temperature to allow for the evaporation of THF. The success of the co-nanoprecipitations was determined initially by visual observations. There were 3 different observations made regarding the formulations. Firstly, there were formulations that showed macroscopic aggregation of polymer, suggesting the co-nanoprecipitation had not been successful and that stable polymer nanoparticles had failed to be generated. Secondly, there were formulations that did not show macroscopic aggregation but appeared 'opalescence', which suggested that polymer nanoparticles had been formed but the encapsulation of SN-38 had not been entirely successful and instead 'free SN-38' (i.e. un-encapsulated SN-38) drug crystals may be present within the aqueous nanoparticle dispersions (Figure 4.6). SEM imaging of these samples confirmed this theory by showing the presence of polymer nanoparticles on large drug crystals (Figure 4.7).

**Figure 4.6** Photographs showing the opalescence appearance of several nanoformulations.

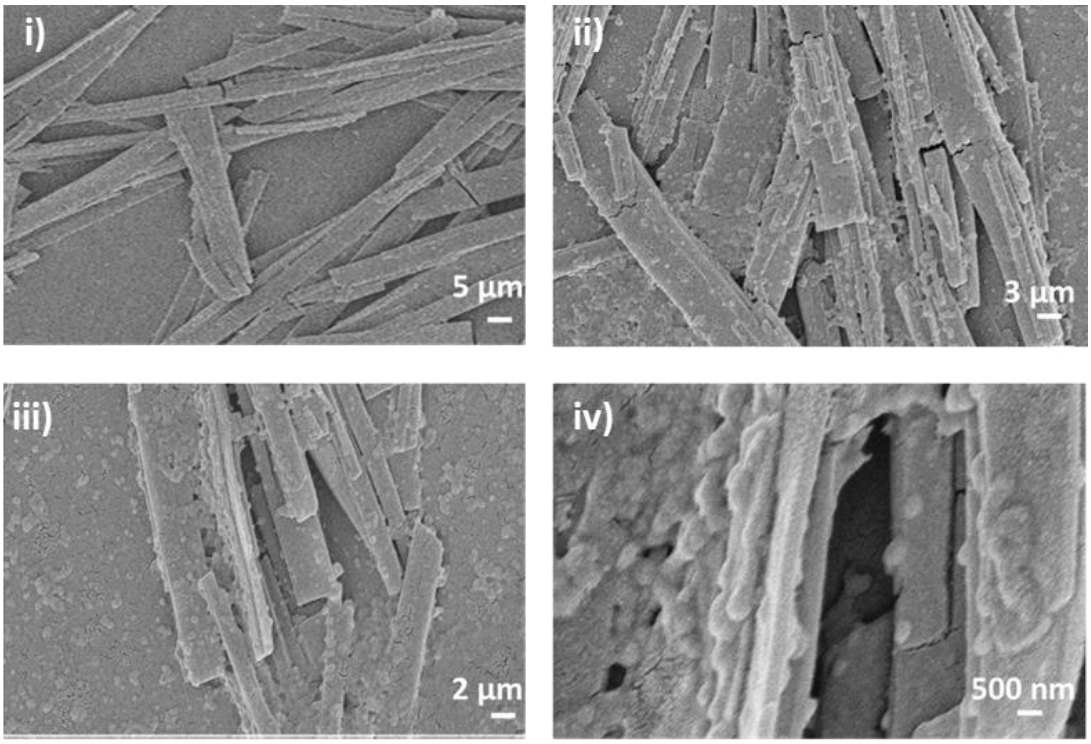


**Figure 4.7** SEM images of co-nanoprecipitations that were described as 'opalescence'. The images show the successful formation of branched vinyl polymer nanoparticles but the unsuccessful encapsulation of SN-38.

Thirdly, and most importantly, there were formulations that remained turbid without the presence of an '*opalescence'* effect or macroscopic aggregation of polymer. This suggests that the encapsulation of SN-38 within branched vinyl polymer nanoparticles had been successful (Figure 4.8).

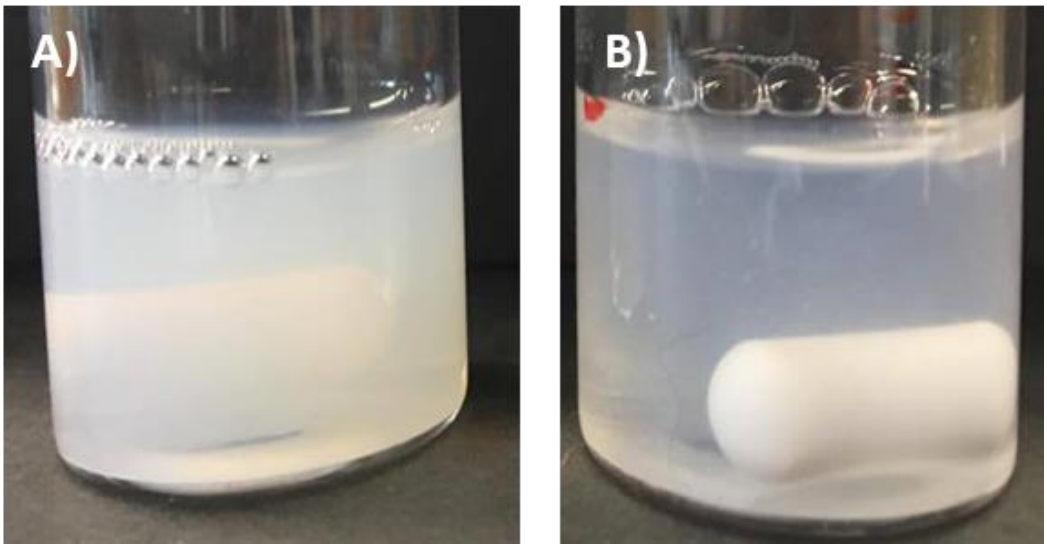


**Figure 4.8** Photographs showing (A) the successful encapsulation of SN-38 within branched vinyl polymer nanoparticles, and (B) its unsuccessful encapsulation, described as 'opalescence' in appearance.

Based on these observations, it was clear that the success of the encapsulation experiments was dependent on the monomer residue functionalities of the AB block copolymers and branched vinyl copolymers, with HPMA monomer residue functionalities proving to be necessary for successful formulation. It is unclear why HPMA was important; however, the potential for strong hydrogen bonding may play a role in interacting with the drug and generating stabilisation or positive interactions that impeded macroscale phase separation. It is important to note that the presence of HPMA did not guarantee success.

The DLS analyses of the aqueous nanoparticle dispersions are presented in Table 4.1. The DLS analyses revealed monomodal intensity-derived particle size distributions (with the exception of one), whereby the nanoparticles had hydrodynamic diameters in the region of 140 – 190 nm and PDI values between 0.099 – 0.333 (Figure 4.9).

**Table 4.1** DLS analyses of SN-38 loaded branched vinyl copolymer nanoparticle dispersions formed *via* co-nanoprecipitation with varying AB block copolymers. Drug loadings of 2.5 and 5 wt. % wrt. total solid mass was targeted.

| | | AB Block Copolymer (40 wt.%) | | | | | | | | |
|---|---|---|---|---|---|---|---|---|---|---|
| | | p(PEG$_{114}$-*b*-BuMA$_{100}$) | | | p(PEG$_{114}$-*b*-EHMA$_{100}$) | | | p(PEG$_{114}$-*b*-HPMA$_{100}$) | | |
| **Polymer Composition** | **SN-38 wt. %** | **$D_z$ (nm)[a]** | **PDI[a]** | **Derived Count Rate (kcps)[a]** | **$D_z$ (nm)[a]** | **PDI[a]** | **Derived Count Rate (kcps)[a]** | **$D_z$ (nm)[a]** | **PDI[a]** | **Derived Count Rate (kcps)[a]** |
| p(BuMA$_{20}$-co-EGDMA$_{0.85}$) | 5 | Opalescence | | | Polymer Aggregate | | | 185 | 0.333 | 531 700 |
| p(EHMA$_{20}$-co-EGDMA$_{0.80}$) | 5 | Opalescence | | | Polymer Aggregate | | | 190 | 0.186 | 325 150 |
| p(HPMA$_{20}$-co-EGDMA$_{0.85}$) | 5 | 115 | 0.237 | 272 400* | Polymer Aggregate | | | 140 | 0.222 | 384 000 |
| p(BuMA$_{100}$-co-EGDMA$_{0.95}$) | 2.5 | Opalescence | | | Polymer Aggregate | | | 160 | 0.099 | 771 100 |
| | 5 | Polymer Aggregate | | | | | | Polymer Aggregate | | |
| p(EHMA$_{100}$-co-EGDMA$_{0.80}$) | 2.5 | Opalescence | | | Polymer Aggregate | | | 175 | 0.123 | 706 450 |
| | 5 | Polymer Aggregate | | | | | | 180 | 0.164 | 760 300 |
| p(HPMA$_{100}$-co-EGDMA$_{0.90}$) | 2.5 | Opalescence | | | Opalescence | | | Opalescence | | |
| | 5 | Polymer Aggregate | | | | | | | | |

[a] Measured using DLS analysis at a concentration of 1 mg mL$^{-1}$, $D_z$ values have been rounded to the nearest 5 nm.
*Non-monomodal size distribution obtained.

These successful nanoprecipitates showed slight deviations in the hydrodynamic diameters and PDI values when compared to the blank nanoparticles (no SN-38) and the 1 wt.% pyrene loaded nanoparticles. In all cases the particle size increased and the particle size distribution became broader for the SN-38 loaded nanoparticles. This effect was more significant for the polymers with a short primary polymer chain length. For example, when comparing blank and SN-38 loaded co-nanoprecipitations of p(BuMA$_{20}$-co-EGDMA$_{0.85}$):p(PEG$_{114}$-*b*-HPMA$_{100}$), the $D_z$ values increased from 155 nm to 185 nm and the PDI values increased from 0.098 to 0.333 when SN-38 was encapsulated. Whereas, the same comparisons for p(BuMA$_{100}$-co-EGDMA$_{0.95}$):p(PEG$_{114}$-*b*-HPMA$_{100}$) showed a small increase in $D_z$ from 145 to 160 nm and the PDI showed minimal deviation from 0.088 to 0.099 when SN-38 was introduced into the co-nanoprecipitation. Again, the direct rationale for this behaviour is unclear.

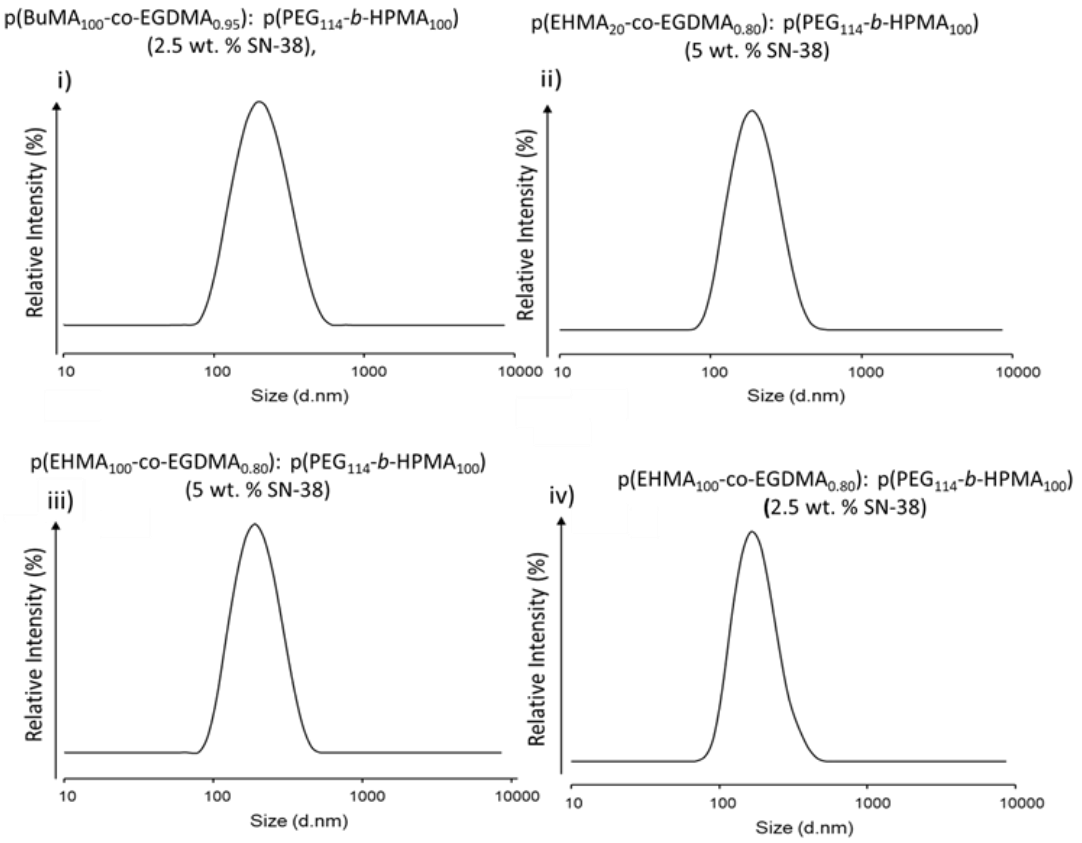


**Figure 4.9** DLS size distribution by intensity traces for SN-38 loaded polymer nanoparticles for i) p(BuMA$_{100}$-co-EGDMA$_{0.95}$): p(PEG$_{114}$-*b*-HPMA$_{100}$) (2.5 wt. % SN-38), ii) p(EHMA$_{20}$-co-EGDMA$_{0.80}$): p(PEG$_{114}$-*b*-HPMA$_{100}$) (5 wt. % SN-38), iii) p(EHMA$_{100}$-co-EGDMA$_{0.80}$): p(PEG$_{114}$-*b*-HPMA$_{100}$) (5 wt. % SN-38), and iv) p(EHMA$_{100}$-co-EGDMA$_{0.80}$): p(PEG$_{114}$-*b*-HPMA$_{100}$) (2.5 wt. % SN-38).

The SN-38 co-nanoprecipitations utilising p(PEG$_{114}$-*b*-EHMA$_{100}$) generated aggregates in all cases, with the exception of combinations containing p(HPMA$_{100}$-co-EGDMA$_{0.90}$). This is in contrast to the blank and pyrene loaded co-nanoprecipitations with this AB block copolymer, which generated sterically stabilised nanoparticles. Clearly the incorporation of SN-38 has impacted the co-nanoprecipitation process of this material. The successful co-nanoprecipitation of p(EHMA$_{20}$-co-EGDMA$_{0.85}$):p(PEG$_{114}$-*b*-HPMA$_{100}$) with 5 wt.% SN-38 was studied using SEM. The images obtained provided evidence for nanoparticle formation and showed that SN-38 had been successfully encapsulated since there were no observable free drug crystals outside of the nanoparticles (Figure 4.10).

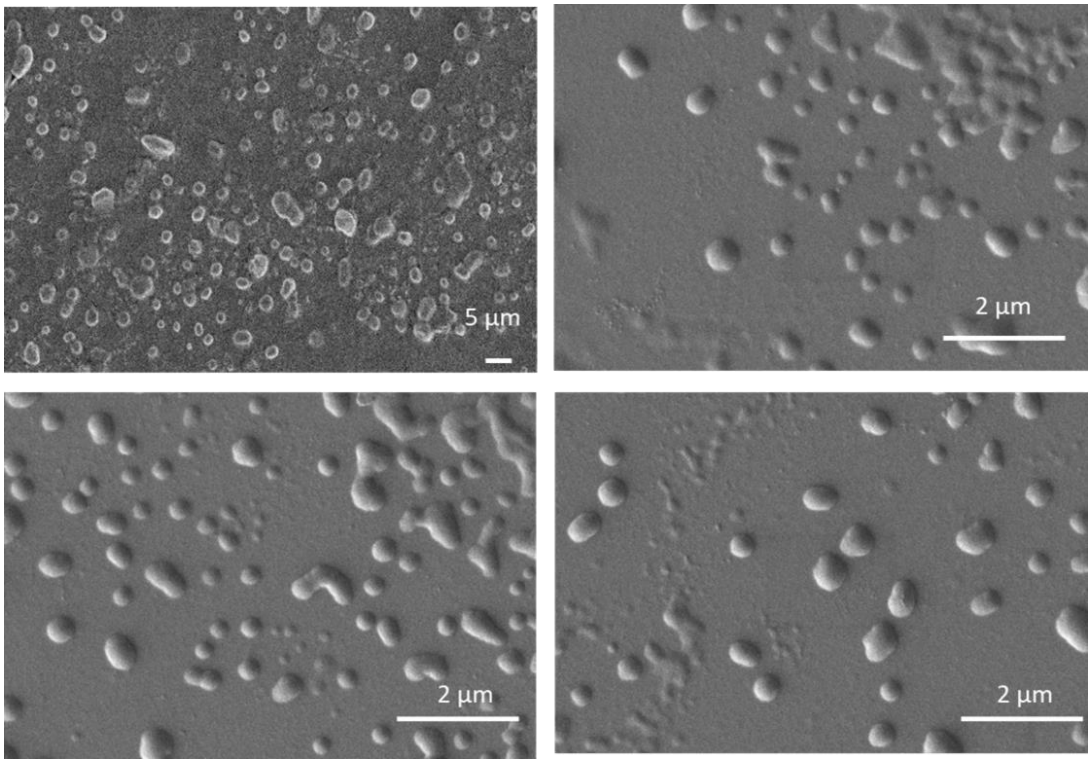


**Figure 4.10** SEM images showing the successful SN-38 encapsulation (5 wt.% drug loading) in p($EHMA_{20}$-co-$EGDMA_{0.85}$): p($PEG_{114}$-*b*-$HPMA_{100}$) nanoparticles at 60:40 wt.% composition, respectively (SEM images obtained at 0.50 mg $mL^{-1}$).

### 4.2.2 Determining the Encapsulation Efficiency of SN-38 Co-nanoprecipitations

When encapsulating SN-38 during a co-nanoprecipitation process it is assumed that all of the drug is located within the core of the branched copolymer nanoparticles. Clearly, it is desirable for this process to be as efficient as possible; however, it is likely that there are small amounts of SN-38 dissolved in the water at the concentration of its thermodynamic equilibrium solubility limit or drug crystals which have not been encapsulated and sedimenting from the saturated aqueous medium. Therefore, quantitative analysis was required in order to evaluate the efficiency and success of the SN-38 encapsulations within the co-nanoprecipitations. The encapsulation efficiency (EE), as described in Equation 4.1, is the concentration of the incorporated material (SN-38) detected in the final formulation divided by the initial concentration used to make the formulation.

$$\mathrm{EE}\ (\%) = \left(\frac{\text{Mass of drug loaded in nanoparticles}}{\text{Total mass of drug loaded}}\right) \times 100 \qquad \textbf{(4.1)}$$

EE was determined by measuring the concentration of SN-38 that remained within the final aqueous nanoparticle dispersion after the nanoparticles were filtered

through an Amicon® ultra-15 centrifugal spin filter tube (MWCO = 30 kDa) and centrifuged (6000 g for 1 hour at 20 °C). The final concentration of SN-38 was determined by monitoring the absorbance at 390 nm using UV-Vis spectroscopy after the water was removed by freeze drying, with a pre-established SN-38 calibration curve (Appendix, Figure A34). The calibration curve was prepared from 8 standard solutions with samples prepared by dissolving the appropriate mass of SN-38 in THF. A linear calibration plot for the above method was obtained over 0 μg $mL^{-1}$ to 15 μg $mL^{-1}$, with a correlation coefficient of 0.99.

The EE was determined for the 2.5 wt.% SN-38 loaded p($BuMA_{100}$-co-EGDMA): p($PEG_{114}$-*b*-$HPMA_{100}$) nanoparticles and both the 2.5 and 5 wt.% SN-38 loaded p($EHMA_{100}$-co-EGDMA):p($PEG_{114}$-*b*-$HPMA_{100}$) nanoparticles. The determined EE values were greater than 98% in all 3 cases. These high values suggest that the SN-38 encapsulation within the branched copolymer co-nanoprecipitates is highly efficient.

### 4.2.3 Studying SN-38-loaded Nanoparticle Formation *via* DLS

As stated earlier, co-nanoprecipitations containing SN-38 using the library of polymers synthesised in Chapter 2, led to either a clear failure, an opalescent dispersion or a turbid aqueous nanoparticle dispersion with no observable particulate material. To study the process of co-nanoprecipitation under these conditions, three combinations of branched and A-B block copolymers were selected with different loadings of SN-38. These were: 1) the opalescent combination of 5 wt.% SN-38 loaded p($HPMA_{100}$-co-$EGDMA_{0.90}$):p($PEG_{114}$-*b*-$HPMA_{100}$), 2) the turbid combination of 5 wt.% SN-38 loaded p($EHMA_{100}$-co-$EGDMA_{0.80}$):p($PEG_{114}$-*b*-$HPMA_{100}$), and the unloaded comparison 3) p($HPMA_{100}$-co-$EGDMA_{0.90}$):p($PEG_{114}$-*b*-$HPMA_{100}$).

During the process of nanoprecipitation and solvent evaporation, DLS analysis was conducted on each sample and compared (Table 4.2). The drug loaded p($EHMA_{100}$-co-$EGDMA_{0.80}$):p($PEG_{114}$-*b*-$HPMA_{100}$) and unloaded p($HPMA_{100}$-co-$EGDMA_{0.90}$): p($PEG_{114}$-*b*-$HPMA_{100}$) co-nanoprecipitations followed a similar trend after addition to water and during the evaporation of THF, leading to monomodal size distributions. Specifically, the hydrodynamic diameters decreased steadily during THF removal

(Figure 4.11), starting at approximately 400 nm for the SN-38 loaded ($EHMA_{100}$-co-$EGDMA_{0.80}$):p($PEG_{114}$-*b*-$HPMA_{100}$) nanoparticles and ending at 180 nm. The unloaded particles comprising p($HPMA_{100}$-co-$EGDMA_{0.90}$):p($PEG_{114}$-*b*-$HPMA_{100}$) decreased from 110 nm to 70nm over the same timescale. The decrease is a result of the initial nanoparticles being swollen with good solvent and collapsing to a final more dense structure as the good solvent is removed. Observation of the same behaviour in presence and absence of SN-38 suggests that the drug substance is compatible with the nanopreciptation timescales, mechanism and environment within ($EHMA_{100}$-co-$EGDMA_{0.80}$):p($PEG_{114}$-*b*-$HPMA_{100}$) combination. Importantly, drug loaded nanoparticles do have a broader size distribution and a larger Dz value which may indicate that the polymer is not fully dominating the process and the drug compound is having a significant influence; however, the distribution was consistent during the evaporation stages.

The behaviour of the p($HPMA_{100}$-co-$EGDMA_{0.90}$):p($PEG_{114}$-*b*-$HPMA_{100}$) nanoprecipitation in the presence of 5 wt% SN-38 is in stark contrast with both the unloaded combination and the loading of SN-38 into p($EHMA_{100}$-co-$EGDMA_{0.80}$):p($PEG_{114}$-*b*-$HPMA_{100}$). Immediately after THF solution addition, a very broad distribution of particles was observed with hydrodynamic diameters of approximately 0.5 μm. The variation in observed hydrodynamic diameter during solvent evaporation was highly irregular although a general trend to smaller values was seen and sedimentation of unstable material was visually observed (Figure 4.12). This suggests a poorly compatible co-nanoprecipitation of polymer and drug, and very inefficient drug encapsulation.

**Table 4.2** DLS analyses of 5 wt.% SN-38 loaded p(HPMA$_{100}$-co-EGDMA$_{0.90}$): p(PEG$_{114}$-b-HPMA$_{100}$), p(EHMA$_{100}$-co-EGDMA$_{0.80}$): p(PEG$_{114}$-b-HPMA$_{100}$) co-nanoprecipitate regimes and non-loaded p(HPMA$_{100}$-co-EGDMA$_{0.90}$): p(PEG$_{114}$-b-HPMA$_{100}$) co-nanoprecipitate over a period of 24 hours.

| Polymer Composition | SN-38 wt.% | Appearance | Time (hour) | $D_z$ (nm)[a] | PDI[a] | Derived Count Rate (kcps)[a] |
|---|---|---|---|---|---|---|
| p(HPMA$_{100}$-co EGDMA$_{0.90}$) | 0 | Turbid | 0 | 110 | 0.055 | 66 350 |
| | | | 1 | 110 | 0.052 | 71 000 |
| | | | 2 | 100 | 0.043 | 43 100 |
| | | | 4 | 95 | 0.045 | 74 250 |
| | | | 5 | 95 | 0.042 | 33 500 |
| | | | 8 | 85 | 0.083 | 64 150 |
| | | | 24 | 70 | 0.049 | 55 000 |
| p(EHMA$_{100}$-co EGDMA$_{0.80}$) | 5 | Turbid | 0 | 400 | 0.188 | 18 900 |
| | | | 1 | 320 | 0.124 | 5200 |
| | | | 2 | 295 | 0.163 | 5600 |
| | | | 4 | 260 | 0.170 | 6400 |
| | | | 5 | 230 | 0.185 | 251 700 |
| | | | 8 | 235 | 0.206 | 122 800 |
| | | | 24 | 180 | 0.210 | 199 300 |
| p(HPMA$_{100}$-co EGDMA$_{0.90}$) | 5 | Opalescence | 0 | 500 | 0.597 | 83 700 |
| | | | 1 | 1215 | 0.938 | 78 550 |
| | | | 2 | 600 | 0.620 | 76 300 |
| | | | 4 | 260 | 0.307 | 60 850 |
| | | | 5 | 415 | 0.498 | 62 600 |
| | | | 8 | 315 | 0.395 | 108 900 |
| | | | 24 | 130 | 0.287 | 69 850 |

[a] Measured using DLS analysis at a concentration of 1 mg mL$^{-1}$.

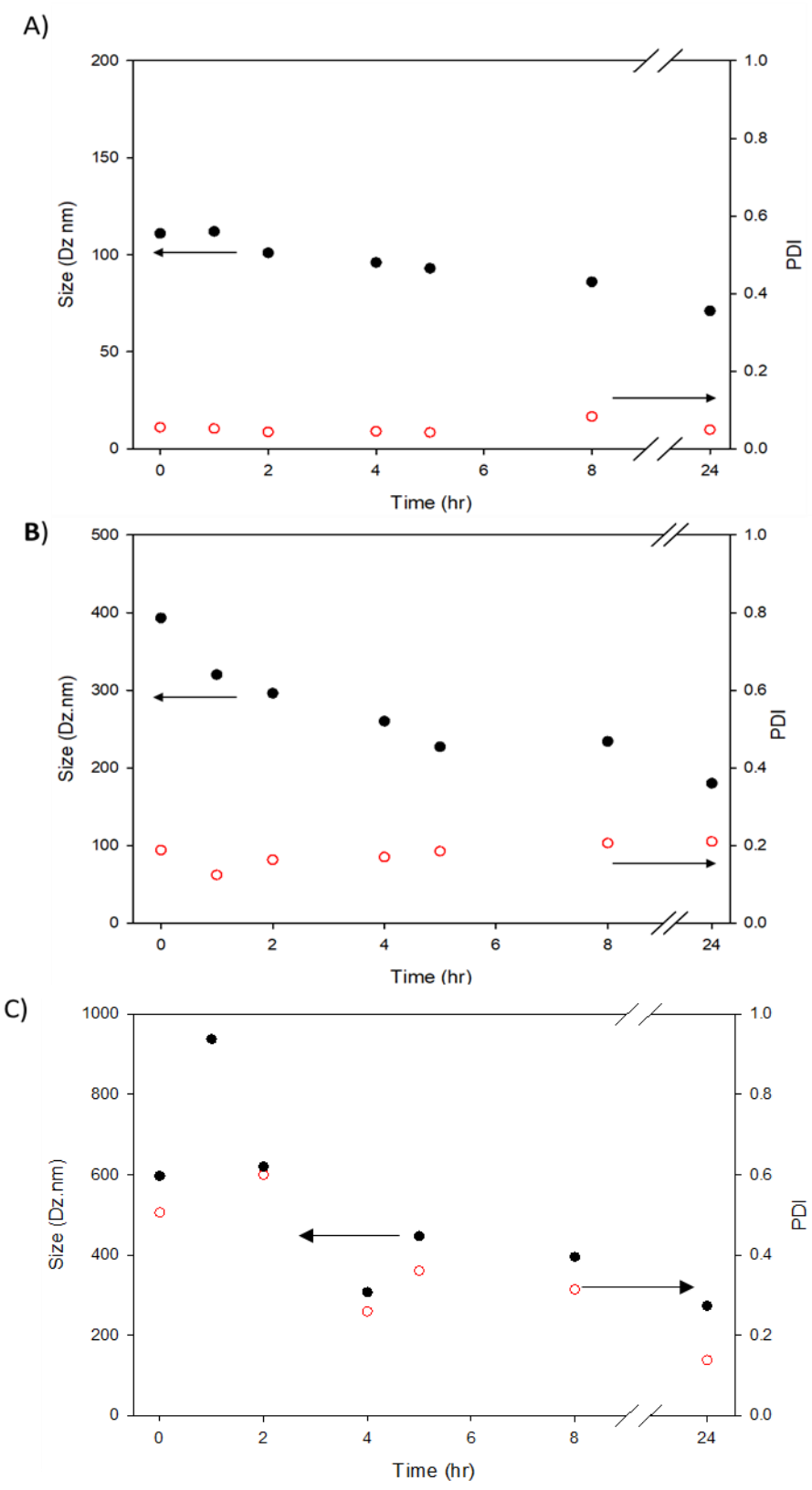


**Figure 4.11** Graphical representation of the changes in hydrodynamic diameter and PDI over 24 hours for A) non-loaded p($HPMA_{100}$-co-$EGDMA_{0.90}$): p($PEG_{114}$-b-$HPMA_{100}$), B) 5 wt. % SN-38 loaded p($EHMA_{100}$-co-$EGDMA_{0.80}$): p($PEG_{114}$-b-$HPMA_{100}$) and C) 5 wt. % SN-38 loaded p($HPMA_{100}$-co-$EGDMA_{0.90}$): p($PEG_{114}$-b-$HPMA_{100}$) co-nanoprecipitate regimes.

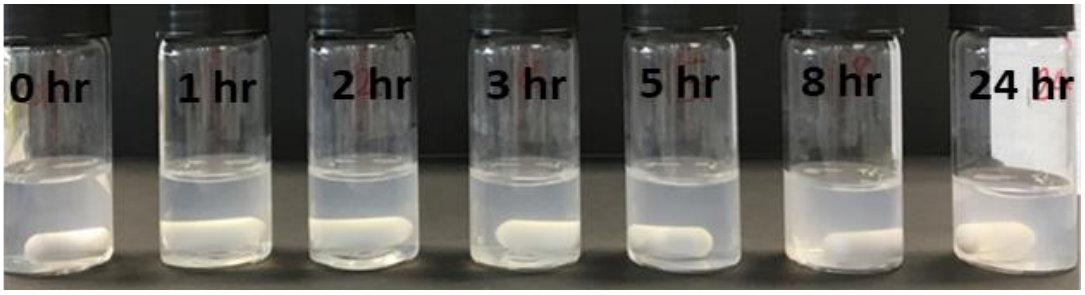


**Figure 4.12** A photograph of 5 wt.% SN-38 loaded p($HPMA_{100}$-co-$EGDMA_{0.90}$): p($PEG_{114}$-b-$HPMA_{100}$) co-nanoprecipitate regime over 24 hours during THF evaporation.

### 4.2.4 Stability of SN-38 Loaded Nanoparticles

The colloidal stability of the SN-38 loaded nanoparticle formulations of p($BuMA_{100}$-co-$EGDMA_{0.95}$):p($PEG_{114}$-*b*-$HPMA_{100}$) (2.5 wt.% SN-38) and p($EHMA_{100}$-co-$EGDMA_{0.80}$):p($PEG_{114}$-*b*-$HPMA_{100}$) (2.5 and 5 wt.% SN-38) was studied by measuring the hydrodynamic diameter, PDI and derived count rate by DLS analysis over a total of 13 weeks of storage (Table 4.3).

**Table 4.3** DLS analyses of SN-38 loaded polymer nanoparticles sterically stabilised with AB block copolymer p($PEG_{114}$-*b*-$HPMA_{100}$) over an extended period of time.

| Nanoparticle Composition | SN-38 wt. % | $D_z$ (nm) [a] | | | PDI | | | Derived count rate (kcps) | | |
|---|---|---|---|---|---|---|---|---|---|---|
| | | Day 1 | Day 8 | Day 91 | Day 1 | Day 8 | Day 91 | Day 1 | Day 8 | Day 91 |
| p($BuMA_{100}$-co-$EGDMA_{0.95}$) | 2.5 | 160 | 160 | 160 | 0.099 | 0.103 | 0.121 | 771 100 | 739 950 | 757 100 |
| p($EHMA_{100}$-co-$EGDMA_{0.80}$) | 2.5 | 175 | 175 | 170 | 0.123 | 0.117 | 0.103 | 706 450 | 836 900 | 767 000 |
| | 5 | 180 | 180 | 175 | 0.177 | 0.125 | 0.134 | 758 450 | 836 900 | 829 350 |

[a] Measured using DLS analysis at a concentration of 1 mg $mL^{-1}$.

Nanoparticle dispersions were stored under ambient conditions out of direct light. In general, monomodal size distributions were observed throughout the storage period (Figure 4.13) and the aqueous SN-38 loaded nanoparticle dispersions remained turbid and free from visible aggregation or drug-crystal formation.

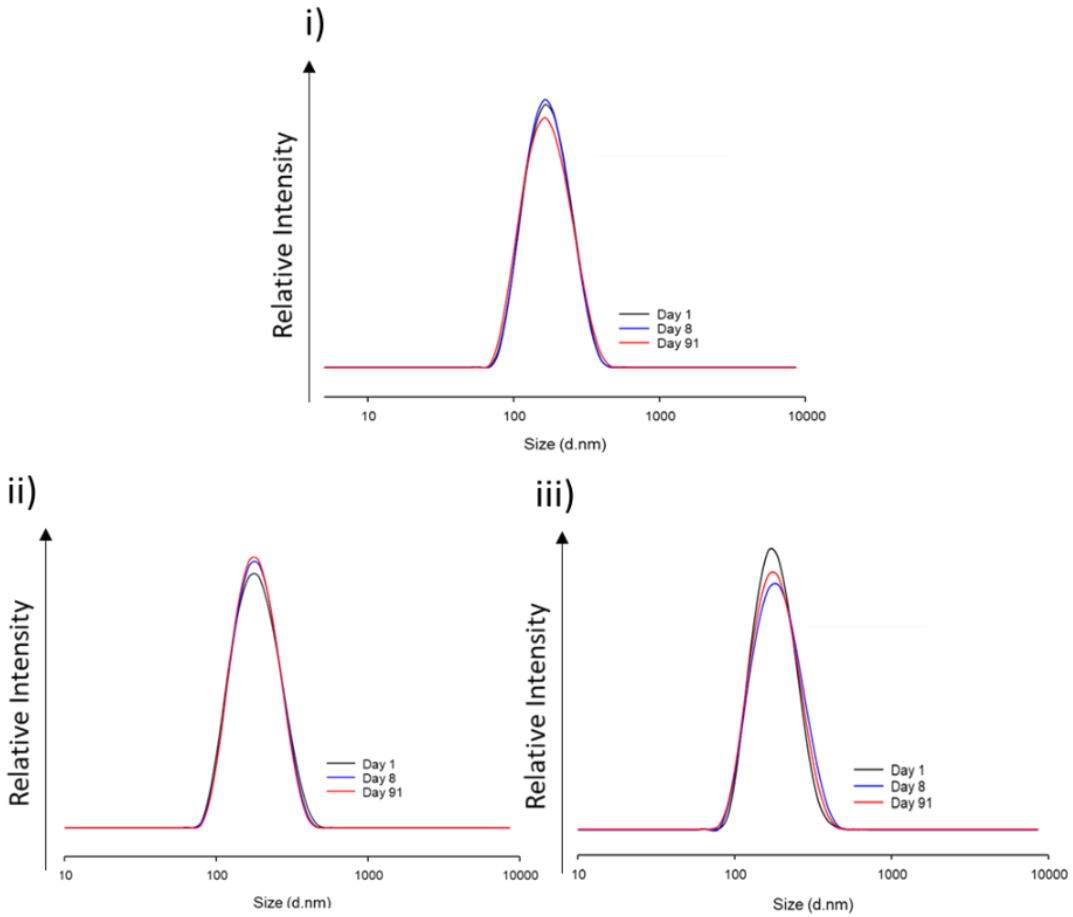


**Figure 4.13** Overlaid DLS size distribution by intensity traces for SN-38 loaded polymer nanoparticles i) p(BuMA$_{100}$-co-EGDMA$_{0.95}$): p(PEG$_{114}$-*b*-HPMA$_{100}$) (2.5 wt.% SN-38), ii) p(EHMA$_{100}$-co-EGDMA$_{0.80}$): p(PEG$_{114}$-*b*-HPMA$_{100}$) (2.5 wt.% SN-38) and iii) p(EHMA$_{100}$-co-EGDMA$_{0.80}$): p(PEG$_{114}$-*b*-HPMA$_{100}$) (5 wt.% SN-38) from day 1, day 8 and 13 weeks.

There was almost no deviation in measured hydrodynamic diameter, PDI and derived count rate compared to the original samples that were measured. These observations confirmed that the SN-38 loaded nanoparticles remained colloidally stable over extended periods of time, as observed for non-drug loaded nanoparticles (Chapter 3.5). The data suggests that the particles maintain their structural integrity during storage and, presumably, after administration which is clearly of importance for DDS. As a comparison, it has been shown that Doxil takes approximately 3-7 days for peak level of drug accumulation within a tumour[46] and other literature reports have shown changes in DDS sizes in much shorter timeframes (< 7 days).[47] Slight decreases in zeta potential values were observed for all 3 of the SN-38 loaded polymer systems from day 1 to day 91. For example, the zeta potential of p(BuMA$_{100}$-co-EGDMA$_{0.95}$):p(PEG$_{114}$-*b*-HPMA$_{100}$) (2.5 wt.% SN-38) decreased from -7.29 mV (day

1) to -11.3 mV (day 91), and that of p(EHMA$_{100}$-co-EGDMA$_{0.80}$):p(PEG$_{114}$-*b*-HPMA$_{100}$) (5 wt.% SN-38) decreased from -12.4 mV (day 1) to -14.2 mV (day 91). These variations are too small to be considered significant.

### 4.2.5 Reproducibility of SN-38 Loaded Nanoparticles

Polymer nanoparticle production is often associated with having poor batch-to-batch variability. Clearly, this is a disadvantage for robust clinical translation as its poor reproducibility will potentially lead to variable pharmacokinetics. It was of importance to check the reproducibility of the SN-38 loaded polymer nanoparticles; therefore, three repeats of the 5 wt.% SN-38 loaded p(EHMA$_{100}$-co-EGDMA$_{0.80}$):p(PEG$_{114}$-*b*-HPMA$_{100}$) co-nanoprecipitations (60:40 wt.%) were conducted under identical conditions, as previously described, but using three different stock solutions to model different manufacturing batches. In all cases, turbid aqueous nanoparticle dispersions were obtained, which were analysed *via* DLS and zeta potential measurements (Table 4.4). Monomodal size distributions were obtained in all cases, with identical hydrodynamic diameters ($D_z$ = 180 nm) and the PDI values varied between 0.167 – 0.196. Zeta potential measurements were all consistent and in the range of -11.3 to -14.2 mV. The results that were obtained suggest that there is very little batch-to-batch variability between the polymer nanoparticles and their physical characteristics.

**Table 4.4** DLS and zeta potential analyses of 5 wt. % SN-38 loaded p(EHMA$_{100}$-co-EGDMA$_{0.80}$): p(PEG$_{114}$-*b*-HPMA$_{100}$) nanoparticles that were prepared from three different stock solutions.

| Polymer Composition | SN-38 wt.% | Stock number | $D_z$ (nm)[a] | PDI[a] | Derived Count Rate (kcps)[a] | ζ (mV)[b] |
|---|---|---|---|---|---|---|
| p(EHMA$_{100}$-co-EGDMA$_{0.80}$): p(PEG$_{114}$-*b*-HPMA$_{100}$) | 5 | 1 | 180 | 0.167 | 628 900 | -11.3 |
| | | 2 | 180 | 0.189 | 744 600 | -12.4 |
| | | 3 | 180 | 0.196 | 699 750 | -14.2 |

[a] Measured using DLS analysis at a concentration of 1 mg mL$^{-1}$.$D_z$ values have been rounded to the nearest 5 nm.
[b] Obtained via measurement of the electrophoretic mobility of aqueous nanoparticle dispersions within zeta cell.

### 4.2.6 Preparation of SN-38 Loaded Nanoparticles Using Statistical Branched Copolymers

The effect of the branched copolymer composition on the degree of SN-38 encapsulation was studied by incorporating statistical branched copolymers within

the co-nanoprecipitation process whilst targeting a 5 wt.% drug loading. For these experiments, the following SN-38 encapsulated co-nanoprecipitated particles were targeted: 1) p(BuMA$_{50}$-*s*-EHMA$_{50}$-co-EGDMA$_{0.95}$), 2) p(BuMA$_{50}$-*s*-HPMA$_{50}$-co-EGDMA$_{0.90}$) and 3) p(HPMA$_{50}$-*s*-EHMA$_{50}$-co-EGDMA$_{0.95}$). All were co-nanoprecipitated with 3 AB block copolymers: p(PEG$_{114}$-*b*-BuMA$_{100}$), p(PEG$_{114}$-*b*-EHMA$_{100}$) and p(PEG$_{114}$-*b*-HPMA$_{100}$) (Figure 4.14).

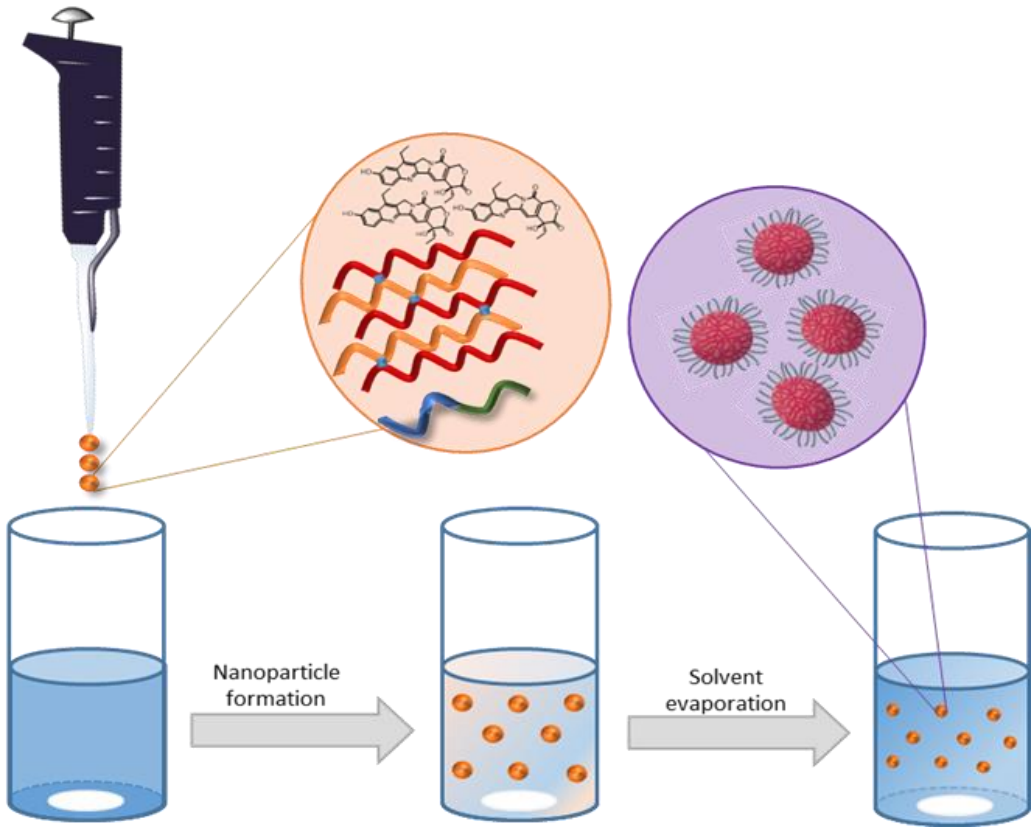


**Figure 4.14** Schematic representation of the co-nanoprecipitation of branched statistical copolymers and AB block copolymers with SN-38 to produce SN-38 loaded branched vinyl copolymer nanoparticles.

SN-38 was prepared, as before, in a THF stock solution (1 mg mL$^{-1}$) that was allowed to equilibrate for 24 hours before addition to the polymer-THF solutions. When this polymer/SN-38 THF stock was co-nanoprecipitated into water, the concentrations of the polymer and drug were $[P]_f$ = 1 mg mL$^{-1}$ and [SN-38] = 0.05 mg mL$^{-1}$. In all cases, the addition of the polymer/SN-38 THF solution resulted in the instantaneous formation of a turbid mixture. The mixtures were left to stir for 24 hours at ambient temperature for THF evaporation and the success of the co-nanoprecipitation was determined by visual observations as previously described. All samples co-nanoprecipitated with p(PEG$_{114}$-*b*-EHMA$_{100}$) resulted in the formation of visual

aggregation, as previously observed (Chapter 4.2.1). In all other cases, except for p(BuMA$_{50}$-*s*-HPMA$_{50}$-co-EGDMA$_{0.90}$):p(PEG$_{114}$-*b*-HPMA$_{100}$), the co-nanoprecipitations resulted in the formation of an opalescent sample, suggesting that the formation of polymeric nanoparticles but the inefficient encapsulation of SN-38. These samples were analysed *via* DLS for information (Table 4.5).

**Table 4.5** DLS analyses of 5 wt.% SN-38 loaded statistical branched copolymers co-nanoprecipitated with varying AB block copolymers (60:40 wt.% respectively).

| | | AB Block Copolymer (40 wt.%) | | | | | | | | |
|---|---|---|---|---|---|---|---|---|---|---|
| | | p(PEG$_{114}$-*b*-BuMA$_{100}$) | | | p(PEG$_{114}$-*b*-EHMA$_{100}$) | | | p(PEG$_{114}$-*b*-HPMA$_{100}$) | | |
| Polymer Composition | SN-38 wt. % | $D_z$ (nm)[a] | PDI[a] | Derived Count Rate (kcps)[a] | $D_z$ (nm)[a] | PDI[a] | Derived Count Rate (kcps)[a] | $D_z$ (nm)[a] | PDI[a] | Derived Count Rate (kcps)[a] |
| p(BuMA$_{50}$-*s*-EHMA$_{50}$-co-EGDMA$_{0.95}$) | 5 | 100 | 0.318* | 139 100 | Polymer Aggregate | | | 180 | 0.250* | 338 900 |
| p(BuMA$_{50}$-*s*-HPMA$_{50}$-co-EGDMA$_{0.90}$) | 5 | *120* | *0.073* | *656 750* | Polymer Aggregate | | | 150 | 0.270* | 331 900 |
| p(HPMA$_{50}$-*s*-EHMA$_{50}$-co-EGDMA$_{0.95}$) | 5 | 100 | 0.318* | 139 200 | Polymer Aggregate | | | 165 | 0.258* | 399 200 |

[a] Measured using DLS analysis at a concentration of 1 mg mL$^{-1}$. * Sample was opalescent and secondary peak present within particle size distribution.

The hydrodynamic diameters obtained for these opalescent samples ranged between 100 ≤ $D_z$ ≤ 180 nm and the recorded PDI values were relatively high (PDI ≥ 0.250). In addition, all samples also contained a secondary peak in the particle size distribution at approximately 5 µm, although the intensity of this peak was significantly less than that of the main population.

The SN-38 loaded p(BuMA$_{50}$-*s*-HPMA$_{50}$-co-EGDMA$_{0.90}$):p(PEG$_{114}$-*b*-HPMA$_{100}$) sample produced nanoparticles with a monomodal size distribution, hydrodynamic diameter of 120 nm and a PDI of 0.073. Long term stability (> 70 days) was also seen for this sample, as shown by the negligible deviation in hydrodynamic diameter (Figure 4.15). This is an interesting observation since the corresponding homopolymers did not successfully encapsulate 5 wt. % SN-38 under the same conditions. This further

suggest that the environment of the core of the nanoparticles is very important for the successful encapsulation of SN-38.

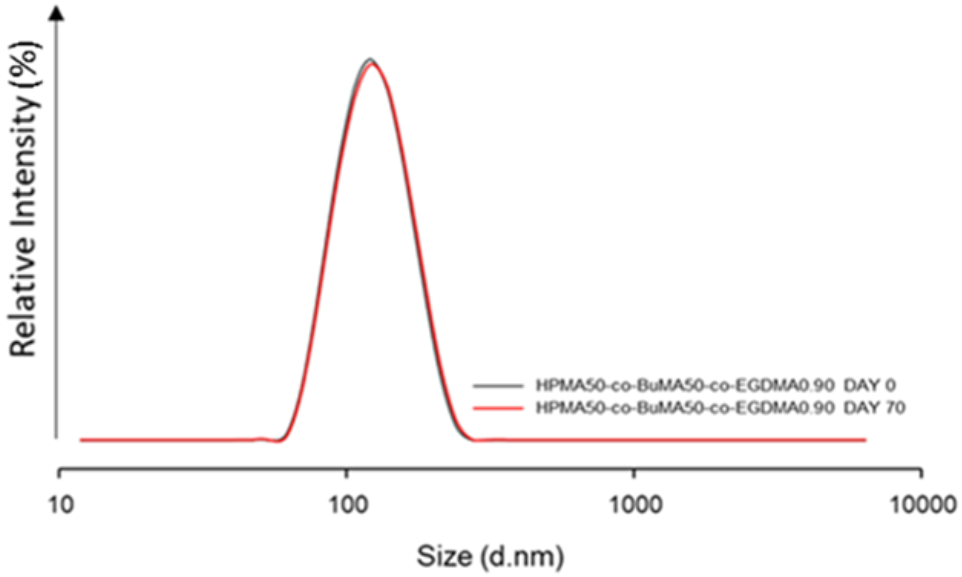


**Figure 4.15** Overlaid DLS size distribution by intensity for 5 wt.% SN-38 loaded p(BuMA$_{50}$-*s*-HPMA$_{50}$-co-EGDMA$_{0.90}$): p(PEG$_{114}$-*b*-HPMA$_{100}$) 60:40 wt. % respectively at day 0 and day 70.

### 4.2.7 Preparation of SN-38 Loaded Nanoparticles Using EHMA Based Branched Polymers with Varying Divinyl Monomer Chemistries

The encapsulation of SN-38 within branched copolymers consisting of EHMA monomer residues at DP 20 and 100 but with varying divinyl monomer residue chemistry was also studied to understand the potential role for drug compatibilization by the branching monomer. Co-nanoprecipitations were conducted as before with p(PEG$_{114}$-*b*-HPMA$_{100}$) as the stabilising block copolymer and a ratio of branched copolymer:AB block polymer of 60:40 wt.%. All of the co-nanoprecipitations were successful in forming colloidally stable nanoparticles encapsulating 5 wt.% SN-38. Analysis *via* DLS showed monomodal particle size distributions for all of the aqueous nanoparticle dispersions (Table 4.6).

**Table 4.6** DLS and zeta potential analyses of 5 wt.% SN-38 loaded aqueous nanoparticle dispersions produced *via* co-nanoprecipitation of the AB block copolymer, p($PEG_{114}$-b-$HPMA_{100}$), with branched p(EHMA) varying in divinyl monomer residue chemistry of with varying primary polymer chain length of DP20 and DP100 monomer units.

| | | $PEG_{114}$-*b*-$HPMA_{100}$ | | | |
|---|---|---|---|---|---|
| **Polymer Composition** | **SN-38 wt. %** | **$D_z$ (nm) [a]** | **PDI [a]** | **Derived Count Rate (kcps) [a]** | **Zeta Potential (mV)[b]** |
| p($EHMA_{100}$-co-$BPDMA_{0.85}$) | 5 | 195 | 0.279 | 447 000 | -14.4 |
| p($EHMA_{100}$-co-$GDMA_{0.85}$) | 5 | 185 | 0.234 | 821 300 | *-20.4* |
| p($EHMA_{100}$-co-$BPGDMA_{0.80}$) | 5 | 180 | 0.238 | 806 150 | -15.9 |
| p($EHMA_{100}$-co-$UDMA_{0.85}$) | 5 | 190 | 0.243 | 693 850 | -15.8 |
| p($EHMA_{100}$-co-$DSDMA_{0.75}$) | 5 | 190 | 0.200 | 781 150 | -13.8 |
| p($EHMA_{20}$-co-$BPDMA_{0.85}$) | 5 | 180 | 0.258 | 455 300 | -14.1 |
| P($EHMA_{20}$-co-$GDMA_{0.85}$) | 5 | 185 | 0.296 | 673 900 | -16.3 |
| p($EHMA_{20}$-co-$BPGDMA_{0.80}$) | 5 | 180 | 0.202 | 729 500 | -14.6 |
| p($EHMA_{20}$-co-$UDMA_{0.85}$) | 5 | 195 | 0.270 | 759 000 | -15.5 |
| p($EHMA_{20}$-co-$DSDMA_{0.75}$) | 5 | 180 | 0.221 | 511 300 | -20.8 |

[a]Measured using DLS analysis at a concentration of 1 mg $mL^{-1}$. [b] Obtained *via* measurement of the electrophoretic mobility within zeta cell.

Drug-loaded nanoparticle dispersions were produced with similar hydrodynamic diameters ($180 \leq D_z \leq 195$ nm) and polydispersity values ($0.200 \leq PDI \leq 0.296$). Comparing these hydrodynamic diameters with that of their unloaded counterparts showed only minor differences in particle size. In all cases, the obtained zeta potential values were relatively low (-13.8 to -20.8 mV), which indicates that colloidal stability was achieved primarily through steric stabilisation. Again, when compared to the range obtained for the comparative blank (no SN-38) polymer nanoparticles (-8.58 to -13.5 mV), a slight decrease (i.e. more negative) zeta potential was observed, although these differences are not highly significant. This may be due to a portion of SN-38 present on the surface of the nanoparticles. Due to the equilibrium between the two forms of SN-38, closed lactone and open carboxylate, this in turn may increase the concentration of charged groups that exist at the nanoparticle surface.

### 4.3 Optimising Drug Loading with Co-nanoprecipitated particles

When considering DDS and how effective they are, drug loading is one of the key characteristics which should be considered. Drug loading refers to the mass of drug present with respect to the total mass of solids which contribute to making polymer nanoparticles. The drug loading can be influenced by the physical and chemical properties of the DDS and, ideally, the drug loading should be as high as possible. High drug loadings, have a range of advantages such as: lower administered dosing volume and a lower concentration of excipients/polymers relative to the dosed drug. Additionally, a high drug loaded nanoparticle dispersion can deliver more active drug to the tumour per particle and may offer improvements to the efficiency and efficacy.[48] However, a challenge that is often associated with polymer nanoparticles is the low drug loading values which plague their development. Often in literature, improvements to the drug loading have required different materials or excipients which can impart specific polymer-drug interactions such as donor-acceptor interactions[49], hydrogen bonding[50] and π–π interactions[51]. In studies described above, drug loadings of 5 wt. % SN-38 have been achieved with the polymers studied here (Section 4.2.1); however, there is a need to establish the range of drug loadings that may be available in order to optimise the clinical relevance of the materials under investigation.

#### 4.3.1 Increased SN-38 Concentrations within the Co-nanoprecipitation

To increase the drug loading of SN-38 within the polymer nanoparticles without material manipulation or compositional changes simply involved increasing the concentration of SN-38 within the SN-38/polymer THF stock solutions over a range of values. Since p($EHMA_{100}$-co-$EGDMA_{0.80}$):p($PEG_{114}$-*b*-$HPMA_{100}$) had proven successful with the incorporation of 5 wt.% SN-38, it was used to study whether higher drug loadings could be achieved. Co-nanoprecipitations were conducted as before using a range of targeted drug loadings: 2.5, 5, 6, 7.5, 10, 20 and 30 wt.%. Immediately following the addition of the stock solutions into water, the initial observations were that turbid dispersions were formed. However, after the evaporation of THF, visible differences between the samples were observed. Samples with drug loadings ≥ 10 wt.% had a white precipitate on the side of each vial, which became more significant as the targeted drug loading increased (Figure 4.16 iv and

v) and may be attributed to free SN-38 that was not successfully encapsulated within the polymer nanoparticles. This white precipitate was not observed for the samples with targeted loadings of ≤ 7.5 wt.% SN-38.

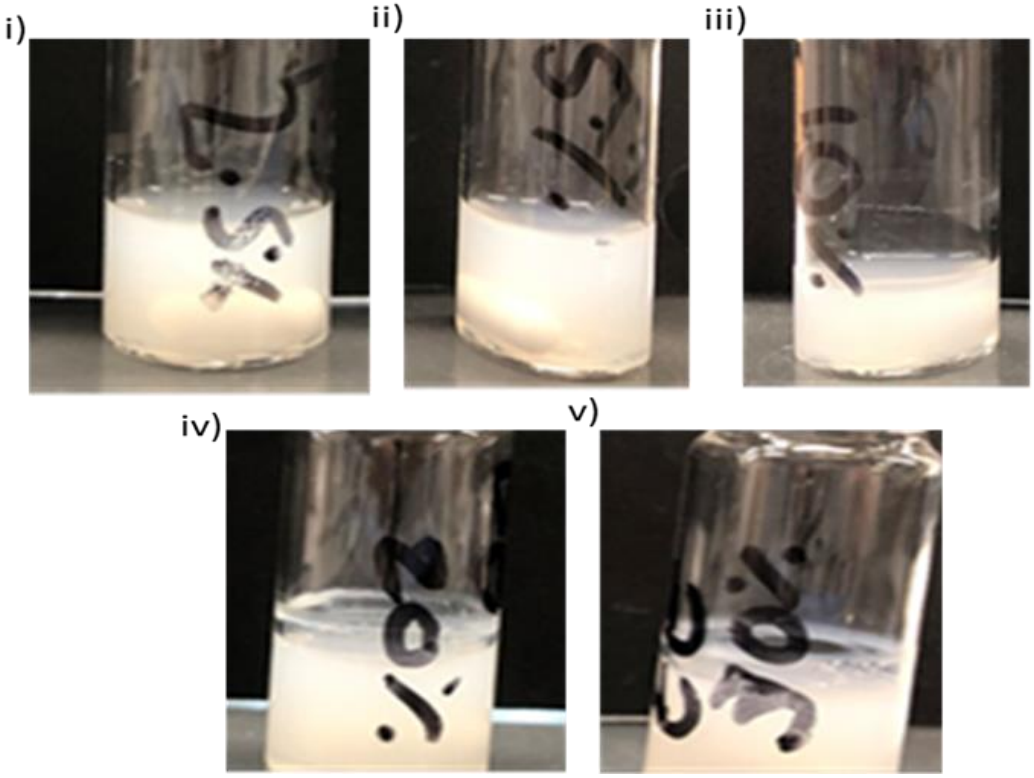


**Figure 4.16** Photographs of p($EHMA_{100}$-co-$EGDMA_{0.80}$): p($PEG_{114}$-*b*-$HPMA_{100}$) co-nanoprecipitations targeting various drug loadings of SN-38, varying from i) 2.5, ii) 5, iii) 10, iv) 20 and v) 30 wt.% SN-38.

The aqueous nanoparticle dispersions were analysed without filtration *via* DLS and zeta potential measurements (Table 4.5).

**Table 4.5** DLS analyses of p($EHMA_{100}$-co-$EGDMA_{0.80}$) branched vinyl copolymer nanoparticle dispersions formed *via* co-nanoprecipitation with $PEG_{114}$-*b*-p$(HPMA)_{100}$. Drug loadings varied between 2.5 and 30 wt.% wrt. total solid mass.

| Polymer Composition | SN-38 (wt.%) | $D_z$ (nm)[a] | PDI[a] | Derived Count Rate (kcps) | ζ(mV)[b] |
|---|---|---|---|---|---|
| p($EHMA_{100}$-co-$EGDMA_{0.80}$) : p($PEG_{114}$-*b*-$HPMA_{100}$) | 2.5 | 175 | 0.123 | 706 450 | -11.9 |
| | 5 | 180 | 0.164 | 760 300 | -12.4 |
| | *6** | *195* | *0.264* | *564 800* | *-12.5* |
| | *7.5** | *215* | *0.288* | *771 550* | *-12.3* |
| | *10** | *220* | *0.305* | *829 600* | *-12.6* |
| | *20** | *245* | *0.481* | *774 300* | *-13.4* |
| | *30** | *320* | *0.736* | *622 000* | *-14.9* |

[a] Measured using DLS analysis at a concentration of 1 mg $mL^{-1}$. [b] Obtained *via* measurement of the electrophoretic mobility in 0.01M KCl aqueous nanoparticle dispersions. *DLS particle size distributions were not monomodal.

The results showed that as the targeted drug loadings increased from 2.5 to 30 wt.%, the Dz increased from 175 to 320 nm and the PDI increased from 0.123 to 0.736. It is worth highlighting that samples targeting ≥ 6 wt.% SN-38 did not possess monomodal particle size distributions, as there was a presence of additional peaks between 1000-5000 nm (Figure 4.17). Although these additional peaks were representative of populations that are low in number, their intensities increased significantly as higher drug loadings were targeted and consequently had a greater bearing on the calculated PDI values.

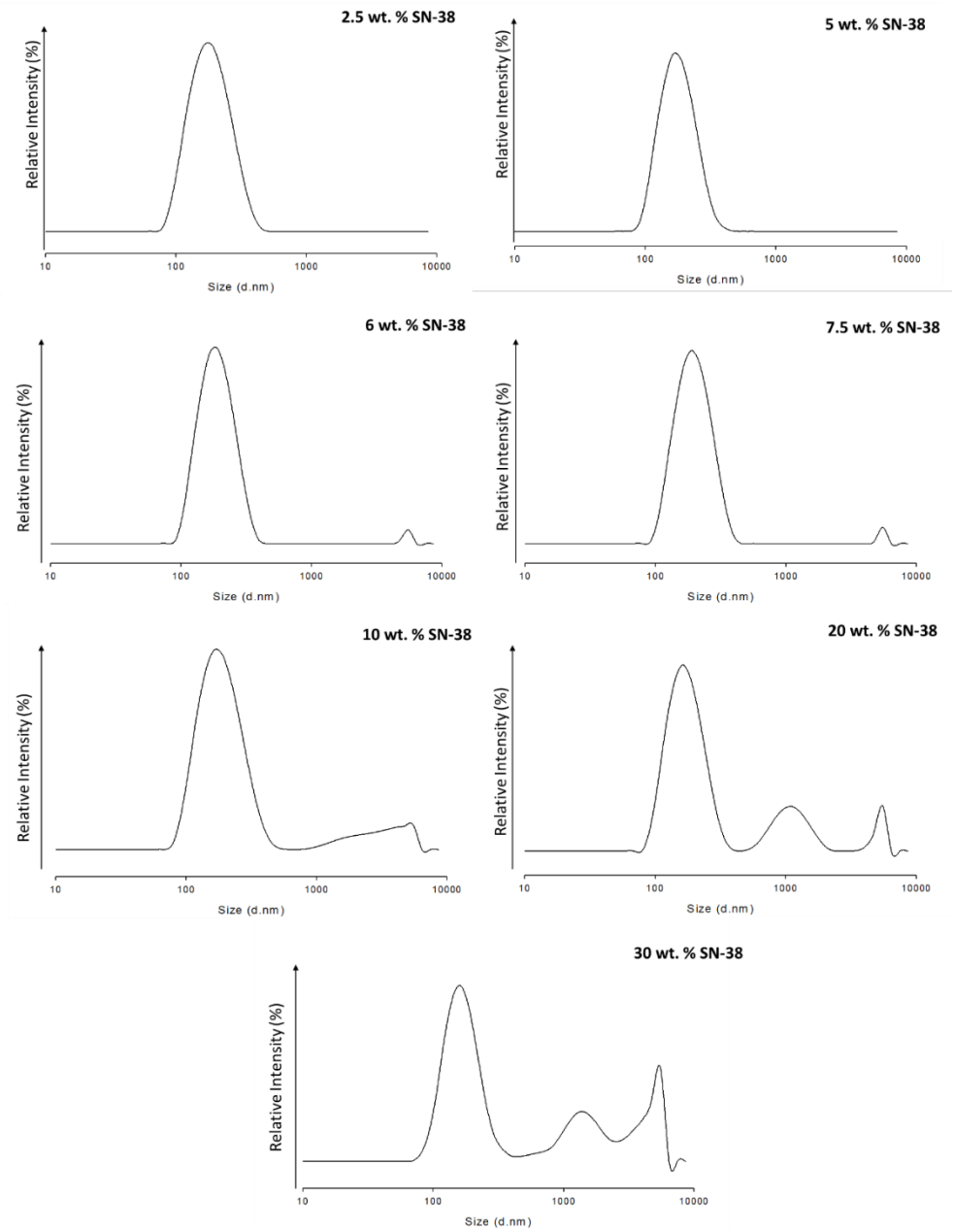


**Figure 4.17** DLS analyses of the SN-38 loaded p(EHMA$_{100}$-co-EGDMA$_{0.80}$): p(PEG$_{114}$-*b*-HPMA$_{100}$) at 60:40 wt. % co-nanoprecipitate regimes with increasing drug loading from 2.5 - 30 wt. %.

The zeta potential measurements were in the range of -11.9 to -14.9 mV, which also increased in negativity as the drug loading increased but show no meaningful differences.

The co-nanoprecipitates targeting the various drug loadings were also studied using SEM (Figure 4.18).

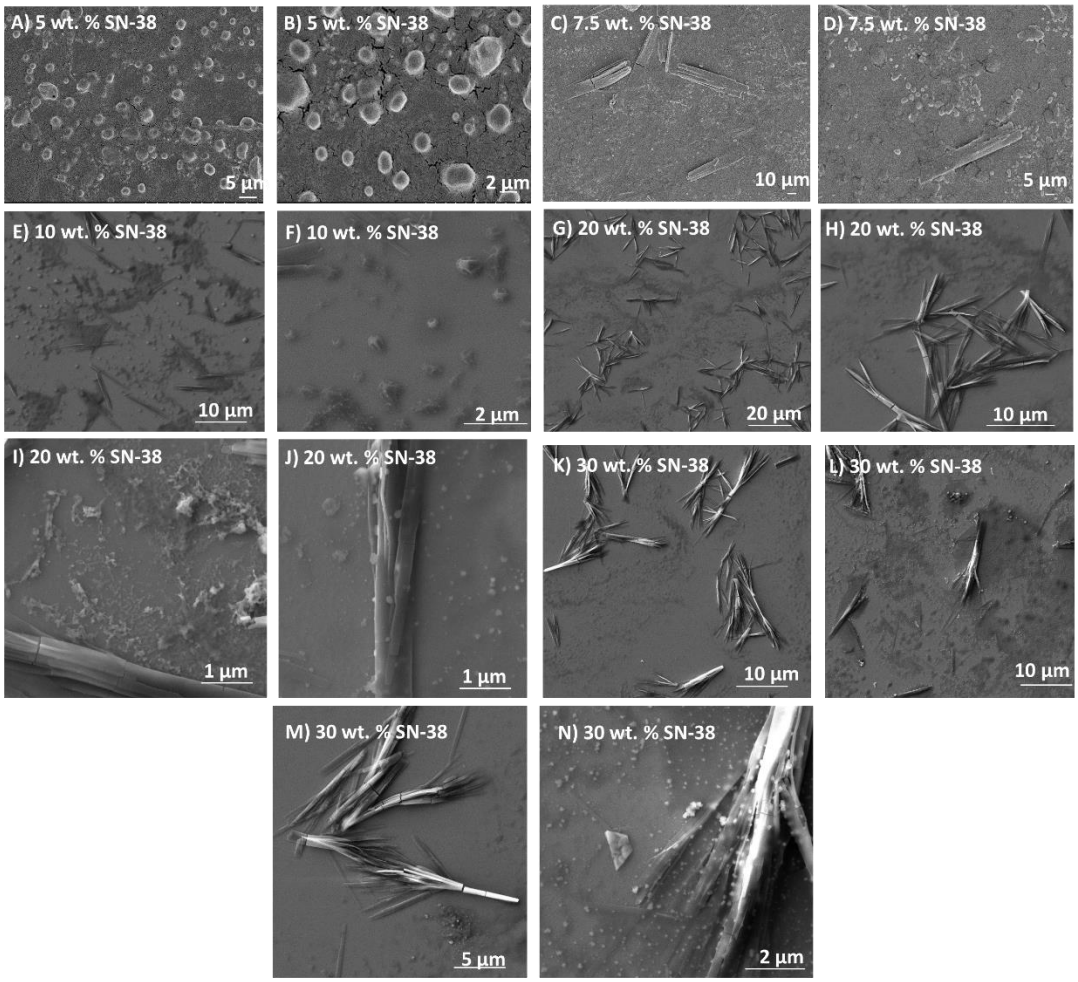


**Figure 4.18** SEM images of SN-38 loaded p(EHMA$_{100}$-co-EGDMA$_{0.80}$): p(PEG$_{114}$-*b*-HPMA$_{100}$) at 60:40 wt. % co-nanoprecipitate regimes. Images obtained of A+B) 5 wt.%, C+D) 7.5 wt.%, E+F) 10 wt.%, G-J) 20 wt.% and K-N) 30 wt.%.

Images obtained for the samples targeting ≤5 wt.% SN-38 showed near-spherical nanoparticles and SN-38 crystals were not observed, suggesting that the SN-38 encapsulations had high efficiency and that there were very low concentrations of free SN-38 within the aqueous phase of the dispersion.

This is consistent with the high encapsulation efficiency values that were determined. However, as the drug loading increased beyond 5 wt.%, long spindle-like crystals

appeared in addition to the polymer nanoparticles, the concentration of which increased as higher loadings were targeted. Whilst it is likely that these crystals are associated with SN-38 that had not been encapsulated and were present as drug crystals in the aqueous dispersion, the crystals could also be as a result of the drying phase of the SEM sample preparation.

Although EE of these co-nanoprecipitations were not determined experimentally, the results of this study strongly suggest that the maximum drug loading that can be successfully achieved is 5 wt.% SN-38. When targeting loadings above this value, a limit to the encapsulation appears to be reached resulting in the formation of multiple populations comprising polymer nanoparticles and free drug crystals. The reasons for this failure may well be due to a saturation of the available polymer encapsulation capacity and the uncontrolled nucleation and growth of SN-38. Additionally, particle density has been reported to have an influence on the degree of encapsulation of hydrophobic guest molecules.[52] Calculations completed by Ribeiro and co-workers on coumarin-6 loaded PCL nanoparticles suggest that the assemblies are loosely packed and represent soft structures compared to hard compact spheres. If this is applicable to the polymer system described here, and the polymer chains are loosely packed, they could be highly swollen by water molecules thereby limiting the degree of encapsulation of SN-38.

### 4.3.2 Varying the Poor Solvent pH during Co-nanoprecipitation and its effects on the Drug Loading

As previously discussed, SN-38 exists in an equilibrium between two forms at pH 7; a closed-ring lactone form and an open-ring carboxylate form. The lactone form is more hydrophobic than the carboxylate form and therefore, has a lower solubility in water.[53, 54] It was hypothesised that through manipulating the pH of the water used in the co-nanoprecipitation process, this could impact the relative concentrations of these two forms; if the pH of the water was acidic, the closed-lactone ring would be present and its greater hydrophobicity would enhance the encapsulation of SN-38 and potentially increase the drug loading. This hypothesis was tested by acidifying the aqueous poor solvent phase to pH 4 before conducting co-nanoprecipitations targeting a 5 wt.% SN-38 loading. However, the results in all cases caused a disruption

to the co-nanoprecipitation process and therefore wasn't studied in any greater detail. It is not clear why the pH was so disruptive to the formation of nanoprecipitated particles; however, the presence of a small concentration of carboxylic acid groups may enable the stabilisation and compatibility of SN-38 during precipitation.

### 4.3.3 Evaluation of SN-38 Pro drugs as options for increased Drug Loadings: SN-38 Pentanoate

Within the literature it has been shown that specific chemical modifications of SN-38 can result in enhanced solubility or lipophilicity of pro-drug formulations compared to their parent compound. These simple chemical modifications involved the esterification at the $C_{10}$ position of SN-38 with different fatty acids of varying length of hydrocarbon chains.[55] It was therefore hypothesised that such lipophilic pro-drugs of SN-38 may enable a more efficient encapsulation within the co-nanoprecipitation process and offer an opportunity to increase the drug loading of the active component, SN-38. This hypothesis was investigated by incorporating SN-38 pentanoate within co-nanoprecipitations of the AB block copolymer, p($PEG_{114}$-*b*-$HPMA_{100}$), and various branched vinyl copolymers. SN-38 pentanoate was synthesised by Dr Andrew Dwyer through the esterification of SN-38 and valeroyl chloride in anhydrous THF, using 4-dimethylaminopyridine (DMAP) as a catalyst and N,N-diisopropylethylamine (DIPEA) as a base (Figure 4.20).

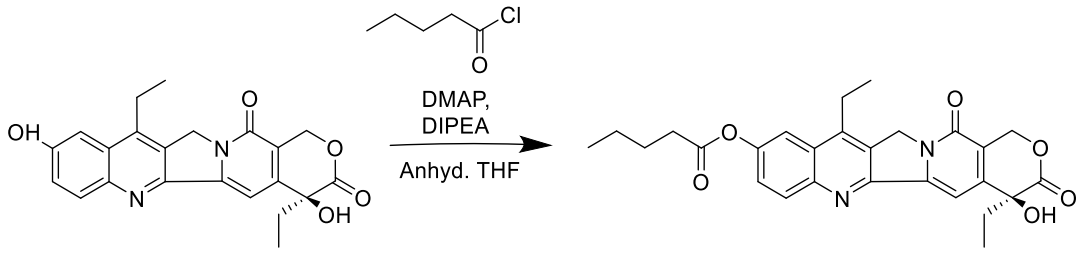


**Figure 4.20** Reaction scheme of the esterification of SN-38 to SN-38 pentanoate.

Andrew is a post-doctoral research associate working in the department of chemistry at the University of Liverpool and was preparing such materials for the use in a different project. He kindly synthesised and supplied SN-38 pentanoate for the use within this experiment.

Co-nanoprecipitations were conducted with the following combinations of polymers: p(BuMA$_{100}$-co-EGDMA$_{0.95}$), p(EHMA$_{100}$-co-EGDMA$_{0.80}$) and p(HPMA$_{100}$-co-EGDMA$_{0.90}$) were each co-nanoprecipitated with the AB block copolymer p(PEG$_{114}$-*b*-HPMA$_{100}$) at a 60:40 wt.% composition. SN-38 pentanoate was incorporated into the co-nanoprecipitations with a targeted drug loading of 2.5 and 5 wt.%. The SN-38 pentanoate/polymer THF stock solution (1 mL) was added to stirred DI water (5 mL). Samples were left for 24 hours to allow for THF evaporation. After evaporation, those samples that did not contain any visible aggregation were analysed *via* DLS and zeta potential measurements (Table 4.6).

**Table 4.6** DLS analyses of SN-38 pentanoate loaded branched vinyl copolymer nanoparticle dispersions formed *via* co-nanoprecipitation with AB block copolymer, p(PEG$_{114}$-*b*-HPMA$_{100}$). Targeted drug loadings of 2.5 and 5 wt.% wrt. total solid mass.

| | | p(PEG$_{114}$-*b*-HPMA$_{100}$) | | | |
|---|---|---|---|---|---|
| **Polymer Composition** | **SN-38 wt. %** | **$D_z$ (nm)[a]** | **PDI[a]** | **Derived Count Rate (kcps)[a]** | **ζ(mV)[b]** |
| p(EHMA$_{100}$-co-EGDMA$_{0.80}$) | 2.5 | 155 | 0.092 | 801 500 | -14.3 |
| p(BuMA$_{100}$-co-EGDMA$_{0.95}$)* | 2.5 | 160 | 0.145 | 816 350 | -15.2 |
| p(BuMA$_{100}$-co-EGDMA$_{0.95}$)* | 5 | 180 | 0.190 | 855 150 | -16.3 |

[a] Measured using DLS analysis at a concentration of 1 mg mL$^{-1}$. $D_z$ values obtained have been rounded to the nearest 5 nm. *Secondary peak present on size distribution by intensity (Figure 4.21B).

SN-38 pentanoate loaded branched vinyl nanoparticles were produced with hydrodynamic diameters in the range of 155 ≤ $D_z$ ≤ 180 nm and PDI values between 0.092 – 0.190. The co-nanoprecipitate of p(EHMA$_{100}$-co-EGDMA$_{0.80}$) with 2.5 wt.% SN-38 pentanoate was successful and produced a monomodal size distribution with a low PDI value of 0.092 (Figure 4.21A). Interestingly, however, the co-nanoprecipitation with 5 wt.% SN-38 pentanoate did not yield an aqueous nanoparticle dispersion, but instead visible aggregation was observed. This observation was surprising for this co-nanoprecipitate regime since it has already been shown that 5 wt. % of the parent drug SN-38 could be incorporated. This may suggest that the phenol ring may play a role in making the drug compatible with the EHMA core, although it is unclear why.

Co-nanoprecipitates with p($BuMA_{100}$-co-$EGDMA_{0.95}$) targeting both 2.5 and 5 wt.% SN-38 pentanoate produced near monodisperse particles, but with the presence of small secondary peaks representative of populations with hydrodynamic diameters > 5000 nm (Figure 4.21B). The intensity of which increased as the pro-drug loading increased from 2.5 to 5 wt.%, suggesting that the encapsulation of SN-38 pentanoate within this co-nanoprecipitate combination was also not optimum.

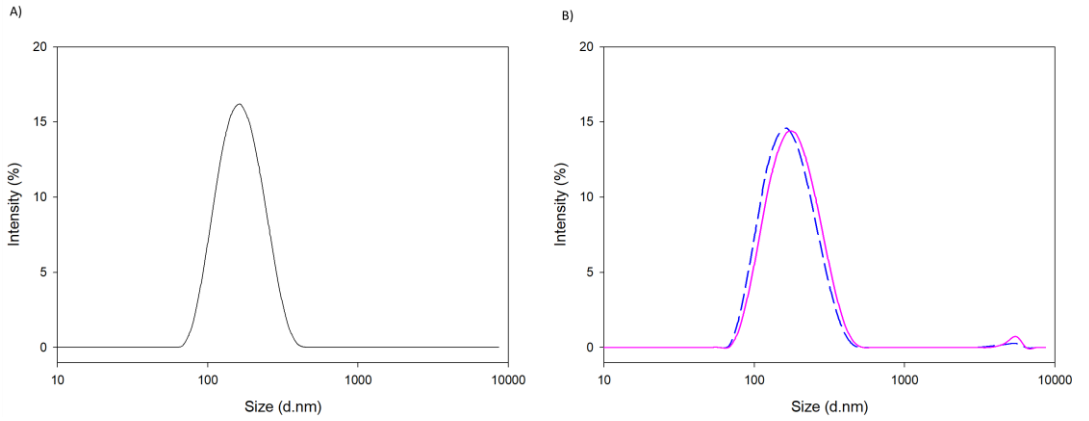


**Figure 4.21** DLS size distribution by intensity traces for SN-38 pentanoate loaded polymer nanoparticles for A) p($EHMA_{100}$-co-$EGDMA_{0.80}$): p($PEG_{114}$-*b*-$HPMA)_{100}$ (2.5 wt.% SN-38 pentanoate) and B) p($BuMA_{100}$-co-$EGDMA_{0.95}$): p($PEG_{114}$-*b*-$HPMA)_{100}$ 2.5 wt.% (blue, dashed line) and 5 wt.% SN-38 pentanoate (pink, solid line).

Both the targeted 2.5 and 5 wt.% SN-38 pentanoate loadings failed to produce nanoparticles (i.e. aggregation was observed) with the p($HPMA_{100}$-co-$EGDMA_{0.90}$) co-nanoprecipitate regime, which was an interesting observation since p($HPMA_{100}$-co-$EGDMA_{0.90}$) has been shown to both solely nanoprecipitate and co-nanoprecipitate successfully, presumably due to its charge stabilisation.

Although SN-38 pentanoate was successfully encapsulated within 2 different co-nanoprecipitate regimes with a maximum drug loading that matched that of SN-38, the difference in mass of the active component did not make the pro-drug approach particularly viable or attractive i.e. 5 wt. % SN-38 pentanoate does not equal 5 wt. % SN-38. Therefore, further studies with more lipophilic pro-drugs were not undertaken.

### 4.4 Increasing the Concentration of SN-38 *via* Multiple Co-nanoprecipitation

SN-38 was successfully loaded at 5 wt.% into branched p(EHMA) based systems (Section 4.2.1) but attempts to increase the drug loading were unsuccessful and had a negative impact on the efficiency and simplicity of the co-nanoprecipitation process

(Section 4.3). When evaluating the viability of these DDS and their potential application within a clinical setting, there are three key factors that need to be considered: 1) drug loading, 2) efficiency of drug loading and 3) the administration dose.

The drug loading achieved within the co-nanoprecipitate regimes appeared modest, but SN-38 is a very potent chemotherapeutic agent and is not currently administered in clinical practice. Therefore, these systems may still be an attractive option for clinical treatments. The candidate therapies containing 5 wt.% drug loaded nanoparticles offered an SN-38 concentration of 0.050 mg $mL^{-1}$. Increasing this concentration without having to adapt the drug loading of the branched vinyl copolymer nanoparticles will only strengthen the attractiveness of the system from a pharmacological perspective as the administered dose required for therapy would be reduced.

Ford *et al*. demonstrated that co-nanoprecipitations involving multiple additions of a polymer solution to a single aqueous phase was possible. This multiple co-nanoprecipitation generated higher concentrations of branched vinyl copolymers within the water phase without any significant impact to the nanoparticle size, but slight increase on particle size distribution which increased from 0.08 to 0.103.[56] This is likely due to the fact that the nanoparticle growth is terminated *via* the steric stabilisation mechanism. Multiple additions of polymer and drug stock may be an attractive way to increase the drug concentration within the aqueous polymeric nanoparticle system without having to alter the drug loading capabilities of the polymer nanoparticles. Therefore, the multiple co-nanoprecipitation of 5 wt.% SN-38 loaded p($EHMA_{20}$-co-$DSDMA_{0.80}$):p($PEG_{114}$-*b*-$HPMA_{100}$) nanoparticles was attempted for the first time. The selection of this specific formulation will be discussed in Chapter 5.

The conditions of the multiple co-nanoprecipitations were kept consistent with previous experiments. The first addition of SN-38/polymer THF stock solution ($[P]_0$ = 5 mg $mL^{-1}$, $[SN\text{-}38]_0$ = 0.25 mg $mL^{-1}$) was rapidly added to stirred DI water (5 mL) to give aqueous SN-38 loaded branched vinyl copolymer nanoparticles ($[P]_f$ = 1 mg $mL^{-1}$, and

final SN-38 concentration, $[SN\text{-}38]_f$ = 0.05 mg $mL^{-1}$). Following THF evaporation overnight, the co-nanoprecipitation was analysed *via* DLS. The subsequent additions were carried out into the same SN-38 loaded aqueous nanoparticle dispersions a further three times to yield aqueous SN-38 loaded branched vinyl copolymer nanoparticles ($[P]_f$ = 4 mg $mL^{-1}$, $[SN\text{-}38]_f$ = 0.20 mg $mL^{-1}$). These turbid aqueous nanoparticle dispersions were assessed *via* DLS at a concentration of $[P]_f$ = 1 mg $mL^{-1}$ following every addition (Table 4.7). It is worth noting that after the first addition, $[P]_f$ = 1 mg $mL^{-1}$, so DLS is obtained as normal. However, following the second, third and fourth addition $[P]_f$ increases to 2, 3 and 4 mg $mL^{-1}$ respectively. The aliquot of the nanoparticle dispersion used for DLS analysis was diluted as required and the aqueous nanoparticle dispersion was topped up by mass to 5 mL by mass before the next addition of polymer/drug stock solution to ensure a constant volume.

**Table 4.7** DLS analyses of 4 sequential multiple co-nanoprecipitations for 2 individual samples of p($EHMA_{20}$-co-$DSDMA_{0.80}$): p($PEG_{114}$-*b*-$HPMA_{100}$) 60:40 wt.% and 5 wt.% SN-38 loaded for p($EHMA_{20}$-co-$DSDMA_{0.80}$): p($PEG_{114}$-*b*-$HPMA_{100}$) 60:40 wt. %.

| | | Sample 1 | | | Sample 2 | | |
|---|---|---|---|---|---|---|---|
| | **Nanoprecipitation addition number** | **$D_z$ [a] (nm)** | **PDI** | **Derived Count Rate (kcps)** | **$D_z$ [a] (nm)** | **PDI** | **Derived Count Rate (kcps)** |
| **5 wt.% SN-38** | 1 | 160 | 0.173 | 797 700 | 170 | 0.229 | 783 200 |
| | 2 | 165 | 0.269 | 513 800 | 165 | 0.205 | 747 300 |
| | 3 | 175 | 0.217 | 773 000 | 185 | 0.219 | 716 300 |
| | 4 | 185 | 0.233 | 626 750 | 185 | 0.204 | 534 400 |
| **No Drug** | 1 | 115 | 0.055 | 460 000 | 120 | 0.036 | 469 900 |
| | 2 | 140 | 0.079 | 466 050 | 140 | 0.075 | 826 250 |
| | 3 | 145 | 0.058 | 426 500 | 145 | 0.058 | 739 450 |
| | 4 | 150 | 0.072 | 594 800 | 155 | 0.116 | 697 500 |

[a] Measured using DLS analysis at a concentration of 1 mg $mL^{-1}$

The recorded $D_z$ values were similar for all four of the additions of the 5 wt.% SN-38 loaded nanoparticle regimes with an observed increase from 160 to 185 nm for sample 1 and from 170 nm to 185 nm for sample 2 after the 1st to the 4th addition, respectively (Figure 4.22).

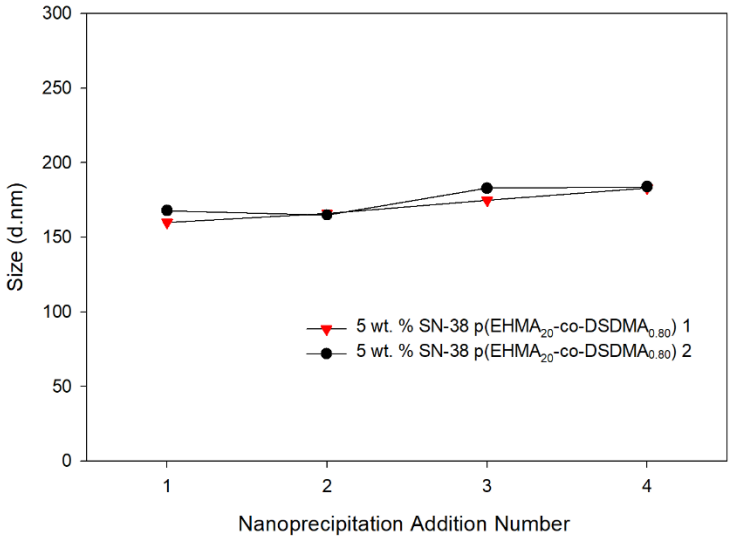


**Figure 4.22** Graphical representation of the changes in hydrodynamic diameter for 5 wt.% SN-38 loaded p($EHMA_{20}$-co-$DSDMA_{0.80}$): p($PEG_{114}$-*b*-$HPMA_{100}$) 60:40 wt.% following 4 sequential additions of 2 different samples: sample 1 (red triangles) and sample 2 (black circles).

There were also some small changes in the PDI values recorded, but the data suggests that multiple additions of SN-38/polymer THF stock solutions are forming new nanoparticle populations and are not causing disruption to the pre-existing population. This is validated by observations when the same co-nanoprecipitate regime was investigated following multiple co-nanoprecipitation in the absence of SN-38.

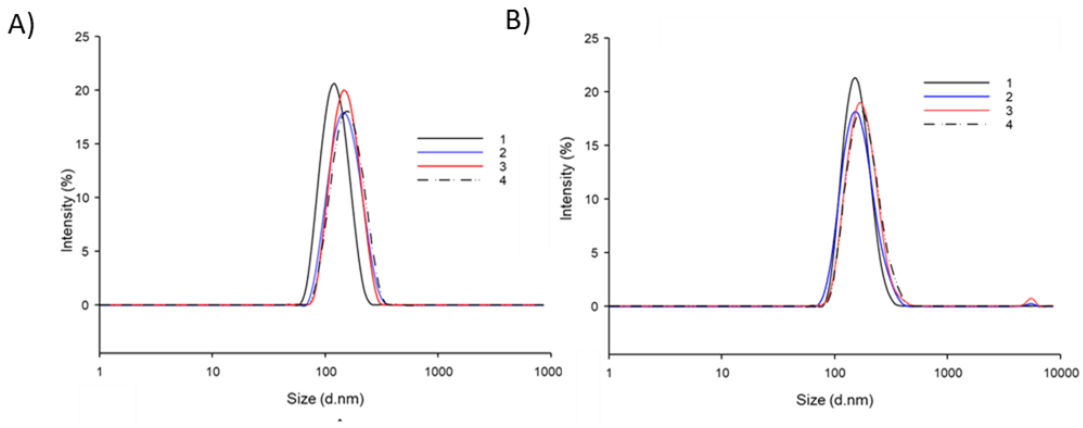


**Figure 4.23** Overlaid DLS size distributions for the four sequential co-nanoprecipitations of A) p($EHMA_{20}$-co-$DSDMA_{0.80}$): p($PEG_{114}$-*b*-$HPMA_{100}$) 60:40 wt.% and B) 5 wt.% SN-38 loaded p($EHMA_{20}$-co-$DSDMA_{0.80}$): p($PEG_{114}$-*b*-$HPMA_{100}$) 60:40 wt.%. 1st addition (black line), 2nd addition (blue line), 3rd addition (red line) and 4th addition (black dashed line).

The derived count rate appears to remain consistent despite the polymer nanoparticle concentration increasing, which may seem counter-intuitive since the derived count rate is a calculated parameter that calculates the number of photons

detected. Given that the light scattered is directly proportional to the size and number of particles present in a sample, it would be expected that this would increase consistently during the multiple co-nanoprecipitation process. However, it is worth reiterating that these DLS measurements of the multiple co-nanoprecipitations were all conducted at the same concentration of 1 mg $mL^{-1}$, since the samples prepared were extremely turbid (Figure 4.24).

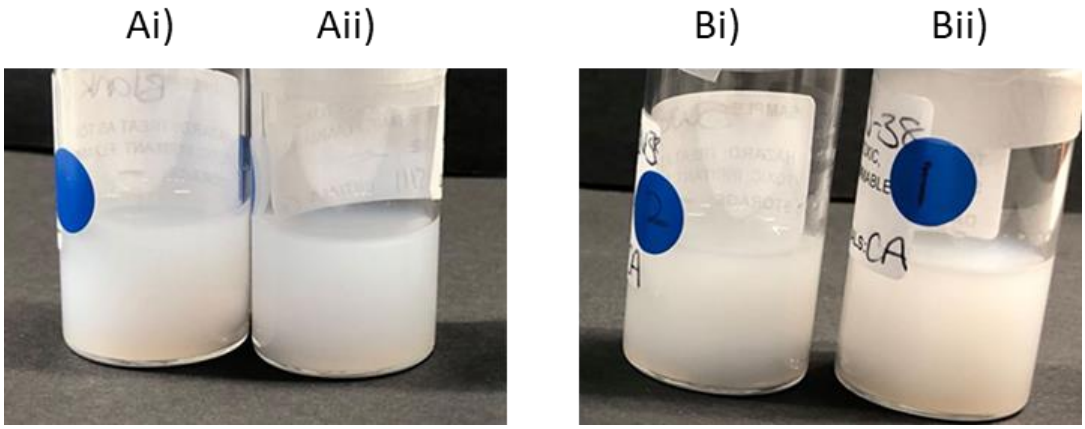


**Figure 4.24** Photographs of A) p($EHMA_{20}$-co-$DSDMA_{0.80}$): p($PEG_{114}$-*b*-$HPMA_{100}$) 60:40 wt.% sample 1 (Ai) and sample 2 (Aii), and B) 5 wt.% SN-38 loaded p($EHMA_{20}$-co-$DSDMA_{0.80}$): p($PEG_{114}$-*b*-$HPMA_{100}$) 60:40 wt.% sample 1 (Bi) and sample 2 (Bii) after four sequential co-nanoprecipitations.

The SEM images obtained after the 1st addition and 4th addition of the SN-38/polymer THF stock solution showed that a homogenous population of polymer nanoparticles was maintained throughout the study (Figure 4.25).

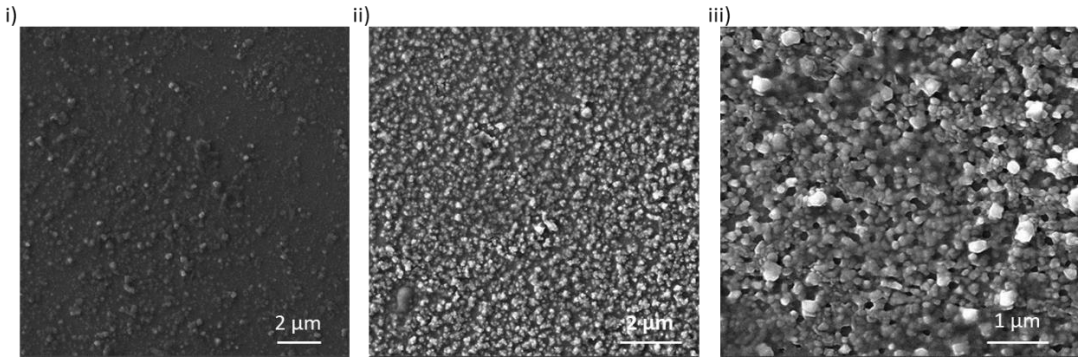


**Figure 4.25** SEM images of 5 wt.% SN-38 loaded p($EHMA_{20}$-co-$DSDMA_{0.80}$): p($PEG_{114}$-*b*-$HPMA_{100}$) following i) initial first addition co-nanoprecipaiton, ii) and iii) after the fourth addition co-nanoprecipitation.

The stability of samples generated by multiple co-nanoprecipitation was measured over an 8-week period *via* DLS following storage of samples under ambient conditions (Table 4.8).

**Table 4.8** DLS analyses over an 8-week period to determine the stability of 2 individual samples: p(EHMA$_{20}$-co-DSDMA$_{0.80}$): p(PEG$_{114}$-*b*-HPMA$_{100}$) 60:40 wt.% and 5 wt.% SN-38 loaded p(EHMA$_{20}$-co-DSDMA$_{0.80}$): p(PEG$_{114}$-*b*-HPMA$_{100}$) 60:40 wt.%.

| | | Sample 1 | | | Sample 2 | | |
|---|---|---|---|---|---|---|---|
| **Nanoparticle Regime** | **Week of measurement** | **$D_z$[a] (nm)** | **PDI** | **Derived Count Rate (kcps)** | **$D_z$[a] (nm)** | **PDI** | **Derived Count Rate (kcps)** |
| p(EHMA$_{20}$-co-DSDMA$_{0.80}$): p(PEG$_{114}$-*b*-HPMA$_{100}$) | 0 | 150 | 0.072 | 594 800 | 155 | 0.116 | 697 500 |
| | 1 | 150 | 0.077 | 668 000 | 150 | 0.096 | 701 350 |
| | 3 | 155 | 0.106 | 663 000 | 155 | 0.116 | 693 550 |
| | 5 | 150 | 0.084 | 502 250 | 155 | 0.071 | 605 500 |
| | 8 | 150 | 0.094 | 482 100 | 155 | 0.063 | 651 100 |
| 5 wt.% SN-38 loaded p(EHMA$_{20}$-co-DSDMA$_{0.80}$): p(PEG$_{114}$-*b*-HPMA$_{100}$) | 0 | 185 | 0.233 | 626 750 | 185 | 0.204 | 534 400 |
| | 1 | 175 | 0.132 | 604 700 | 175 | 0.132 | 638 250 |
| | 3 | 170 | 0.083 | 564 250 | 190 | 0.208 | 675 900 |
| | 5 | 170 | 0.085 | 541 900 | 180 | 0.088 | 478 350 |
| | 8 | 175 | 0.105 | 514 600 | 180 | 0.160 | 511 800 |

[a] Measured using DLS analysis at a concentration of 1 mg mL$^{-1}$, Dz values obtained have been rounded to the nearest 5 nm.

Minimal changes were observed for the measurements of the hydrodynamic diameter over the 8-week period (Figure 4.26).

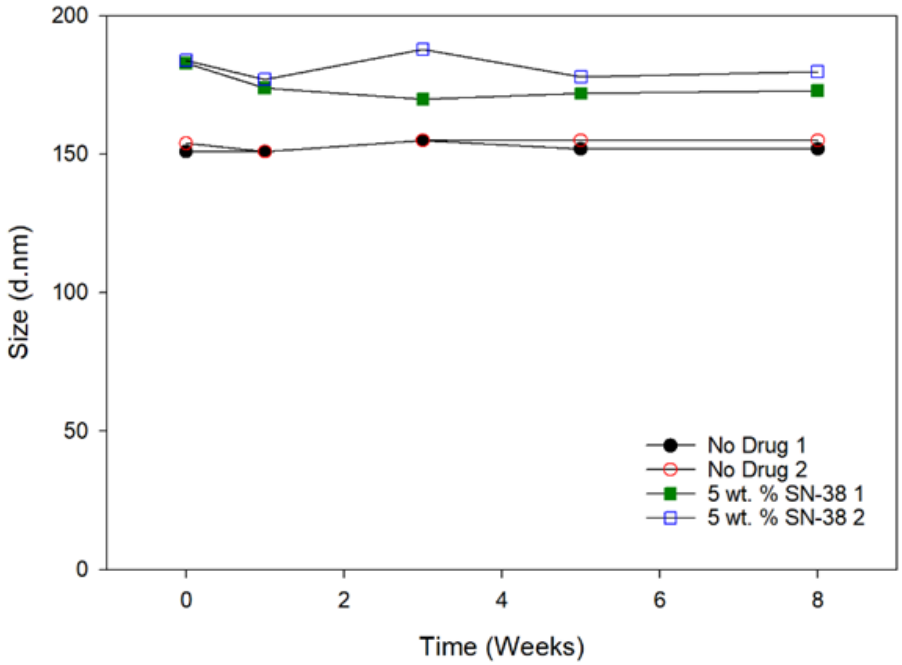


**Figure 4.26** Graphical representation of the changes in hydrodynamic diameter over 8 weeks *via* DLS of p(EHMA$_{20}$-co-DSDMA$_{0.80}$): p(PEG$_{114}$-*b*-HPMA$_{100}$) 60:40 wt.% sample 1 (black, closed circle), sample 2( red, open circle) and 5 wt.% SN-38 loaded p(EHMA$_{20}$-co-DSDMA$_{0.80}$): p(PEG$_{114}$-*b*-HPMA$_{100}$) 60:40 wt.% sample 1 (green, closed squares) and sample 2 (blue, open squares).

Monomodal size distributions were obtained for the blank (no SN-38) p(EHMA$_{20}$-co-DSDMA$_{0.80}$):p(PEG$_{114}$-*b*-HPMA$_{100}$) co-nanoprecipitates (Figure 4.27A). However, a

small secondary population ≥ 5000 nm was observed for 5 wt.% SN-38 loaded p(EHMA$_{20}$-co-DSDMA$_{0.80}$):p(PEG$_{114}$-*b*-HPMA$_{100}$) co-nanoprecipitate on the 3-week and 8-week measurements (Figure 4.27B). This secondary peak may be representative of SN-38 drug crystals that had formed during storage and it is important to note that after 5 weeks of sample storage, a cream coloured sediment was evident at the bottom of the vials, suggesting that these secondary populations were not stable within the dispersion (Appendix, Figure A.35).

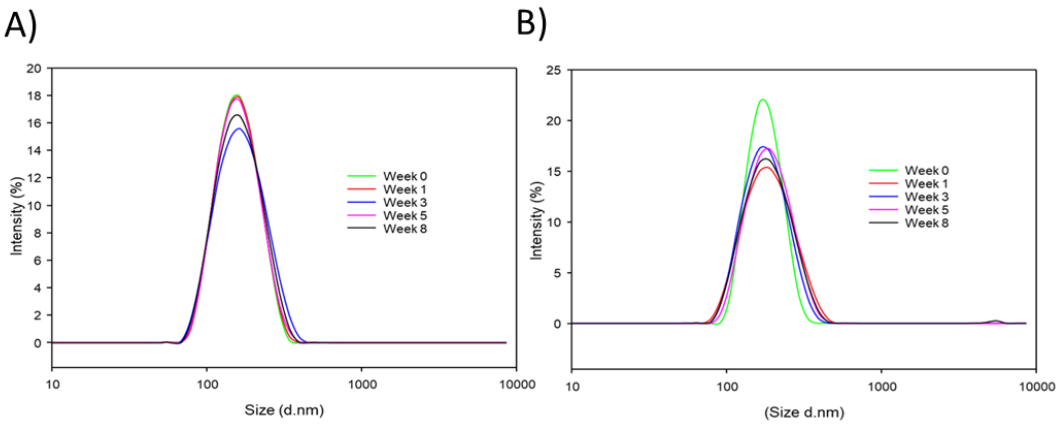


**Figure 4.27** Overlaid DLS size distribution by intensity traces for A) p(EHMA$_{20}$-co-DSDMA$_{0.80}$): p(PEG$_{114}$-*b*-HPMA$_{100}$) co-nanoprecipitate regime and B) 5 wt.% SN-38 loaded p(EHMA$_{20}$-co-DSDMA$_{0.80}$): p(PEG$_{114}$-*b*-HPMA$_{100}$) co-nanoprecipitate regime measured over 8 weeks.

The ability to increase the concentration of SN-38 loaded polymer nanoparticles *via* sequential low volume additions of the polymer-drug stock solution, coupled with extended stability, is very appealing. Especially since the concentration of SN-38 has been increased by a factor of four whilst maintaining a constant volume of water. This methodology is very attractive and generates an opportunity to create materials that can be taken forward and analysed in *in vivo* studies.

## 4.5 Quantitative Analysis of SN-38 Release from Branched Vinyl Copolymer Nanoparticles Using Tritium Labelled SN-38

One of the leading advantages of DDS from a pharmacological perspective is the opportunity to offer controlled drug release. It is highly desirable that the drug release from a DDS is slow and sustained. This temporal control provided by DDS can potentially allow for the maintenance of therapeutic and efficacious drug concentrations in the blood or at the targeted tissues. If the release of the drug is too fast, this can result in a large concentration of the drug being released from the DDS in a short time, which is often referred to as a burst release. Such release could

result in premature clearance of the drug, off-site toxicities, and reduced efficacies as a result of inadequate concentrations of drug reaching the target tissues. Whereas if the release of the drug is too slow, then the DDS could potentially be cleared from the body before depositing a therapeutic concentration of the drug.

Given that the successful encapsulation of SN-38 within branched vinyl co-polymer nanoparticles formed *via* co-nanoprecipitation had been demonstrated, this offered the opportunity to study the release rates of SN-38 from the polymer nanoparticles. Therefore, release experiments were conducted to observe the release behaviour of SN-38 from the polymer nanoparticles. A number of different experimental methods have been used for the determination of drug release profiles from dispersed systems including, sample and separate, continuous flow and dialysis membrane methods. (ref) These are typically used in combination with an analytical technique, such as UV-Vis spectroscopy which can be used to quantify drug concentrations.

Radiolabelling of SN-38 with Tritium ($^{3}H$) and subsequent membrane dialysis coupled with liquid scintillation counting (LSC) also offers as a quantitative analytical technique that can be used to accurately detect concentrations of SN-38. $^{3}H$ is a beta (β) emitting radio nuclide, which exhibits low energy (0.0186 MeV) and has a half-life of > 12 years. Since the β emission is of low energy, this results in low penetration distances in air from emitted electrons and an inability to penetrate through the top layer of any exposed skin. All experiments conducted using $^{3}H$-labelled SN-38 required basic radiation protection training at the University of Liverpool and all experiments were conducted within the Rannard Group Radio Materials Laboratory under the supervision of an accredited radiation protection supervisor, Dr Helen Cauldbeck. The high accuracy and precision that accompanies radiometric analysis means that EE, drug loading and drug release rates can be accurately determined.

### 4.5.1 Quantification of SN-38 Encapsulation Efficiency and Drug Loading Achieved During Nanoparticle Formation *via* Co-Nanoprecipitation

The use of radio-experiments and LSC for the monitoring of SN-38 release allows for the detection of extremely low concentrations and highly accurate quantification due to the highly sensitive nature that is associated with experiments using radio-labelled

molecules. The intensity of β-emissions that are emitted from $^{3}H$ nuclei per unit mass is referred to as the specific activity (SA). Using LSC, the total radiation (TR) from a sample is detected. The relationship between TR, mass of SN-38 and the SA is presented in Equation 4.2. This allows for the SN-38 mass to be calculated at any given time point.

$$\text{Mass of SN-38(mg)} = \text{TR}\,(\mu\text{Ci})/\text{SA}\,(\mu\text{Ci mg}^{-1}) \quad \textbf{(4.2)}$$

Co-nanoprecipitations were conducted using $^{3}H$-labelled SN-38 containing SA ranging from 31.16 - 38.67 μCi $mg^{-1}$. The co-nanoprecipitations for the radio-dialysis experiments were conducted with various branched vinyl polymers in combination with p($PEG_{114}$-*b*-$HPMA_{100}$) at a composition of 60:40 wt.%, respectively. Drug loading of SN-38 was fixed at 5 wt.% for all co-nanoprecipitate regimes. Co-nanoprecipitations were left for 24 hours to allow for THF evaporation. DLS analysis and quantification of EE and drug loading were conducted on all the samples prepared using $^{3}H$-labelled SN-38 and are presented with the corresponding radio-dialysis. Analyses by LSC were conducted on co-nanoprecipitates, which allowed for the quantification of the accurate mass of SN-38 present. Following this, centrifugation was conducted on an aliquot to separate the free SN-38 dissolved in the aqueous media from the nanoparticles. This allowed for the EE and drug loading to be quantified.

### 4.5.2 Determining SN-38 Release Rates *via* $^{3}H$ Radio-dialysis

Radio-dialysis experiments were conducted to determine the percentage release of SN-38 from p($EHMA_{100}$-co-$EGDMA_{0.80}$): p($PEG_{114}$-*b*-$HPMA_{100}$) nanoparticles over 24 hours. Dialysis as mentioned, is a well-established and useful technique to determine *in vitro* release. These were conducted using $^{3}H$-labelled SN-38 within the co-nanoprecipitation. The $^{3}H$-labelled SN-38 polymer nanoparticles (1 mL) were added to a double-sided bio-dialyser, which was sealed with a 3.5 kDa molecular weight cut off (MWCO) membrane. This bio-dialyser was then placed into a sealed reservoir (100 mL) of stirred DI water at 37 °C to ensure sink conditions (Figure 4.28).

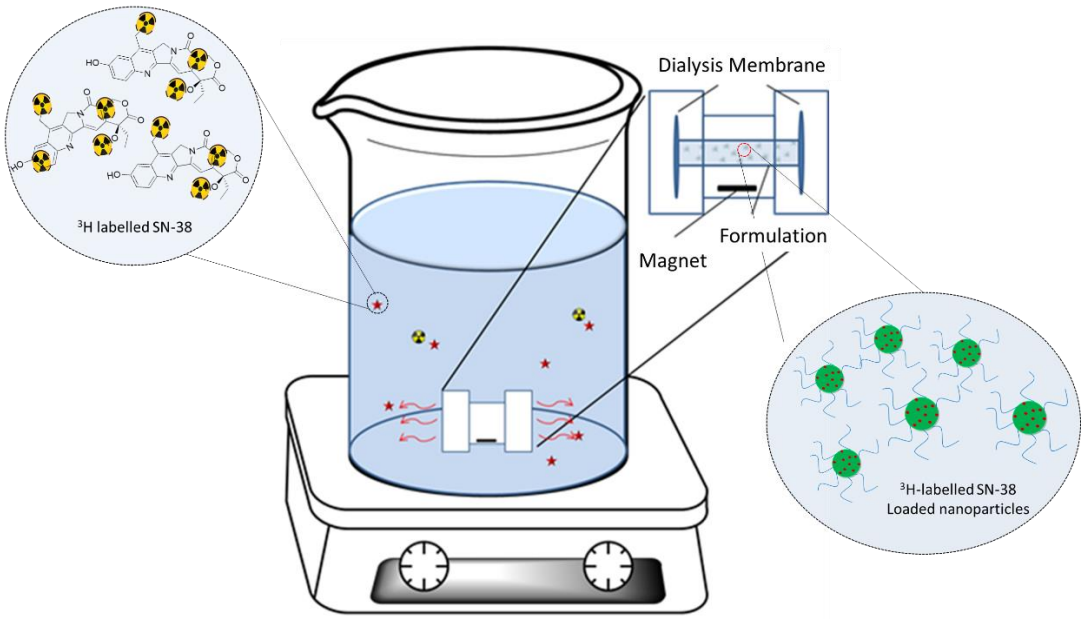


**Figure 4.28** Schematic representation of how the release rate of SN-38 from branched vinyl copolymer nanoparticles were determined over time *via* radio-dialysis. Branched vinyl copolymer nanoparticles were loaded with $^3$H-labelled SN-38 and added into a bio-dialyser (3.5 kDa MWCO), which was placed in DI water and stirred under sink conditions.

During the release experiment, the bio-dialyser was removed and transferred to fresh pre-heated reservoirs at regular time intervals of: 0.5, 1, 2, 3, 4, 5, 6, 7, 8 and 24 hours. This ensured that sink conditions were maintained and that any hazards or risks associated with the use of radio-labelled SN-38 were minimised as the rigid structure of the bio-dialyser provides more secure containment of $^3$H-labelled SN-38. An aliquot (1 mL) was removed from each reservoir and added to a scintillation cocktail (10 mL) to enable LSC analyses of the $^3$H-labelled SN-38 within the aqueous solution. Measuring the activity at each time point enabled the mass of SN-38 to be determined following its release from the polymer nanoparticles. These values were then used to plot a cumulative release curve against time. Given the significant accuracy associated with LSC analyses, it was deemed unnecessary to run the measurements in triplicate.

#### 4.5.2.1 The Impact of pH on SN-38 Release Rates

Given that SN-38 has pH dependant behaviour, it was of interest to understand whether this would impact the release of the SN-38 from the branched vinyl copolymer nanoparticles as studies have shown that the release of SN-38 from chitosan nanoparticles can be impacted by pH.[57] The release of SN-38 from p(EHMA$_{100}$-co-EGDMA$_{0.80}$):p(PEG$_{114}$-*b*-HPMA$_{100}$) nanoparticles at pH7 and pH 4 was

studied by radio-dialysis using $^{3}$H-labelled SN-38. To enable this, a co-nanoprecipitation was conducted in the exact same manner that has previously been described, with a composition of 60:40 wt.% branched vinyl polymer:AB block copolymer ratio but with the incorporation of $^{3}$H-labelled SN-38 at a drug loading of 5 wt.%. A turbid aqueous nanoparticle dispersion was obtained and analysed *via* DLS. A monomodal size distribution was obtained with the hydrodynamic diameter (180 nm) and PDI (0.178) values consistent with those previously obtained for this system when using unlabelled SN-38, suggesting that the encapsulation of $^{3}$H-labelled SN-38 had been successful. The EE value was also determined (92 %), which corresponded to a drug loading of 4.78%, consistent with the 5 wt. % which was being targeted. The radio dialysis experiments were conducted as before after adjusting the pH of the aqueous medium to pH 4 and pH 7. The cumulative release plot showed that similar release profiles were obtained but the release rates were different for the experiments performed at the two different pH values (Figure 4.29). Release profiles were also determined at pH7 and pH4 for non-encapsulated SN-38 (Appendix, Figure A.36).

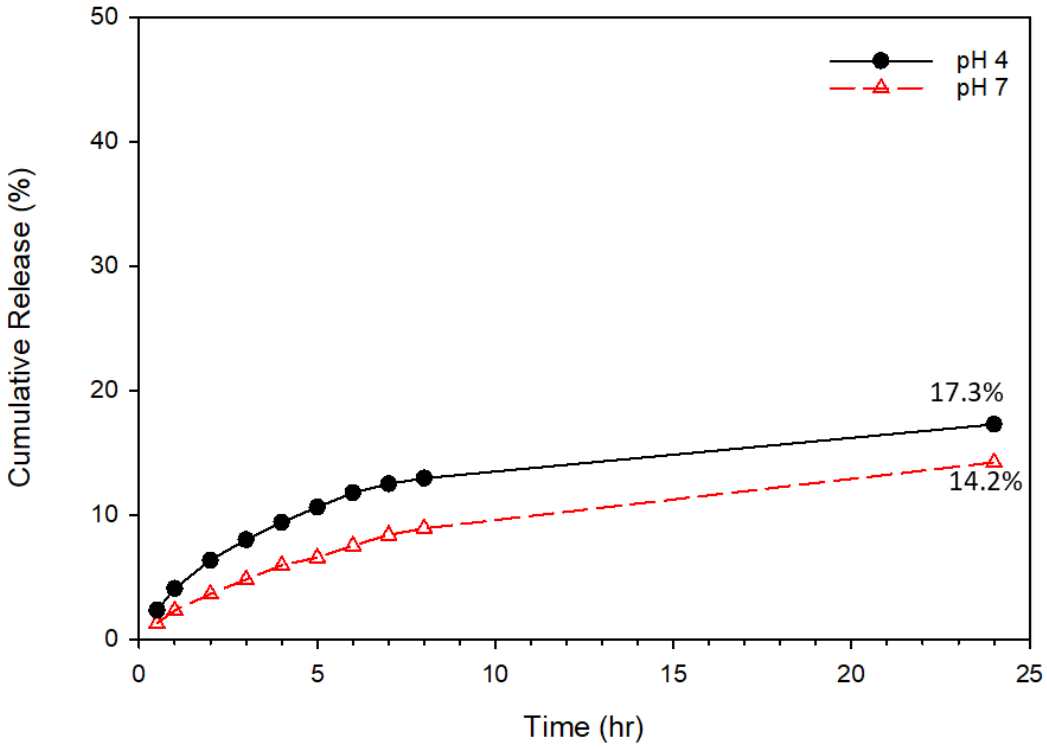


**Figure 4.29** Cumulative $^{3}$H-labelled SN-38 release (%) data obtained over 24 hours *via* radio-dialysis of

p(EHMA100-co-EGDMA0.80):p($PEG_{114}$-*b*-$HPMA_{100}$) nanoparticles at pH 4 (black, closed circles) and pH 7 (red, open triangles) at 37 °C.

The release of SN-38 after 24 hours at pH 7 was 14.2%, whereas the release of SN-38 at pH 4 after 24 hours was 17.3%. It can be postulated that the differences observed between the two release rates could be as a result of the shift in the equilibrium that exists between SN-38 lactone and carboxylate form. As previously discussed, SN-38 exists as a closed lactone ring at pH 4. Therefore, removing the possible ionic interactions that were occurring between the carboxylate form of SN-38 and the ester functionality on the polymer backbone or the hydroxyl group present on the hydrophobic segment (HPMA) of the AB block copolymer. Similar observations have been reported for the release of SN-38 from poly(amidoamine) dendrimers, whereby a difference in release rate was observed for pH 7.4 and pH 5.[58] At pH 7.4, the authors reported that 20% of the total SN-38 had been released within 2 hours, which increased significantly to 85% SN-38 released in 2 hours when the pH was decreased. Another study conducted by Seperhri and co-workers also observed a difference in release rates of SN-38 from PLGA nanoparticles at different pH values.[16] Release rates at pH 7.4 saw ~15% of SN-38 being released in 24 hours, which increased to ~ 30% SN-38 being released in 24 hours at pH 5.2.

DLS analysis of the $^{3}$H-labelled SN-38 loaded p($EHMA_{100}$-co-$EGDMA_{0.80}$):p($PEG_{114}$-*b*-$HPMA_{100}$) nanoparticles after the radio-dialysis showed minimal impact on the nanoparticle size or stability ($D_z$ = 174 nm, PDI = 0.183) when compared to the values obtained before radio-dialysis. As expected, this result suggests that the mechanism of SN-38 release from the branched vinyl polymer nanoparticles is most likely to be diffusion-based rather than erosion or degradation of the nanoparticulate structure.

The release rate of SN-38 from p($EHMA_{100}$-co-$EGDMA_{0.80}$):p($PEG_{114}$-*b*-$HPMA_{100}$) nanoparticles in a changing pH environment was also studied. This experiment was designed to simulate what would happen to the release rate when the SN-38 loaded nanoparticles were administered *in vivo* at the initial pH of blood and as they progressed to the lower pH condition typically exhibited within a tumour microenvironment. The radio-dialysis was conducted as described previously, but the pH of the reservoir was changed from pH 7 to pH 4 at the 4-hour time point.

SN-38 cumulative release (%) was plotted against time (Figure 4.30). The cumulative release graph clearly shows the presence of two different release profiles. Initially, there was a release profile at pH 7 where there had been a 13% cumulative release of SN-38 over 4 hours, but when the media was changed to pH 4 there was a subtle change in the release profile that is indicated by the appearance of a step-like change, which is highlighted on the figure with an arrow. After 24 hours, the cumulative release of SN-38 was 29%. This change, although only subtle, suggests that the rate of release of SN-38 is increased when the environment of the nanoparticles is changed to more acidic conditions. Both experiments have shown that the percentage release of SN-38 from p($EHMA_{100}$-co-$EGDMA_{100}$):p($PEG_{114}$-*b*-$HPMA_{100}$) nanoparticles is dependent on the pH of the reservoir media. The faster release observed for pH 4 is desirable for exploiting tumour environmental factors, such as acidic pH, to ensure an increased concentration of SN-38 released into the tumour tissue. Additionally, the slow release of SN-38 at biological pH suggests that the nanoparticles are maintaining their structural integrity and burst release profiles are avoided. This is essential of any DDS if the primary aim is to release concentrations that are sufficient for a therapeutic effect.

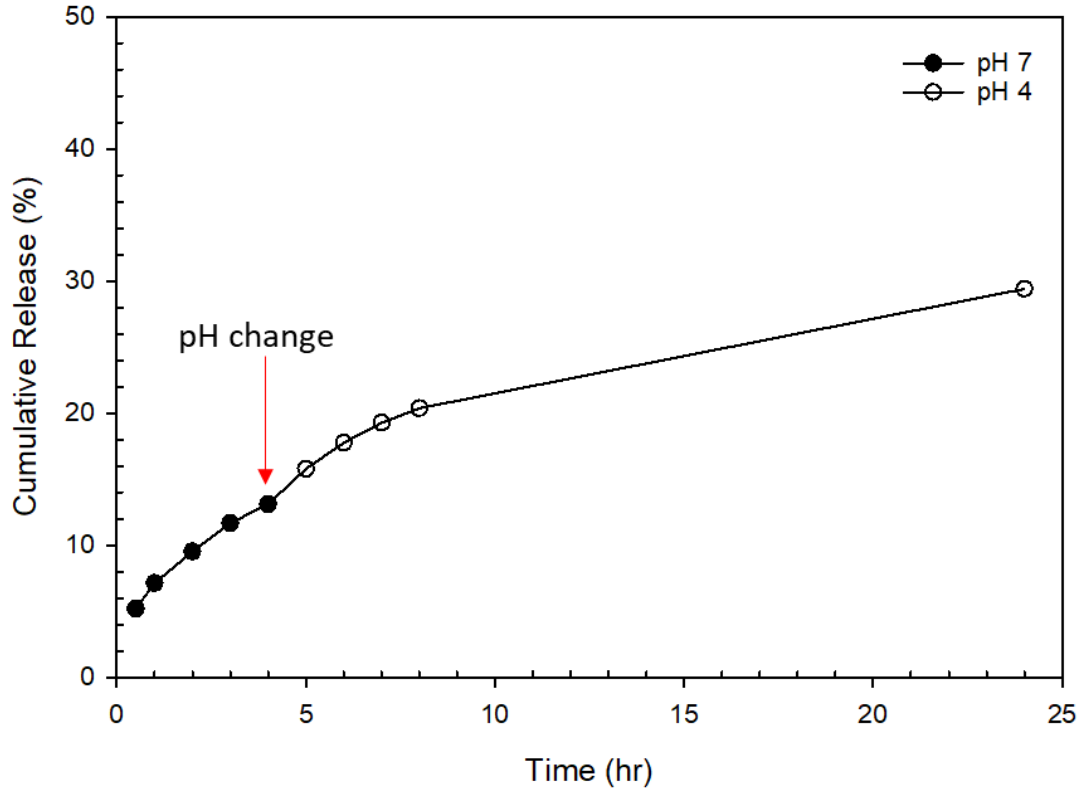


**Figure 4.30** Cumulative $^{3}$H-labelled SN-38 release data obtained over 24 hours *via* radio-dialysis of p(EHMA$_{100}$-co-EGDMA$_{0.80}$):p(PEG$_{114}$-*b*- HPMA$_{100}$) nanoparticles at pH 7 (black, closed circles) initially between 0 and 4 hour and then following the subsequent pH change to pH 4 (black, open circles) at 37 °C.

### 4.5.2.2 The Impact of Divinyl Monomer Chemistry on SN-38 Release Rates

Manipulating the polymer-drug interactions have also been shown to modulate the rate of drug release in previous reports.[59] It was hypothesised that changes to the release rate may be observed through different polymer-drug interactions, which may arise following the changes to the divinyl monomer chemistry. Therefore, the release rates of branched p(EHMA$_{20}$-co-DVM$_{y}$) synthesised with different branching agents was investigated using radio-dialysis, were DVM represents divinyl monomer. The co-nanoprecipitations were performed as previously described with the inclusion of 5 wt.% $^{3}$H-labelled SN-38 for the following polymers: p(EHMA$_{20}$-co-DSDMA$_{0.80}$), p(EHMA$_{20}$-co-BPGDMA$_{0.80}$) and p(EHMA$_{20}$-co-EGDMA$_{0.80}$) with p(PEG$_{114}$-*b*-HPMA$_{100}$) at 60:40 wt.%, respectively. The branched polymers with the lower DP$_{n}$ of the primary polymer chains were chosen to maximise any effect that the divinyl monomer residue chemistries had on the polymer-drug interactions. Turbid aqueous nanoparticle dispersions were obtained by co-nanoprecipitation and were analysed

*via* DLS. Monomodal size distributions with hydrodynamic dimeters and PDI values were obtained as follows: p(EHMA$_{20}$-co-DSDMA$_{0.80}$) ($D_z$ = 160 nm, PDI = 0.161), p(EHMA$_{20}$-co-BPGDMA$_{0.80}$) ($D_z$ = 165 nm, PDI = 0.178) and p(EHMA$_{20}$-co-EGDMA$_{0.80}$) ($D_z$ = 180 nm, PDI = 0.160). All of which were successfully loaded with 5 wt.% $^3$H-labelled SN38. The physicochemical properties of these co-nanoprecipitates were consistent with those following the co-nanoprecipitation of non-radio labelled SN-38 loaded co-nanoprecipitate regimes described in Chapter 4.2.1 which were as follows: p(EHMA$_{20}$-co-DSDMA$_{0.80}$) ($D_z$ = 180 nm, PDI = 0.221), p(EHMA$_{20}$-co-BPGDMA$_{0.80}$) ($D_z$ = 180 nm, PDI = 0.202) and p(EHMA$_{20}$-co-EGDMA$_{0.80}$) ($D_z$ = 190 nm, PDI = 0.186). The radio-dialysis proceeded over 24 hours with the reservoir medium at pH 7. Cumulative release (%) plots were obtained (Figure 4.31).

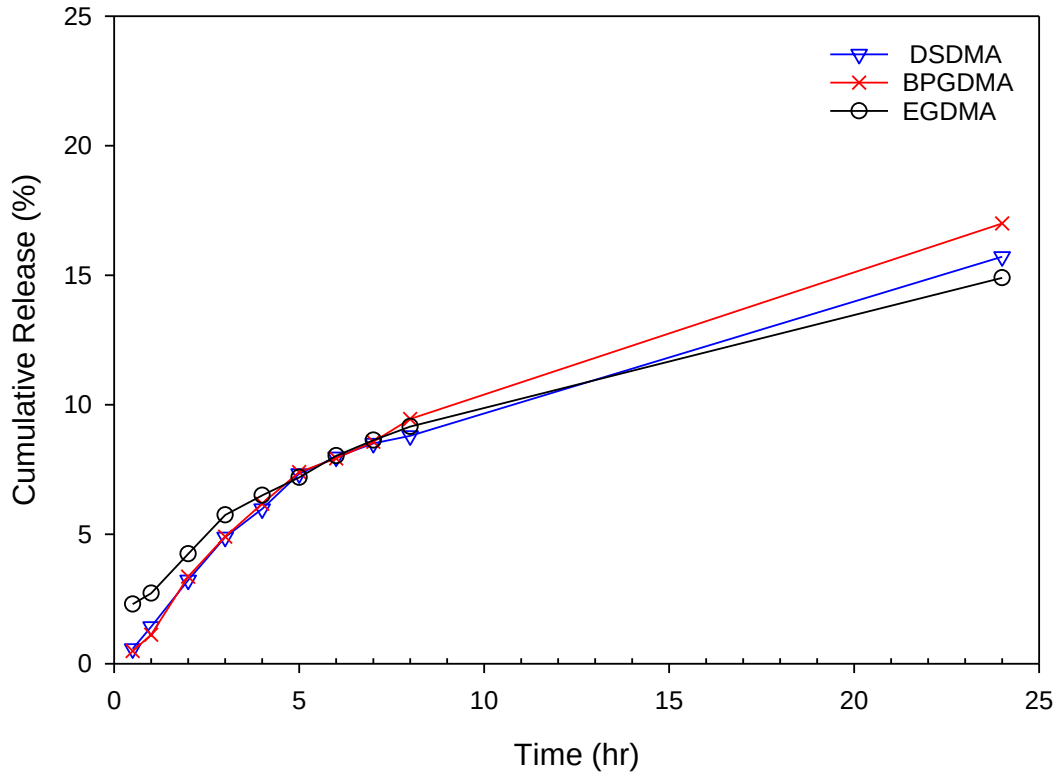


**Figure 4.31** Cumulative $^3$H-labelled SN-38 release data obtained over 24 hours at pH 7 *via* radio-dialysis of p(EHMA$_{100}$-co-EGDMA$_{0.80}$)(black, open circles), p(EHMA$_{100}$-co-DSDMA$_{0.80}$) (red, crosses), p(EHMA$_{100}$-co-BPGMA$_{0.80}$)(blue, open triangles): p(PEG$_{114}$-*b*- HPMA$_{100}$) nanoparticles at 37 °C.

The 3 different branched polymers all followed the same release profile, with minimal differences in the cumulative release (%) of SN-38 over 24 hours. The cumulative release of SN-38 after 24 hours was greatest for p(EHMA$_{20}$-co-BPGDMA$_{0.80}$) (17.0 %), followed by p(EHMA$_{20}$-co-DSDMA$_{0.80}$) (15.7 %) and p(EHMA$_{20}$-

co-EGDMA$_{0.80}$) (14.9 %). The ordering of these systems in terms of cumulative percentage release may seem counter-intuitive, since it would be expected that the greater hydrogen bonding capabilities of the BPGDMA divinyl monomer residues would increase the polymer-SN-38 interactions and therefore slow the release. However, the EE for these systems were determined by radiometric analyses and were calculated as follows: 92%, 87% and 83% for the EGDMA, DSDMA and BPGDMA divinyl monomer residues, respectively. Therefore, from this observation it is apparent that EE has a direct effect on the rate of release. Although, the observed changes were only minimal and may be as a result of EE instead of differing polymer-SN-38 interactions, this experiment has highlighted that the release of SN-38 from branched p(EHMA$_{20}$-co-DVM$_y$) based co-nanoprecipitates is reproducible, since three different stock solutions showed similar release profiles and results.

#### 4.5.2.3 The Impact of Higher SN-38 Concentrations Following Multiple Co-Nanoprecipitations on the Rate of Release

Multiple co-nanoprecipitations successfully increased the concentration of SN-38 within 1 mL of aqueous nanoparticle dispersion (Section 4.4). The radio-dialysis of these dispersions with higher SN-38 concentrations (0.20 mg mL$^{-1}$) was conducted to establish observable differences to the release of SN-38 at lower concentrations (0.05 mg mL$^{-1}$). Multiple co-nanoprecipitations of $^3$H-labelled SN-38 were conducted as before. Turbid aqueous nanoparticle dispersions were obtained, which were analysed *via* DLS at $[P]_f$ = 1 mg mL$^{-1}$. Monomodal size distributions were obtained for the different SN-38 concentrations, with the hydrodynamic diameters in the range of 155 to 193 nm and the PDI values between 0.170 and 0.204. Release of SN-38 was monitored following the first, second, third and fourth addition of SN-38/polymer THF stock at SN-38 concentrations of 0.05, 0.10, 0.15 and 0.20 mg mL$^{-1}$. Accurate quantification of SN-38 concentrations was obtained by LSC as follows: 0.0524, 0.0902, 0.1402 and 0.1912 mg mL$^{-1}$. High EE values were determined in the range of 89-94%. The radio-dialysis was conducted at pH 7 for 24 hours. The cumulative release plot showed that the same release profiles were obtained for all four concentrations with comparable release rates (Figure 4.32). The cumulative release of SN-38 after 24 hours was in the range of 13 – 16%.

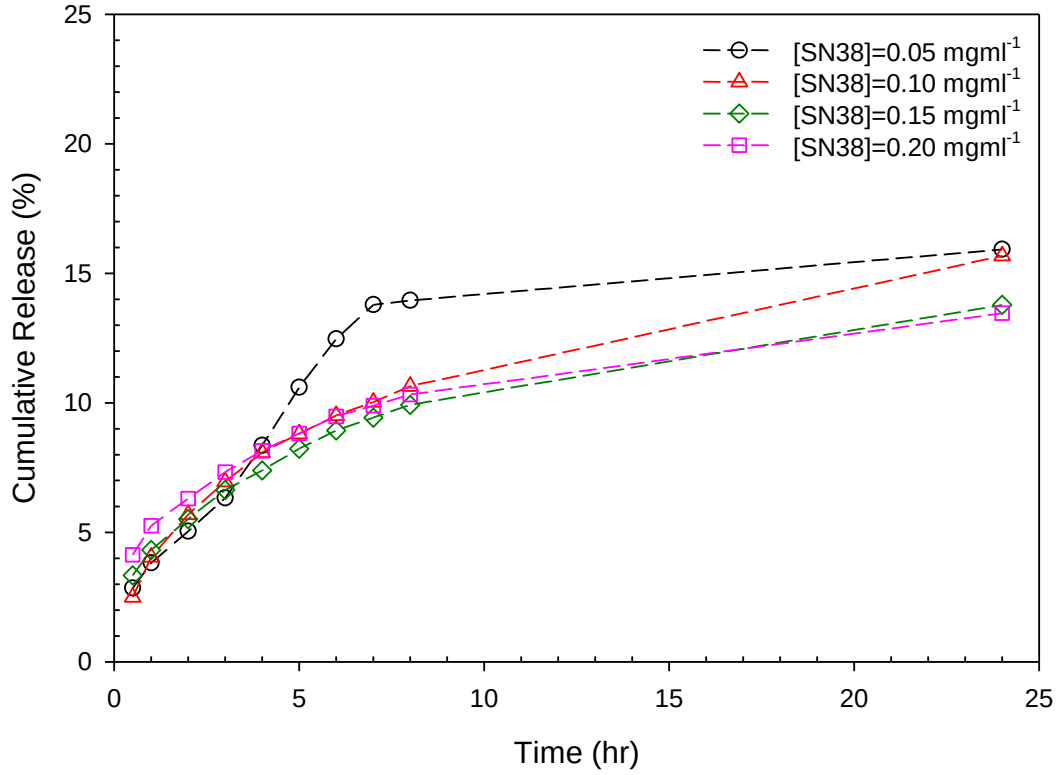


**Figure 4.32** Cumulative $^{3}$H-labelled SN-38 release data obtained over 24 hours at pH 7 via radio-dialysis of 5 wt.% $^{3}$H-labelled SN-38 loaded p(EHMA$_{100}$-co-EGDMA$_{0.80}$): p(PEG$_{114}$-*b*- HPMA$_{100}$) nanoparticles with increasing SN-38 concentrations prepared *via* multiple co-nanoprecipitations. SN-38 concentrations: 0.05 mg mL$^{-1}$ (black, open circle), 0.10 mg mL$^{-1}$ (red, open triangle), 0.15 mg mL$^{-1}$ (green, open diamond) and 0.20 mg mL$^{-1}$ (pink, open square).

### 4.5.3 Mathematical Modelling of SN-38 Release

The term drug release actually refers to a multi-step complex process. Initially, drug molecules migrate from their original position to the outer surface of the polymeric system (polymer-water interface). This is then followed by the movement of the drug particles into the release medium.[60] This in turn generates a two-stage release profile: the initial release from the particle surface, often described as a burst release, followed by the second more stable release of the drug that is dependent on the mechanism of release. There are many mechanisms that control this release, which are usually determined by the physical or chemical characteristics of the polymer. The most common are diffusion, swelling or erosion based.[61] Simple mathematical models can be employed to provide information and understanding of the drug release kinetics and mechanism. Solute transport from non-degradable polymers is mainly considered as diffusion based and drug release occurs due to a concentration gradient. There are several different diffusion-based models that can be used to

describe release profiles, such as zero order, first order and Highuci model, each of which are described below. [62-64]

Zero order kinetics can be described by the following relationship (Equation 4.3).

$$C_t = k_t + C_0 \qquad \textbf{(4.3)}$$

Whereby $C_t$ represents the concentration of drug at time t, $k_t$ is the rate constant at time (t) and $C_0$ is the initial drug concentration. A plot of cumulative release vs time would yield a straight line. If a strong correlation was observed, it would suggest that the rate of release is dependent on drug dissolution and not the disaggregation of the polymer system.

First order kinetics can be described by the following relationship (Equation 4.4).

$$C_t = C_0\, e^{-kt} \qquad \textbf{(4.4)}$$

A plot of log ($C_t$) against time yields a straight line whose gradient is equal to the rate constant. If the release kinetics are first order, then the release rate is directly proportional to the concentration of the drug. It is often used to describe the dissolution of a poorly water-soluble drug, which is embedded in a water-soluble matrix.

The Higuchi model is described by the following relationship (Equation 4.5).

$$\mathrm{C_t} = \mathrm{k_H t^{0.5}} \qquad \textbf{(4.5)}$$

Where $k_H$ represents the Higuchi rate constant. A plot of drug concentration vs square root of time yields a straight line. The Higuchi model is based on several assumptions: the initial concentration of the drug in the formulation is higher than the drug thermodynamic equilibrium solubility, sink conditions are maintained, polymer swelling and dissolution is negligible, the drug particles are much smaller than the nanoparticle carrier, and finally, that the drug diffusivity does not change rate.

The obtained release profiles for 5 wt.% $^3$H-labelled SN-38 loaded (EHMA$_{20}$-co-DSDMA$_{0.80}$), p(EHMA$_{20}$-co-BPGDMA$_{0.80}$) and p(EHMA$_{20}$-co-EGDMA$_{0.80}$) with p(PEG$_{114}$-

*b*-HPMA$_{100}$) co-nanoprecipitate regimes were analysed using the zero-order, the first-order and the Higuchi model (Figure 4.33).

Linear regression analysis was employed to study the linearity of the kinetic plots and to determine the correlation coefficients ($R^2$). The model that yielded the best $R^2$ values was the Higuchi model (≥ 0.98), followed by the zero-order kinetic model (0.89 – 0.96). The worst fitting model was the first order kinetic model, as indicated by the low $R^2$ values (0.76 – 0.89). These results suggest that the release of SN-38 was not concentration dependent, which is clearly advantageous when designing a DDS. It can be concluded from the obtained high linearity values that the mechanism of release has a high reliance on drug diffusion. The Higuchi model has been derived from Fick's first law of diffusion and the suitability of the model fit indicates that the drug release is *via* drug diffusion over time from a homogenous environment i.e. the polymer nanoparticle is not degrading.

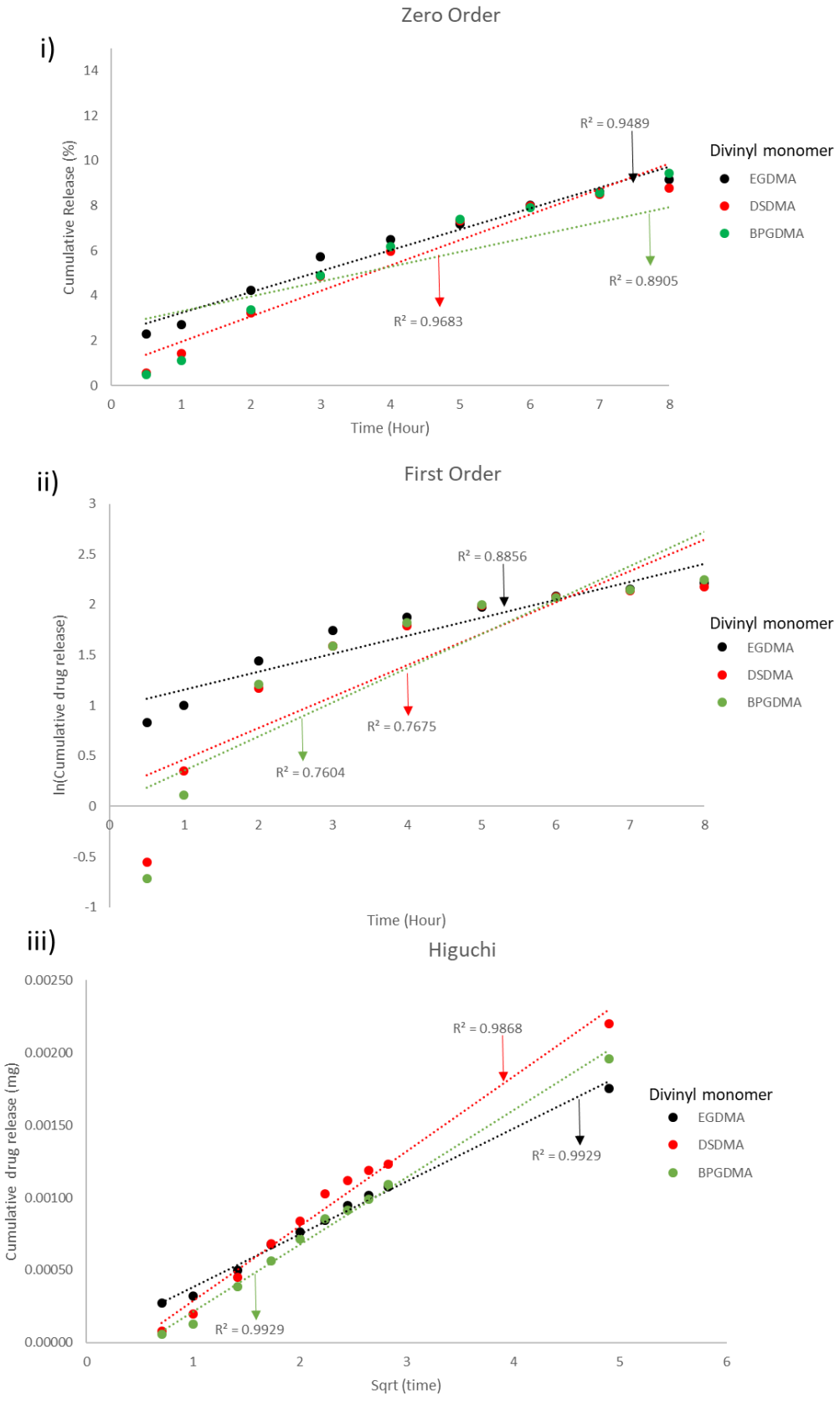


**Figure 4.33** Release kinetic plots of 5 wt.% SN-38 loaded ($EHMA_{20}$-co-$DSDMA_{0.80}$), p($EHMA_{20}$-co-$BPGDMA_{0.80}$) and p($EHMA_{20}$-co-$EGDMA_{0.80}$) with p($PEG_{114}$-b-$HPMA_{100}$) co-nanoprecipitate regimes according to i) zero-order model, ii) first-order model, and iii) the Higuchi model.

## 4.6 Conclusion

SN-38 loaded branched vinyl copolymer nanoparticles have been successfully prepared at a drug loading of 5 wt.% *via* co-nanoprecipitation. The production of which proved to be facile, efficient and reproducible, as demonstrated by the high EE values (≥ 83%) and the similarities in both particle size and PDI values across different batches. The drug loaded nanoparticles that were generated were of an acceptable particle size for the intended application and were also found to exhibit stability over prolonged periods of time (13 weeks). Studies were conducted to try to increase the drug loading beyond 5 wt.% but were unsuccessful as they resulted in multiple populations being observed, the formation of drug crystals and polymer aggregates. However, multiple co-nanoprecipitation proved to be a successful, simple method to increase the concentration of SN-38 within a single formulation whilst still targeting a 5 wt.% drug loading. The use of $^{3}$H-labelled SN-38 provided a highly accurate quantification platform to analyse the release rates of SN-38 from branched vinyl co-polymer nanoparticles *via* radio-dialysis. The findings from these studies show that the release of SN-38 from polymer nanoparticles could be sustained over time at a physiological relevant temperature and pH. SN-38 remained within the nanoparticles for 24 hours with < 16% release. Studies were also performed to study the effect of pH, polymer-drug interactions and initial drug concentration on the release rates of SN-38. It was shown that release rates were greater when the radio-dialysis medium was acidic in pH, which is potentially advantageous for a DDS to exploit the tumour environmental factors. Simple mathematical modelling of the obtained release profiles confirmed that the release was diffusion based and followed a release profile best fitted to the Higuchi model. The findings within this chapter highlight the promising potential and suitability of these SN-38 loaded nanoparticles to be considered for further *in vitro* and *in vivo* analysis.

All of the attempts described above (Section 4.3) to increase the drug loading of SN-38 within nanoparticle regimes above 5 wt.% offered limited success. However, whilst this value may initially seem modest, it is not uncommon that reported drug loadings for polymer nanoparticles do not exceed 10 wt.% [65-67] and even less

(1-5 wt.%) for those prepared by nanoprecipitation methods.[68,69] These loading values are likely due to the different solubilities exhibited by the individual components, which lead to different precipitation times. However, one of the main advantages of working with SN-38 is the extreme level of potency it exhibits,[70-72] which in turn may see the reduction in the dose that would achieve an equivalent therapeutic effects to that of IR.

In an attempt to estimate the possible clinical value of a 5 wt.% loaded SN-38 containing polymer nanoprecipitate, it is useful to compare the commercial products that attempt to deliver the benefits of SN-38 in the clinic. Campto, the marketed brand of IR, is currently sold as IR hydrochloride and sorbitol at concentrations of 20 mg $mL^{-1}$ (17.33 mg $mL^{-1}$ of IR).[73] Currently, IR in monotherapy is dosed at a 350 mg $m^{-2}$.[74] The average person is 1.75 $m^2$, so the average dose of IR administered is 612.5 mg (1.75 $m^2$ x 350 mg $m^{-2}$), which equates to approximately 30.6 mL of Campto being required (612.5 mg; 20mg$mL^{-1}$). Within this solution there is 530.73 mg of IR (30.6 mL x 17.33 mg $mL^{-1}$). Literature has shown that SN-38 is up to 1000 times more potent than IR.[72] If potency is assumed to be 1000 times greater than IR, the dose required to achieve the same therapeutic effect as IR would only be 0.531 mg $m^{-2}$. The concentration of the 5 wt.% SN-38 loaded formulations is 0.05 mg $mL^{-1}$, meaning that only 10.62 mL would be required of these formulations. This sees a reduction of 65% of total volume of formulation required. If we take the more modest potency level of 100-fold higher than IR, the same calculations would equate to 106 mL being required of our formulation. Whilst this volume is greater than required for Campto, the advantage is the delivery of SN-38 as an active parent compound. Multiple co-nanoprecipitations increased the concentration of SN-38 from 0.05 mg $mL^{-1}$ to 0.2 mg $mL^{-1}$; this would potentially reduce the administered volume by a factor of 4 and into the range of the Campto product if the conservative potency of 100-fold is correct (26.5 mL). These calculations do not consider factors such as metabolism and clearance rates that are drug-specific and are purely deriving an SN-38 equivalence basis; however, it is important to note that the formulation (from this perspective) does provide an ethical foundation to conduct *in vivo* studies that are described in Chapter 5.

## 4.7 References


1. B. E. N. Sprangers, L. Cosmai and C. Porta, in *Onco-Nephrology*, eds. K. W. Finkel, M. A. Perazella and E. P. Cohen, 2020, **11**, 127-153
2. R. C. Gallo, J. Whang-Peng and R. H. Adamson, *JNCI: Journal of the National Cancer Institute*, 1971, **46**, 789-795.
3. U. Schaeppi, R. W. Fleischman and D. A. Cooney, *Cancer Chemotherapy Reports*, 1974, **5**, 25-36.
4. C. G. Moertel, A. J. Schutt, R. J. Reitemeier and R. G. Hahn, *Cancer Chemotherapy Reports*, 1972, **56**, 95-101.
5. F. Muggia, in *Twenty Years Later: Review of Clinical Trials with Camptothecin Sodium)*, CRC Press: Boca Raton, FL, 1995.
6. F.M. Muggia, P.J. Creaven, H.H. Hansen, M.H. Cohen, O.S. Selawry, *Cancer Chemotherapy Reports.* 1972, **4,** 515-21.
7. R. H. J. Mathijssen, R. J. van Alphen, J. Verweij, W. J. Loos, K. Nooter, G. Stoter and A. Sparreboom, *Clinical Cancer Research*, 2001, **7**, 2182-2194.
8. K.-i. Fujita, Y. Kubota, H. Ishida and Y. Sasaki, *World J Gastroenterol*, 2015, **21**, 12234-12248.
9. C. Gerrits, M. De Jonge, J. Schellens, G. Stoter and J. Verweij, *British journal of cancer*, 1997, **76**, 952-962.
10. T. Kunimoto, K. Nitta, T. Tanaka, N. Uehara, H. Baba, M. Takeuchi, T. Yokokura, S. Sawada, T. Miyasaka and M. Mutai, *Cancer Res*, 1987, **47**, 5944-5947.
11. T. Tsuruo, T. Matsuzaki, M. Matsushita, H. Saito and T. Yokokura, *Cancer Chemotherapy and Pharmacology*, 1988, **21**, 71-74.
12. T. Matsuzaki, T. Yokokura, M. Mutai and T. Tsuruo, *Cancer chemotherapy and pharmacology*, 1988, **21**, 308-312.
13. Cancer Research UK, https://www.cancerresearchuk.org/about-cancer/cancer-in-general/treatment/cancer-drugs/drugs/irinotecan, (accessed 07/10/2020).
14. Y. Kawato, M. Aonuma, Y. Hirota, H. Kuga and K. Sato, *Cancer research*, 1991, **51**, 4187-4191.
15. A. Wang and S. Li, *BMC biotechnology*, 2008, **8**, 1-7.
16. N. Sepehri, H. Rouhani, F. Tavassolian, H. Montazeri, M. R. Khoshayand, M. H. Ghahremani, S. N. Ostad, F. Atyabi and R. Dinarvand, *International Journal of Pharmaceutics*, 2014, **471**, 485-497.
17. S. Ge, Y. Tu and M. Hu, *Current Pharmacology Reports*, 2016, **2**, 326-338.
18. S. Palakurthi, *Expert Opinion on Drug Deliv*ery, 2015, **12**, 1911-1921.
19. H. Zhao, B. Rubio, P. Sapra, D. Wu, P. Reddy, P. Sai, A. Martinez, Y. Gao, Y. Lozanguiez, C. Longley, L. M. Greenberger and I. D. Horak, *Bioconjugate Chemistry*, 2008, **19**, 849-859.
20. F. Atyabi, A. Farkhondehfai, F. Esmaeili and R. Dinarvand, *Acta Pharm*, 2009, **59**, 133-144.
21. O. Mert, G. Esendağlı, A. L. Doğan and A. S. Demir, *RSC advances*, 2012, **2**, 176-185.
22. J. Fassberg and V. J. Stella, *Journal of Pharmaceutical Sciences*, 1992, **81**, 676-684.
23. W. J. Slichenmyer, E. K. Rowinsky, R. C. Donehower and S. H. Kaufmann, *Journal of the National Cancer Institute*, 1993, **85**, 271-291.
24. T. G. Burke and Z. H. Mi, *Analytical Biochemistry*, 1993, **212**, 285-287.
25. T. G. Burke, C. B. Munshi, Z. Mi and Y. Jiang, *Journal of Pharmaceutical Sciences*, 1995, **84**, 518-519.
26. R. Kurzrock, S. Goel, J. Wheler, D. Hong, S. Fu, K. Rezai, S. K. Morgan-Linnell, S. Urien, S. Mani, I. Chaudhary, M. H. Ghalib, A. Buchbinder, F. Lokiec and M. Mulcahy, *Cancer*, 2012, **118**, 6144-6151.
27. D. S. Goldberg, N. Vijayalakshmi, P. W. Swaan and H. Ghandehari, *Jounral of Controlled Release*, 2011, **150**, 318-325.
28. S. Lei, P. Y. Chien, S. Sheikh, A. Zhang, S. Ali and I. Ahmad, *Anticancer Drugs*, 2004, **15**, 773-778.
29. Y. Sadzuka, H. Takabe and T. Sonobe, *Jounral of Controlled Release*, 2005, **108**, 453-459.
30. J. A. Zhang, T. Xuan, M. Parmar, L. Ma, S. Ugwu, S. Ali and I. Ahmad, *International Journal of Pharmaceutics*, 2004, **270**, 93-107.
31. Q. Gu, J. Z. Xing, M. Huang, C. He and J. Chen, *Nanotechnology*, 2012, **23**, 205101.
32. M. Gan, W. Zhang, S. Wei and H. Dang, *Artificial Cells, Nanomedicine, and Biotechnology*, 2017, **45**, 389-397.

33. P. Ebrahimnejad, R. Dinarvand, S. A. Sajadi, F. Atyabi, F. Ramezani and M. R. Jaafari, *PDA Journal of Pharmaceutical Science and Technology*, 2009, **63**, 512-520.
34. P. Ebrahimnejad, R. Dinarvand, A. Sajadi, M. R. Jaafari, A. R. Nomani, E. Azizi, M. Rad-Malekshahi and F. Atyabi, *Nanomedicine*, 2010, **6**, 478-485.
35. J. Williams, R. Lansdown, R. Sweitzer, M. Romanowski, R. LaBell, R. Ramaswami and E. Unger, *Jounral of Controlled Release*, 2003, **91**, 167-172.
36. F. Koizumi, M. Kitagawa, T. Negishi, T. Onda, S.-i. Matsumoto, T. Hamaguchi and Y. Matsumura, *Cancer Research*, 2006, **66**, 10048-10056.
37. T. Nagano, M. Yasunaga, K. Goto, H. Kenmotsu, Y. Koga, J.-i. Kuroda, Y. Nishimura, T. Sugino, Y. Nishiwaki and Y. Matsumura, *Clinical Cancer Research*, 2009, **15**, 4348-4355.
38. T. Eguchi Nakajima, K. Yanagihara, M. Takigahira, M. Yasunaga, K. Kato, T. Hamaguchi, Y. Yamada, Y. Shimada, K. Mihara, T. Ochiya and Y. Matsumura, *Cancer Research*, 2008, **68**, 9318-9322.
39. Y. Saito, M. Yasunaga, J. Kuroda, Y. Koga and Y. Matsumura, *Cancer Science*, 2008, **99**, 1258-1264.
40. M. Sumitomo, F. Koizumi, T. Asano, A. Horiguchi, K. Ito, T. Asano, T. Kakizoe, M. Hayakawa and Y. Matsumura, *Cancer Research*, 2008, **68**, 1631-1635.
41. T. E. Nakajima, M. Yasunaga, Y. Kano, F. Koizumi, K. Kato, T. Hamaguchi, Y. Yamada, K. Shirao, Y. Shimada and Y. Matsumura, *International Journal of Cancer*, 2008, **122**, 2148-2153.
42. H. Zhao, B. Rubio, P. Sapra, D. Wu, P. Reddy, P. Sai, A. Martinez, Y. Gao, Y. Lozanguiez, C. Longley, L. M. Greenberger and I. D. Horak, *Bioconjugate Chemistry*, 2008, **19**, 849-859.
43. A. Patnaik, K. P. Papadopoulos, A. W. Tolcher, M. Beeram, S. Urien, L. J. Schaaf, S. Tahiri, T. Bekaii-Saab, F. M. Lokiec, K. Rezaï and A. Buchbinder, *Cancer chemotherapy and pharmacology*, 2013, **71**, 1499-1506.
44. H. Zhang, J. Wang, W. Mao, J. Huang, X. Wu, Y. Shen and M. Sui, *Journal of Controlled Release*, 2013, **166**, 147-158.
45. E. Roger, F. Lagarce and J.-P. Benoit, *European Journal of Pharmaceutics and Biopharmaceutics*, 2011, **79**, 181-188.
46. A. Gabizon, R. Catane, B. Uziely, B. Kaufman, T. Safra, R. Cohen, F. Martin, A. Huang and Y. Barenholz, *Cancer research*, 1994, **54**, 987-992.
47. H. Liu, H. Lu, L. Liao, X. Zhang, T. Gong and Z. Zhang, *Drug Delivery*, 2015, **22**, 701-709.
48. J. Della Rocca, D. Liu and W. Lin, *Nanomedicine (Lond)*, 2012, **7**, 303-305.
49. S. Lv, Y. Wu, K. Cai, H. He, Y. Li, M. Lan, X. Chen, J. Cheng and L. Yin, *Journal of the American Chemical Society*, 2018, **140**, 1235-1238.
50. S. Wieczorek, A. Dallmann, Z. Kochovski and H. G. Börner, *Journal of the American Chemical Society*, 2016, **138**, 9349-9352.
51. Y. Shi, M. J. van Steenbergen, E. A. Teunissen, L. s. Novo, S. Gradmann, M. Baldus, C. F. van Nostrum and W. E. Hennink, *Biomacromolecules*, 2013, **14**, 1826-1837.
52. C. A. S. Ribeiro, C. E. de Castro, L. J. C. Albuquerque, C. C. S. Batista and F. C. Giacomelli, *Colloid and Polymer Science*, 2017, **295**, 1271-1280.
53. V. Peikov, S. Ugwu, M. Parmar, A. Zhang and I. Ahmad, *International Journal of Pharmaceutics,* 2005, **299**, 92-99.
54. J. A. Zhang, T. Xuan, M. Parmar, L. Ma, S. Ugwu, S. Ali and I. Ahmad, *International Journal of Pharmaceutic*s, 2004, **270**, 93-107.
55. V. Bala, S. Rao, P. Li, S. Wang and C. A. Prestidge, *Molecular Pharmaceutics*, 2016, **13**, 287-294.
56. J. Ford, *PhD Thesis*, Univerisity of Liverpool, 2015. (https://livrepository.liverpool.ac.uk/2052220/1/FordJan_Sept2015_2052220.pdf.pdf)
57. S. Prasad and J. S. Dangi, *Artificial Cells, Nanomedicine, and Biotechnology*, 2016, **44**, 1824-1834.
58. R. B. Kolhatkar, P. Swaan and H. Ghandehari, *Pharmaceutical research*, 2008, **25**, 1723-1729.
59. M. D. Blanco and M. J. Alonso, *European Journal of Pharmaceutics and Biopharmaceutics*, 1997, **43**, 287-294.
60. R. Langer, *Science*, 1990, **249**, 1527-1533.
61. M. L. Bruschi, in *Strategies to Modify the Drug Release from Pharmaceutical Systems*, Woodhead Publishing, 2015, 37-62.

62. C. Mircioiu, V. Voicu, V. Anuta, A. Tudose, C. Celia, D. Paolino, M. Fresta, R. Sandulovici and I. Mircioiu, *Pharmaceutics*, 2019, **11**, 140.
63. T. Higuchi, *Journal of pharmaceutical sciences*, 1961, **50**, 874-875.
64. T. Higuchi, *Journal of pharmaceutical sciences*, 1963, **52**, 1145-1149.
65. Z. Liu, Y. Jiao, Y. Wang, C. Zhou and Z. Zhang, *Advanced Drug Delivery Reviews*, 2008, **60**, 1650-1662.
66. L. Zhang, J. M. Chan, F. X. Gu, J. W. Rhee, A. Z. Wang, A. F. Radovic-Moreno, F. Alexis, R. Langer and O. C. Farokhzad, *ACS Nano*, 2008, **2**, 1696-1702.
67. G. A. Husseini and W. G. Pitt, *Advanced Drug Delivery Review*, 2008, **60**, 1137-1152.
68. J. Hrkach, D. Von Hoff, M. Mukkaram Ali, E. Andrianova, J. Auer, T. Campbell, D. De Witt, M. Figa, M. Figueiredo, A. Horhota, S. Low, K. McDonnell, E. Peeke, B. Retnarajan, A. Sabnis, E. Schnipper, J. J. Song, Y. H. Song, J. Summa, D. Tompsett, G. Troiano, T. Van Geen Hoven, J. Wright, P. LoRusso, P. W. Kantoff, N. H. Bander, C. Sweeney, O. C. Farokhzad, R. Langer and S. Zale, *Science Translational Medicine*, 2012, **4**, 128ra139.
69. Y. Liu, G. Yang, T. Baby, Tengjisi, D. Chen, D. A. Weitz and C.-X. Zhao, *Angewandte Chemie International Edition*, 2020, **59**, 4720-4728.
70. J.-i. Kuroda, J.-i. Kuratsu, M. Yasunaga, Y. Koga, Y. Saito and Y. Matsumura, *International Journal of Cancer*, 2009, **124**, 2505-2511.
71. P. J. Houghton, G. S. Germain, F. C. Harwood, J. D. Schuetz, C. F. Stewart, E. Buchdunger and P. Traxler, *Cancer research*, 2004, **64**, 2333-2337.
72. Y. Yao, X. Su, Y. Xie, Y. Wang, T. Kang, L. Gou, C. Yi and J. Yang, *Anti-cancer drugs*, 2013, **24**, 270-277.
73. M. Hoyle, L. Crathorne, J. Peters, T. Jones-Hughes, C. Cooper, M. Napier, P. Tappenden and C. Hyde, *Health Technology Assessment,*2013*,* **17**,14.
74. Electronic medicines compendiu, https://www.medicines.org.uk/emc/product/2213/smpc, (accessed October 2020).

# Chapter 5

*In Vitro* and *In Vivo* Pharmacological Assessment of SN-38 Loaded Branched Vinyl Co-Polymer Nanoparticles

## 5.1 Pharmacological Studies of SN-38 Loaded Co-nanoprecipitated Nanoparticles

Polymer nanoparticles administered *in vivo* can initiate a myriad of different biological responses, as discussed in Chapter 1.4, but their overall effect, whether valuable or deleterious, is governed by their interactions at a cellular level.[1] The interactions of polymer nanoparticles with cells can modulate cellular fate, induce or prevent mutations, initiate cell-cell communication, and modulate their cellular structure in a way that is largely dictated by phenomena occurring at the nano-bio interface.[1] When in biological fluids nanoparticles can acquire different physicochemical properties, and typically the surface of the nanoparticle can be dramatically modified through the adsorption of proteins.[2] This protein-corona alters the size and the interfacial composition of the nanoparticles, thereby creating a biological identity that is distinctly different to its original chemistry.[3] This biological identity determines the physiological response including accumulation and toxicity. There are several factors that may affect the polymer nanoparticle's biological identity: 1) its physical characteristics such as size, polydispersity, shape, charge and surface chemistry, 2) the nature of the physiological environment (e.g. blood type, cell cytoplasm, protein abundance), and 3) experimental parameters, including duration of exposure.[4, 5]

One of the primary assessments of chemotherapeutics for cancer and their therapeutic utility is their ability to cause cellular death. This potency is a crucial parameter to consider when evaluating anti-cancer DDS. Additionally, for an anti-cancer DDS to achieve high therapeutic efficacy and success, the intercellular fate of the nanoparticle is also critical. In order to evaluate how SN-38 loaded branched vinyl polymer nanoparticles would behave in biological environments and to assess their cellular toxicity, a series of *in vitro* and *in vivo* pharmacological evaluations were conducted using the materials described in Chapter 4. All of the pharmacological experiments presented within this chapter were completed by Usman Arshad in the Molecular and Clinical Pharmacology Department at the University of Liverpool under the supervision of Professors Andrew Owen and Chris Goldring; however, the presentation and interpretation of the data are that of the author. Fourteen of the

SN-38 encapsulated nanoparticles prepared and presented in Chapter 4 were taken forward for *in vitro* analysis.

### 5.1.1 Determining SN-38 Equilibration Rate *via* Rapid Equilibrium Dialysis

To facilitate a quick screening of the SN-38 loaded nanoformulations that were described in Chapter 4, *in vitro* release kinetics were studied using rapid equilibrium dialysis (RED) devices (Figure 5.1). The RED device insert is made up of two side-by-side compartments, one donor and one acceptor, which are separated by a cellulose dialysis membrane with a specified molecular weight cut-off (MWCO). The insert is then used within a base plate that can hold up to 48 RED device inserts, which allows for high throughput screening. The high surface area-to-volume ratio of the dialysis membrane enabled rapid equilibration and allowed any differences in equilibration times i.e. release rates between drug loaded formulations to be identified. SN-38 loaded nanoparticles were added to the donor compartment and the concentration of SN-38 in the acceptor compartment was determined at time intervals. This was then used to generate a qualitative assessment of overt differences in behaviour between the formulations. A similar study has been reported on SDN-based DDS of atovaquone, an antimalarial drug.[6]

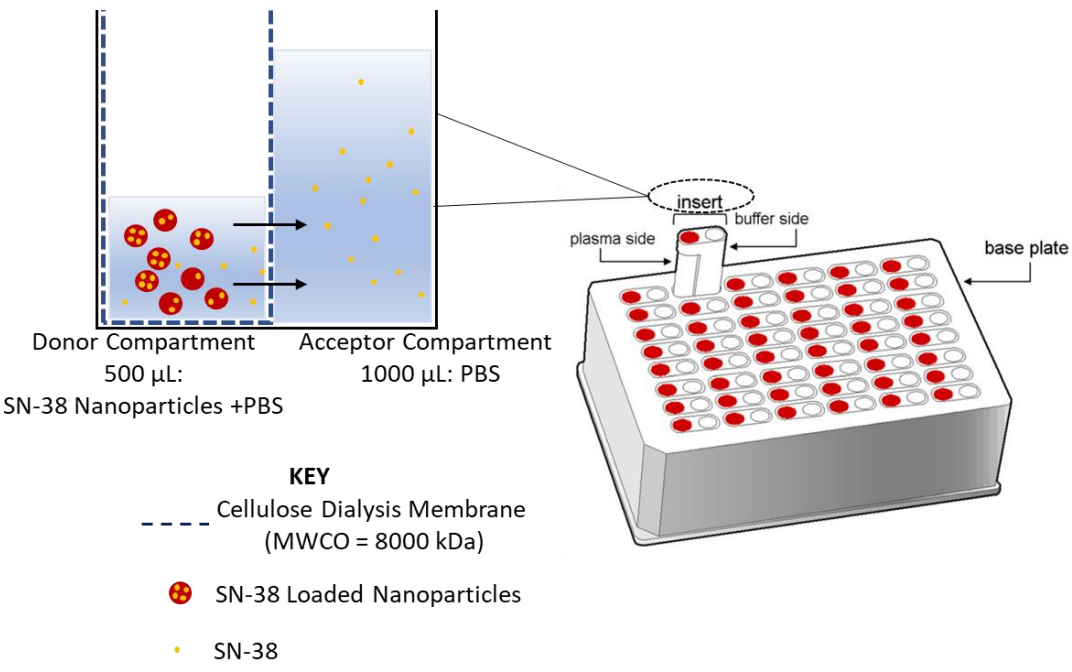


**Figure 5.1** A schematic representation of the Rapid Equilibrium Dialysis setup.

To determine whether there were any differences in equilibration between the SN-38 nanoformulations, 5 wt.% SN-38 loaded nanoparticles were diluted to 250 ng $mL^{-1}$ in PBS (pH 7.4) and compared to free SN-38. Free SN-38 was dissolved in DMSO prior to dilution with PBS, such that DMSO comprised < 1% of the final volume. To assess the SN-38 release kinetics, 0.5 mL of the samples were added to the donor compartments of 8 kDa MWCO RED inserts and 1 mL PBS was added to the acceptor compartments. Plates containing the inserts were placed on an orbital shake which was set at 37 °C. Each insert represented a single time-point and at 0.5, 1, 2, 3, 4, 5, 6, 7, 8 and 24 hours both the acceptor fluids (1 mL) and donor fluids (0.5 mL) were removed. Aliquots of each time-point sample were then used to determine concentrations of SN-38 in each compartment using a validated liquid chromatography with tandem mass spectrometry (LC-MS) method. Since this experiment represents an equilibrium assay, the experiment was completed once the concentration of SN-38 in each compartment was the same (i.e. 50% of the initial SN-38 concentration was detected in the acceptor compartment). Data is shown as the cumulative release (%) of SN-38 that has been determined to have diffused across the membrane at the set time-points (Figure 5.2-5.4). It is important to reiterate that each time-point is represented by a single insert and that the experiment is completed once 50 % of the total SN-38 concentration has been detected. This experiment differs from the radio-dialysis described in Chapter 4.5 and the two experiments and their results are not inter-changeable or comparable.

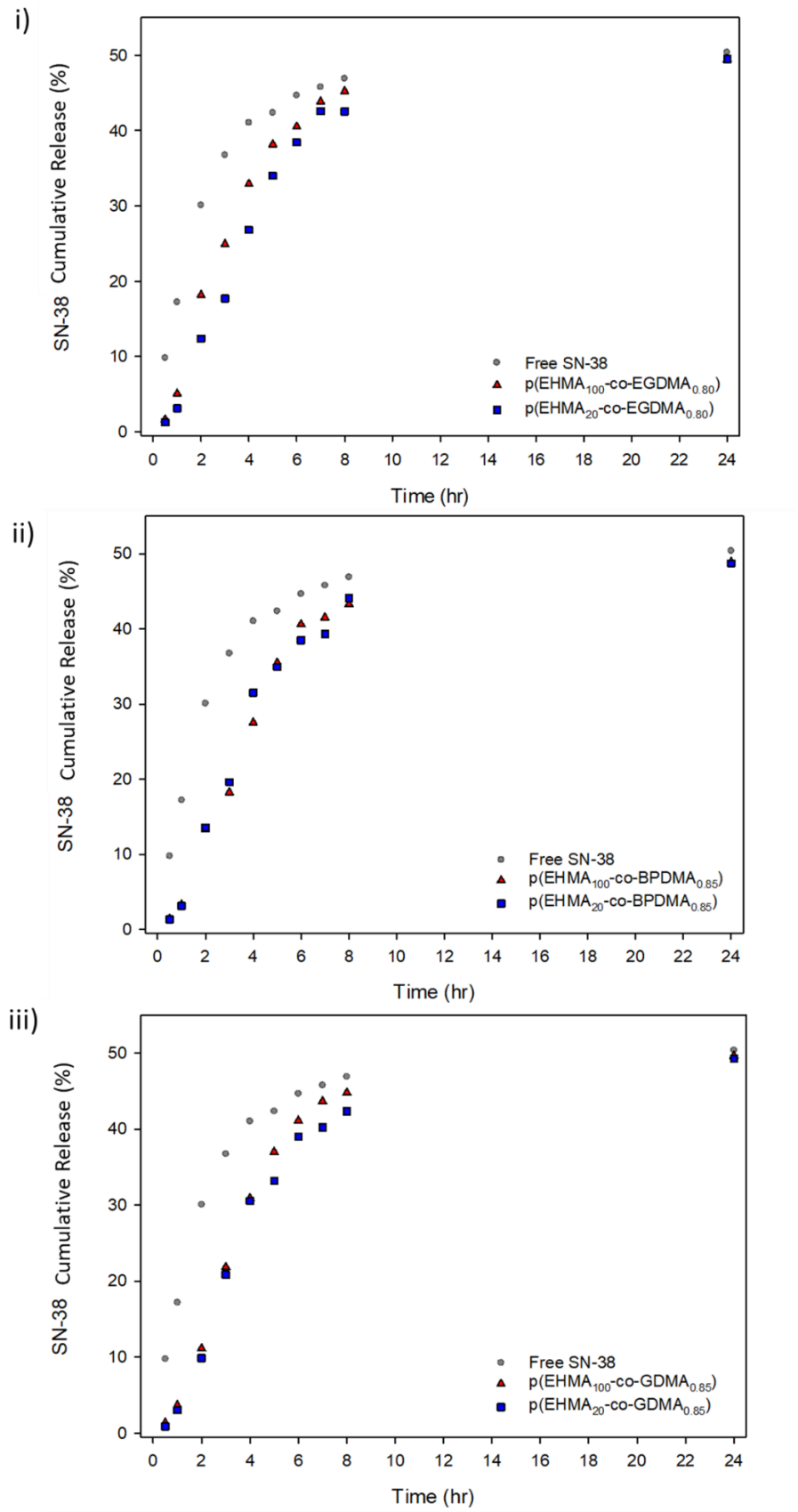


**Figure 5.2** SN-38 cumulative release (%) data obtained over a period of 24 hours *via* RED of SN-38 loaded: i) p(EHMA$_n$-co-EGDMA), ii) p(EHMA$_n$-co-BPGDMA) and iii) p(EHMA-co-GDMA) branched vinyl copolymers co-nanoprecipitated with AB block copolymer p(PEG$_{114}$-*b*-HPMA$_{100}$) (60:40 wt. % respectively), compared to free SN-38 (grey circles). Where, n represents DP$_{20}$ or DP$_{100}$ monomer units.

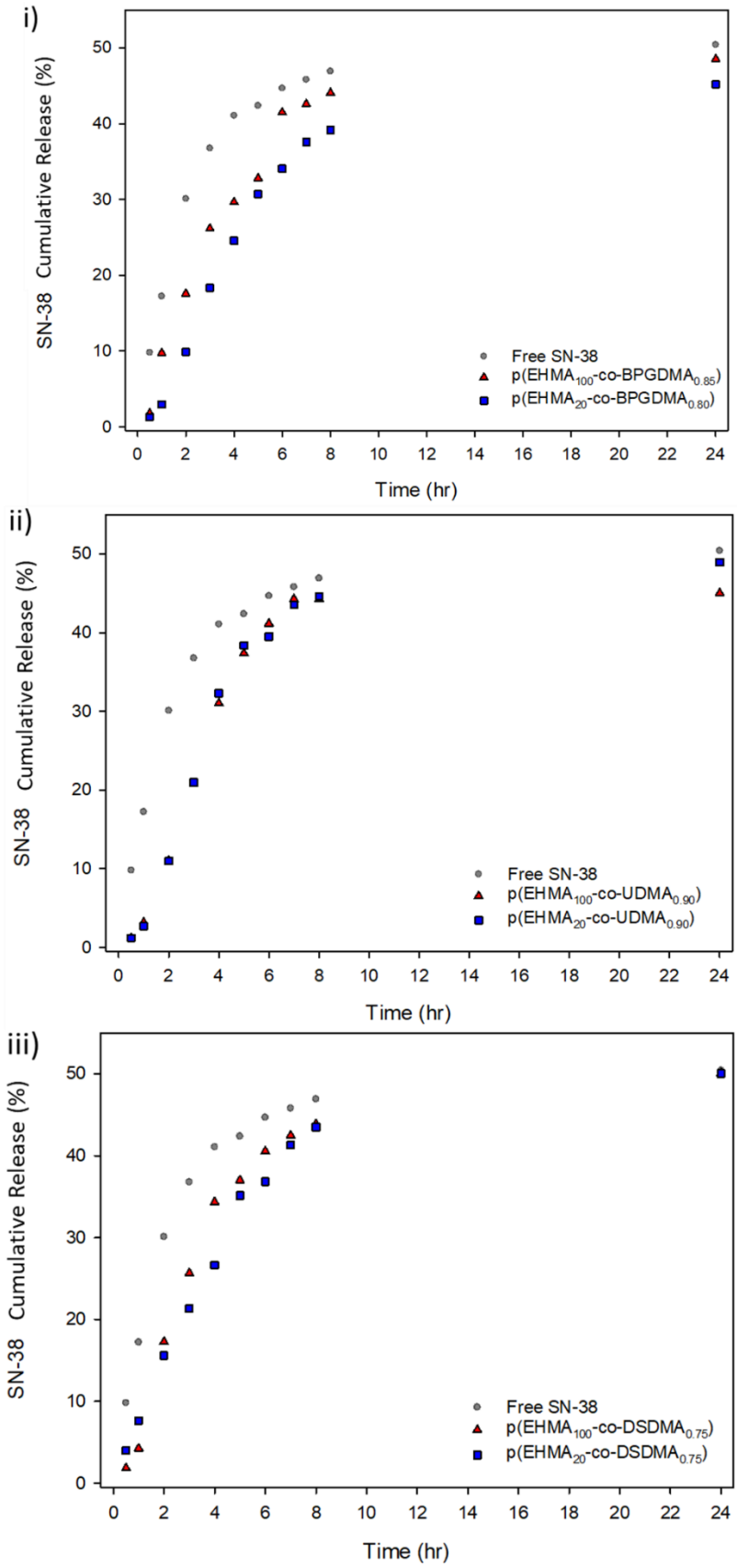


**Figure 5.3** SN-38 cumulative release (%) data obtained over a period of 24 hours *via* RED of SN-38 loaded: i) p(EHMA$_n$-co-BPGDMA), ii) p(EHMA-co-UDMA) and iii) p(EHMA-co-DSDMA) branched vinyl copolymers co-nanoprecipitated with AB block copolymer p(PEG$_{114}$-*b*-HPMA$_{100}$) (60:40 wt. % respectively), compared to free SN-38 (grey circles). Where, n represents DP$_{20}$ or DP$_{100}$ monomer units.

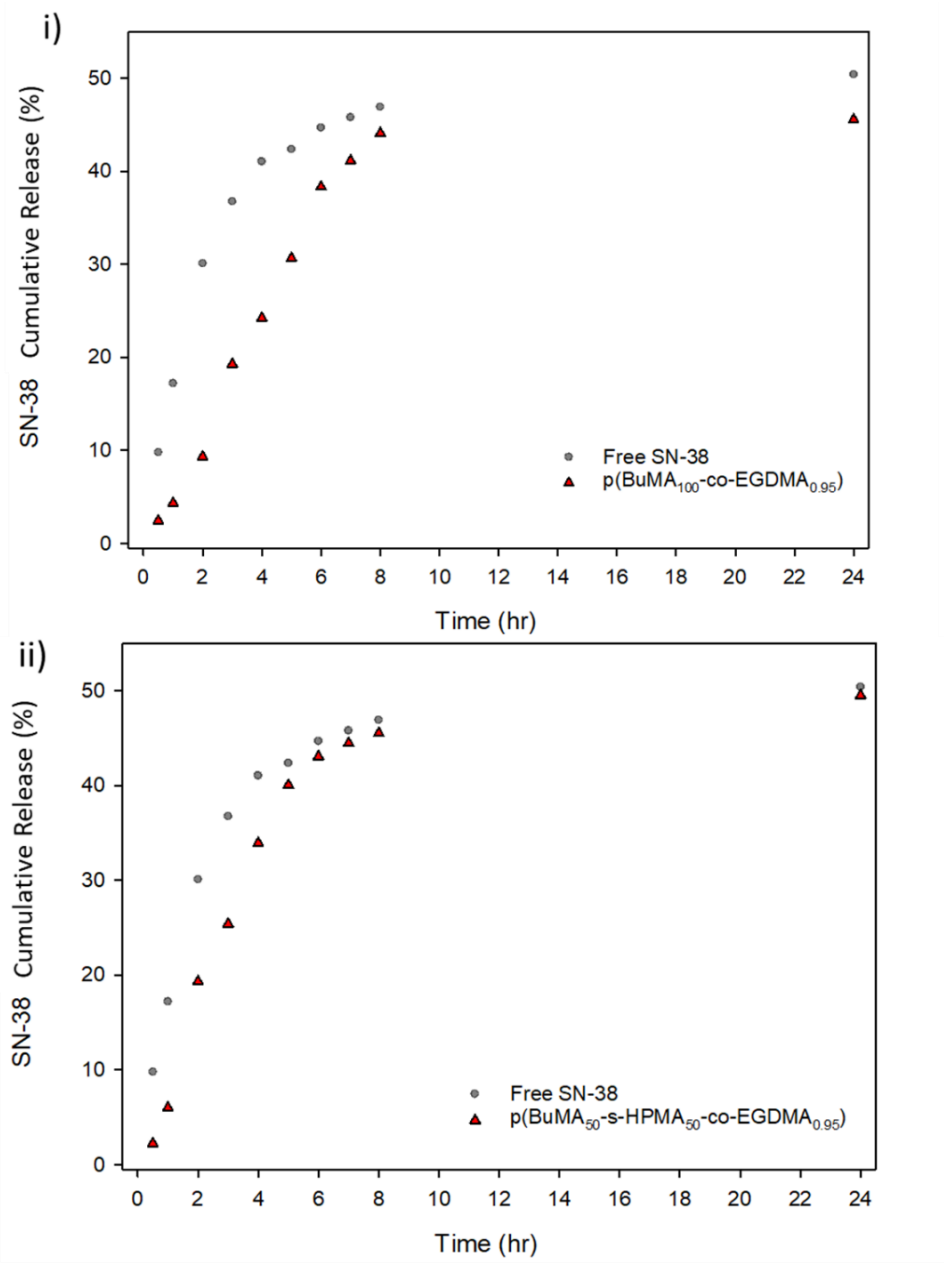


**Figure 5.4** SN-38 cumulative release (%) data obtained over a period of 24 hours *via* RED of SN38 loaded: i) p(BuMA$_{100}$-co-EGDMA$_{0.95}$) and ii) p(BuMA$_{50}$-*s*-HPMA$_{50}$-co-EGDMA$_{0.95}$) compared to free SN-38 (grey circles). Where, n represents DP$_{20}$ or DP$_{100}$ monomer units.

In all cases, it is evident that SN-38 loaded nanoparticles have a slower equilibration in comparison to free SN-38. This is consistent with previous observations from the radio release experiments presented in Chapter 4.5 and further suggests that very little free drug is present in the aqueous solution and that the majority of SN-38 is encapsulated within the polymer nanoparticles, since no burst release was observed. The equilibration profiles seem to vary between the fourteen tested SN-38 nanoformulations, although none of the variations in polymer functionality or branching chemistry had any meaningful or significant influence on the cumulative

release after 24-hours. However, reducing the $DP_n$ value from 100 to 20 monomer units showed a reduction in the SN-38 equilibration of the SN-38 loaded polymer co-nanoprecipitates within the 8-hour time frame for: p($EHMA_{20}$-co-$EGDMA_{0.80}$) (Figure 5.2i) and p(EHMA-co-$BPGDMA_{0.80}$) co-nanoprecipitated with AB block copolymer p($PEG_{114}$-*b*-$HPMA_{100}$) (60:40 wt. % respectively) (Figure 5.3i). For example, after 3 hours equilibration time, p($EHMA_{100}$-co-$EGDMA_{0.80}$) had a cumulative release of approximately 26 % compared to p($EHMA_{20}$-co-$EGDMA_{0.80}$) which had a cumulative release of approximately 17 %, which equates to a reduction of approximately 34.6 % less SN-38 released under the same conditions within the same time. Additionally, similar was observed for p($EHMA_{100}$-co-$BPGDMA_{0.85}$) after 3 hours equilibration time, which had cumulative release of approximately 26 %, compared to approximately 18 % cumulative release for p($EHMA_{20}$-co-$BPGDMA_{0.80}$), a reduction of approximately 30.8 % in SN-38 release. Since the monomer and divinyl chemistry is remaining the same, one of the only known differences is the polymer primary chain length and the subsequent mass of divinyl monomer present per unit of polymer mass. Therefore, it can be postulated that these reductions to the SN-38 equilibration may be due to a number of factors; for example, SN-38 interactions with the polymeric core of the nanoparticle may be affected by 1) the increased relative mass of divinyl monomer, 2) the increase in chain-end concentration, or 3) the variation in *Tg* that would be present as the primary chain length decreases. Variations to the $DP_n$ value within the other polymeric systems had little effect on SN-38 equilibration.

Five candidates were selected for further *in vitro* studies due to time and experimental constraints; however, it was difficult to identify these candidates as the differences in the extent of drug release was relatively small and there was no single candidate that appeared to dramatically delay drug release compared to each other.

Since the optimal equilibration rate for these DDS was unknown, in order to select a broad range of candidates for further *in vitro* studies, analysis of the curves was conducted that allowed an evaluation of the differences at specific times and identification of formulations that appeared to have the fastest or most delayed release. Comparisons of cumulative release to free SN-38 were chosen at four time points to provide this analysis: early time-points (0.5 and 1 hours), an intermediate time-point (6 hours) and the final time-point (24 hours), each of which are represented in Figure 5.3i-iii.

Analysis at 0.5 hours equilibration showed that all 14 nanoformulations did not demonstrate a burst release as their cumulative release rates were all lower (< ~4 %) than that obtained for free SN-38 (~ 10%). In addition, the initial equilibration of these formulations was all similar, except for p($EHMA_{20}$-co-$DSDMA_{0.75}$) (Figure 5.5iii) which had the largest SN-38 cumulative release (~ 4%). Since this suggests it has the fastest SN-38 release rate at this time point under these conditions, it was of interest to study this formulation with further *in vitro* studies, therefore it was selected.

The cumulative release after 1 hour was compared, and two formulations were chosen: p($EHMA_{100}$-co-$BPGDMA_{0.85}$) (Figure 5.5ii) and p($EHMA_{20}$-co-$UDMA_{0.90}$) (Figure 5.5iii), which had the highest and lowest cumulative release with approximate values of 10 % and 3 %, respectively, compared to free SN-38 which had a cumulative release of approximately 17 % after 1 hour. These cumulative release values correspond to the “fastest” and “slowest” SN-38 release at 1 hour.

Input from an industrial collaborator, AstraZeneca, suggested that differences within the first 8 hours was important for seeing *in vivo* differences between formulations, the 6-hour timepoint was therefore selected as a key determinant of potential benefit. Overall, p($BuMA_{50}$-*s*-$HPMA_{50}$-co-$EGDMA_{0.95}$) exhibited the highest cumulative release (~ 43 %) and was similar to that compared of free SN-38 (~ 44 %). This increased cumulative release value compared to the other formulations was likely due to weaker polymer-drug intermolecular interactions experienced.

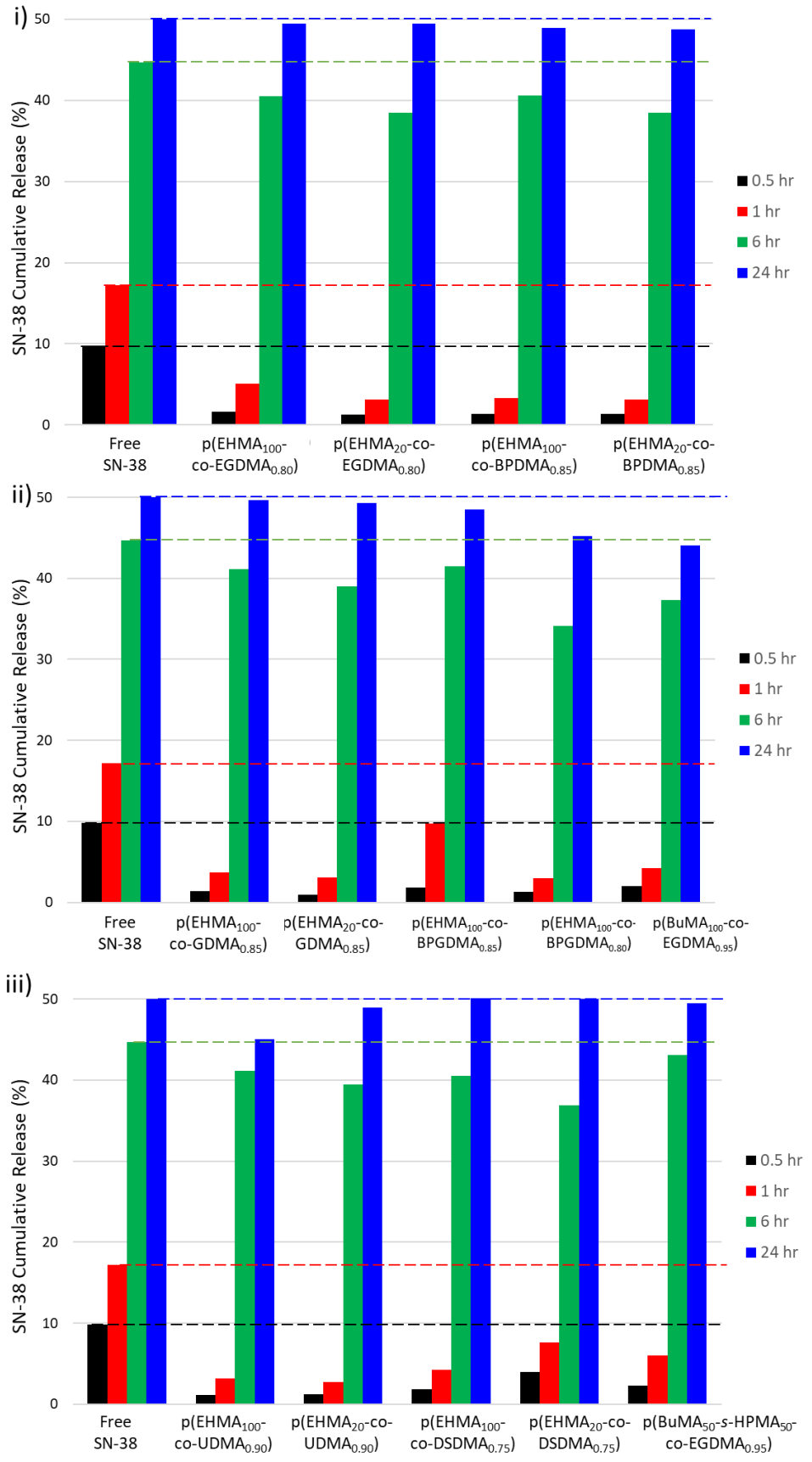


**Figure 5.5** Graphical representation of the SN-38 loaded nanoformulations cumulative release at 0.5 hour (black bar), 1 hour (red bar), 6 hours (green bar) and 24 hours (blue bar) compared to free SN-38 (dashed lines).

Looking at the equilibration after 24 hours, the nanoformulation with the "slowest" equilibration rate compared to free SN-38 was selected, which corresponded to p($BuMA_{100}$-co-$EGDMA_{0.95}$) with a cumulative release of approximately 44 %. The selection of SN-38 nanoformulations for further *in vitro* and *in vivo* studies effectively bracketed the range of release behaviours available within the library of materials generated within this programme. The chosen candidates are presented in Table 5.1.

**Table 5.1** SN-38 nanoparticle formulations that were selected for further *in vitro* pharmacological assessment.

| Nanoparticle Composition (60:40 wt. %) | Reason for Selection |
|---|---|
| p($BuMA_{100}$-co-$EGDMA_{0.95}$):p($PEG_{114}$-$HPMA_{100}$) | "Slowest" equilibration (24 hours) |
| p($EHMA_{20}$-co-$UDMA_{0.90}$):p($PEG_{114}$-$HPMA_{100}$) | "Slowest" equilibration (1 hours) |
| p($EHMA_{20}$-co-$DSDMA_{0.75}$):p($PEG_{114}$-$HPMA_{100}$) | "Fastest" equilibration (0.5 hours) |
| p($EHMA_{100}$-co-$BPGDMA_{0.90}$):p($PEG_{114}$-$HPMA_{100}$) | "Fastest" equilibration (1 hours) |
| p($BuMA_{50}$-*s*-$HPMA_{50}$-co-$EGDMA_{0.95}$):p($PEG_{114}$-$HPMA_{100}$) | "Highest" equilibration (6 hours) |

### 5.1.2 ATP assays to Determine Cytotoxicity of SN-38 Nanoformulations in 2D *HCT-116, CT-26, LoVo* and *DLD-1* cell lines and 3D Spheroids from *HCT-116* and *CT-26*

The treatment of cells with a cytotoxic compound can result in a variety of different cell fates such as: necrosis (accidental cell death), apoptosis (programmed cell death), or a decrease in cell viability. Cytotoxicity assays are widely used to determine how toxic compounds are to cells.[7, 8] One method commonly used to assess the cytotoxicity is the use of adenosine triphosphate (ATP) assays, which quantify ATP levels. ATP can be used as a marker of cell-viability since only metabolically active cells produce ATP, whereas dead cells do not.[9] DDS encapsulating chemotherapeutic agents should aim to at least maintain, if not decrease, the cell viability level compared to the non-formulated chemotherapeutic.

Experiments were conducted to evaluate the cytotoxicity of the SN-38 loaded nanoformulations in both human and murine CRC cell lines. The cytotoxicity's of the selected SN-38 loaded nanoformulations were compared against free SN-38 and IR. ATP assays were conducted using CellTiter-Glo® Luminsecent cell viability assays (Promega, UK) according to manufacturer's instructions. Four different cell lines obtained from humans and mice were investigated: human colorectal cancer *(HTC-116)*, murine colorectal cancer (*CT-26)*, human colorectal adenocarcinoma (*LoVo)*, and Dukes' type C colorectal adenocarcinoma (*DLD-1)*. ATP quantification was measured by a luciferin-luciferase assay using a Varioscan flash fluorescent plate reader measuring the luminescence at 570 nm wavelength. Cell viability was calculated as a percentage of untreated vehicle control (DMSO – 0.1%) or blank nanoformulation sample and used to determine the half maximal inhibitory concentration ($IC_{50}$) value (mean ± SD, n=3) after 48, 72, and 96-hours incubation time. ATP assays were conducted across a range of concentrations ([SN-38] = 0.5 to 400 nM and [IR] = 0.01 to 100 µM), with free SN-38 and IR in solutions with 0.1% DMSO. The *in vitro* cytotoxic effect of SN-38 loaded nanoformulations, free SN-38 and IR is presented in Figure 5.6 and Figure 5.7 A-D. Additionally, the *in vitro* cytotoxicity of the polymer nanoparticles without SN-38 was also tested.

For all five of the nanoformulations with no SN-38 loaded, $IC_{50}$ values were not obtained since the blank nanoformulations were not cytotoxic at the concentration range used (i.e. the value for cell viability = 100 %). This is a positive observation as it suggests that the polymer-based nanoparticles did not disrupt any of the cellular membranes or elicit any toxicity. This means that any toxicity observed after the incorporation of SN-38 is a direct result of the inclusion of the potent payload.

Through the incorporation of SN-38 within the nanoformulations a decrease in cell viability was observed, indicating that the SN-38 nanoformulations were toxic (Figure 5.6 and 5.7). This was to be expected since SN-38 is the toxic, active metabolite of IR that is used clinically as a chemotherapeutic. When compared to IR, the *in vitro* cytotoxicity experiments demonstrated that the SN-38 loaded nanoparticles had superior cytotoxicity in all four cell lines and the $IC_{50}$ values were significantly lower

than the $IC_{50}$ values of IR (Table 5.2). The symbol X, included on Figure 5.6 and 5.7 represents were an $IC_{50}$ was not calculated within this concentration range or incubation time. Except, in the instance of the missing $IC_{50}$ value for co-nanoprecipitate regime, p($BuMA_{100}$-co-$EGDMA_{0.95}$), after 72 hours incubation which was not determined due to experimental error.

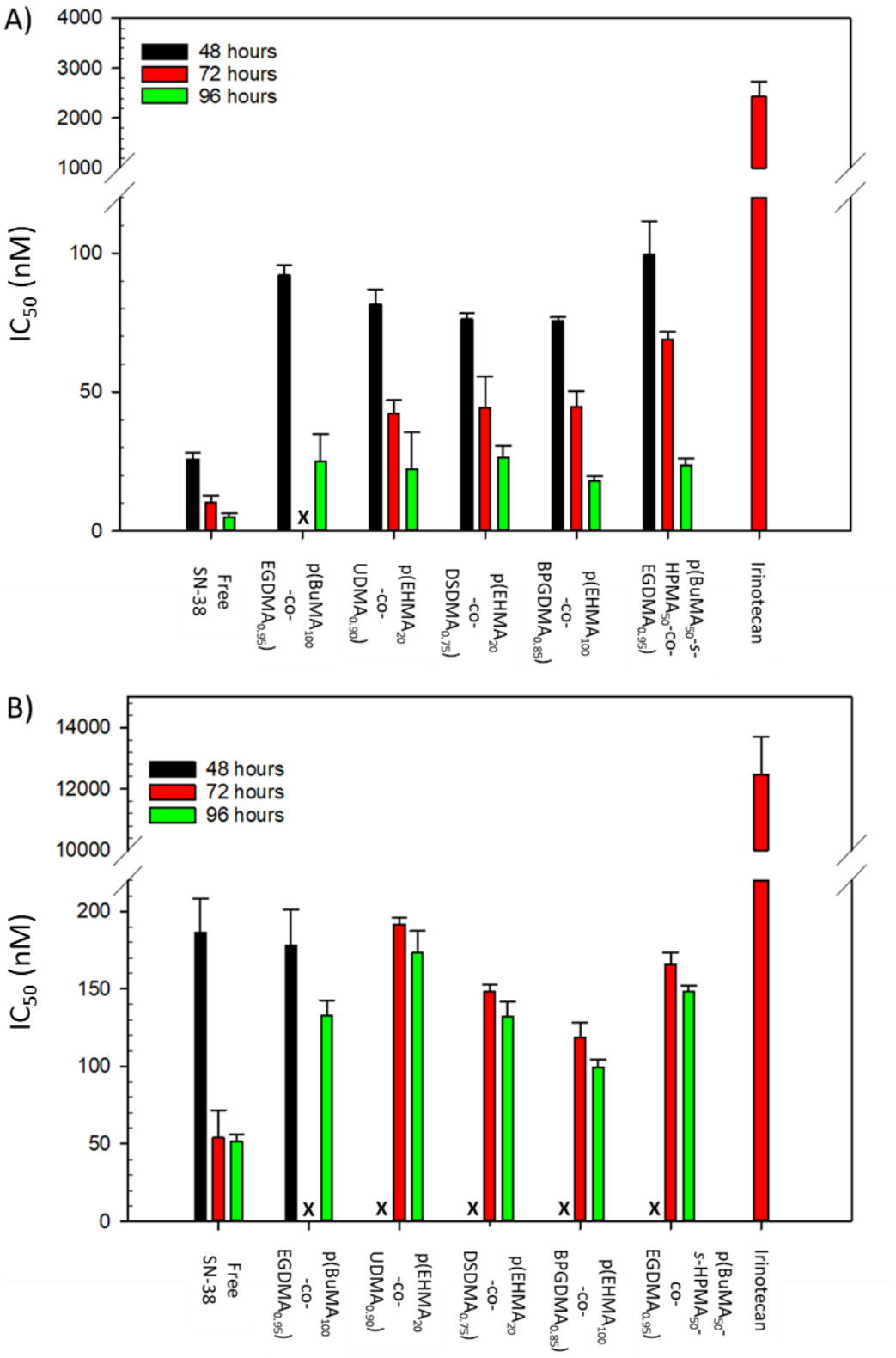


**Figure 5.6** *In-vitro cell* viability study of A) HCT 116 and B) CT 26 cancer cells after treatment with free SN-38, SN-38 loaded: (p($BuMA_{100}$-co-$EGDMA_{0.95}$):p($PEG_{114}$-*b*-$HPMA_{100}$) 60:40 wt.%), (p($EHMA_{20}$-co-$UDMA_{0.90}$):p($PEG_{114}$-*b*-$HPMA_{100}$) 60:40 wt.%) , p($EHMA_{20}$-co-$DSDMA_{0.75}$), (p($EHMA_{20}$-co-$BPGDMA_{0.80}$):p($PEG_{114}$-*b*-$HPMA_{100}$) 60:40 wt.%) and (p($BuMA_{50}$-*s*-$HPMA_{50}$-*co*-$EGDMA_{0.90}$):p($PEG_{114}$-*b*-$HPMA_{100}$) 60:40 wt.%) after 48 (black), 72 (red) and 96 hours (green) incubation. X represents were an $IC_{50}$ was not calculated within this concentration range.

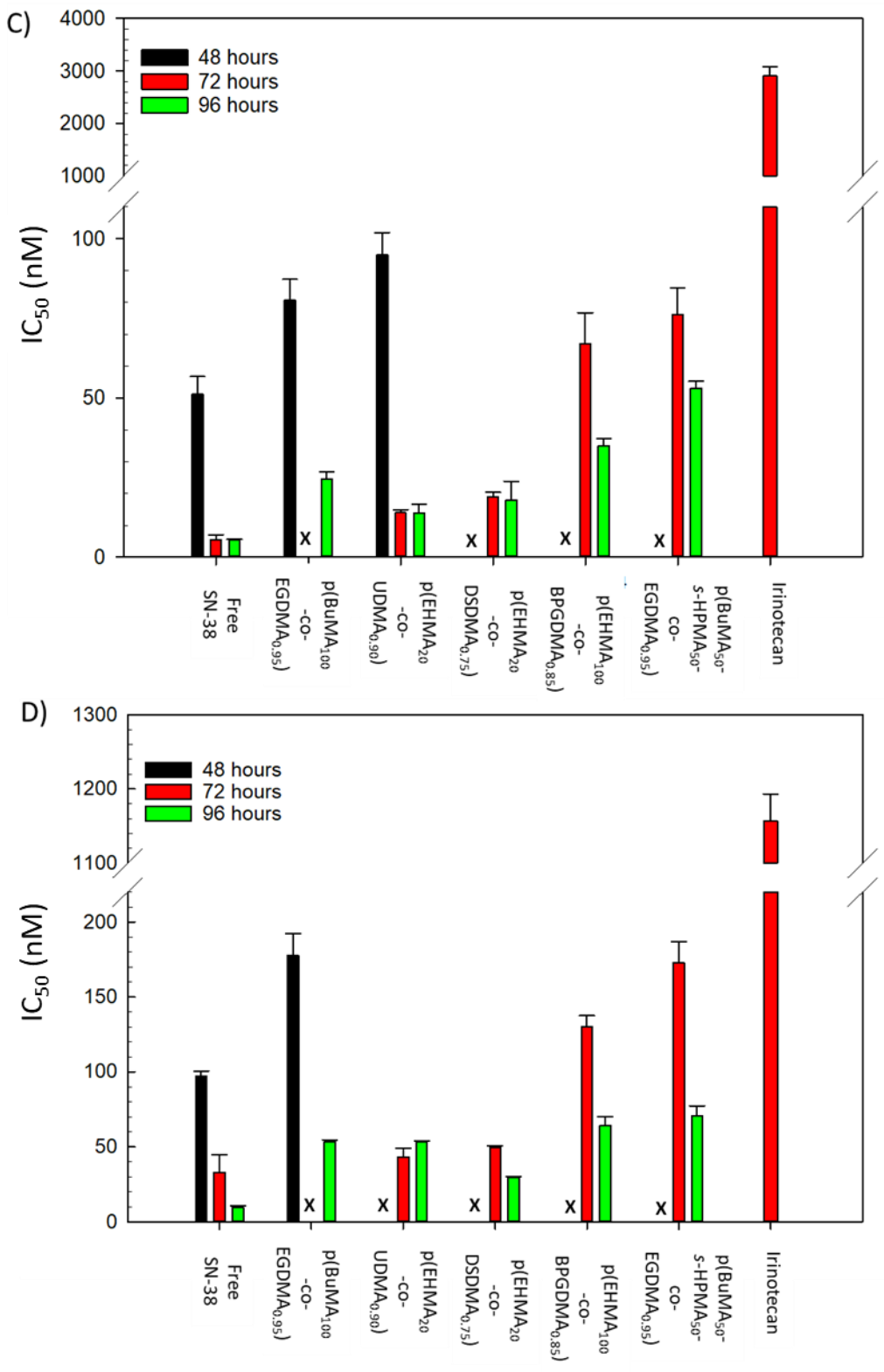


**Figure 5.7** *In-vitro cell* viability study of C) LoVo and D) DLD-126 cancer cells after treatment with free SN-38, SN-38 loaded: (p($BuMA_{100}$-co-$EGDMA_{0.95}$):p($PEG_{114}$-*b*-$HPMA_{100}$) 60:40 wt.%), (p($EHMA_{20}$-co-$UDMA_{0.90}$):p($PEG_{114}$-*b*-$HPMA_{100}$) 60:40 wt.%) , p($EHMA_{20}$-co-$DSDMA_{0.75}$), (p($EHMA_{20}$-co-$BPGDMA_{0.80}$):p($PEG_{114}$-*b*-$HPMA_{100}$) 60:40 wt.%) and (p($BuMA_{50}$-*s*-$HPMA_{50}$-*co*-$EGDMA_{0.90}$):p($PEG_{114}$-*b*-$HPMA_{100}$) 60:40 wt.%) after 48 (black), 72 (red) and 96 hours (green) incubation. X represents were an $IC_{50}$ was not calculated within this concentration range.

**Table 5.2** $IC_{50}$ values of SN-38 nanoformulations 1-5, free SN-38 and irinotecan on HCT-116, CT-26, LoVo and DLD-1 cell lines after 48, 72 and 96-hour incubation times. Cell viability was determined by CellTiter-Glo® Luminsecent cell viability assay. Values are mean ± SD (*n* = 3).

| [a] Nanoparticle Formulation | Incubation time (h) | $IC_{50}$ (nM) HCT-116 | $IC_{50}$ (nM) CT-26 | $IC_{50}$ (nM) LoVo | $IC_{50}$ (nM) DLD-1 |
|---|---|---|---|---|---|
| p(BuMA$_{100}$-co-EGDMA$_{0.95}$): | 48 | 92 ± 3 | 178 ± 23 | 81 ± 7 | 178 ± 15 |
| p(EHMA$_{20}$-co-UDMA$_{0.90}$) | | 82 ± 5 | - | 95 ± 7 | - |
| p(EHMA$_{20}$-co-DSDMA$_{0.75}$) | | 76 ± 2 | - | - | - |
| p(EHMA$_{100}$-co-BPGDMA$_{0.90}$) | | 76 ± 1 | - | - | - |
| p(BuMA$_{50}$-*s*-HPMA$_{50}$-co-EGDMA$_{0.95}$) | | 99 ± 12 | - | - | - |
| SN-38 | | 26 ± 2 | 186 ± 22 | 51 ± 6 | 97 ± 3 |
| Irinotecan | | 95252 ± 391 | 18381 ± 1082 | 17914 ± 637 | 4259 ± 530 |
| p(BuMA$_{100}$-co-EGDMA$_{0.95}$): | 72 | - | - | - | - |
| p(EHMA$_{20}$-co-UDMA$_{0.90}$) | | 42 ± 5 | 192 ± 4 | 14 ± 1 | 43 ± 5 |
| p(EHMA$_{20}$-co-DSDMA$_{0.75}$) | | 44 ± 11 | 148 ± 4 | 19 ± 1 | 49 ± 1 |
| p(EHMA$_{100}$-co-BPGDMA$_{0.90}$) | | 45 ± 6 | 119 ± 9 | 67 ± 10 | 129 ± 8 |
| p(BuMA$_{50}$-*s*-HPMA$_{50}$-co-EGDMA$_{0.95}$) | | 69 ± 3 | 166 ± 8 | 76 ± 8 | 173 ± 14 |
| SN-38 | | 10 ± 2 | 54 ± 18 | 6 ± 1 | 33 ± 12 |
| Irinotecan | | 2430 ± 311 | 12478 ± 1236 | 2906 ± 171 | 1156 ± 37 |
| p(BuMA$_{100}$-co-EGDMA$_{0.95}$): | 96 | 24 ± 10 | 133 ± 10 | 24 ± 2 | 53 ± 1 |
| p(EHMA$_{20}$-co-UDMA$_{0.90}$) | | 22 ± 13 | 173 ± 14 | 14 ± 3 | 53 ± 1 |
| p(EHMA$_{20}$-co-DSDMA$_{0.75}$) | | 26 ± 4 | 132 ± 10 | 18 ± 6 | 30 ± 1 |
| p(EHMA$_{100}$-co-BPGDMA$_{0.90}$) | | 17 ± 2 | 99 ± 5 | 35 ± 2 | 64 ± 6 |
| p(BuMA$_{50}$-*s*-HPMA$_{50}$-co-EGDMA$_{0.95}$) | | 26 ± 2 | 148 ± 4 | 53 ± 2 | 71 ± 6 |
| SN-38 | | 5 ± 1 | 51 ± 4 | 6 ± 1 | 10 ± 1 |
| Irinotecan | | 906 ± 141 | 2596 ± 236 | 926 ± 71 | 832 ± 120 |

[a] All branched copolymer nanoparticle included AB block copolymer p(PEG$_{114}$-*b*-HPMA$_{100}$) 60:40 wt. %

For example, in HCT-116 cell line, a range of low $IC_{50}$ values for SN-38 loaded nanoformulations were obtained ($76 \pm 1 \leq IC_{50} \leq 99 \pm 12$ nM) compared to the higher $IC_{50}$ value for IR ($95253 \pm 391$ nM) after 48 hours incubation time. These $IC_{50}$ values for the SN-38 loaded nanoformulations suggest that they demonstrate more than a 1000-fold greater cytotoxic behaviour compared to IR alone.

When compared to free SN-38 $IC_{50}$ values in all four cell lines and at all three-incubation time points, the obtained $IC_{50}$ values for the five SN-38 loaded nanoformulations were slightly higher. For example, in HCT-116 cell lines the $IC_{50}$ values for all of the SN-38 loaded nanoformulations ($18 \pm 2 \leq IC_{50} \leq 27 \pm 2$ nM) were slightly higher than the $IC_{50}$ value obtained for free SN-38 ($5 \pm 1$ nM). This indicates that free SN-38 showed greater cytotoxicity than the SN-38 loaded nanoparticles. Which is indicative of a fraction of the SN-38 being within the nanoparticles and therefore acting as if it is a lower concentration of available free SN-38. Therefore, whilst the SN-38 loaded nanoformulations were slightly less cytotoxic compared to free SN-38, they are representative of SN-38 that can potentially be administered *in vivo* and have a significantly greater cytotoxic effect than IR. The apparent decrease in direct toxicity, observed for encapsulated SN-38, may offer additional advantages *in vivo* as high concentrations of IR induces intestinal toxicity and severe diarrhoea;[10, 11] the direct cause of which is believed to be associated by the reconversion of SN-38 glucuronide, a waste metabolite of SN-38, back into SN-38 which is then retained for long periods in the intestine.

In all four cell lines, a time response is observed for free SN-38, SN-38 loaded nanoformulations and IR. This time response indicates that cell viability continues to decrease with time following the initial treatment with the formulations. Within error, the five different SN-38 loaded nanoformulations did not differ with any statistical significance in cytotoxicity behaviour following statistical analysis which was conducted *via* a two-way ANOVA and a Holm-Šídák post-hoc analysis.

Additional studies were also conducted using 3D spheroids created with HCT-116 and CT-26 cells after incubation for 72 and 144 hours. Cellular viability decreased

proportionally with increasing SN-38 concentration and tumour size was seen to decrease (Figure 5.8-5.13).

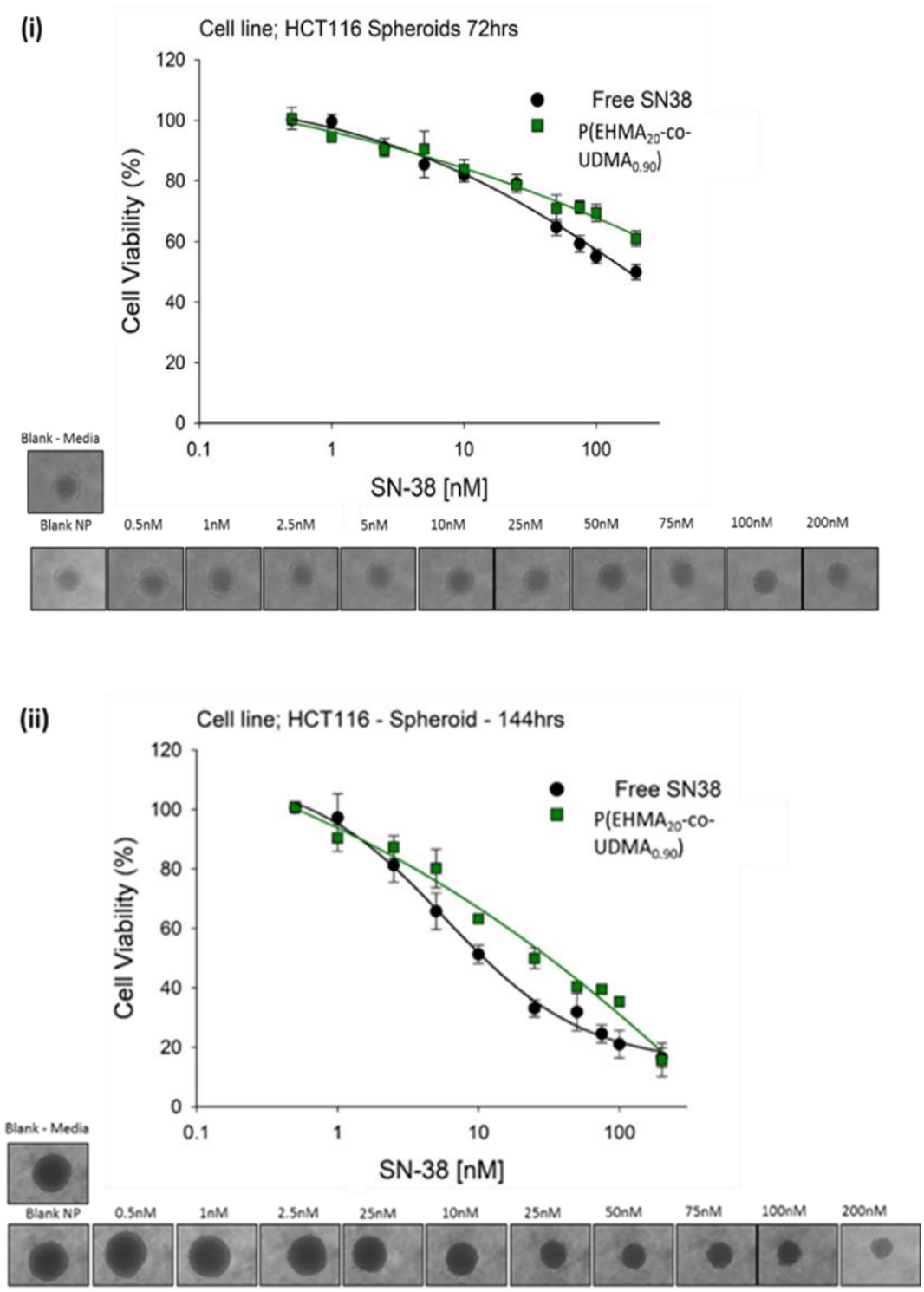


**Figure 5.8** Cell viability graphs for SN-38 loaded p(EHMA$_{20}$-co-UDMA$_{0.90}$):p(PEG$_{114}$-*b*-HPMA$_{100}$) (60:40 wt. %) nanoparticles in 3D spheroids grown from HCT 116 cell lines after i) 72 hours incubation time and ii) 144 hours incubation time. Microscope images also displaying tumour shrinkage following the administration of the SN-38 loaded p(EHMA$_{20}$-co-UDMA$_{0.90}$):p(PEG$_{114}$-*b*-HPMA$_{100}$) (60:40 wt. %) nanoparticles at varying concentrations.

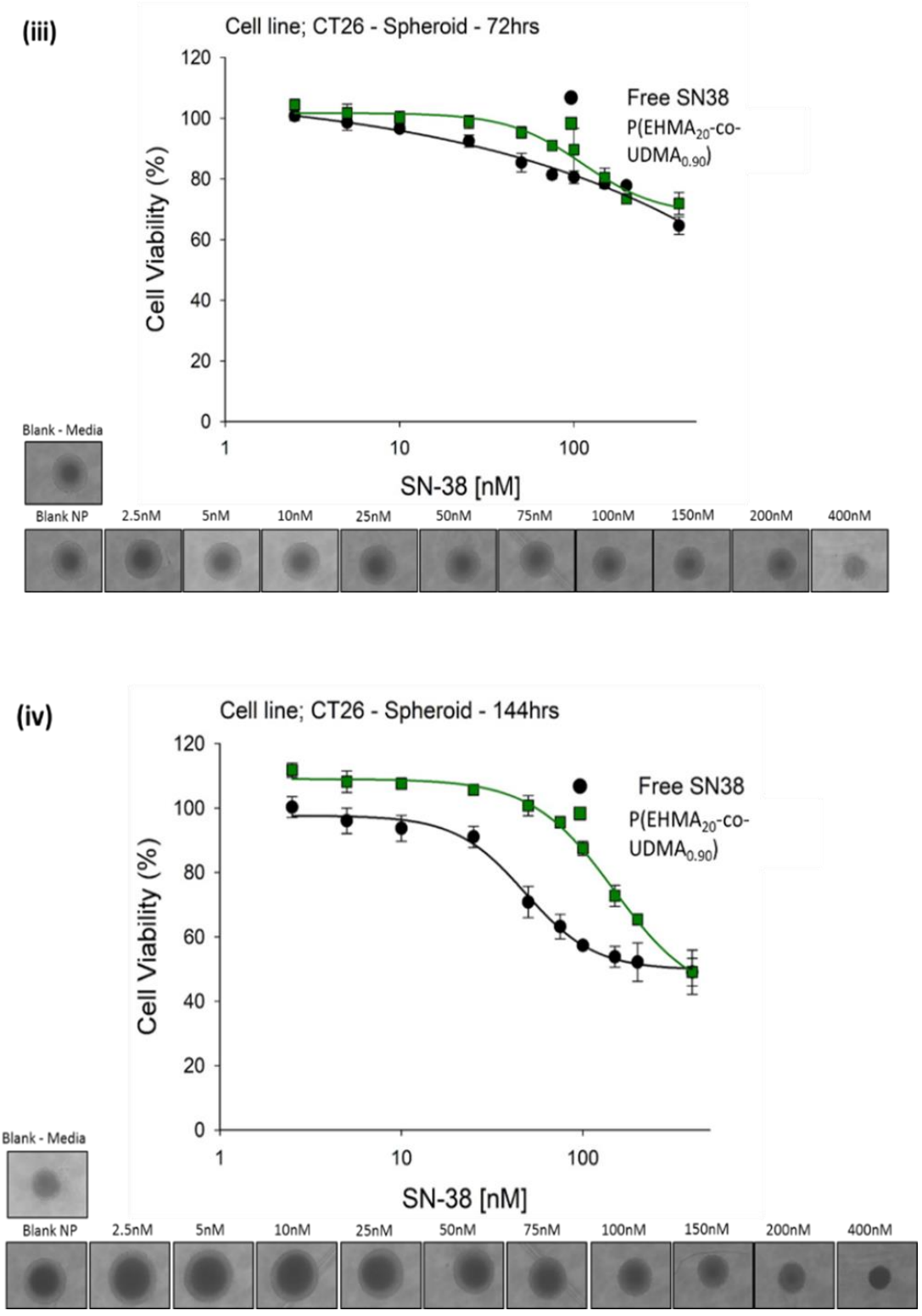


**Figure 5.9** Cell viability graphs for SN-38 loaded p($EHMA_{20}$-co-$UDMA_{0.90}$):p($PEG_{114}$-*b*-$HPMA_{100}$) (60:40 wt. %) nanoparticles in 3D spheroids grown from CT-26 cell lines after iii) 72 hours incubation time and iv) 144 hours incubation time. Microscope images also displaying tumour shrinkage following the administration of the SN-38 loaded p($EHMA_{20}$-co-$UDMA_{0.90}$):p($PEG_{114}$-*b*-$HPMA_{100}$) (60:40 wt. %) nanoparticles at varying concentrations.

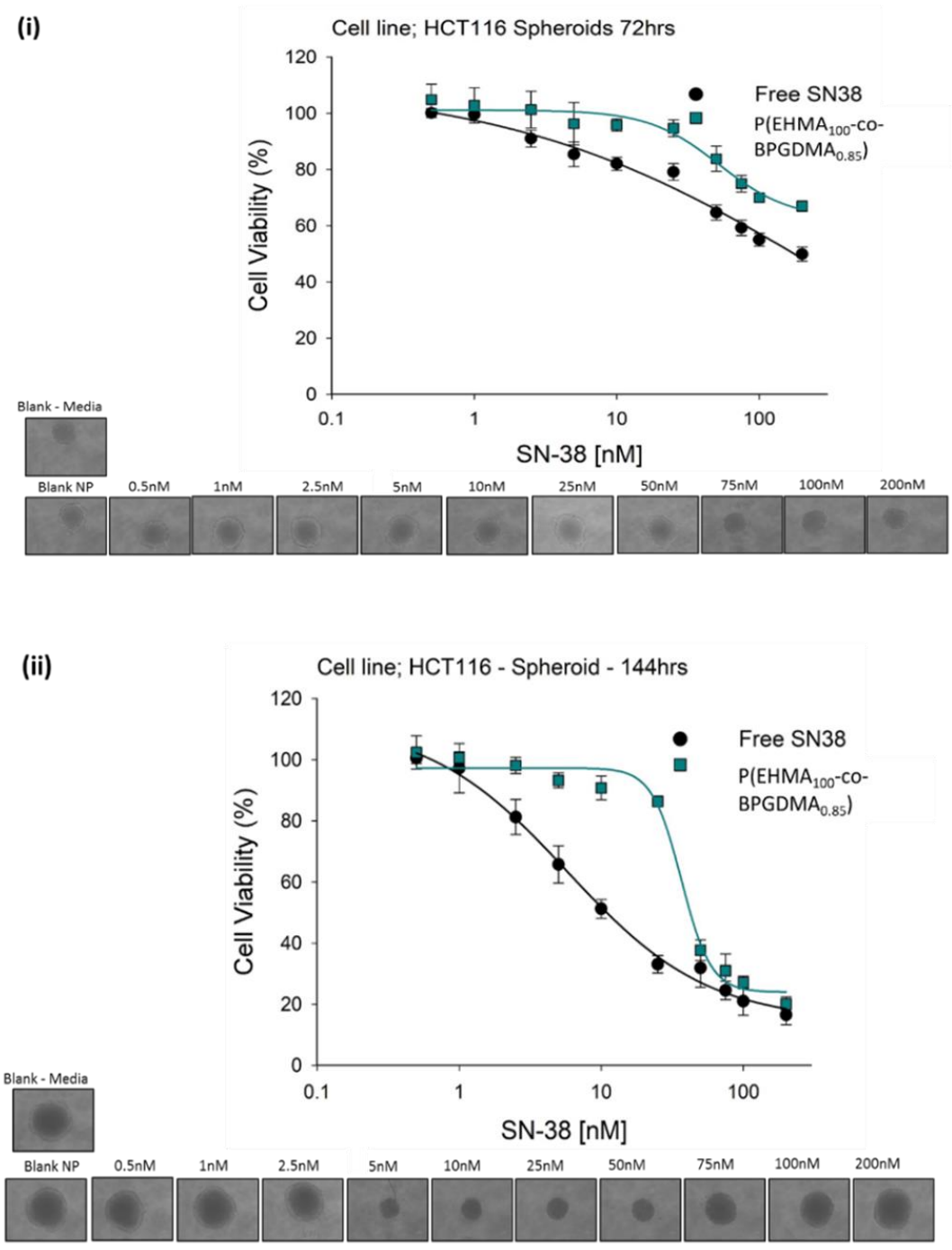


**Figure 5.10** Cell viability graphs for SN-38 loaded p($EHMA_{100}$-co-$BPGMA_{0.95}$):p($PEG_{114}$-*b*-$HPMA_{100}$) (60:40 wt. %) nanoparticles in 3D spheroids grown from HCT 116 cell lines after i) 72 hours incubation time and ii) 144 hours incubation time. Microscope images also displaying tumour shrinkage following the administration of the SN-38 loaded p($EHMA_{100}$-co-$BPGMA_{0.95}$):p($PEG_{114}$-*b*-$HPMA_{100}$) (60:40 wt. %) nanoparticles at varying concentrations.

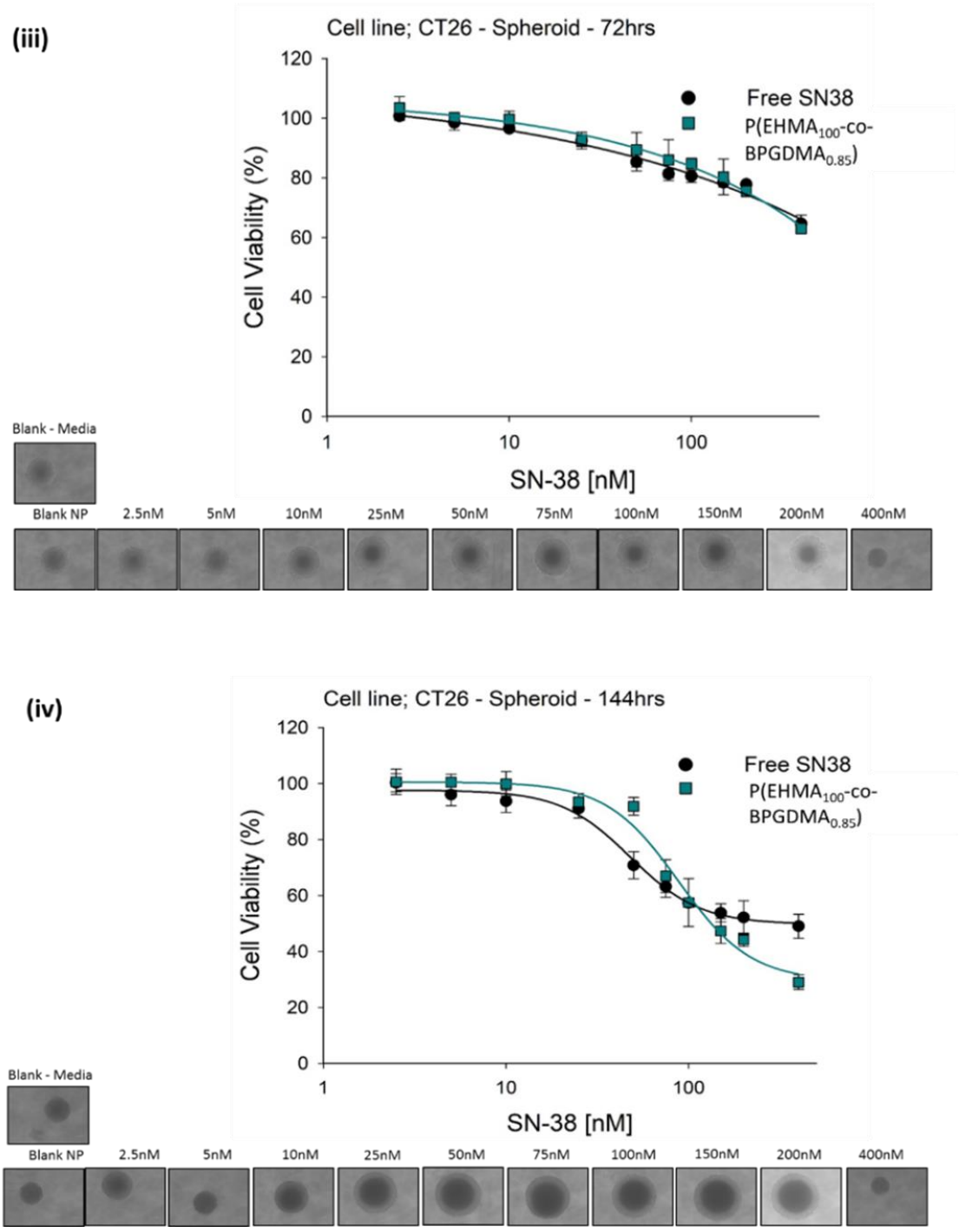


**Figure 5.11** Cell viability graphs for SN-38 loaded p(EHMA$_{100}$-co-BPGMA$_{0.95}$):p(PEG$_{114}$-*b*-HPMA$_{100}$) (60:40 wt. %) nanoparticles in 3D spheroids grown CT-26 cell lines after iii) 72 hours incubation time and iv) 144 hours incubation time. Microscope images also displaying tumour shrinkage following the administration of the SN-38 loaded p(EHMA$_{100}$-co-BPGMA$_{0.95}$):p(PEG$_{114}$-*b*-HPMA$_{100}$) (60:40 wt. %) nanoparticles at varying concentrations.

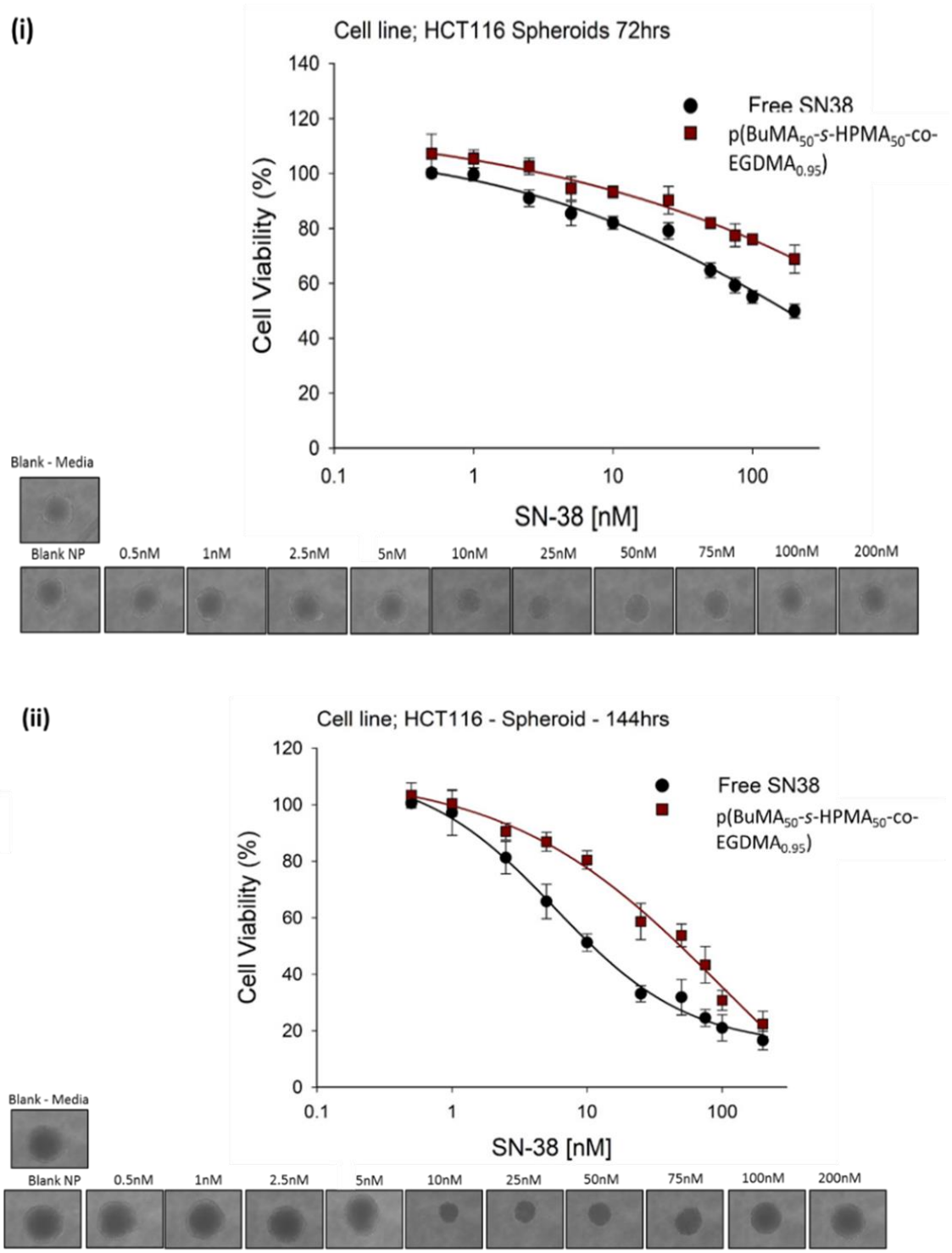


**Figure 5.12** Cell viability graphs for SN-38 loaded p(BuMA$_{50}$-*s*-HPMA$_{50}$-co-EGDMA$_{0.95}$):p(PEG$_{114}$-*b*-HPMA$_{100}$) (60:40 wt. %) nanoparticles in 3D spheroids grown from HCT 116 cell lines after i) 72 hours incubation time and ii) 144 hours incubation time. Microscope images also displaying tumour shrinkage following the administration of the SN-38 loaded p(BuMA$_{50}$-*s*-HPMA$_{50}$-co-EGDMA$_{0.95}$): p(PEG$_{114}$-*b*-HPMA$_{100}$) (60:40 wt. %) nanoparticles at varying concentrations.

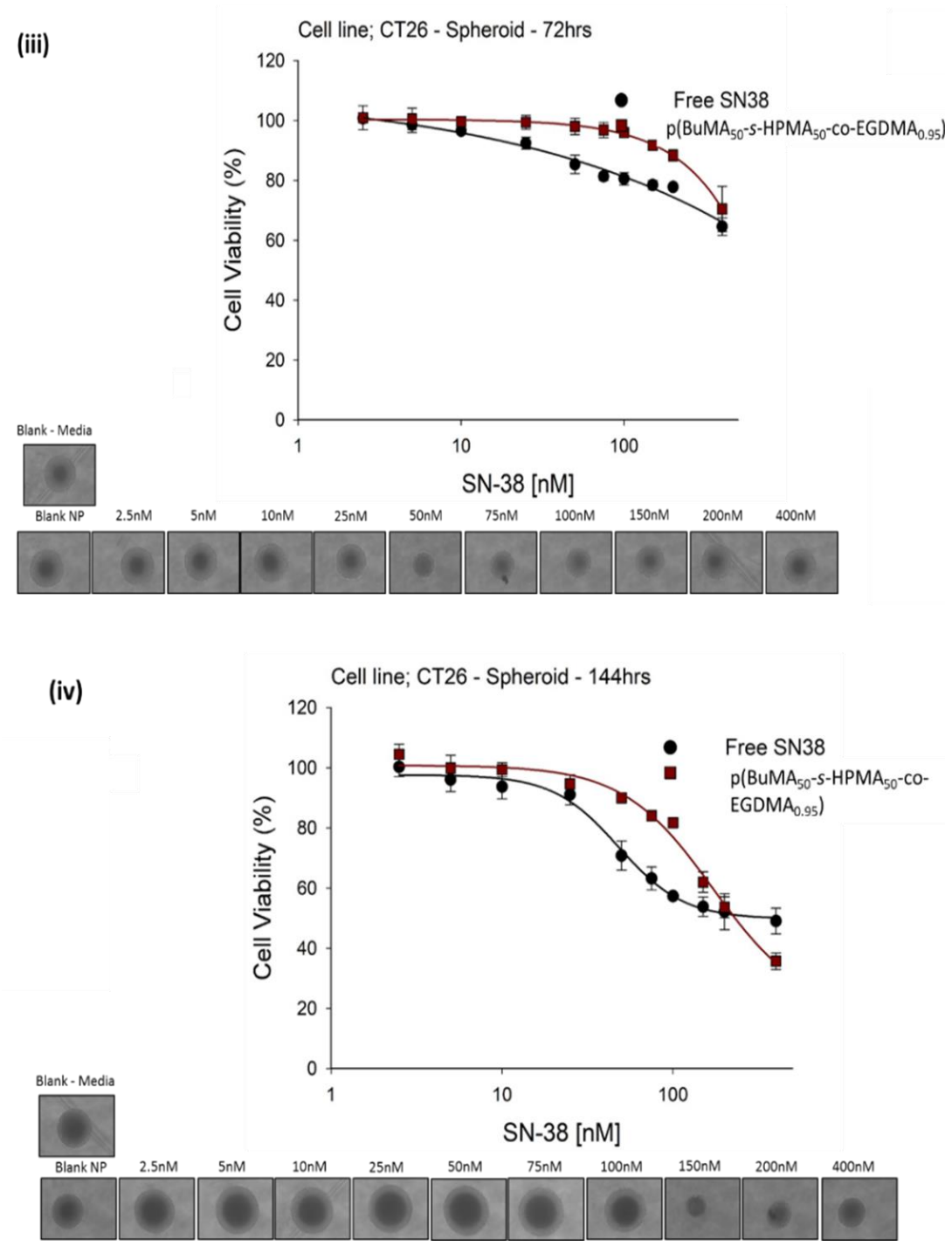


**Figure 5.13** Cell viability graphs for SN-38 loaded p(BuMA$_{50}$-*s*-HPMA$_{50}$-co-EGDMA$_{0.95}$):p(PEG$_{114}$-*b*-HPMA$_{100}$) (60:40 wt. %) nanoparticles in 3D spheroids grown CT-26 cell lines after iii) 72 hours incubation time and iv) 144 hours incubation time. Microscope images also displaying tumour shrinkage following the administration of the SN-38 loaded p(BuMA$_{50}$-*s*-HPMA$_{50}$-co-EGDMA$_{0.95}$): p(PEG$_{114}$-*b*-HPMA$_{100}$) (60:40 wt. %) nanoparticles at varying concentrations

However, $IC_{50}$ values were only obtained at 144 hours and were not obtained at 72 hours at the tested concentration range (Figure 5.14). Again, the symbol X has been used to represent were $IC_{50}$ was not reached within the tested concentration range.

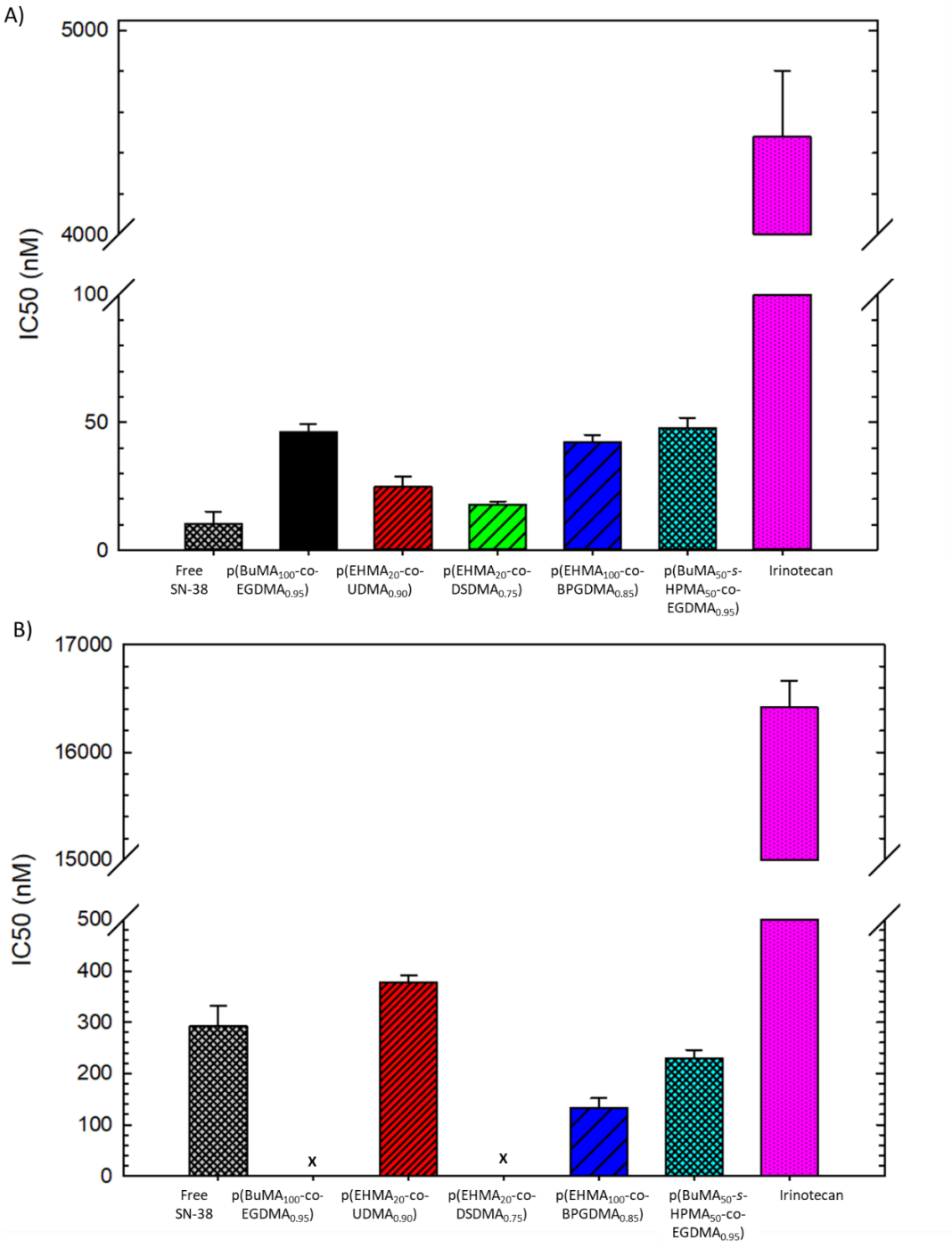


**Figure 5.14** *In-vitro* cell viability in 3D spheroids from A) HCT 116 and B) CT 26 cancer cells after treatment with free SN-38 (grey bar), p(BuMA$_{100}$-co-EGDMA$_{0.95}$ (black bar), p(EHMA$_{20}$-co-UDMA$_{0.90}$)(red bar, fine), p(EHMA$_{20}$-co-DSDMA$_{0.75}$) (green bar, medium), p(EHMA$_{20}$-co-BPGDMA$_{0.80}$) (blue bar, coarse), p(BuMA$_{50}$-*s*-HPMA$_{50}$-*co*-EGDMA$_{0.90}$) (turquoise, fine check) and irinotecan (pink bar) after incubation for 144 hours. All branched copolymers were co-nanoprecipitated with p(PEG$_{114}$-*b*-HPMA$_{100}$) at 60:40 wt. % composition respectively. X represents were $IC_{50}$ was not reached within the tested concentration range.

As depicted in Figure 5.9A, the cell viability of the HCT-116 3D spheroids was affected after a 144-hour incubation with each of the SN-38 loaded nanoparticles, as well as with free SN-38 and IR. Whereas, in the CT-26 3D spheroids, only three of the SN-38 loaded nanoformulations: (p(EHMA$_{20}$-co-UDMA$_{0.90}$), p(EHMA$_{20}$-co-BPGDMA$_{0.80}$) and p(BuMA$_{50}$-*s*-HPMA$_{50}$-*co*-EGDMA$_{0.90}$) generated an $IC_{50}$ value at the tested concentration range. The $IC_{50}$ values obtained for SN-38 loaded nanoformulations were significantly lower than those obtained for IR in both 3D spheroids from HCT-116 and CT-26 cell lines (Table 5.3).

**Table 5.3** $IC_{50}$ values of free SN-38 and irinotecan and five SN-38 nanoformulations, on 3D spheroids created from HCT-116 and CT-26 cell lines after 144-hour incubation time. Cell viability was determined by CellTiter-Glo® Luminescent cell viability assay. Values are mean ± SD (*n* = 3).

| Formulation | **$IC_{50}$ (nM) 3D Spheroids (HCT-116)** | **$IC_{50}$ (nM) 3D Spheroids (CT-26)** |
|---|---|---|
| SN-38 | 10 ± 5 | 292 ± 40 |
| Irinotecan | 4480 ± 324 | 16 419 ± 247 |
| p(BuMA$_{100}$-co-EGDMA$_{0.95}$) | 47 ± 3 | - |
| p(EHMA$_{20}$-co-UDMA$_{0.90}$) | 25 ± 4 | 378 ± 14 |
| p(EHMA$_{20}$-co-DSDMA$_{0.75}$) | 18 ± 1 | - |
| p(EHMA$_{100}$-co -BPGDMA$_{0.90}$) | 42 ± 3 | 133 ± 19 |
| p(BuMA$_{50}$-*s*-HPMA$_{50}$-co-EGDMA$_{0.95}$) | 48 ± 4 | 229 ± 17 |

Furthermore, the obtained $IC_{50}$ values were lower for the 3D spheroids grown from HCT-116 cells compared to those obtained for the 3D spheroids grown from CT-26 cells for all SN-38 nanoformulations, free SN-38, and IR. This may be as a result of better penetration of SN-38 within HCT-116 spheroids compared to CT-26 spheroids.

In the study using HCT-116 3D spheroids, the SN-38 loaded nanoformulations p(EHMA$_{20}$-co-UDMA$_{0.90}$) and p(EHMA$_{20}$-co-DSDMA$_{0.75}$) had the lowest IC$_{50}$ values within the nanoformulation series (IC$_{50}$ = 25 ± 4 and 18 ± 1 nM, respectively). The latter demonstrating similar values compared to unformulated SN-38 (IC$_{50}$ = 10 ± 5 nM), indicating that they are exhibiting similar cytotoxicity as the free drug. This observation is not that surprising since p(EHMA$_{20}$-co-DSDMA$_{0.75}$) also displayed the fastest initial equilibration rate when assessed *via* RED (Section 5.1.1).

The IC$_{50}$ values obtained for the SN-38 nanoformulations in the 3D spheroids from CT-26 cells were as follows. For SN-38 loaded: p(BuMA$_{100}$-co-EGDMA$_{0.95}$) and p(EHMA$_{20}$-co-DSDMA$_{0.75}$), no IC$_{50}$ value was obtained over the tested concentration range as previously mentioned. The lowest IC$_{50}$ value was exhibited by SN-38 loaded p(EHMA$_{20}$-co-BPGDMA$_{0.80}$) (133 ± 19 nM), which was lower than that obtained for free SN-38 (292 ± 40 nM) and considerably lower than that obtained for IR (16 419 ± 247 nM). The IC$_{50}$ value obtained for SN-38 loaded p(BuMA$_{50}$-*s*-HPMA$_{50}$-*co*-EGDMA$_{0.90}$) (229 ± 17) was similar in cytotoxicity as free SN-38. SN-38 loaded p(EHMA$_{20}$-co-UDMA$_{0.90}$) (378 ± 14 nM) was the least cytotoxic out of the SN-38 formulations on this tested cell line.

The IC$_{50}$ values collected from both 3D spheroids cell lines, further confirm the superior cytotoxicity of the SN-38 loaded nanoformulations compared to IR.

### 5.1.3 Determining Cellular Accumulation Ratios of SN-38 Nanoformulations in M1 and M2 Macrophages

When a host is exposed to nanomaterials, phagocytes are key cellular participants in determining the fate of the nanoparticles within the body. In particular, macrophages are believed to be the first cell-type involved in the detection of nanoparticles that can mediate host inflammatory and immunological biological responses. When a nanoparticle reaches the exterior membrane of a phagocyte, interactions can occur between the nanoparticle and the plasma membrane components or the extracellular matrix. These interactions permit and facilitate entry into the cell mainly *via* endocytosis. This is a distinct process whereby nanoparticles are engulfed in membrane invaginations, which then bud off inside the cell to form a vesicle

containing the ingested nanoparticle.[12] One of the main endocytosis mechanisms is phagocytosis. Generally, wherever nanoparticles are detected phagocytosis occurs ubiquitously, since macrophages play a crucial role in the defence system of the body. Macrophages can be divided into M1-type (classically activated) and M2-type (alternatively activated), both of which produce an array of cytokines, chemokines, hormones, proteases and polypeptide growth factors.[13, 14] The role of M1 macrophages is to function as a immune monitor, secrete pro-inflammatory cytokines and present antigens. Whereas, M2 macrophages primarily reduce inflammation by secretion of anti-inflammatory cytokines.[15] The phagocytosis by macrophages can result in the rapid systemic clearance of the nanoparticles, which in-turn limits the nanoparticles ability to accumulate at the target delivery site. The extent of this phagocytic uptake is largely governed by the physiochemical characteristics of the nanoparticles, such as size, shape, and surface properties.[16] With regard to the latter, studies have shown that "stealth" surface functionalities such as PEG can reduce such phagocytic uptake and enhance systemic circulations times, as discussed in detail in Chapter 1.5.

For the treatment of certain infection diseases such as HIV, accumulation of nanoparticles in macrophages is highly advantageous, since it has been shown that macrophages can act as latent reservoirs of the HIV virus.[17-19] There are also emerging reports within recent literature of macrophages being targeted for anti-cancer therapies, since macrophages are a major constituent of the tumour microenvironment.[20-22] Within this environment, the macrophages promote pro-tumour functions such as proliferation, angiogenesis and metathesis, so targeting of macrophages may prove advantageous, although there is a lot unknown about macrophages ontogeny as it is very much still in its infancy. In general, anti-cancer DDS are designed and engineered to limit and minimise the macrophage uptake in order to facilitate long systemic circulation times to enable high therapeutic efficacy. The cellular accumulation ratio (CAR) of five SN-38 loaded nanoformulations was investigated in M1-type and M2-type macrophages. CAR is given as the ratio of the intracellular to the extracellular SN-38 concentration. The CAR of the five different

SN-38 nanoformulations in M1 and M2 macrophages was compared directly to free SN-38 after a 24-hour incubation time (Figure 5.15).

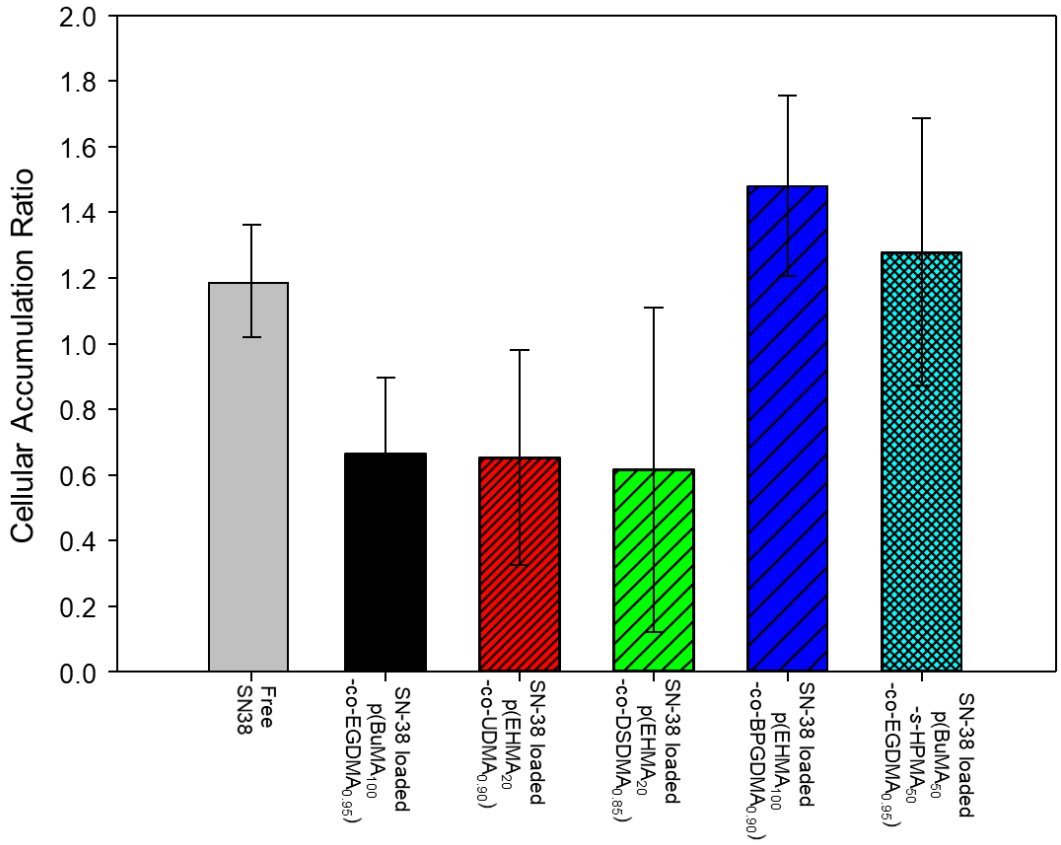


**Figure 5.15** Cellular accumulation (ratio of cellular to extracellular concentration) of: free SN-38 (grey bar), SN-38 loaded (p($BuMA_{100}$-co-$EGDMA_{0.95}$) (black bar), SN-38 loaded (p($EHMA_{20}$-co-$UDMA_{0.90}$) (red bar, fine), SN-38 loaded p($EHMA_{20}$-co-$DSDMA_{0.75}$) (green bar, medium), SN-38 loaded p($EHMA_{20}$-co-$BPGDMA_{0.80}$) (blue bar, coarse) and SN-38 loaded p($BuMA_{50}$-*s*-$HPMA_{50}$-*co*-$EGDMA_{0.90}$) (turquoise, fine check). All of which are sterically stabilised with AB block copolymer p($PEG_{114}$-*b*-$HPMA_{100}$) (60:40 wt. % branched copolymer: AB block copolymer respectively. Macrophages were treated with 50 µM of sample for 24 hours. Values are mean ± standard deviation from three experiments.

The CAR values after incubation with SN-38 loaded: p($BuMA_{100}$-co-$EGDMA_{0.95}$), p($EHMA_{20}$-co-$UDMA_{0.90}$) and p($EHMA_{20}$-co-$DSDMA_{0.75}$) (0.66 ± 0.23, 0.65 ± 0.33 and 0.62 ± 0.49, respectively) were identical within experimental error and were lower than the CAR value for free SN-38 (1.19 ± 0.17). This suggests that the uptake of free SN-38 by macrophages was greater than that of the SN-38 loaded nanoparticles, although not statistically significant. This decreased uptake may be as result of the formulation including PEG moieties, which may have reduced the protein corona formed compared to that of free SN-38. The CAR values obtained for SN-38 loaded: p($EHMA_{20}$-co-$BPGDMA_{0.80}$) and p($BuMA_{50}$-*s*-$HPMA_{50}$-*co*-$EGDMA_{0.90}$) (1.48 ± 0.28 and

1.278 ± 0.41) were similar to that of free SN-38. These 2 formulations also exhibited the two highest cumulative release of SN-38 when tested by RED, as discussed in Section 5.1.1. The increased equilibration compared to the other 3 formulations may also explain the increased accumulation within macrophages: if the nanoformulations release more SN-38 or present more SN-38 at the surface of the particle, then they may have a greater protein corona that would subsequently trigger an increase in macrophage uptake. Despite being similar to SN-38 uptake, it was observed that formulating SN-38 within polymer nanoparticles did not increase macrophage uptake.

### 5.1.4 *In vivo* PK Studies

A pharmacokinetic study was conducted with 5 wt.% SN-38 loaded p($EHMA_{20}$-co-$DSDMA_{0.80}$):p($PEG_{114}$-*b*-$HPMA_{100}$) 60:40 wt.% co-nanoprecipitate, which was administered to healthy male BALB/c mice at [SN-38] = 0.40 mg $mL^{-1}$. BALB/c represents an albino, immunodeficient inbred mouse strain, which serves as a useful murine model in cancer therapy research.[23] This material was selected due to the fact that it had the lowest CAR value following the *in vitro* study involving M1 and M2 macrophages (Section 5.1.3), which suggested that it would likely have the greatest systemic circulation time following intravenous administration.

Unfortunately, due to undue stress the mice were sacrificed after administration and before any evaluation could be conducted, which is concerning from the perspective of the future application of this material. Investigations have been initiated in order to provide an explanation for the failure of the *in vivo* study, however, due to the COVID-19 pandemic these were unable to be completed before the completion of this thesis.

## 5.2 Conclusion

The pharmacological behaviour of fourteen different SN-38 loaded nanoformulations were assessed. RED assays were used as a rapid screening process to evaluate the SN-38 release rates of these formulations compared to free SN-38. All fourteen of the SN-38 nanoformulations showed no evidence of any burst release and it was shown that the formulations have a reduced equilibration compared to free SN-38 within 8 hours of equilibration time. This observation provides further validation that

the vast majority of the SN-38 concentration is encapsulated within the nanoparticles as previously demonstrated through encapsulation efficiency calculations (Chapter 4, Section 2.2).

Although the equilibration profiles of the nanoformulations were slightly different, they did not differ significantly between the fourteen samples and it was shown that variations in polymer functionality and brancher chemistry had little influence on SN-38 release under these conditions. However, it was indicated that variations to $DP_n$ value may modulate SN-38 release rate through increased polymer-drug interactions, although it is currently unclear why this variation has an impact in this way. It is recognised that a more comprehensive study with more varying $DP_n$ values would be required before drawing on that conclusion.

Five nanoformulations were chosen to progress with further *in vitro* cytotoxicity and cellular uptake studies: p(BuMA$_{100}$-co-EGDMA$_{0.95}$), p(EHMA$_{100}$-co-BPGDMA$_{0.85}$), p(EHMA$_{20}$-co-UDMA$_{0.90}$), p(EHMA$_{20}$-co-DSDMA$_{0.75}$) and p(BuMA$_{50}$-s-HPMA$_{50}$-co-EGDMA$_{0.95}$), all co-nanoprecipitated with AB block copolymer p(PEG$_{114}$-*b*-HPMA$_{100}$) at a compositional ratio of 60:40 wt. % respectively. These were chosen based on their "slow and fast" equilibration rates at four chosen time points compared to free SN-38 and the other SN-38 nanoformulations.

Cytotoxicity studies of these five formulations demonstrated that the corresponding non-loaded polymer nanoparticles were not cytotoxic, which is a highly advantageous attribute and suggestive that the material is suitable and safe for its intended application as described in Chapter 1, Section 4.1. The studies confirmed that through the encapsulation of SN-38 within the polymer nanoparticles that a decrease to cellular viability was observed and therefore an increase in the material's cytotoxic behaviour. This observation was consistent with what was expected since SN-38 is reported to have anti-cancer properties. Additionally, it also demonstrated that all five of the SN-38 nanoformulations had superior cytotoxicity compared to IR with extremely low $IC_{50}$ values in nM being obtained for all five of the SN-38 nanoformulations. This result is extremely promising and combined with the fact that the formulations represent SN-38 that could be directly administered intravenously

indicates that these nanoformulations have potential to act as SN-38 DDS with encouraging *in vitro* anti-cancer properties. This was then further reiterated when further cytotoxicity studies were conducted in 3D spheroids which also demonstrated that the five SN-38 nanoformulations had extremely low $IC_{50}$ values and had the ability to cause tumour shrinkage under these tested conditions. Again, it was highlighted that the SN-38 nanoformulations were significantly more toxic than IR further validating the desire to be able to formulate and deliver SN-38 directly.

The CAR values were determined for the five SN-38 loaded nanoformulations. through *in vitro* macrophage uptake studies. Interestingly, three of the SN-38 loaded nanoformulations: p($BuMA_{100}$-co-$EGDMA_{0.95}$), p($EHMA_{20}$-co-$UDMA_{0.90}$) and p($EHMA_{20}$-co-$DSDMA_{0.75}$) all co-nanoprecipitated with AB block copolymer p($PEG_{114}$-$HPMA_{100}$) (60:40 wt. % composition) all demonstrated lower cellular uptake (0.66 ± 0.23, 0.65 ± 0.32 and 0.62 ± 0.49, respectively) compared to free SN-38 (1.19 ± 0.17). This reduced cellular uptake may be as a result of the reduced recognition by the macrophages caused through the incorporation of the PEG functionalities from the AB block copolymer. But it is unclear at this stage why the other two SN-38 nanoformulations: p($EHMA_{100}$-co-$BPGDMA_{0.90}$) and p($BuMA_{50}$-s-$HPMA_{50}$-co-$EGDMA_{0.95}$) with AB block copolymer p($PEG_{114}$-$HPMA_{100}$) showed similar uptake (1.48 ± 0.28 and 1.28 ± 0.41 respectively) to that of free SN-38. However, it is worth noting that although there were differences observed there was no statistical significance. Positively, it was seen that encapsulating SN-38 within polymer nanoparticles did not increase the cellular accumulation, i.e., the macrophage uptake was not increased, and the polymer nanoparticles do not increase the cellular interaction with macrophages.

The failing of the *in vivo* PK studies of SN-38 loaded nanoformulation p($EHMA_{20}$-co-$DSDMA_{0.75}$):p($PEG_{114}$-*b*-$HPMA_{100}$) (60:40 wt. % respectively) at this stage is unclear and although concerning given the intended application of the SN-38 DDS, investigations will resume following the return of research from COVID19. However, despite this, the initial preliminary results from the *in vitro* work are still suggestive

that these SN-38 nanoformulations have the capability to act as DDS of the currently un-administrable SN-38.

## 5.3 References


1. S. Behzadi, V. Serpooshan, W. Tao, M. A. Hamaly, M. Y. Alkawareek, E. C. Dreaden, D. Brown, A. M. Alkilany, O. C. Farokhzad and M. Mahmoudi, *Chemical Society reviews*, 2017, **46**, 4218-4244.
2. C. D. Walkey and W. C. Chan, *Chemical Society Reviews*, 2012, **41**, 2780-2799.
3. D. Walczyk, F. B. Bombelli, M. P. Monopoli, I. Lynch and K. A. Dawson, *Journal of the American Chemical Society*, 2010, **132**, 5761-5768.
4. U. Prabhakar, H. Maeda, R. K. Jain, E. M. Sevick-Muraca, W. Zamboni, O. C. Farokhzad, S. T. Barry, A. Gabizon, P. Grodzinski and D. C. Blakey, *Cancer research*, 2013, **8**, 2412-2417.
5. S. Sharifi, S. Behzadi, S. Laurent, M. L. Forrest, P. Stroeve and M. Mahmoudi, *Chemical Society Reviews*, 2012, **41**, 2323-2343.
6. R. P. Bakshi, L. M. Tatham, A. C. Savage, A. K. Tripathi, G. Mlambo, M. M. Ippolito, E. Nenortas, S. P. Rannard, A. Owen and T. A. Shapiro, *Nature Communications*, 2018, **9**, 315.
7. T. Riss, A. Niles, R. Moravec, N. Karassina and J. Vidugiriene, in *Assay Guidance Manual*, Eli Lilly & Company and the National Center for Advancing Translational Sciences, Bethesda (MD), 2004.
8. W. Li, J. Zhou and Y. Xu, *Biomedical reports*, 2015, **3**, 617-620.
9. F. Chen and M. T. Cushion, *Journal of clinical microbiology*, 1994, **32**, 2791-2800.
10. R. Sun, L. Zhu, L. Li, W. Song, X. Gong, X. Qi, Y. Wang, R. Ghose, S. Gao, M. Hu and Z. Liu, *Toxicology and Applied Pharmacology*, 2020, **398**, 115032.
11. E. Araki, M. Ishikawa, M. Iigo, T. Koide, M. Itabashi and A. Hoshi, *Jpn Journal of Cancer Research*, 1993, **84**, 697-702.
12. S. Kumari, S. Mg and S. Mayor, *Cell Research*, 2010, **20**, 256-275.
13. D. M. Mosser and J. P. Edwards, *Nature Reviews Immunology*, 2008, **8**, 958-969.
14. R. Noy and J. W. Pollard, *Immunity*, 2014, **41**, 49-61.
15. G. Germano, R. Frapolli, C. Belgiovine, A. Anselmo, S. Pesce, M. Liguori, E. Erba, S. Uboldi, M. Zucchetti, F. Pasqualini, M. Nebuloni, N. van Rooijen, R. Mortarini, L. Beltrame, S. Marchini, I. Fuso Nerini, R. Sanfilippo, P. G. Casali, S. Pilotti, C. M. Galmarini, A. Anichini, A. Mantovani, M. D'Incalci and P. Allavena, *Cancer Cell*, 2013, **23**, 249-262.
16. H. Hillaireau and P. Couvreur, *Cellular and Molecular Life Sciences*, 2009, **66**, 2873-2896.
17. D. D. Richman, D. M. Margolis, M. Delaney, W. C. Greene, D. Hazuda and R. J. Pomerantz, *Science*, 2009, **323**, 1304-1307.
18. M. D. Marsden and J. A. Zack, *Jourmal of Antimicrobial Chemotherapy*, 2009, **63**, 7-10.
19. T. Mamo, E. A. Moseman, N. Kolishetti, C. Salvador-Morales, J. Shi, D. R. Kuritzkes, R. Langer, U. von Andrian and O. C. Farokhzad, *Nanomedicine (Lond)*, 2010, **5**, 269-285.
20. B. Ruffell and L. M. Coussens, *Cancer Cell*, 2015, **27**, 462-472.
21. M. Erreni, A. Mantovani and P. Allavena, *Cancer Microenviron*, 2011, **4**, 141-154.
22. J. L. Guerriero, *Trends in Molecular Medicine*, 2018, **24**, 472-489.
23. A. Gharib, Z. Faezizadeh, S. A. R. Mesbah-Namin and R. Saravani, *Pharmacognosy magazine*, 2015, **11**, S117-S122.

# Chapter 6

## Conclusions & Future Work

## 6.1 Conclusions

The main objective of this research was to encapsulate the anti-cancer drug SN-38, within a novel polymeric based drug delivery platform and assess its applicability as a biologically, and clinically, relevant therapy candidate. At the highest level, this has been successfully achieved and the results presented within this thesis have shown that a wide variety of sterically stabilised branched vinyl polymer nanoparticles loaded with SN-38 can be prepared, with relative ease, high efficiency and reproducibility *via* co-nanoprecipitation. Additionally, it was demonstrated through radiometric analysis and *in vitro* studies that these polymer nanoparticles may be potentially useful as drug delivery systems of SN-38. This research has also provided an understanding of how the chemistry of the polymers and the subsequent core of the nanoparticles may govern the success of the encapsulation and how it can modulate the drug release. Furthermore, it has also highlighted and allowed the identification of a number of factors within the polymerisation and co-nanoprecipitation processes which influence the successful formation of the polymers and nanoparticles, respectively.

Methanolic ATRP proved to be a robust synthetic technique which allowed for the synthesis of a wide range of polymeric materials with well-defined architectures including, linear homo and statistical copolymers, statistical branched and AB block copolymers, with varying degrees of polymerisation. The synthetic versatility which ATRP exhibited allowed for various different chemical compositions to be synthesised with relative ease and control, through the incorporation of different vinyl, divinyl monomers and initiators, expanding on previously reported materials. It also facilitated the generation of a novel library of soluble hydrophobic branched materials, which were obtained *via* a 'modified Strathclyde approach'. As expected, an influence on the polymer's physical properties, specifically the glass transition temperature and polarity were observed when varying the chemistries and architectures. Which in turn, also influenced the success of drug encapsulation and varied release profiles which will be discussed below.

Before the encapsulation of SN-38, further essential studies were required to gain an understanding of polymer nanoparticle synthesis *via* nanopreciptation and co-

nanoprecipaiton, in the context of this new polymer library. Findings from both the nanoprecipitation and co-nanoprecipitation studies confirmed that high molecular weight branched copolymers were an essential requirement in the formation of stable and highly monodispersed aqueous nanoparticle dispersions. Furthermore, the failing of the vast majority of the polymers during the sole nanoprecipitation experiments also emphasised the importance of the presence of an AB block copolymer to provide steric stabilisation; as confirmed during the initial co-nanopreciptation studies, undertaken with p($PEG_{114}$-*b*-$HPMA_{100}$) and branched polymers: p($HPMA_{100}$-co-$EGDMA_{0.90}$), p($BuMA_{100}$-co-$EGDMA_{0.95}$) and p($EHMA_{100}$-co-$EGDMA_{0.80}$).

During these studies it was determined that the optimal composition ratio required between branched vinyl polymer and AB block copolymer was ≥ 40 wt.% of AB block copolymer to provide sufficient steric stabilisation upon dilution and exposure to salt whilst also facilitating the successful formation of monodisperse nanoparticles within the ideal size range for anti-cancer DDS (< 200 nm). It was also highlighted that variation of this ratio had a direct impact on particle size, whereby increasing the % wt. of AB block copolymer decreased the particle hydrodynamic diameter, which provides a future formulation strategy to reduce the nanoparticle hydrodynamic diameter. Additionally, it was observed that this ratio also governed the success of the co-nanoprecipitations, which was entirely dependent on the chemical nature of the monomer residue within the branched polymer backbone. It was observed that p($EHMA_{100}$-co-$EGDMA_{0.80}$) nanoprecipitates required a much larger content of p($PEG_{114}$-b-$HPMA_{100}$) (≥ 70 wt.%), compared to the p($BuMA_{100}$-co-$EGDMA_{0.95}$) nanoprecipitates (≥ 40 wt.%) in order to achieve colloidal stability.

Following these findings, it was assumed that the nanoprecipitates of the EHMA-based polymers would not be suitable for DDS due to the larger content of AB block copolymer required to provide steric stability. However, interestingly, when pyrene was encapsulated during the co-nanoprecipitation process it was shown that whilst there was almost no impact on the size and dispersity of the polymer nanoparticles, the presence of a hydrophobic guest macromolecule seemed to influence the overall success of the co-nanopreciptation process, particularly for p($EHMA_{100}$-co-

$EGDMA_{0.80}$). This observation was somewhat surprising and was further observed when the guest molecule was substituted with SN-38, which also appeared to aide nanoparticle formation. Unexpectedly, it transpired that all the polymers involving EHMA monomer residues ultimately became the lead candidates for successful SN-38 loaded nanoparticle regimes and subsequent pharmacological studies.

For the first time, the complimentary chemistry of the B segment of the AB block copolymer, to the branched vinyl polymer core, was shown as not being a prerequisite to produce sterically stabilised nanoparticles, and it was observed that by varying of the hydrophobic segment of the AB block copolymer an impact on the core polarity was seen. This new-found ability to manipulate and tune both the chemistry of the branched polymer and the AB block copolymer and, in-turn, the core of the nanoparticle is very appealing when considering a new drug delivery nanocarrier and provides an expansion to the scope of co-nanopreciptation to produce branched vinyl copolymer nanoparticles, which seek to complement guest drug molecule chemistries.

All the studies conducted proved that the co-nanoprecipitation approach provided a fast and efficient route to sterically stabilised, highly monodisperse, aqueous vinyl polymer nanoparticles. This was achieved without the need for any additives, such as polymeric surfactants within the aqueous phase. *In vitro* cytotoxicity studies of blank unloaded branched vinyl copolymer nanoparticles confirmed that these materials did not cause any decrease in cell viability, which is a critical feature of any potential DDS and means that they are fit for their intended purpose.

The applicability of the co-nanoprecipitation technique for the generation of guest loaded sterically stabilised aqueous polymer nanoparticles was demonstrated *via* low loading of hydrophobic guest molecule pyrene which, thanks to its fluorescent chemical nature, characterised the internal polarity of the nanoparticles i.e. hydrophobicity of the core, was varied through copolymerisation of different vinyl and divinyl monomers into the polymers and also through the incorporation of different AB block copolymers.

Again, when SN-38 was encapsulated, minimal changes to nanoparticle size, monodispersity, charge and stability were observed. However, the success of the encapsulation was largely dictated by the chemistry of the vinyl monomer residue and a strong dependency on EHMA was observed. One possible explanation of this dependency, may arise from the observation that the core of nanoparticles consisting of EHMA polymers, was found to be the least polar and therefore most hydrophobic, meaning that it is more suited as a host environment for SN-38. Additionally, it was observed that the most successful SN-38 loaded formulations all contained the AB block copolymer, p($PEG_{114}$-*b*-$HPMA_{100}$).

The maximum SN-38 drug loading achieved under the studied conditions was determined to be 5 wt. % with respect to total mass. Efforts were made to increase this value through increasing the SN-38 concentration in the THF solvent phase, *via* pH variations and SN-38 drug modifications; however, all were unsuccessful. Alternatively, as per the hypothesis laid out in Chapter 1, investigations were conducted into whether drug loading could be optimised and influenced through manipulations to core chemistries, specifically through varying the divinyl monomer, but again minimal impact was observed. Whilst this value may appear to be modest, it is worth reiterating the extreme potency SN-38 exhibits compared to the prodrug irinotecan (up to a 1000- fold increase) and that SN-38 is not currently directly administered due to its extreme hydrophobicity and instability, therefore, these systems are still an attractive option for clinical treatments. This SN-38 drug loading value is also particular noteworthy, since this drug loading achieved through co-nanopreciptation of SN-38 is higher than those previously reported using alternative nanoformulation techniques.[1]

Successful multiple co-nanopreciptation allowed for the concentration of SN-38 to be increased (four-fold), whilst maintaining the nanoparticles hydrodynamic diameter, dispersity and stability, without any additional chemical adaptations or modifications to the polymeric nanoparticles. This was the first demonstration of a three-component multiple nanoprecipitation, in the presence of a guest molecule.

Increasing the drug concentration *via* such a simple methodology only strengthens the attractiveness of these SN-38 loaded nanoparticle systems from a pharmacological perspective, since it means that the administered dose required for therapy would be reduced. Even at the lowest SN-38 concentration ([SN-38] = 0.05 mg $mL^{-1}$), an impressive dosing volume reduction of 65 % was determined for the SN-38 loaded nanoparticles compared to Campto (marketed product of IR), when the potency of SN-38 is assumed to be 1000- fold greater than IR. When a highly conservative potency value of SN-38 is used (100- fold), the total volume of formulation required does increase (106 mL), compared to Campto (30.6 mL), but this value is not thought to be unrealistic for infusion from a clinical perspective. Whilst it is noted that this may not be ideal from a formulation perspective, it is worth reiterating that the conversion of IR to SN-38 does vary considerably between patients and that these SN-38 loaded nanoparticle formulations provide the unique advantage of directly administrating aqueous SN-38, something which is not currently reported. Additionally, the determined value for total volume required was reduced significantly (26.5 mL), when the concentration of SN-38 was increased four-fold ([SN-38] = 0.20 mg $mL^{-1}$) *via* multiple co-nanopreciptation, assuming SN-38 has 100-fold increased potency. This new determined value is within the range of the Campto product.

Of course, it is recognised that these values determined are subjective and do not consider factors such as metabolism and clearance rates, but they do help to provide some context into the relevance of these SN-38 nanoformulations as clinical DDS which may help to direct future work. This SN-38 potency was also highlighted when it was determined that the SN-38 nanoformulations had superior cytotoxicity compared to prodrug IR during *in vitro* cytotoxicity studies.

In addition to this, the attractiveness of these SN-38 loaded nanoparticles were further validated through a series of different radiometric analyses and *in vitro* experiments. Radio dialysis highlighted that the majority of SN-38 mass (> 83 %) was encapsulated within the core, since no burst release was observed unlike many reported DDS, and that the branched vinyl copolymer nanoparticles retained sufficient levels of SN-38 over a period of 24 hours at different pH values (85.8 % SN-

38 retained at pH 7 and 82.7 % SN-38 retained at pH4). Therefore, this suggests that the SN-38 concentration within the branched vinyl copolymer nanoparticles would remain significant over time and would potentially allow for the nanoparticles to accumulate at the intended delivery site *via* EPR effect and deliver a sufficient concentration of SN-38 to maximise their therapeutic effectiveness. It was also established through modelling of the release rate data, that SN-38 release from the polymer nanoparticles was entirely diffusion based.

A subtle pH dependency was determined through the release profiles and it was observed that by decreasing the pH from 7 to 4, saw the release rate of SN-38 increase. This was particularly interesting as it suggested that the polymer nanoparticles may release more SN-38 at the tumour site, an obvious benefit, since it is characteristically a lower pH condition than typically exhibited from blood.

It was hypothesised that SN-38 release from the polymer nanoparticles may have been manipulated and altered through the variations to core chemistry, and in turn variations in polymer $T_g$ and polarity. However, despite varying equilibration profiles being obtained during RED, no significant difference was observed for the varying chemistries and since the majority of successful formulations involved the vinyl monomer residue, EHMA, studying the real impact of varying core polarity on drug release was not possible. However, it was observed that shorter primary polymer chain lengths may cause slower drug release.

An additional positive effect of the incorporation of an AB block copolymer and subsequent PEG moieties, was observed when a reduced cellular accumulation ratio was determined for SN-38 loaded: p(BuMA$_{100}$-co-EGDMA$_{0.95}$), p(EHMA$_{20}$-co-UDMA$_{0.90}$) and p(EHMA$_{20}$-co-DSDMA$_{0.75}$) all co-nanoprecipitated with AB block copolymer p(PEG$_{114}$-HPMA$_{100}$) (60:40 wt. % composition) compared to free SN-38. This suggests that there was a reduction in cellular uptake, potentially caused through the reduced recognition of the nanoparticles from the stealth characteristics PEG provides. Despite this not being consistently observed across all the formulations, positively, it can be confirmed that encapsulating SN-38 within polymer nanoparticles did not increase cellular accumulation within macrophages.

The work presented within this thesis shows that aqueous branched vinyl copolymer nanoparticles prepared *via* a simple formulation strategy, co-nanoprecipaiton, can act as a suitable DDS for the direct delivery of SN-38 with promising potential. This ability to formulate an aqueous SN-38 formulation at clinically viable drug concentrations may facilitate a more convenient and efficient delivery of SN-38 and would remove the need to utilise the currently administered prodrug IR. SN-38 polymer nanoparticles detailed within literature reports predominantly focus on the utilisation of polyesters, specifically PLGA, for the synthesis of nanoparticles, whereas here it has been demonstrated, for the first time that methacrylate-based polymers are also suitable. This may help to overcome some of the disadvantages associated with the use of PLGA nanoparticles as drug carriers such as: unpredictable degradation profile of PLGA, which has been shown to affect the activity of the encapsulated drug and the poor drug loading and burst release.[2, 3]

Although the primary objective of this study was successfully met, the study did present some limitations. First of all, although a wide library of materials was generated, the scope of the project was limited to the chemistries which were explored and it may have been that alternative, more beneficial chemistries were missed i.e. the chemistry chosen may not have been broad enough or the right chemistry for SN-38. However, the chemistries studied here do provide good foundational knowledge to build from. Furthermore, SN-38 was difficult and complex to work with, due to its instability with pH change and the extremely limited solubility exhibited by SN-38. These complexities of SN-38 may have prevented the true impact of the designed chemical variations and their influence on drug encapsulation, release and pharmacological behaviour to be seen.

### 6.2 Future Work

The work presented within this thesis has shown that co-nanoprecipitation has provided a reliable and fast method to generate sterically stabilised SN-38 loaded branched vinyl nanoparticles with reproducibility and high efficiency. However, there are multiple different avenues which could be explored should the research in this thesis be taken forward for further studies. These are highlighted and discussed below:

- Further *in vivo* investigations to gain detailed understanding into the off-site accumulation of the polymer nanoparticles within lung tissue.
- Making the internal nanoparticle core chemistry more like SN-38.
    - Incorporating complimentary SN-38 chemistries within the polymer core through monomer and initiator design may promote and increase polymer-drug interactions. In turn, this may increase the drug loading and modulate drug release.
- Expanding the scope of the chemistry library further through the use of different vinyl monomers which vary more significantly in pendant group functionality.
    - This variation may permit the influence of these changes to drug encapsulation and release to be observed if the library of the monomers used was extended.
- Applicability of the formulation technique in a scaled-up setting.
- Encapsulating an alternative anti-cancer drug (e.g. docetaxel, paclitaxel and doxorubicin)
    - Utilising the same chemistry discussed but co-nanoprecipitating with an alternative drug which is not limited by its extreme hydrophobicity and instability. This may provide opportunity to gain more detailed understanding into: 1) what limits drug loading capacity, 2) whether the effect of chemical manipulation i.e. physicochemical properties have on the pharmacological behaviour (e.g. drug release).

## 6.3 References

1. V. Bala, S. Rao, B. J. Boyd and C. A. Prestidge, *J Control Release*, 2013, **172**, 48-61.
2. S. Sharma, A. Parmar, S. Kori and R. Sandhir, *TrAC trends in analytical chemistry*, 2016, **80**, 30-40.
3. D. Essa, P. P. D. Kondiah, Y. E. Choonara and V. Pillay, *Front Bioeng Biotechnol*, 2020, **8**, 48-48.

# Chapter 7

## Experimental

## 7.1 Materials

Butyl methacrylate (BuMA, contains 10 ppm monomethyl ether hydroquinone as inhibitor 99%), 2-ethyl hexyl methacrylate (EHMA, 99%), 2-hydroxypropyl methacrylate (HPMA, 97% mixture of isomers, contains 180-220 ppm monomethyl ether hydroquinone as inhibitor), copper (I) chloride (Cu(I)Cl, 99%), α-bromo isobutyryl bromide (EBiB 99%), 2,2'–bipyridine (bpy, 99%), anhydrous methanol (anhydrous MeOH, 99.8%), aluminium oxide (activated, neutral), deuterated chloroform ($CDCl_3$, 98.8 atom %), ethylene glycol dimethacrylate (EGDMA, 98%), bisphenol A dimethacrylate (BPDMA, > 98%)**,** bisphenol A glycerolate dimethacrylate (BPGDMA, 98%), bis(2-methacryloyl)oxyethyl disulphide (DSDMA, contains 6000 ppm hydroquinone as inhibitor, 99%), Diurethane dimethacrylate (UDMA, mixture of isomers contains 225 ± 25 ppm topanol as inhibitor, ≥ 97%), Glycerol dimethacrylate (GDMA, mixture of isomers, contains 200 ppm monomethyl ether hydroquinone as inhibitor, 85%), poly(ethylene glycol) monomethyl ether ($M_n$ ~5,000 g $mol^{-1}$), pyrene (98%), dithiothreitol (DTT), basic aluminium oxide and Dowex marathon exchange beads were purchased from Sigma Aldrich. Anhydrous triethylamine (TEA, 99%), 4-(dimethylamino) pyridine (DMAP, 99%) and all solvents were analytical grade and purchased from Fisher scientific and used as received.

7-ethyl-10-hydroxycamptothecin (SN-38) was purchased from Chemleader Biochemical. SN-38 as purchased was sent to RCTritec, Switzerland for direct tritiation (H/T exchange). Tritiated SN-38 was stored in a THF solution until used. THF was removed before experiments were conducted. ProSafe+ scintillation cocktail was purchased from Meridian Biotechnologies Ltd. and was added to radio samples before LSC. All materials were used as received. SN-38 Pentanoate was synthesised and supplied by Dr Andrew Dwyer, PDRA in the department of chemistry at the University of Liverpool.

## 7.2 Instrumentation

$^1H$ and $^{13}C$ nuclear magnetic resonance (NMR) spectra were recorded in chloroform-d, methanol-$d_4$, DMSO-$d_6$ or $D_2O$ using a 400 MHz Bruker Avance spectrometer operating at 400 and 100 MHz, respectively. Chemical shifts (δ) are reported in parts per million (ppm) with respect to an internal reference of tetramethylsilane (TMS).

Triple detection size exclusion chromatography (SEC) was conducted using either: i) a Malvern Viscotek instrument equipped with a GPC max VE2001 auto-sampler, two viscotek T6000 columns (and a guard column), a refractive index (RI) detector VE3580 and a dual 270 detector (light scattering and viscometer), or ii) a Malvern Viscotek equipped with D6000 columns (and a guard column) and a triple detector array TDA305 (refractive index, light scattering and viscometer). Analysis was conducted using a mobile phase of either i) DMF (containing 0.01 M lithium bromide) at 60 °C, or ii) THF (containing 2 v/v % TEA), at 35 °C both at a flow rate of 1 mL $min^{-1}$. Polymer thermal characteristics were analysed using differential scanning calorimetry (DSC), utilising a DSC Discovery instrument using a T4P calibration of samples held within Tzero pans. Samples were analysed at temperatures between -90 and 270 °C under a nitrogen atmosphere at a pressure of 0.1 MPa with a heating rate of 5 °C $min^{-1}$. Dynamic light scattering (DLS) measurements and zeta potentials were performed using a Malvern Zetasizer Nano ZS instrument with a wavelength of 630 nm. Measurements were performed at 25 °C at a nanoparticle concentration of 1 mg $mL^{-1}$ unless stated otherwise. Dispersions were measured without additional filtration or centrifugation, unless stated otherwise, in a polystyrene disposable fluorometric cuvette (size measurements) or a disposable capillary zeta flow cell (zeta measurements). Size measurements were obtained as an average of 3 individual measurements and were rounded to the nearest 5 nm. Scanning electron microscopy (SEM) images were obtained using a Hitachi S-4800 FE-SEM and a Tescan FIB SEM S8000G. Aqueous nanoparticle samples were prepared for analysis by dropping 10 µL sample (0.5 mg $mL^{-1}$) onto a silicon wafer, which was mounted on an aluminum stub with silver electroconductive paste. Samples were placed in a desiccator overnight and allowed to dry at ambient temperature and then chromium sputter-coated (120 mA for 60 seconds). Fluorescence spectra were obtained using a Shimadzu RF-5301PC spectrofluorophotometer. Emission spectra for pyrene were recorded between 300 and 500 nm. An excitation wavelength of $\lambda_{ex}$ = 335 nm was used for all studies, as well as an excitation slit width of 2.5 nm and an emission slit width of 2.5 nm with a scan rate of 60 nm $min^{-1}$. Electrospray ionisation (ESI) mass spectrometry data were recorded in the Mass Spectrometry Laboratory at the University of Liverpool using a MicroMass LCT mass spectrometer, electron

ionisation and direct infusion syringe pump sampling. All materials were diluted with methanol. Elemental analyses were obtained from a Thermo FlashEA 1112 series CHNSO elemental analyser. All radiation measurements were carried out using a liquid scintillation counter (Packard Tri-Carb 3100TR; Isotech) and radio-TLC analysed on an AR-2000 radio-TLC imaging scanner (Bioscan Inc.)

## 7.3 Experimental Methods

### 7.3.1 Chapter 2

#### 7.3.1.1 General Synthesis of p(BuMA)$_{100}$ *via* ATRP

Prior to use, anhydrous MeOH and BuMA were deoxygenated *via* gentle bubbling with Ar for 60 minutes. In a typical ATRP synthesis of p(BuMA)$_{100}$, bpy (0.110 g, 0.704 mmol, 2 eq.), BuMA (5 g, 35.2 mmol, 100 eq.), was added to an oven dried round-bottomed flask (25 mL) equipped with an argon inlet/outlet and a magnetic stirrer bar. Anhydrous MeOH was added (6.58 mL, 50 wt.% based on total solid mass) and the solution was degassed *via* Ar sparge for 30 minutes. Copper catalyst Cu(I)Cl (0.038 g, 0.352 mmol, 1 eq.) was added rapidly to the flask forming a brown coloured solution, and the reaction was further degassed for 5 mins. EBiB (52 µL, 0.352 mmol, 1 eq.) was rapidly injected into the solution and the Ar inlet and outlet was removed. The reaction flask was inverted and shaken, the septum was sealed with grease and flask was swiftly submerged into a preheated oil bath (50 °C). The reactions proceeded as homogeneous solution, for 72 hours. The polymerisation was terminated by exposure to air and a small sample was removed to calculate the monomer conversion by $^{1}$H-NMR ($CDCl_3$) (Figure 7.1). The reaction mixture was diluted further with the addition of THF, forming a bright green coloured solution. The polymer was then purified by passing the sample through a neutral alumina column to remove the copper catalytic system. Excess THF was removed under vacuum to concentrate the sample before precipitation from THF into ice cold MeOH, yielding a white solid, which was dried in a vacuum oven (40 ˚C, 24 hours) The resulting polymer was characterised by $^{1}$H NMR in $CDCl_3$ (Figure 7.2) and TD-SEC with a mobile phase of THF/TEA (98/2 v/v %) using a narrow poly(styrene) standard calibration.

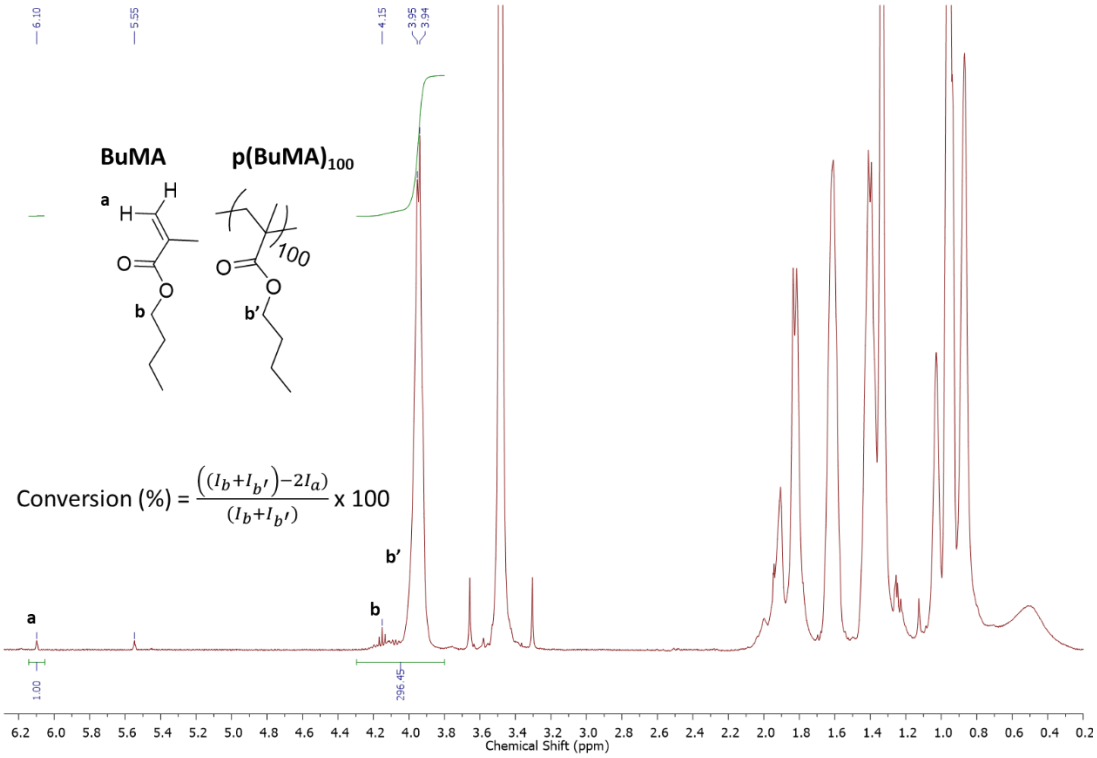


**Figure 7.1** Crude $^1$H-NMR ($CDCl_3$) taken to allow for the quantification of monomer conversion achieved during the polymerisation of $p(BuMA)_{100}$ after 72 hours.

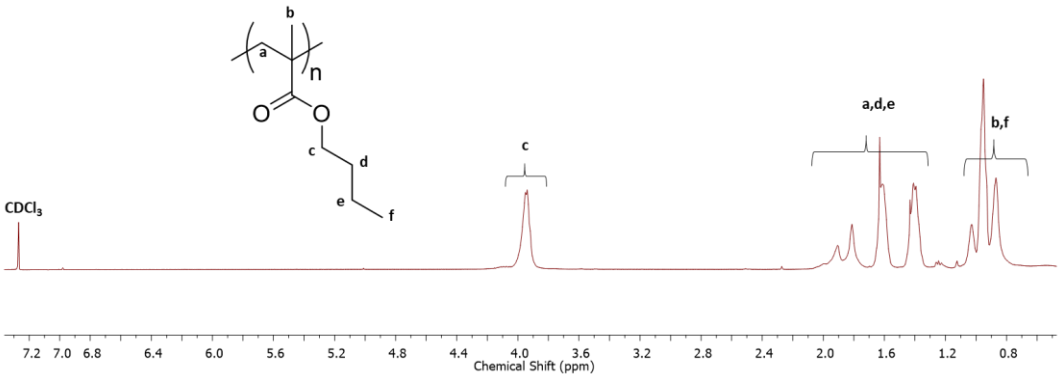


**Figure 7.2** $^1$H-NMR ($CDCl_3$) of pure $p(BuMA)_{100}$.

This method outlined was also used for the synthesis of p(BuMA)20, $p(EHMA)_{20}$, $p(EHMA)_{100}$, $p(HPMA)_{20}$ and $p(HPMA)_{100}$. The polymerisation of EHMA, became biphasic as the polymerisation progressed. Due to this biphasic nature of the EHMA polymerisation, termination occurred through the exposure to air and the addition of $CDCl_3$ so that a homogenous solution could be formed before collecting a crude $^1$H-NMR sample. Purification by precipitation of HPMA based polymer occurred in ice - cold hexane.

### 7.3.1.2 Determination of p(BuMA)$_{60}$ Polymerisation Kinetics

Kinetic studies were performed by taking samples from the polymerisation of p(BuMA)$_{60}$ under positive Ar pressure. The polymerisation was prepared as stated in Section 7.3.1.1. Aliquots were analysed by $^{1}$H NMR ($CDCl_3$) to determine the conversion and by TD-SEC with a mobile phase of THF/TEA 98:2 v/v % after the catalyst was removed from the samples by passing through a small neutral alumina column. Monomer conversion was determined by NMR spectroscopy using crude samples of the reaction medium. Integrals of the vinyl protons of the unreacted monomer (5.55 ppm and 6.10 ppm) were compared with the integrals of the $CH_2$ signal adjacent to the ester group of both the polymer repeat units and the monomer (3.95 ppm and 4.15 ppm, respectively).

### 7.3.1.3 Synthesis of poly(ethylene glycol) mono-functional ATRP macro-initiator (MeO-PEG$_{114}$-Br)

Poly(ethylene glycol) methyl ether, MeO-PEG$_{114}$-OH (32.15 g, 6 mmol, 1 eq.) was added to anhydrous toluene (100 mL) in the presence of TEA (1.21 g, 12 mmol, 2 eq.) in a two necked round-bottomed flask fitted with a dropping funnel, an Ar inlet/outlet and a magnetic stirrer bar. The reaction mixture was heated to 40 °C to help solublise the MeO-PEG$_{114}$-OH. After 30 minutes of heating and stirring, MeO-PEG$_{114}$-OH was full dissolved. The reaction mixture was then left to cool to ambient temperature. α-bromoisobutyryl bromide (23.76 g, 12 mmol, 2 eq.) diluted with toluene (20 mL) was placed into the dropping funnel. The reaction was placed in an ice bath and the α-bromoisobutyryl bromide solution was added slowly over 30 mins. The ice bath was removed and the reaction mixture was left to stir at ambient temperature for 24 hours. Upon return, the reaction mixture had formed a white precipitate (triethylamine salt $Et_3NH^+Br^-$) which provided indication of the reaction progress. A hot filtration (50 ˚C) was performed using small amounts of hot toluene to wash the salt. The reaction medium was filtered through a short basic alumina column with toluene as the eluent and concentrated on the rotary evaporator. The resulting product was diluted in THF and purified by precipitation into room temperature hexane to yield a fine white powder. Solvent was removed by decantation. The precipitation step was repeated, and the product was finally dried under vacuum at 40 °C for 72 hours. The chemical structure of resulting mono-

functional macro-initiator (MeO-$PEG_{114}$-Br) (white powder, 21 g, 66%) was confirmed by $^1H$ NMR in $CDCl_3$, and TD-SEC with a mobile phase of DMF (containing 0.01 M lithium bromide).

**7.3.1.4 Synthesis of $PEG_{114}$ AB block Copolymer p($PEG_{114}$-*b*-$BuMA_{100}$) by Cu-ATRP.**

Prior to use, anhydrous MeOH and BuMA were deoxygenated *via* gentle bubbling with Ar for 60 minutes. In a typical reaction, targeting a number average $DP_n$ of 100 monomer units for BuMA, using MeO-$PEG_{114}$-Br macroinitiator (1.81 g, 0.352 mmol, 1 eq.), BuMA (5 g, 35.2 mmol, 100 eq.) and bpy (0.11 g, 0.704 mmol, 2 eq.) were added to a round bottomed flask (25 mL) equipped with an Ar inlet/outlet and a magnetic stirrer bar. Anhydrous MeOH (50 wt.%, based on total solid mass, 8.79 mL) was added and the solution was degassed *via* Ar sparge for a further 15 minutes. Cu(I)Cl (0.035 g, 3.52 mmol, 1 eq.) was rapidly added to the flask and the reaction medium turned dark brown immediately. The reaction mixture was further degassed for 60 seconds, sealed with grease and submerged into a preheated oil bath (50 ˚C). The reaction was allowed to proceed for 72 hours. The polymerisations were cooled and terminated by exposure to air and a small sample was removed and diluted with $CDCl_3$ to determine the monomer conversion ($^1H$-NMR, Figure 7.3). The reaction mixture was diluted with the addition of DCM. The copper catalytic system was removed by passing the polymer solution through a neutral alumina column using DCM as the mobile phase. The resulting solution was concentrated *in-vacuo* and the AB block copolymer was purified by precipitation from THF into ice-cold diethyl ether and dried *in vacuo* at 40 ˚C for 24 hours. The resulting AB block copolymer was characterised by $^1H$ NMR ($CDCl_3$) and TD-SEC with a mobile phase of THF/TEA (98:2% v:v). The procedure outlined above was followed for the synthesis of p($PEG_{114}$-*b*-$HPMA_{100}$) and p($PEG_{114}$-*b*-$EHMA_{100}$).

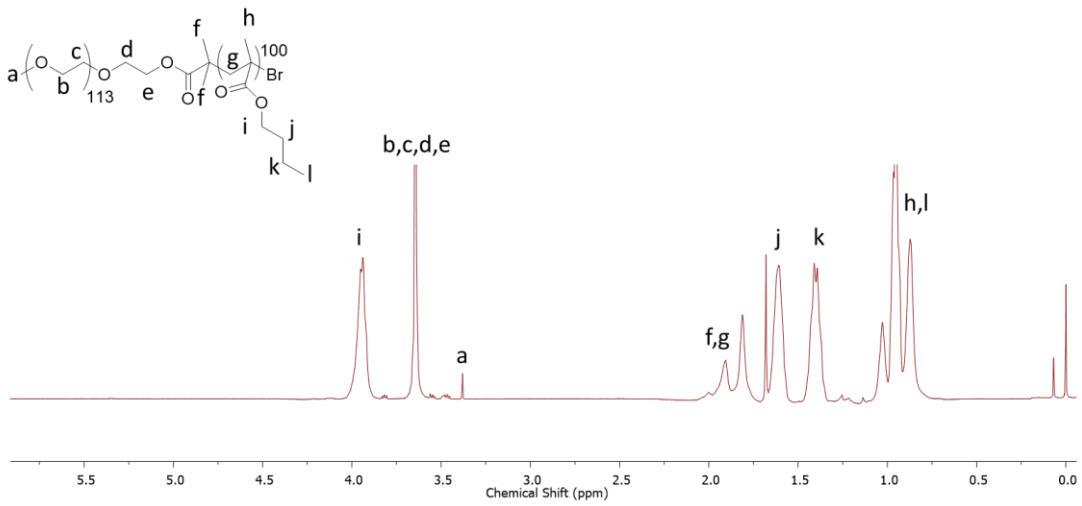


**Figure 7.3** $^{1}$H-NMR ($CDCl_3$) of p($PEG_{114}$-*b*-$BuMA_{100}$).

### 7.3.1.5 General Synthesis of EGDMA branched copolymer *via* methanolic ATRP (BuMA, HPMA and EHMA)

Prior to use, anhydrous MeOH and all monomers were deoxygenated *via* gentle bubbling with Ar for 60 minutes. In a typical reaction, targeting a number average $DP_n$ of 100 monomer units for BuMA, the branched copolymer, p($BuMA_{100}$-*co*-$EGDMA_{0.95}$), was synthesised and purified using the procedure described above for linear *p*($BuMA_{100}$) with the addition of the branching agent/ divinyl co-monomer EGDMA. In brief, BuMA (5 g, 35.2 mmol, 100 eq.), EGDMA 66.3 mg, 0.342 mmol, 0.95 eq. wrt.to initiator amount), bpy (0.110 g, 0.704 mmol, 2 eq.) were added to a round bottom flask (25 mL) equipped with an Ar inlet/outlet and a magnetic stirrer bar. Anhydrous MeOH (50 wt.%, based on total solid mass, 6.67 mL) was added and the solution was degassed *via* Ar sparge for a further 30 minutes. Cu(I)Cl (34.8 mg, 0.352 mmol, 1 eq.) was added rapidly, forming a dark brown coloured solution. The reaction mixture was purged further with Ar for 30 minutes. EBiB (51.7 µL, 0.361 mmol, 1 eq.) was injected into the reaction mixture, and the reaction mixture was further purged with Ar for approximately 1 minute. The Ar inlet and outlet were removed from the flask, which was then inverted, sealed with grease and submerged into a pre-heated oil bath (50 ˚C). The reaction was allowed to proceed for 72 hours. The polymerisation was terminated by exposure to air and a small sample removed to calculate the monomer conversion by $^{1}$H-NMR ($CDCl_3$). The reaction mixture was diluted using $CHCl_3$, which rapidly turned bright green in colour. The solution was passed over a neutral alumina column to remove the catalytic complex and

concentrated *in vacuo*. The branched copolymer was then purified by precipitation from THF into ice-cold MeOH to yield white solid powder. The supernatant was decanted and the residual powder was dried *in vacuo* at 40 ˚C for 24 hours. The resulting branched material was characterised by $^1$H NMR in $CDCl_3$ and TD-SEC with a mobile phase of THF/TEA eluent (98/2 v/v %).

#### 7.3.1.6 General Synthesis of statistical linear copolymers *via* methanolic ATRP (BuMA, HPMA and EHMA)

In a typical ATRP synthesis of a linear statistical copolymer p($BuMA_{50}$-*s*-$HPMA_{50}$) targeting $DP_n$ = 100 monomer units overall, anhydrous MeOH and all monomers were deoxygenated *via* gentle bubbling with Ar for 60 minutes prior to use. BuMA (1 g, 7.08 mmol, 50 eq.), HPMA (1.02 g, 7.08 mmol, 50 eq.) and bpy (44.36 mg, 0.284 mmol, 2 eq.) were added to an oven dried round-bottomed flask (10 mL) equipped with an Ar inlet/outlet and a magnetic stirrer bar. Anhydrous MeOH was added (2.63 mL, 50 wt.% based on total solid mass) and the solution was degassed *via* Ar sparge for 30 minutes. Copper catalyst Cu(I)Cl (0.0140 g, 0.142 mmol, 1 eq.) was added rapidly to the flask forming a brown coloured solution, and the reaction was further degassed for 5 mins. EBiB (20.8 µL, 0.142 mmol, 1 eq.) was rapidly injected into the solution and the Ar inlet and outlet was removed. The reaction flask was inverted and shaken, the septum was sealed with grease and the flask was swiftly submerged into a preheated oil bath (50 °C). The reactions proceeded as homogenous solutions, except for p($BuMA_{50}$-*s*-$EHMA_{50}$) which became biphasic as the polymerisation progressed towards the late stages. Reactions proceeded for up to 72 hours and the polymerisations were terminated by exposure to air. In the cases of homogenous reaction mixtures, a small sample was removed for $^1$H-NMR ($CDCl_3$ or MeOD) analysis to determine monomer conversion followed by the addition of THF to the reaction medium. The biphasic polymerisation was diluted with $CDCl_3$ to allow for a crude sample to be taken for $^1$H-NMR analysis to determine monomer conversion. All the polymers were purified by passing the samples through a neutral alumina column to remove the copper catalytic system. Excess THF (or $CHCl_3$) was removed under vacuum to concentrate the sample before precipitation from THF into ice cold MeOH, yielding a white solid that was dried in a vacuum oven (40 ˚C, 24 hours) The resulting

polymers were characterised by $^1$H NMR in $CDCl_3$ and TD-SEC with a mobile phase of THF/TEA (98/2 v/v %) using a narrow and broad poly(styrene) standard calibration.

### 7.3.1.7 General Synthesis of statistical branched copolymer *via* methanolic ATRP (BuMA, HPMA and EHMA)

The synthesis and purification of statistical branched copolymers followed the same procedure as that described for linear p($BuMA_{50}$-*s*-$HPMA_{50}$), but with the inclusion of EGDMA divinyl monomer. BuMA (2.50 g, 17.6 mmol, 50 eq.), HPMA (2.54 g, 17.6 mmol, 50 eq.), EGDMA (62.8 mg, 3.168 mmol, 0.9 eq.) and bpy (0.110 g, 0.704 mmol, 2 eq.) were added to a reaction flask (25 mL) fitted with a magnetic stirrer bar and an Ar inlet and outlet. Anhydrous MeOH (50 wt.% wrt. total solid mass, 6.71 mL) was added and the solution was degassed *via* Ar sparge for 30 minutes. Copper catalyst Cu(I)Cl (34.8 mg, 0.352 mmol, 1 eq.) was added rapidly to the flask forming a brown coloured solution, and the reaction was further degassed for 5 mins. EBiB (68.7 µL, 0.352 mmol, 1 eq.) was rapidly injected into the solution and the Ar inlet and outlet was removed. The reaction was then carried out in an identical manner to that described in section 7.3.1.7 with precipitation of polymer into ice-cold hexane. The resulting polymer was characterised by $^1$H NMR in $CDCl_3$ and TD-SEC with a mobile phase of THF/TEA (98/2 v/v%) using a narrow and broad poly(styrene) standard calibration.

### 7.3.1.8 General Synthesis of branched EHMA copolymers with varying divinyl monomers (BPGDMA, BPDMA, DSDMA, UDMA, GDMA)

Prior to use, anhydrous MeOH and EHMA monomer were deoxygenated *via* gentle bubbling with Ar for 60 minutes. In a typical reaction, targeting a number average $DP_n$ of 20 monomer units for p($EHMA_{20}$-co-$UDMA_{0.90}$), EHMA (2 g, 10 mmol, 20 eq.), UDMA (0.2139 g, 0.4545 mmol, 0.90 eq. wrt. to initiator amount) and bpy (0.1567 g, 1.01 mmol, 2 eq.) were added to a round bottomed flask (25 mL) equipped with an Arinlet/outlet and a magnetic stirrer bar. Anhydrous MeOH (50 wt.%, based on total solid mass, 3.24 mL) was added and the solution was degassed *via* Ar sparge for a further 30 minutes. Cu(I)Cl (49.6 mg, 0.502 mmol, 1 eq.) was added rapidly, forming a dark brown solution. The reaction mixture was purged further with Ar for 30 minutes. EBiB (73.7 µL, 0.502 mmol, 1 eq.) was injected into the reaction mixture, and the reaction mixture was further purged with Ar for approximately 1 minute. The

Ar inlet and outlet were removed from the flask, which was then inverted, sealed with grease and submerged into a pre-heated oil bath (50 ˚C). The reaction was allowed to proceed for 48 hours, and become biphasic as the reaction progressed. The polymerisation was terminated by exposure to air and the reaction medium was diluted using $CDCl_3$ to give a bright green and homogenous mixture. The mixture was passed over a neutral alumina column to remove the catalytic complex and concentrated *in vacuo*. The branched copolymer was then purified by precipitation from THF into ice-cold MeOH to yield white powder. The supernatant was decanted, and the residual polymer was dried *in vacuo* at 40 ˚C for 24 hours. The resulting branched material was characterised by $^1$H NMR in $CDCl_3$ and TD-SEC with a mobile phase of THF/TEA eluent (98/2 v/v %).

### 7.3.2 Chapter 3

#### 7.3.2.1 Aqueous nanoparticle formation

#### 7.3.2.2 Sole Nanoprecipitations

During a typical sole nanoprecipitation experiment, polymeric material (50 mg) was dissolved in 10 mL of analytical grade THF in a glass vial and sealed. The vial was placed on a roller mixer at ambient temperature for 18-24 hours to allow for complete solubilisation. The polymer concentration within this stock was $[P]_0$ = 5 mg $mL^{-1}$. The polymer/THF stock solution (1 mL) was rapidly added to a glass vial containing deionized water (5 mL) which was stirring (450 rpm). This mixture was then left for 24 hours at ambient temperature to allow for THF evaporation, resulting in an aqueous nanoparticle dispersion at final polymer concentration $[P]_f$ = 1 mg $mL^{-1}$. These nanoparticle dispersions were assessed initially by visual observation for any signs of sedimentation or polymer aggregates. DLS analysis of the aqueous dispersions (1 mL) was then performed to obtain the hydrodynamic diameter and zeta potential measurements. This method was used for the sole nanoprecipitations of: linear homopolymers, branched copolymers, AB block copolymers and statistical linear and branched copolymers.

#### 7.3.2.3 Co-nanoprecipitations

During a typical co-nanoprecipitation targeting a weight fraction of 40 wt.% AB block copolymer and 60 wt.% hydrophobic polymers, a total mass of 50 mg of material was

weighed out (20 mg of AB block copolymer and 30 mg of hydrophobic polymer) into a glass vial followed by the addition of THF (10 mL). The solutions were sealed and placed on a roller mixer for 24 hours to allow for solubilisation. The polymer concentration within this stock solution was $[P]_0$ = 5 mg $mL^{-1}$. The polymer/THF stock solution (1 mL) was added to a glass vial containing stirring (450 rpm) deionized water (5 mL). This mixture was then left for 24 hours at ambient temperature to allow for THF evaporation, resulting in an aqueous nanoparticle dispersion at final polymer concentration $[P]_f$ = 1 mg $mL^{-1}$. These nanoparticle dispersions were assessed initially by visual observation for any signs of sedimentation or polymer aggregates. DLS was then used to obtain the hydrodynamic diameter and zeta potential measurements.

#### 7.3.2.4 Varying the Weight Compositional Ratio of Each Polymeric Component Within Co-nanoprecipitation

Co-nanoprecipitation studies were conducted using branched copolymer and AB block copolymer weight percentages of: 100:0, 90:10, 80:20, 70:30, 60:40, 50:50, 40:60, 30:70, 20:80, 10: 90 and 0:100. A total mass of 50 mg of material was weighed out into a glass vial followed by the addition of THF (10 mL). The solutions were sealed and placed on a roller mixer for 24 hours to allow for solubilisation. Polymer concentration within this stock was $[P]_0$ = 5 mg $mL^{-1}$. The polymer/THF stock solution (1 mL) was added to a glass vial containing stirring (450 rpm) deionized water (5 mL). This mixture was then left for 24 hours at ambient temperature to allow for THF evaporation, resulting in an aqueous nanoparticle dispersion at final polymer concentration $[P]_f$ = 1 mg $mL^{-1}$. These nanoparticle dispersions were assessed initially by visual observation for any signs of sedimentation or polymer aggregates. DLS was then used to obtain the hydrodynamic diameters. This method was used for the co-nanoprecipitations of p($HPMA_{100}$-co-$EGDMA_{0.90}$), p($BuMA_{100}$-co-$EGDMA_{0.95}$) and p($EHMA_{100}$-co-$EGDMA_{0.80}$) with p($PEG_{114}$-b-$HPMA_{100}$). Samples were left at ambient temperature on the benchtop for 10 days and DLS measurements were repeated to assess stability.

#### 7.3.2.5 Nanoparticle Stability to Addition of PBS

Five THF stock solutions of p($HPMA_{100}$-co-$EGDMA_{0.90}$): p($PEG_{114}$-*b*-$HPMA_{100}$) were prepared with compositional ratios varying from 100:0 – 50:50 wt.%, respectively. The polymer concentration within this stock solution was 5 mg $mL^{-1}$. The polymer-THF stock solution (1 mL) was added to stirring DI water (5 mL, 450 rpm) to produce a final polymer concentration of 1 mg $mL^{-1}$, and THF was allowed to evaporate overnight. Initial $D_z$, PDI and derived count rate values were determined *via* DLS prior to dilution. PBS (pH 7.4) was added over a 100-fold dilution factor to produce polymer concentrations at 0.5, 0.25, 0.1 and 0.01 mg $mL^{-1}$. The aqueous nanoparticle dispersions were sealed and placed on a roller mixer overnight following dilution and then assessed initially by visual observations for any sign of polymer aggregation or sedimentation and then *via* DLS at $[P]_f$ = 1 mg $mL^{-1}$.

#### 7.3.2.6 SEM Sample Preparation of Nanoparticles

In a typical preparation of a sample for SEM analysis, aqueous nanoparticle dispersion (1 mL, 1 mg $mL^{-1}$) was added to a glass vial containing deionised water (1 mL) to give a diluted aqueous nanoparticle dispersion at a concentration of 0.5 mg $mL^{-1}$ . Aqueous nanoparticle dispersion (10 µL) was dropped onto a silicon wafer, which was mounted on an aluminum stub with silver DAG and left to dry overnight in a desiccator. Dried samples were chromium sputter-coated (120 mA for 60 seconds).

#### 7.3.2.7 Encapsulation of the Hydrophobic Guest Molecule Pyrene

In a typical encapsulation of pyrene, a stock solution of pyrene was prepared in acetone (0.1 mg $mL^{-1}$). The stock solution (300 µL, 0.1 mg $mL^{-1}$) was added to a glass vial and the acetone was allowed to evaporate overnight to leave pyrene dye (30 µg). For a typical co-nanoprecipitation targeting a 60:40 wt.% composition, *p*($HPMA_{100}$-*co*-$EGDMA_{0.95}$) (18 mg), *p*($PEG_{114}$-*b*-$HPMA_{100}$) (12 mg) and THF (6 mL) were added to the vial to give $[P]_0$ = 5 mg $mL^{-1}$ and $[pyrene]_0$ = 5 µg $mL^{-1}$. The solution was sealed and placed on a roller mixture for 24 hours for complete solubilisation. The pyrene loaded nanoparticles were then prepared by rapid addition of copolymers/pyrene/THF (1 mL) into vigorously stirring deionised water (5 mL, 450 rpm). The mixture was left for 24 hours at ambient temperature to ensure complete

THF evaporation leading to a $[P]_f$ = 1 mg $mL^{-1}$ and $[pyrene]_f$ = 1 µg $mL^{-1}$. Samples were assessed initially by visual observations to look for any signs of visible polymer aggregation or sedimentation, then the samples were assessed *via* DLS.

#### 7.3.2.8 Evaluating the Stability of Pyrene Loaded p(EHMA$_{100}$-co-EGDMA$_{0.80}$): p(PEG$_{114}$-*b*-HPMA$_{100}$) Nanoparticles to PBS Addition

A stock solution of pyrene was prepared in acetone (0.1 mg $mL^{-1}$). The stock solution (300 µL, 0.1 mg $mL^{-1}$) was added to glass vials and the acetone was allowed to evaporate overnight to leave pyrene dye (30 µg). Five stock solutions of p(EHMA$_{100}$-co-EGDMA$_{0.80}$): p(PEG$_{114}$-*b*-HPMA$_{100}$) were prepared with compositional ratios varying from 100:0 – 50:50 wt.%, respectively. The polymer concentration within this stock solution was 5 mg $mL^{-1}$. The solution was sealed and placed on a roller mixture for 24 hours for complete solubilisation. The pyrene loaded nanoparticles were then prepared by rapid addition of copolymers/pyrene/THF (1 mL) into vigorously stirring deionised water (5 mL, 450 rpm). The mixture was left for 24 hours at ambient temperature to ensure complete THF evaporation leading to a $[P]_f$ = 1 mg $mL^{-1}$ and $[pyrene]_f$ = 1 µg $mL^{-1}$. Samples were assessed *via* DLS before addition of PBS. Following this, PBS (pH 7.4) was added over a 100-fold dilution factor to produce polymer concentrations at 0.5, 0.25, 0.1 and 0.01 mg $mL^{-1}$. The aqueous nanoparticle dispersions were sealed and placed on a roller mixer overnight following dilution and then assessed initially by visual observations for any sign of polymer aggregation or sedimentation and then *via* DLS at $[P]_f$ = 1 mg $mL^{-1}$.

### 7.3.3 Chapter 4

#### 7.3.3.1 Preparation of Aqueous SN-38 Loaded Nanoparticles (5 wt.% drug loading)

Before conducting the co-nanoprecipitation experiments, a stock solution of SN-38 was prepared in THF (1 mg $mL^{-1}$). During a typical co-nanoprecipitation, 2.5 mL of the SN-38 stock solution was added to a vial and to this, 30 mg of a branched copolymer and 20 mg of AB block copolymer were added and dissolved in 7.5 mL of THF. The solution was tightly sealed and placed on a roller mixer overnight to ensure complete solubilisation. SN-38/polymer THF stock (1 mL, $[P]_0$= 5 mg $mL^{-1}$) was added rapidly to stirring DI water (5 mL). The mixture was left for 24 hours at ambient temperature to ensure complete THF evaporation to yield SN-38 loaded aqueous polymer

nanoparticles ($[P]_f$ = 1 mg $mL^{-1}$ and [SN-38] = 0.050 mg $mL^{-1}$. These nanoparticle dispersions were assessed initially by visual observation for any signs of sedimentation or polymer aggregates. DLS was then used to obtain the hydrodynamic diameter and zeta potential measurements. The same procedure was followed when targeting drug loading values of 2.5, 6, 7.5, 10, 20 and 30 wt.%.

#### 7.3.3.2 Determining the Encapsulation Efficiency of SN-38 During Co-Nanoprecipitation *via* UV-Vis Spectroscopy

SN-38 loaded aqueous nanoparticle dispersions were prepared as previously described in Section 7.3.3.1. An aliquot of SN-38 loaded aqueous nanoparticle dispersion (1 mL, $[P]_f$ = 1 mg $mL^{-1}$) was added to a glass vial and rapidly cooled using liquid $N_2$ and $H_2O$ was removed *via* freeze drying over 48 hours. The same SN-38 loaded aqueous nanoparticle dispersion (1.5 mL, $[P]_f$ = 1 mg $mL^{-1}$) was added to an Amicon® ultra-15 centrifugal filter unit (MWCO = 3 kDa) with a regenerated cellulose membrane and placed under high centrifugation (6000 xg, 20 °C) for 60 minutes. The filtrate (1 mL), located in the bottom compartment of the centrifugal filter unit, was removed and added to a glass vial. DI $H_2O$ (1 mL) was added to the top compartment and the sample was placed under high centrifugation (6000 xg, 20 °C) for 30 minutes. The SN-38 loaded nanoparticles were washed a further 2 times. The aliquots (total volume = 4 mL) were combined and rapidly cooled under liquid $N_2$ and freeze dried for 72 hours. Following the removal of $H_2O$, both the filtrate and unfiltered SN-38 loaded aqueous nanoparticle monoliths were re-solvated with a known volume of inhibitor-free THF. The SN-38 mass concentration was determined from the UV-Vis absorption at 390 nm, using a pre-established SN-38 calibration curve, which was prepared for SN-38 from 8 standard THF stock solutions obtained over 0.1 µg $mL^{-1}$ to 15 µg $mL^{-1}$. SN-38 encapsulation efficiency was determined by using Equation 7.1. Where, $[SN\text{-}38]_{total}$ represents the SN-38 concentration determined prior to ultracentrifugation and $[SN\text{-}38]_{free}$ represents the SN-38 concentration determined from the filtrate following the ultracentrifugation.

$$\mathrm{EE}\ (\%) = \left(\frac{[\mathrm{SN{-}38\ total}]-[\mathrm{SN{-}38\ free}]}{[\mathrm{SN{-}38\ total}]}\right) \mathrm{x}\ 100 \qquad \textbf{(7.1)}$$

### 7.3.3.3 Stability of SN-38 Loaded Nanoparticles

SN-38 loaded nanoparticle formulations of p($BuMA_{100}$-co-$EGDMA_{0.95}$): p($PEG_{114}$-*b*-$HPMA_{100}$) (2.5 wt.% SN-38) and p($EHMA_{100}$-co-$EGDMA_{0.80}$): p($PEG_{114}$-*b*-$HPMA_{100}$) (2.5 and 5 wt.% SN-38) were prepared as described in Section 7.3.3.1, with composition of branched polymer: AB block copolymer at 60:40 wt.%, respectively. Initial $D_z$, PDI, derived count rate and zeta potential measurements were obtained *via* DLS following THF evaporation after 24 hours. Nanoparticle dispersions were then stored out of direct light at ambient temperature, and the measurements repeated after 7 days and 13 weeks of storage.

### 7.3.3.4 Reproducibility Studies on SN-38 Loaded Nanoparticles

Three independent co-nanoprecipitations of 5 wt.% SN-38 loaded p($EHMA_{100}$-co-$EGDMA_{0.80}$): p($PEG_{114}$-*b*-$HPMA_{100}$) at 60:40 wt.% compositions were conducted under identical conditions from three different stock solutions as previously described in Section 7.3.3.1. $D_z$, PDI, derived count rate and zeta potential measurements were obtained *via* DLS after THF evaporation after 24 hours.

### 7.3.3.5 Modifying pH of Nanoprecipitation Environment

SN-38 loaded co-nanoprecipitation regimes were prepared as described in Section 7.3.3.1, but the pH of the deionised water was altered to pH 4 by the addition of $H_2SO_{4\,(aq.)}$ (1 M). SN-38/polymer THF stock solution (1 mL, $[P]_0$ = 5 mg $mL^{-1}$) was added rapidly to stirring water (5 mL, pH 4). The mixture was left for 24 hours at ambient temperature to ensure complete THF evaporation to yield SN-38 loaded aqueous polymer nanoparticles ($[P]_f$ = 1 mg $mL^{-1}$ and [SN-38] = 0.050 mg $mL^{-1}$. These nanoparticle dispersions were assessed initially by visual observation for any signs of sedimentation or polymer aggregates. DLS was then used to obtain the hydrodynamic diameter and zeta potential measurements.

### 7.3.3.6 Multiple Co-nanoprecipitations

During a typical multiple co-nanoprecipitation, a THF stock solution of 5 wt.% SN-38 loaded p($EHMA_{100}$-co-$EGDMA_{0.80}$): p($PEG_{114}$-*b*-$HPMA_{100}$) was prepared as described in Section 7.3.3.1, at 60:40 wt.% composition of branched polymer: AB block copolymer, respectively, and a concentration of polymer = 5 mg $mL^{-1}$. The SN-38/polymer – THF stock solution (1 mL) was added to stirring DI water (5 mL) and the

sample was left to stir for 24 hours to allow for THF evaporation. To this aqueous nanoparticle dispersion, SN-38/polymer-THF stock solution (1 mL) was then added again with rapid stirring and left for 24 hours. A further two additions were made in the same manner, to generate aqueous SN-38 loaded nanoparticle dispersions with $[P]_f$ = 4 mg $mL^{-1}$ and [SN-38] = 0.20 mg $mL^{-1}$. $D_z$, PDI and derived count rate values were determined *via* DLS measurements.

#### 7.3.3.7 Assessment of $^3$H-Labelled SN-38 Radio Purity *via* Radio Thin-Layer Chromatography

Thin-layer chromatography (TLC) analysis was conducted on SN-38 in order to establish a suitable eluent system and $R_f$ values; these were determined to be ethyl acetate (100%) and $R_{f1}$ = 0.25 and $R_{f2}$ = 0.88 associated with the open and closed lactone form of SN-38. Using the same mobile phase, radio-TLC was conducted to check radio purity of $^3$H-labelled SN-38, which was ran in parallel to unlabelled SN-38. TLC plate was dried and analysed using a radio-TLC imaging scanner which generates $R_f$ values *via* digital counting of $^3$H isotopes. The $R_f$ values obtained for the radio-labelled and unlabelled SN-38 were compared and found to be in good agreement.

#### 7.3.3.8 Preparation of $^3$H-SN-38 Loaded Branched Vinyl Copolymer Nanoparticles *via* Co-Nanoprecipitation

$^3$H-SN-38 loaded nanoparticles were prepared targeting a SN-38 drug loading of 5 wt.% using a compositional ratio of branched polymer: AB block copolymer at 60:40 wt.%, respectively. Total solid mass was 50 mg and $[P]_0$ = 5 mg $mL^{-1}$. For a typical co-nanoprecipitation of 5 wt.% $^3$H-SN-38 loaded p($EHMA_{100}$-co-$EGDMA_{0.80}$): p($PEG_{114}$-*b*-$HPMA_{100}$), a stock solution of $^3$H labelled SN-38 (5-135 µL, 5.418-37.133 µCi $mg^{-1}$) was prepared in EtOH and added to a glass vial and left at ambient temperature overnight to allow complete EtOH evaporation. A stock solution of p($EHMA_{100}$-co-$EGDMA_{0.80}$): p($PEG_{114}$-*b*-$HPMA_{100}$) was prepared in THF ($[P]_0$ = 5 mg $mL^{-1}$), sealed and placed on a roller mixer for 24 hours. To the glass vial containing dried $^3$H-SN-38, an aliquot of polymer stock solution was added; the glass vial was then sealed and the contents were mixed using a vortex mixer for approx. 1 minute. Co-nanoprecipitation was conducted by rapidly adding this solution (1 mL) into stirring DI water (5 mL), and the sample was left for 24 hours at ambient temperature to allow for THF evaporation

and to yield $^{3}$H-SN-38 loaded p(EHMA$_{100}$-co-EGDMA$_{0.80}$): p(PEG$_{114}$-*b*-HPMA$_{100}$) nanoparticles with $[P]_f$ = 1 mg mL$^{-1}$ which were analysed by DLS.

### 7.3.3.9 Determining Radiometric Encapsulation Efficiency

The encapsulation efficiency of $^{3}$H-SN-38 loadings was determined by using LSC to obtain the total mass of SN-38 present within the aqueous nanoparticle dispersions prepared as described in Section 7.3.3.11. Following this, the aqueous nanoparticle dispersions (0.5 mL, $[P]_f$ = 1 mg mL$^{-1}$) were placed in centrifugal tubes and centrifuged (14 000 rpm, 1 hour). The filtrates were collected and analysed *via* LSC, which determined the mass of the free SN-38 present. Encapsulation efficiencies were calculated using Equation 7.2.

$$\text{EE}\ (\%) = \frac{(\text{Total mass of SN}-38)-(\text{Free SN}-38)}{(\text{Total mass of SN}-38)}\ \text{x}\ 100 \quad \textbf{(7.2)}$$

### 7.3.3.10 Determining SN-38 Release Rates *via* $^{3}$H Radio-dialysis at pH 7 and pH 4

SN-38 release rates were determined at pH 7 and pH 4 using radio dialysis of p(EHMA$_{100}$-co-EGDMA$_{0.80}$): p(PEG$_{114}$-*b*-HPMA$_{100}$) aqueous nanoparticle dispersion. The $^{3}$H-SN-38 loaded nanoparticle dispersion was prepared as described in Section 7.3.3.11, with a targeted SN-38 loading of 5 wt.% and $[P]_f$ = 1 mg mL$^{-1}$. Loaded $^{3}$H-SN-38 p(EHMA$_{100}$-co-EGDMA$_{0.80}$): p(PEG$_{114}$-*b*-HPMA$_{100}$) (1 mL) nanoparticle dispersion was added to a double-sided dialyser (MWCO = 3.5 kDa regenerated cellulose membrane). This was placed in a preheated (37 °C) glass jar containing DI water (100 mL, pH 7), which was then placed in a preheated oil bath and stirred (100 rpm). SN-38 release rate was monitored at pre-determined time points of 0.5, 1, 2, 3, 4, 5, 6, 7, 8 and 24 hours. At each time point the bio-dialyser was removed and added to a new jar with pre-heated $H_2O$ (100 mL). SN-38 release rate was determined using LSC after removing an aliquot (1 mL) from each independent time point reservoir and adding scintillation cocktail (10 mL). The release rate of SN-38 was also determined in an identical manner at pH 4, with the only difference being the pH of the DI water in the reservoir was acidified to pH4 using 1 M $HCl_{(aq.)}$. Cumulative release was calculated using Equation 7.3.

$$\text{Cumulative Release}\ (\%) = \left(\frac{(\text{concentration drug release})_t}{(\text{total drug concentration})}_{t=0}\right) \text{x}\ 100 \quad \textbf{(7.3)}$$

#### 7.3.3.11 Determining SN-38 Release Rates *via* $^{3}$H Radio-dialysis with a pH step change from pH 7 to pH 4.

SN-38 release rates from 5 wt.% $^{3}$H-SN-38 loaded p(EHMA$_{100}$-co-EGDMA$_{0.80}$): p(PEG$_{114}$-*b*-HPMA$_{100}$) nanoparticles were determined as per Section 7.3.3.13. However, at the time point of 4 hours, the pH of the water in the reservoir was changed from pH 7 to pH 4.

#### 7.3.3.12 Determining SN-38 Release Rates *via* $^{3}$H Radio-dialysis of 5 wt. % $^{3}$H-SN-38 loaded p(EHMA$_{20}$-co-DSDMA$_{0.80}$), p(EHMA$_{20}$-co-BPGDMA$_{0.80}$) and p(EHMA$_{20}$-co-EGDMA$_{0.80}$): p(PEG$_{114}$-*b*-HPMA$_{100}$) Nanoprecipitate Regimes

SN-38 release rates from 5 wt.% $^{3}$H-SN-38 loaded p(EHMA$_{20}$-co-DSDMA$_{0.80}$), p(EHMA$_{20}$-co-BPGDMA$_{0.80}$) and p(EHMA$_{20}$-co-EGDMA$_{0.80}$) with p(PEG$_{114}$-*b*-HPMA$_{100}$) at 60:40 wt.%, respectively, were determined using radio-dialysis following the same method outlined in Section 7.3.3.13.

#### 7.3.3.13 Determining SN-38 Release Rates *via* $^{3}$H Radio-dialysis of Increased $^{1}$H-SN-38 Drug Concentrations

Multiple co-nanoprecipitations of 5 wt.% loaded $^{3}$H-SN-38 p(EHMA$_{20}$-co-EGDMA$_{0.80}$): p(PEG$_{114}$-*b*-HPMA$_{100}$) with a compositional ratio of 60:40 wt.%, respectively, were conducted. A SN-38/polymer-THF stock solution was prepared and co-nanoprecipitated as described in Section 7.3.3.11 to produce four samples. Each sample would be used to monitor the release at the corresponding addition number (i.e. the sample that was analysed after the first stock addition did not receive an additional subsequent addition). Release studies were conducted *via* radio-dialysis with SN-38 concentrations of 0.05, 0.10, 0.15 and 0.20 mg mL$^{-1}$ after THF evaporation at pH 7, 37 °C.

### 7.3.4 Chapter 5

#### 7.3.4.1 Pharmacology Studies

As discussed throughout, pharmacology assessment of various co-nanoprecipitated materials was conducted by Usman Arshad, supervised by Joanne Sharp and Helen Box. The SN-38 encapsulated materials were studied to assess their release rates, cellular accumulation in macrophages and cytotoxicity to HTC-116, CT-26, LoVo, DLD-1 cell lines.

#### 7.3.4.2 Materials

Dulbecco's Modified Eagles Medium (DMEM), Hanks buffered saline solution (HBSS), Trypsin-EDTA, bovine serum albumin (BSA), Formic acid (FA), 3-(4,5-Dimethylthiazol-2-yl)-2,5-diphenyltetrazolium bromide (MTT reagent), acetonitrile (ACN) and all general laboratory reagents were purchased from Sigma (Poole, UK). Foetal bovine serum (FBS) was purchased from Gibco (Paisley, UK). The CellTiter-Glo® Luminescent Cell Viability Assay kit was from Promega (UK). The 24-well HTS transwell plates were obtained from Corning (New York, USA). The 96-well black walled, flat bottomed plates were from Sterilin (Newport, UK). Rotenone, 2-deoxyglucose, chlorpromazine hydrochloride, dansylcadaverine, indomethacin, genistein, dynasore hydrate were all purchased from Sigma Aldrich.

#### 7.3.4.3 *In vitro* Release of SN-38 *via* Rapid Equilibrium Dialysis

Candidates from physicochemical characterisation were progressed to *in vitro* release kinetics using a rapid equilibrium dialysis setup. SN-38 NPs were diluted to 250 ng $ml^{-1}$ in PBS (pH 7.4*).* Free SN-38 was dissolved in DMSO prior to dilution with PBS, such that DMSO comprised < 1% of final volume. To assess release, 0.5 mL of samples were added to the donor compartment of an 8 kDa MWCO rapid equilibrium dialysis inserts (ThermoFisher Scientific) and 1 mL PBS was added to the acceptor compartment. Plates containing the inserts were placed on an orbital shaker (Heidolph Rotomax 120; 100 rpm, 48 hours, 37 ± 1 °C). Each insert represented a single time-point and at specified time intervals both acceptor (1 mL) and donor fluid (0.5 mL) were removed. Aliquots of each timed sample were then used to determine levels of SN-38 in each compartment using a validated LC-MS method. Data are shown as the % release of SN-38 (diffused across the membrane).

#### 7.3.4.4 *In vitro* Cytotoxicity

The cytotoxicity of selected nano-formulations was tested on CT26, DLD-1, HCT116 and LoVo colorectal cancer cell lines. The toxicity was also compared to irinotecan and free SN-38 solution in 0.1% DMSO. Monolayer cells were seeded on 96-well plates at density of 2000-5000 cells/well and incubated for 24 hours at 37 °C under 5% $CO_2$. Additionally, HCT116 (1250 cells/well) and CT26 (1000 cells/well) were seeded as spheroids for 5 days using ultra low attachment plates (Corning). Following

incubation, the medium was replaced with increasing NP and free SN-38 concentrations (0.5 to 400 nM) or irinotecan (0.01 to 100 µM) and left for 24-144 hours. Cell viability was measured using the CellTiter-Glo® Luminsecent cell viability assay (Promega, UK) according to manufacturer's instructions. Luminescence was then measured at 570 nm wavelength using a Varioscan flash fluorescent plate reader. Cell viability was calculated as a percentage of untreated vehicle control (DMSO – 0.1%) or blank NP samples and used to determine an $IC_{50}$ value (mean ± SD, n = 3).

#### 7.3.4.5 Macrophage Uptake

Monocytes were isolated by ficoll plaque separation of buffy coats purchased from the NHS Blood and Transfusion Service. The CD14+ monocytes were then differentiated into M1/M2 macrophages using macrophage generation media DXF. Macrophages ($1 \times 10^6$) were plated out in 6 well plates and treated (50 µM) for 24 hours with the various nano-formulations. Both extracellular and intracellular (following lysis with $H_2O$) levels of SN-38 were quantified using the LC MS/MS method. Data was shown as a cellular accumulation ratio (mean ± SD, n = 3).

# Appendix

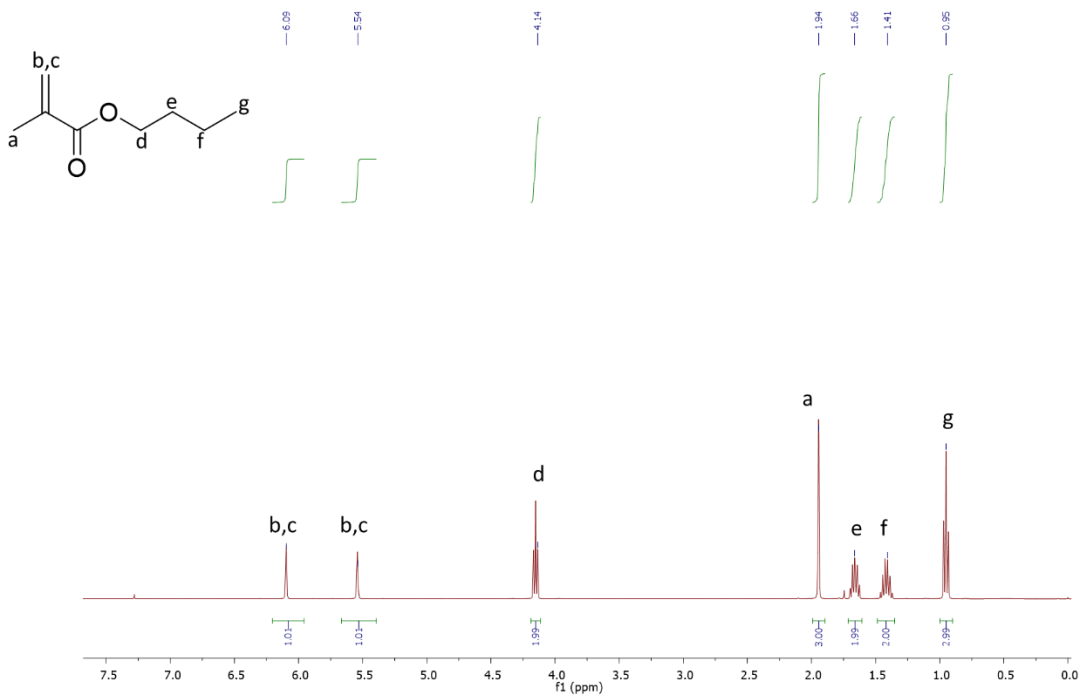


**Figure A.1** $^{1}$H-NMR ($CDCl_3$,400 MHz) of BuMA monomer.

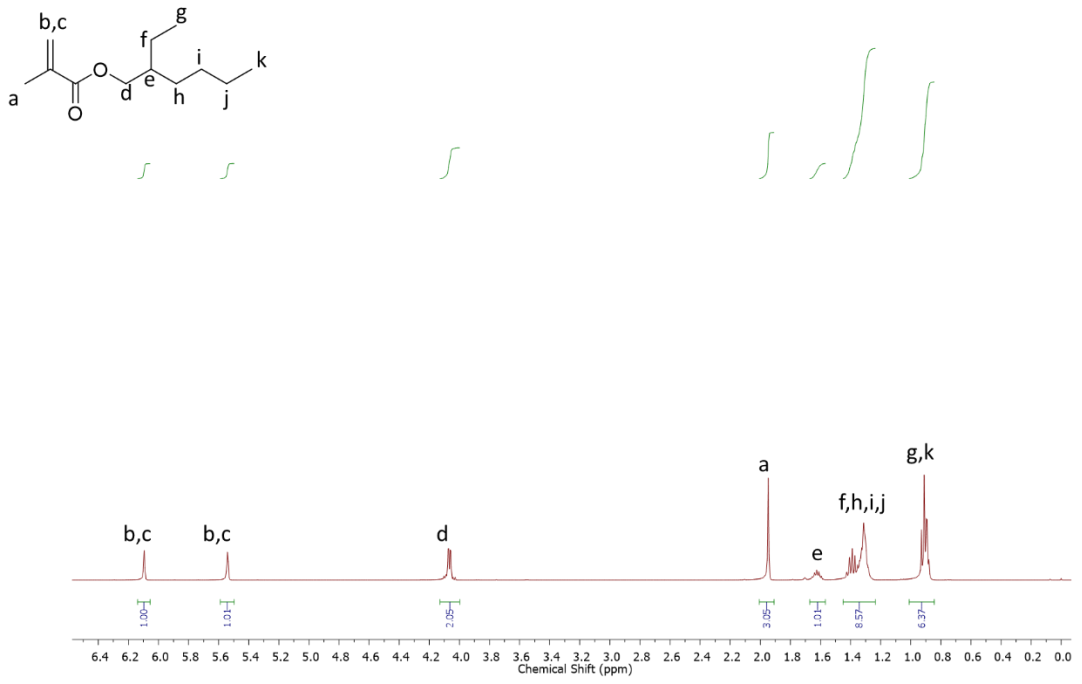


**Figure A.2** $^{1}$H-NMR ($CDCl_3$,400 MHz) of EHMA monomer.

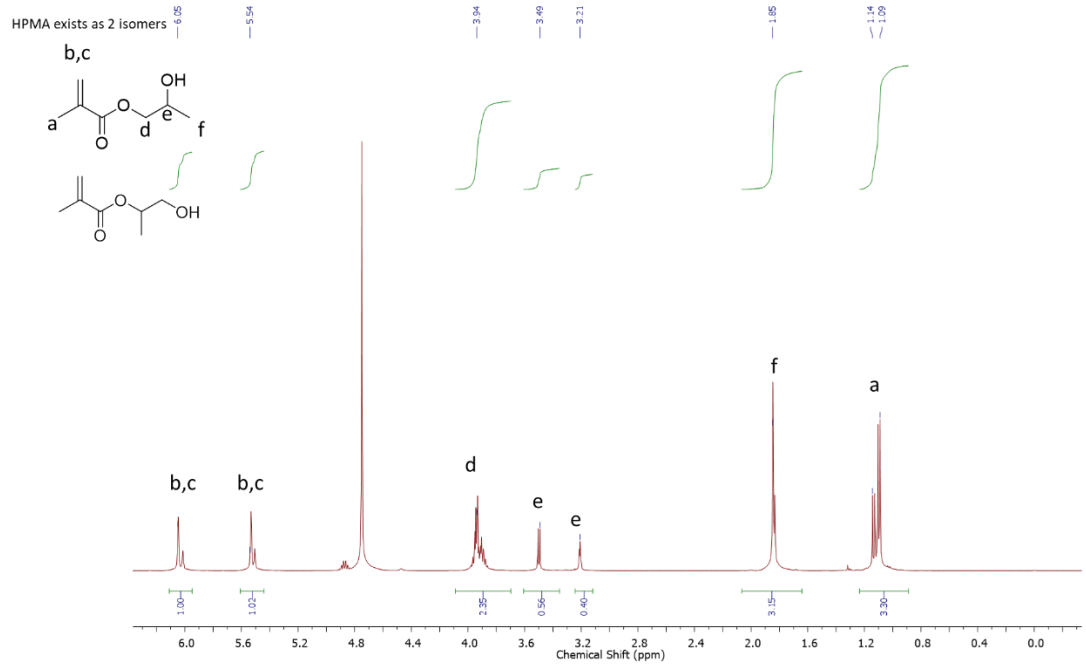


**Figure A.3** $^{1}$H-NMR (MeOD,400 MHz) of HPMA monomer.

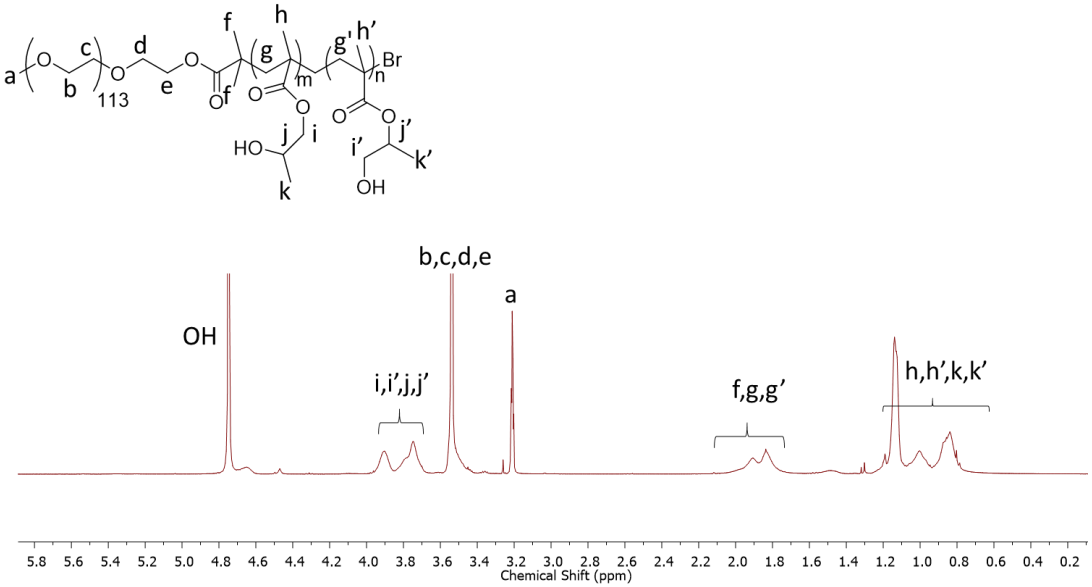


**Figure A.4** $^{1}$H-NMR (MeOD,400 MHz) of p($PEG_{114}$-*b*-$HPMA_{100}$).

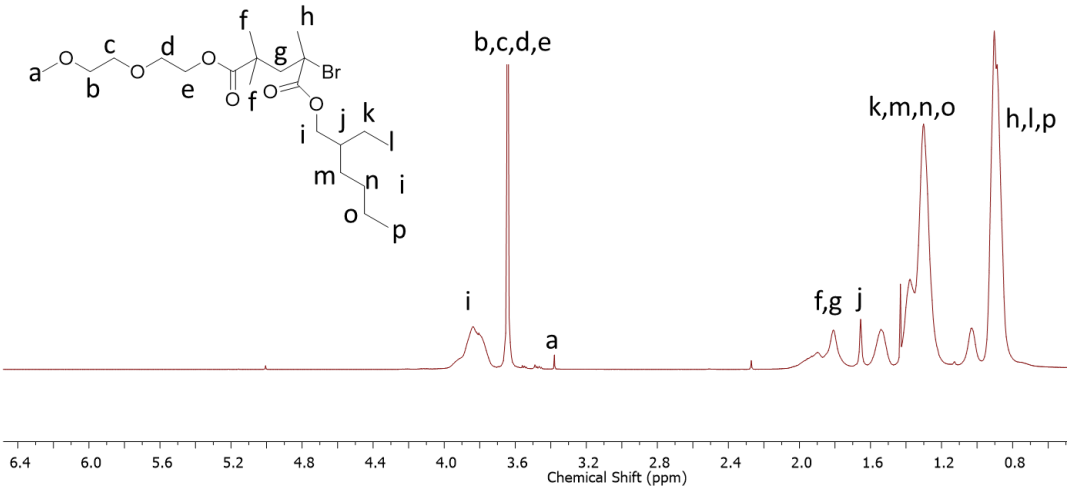


**Figure A.5** $^{1}$H-NMR ($CDCl_3$, 400 MHz) of p($PEG_{114}$-*b*-$EHMA_{100}$).

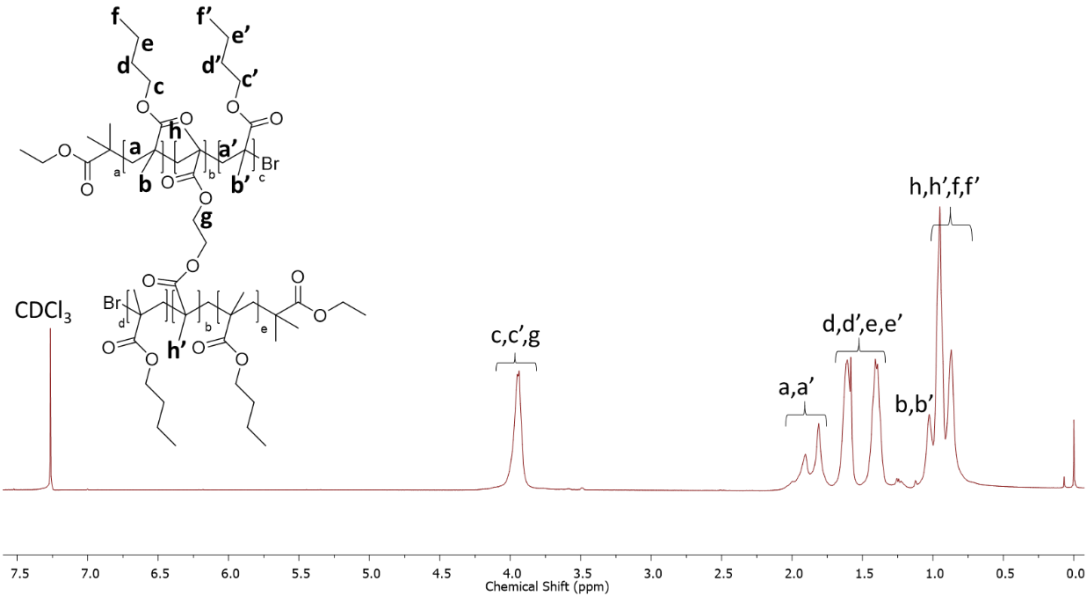


**Figure A.6** $^{1}$H-NMR ($CDCl_3$, 400 MHz) of p($BuMA_{100}$-co-$EGDMA_{0.95}$).

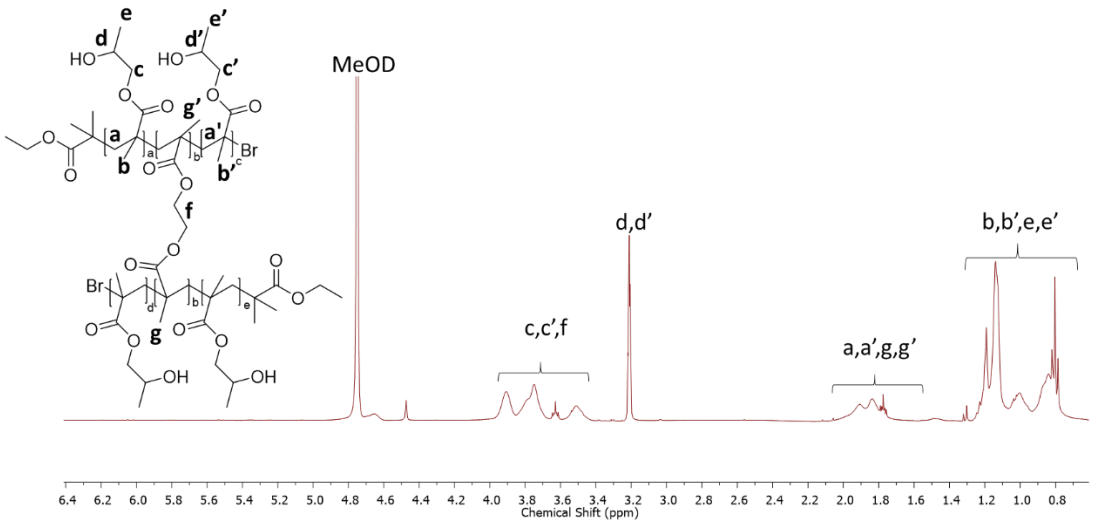


**Figure A.7** $^{1}$H-NMR (MeOD, 400 MHz) of p(HPMA$_{100}$-co-EGDMA$_{0.95}$).

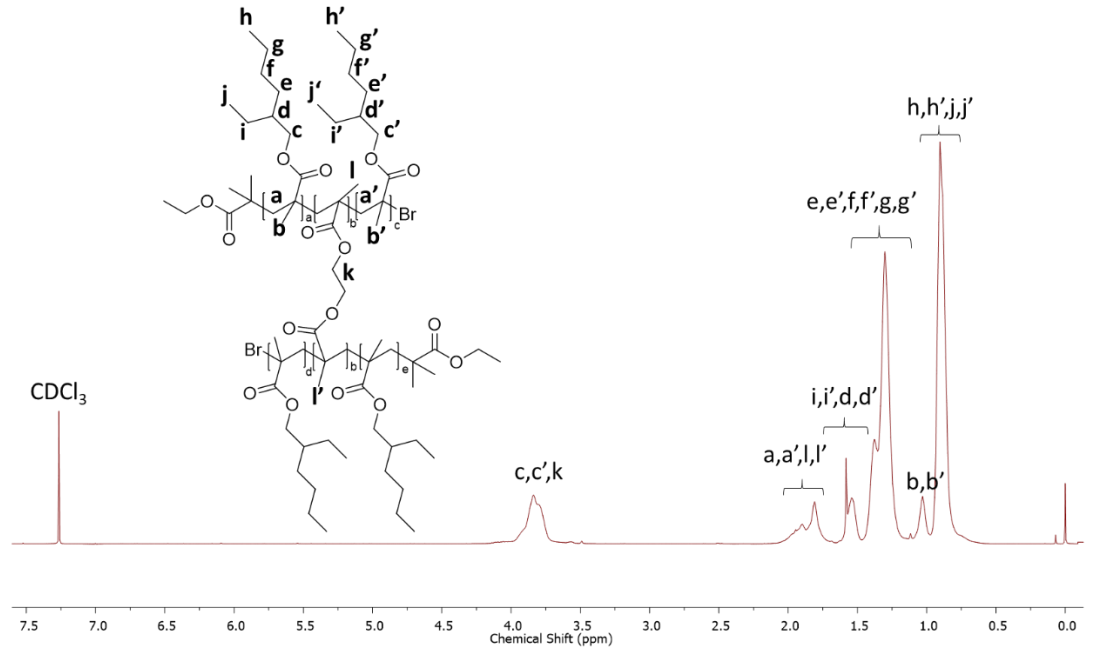


**Figure A.8** $^{1}$H-NMR (MeOD, 400 MHz) of p(EHMA$_{100}$-co-EGDMA$_{0.80}$).

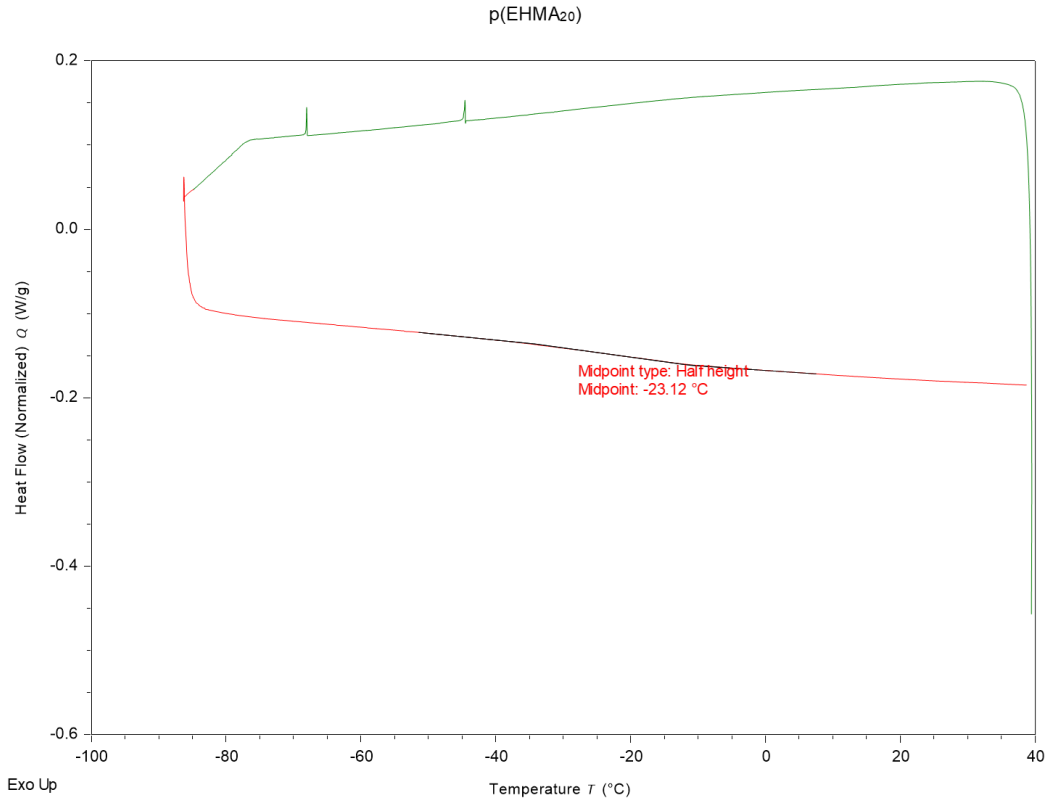


**Figure A.9** DSC thermogram obtained for p(EHMA$_{20}$).

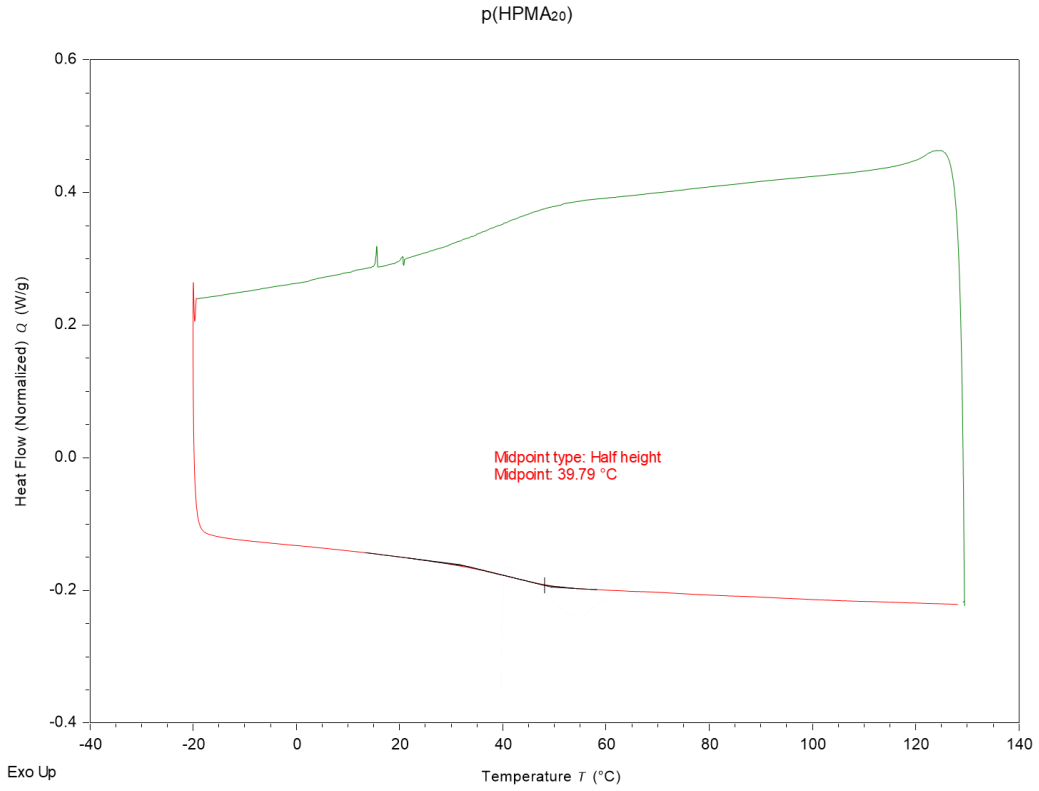


**Figure A.10** DSC thermogram obtained for p(HPMA$_{20}$).

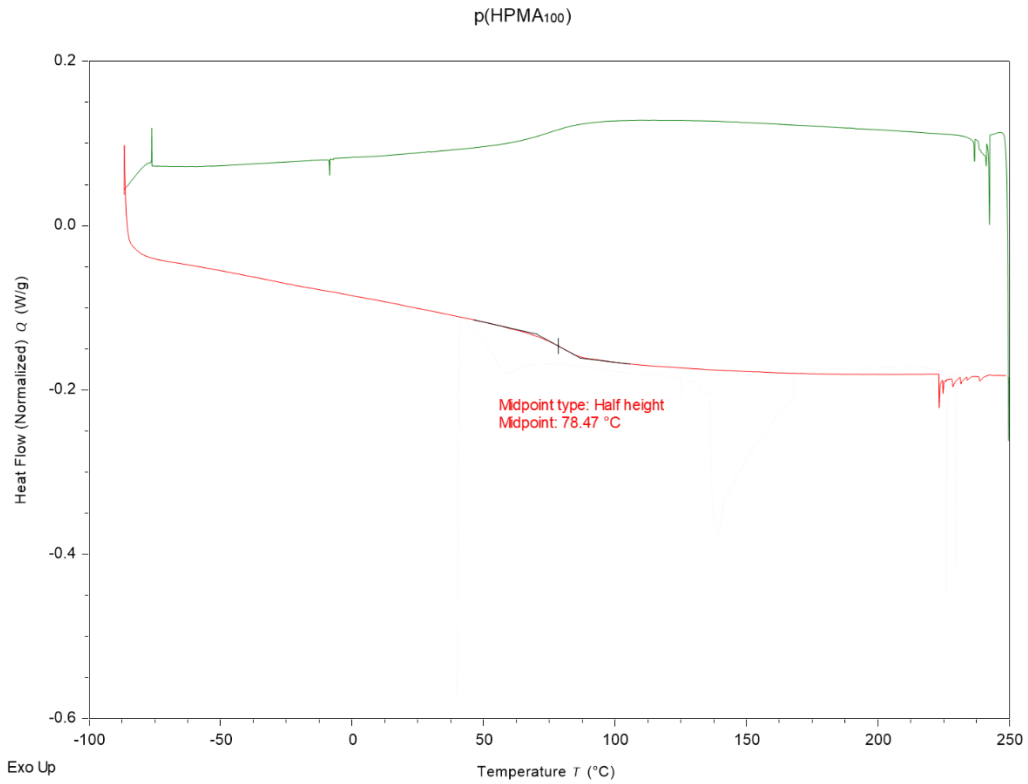


**Figure A.11** DSC thermogram obtained for p(HPMA$_{100}$).

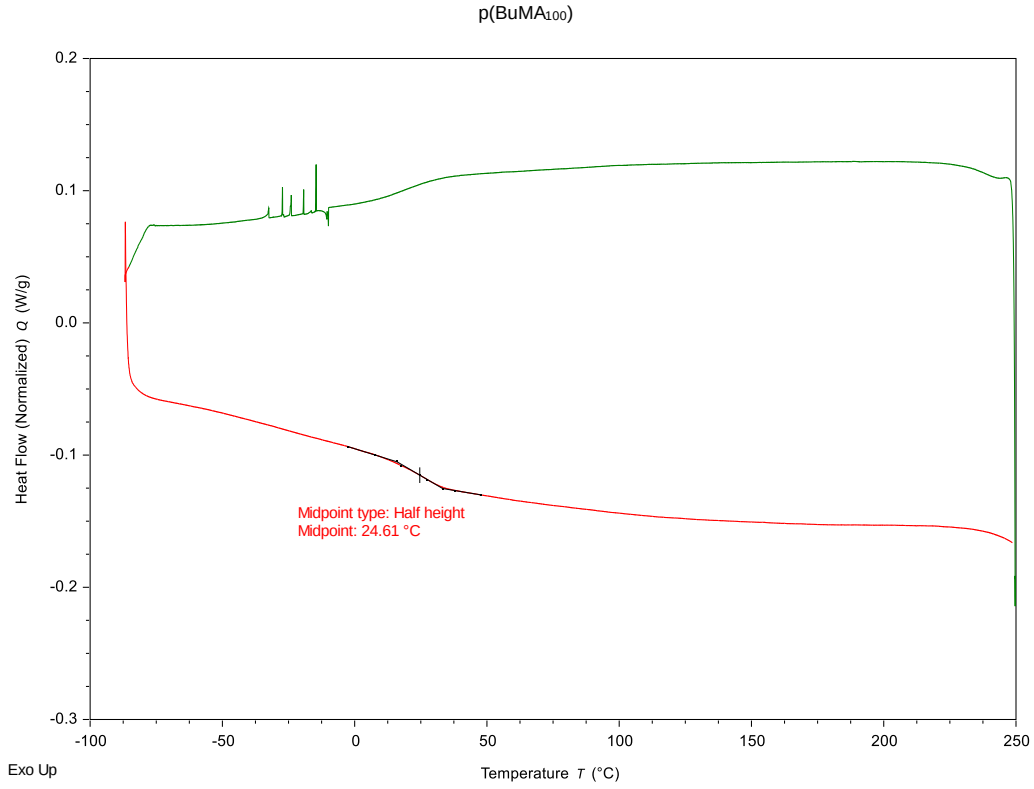


**Figure A.12** DSC thermogram obtained for p(BuMA$_{100}$).

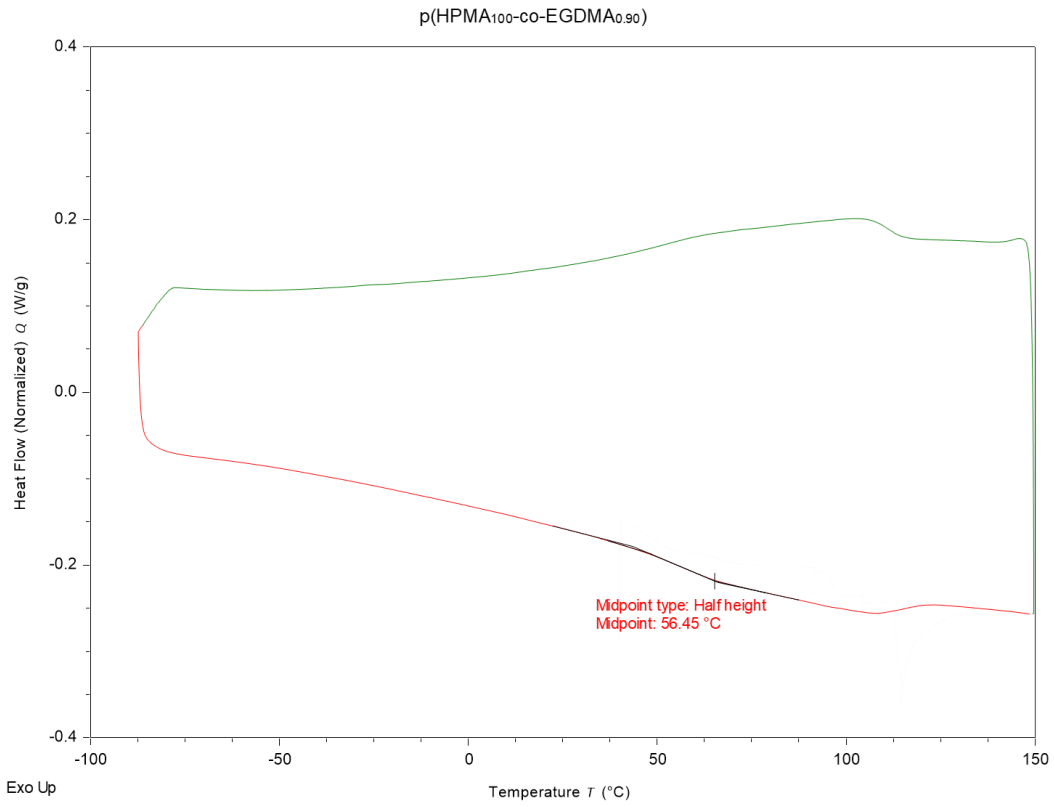


**Figure A.13** DSC thermogram obtained for p(HPMA$_{100}$-co-EGDMA$_{0.90}$).

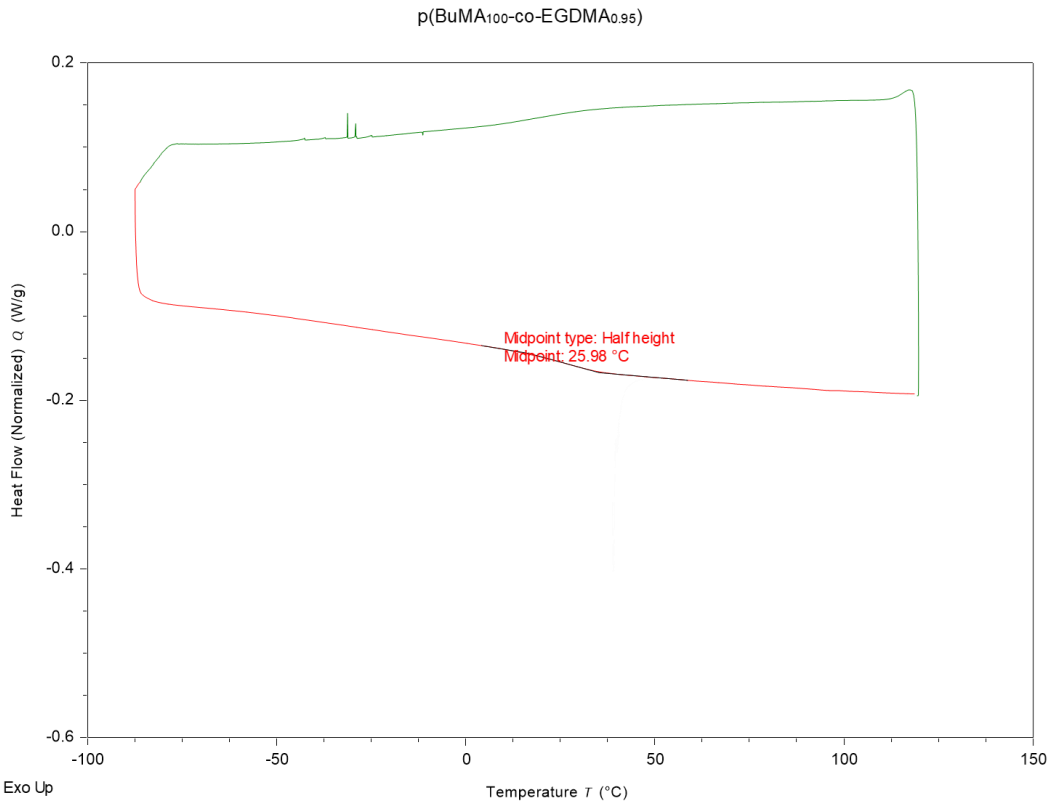


**Figure A.14** DSC thermogram obtained for p(BuMA$_{100}$-co-EGDMA$_{0.95}$).

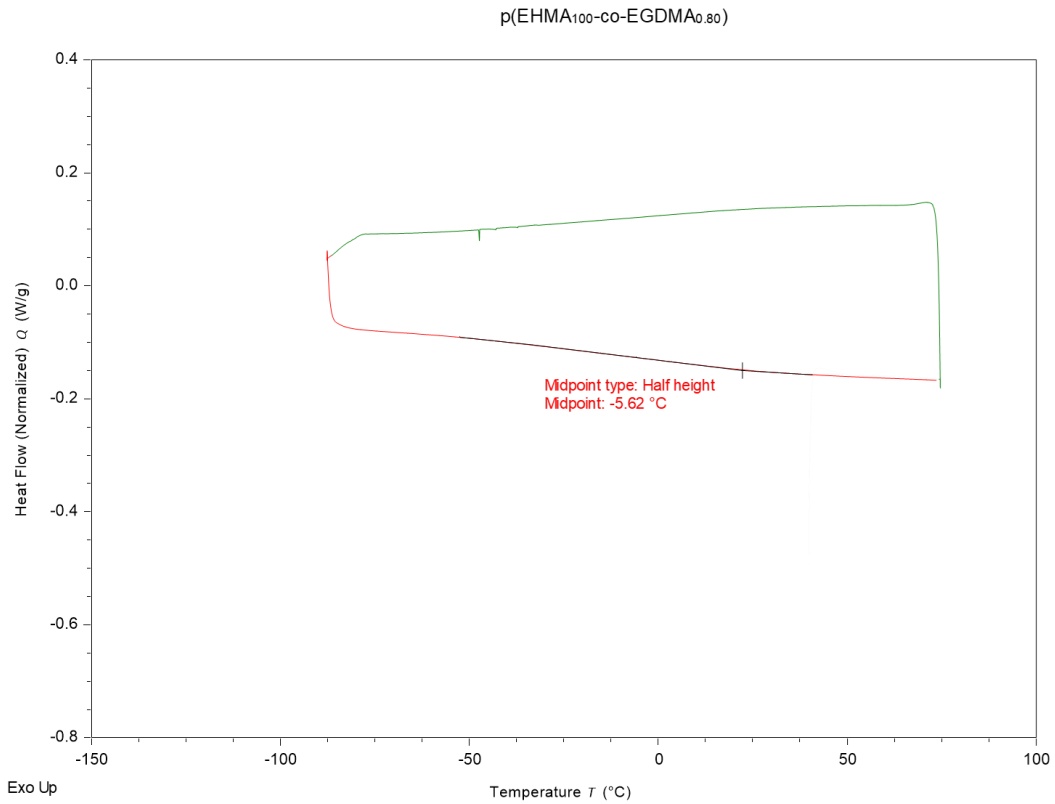


**Figure A.15** DSC thermogram obtained for p(EHMA$_{100}$-co-EGDMA$_{0.80}$).

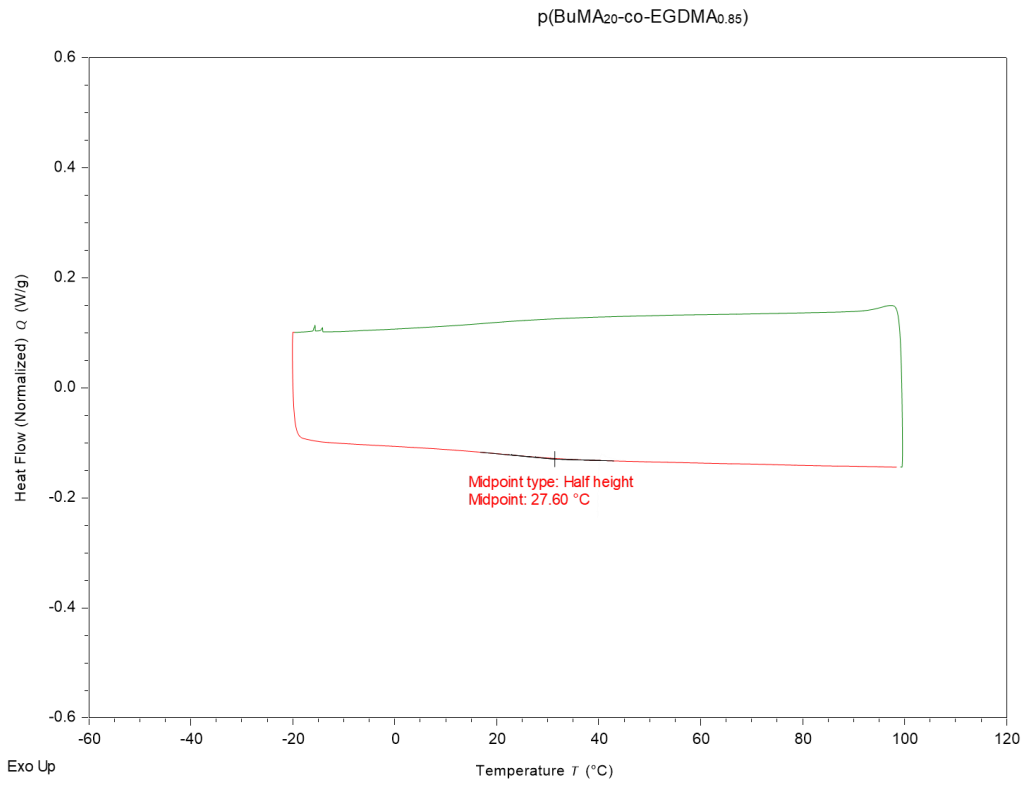


**Figure A.16** DSC thermogram obtained for p(BuMA$_{20}$-co-EGDMA$_{0.85}$).

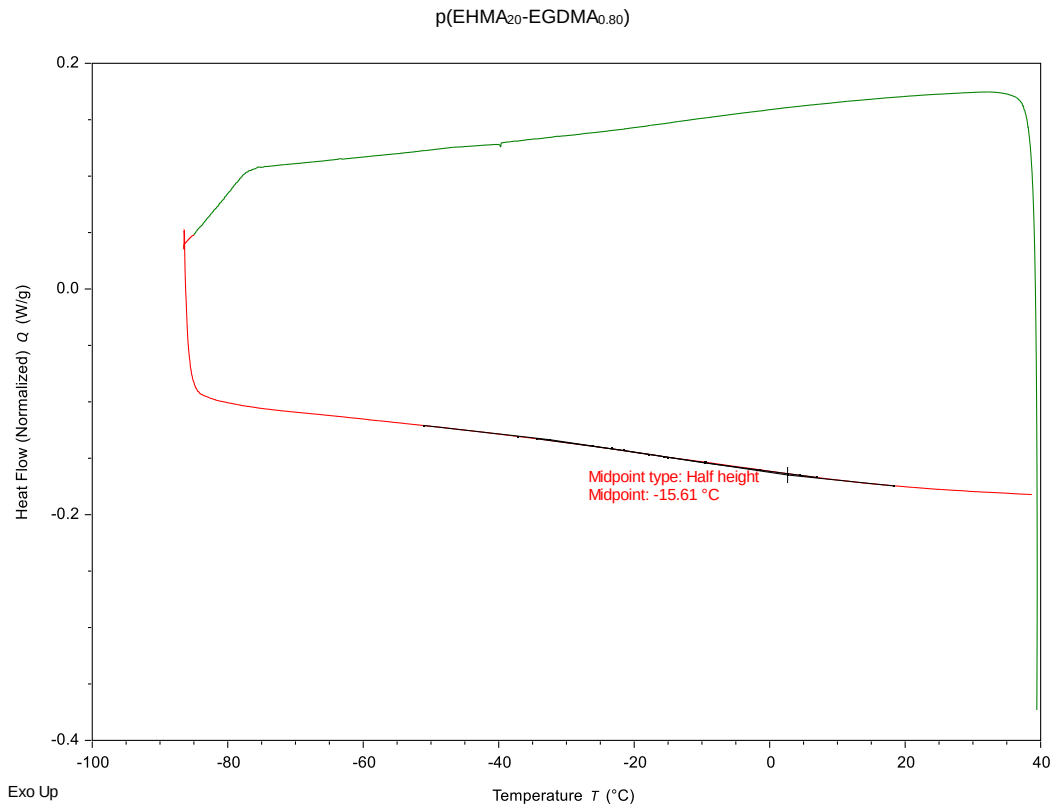


**Figure A.17** DSC thermogram obtained for p(EHMA$_{20}$-co-EGDMA$_{0.80}$).

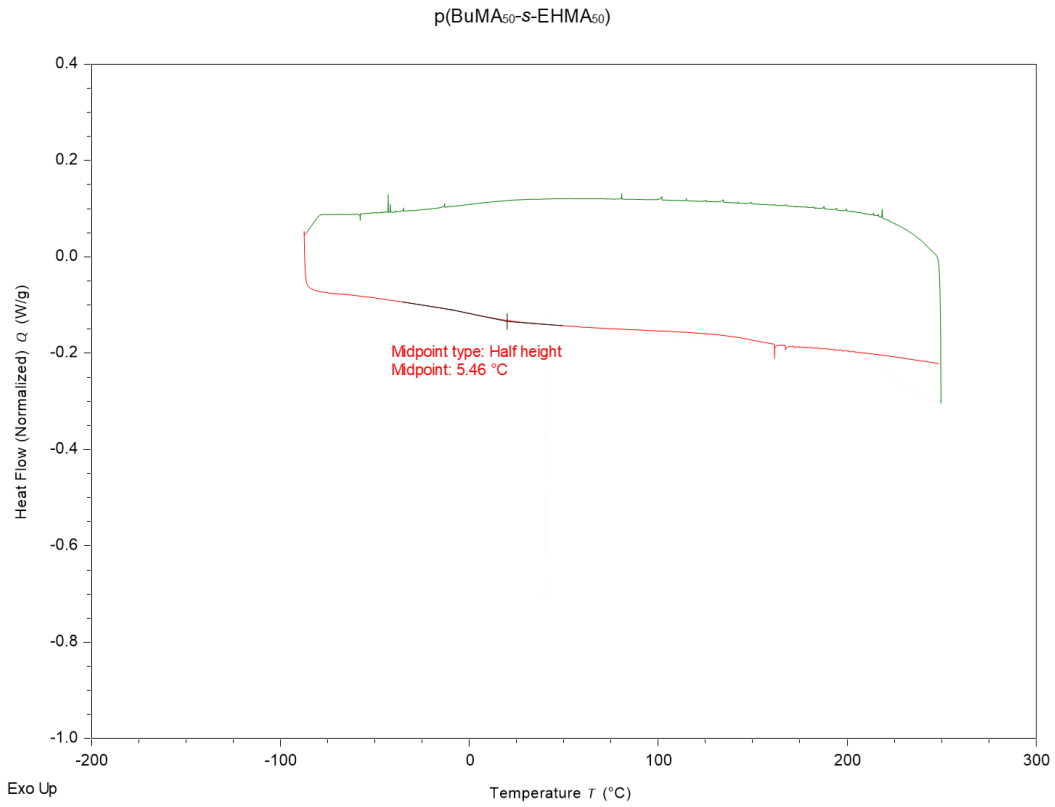


**Figure A.18** DSC thermogram obtained for p(BuMA$_{50}$-*s*-EHMA$_{50}$).

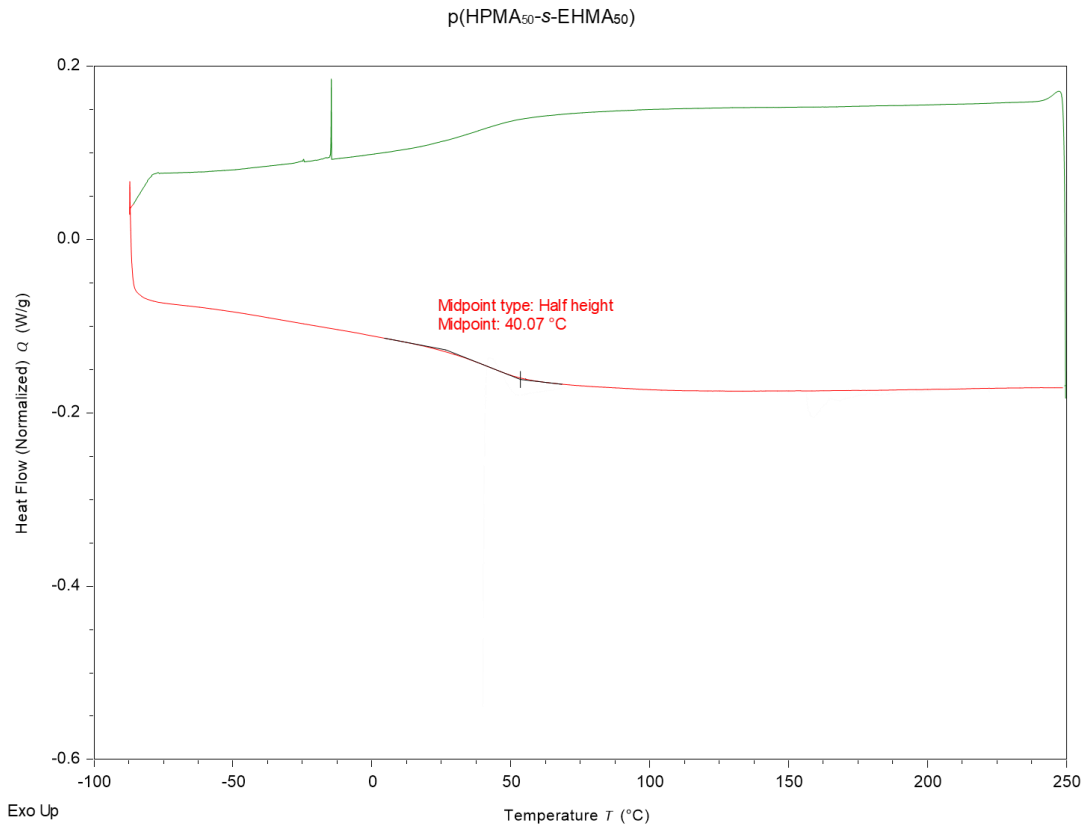


**Figure A.19** DSC thermogram obtained for p(HPMA$_{50}$-*s*-EHMA$_{50}$).

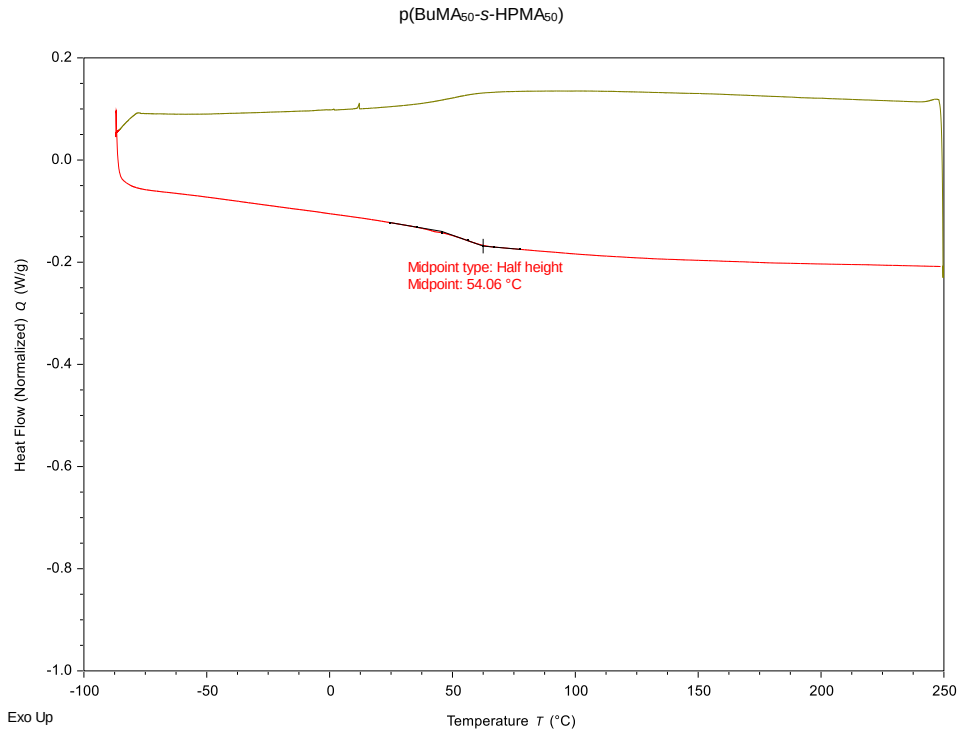


**Figure A.20** DSC thermogram obtained for p(BuMA$_{50}$-*s*-HPMA$_{50}$).

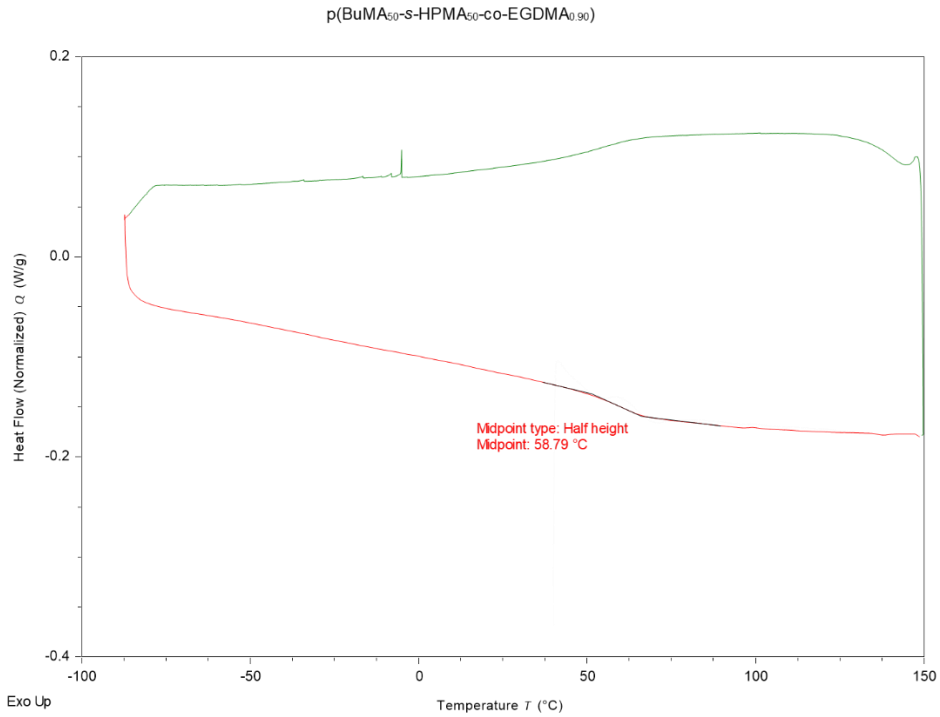


**Figure A.21** DSC thermogram obtained for p(BuMA$_{50}$-*s*-HPMA$_{50}$-co-EGDMA$_{0.90}$).

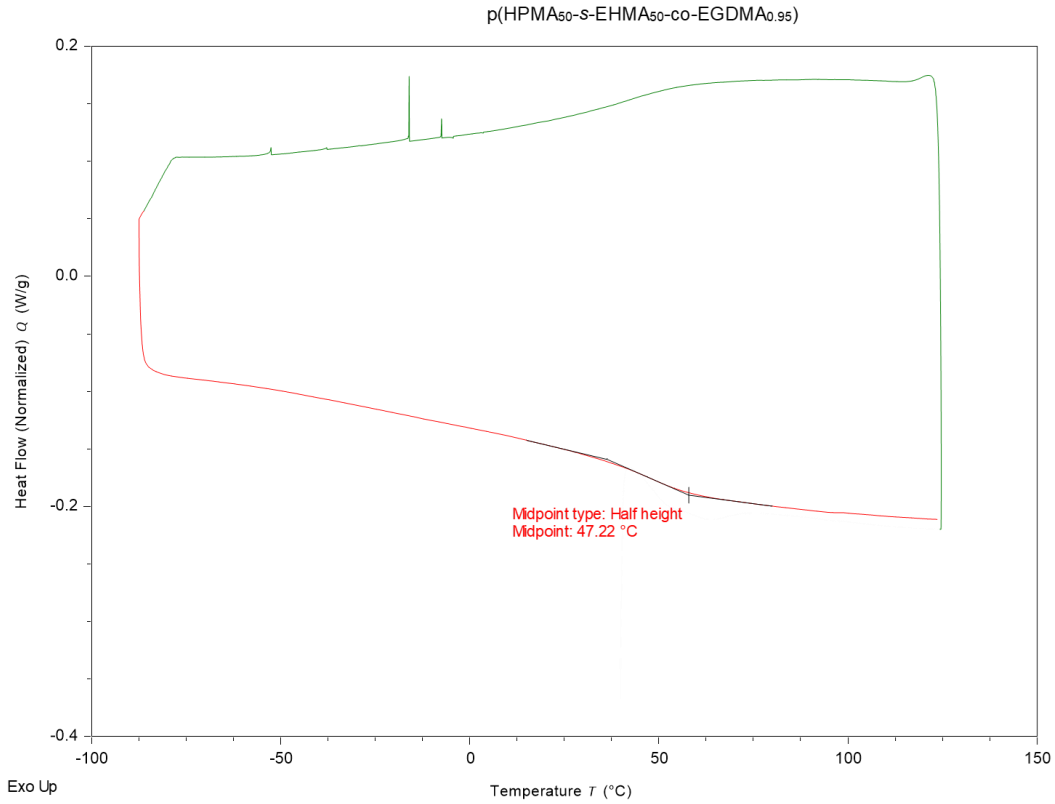


**Figure A.22** DSC thermogram obtained for p(EHMA$_{50}$-*s*-HPMA$_{50}$-co-EGDMA$_{0.95}$).

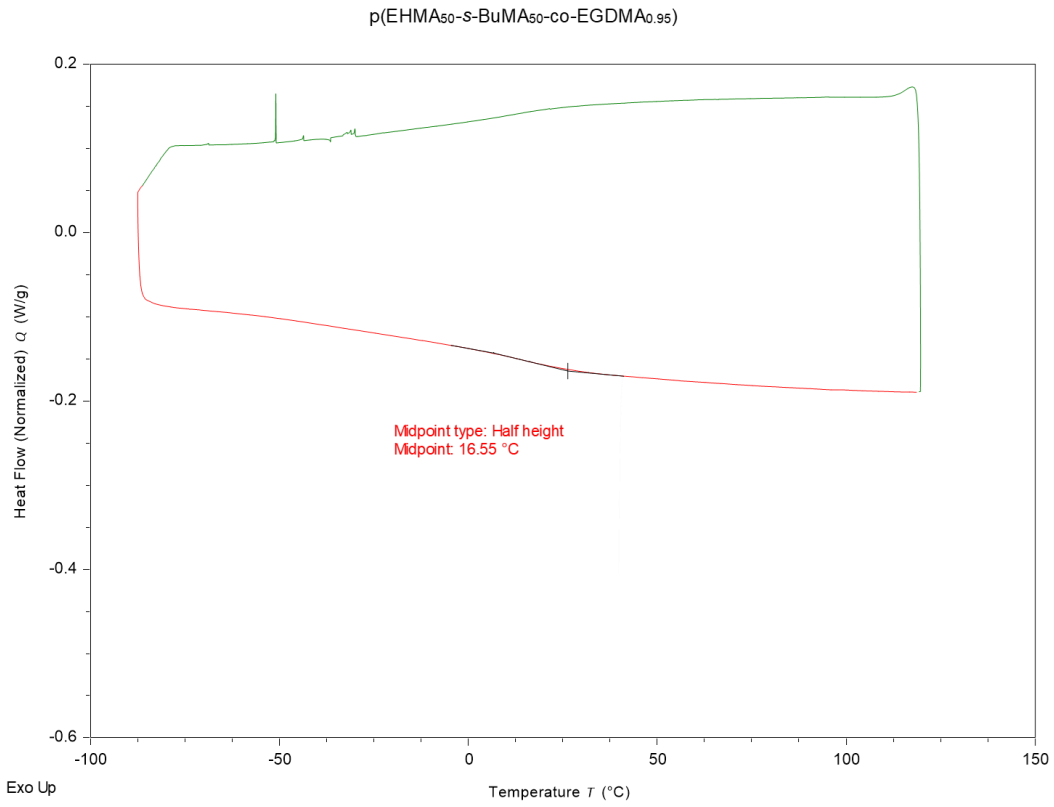


**Figure A.23** DSC thermogram obtained for p(BuMA$_{50}$-*s*-EHMA$_{50}$-co-EGDMA$_{0.95}$).

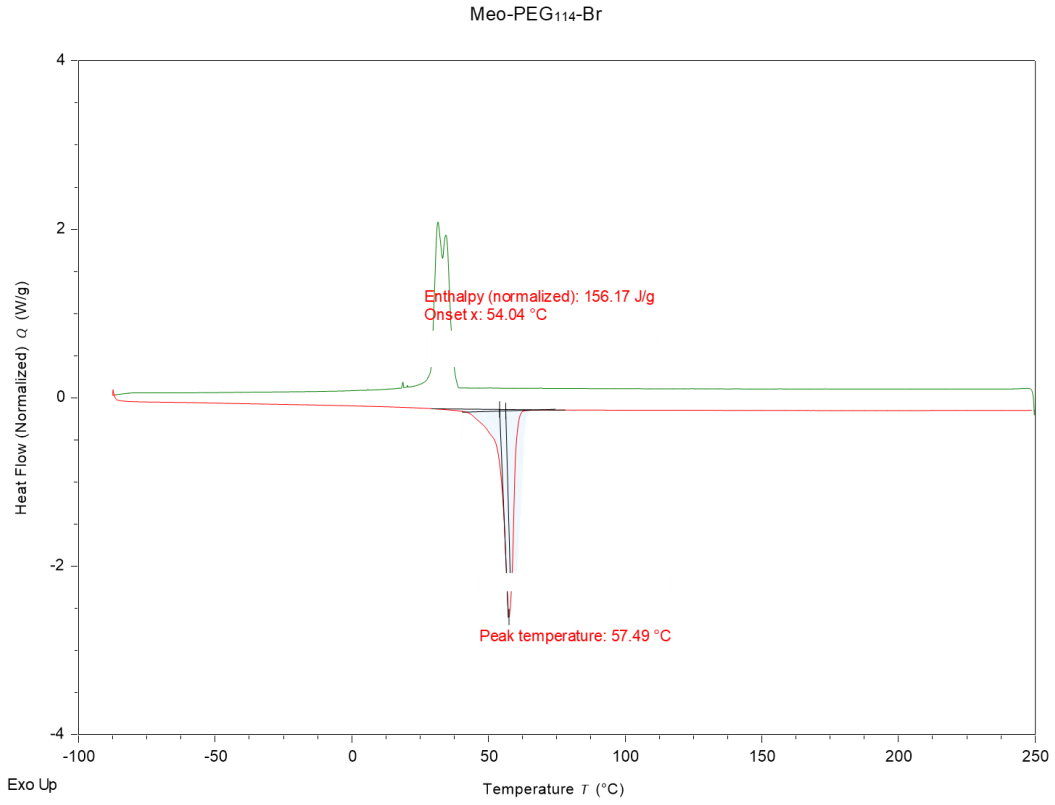


**Figure A.24** DSC thermogram obtained for Meo-PEG$_{114}$-Br.

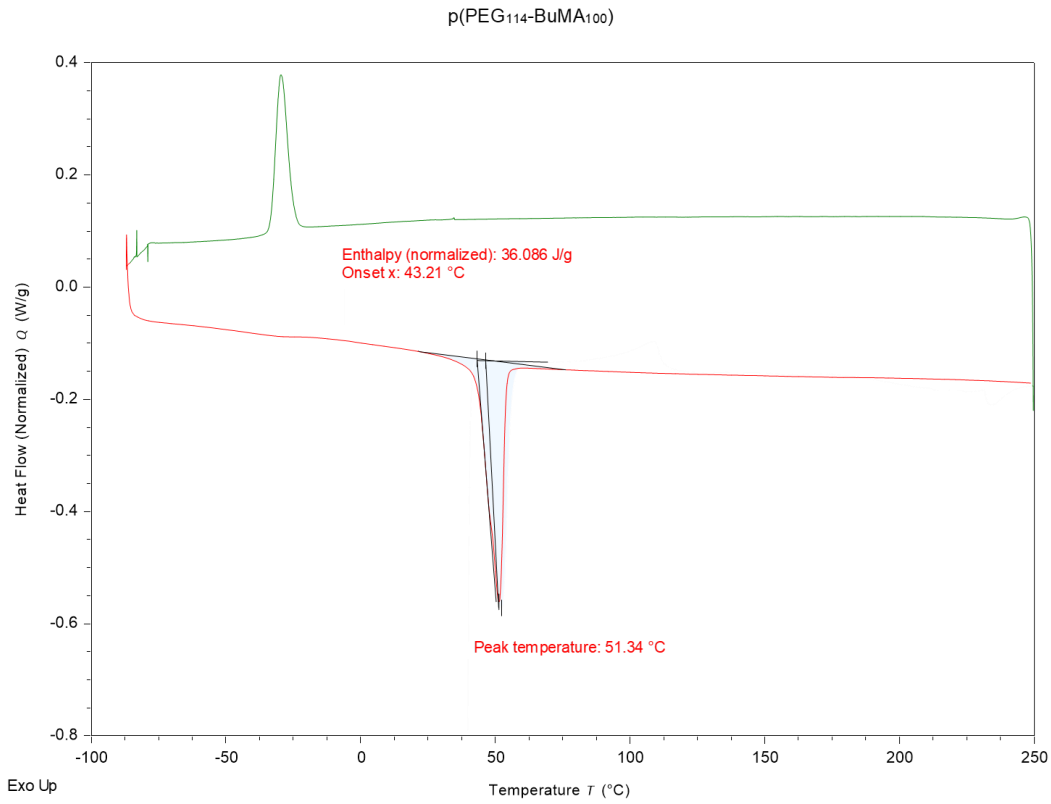


**Figure A.25** DSC thermogram obtained for p(PEG$_{114}$-*b*-BuMA$_{100}$).

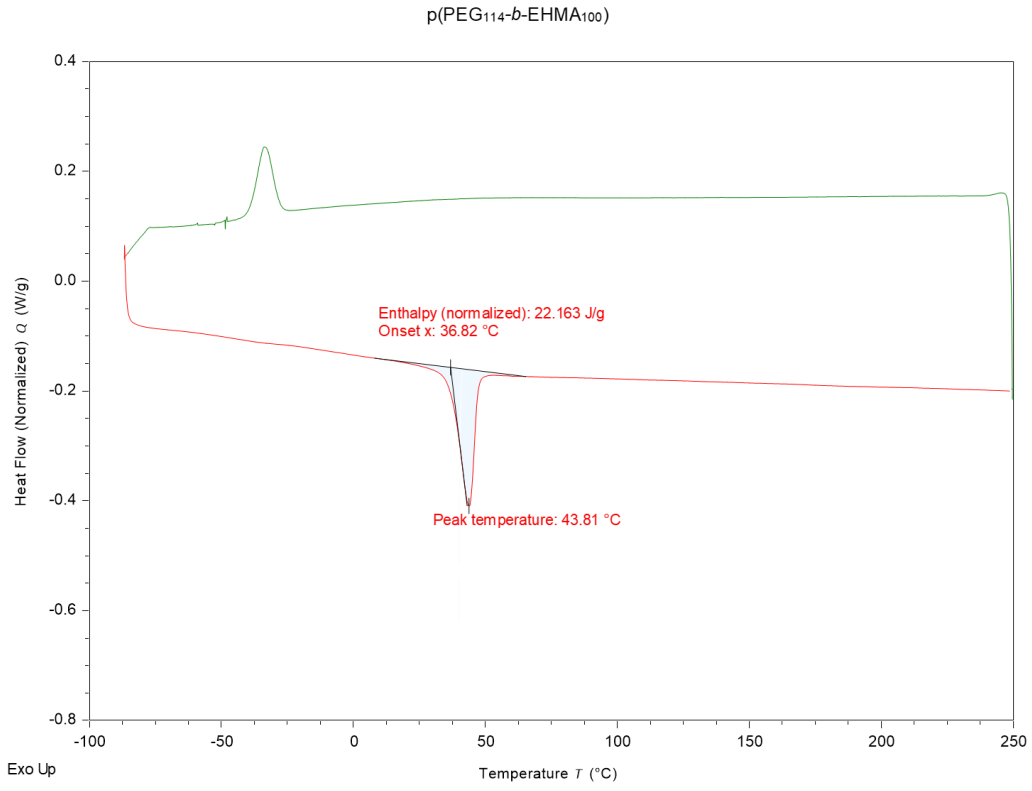


**Figure A.26** DSC thermogram obtained for p(PEG$_{114}$-*b*-EHMA$_{100}$).

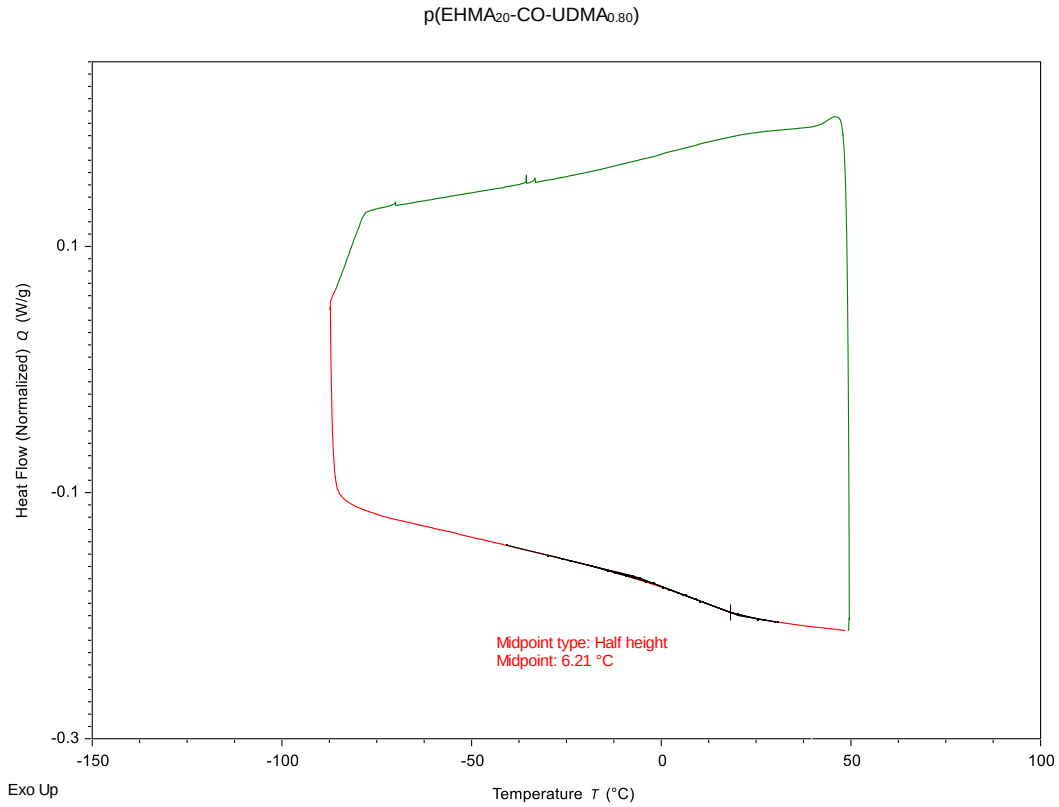


**Figure A.27** DSC thermogram obtained for p(EHMA$_{20}$-co-UDMA$_{0.80}$).

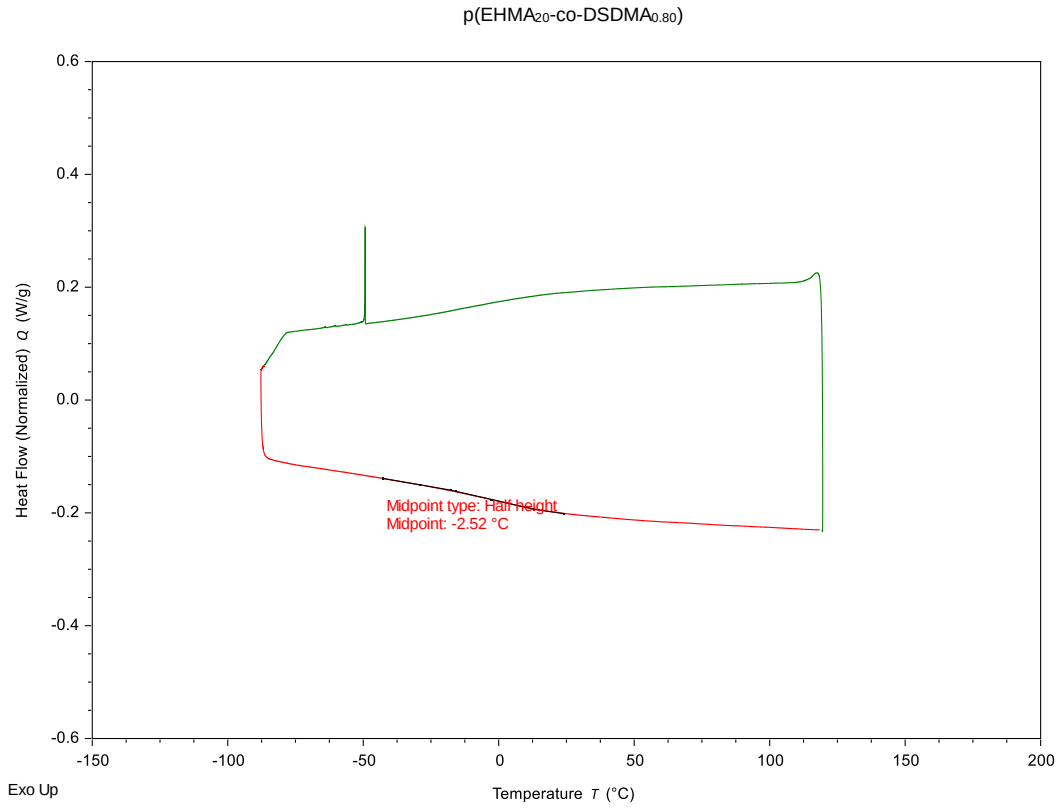


**Figure A.28** DSC thermogram obtained for p(EHMA$_{20}$-co-DSDMA$_{0.80}$).

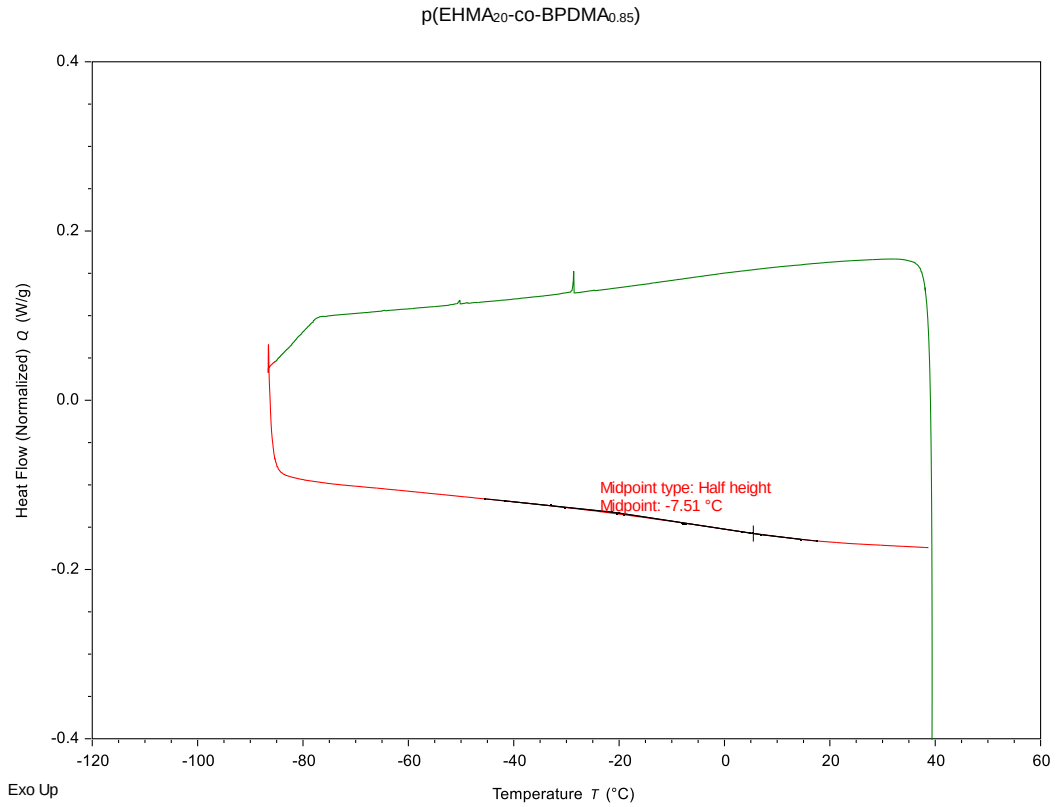


**Figure A.29** DSC thermogram obtained for p(EHMA$_{20}$-co-BPDMA$_{0.85}$).

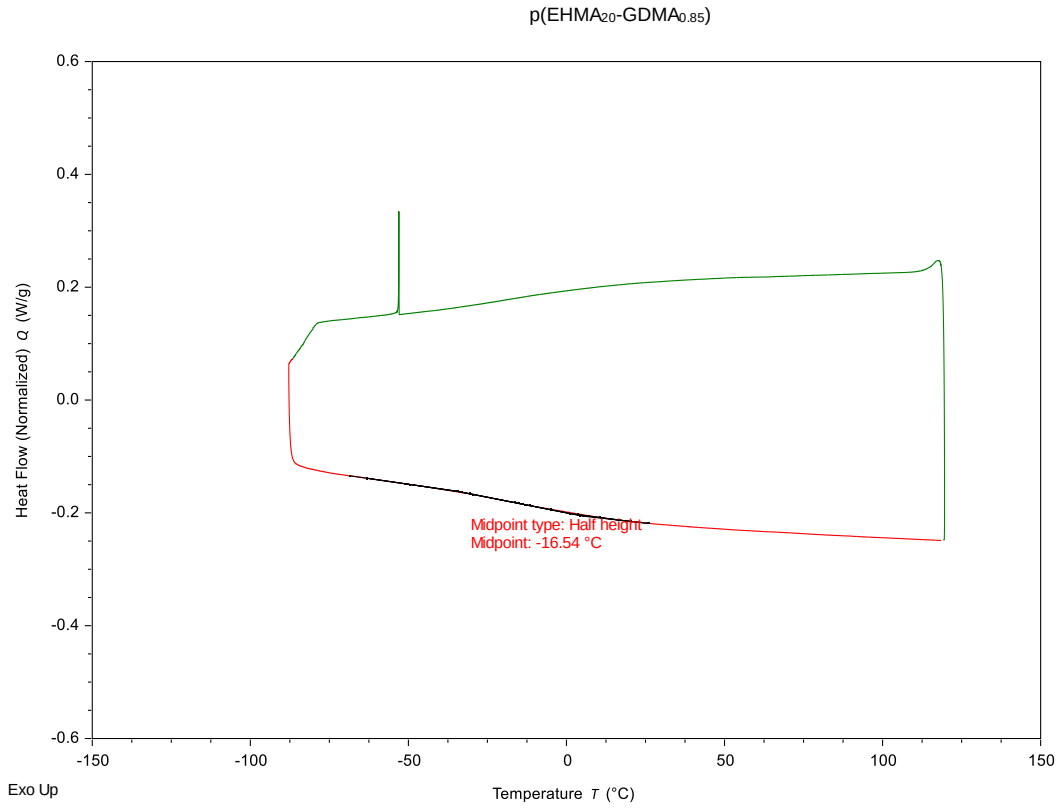


**Figure A.30** DSC thermogram obtained for p(EHMA$_{20}$-co-GDMA$_{0.85}$).

**Table A.1** DLS analyses of p(HPMA$_{100}$-co-EGMDA$_{0.90}$) co-nanoprecipitates varying in wt. % of p(PEG$_{114}$-b- HPMA$_{100}$) from 0 – 50 wt.%, respectively, following the serial dilution with PBS addition at 0.10 & 0.01 mg mL$^{-1}$.

| Polymer Concentration | Wt.% of Branched Polymer | Wt.% of AB block co-polymer | $D_z$ (nm) | PDI | Derived count rate (kcps) |
|---|---|---|---|---|---|
| 0.10 mg mL$^{-1}$ (PBS) | 100 | 0 | *Polymer aggregation* | | |
| | 90 | 10 | *Polymer aggregation* | | |
| | 80 | 20 | 160 | 0.098 | 51 200 |
| | 70 | 30 | 80 | 0.129 | 12 255 |
| | 60 | 40 | 60 | 0.133 | 5400 |
| | 50 | 50 | 240 | 0.307 | 6000 |
| 0.01 mg mL$^{-1}$ (PBS) | *100* | *0* | *Polymer aggregation* | | |
| | *90* | *10* | *Polymer aggregation* | | |
| | 80 | 20 | 160 | 0.142 | 6000 |
| | 70 | 30 | 85 | 0.235 | 1300 |
| | 60 | 40 | 125 | 0.350 | 850 |
| | 50 | 50 | 120 | 0.225 | 650 |

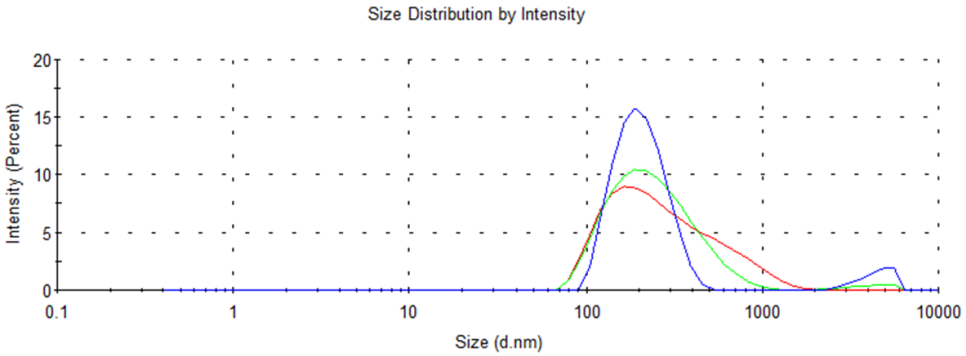


**Figure A.31** Size distribution by intensity of p(EHMA$_{100}$-co-EGMDA$_{0.90}$) and 10 wt. % AB block copolymer p(PEG$_{144}$-*b*-HPMA$_{100}$) polymer nanoparticles at dilution concentration of 0.25 mg mL$^{-1}$ with PBS over 3 runs.

**Table A.2** DLS and zeta potential analyses of aqueous nanoparticle dispersions produced via co-nanoprecipitation of the AB block copolymer, p($PEG_{114}$-b-$HPMA_{100}$), with branched p(EHMA) varying in divinyl monomer residue chemistry after 80 days storage.

| | | AB Block copolymer: p($PEG_{114}$-*b*-$HPMA_{100}$) | | | |
|---|---|---|---|---|---|
| **$DP_n$ of branched copolymer (monomer units)** | **Branching Agent** | **$D_z$ (nm)[a]** | **PDI[a]** | **Derived count rate (kcps)[a]** | **ζ (mV)[b]** |
| 20 | GDMA | 165 | 0.131 | 574 300 | -11.9 |
| | UDMA | 160 | 0.084 | 765 000 | -7.79 |
| 100 | GDMA | 165 | 0.104 | 689 500 | -8.45 |
| | UDMA | 160 | 0.038 | 627 900 | -10.4 |

[a] Measured using DLS analysis at a concentration of 1 mg $mL^{-1}$. [b] Obtained via measurement of the electrophoretic mobility of aqueous nanoparticle dispersions within zeta cell.

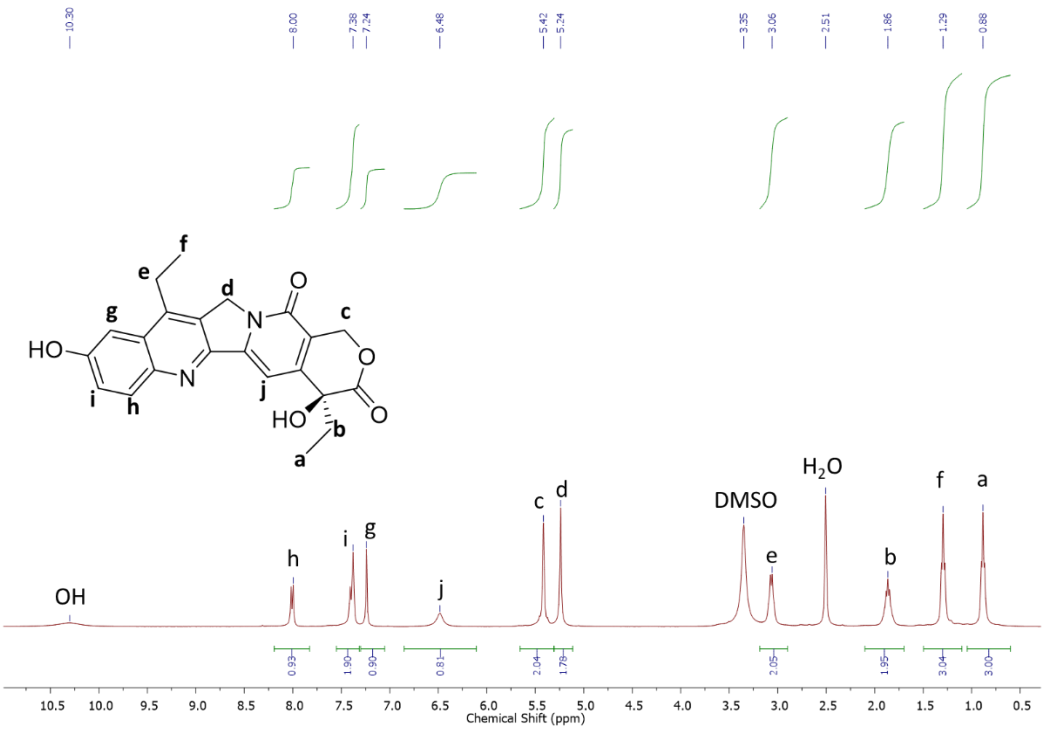


**Figure A.32** $^1$H-NMR (DMSO-$D_6$, 400 MHz) of SN-38.

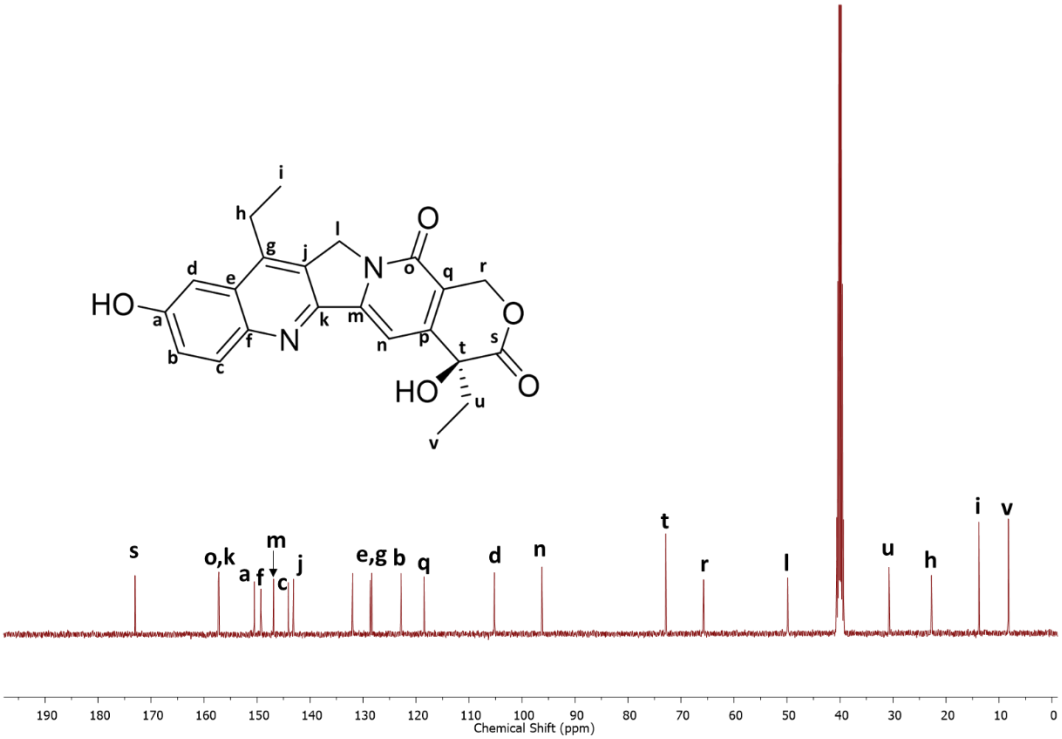


**Figure A.33** $^{13}$C-NMR analysis of SN-38 (DMSO-$d_6$,400 MHz).

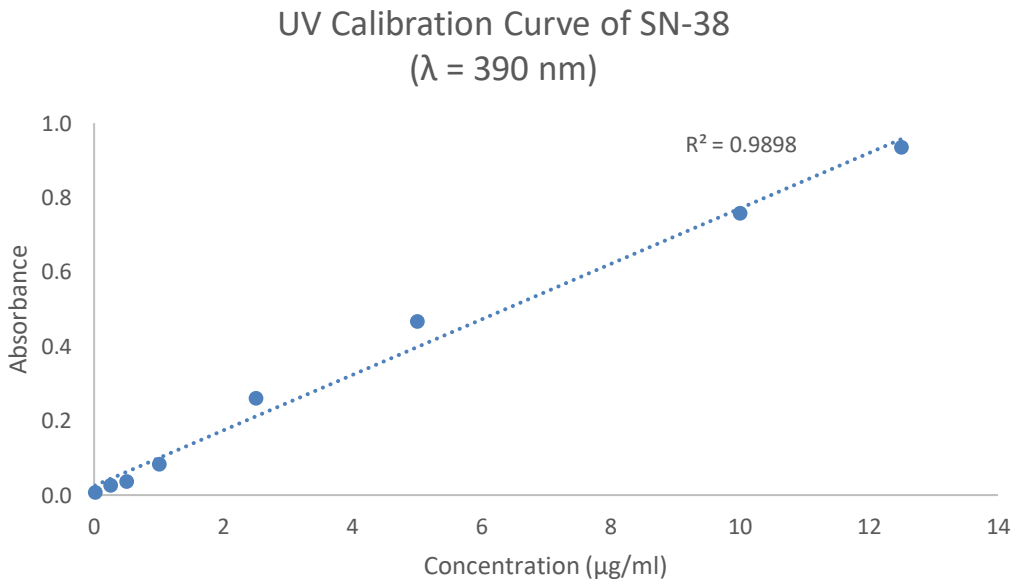


**Figure A.34** UV-Vis calibration curve for SN-38 absorbance at wavelength of 390 nm, concentration range of 0 to 12 µg mL$^{-1}$.

**Figure A.35** A photograph of 5 wt. % SN-38 loaded p(EHMA$_{20}$-co-DSDMA$_{0.80}$): p(PEG$_{114}$-*b*-HPMA$_{100}$) co-nanoprecipitate regime with increased SN-38 concentration and polymer concentration after 5 weeks following the multiple nanoprecipitation.

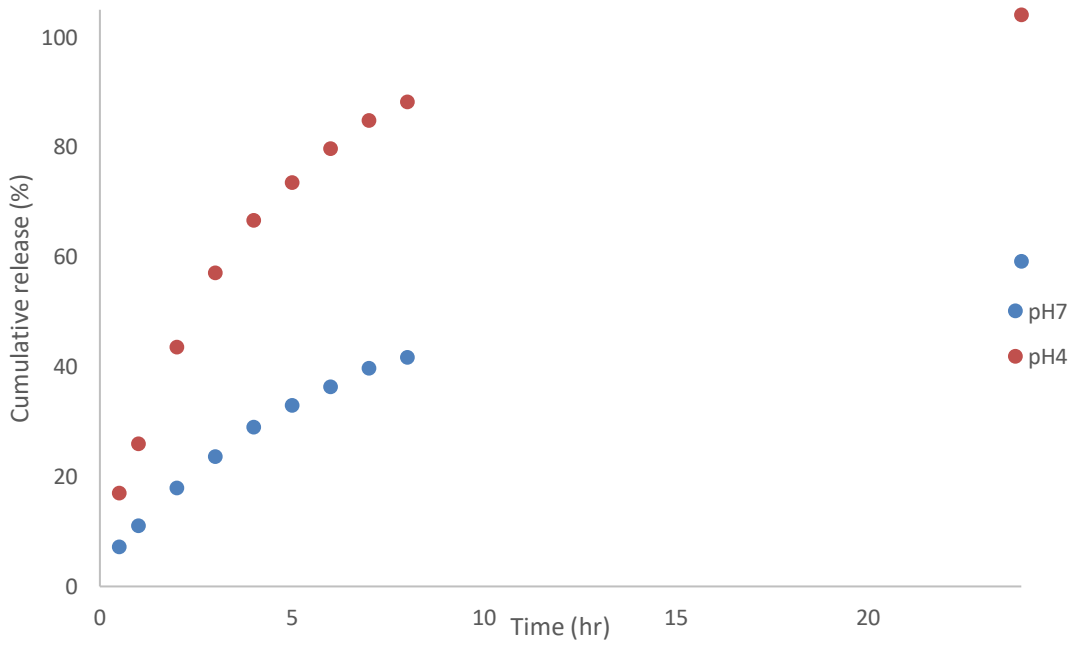


**Figure A.36** The rate of free SN-38 diffusion determined by radio-dialysis at pH7 and pH4 (37 °C).